

UNIVERSITY OF BREMEN

DOCTORAL THESIS

**Deciphering past and present ice flow
patterns from radar reflections**

Author:
Steven FRANKE

Supervisors:
Dr. Daniela JANSEN
Prof. Dr. Olaf EISEN

Referees:
Prof. Dr. Olaf EISEN
Dr. Christoph MAYER

*A thesis submitted in fulfillment of the requirements
for the degree of Doctor Rerum Naturalium*

in the

Department of Geosciences

Date of submission: May 27, 2021

Date of defense: September 22, 2021

Versicherung an Eides Statt

gem. § 5 Abs. 5 der Promotionsordnung vom 18.06.2018

Ich, Steven FRANKE (Matr. Nr.: 3164006),

versichere an Eides Statt durch meine Unterschrift, dass ich die vorstehende Arbeit, "Deciphering past and present ice flow patterns from radar reflections" selbständig und ohne fremde Hilfe angefertigt und alle Stellen, die ich wörtlich dem Sinne nach aus Veröffentlichungen entnommen habe, als solche kenntlich gemacht habe, mich auch keiner anderen als der angegebenen Literatur oder sonstiger Hilfsmittel bedient habe.

Ich versichere an Eides Statt, dass ich die vorgenannten Angaben nach bestem Wissen und Gewissen gemacht habe und dass die Angaben der Wahrheit entsprechen und ich nichts verschwiegen habe.

Die Strafbarkeit einer falschen eidesstattlichen Versicherung ist mir bekannt, namentlich die Strafandrohung gemäß § 156 StGB bis zu drei Jahren Freiheitsstrafe oder Geldstrafe bei vorsätzlicher Begehung der Tat bzw. gemäß § 161 Abs. 1 StGB bis zu einem Jahr Freiheitsstrafe oder Geldstrafe bei fahrlässiger Begehung.

Signed:

Date:

"Respect the old but break new ground too."

Madball - A band based in NYC

UNIVERSITY OF BREMEN

Abstract

Department of Geosciences

Doctor Rerum Naturalium

Deciphering past and present ice flow patterns from radar reflections

by Steven FRANKE

The large ice sheets on Earth respond to changes in the global climate. Ice mass loss increases with rising global mean temperature and thus is a major contributor to sea-level rise. In order to reduce the uncertainty to predict the contributions to sea-level rise of ice sheets, it is crucial to study how the ice sheets' fast-flowing drainage pathways (so-called ice streams) have evolved over the last thousand to millions of years. In this thesis, a contribution to the understanding of the flow characteristics of large ice streams in Greenland and Antarctica is performed by an analysis of (ice-penetrating) radar reflections within the ice column and at the ice base. My focus lies on the question how these data can be used to obtain information about present and paleo ice-flow regimes. I concentrate on radar data acquired in Northeast Greenland in the upstream regions of the North East Greenland Ice Stream (NEGIS) and in the upstream catchment of the Nioghalvfjærdsbrae (79° N Glacier) as well as on data recorded at the onset of the Jutulstraumen Glacier in Antarctica. In my studies, I show that the NEGIS in its present form is a relatively young feature and that its geometry and flow characteristics are intertwined with the subglacial topography. I also found indications for a re-organization of ice stream activity in the NEGIS catchment during the Holocene. This suggests that ice streams are probably less persistent than previously thought and adapt in their entire length to the changing geometry of the ice sheet on short time scales. In Antarctica, I investigate past ice flow patterns over a period of millions of years, as in the example of the Jutulstraumen Glacier basin in Antarctica. Many of the glacial and fluvial landscapes, which developed since the glaciation of Antarctica, have been mostly preserved under the contemporary thick ice sheet, and some even serve as basins for active subglacial lakes today.

UNIVERSITÄT BREMEN

Zusammenfassung

Fachbereich Geowissenschaften | FB5

Doctor Rerum Naturalium

Deciphering past and present ice flow patterns from radar reflections

von Steven FRANKE

Die großen Eisschilde der Erde reagieren auf Veränderungen des globalen Klimas. Der Eismassenverlust nimmt mit steigender globaler Mitteltemperatur zu und trägt somit wesentlich zum Meeresspiegelanstieg bei. Um die Unsicherheiten bei der Vorhersage der Beiträge von Eisschilden zum Meeresspiegelanstieg zu reduzieren, ist es von entscheidender Bedeutung zu untersuchen, wie sich Eisschilde und ihre schnell fließenden "Förderbänder" (sogenannte Eisströme) in den letzten Tausenden bis Millionen von Jahren entwickelt haben. Diese Arbeit ist ein Beitrag zum Verständnis des Fließverhaltens der großen Eisschilde in Grönland und der Antarktis anhand einer Analyse von Radarreflexionen innerhalb der Eissäule und an der Eisbasis. Mein Schwerpunkt liegt auf der Darstellung der Möglichkeiten, wie diese Daten genutzt werden können, um Informationen über gegenwärtige und vergangene Fließkonfigurationen zu erhalten. Ich konzentriere mich auf Radardaten, die in Nordostgrönland in den stromaufwärts gelegenen Regionen des Nordostgrönländischen Eisstroms (NEGIS) und im stromaufwärts gelegenen Einzugsgebiet des Nioghalvfjerdsbrae (79° N Gletscher) gewonnen wurden, sowie auf Daten, die am Onset des Jutulstraumen Gletschers in der Antarktis erhoben wurden. In meinen Studien zeige ich, dass der NEGIS in seiner heutigen Form ein relativ junger Eisstrom ist und dass seine Geometrie und Fließeigenschaften mit der subglazialen Topographie zusammenhängen. Ich zeige auch, dass sich die Eisströmungsbedingungen in Nordgrönland von einem weit ins Landesinnere reichenden, lokalisierten Strömungsregime zu dem heutigen Fließregime verschoben haben. Dies deutet darauf hin, dass Eisströme wahrscheinlich viel kurzlebiger sind als bisher angenommen und sich im Laufe der Zeit an die veränderte Geometrie des Eisschildes anpassen. In der Antarktis untersuche ich vergangene Eisflussmuster über einen Zeitraum von Millionen von Jahren, wie am Beispiel des Jutulstraumen-Gletscherbeckens im Dronning Maud Land. Viele der Gletscher- und Flusslandschaften, die sich seit der Vergletscherung der Antarktis entwickelt haben, sind größtenteils unter dem heutigen dicken Eisschild erhalten geblieben und einige dienen heute sogar als Becken für aktive subglaziale Seen.

Acknowledgements

Above all, I want to thank my supervisor and mentor **Daniela Jansen** as well as my co-supervisors **Olaf Eisen** and **Ilka Weikusat**. They created an environment in which I could be myself. I truly believe that interpersonal respect and mutual acceptance of one's own and the other's strengths and weaknesses are the most important qualities of a supervisor for a successful doctoral period. **Daniela**, you are a wonderful person. I was lucky to be at the right moment at the right place. You gave me the chance to work on a great project, visit phenomenal places, and I am very thankful for everything you did for me. **Olaf**, thanks for being so reliable and supporting all the way. You had the right ideas at the right time. Our paths did not cross so many times in person, but still after all this time, I have to say that I am a big fan of you. And **Ilka**, thanks for letting me be a tiny part of the ice crystal world. All the things you do for your colleagues at work are immensely important. I will never forget the time with you and **David** in the PP-(rave)-cave.

I consider myself lucky to have met **Jölund Asseng**, already before I started my PhD. I appreciate him as a wonderful colleague, a true friend and a person who has probably influenced me the most during the last years. We share a passion for bad jokes, coffee breaks, V1 at Bao Mi and the creation of GIS maps.

I have benefited immensely from my colleagues: **Ole, Nico, Alex** (all three great office mates), **Hannah, Hannes, Emma, Remi, Ursel, Jakob, Jan, Damien, Nico** (the one with the afro), **Nils** (the tall one) at AWI, and also **Julien** and **Tamara** at University of Copenhagen, it was a pleasure to have you guys around me. The person I have to thank the most during the last one and a half years is **Niklas Neckel**. Not only that we share a passion for climbing, chilli-cheese burger menus and Python, we also became good friends and found some subglacial water in Antarctica.

A special thanks goes to **John Paden**, who is an extraordinary human being. At the end of my PhD, I revealed to him that I am starting to understand tiny first bits of the radar system I was working with. He made me feel so much better when he told me, that he is still beginning to understand glaciology after 20 years. John, thanks for teaching me these tiny bits! In respect to ice-penetrating radar, I haven't met anyone who knows as many details about radars and radioglaciology as **Daniel Steinhage**. He is a modest, hard-working and extremely valuable colleague with a good sense of humor. I also want to thank **Veit Helm**, just for being Veit Helm. He might be the only person I know who might be able to solve just everything. But most of all, I have not forgotten all the work of **Tobias Binder**. Because of him, I was lucky to be able to work with incredible radar data.

Frank Wilhelms is a magnificent leader of the glaciology department. His commitment to the doctoral students is characterized by prompt assistance regarding any subject. He always supported me on my way in administrative and personal matters and took care of my concerns. The same accounts for **Heinz Miller**. Some of his fascination for glaciology and radar data has jumped over to me. And what would be AWI Glaciology without **Constance**. Thank you for all your invaluable help.

One of the most memorable and saddest moments during my PhD was when **Nils Dörr** left Bremerhaven. I truly believe that he is one of the smartest geophysicists I have ever met. I could always count on him and he is still the person I contact when I am not sure what is going on with the UWB radar data processing.

From **Paul Bons**, I learned a good deal of scientific practice. Although it is sometimes difficult to keep up with him and to follow his ideas, he was an inspiration for me and will be even more for the whole glaciological community. And I will keep in mind the following sentence you once said: "It doesn't mean that I'm right, it's just an idea...".

Like many other PhD students, I really appreciated all the help and support from the **Claudias** (POLMAR) and in this context I would also like to thank **Gunther Tress** for his many valuable courses on paper writing. That being said, I want to mention **Nick Holschuh**, who reviewed one of my manuscripts (he is aware that he is mentioned here) and from whom I learned so much during the review process. I had the feeling that he was even more interested in the study than I was.

I want to thank **Kinga** and **Ruth** from AWI K&M. Every time I spend my free time helping out AWI on a public event as a volunteer, I did it because they are just fun to be around.

Finally, a big thank goes to **Sarah**, my home office mate for the last year. Thank you for being so patient with me, for selecting the appropriate colors for my figures in this thesis and for making me stay in Bremen. And of course, I have not forgotten all the things my family has done for me. Thank you for creating an environment for me that has made everything possible so far.

Contents

Abstract	iii
Acknowledgements	v
1 Introduction	1
1.1 Scope of the thesis	1
1.2 Structure of the thesis	2
1.3 Background	3
1.3.1 Ice sheets and glaciers	4
1.3.2 The flow and deformation of ice	6
1.3.3 Ice-sheet bed and internal processes	8
1.4 Ultra-wideband radar	12
1.4.1 Radioglaciology	12
1.4.2 UWB radar data	13
1.5 Methods for radar data analysis	17
1.6 Study sites and regional overview	21
2 Summary of scientific contributions	24
Paper I NEGIS Onset Bed Topography	24
Paper II NEGIS Onset Basal Conditions	25
Paper III Jutulstraumen Geomorphology	26
Paper IV Jutulstraumen Subglacial Hydrology	27
Paper V EGRIP-NOR-2018 Radar Data	28
Paper VI Deciphering NEGIS' folds	29
Paper VII Ice Stream Regime Shift in NE Greenland	30
Paper VIII A 3D View on Folded Radar Stratigraphy	31
3 Discussion and outlook	32
3.1 Ice flow and its imprint in the subglacial environment	32
3.1.1 Subglacial geomorphology and its link to the ice dynamics of localised ice flow	32
3.1.2 Reconstruction and modification of the ice base by former ice flow	33
3.2 Past ice-flow patterns captured in the englacial deformation history	34
3.3 Perspectives	37
Bibliography	38

A	UWB radar: theoretical background	49
A.1	Electromagnetic wave propagation	49
A.2	AWI UWB radar system	52
A.3	UWB radar data acquisition	53
A.4	UWB radar data processing	54
B	UWB radar: acquisition and processing tests	61
B.1	Data acquisition tests	61
B.2	Data processing tests	61
B.3	Image mode	65
B.4	Recommendations	67
C	Software, data and documentation	70
D	Further contributions	73
E	Paper I NEGIS Onset Bed Topography (<i>published</i>)	75
F	Paper II NEGIS Onset Basal Conditions (<i>published</i>)	92
G	Paper III Jutulstraumen Geomorphology (<i>published</i>)	119
H	Paper IV Jutulstraumen Subgl. Hydrology (<i>in review</i>)	140
I	Paper V EGRIP-NOR-2018 Radar Data (<i>in review</i>)	151
J	Paper VI Deciphering NEGIS' folds (<i>in prep.</i>)	169
K	Paper VII Ice Stream Regime Shift (<i>in prep.</i>)	180
L	Paper VIII A 3D View on Folded Radar Stratigraphy (<i>in prep.</i>)	191

List of Figures

1.1	Glacial cycles in atmospheric CO ₂ concentration	4
1.2	Overview of the polar regions	5
1.3	The flow of ice	6
1.4	Ice stream locations of the Laurentide Ice Sheet	7
1.5	Schematic illustration of subglacial landscapes	9
1.6	Folds in ice sheets on different spatial scales	10
1.7	Illustration of the general principle in radioglaciology.	12
1.8	AWI UWB setup on Polar 6	13
1.9	AWI UWB radar data workflow.	15
1.10	Diagram explaining the analysis of basal properties from radar data	18
1.11	3D surface reconstruction from IRHs	19
1.12	Full workflow for 3D surface construction on the basis of radar data	20
1.13	Overview of the locations of the two radar survey in Greenland	21
1.14	Overview of the locations of the two radar survey in Antarctica	22
3.1	Cartoon illustration of subglacial environments in Greenland and Antarctica	33
3.2	Ice-flow reconstruction methods based on radar stratigraphy	36
A.1	Crystal orientation fabric distribution in ice.	50
A.2	Sloping layer effect on radar processing.	52
A.3	AWI UWB radar system on <i>Polar6</i>	52
A.4	Schematic illustration of chirped waveforms and reflections.	53
A.5	Amplitude, time and phase correction.	53
A.6	CRISIS radar data processing.	54
A.7	SAR coordinate system.	54
A.8	Combination of waveform images.	56
A.9	Principle of 3D swath tomography.	56
B.1	Radargrams showing four different acquisition modes.	62
B.2	Comparison between two different processing methods.	63
B.3	Sketch showing the principle of sub-aperture processing.	64
B.4	Bed topography imaging with 3D swath processing.	66
B.5	UWB acquisition modes over different glaciological settings	67
E.1	Paper 1: Overview of the survey area.	78
E.2	Paper 1: Map of ice thickness distribution at the NEGIS onset.	80
E.3	Paper 1: Comparison of BMv3 and EGRIP-NOR-2018 bed topography.	81
E.4	Paper 1: Echogram from profile 20180508_06_003.	82
E.5	Paper 1: Radargrams showing off-nadir reflection patterns.	83
E.6	Paper 1: Sketch of the interpretation of off-nadir bed reflections.	84
F.1	Paper 2: Overview of the survey area	96
F.2	Paper 2: Vertical roughness profiles in along- and cross-flow	99
F.3	Paper 2: Flux gate analysis at the onset of the NEGIS	101
F.4	Paper 2: NEGIS' basal and englacial properties' evolution.	102

F.5	Paper 2: Bed and flow properties in the downstream survey region.	103
F.6	Paper 2: Bed return power and waveform abruptness	104
F.7	Paper 2: Radar cross-sections with BRP and waveform abruptness	105
F.8	Paper 2: Basal routing pathways calculates with different DEMs	107
F.9	Paper 2: Histograms showing the roughness anisotropy	108
F.10	Paper 2: Summary of basal properties at the onset of the NEGIS	110
G.1	Paper 3: Distribution of geological units within Gondwana	120
G.2	Paper 3: Geographical and glaciological setting of the JG drainage basin.	121
G.3	Paper 3: Flight tracks in the Jutulstraumen drainage basin.	122
G.4	Paper 3: Sketch of parameters used to describe the geometries of valleys	124
G.5	Paper 3: Bed topography in survey area.	125
G.6	Paper 3: JURAS-2018 radargrams.	126
G.7	Paper 3: Analysis of valley geometries.	127
G.8	Paper 3: Basal roughness, water flow routing and hypsometric analyses.	128
G.9	Paper 3: Landscape interpretation for the JG drainage system.	133
H.1	Paper 4: Subglacial lake locations at the onset of the Jutulstraumen Glacier	142
H.2	Paper 4: Ice surface displacements derived from DInSAR and ICESat-2	144
H.3	Paper 4: Propagation of ice surface uplift and subsidence events	145
I.1	Paper 5: Location of the EGRPI-NOR-2018 survey area in NE Greenland.	152
I.2	Paper 5: EGRIP-NOR-2018, flow parallel radar profile.	156
I.3	Paper 5: EGRIP-NOR-2018, flow perpendicular radar profiles.	158
I.4	Paper 5: EGRIP-NOR-2018 data products.	159
I.5	Paper 5: EGRIP-NOR-2018 waveforms.	160
I.6	Paper 5: EGRIP-NOR-2018 segment overview.	163
J.1	Paper 6: Overview map of survey area and radar lines	170
J.2	Paper 6: Fold amplitude vs depth plots	172
J.3	Paper 6: Situation before localisation of strain	173
K.1	Paper 7: Study site overview and key radar observations	181
K.2	Paper 7: Folded radiostratigraphy in NE Greenland	183
K.3	Paper 7: Ice-dynamic reconstruction from folds in NE Greenland	184
L.1	Paper 8: 3D englacial stratigraphy horizons in northern Greenland	192
L.2	Paper 8: Workflow sequence for 3D horizon construction.	194
L.3	Paper 8: Individual 3D horizons.	196

List of Tables

1.1	AWI UWB processing and acquisition parameters.	13
A.1	Reflectivity values for subglacial materials	51
E.1	Acquisition parameters of AWI’s UWB radar campaign in Greenland 2018. . .	77
I.1	Paper 5: Acquisition parameters of the EGRIP-NOR-2018 radar campaign. . .	154
I.2	Paper 5: Data record properties.	156
I.3	Paper 5: EGRIP-NOR-2018 segment specifications.	161
L.1	Paper 8: Radar data used for 3D horizon construction.	193
L.2	Paper 8: 3D horizon specifications of the three survey regions.	197
L.3	Paper 8: Data format specifications, description and usage.	197

Chapter 1

Introduction

Why study ice sheet and glacier motion? The large ice sheets on Earth respond to changes of the global climate. The presently ongoing ice mass loss increases linearly with global mean temperature (Edwards et al., 2021) and is, thus, a major contributor to sea-level rise (Church et al., 2013). Sea-level rise in the twentieth century was mainly dominated by thermal expansion of seawater. Still mass loss from grounded glaciers and ice sheets are becoming the major contributor in the future (IPCC Special Report on the Ocean and Cryosphere in a Changing Climate (Polar Regions), 2019; Meredith et al., 2019). Beyond the projections in sea-level rise, the IPCC acknowledged that greater sea-level increase is possible through mechanisms not fully incorporated in models used in the assessment (Siegert et al., 2020). In this context, studies of paleo-ice streams show that ice-dynamic processes play a major role in continent-scale deglaciation, but the mechanisms are not yet fully understood. Therefore studies of the flow characteristics of the large ice sheets (in Greenland and Antarctica) are essential for understanding and predicting changes in the dynamics of the ice sheets as a whole.

1.1 Scope of the thesis

One major source of uncertainty to predict the contributions to sea-level rise of ice sheets is that the observations used for model initialisation and calibration only cover a time period of several decades (Stokes et al., 2016). Therefore, it is crucial to study how ice sheets and their fast-flowing drainage pathways (so called ice streams) have evolved over the last thousand of years. Modern ice streams represent the main drainage pathways in present ice sheets. It has been shown that changes in ice stream dynamics could introduce a considerable non-linearity into the ice-sheet response to a warming climate forcing (Golledge et al., 2015; Joughin et al., 2014).

New constraints on paleo ice dynamics are required to improve our understanding of past ice sheet and climate interactions and improve ice-sheet projections. Many studies concentrate on reconstructing ice streams of contemporary non-glaciated areas in the northern hemisphere, such as the Laurentide Ice Sheet (Stokes and Clark, 2001; Stokes et al., 2016). Still, these proxies for past ice-sheet motion are not available on many temporal and spatial scales for the regions of Greenland and Antarctica. A much more relevant but also more challenging task is to infer the ice-sheet configurations of the Greenland and Antarctic Ice Sheet for the last thousands of years (e.g. since the Last Glacial Maximum (LGM) 26.5–19 ka BP; Clark et al. 2009). To address this issue, we can use information acquired from airborne ice-penetrating radars about the internal architecture of the ice and the ice–bed interface to constrain today's and historic ice-flow patterns. In this thesis, I will investigate the following:

Research questions

RQ1 What can radar reflections at the ice–bed interface tell us about current and past ice stream motion?

RQ2 How can we decipher and use the deformation history engraved in the radar stratigraphy to reconstruct past ice-flow patterns?

1.2 Structure of the thesis

I present my research as a cumulative dissertation. Hence, this thesis is composed of a collection of publications in recognised scientific journals. Some of the publications are already published, and others are currently in review or close to submission. In the central part of my thesis (Chapter 1–3), I explain the scientific background and the data and methods I use for my research. Then, I focus on the summary and key messages of my publications and discuss my findings within the scope of the current state of the science.

The common thread running through the publications is the radar-based analysis of ice-internal and bed structures, which provide information about the past and present ice-flow characteristics. Further details of the background in radar data and all publications in full length are provided in the appendix. This results in the following structure of my thesis:

Thesis structure

Chapter 1 gives an overview of the scientific background as well as a summary of the materials and methods I used. Further details in radar theory and data processing are provided in Appendix A and B.

Chapter 2 provides a summary of scientific publications. In this chapter, I also describe in detail the motivation and conclusions of the publications, as well as my contribution to each article. Moreover, I link the findings of each publication to my research questions.

Chapter 3 In this chapter, I draw connections between the findings of my studies and discuss the key outcomes based on my research questions as well as their implications for the system as a whole.

Appendix A gives a detailed overview of the theoretical background of AWI's (Alfred Wegener Institute, Helmholtz Centre for Polar and Marine Research) ultra-wideband radar (UWB). I explain the fundamentals of electromagnetic wave propagation as well as all aspects which are relevant for my work. Furthermore, I introduce the radar data acquisition and processing steps for the AWI UWB radar.

Appendix B summarises AWI UWB radar acquisition and processing tests, which I performed during my PhD work. Some of the test results are not related to the findings or interpretations made in this thesis but are of potential use for future surveys and scientific questions.

Appendix C provides a detailed description of the software I used for my work and where it can be obtained. I also document my own code I used for analysis and where to find it. Additionally, I describe the data products I created during my PhD and where they are available.

Appendix D provides an overview of further scientific contributions, such as co-authored manuscripts, which are not included in this thesis and presentations at international conferences.

Appendix E–L contains the scientific publications from Chapter 2 in full length.

1.3 Background

"The polar regions are losing ice, and their oceans are changing rapidly. The consequences of this polar transition extend to the whole planet, and are affecting people in multiple ways."

IPCC - Special Report on the Ocean and Cryosphere in a Changing Climate (Polar Regions), 2019, [Meredith et al. \(2019\)](#)

Around 71 % of the Earth surface are covered by the ocean, and another 10 % of the land area by glaciers and ice sheets. Both systems are responsible for the distribution and storage of heat and carbon dioxide (CO₂). The ice sheets of Antarctica and Greenland hold a respective water equivalent to raise global sea level by 58 m ([Fretwell et al., 2013](#)) and 7.4 m ([Morlighem et al., 2017](#)). The fate of coastal cities as well as the heritage of many ecosystems depend on their long-term stability. In order to predict the changes in the polar regions due to a warming climate as well as their consequences for the entire Earth system, we have to understand the processes governing the dynamics of polar ice sheets.

99 % of all ice mass on Earth is stored in the Greenland (11 %) and Antarctic (88 %) Ice Sheet ([Allison et al., 2009](#)). Mass and energy are constantly exchanged between glaciers, oceans, the atmosphere, biosphere and the solid Earth and thus, play a central role in the global hydrological system. Ice mass loss occurs due to meltwater runoff at the ice base and surface as well via calving at marine-terminating outlet glaciers. The regrowth of the collapse of marine ice sheets would require more than ten thousand years, considering the current rates of accumulation ([Michael Oppenheimer, 1998](#)). However, when global warming exceeds critical temperature thresholds, substantial ice loss is irreversible and ice masses would not regrow to its contemporary extent, even if the increase of the global mean temperature is reversed ([Garbe et al., 2020](#)).

The importance and potential of sea level fluctuations is revealed by ocean sediment and ice core records. For the last several million years (Pleistocene epoch) the Earth is experiencing cycles of extensive glaciation and warmer times called glacial and interglacial periods. These cycles currently last approximately 100 000 years, where the interglacial periods like the present Holocene (with high sea level and low ice volume) make up around 10 % of the time ([Allen et al., 2005](#)). Changes between glacial and interglacial periods correlate with variations in the atmospheric CO₂ concentration (Figure 1.1), which causes a substantial fraction of ice-age cooling and helps to explain why the climate forcing is distributed globally ([Sigman et al., 2010](#)). Variations in sea level over the glacial cycles are mainly caused by the accretion or melt of continental ice (in contrast to sea ice) with a small contribution from thermal expansion of ocean water. In the past glacial periods, two additional large ice sheet covered Northern Europe (the Fennoscandian Ice Sheet) and North America (the Laurentide Ice Sheet). The maximum extension during the last glacial period occurred around 21 000 years ago. During the past interglacials, the extent of the Greenland and Antarctic Ice Sheet decreased but the ice sheets never fully disappeared. In this respect, it is timely to remember that simulations based on the RCP 8.5 scenario (Representative Concentration Pathway on greenhouse gas concentration; see IPCC AR5; [IPCC 2013](#)), suggest that the Greenland Ice Sheet will potentially disappear within a millennium ([Aschwanden et al., 2019](#)).

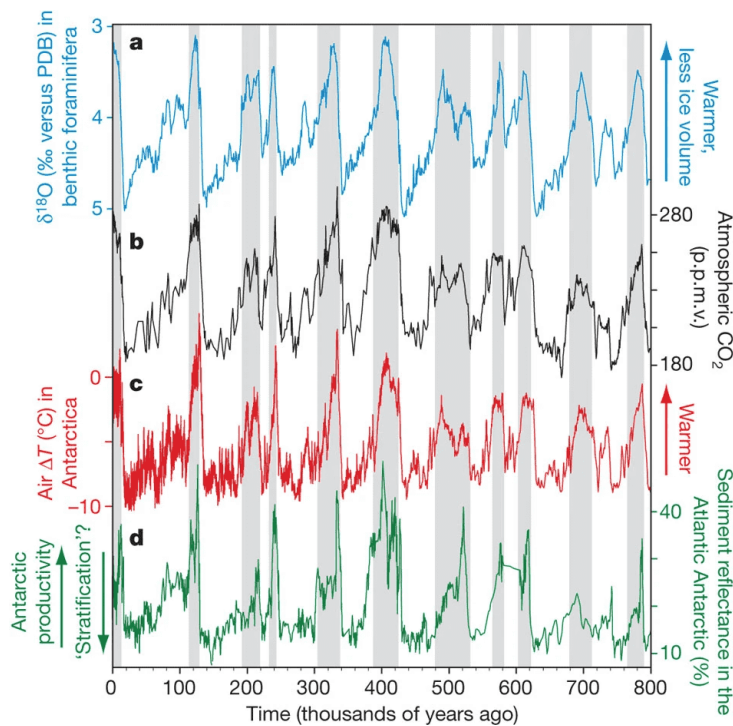


Figure 1.1: Atmospheric CO₂ record, temperature and ice volume during the glacial cycles over the last 800 ka. Panel (a) shows a compilation benthic foraminiferal $\delta^{18}\text{O}$ (Lisiecki and Raymo, 2005), which reflect changes in continental glaciation and deep ocean temperature. (b) shows atmospheric CO₂ reconstructed from ice cores (Lüthi et al., 2008). Panel (c) shows reconstructed Antarctic air temperature from deuterium (Jouzel et al., 2007) and (d) a reconstruction of biogenic material of the surface ocean from Antarctic deep sea sediment cores. The grey bars mark the interglacial (warm) periods, which are characterised by less ice cover, high atmospheric CO₂ concentration, warm air temperature and high Antarctic biomass production. The figure and caption text was taken from Sigman et al. (2010).

The decisions and actions taken within the next decade will determine whether greenhouse gas emissions will remain high and climate continues to warm with an increasing risk of out-of-control consequences, for instance induced by tipping points in the climate system or if ambitious action is taken to decrease greenhouse gas emission to net zero and reduce anthropogenic pressure on the environment.

1.3.1 Ice sheets and glaciers

Ice sheets and glaciers are formed from snowfall, which metamorphoses into ice over several years to centuries at temperatures well below the melting point (Allison et al., 2009). The two contemporary ice sheets cover Greenland and the Antarctic continent (Figure 1.2 a and 1.3 a). Gravity makes the ice sheets flow towards their margins by internal deformation and sliding at the ice-sheet base. This process is the primary mechanism transferring ice mass from the interior towards the ocean. Since the Pleistocene epoch (2.58 million years ago), the Earth has been subject to periodic climatic fluctuations between ice ages when ice sheets and glaciers were up to three times larger as today and warmer times when ice cover was at a comparable extent as today (Benn and Evans, 2010). Growth and shrinkage of ice masses have profoundly shaped the landscape of the Earth. During the last cold period, much of North America and Scandinavia were also covered by extensive ice sheets.

The Antarctic Ice Sheet (AIS; Figure 1.2 b and d) covers an area of approximately 14 million km² and contains a volume of 30 million km³ of ice. The ice column is up to 4 km thick and holds enough fresh water to raise sea level by 58 m (Figure 1.3 a; Fretwell et al. 2013). The ice sheet is composed of a large inland catchment and channels of high ice-flow velocities (Figure 1.2 b) where the ice is transported towards the ocean (Rignot et al., 2013). The AIS is divided into three main sections: the East Antarctic Ice Sheet (EAIS), The West Antarctic Ice Sheet (WAIS) and the Antarctic Peninsula (Figure 1.2 b and d). Due to the weight of the thick ice cover and long-term erosional activity, large areas of the Antarctic bed topography are (up to -3 500 m) below sea level (Morlighem et al., 2019). A mass balance analysis between 1992 and 2017 shows that the AIS has lost $2\,720 \pm 1\,290$ billion tonnes of ice, which corresponds to a rise in mean sea

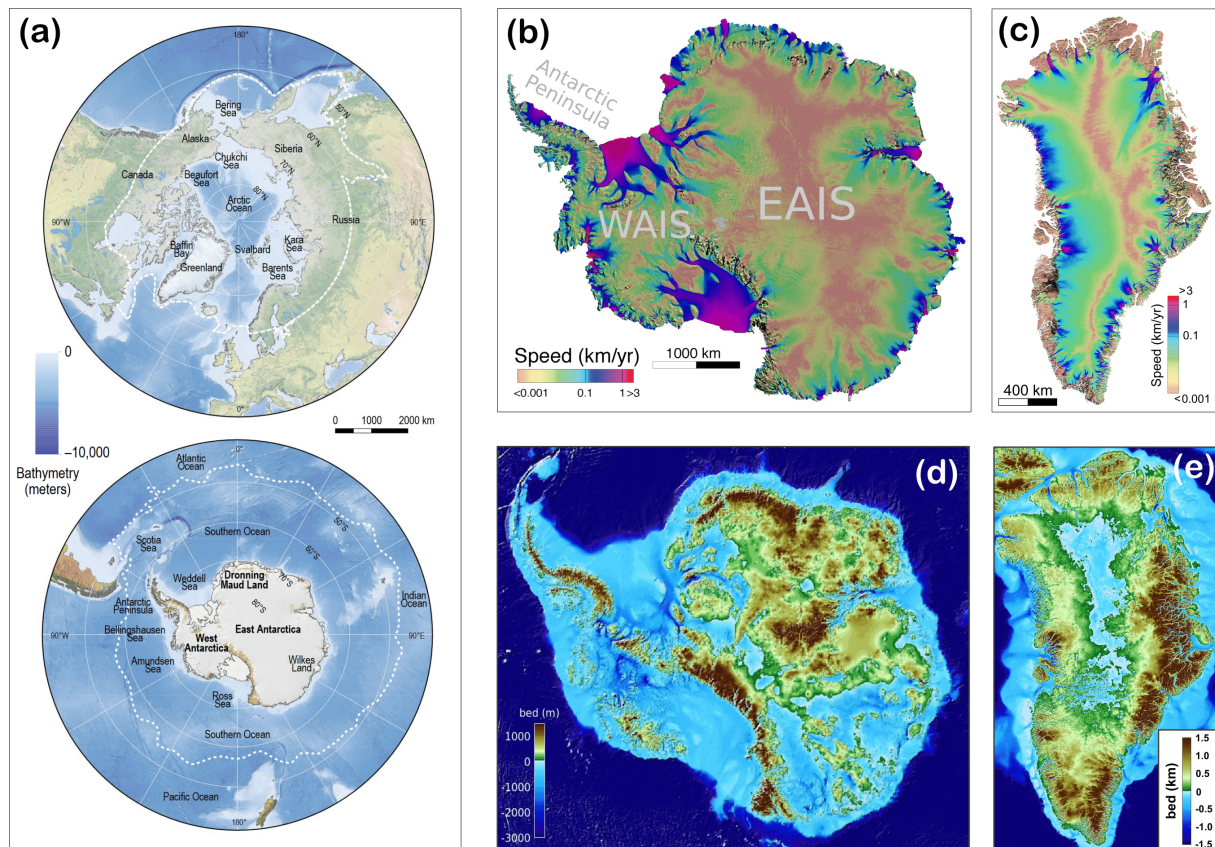


Figure 1.2: Overview of the polar regions. Panel (a) shows the geographic setting of the northern and southern hemisphere centred at the geographic poles. (b) and (c) display the ice surface velocity of the Antarctic and Greenland Ice Sheet and (d) and (e) the respective elevation of the bed topography. Image (a) is taken from the Special Report on the Ocean and Cryosphere in a Changing Climate: Polar Regions (Meredith et al., 2019), (b) and (c) from Mouginot et al. (2017), (d) from Morlighem et al. (2019) and (e) from Morlighem et al. (2017). Emphasis must be placed on the different spatial scales between the Antarctic and Greenland Ice Sheet in (b)–(e).

level of 7.6 ± 3.9 millimetres (Shepherd et al., 2018). Today’s net mass loss from Antarctic ice is small in comparison to the GrIS and other ice masses. However, it is to be expected to increase with ongoing global warming eventually. The future behaviour of the AIS will be determined by the interplay between dampening (negative) and amplifying (positive) feedbacks (Meredith et al., 2019). The ice sheet has the potential to cross critical thresholds, where positive feedbacks will cause an irreversible dynamic, further increasing sea-level rise (Garbe et al., 2020).

The Greenland Ice Sheet (GrIS; Figure 1.2 c and e) yields a total ice volume of 2.99 ± 0.02 million km^3 on an area of 1.71 million km^2 . Near the central ice divide, the ice column is more than 3 000 m thick and the bed several hundred metres below sea level (Figure 1.3 a; Morlighem et al. 2017). Similarly to the AIS, ice flows towards the ocean via a network of glaciers and ice streams (Joughin et al., 2010), some of them reaching far inland. Warming of the Arctic has a profound impact on the GrIS. Ice loss has accelerated over the last two decades (IPCC 2013) and makes it one of the largest contributors to eustatic sea level rise over the last decade (e.g. Shepherd et al., 2012; Helm et al., 2014; Khan et al., 2014). The cumulative mass loss between 1992 to 2017 was $3\,902 \pm 342$ billion tonnes causing a mean sea level rise of 10.8 ± 0.9 millimetres (Shepherd et al., 2020). Ongoing ice loss acceleration of the GrIS has the potential to contribute as much as 9 cm of sea-level rise by 2050 (Church and White, 2006).

Ice loss of contemporary ice sheets can be partitioned into two main processes: (i) ice discharge and (ii) melt induced mass losses (Khan et al., 2015). Both processes mainly depend on changes in atmospheric and oceanic conditions (Holland et al., 2008). Mass loss from ice

discharge is dynamically induced and related to changes in the ice movement (e.g. increase in ice flow due to a reduction of marine ice shelf buttressing (see Dupont and Alley, 2005; Gagliardini et al., 2010) or a reduction of the resistance at the glacier bed). Melt induced ice loss is expressed by changes in the surface mass balance (SMB), which represents the difference between accumulation (via snow deposition and refreezing rain) and ablation (via sublimation, meltwater runoff and snow erosion).

1.3.2 The flow and deformation of ice

Large bodies of ice are subject to motion (ice flow) and deformation. On polar ice caps, snow is accumulated in the central parts of the ice sheets. The ice column is compressed under its own weight, and ice flows driven by gravity slowly towards the margins (Figure 1.3 b). Ice temperature and the resistance at the ice-sheet base are the two most important factors controlling ice flow. Ice is removed at the ice-sheet margins by the discharge of icebergs into the ocean or by melting. Changes in the amount of snowfall or variations in ocean or atmospheric temperature influence the ice sheets' extent and thickness. Horizontal ice flow at the surface can be measured with GPS measurements or remote sensing. Internal velocities measurements and in particular the velocity at the glacier bed are only possible to be measured through boreholes. The ice at the bed can slide (low resistance and less deformation) over the ground or remain frozen to a substrate (high resistance and strong deformation).

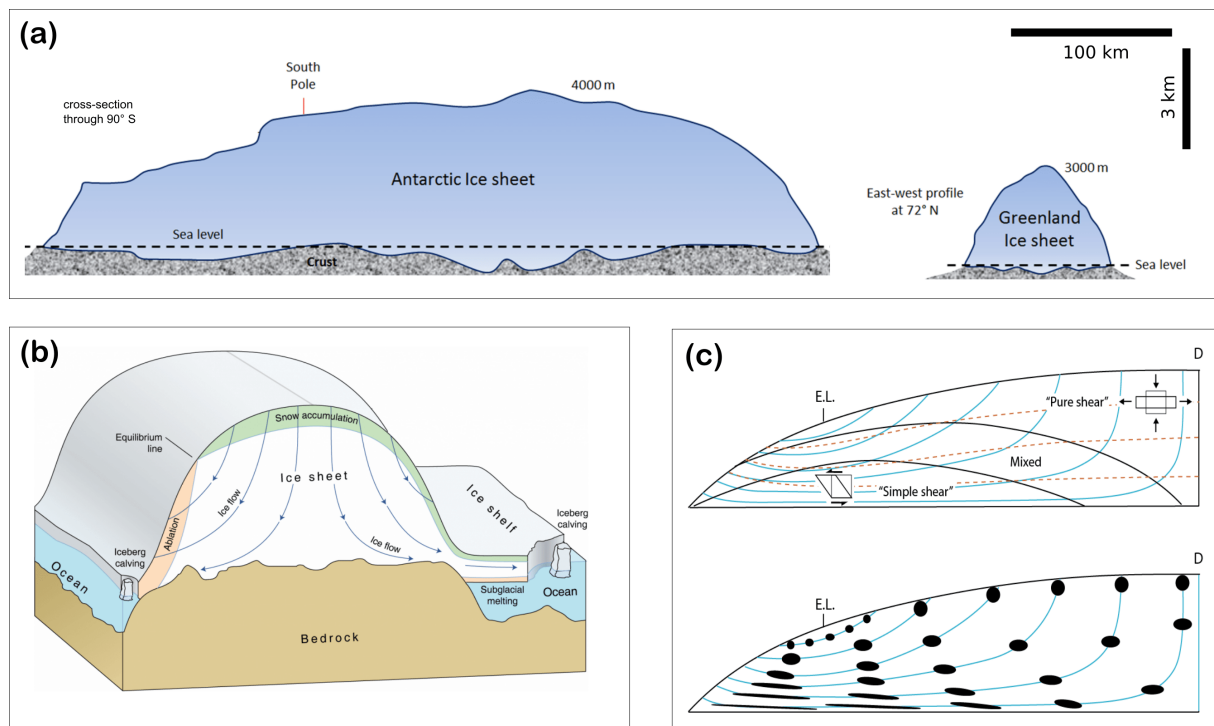


Figure 1.3: The flow of ice. The image in panel (a) shows a simplified cross section through the AIS and GrIS and was modified from opentextbc.ca (Earle, 2019). Panel (b) shows the general ice-flow pathways from the central accumulation region of an ice sheet towards the margins (image taken from the Landsat Image Mosaic Of Antarctica; LIMA). Panel (c) illustrates the principle deformation regimes for ice following the flow trajectories shown in (b). The image is taken from Hudleston (2015).

As ice deforms, it leaves traces on a small and large scale. Most deformation is dominated by plastic flow and recrystallization and locally by fracture under tension (Hudleston, 2015). If we consider ice motion on a large scale in two dimensions (e.g. in Figure 1.3 b), we can discriminate between pure shear in the upper ice column, simple shear in the near-bed area and a mix between the two in the middle part of the ice column (Figure 1.3 c). A variety of structures are

the result of cumulative deformation. For instance, foliation or folding can be identified in ice sheets because new layers of snow are deposited horizontally on the ice sheet representing an undisturbed horizon. Variations in ice flow over time or inhomogeneities in the flow associated with shear zones (Hudleston, 2015) are one possible mechanism for ice deformation. A typical regime in an ice sheet where strong deformations are occurring are so-called ice streams.

In the AIS and GrIS, ice streams are commonly referred to as corridors of fast ice flow within an ice sheet, responsible for discharging the majority of the ice and sediment within them (Bennett, 2003). Ice streams were first defined by Swithinbank (1954) as a part of an inland ice sheet that flows faster than the surrounding ice. Six decades ago, Henri Bader provided another definition for an ice stream (Bader, 1961): *An "ice stream" is something akin to a mountain glacier consisting of a broad accumulation basin and a narrower outlet valley glacier: but a mountain glacier is laterally hemmed in by rock slopes, while the ice stream is contained by slower moving surrounding ice.*

Ice streams play a key role in the stability of ice sheets. As all ice from the AIS and GrIS is discharged into the ocean, ice streams provide a link between the cryosphere and the ocean. Today, ice streams discharge over 90% of all the ice and sediment of the AIS (Bamber et al., 2000). Episodes of intensive ice streaming have been suggested to trigger a climate response of a global extent (Broecker, 1994). Therefore, it is important to understand the mechanics of fast ice flow and to investigate the controlling factors for ice stream initiation and shut down to decode past glacial activity as well as to predict the future evolution of an ice sheet (Bennett, 2003). Winsborrow et al. (2010) identified potential controls on ice stream locations in the literature, such as topographic focusing, topographic steps, topographic roughness, calving margin, subglacial geology, geothermal heat flux and subglacial meltwater routing. When investigating the controls on ice stream geometry and location, it can be difficult to distinguish the cause and effect of ice stream activity. E.g. does a smooth bed initiate or favour ice stream initiation, or is a smooth bed the result of ice stream activity?

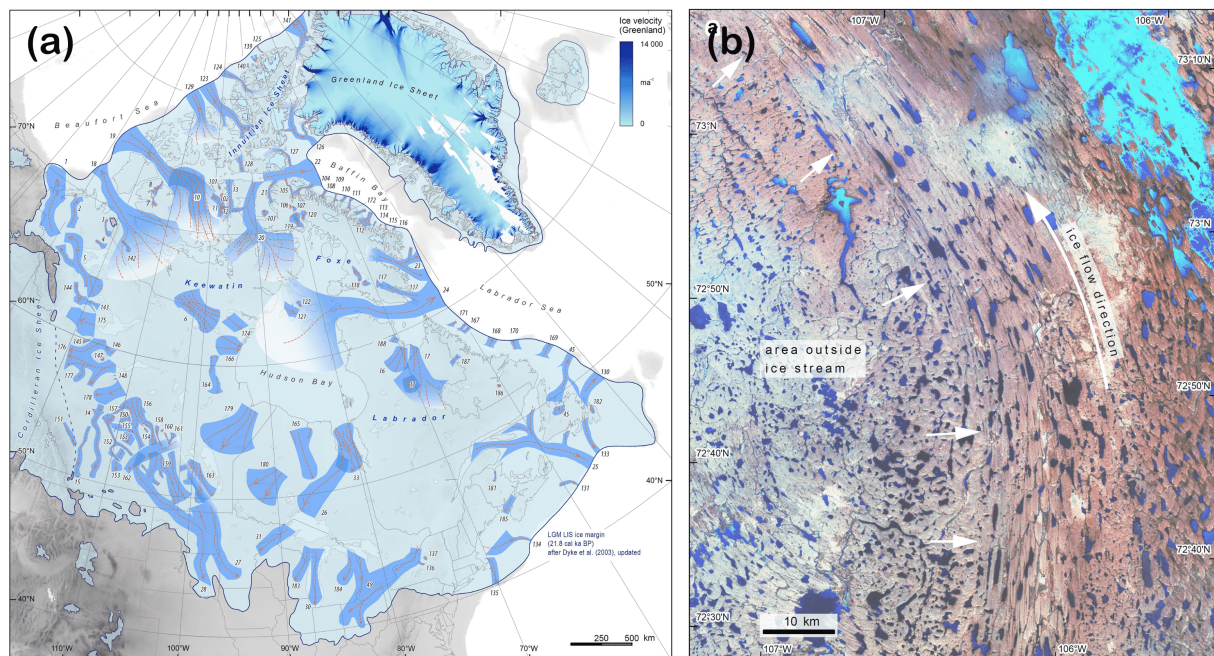


Figure 1.4: Reconstructed ice stream locations and bed morphology after deglaciation of the Laurentide Ice Sheet. Panel (a) shows the Extended Data Figure 1 (Location of 117 ice streams from a recently compiled inventory based on previous work and systematic mapping across the LIS bed) and panel (b) the Extended Data Figure 5a (Landsat imagery of lateral shear margin moraines in the Canadian Arctic Archipelago) from Stokes et al. (2016).

The fast ice-flow velocities of ice streams can be explained by two general mechanisms (Stokes et al., 2007): The fast motion of ice streams which are located in deep topographic

troughs is enabled by the so-called *creep instability* (Clarke et al., 1977). Ice streams that are not constrained by a subglacial valley require a layer where sliding is facilitated, such as a lubricated bed or soft and deformable sediment (Anandakrishnan and Alley, 1997). Furthermore, it was shown that ice streams can be highly dynamic and are subject to rapid changes. Changes in the ice-sheet configuration, such as continuing thinning or thickening are presumably responsible for a switch in flow direction of the Whillans ice stream (Conway et al., 2002). Also, numerous ice streams show a decrease or increase in ice-flow velocity over time (Stephenson and Bindshadler, 1988; Joughin et al., 2003). Changes in ice stream behaviour are either driven by external forcing (e.g., changes in the atmosphere or ocean) or internal forcing at the ice stream bed Margold et al. (2015).

In contrast to atmospheric and oceanic measurements, it is far more challenging to investigate the glacier bed. Only a few single borehole locations in Greenland and Antarctica give insight into the *in-situ* physical and material properties. However, the bed characteristics of paleo ice streams can be reconstructed from sedimentary records and the analysis of former subglacial landforms (Stokes and Clark, 2001). A large number of former ice streams of the Laurentide Ice Sheet (LIS; former largest of the Northern Hemisphere ice sheets during the last ice ages) have been reconstructed and described by Margold et al. (2015) (Figure 1.4). Stokes et al. (2016) investigated the potential impact of ice streams of the former LIS during deglaciation after its maximum extent approximately 22 000 years ago. The drainage network of the LIS had a comparable extent as the AIS and GrIS. The authors find evidence that depending on the ice-sheet scale, its drainage network adjusted to the changes in ice-sheet volume. It is possible that ice streams had a less severe impact on the ice-sheet mass balance during the retreat of the LIS as hypothesised for modern ice streams. However, it is unclear if these findings can be translated to modern ice sheets (Stokes et al., 2016).

1.3.3 Ice-sheet bed and internal processes

Processes at the ice-sheet bed ice-flow patterns can be complex and the basal properties render one of the most important parametrisations in ice-flow modelling, such as bed type and structure and availability of liquid water (Wilkens et al., 2015). The ice base (also referred to as the interface between ice and the underlying material) of glaciers and ice sheets is one of the most difficult to access parts of an ice sheet. The way the ice sheet behaves depends on the conditions underneath the ice. In particular, the geometry of the bed topography, the physical conditions (e.g. temperature, softness of the bed and liquid water content and subglacial water pressure) and material properties of the basal ice influence ice flow. At the same time, ice flow affects the ice-underlying material. For example the removal of material at the ice base contributes to the sculpting of the subglacial environment and transportation of material downstream. Furthermore, increased sliding increases the temperature at the ice base, which in turn plays a major role in respect to the availability of subglacial water.

Glacial erosion has contributed to the creation of alpine landscapes, scouring of areas and transportation and deposition of sediments (Cook and Swift, 2012). Formerly glaciated regions give insight into the evolution of glacial landscapes. The distribution of large erosional landforms, such as U-shaped valleys, scoured areas, cirques and overdeepenings can be used to reconstruct the paleo-glaciological conditions (Glasser and Bennett, 2004). In this context, geomorphological observations of the bed can also be used to infer the glacial history beneath contemporary ice sheets (Bingham et al., 2010). In particular, the widening and deepening of subglacial valleys, starting from pre-glacial fluvial erosion with successive glacial cycles (Figure 1.5 a), have the potential to constrain the evolution, dynamics and ice extent of former and contemporary ice sheets (e.g. Cook and Swift, 2012; Taylor et al., 2004; Kessler et al.; Kaplan et al., 2009).

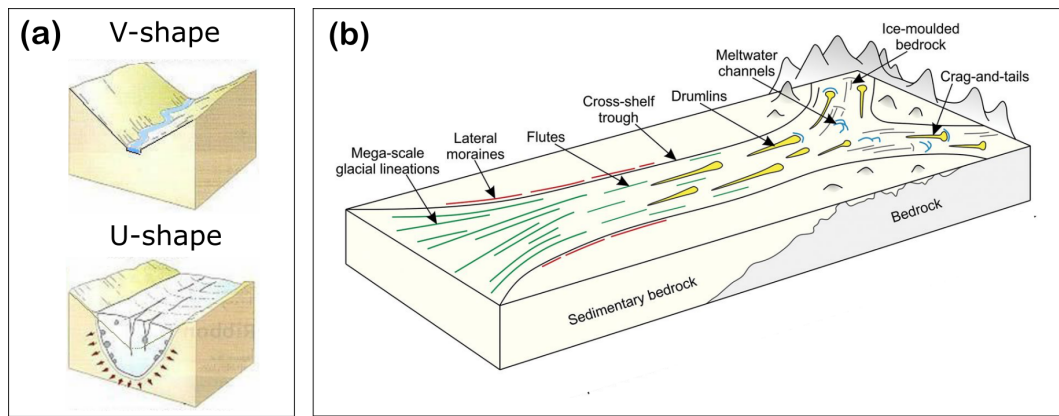


Figure 1.5: Schematic illustration of subglacial landscapes. Panel (a) shows valleys shaped by fluvial (V-shape) and subsequent glacial activity (U-shaped). Panel (b) illustrates a selection of common (mostly submarine) glacial landforms, created by ice flow. Image (a) is taken from the IAS Academy and image (b) from Dowdeswell et al. (2016).

The study of the geomorphology of the bed can also be used to understand ice-flow behaviour on a smaller spatial scale and on shorter time scales. Particular landforms beneath ice streams are the result of local erosion, transport and deposition of sediments (e.g. King et al., 2009) (Figure 1.5b). These processes are tightly linked to the mechanisms through which ice streams flow (Stokes, 2018; Bingham and Siegert, 2009). Ice flow causes an ongoing evolution of the subglacial geomorphology and influences the bed's roughness and propagation pathways and pressure of the subglacial hydrological system (Stokes, 2018; Schoof, 2002). In turn the subglacial hydrology controls subglacial erosion rates and mechanisms (Ugelvig et al., 2018).

Next to the controls on subglacial erosion, the subglacial hydrology system has become a crucial component for the understanding of ice-sheet behaviour and evolution. The presence of subglacial water underneath ice sheet is being recognised to control basal sliding and the deformation of soft beds, episodic lake drainage events correlated with subglacial pressure fluctuations and changing basal traction via basal freeze-on (see Greenwood et al. 2016 and the references therein). Thus, it is crucial to constrain the propagation of subglacial water on an ice-sheet scale. For Antarctica, repeated drainage events between neighbouring subglacial lakes reveal that basal water is transported hundreds of kilometres from the ice-sheet interior towards the margins (Fricker et al., 2007).

Ice internal processes The flow of ice does not solely leave traces at the ice base. One of the major drawbacks of characterising ice flow via observations at the base of the ice is that direct information beneath contemporary ice sheets is difficult to acquire. Moreover, the observations from paleo ice sheets are mostly useful to characterise ice-sheet behaviour of ice bodies that have already disappeared. The interpretation of folded englacial stratigraphic structures (mostly made visible through the shape of continuous reflections detected with radio-echo sounding) is another way to infer the history of motion of contemporary ice sheets at more recent time scales (e.g. the last thousands of years).

Folds have been described in all glacier and types and occur on scales from centimetres to kilometres (Hudleston, 2015). The shape, orientation and location of folded ice structures reflect different formation processes. We generally assume that planar stratification is the original state in an ice sheet because accumulation can be considered to be homogeneous on the spatial scales that we are investigating. Therefore, we consider stratified layers to be isochronous (layers representing the same age). In this case, folding is a consequence of non-uniform flow on different time and spatial scales, resulting in the passive deformation of planar markers (Hudleston, 2015). Horizontal shortening and shearing are the two most important processes.

Planar markers can be optically visible features (e.g. crevasses, veins or dust layers) or, as in the sense of this thesis, reflections from radio-echo sounding surveys.

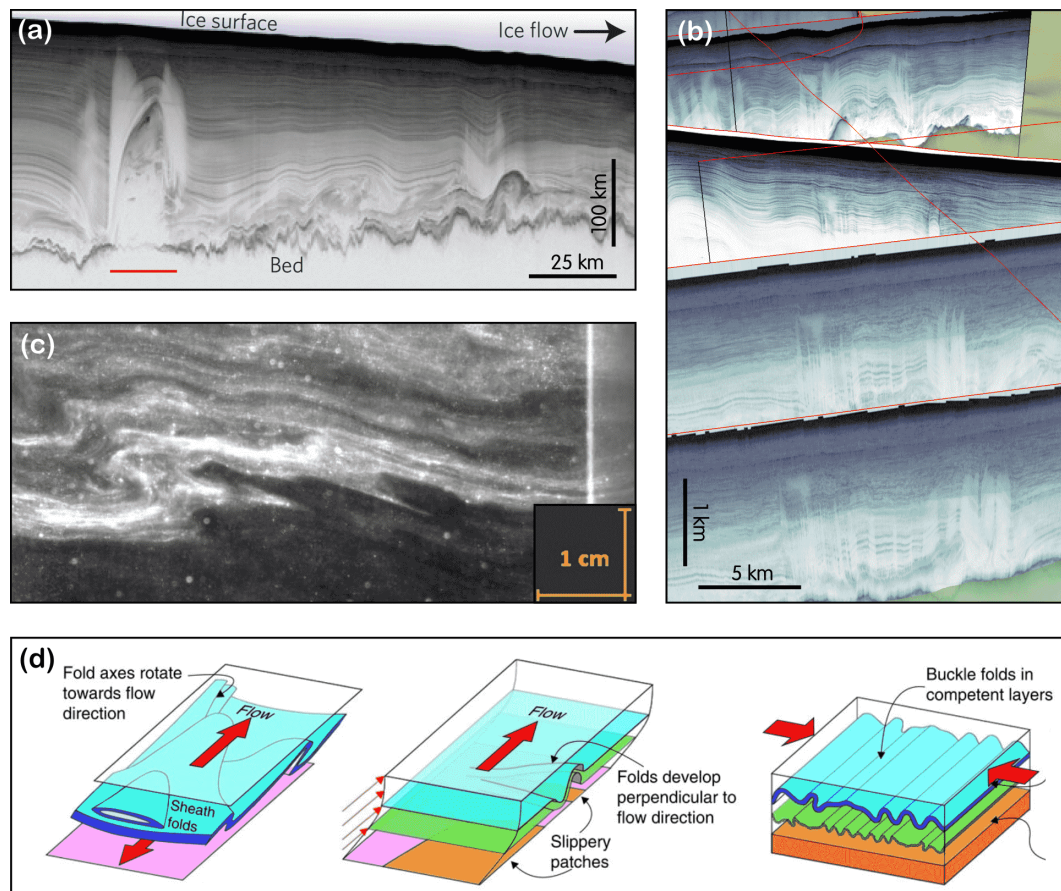


Figure 1.6: Folds in ice sheets on different spatial scales. Panel (a) shows a radargram from Bell et al. (2014) highlighting folded radar stratigraphy closely to the bed and reaching up several kilometres in the ice column. In panel (b) we can observe reoccurring sequences of folded radar stratigraphy in several radargrams (from Paper VI). Panel (c) highlights centimetre-scale disturbances in the NEEM ice core visualised with the line scanner (image taken from the B.Sc. thesis of Julien Westhoff (with permission); Westhoff 2014). Possible folding mechanisms elaborated by Bons et al. (2016) are shown in panel (d).

In most cases of steady ice flow, folds are amplified by horizontal shortening or shearing at various locations of the glacier (Hudleston, 2015). One prominent feature are upright folds, found for instance in the ablation zones of valley glaciers (particularly at their margins (e.g. Allen et al., 1960; Hambrey and Glasser, 2003)). Moreover, the axial planar foliation is associated with strong horizontal shortening due to the reduction of width in convergent flow regimes (e.g. Bons et al., 2016) or the joining of two ice streams (Lawson et al., 1994). Alternatively, steady-state flow may form folds due to the bed topography or in combination with snow accumulation at steady or migrating ice divides (e.g. recumbent folding of divide arches and Raymond bumps; Jacobson and Waddington 2005; Raymond 1983).

Ice deformation and folding are also common at the ice-sheet bed. The general deformation style is close to simple shear (Figure 1.2 c). The resulting deformation geometries can deviate from the expected one due to rheological contrasts produced by variations in bubble content, crystallographic fabric or impurities (Hudleston, 2015). Furthermore, the deformations close to the bed are generally characterised by large displacements and high strains.

Different types and magnitudes of deformed internal layers were found in Greenland (MacGregor et al., 2015; Leysinger Vieli et al., 2018; Panton and Karlsson, 2015; Bell et al., 2014) and Antarctica (Drews et al., 2009; Bell et al., 2011; Ross et al., 2020). They range from

overturned and sheath folds as well as plume-like structures associated with large units of disrupted stratigraphy at the ice base (see [MacGregor et al. 2015](#); [Bell et al. 2014](#); [Bons et al. 2016](#); [Leysinger Vieli et al. 2018](#) and Figure 1.6 a), over tight folds that extend almost over the entire ice column with a fold axis oriented parallel to the shear margins of ice streams (see [Franke et al. 2020](#), Paper VI–VII and Figure 1.6 b), to small folds visible in ice cores (Figure 1.6 c), such as centimetre-scale undulations observed in the visual stratigraphy of ice cores ([NEEM community members, 2013](#); [Jansen et al., 2016](#); [Westhoff et al., 2020](#)).

The overview given here, of course, represents only a fraction of the background information that is important for ice-dynamic processes in ice sheets. More detailed information can be found in the individual manuscripts. The majority of the studies (Papers I, II and V–VIII) focus on the Greenland Ice Sheet. Studies III and IV, on the other hand, analyse data from Antarctica. The exact survey areas are described in Section 1.6. The manuscripts are basically divided into two groups, with papers I–IV dealing with processes and findings from the base of the ice sheet and papers V–VIII dealing with processes within the ice.

1.4 Ultra-wideband radar

The results of this thesis are based on radio-echo sounding (radar) data acquired with a multi-channel ultra wideband (UWB) radar system mounted on AWI's polar research aircraft Polar 6. In this section, I introduce the radar based measurement principle to investigate ice sheets and glaciers (radioglaciology), the acquisition system, data processing steps as well as the methods I use to analyse the data. More specific information can be found in the Appendix A and B and in the method sections in the scientific publications.

1.4.1 Radioglaciology

Radioglaciology is a discipline that uses radio waves to investigate ice masses of all types (Schroeder et al., 2020). Airborne radio-echo sounding is the most important tool for observations inside and beneath ice sheets. The majority of data is collected by radars mounted on aeroplanes. The radar is used to transmit electromagnetic signals down into the ice and record the reflected echos, which contain information about the physical properties inside and underneath the ice sheet. The recorded data are visualised in radargrams, which are vertical profiles through the ice column (Figure 1.7). Radar waves have been used for more than five decades to sound ice masses (e.g. ice sheets, ice shelves, mountain glaciers and sea ice). Large-scale data collection surveys across the Greenland and Antarctic Ice Sheet started in the late 1960s and 1970s and were only made possible by collaborations of multiple countries (Schroeder et al., 2020).

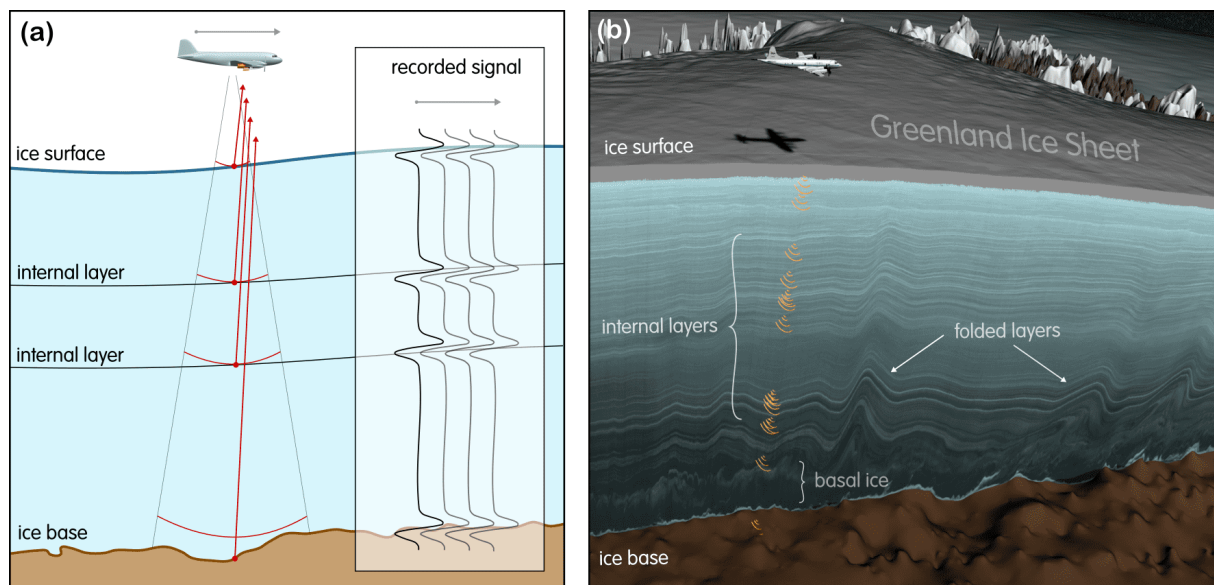


Figure 1.7: Illustration of the general principle in radioglaciology and the typical reflections in ice sheets (e.g. ice surface, internal layers and the ice base). The sketch in panel (a) is adapted from Reynolds (2011) and the image in panel (b) is taken from the NASA Goddard's Scientific Visualisation Studio.

Radio-echo sounding systems span a variety of frequency ranges, antenna configurations and include both mono-pulse and chirped-waveform transmission systems. Since the 1990s a major development step was made with phase-sensitive radars designed with multi-element cross-track antenna arrays in combination with coherent synthetic aperture radar (SAR) processing (Gogineni et al., 1998; Leuschen et al., 2000; Legarsky et al., 2001). This new generation of radar systems is able to achieve a much higher signal-to-noise ratio (SNR) as well as an improved azimuth resolution. Moreover, radar systems are nowadays able to record and emit radar waves at multiple polarizations (e.g. Dall et al., 2018).

Regardless of the type of radar system, the analysis of the data is based on the same physical principles. Radar waves travelling through the ice get reflected at every interface separating materials of contrasting electromagnetic properties (in particular, the dielectric properties). These reflections are referred to as internal reflection horizons IRHs and their geometry contains information about the history of the ice sheet. In combination with ice core dating, IRHs can be used to reconstruct accumulation rates or historic ice flow (e.g. [Paren and Robin, 1975](#); [Jacobel and Hodge, 1995](#); [Cavitte et al., 2016](#)). Next to the analysis of englacial properties, the primary objective of the vast majority of radar soundings was to locate the bed reflection and obtain information about the ice thickness ([Bailey et al., 1964](#); [Bamber et al., 2013](#); [Fretwell et al., 2013](#)).

In this thesis, I build my analysis on radar data, which has been acquired with one of the most modern airborne radio-echo sounding systems at the present time. The radar system and data, as well as the survey regions are introduced in the upcoming sections. Details about the specific survey and acquisition can be found in the respective manuscripts. Two sections in the Appendix provide further details on the theoretical background of the radar system (Appendix A) and on acquisition and processing tests I performed during my PhD work (Appendix B).

1.4.2 UWB radar data

The core data and foundation for most of the results generated and presented in this thesis is airborne radar data acquired with the multi-channel ultra-wideband (UWB) radar of the Alfred Wegener Institute, Helmholtz Centre for Polar and Marine Research (AWI; Figure 1.8 a). The AWI UWB RDS/I (radar depth sounder and imager) was developed by the Centre of Remote Sensing of Ice Sheets (CRE SIS) at the University of Kansas in collaboration with AWI ([Hale et al., 2016](#); [Arnold et al., 2019](#)). The 150–600 MHz bandwidth offers an improved vertical resolution in ice and supports up to eight transmit channels (Tx) and 24 receive channels (Rx; Figure 1.8 and Table 1.1). The large number of channels results in the highest transmit power as well as the best cross-track resolution out of all the RDS systems ([Arnold et al., 2019](#)).

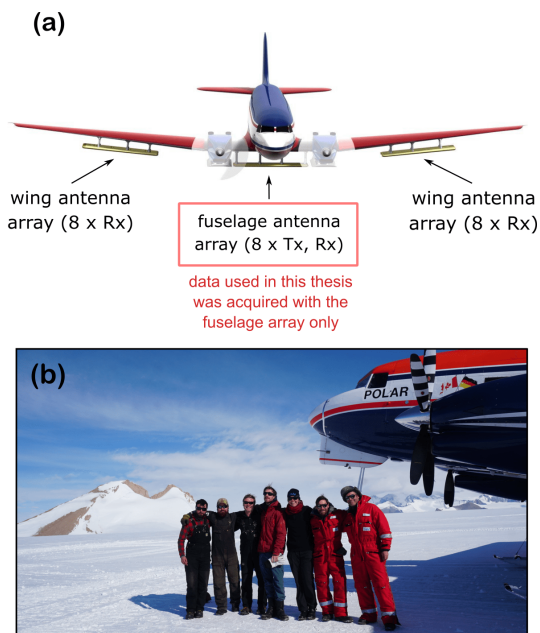


Figure 1.8: AWI UWB radar setup on Polar 6 (a) and field team in Antarctica 2018/19 (b)

Table 1.1: AWI UWB processing and acquisition parameters.

Parameter	Value
frequency	150–600 MHz
Tx channels	8
max. Rx channels	24
Tx power (total)	6000 W
PRF	12 kHz nominal
max. num. waveforms	12
sampling rate	625 or 1250 MSPS*
max data per flight	12 TB
record window	32 000 or 64 000 samples
acquisition modes	sounding (2D) & imaging (3D)
*MSPS = mega samples per second	
acquisition parameters	num. of waveforms pulse length intensity transmission angle
processing parameters	pulse compression SAR processing array processing

The radar can resolve details of the lower ice stratigraphy, which allow new possibilities for the interpretation of englacial structures. In my thesis, I used data from three different surveys of the Greenland campaign 2018 and from one survey in Antarctica in austral summer 2018/19:

1. **EGRIP-NOR-2018**: A survey in the vicinity of the EastGRIP (East Greenland Ice-Core Project) drill site on the Northeast Greenland Ice Stream (NEGIS) (Figure 1.13 a and c). The focus of this survey was to image the ice thickness and bed properties as well as the stratigraphy of the whole ice column, in particular at the ice streams shear margins.
2. **FINEGIS**: A survey in Northern Greenland upstream of the 79°NG (Figure 1.13 a and b). The survey lines cover a set of cylindrical folds, and the aim of the survey was to image the deformation structures of the folds.
3. **JURAS**: A survey at the onset of the Jutulstraumen Glacier, Dronning Maud Land, Antarctica (Figure 1.14). The survey area is located between Troll (Norway) and Kohlen (Germany) station. The focus of the survey was to map the radar stratigraphy perpendicular to ice flow as well as close substantial gaps in the bed topography data.

In the following, I will (i) show how the radar data is acquired and processed to generate high-resolution radargrams, (ii) introduce the methods used to infer the physical conditions and erosional activity at the ice base and (iii) the procedure for the construction and analysis of 3D surfaces of englacial layers.

General workflow of radar data acquisition and processing

Figure 1.9 illustrates the complete workflow starting with the radar data acquisition in the field until the generation of data products, which are used for scientific analysis. The raw radar data as well as GPS positioning data is initially saved on a large raid set of SSD disks on the acquisition server. A backup is created after every flight, either on a second set of SSD disks or on HDD disks. A first so-called *qlook* processing is applied to check the quality and generate first radargrams. Complete SAR processing in the field is usually too time consuming and requires further computational resources.

After a field season, the AWI aircraft team stores all GPS/INS and metadata as well as the data from other instruments (e.g. Laserscanner data) in the DMS archive. UWB raw radar data can be transferred to the AWI servers via the Ground 3 server. A compressed version of the raw data is transferred to the AWI HSM server and stored at the WORM (write once read many) file system. This has the advantage that the raw data is highly protected and cannot be deleted easily. The uncompressed raw data is transferred to the HPC (High Performance Computation) server *Ollie* for full data processing.

The option for parallel processing of the radar data reduces the time needed to generate results. For the processing, we use the CReSIS Toolbox (CReSIS-Toolbox, 2019), developed by the team of John Paden from the Centre for Remote Sensing of Ice Sheets at the University of Kansas. The toolbox generates various types of high-resolution radargrams in the form of matfiles (hd5 format). We can consider three typical types of results:

1. The **qlook** data product, which is an efficiently produced output and only performs stacking (averaging followed by decimation) in the along-track dimension without any kind of migration/focusing in the along-track.
2. The **SAR** data product uses fk-migration to focus scattered energy back to their reflection origin (Leuschen et al., 2000).

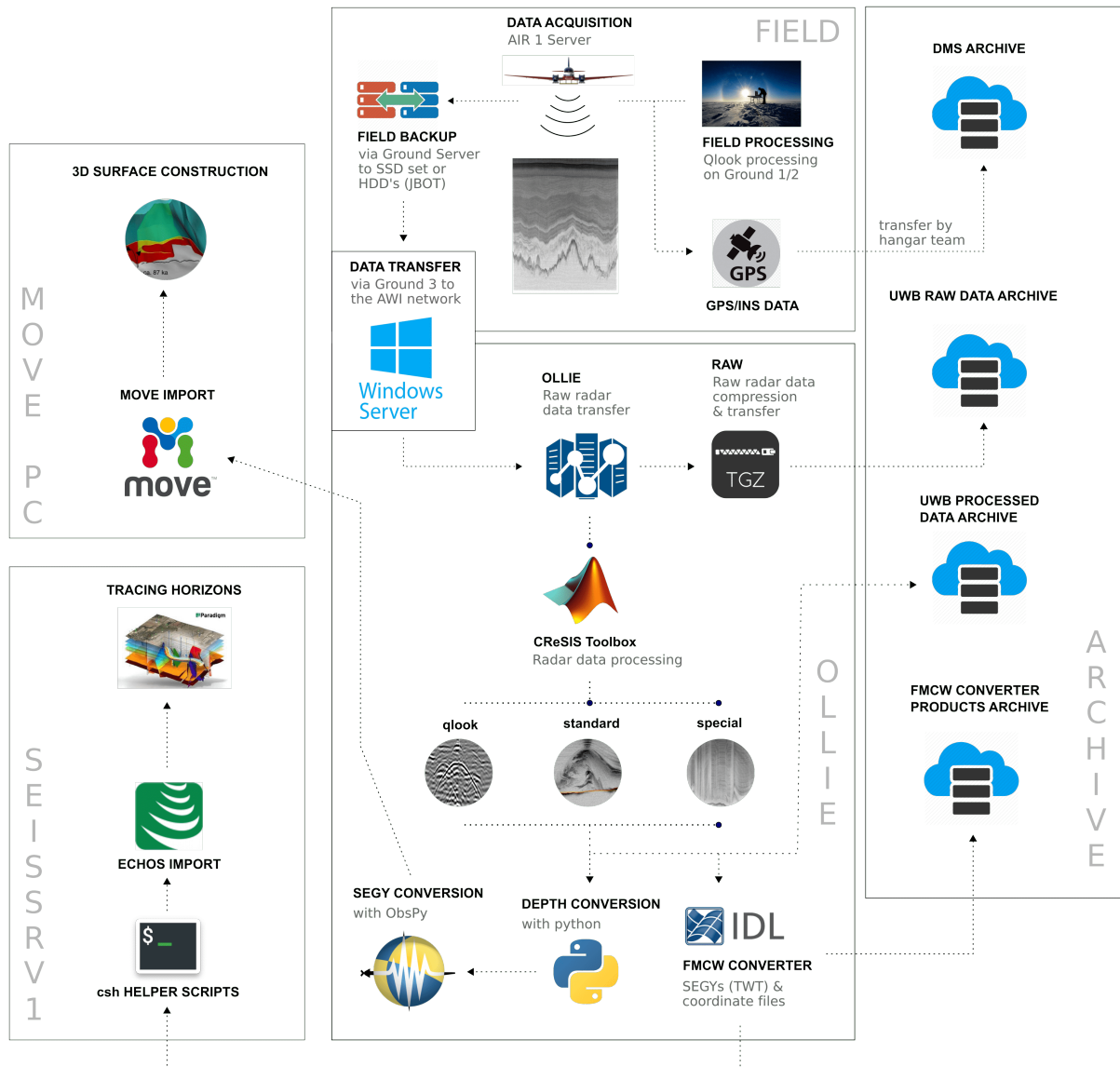


Figure 1.9: Schematic AWI UWB radar data acquisition, data processing and backup storage workflow.

3. With the **special** data product I summarise any data products which are created with a more complex approach and deviate from the two standard products (*qlook* and *SAR* with standard settings). This could be the combination of radargrams from several sub-apertures or results from the 3D imaging processing of the bed topography.

After generating radar data products with the CReSIS Toolbox, I apply two different workflows. The first converts the matfiles in several data formats with an IDL converter, written by Veit Helm (AWI). All files generated in this step are transferred to the data archive on the AWI HSM server (see Figure 1.9). In addition, I save all relevant outputs from the CReSIS Toolbox on this server. A part of the converted files can be used for the import of the radar data into the ECHOS database. A set of helper scripts (by Daniel Steinhage, AWI) can be used to create a script-based automated import to ECHOS. Once the data is imported in ECHOS, it is possible to trace layers, filter or manipulate the radar data.

For the second workflow, I convert the radar data (which are originally available in the TWT domain) to elevation with Python scripts. For this step, it is required that the ice surface

reflection is available and correct. After that, I convert the data to the SEG-Y format to import the files to the Move software. Move is afterwards used to generate 3D surfaces of englacial structures.

1.5 Methods for radar data analysis

In this section, I introduce the methods I apply and describe how they are used to gain information on ice-sheet motion. The focus lies on their general description and how I use them to answer my research questions. For an in-depth description, I refer to the manuscripts in which they are used, as well as to other literature.

Methods

1. Analysis of the geometry/geomorphology of the bed
2. Analysis of reflection patterns and intensities at the bed
3. Analysis of subglacial water transport and ice mass flux
4. Two- and three-dimensional analysis of radar stratigraphy

1. Analysis of the geometry/geomorphology of the ice-sheet bed

The base of a glacier is the most difficult part of an ice sheet to access. At the same time, it contains many of the most important parameters to understand ice flow, such as the geological type of the bed, its ability to deform, the temperature regime and the availability of subglacial water. Next to seismic surveys and *in-situ* information acquired by drilling through the ice, radar surveys are the most effective way to infer the physical properties of the base.

We use the reflection of the ice surface and ice–bed interface in our radar data to calculate the ice thickness and the elevation of the bed topography. As a result, we obtain the bed topography along the flight path of our instrument. I use this purely geometric information to:

- (A) **Create and analyse a digital elevation model (DEM) of bed topography elevation** (see Paper I, III). The bedrock topography is an essential boundary condition for numerical modelling studies of the Greenland and Antarctic Ice Sheet (Bamber et al., 2001). Furthermore, it provides essential information on the large-scale morphology of the bed. Airborne radar data provide bed elevation measurements directly beneath the flight trajectory. Hence, depending on the flight line coverage, major data gaps remain. Therefore, we extrapolate the point measurements to a two-dimensional DEM. The actual resolution depends on the measurement density, which can introduce errors (Morlighem et al., 2019).
- (B) **Analyse the roughness of the bed topography** (see Paper II, III and Figure 1.10 a), which is a geomorphological parametrisation of the undulations of the bed beneath an ice mass (Lindbäck and Pettersson, 2015). It can be determined via statistical analysis of vertical variation in along-track bed topography (e.g. Siegert et al., 2005; Cooper et al., 2019). Basal roughness has become an indicator of subglacial conditions for past ice-flow activity and potential control for current ice-sheet dynamics (Rippin et al., 2014). For this study, we employ a spectral method to analyse the vertical and horizontal roughness with the application of fast Fourier transforms (FFT; Hubbard et al. 2000).
- (C) **Analyse specific subglacial structures, such as subglacial valleys** (Paper III and Figure 1.10 b). Knowledge of their location, extent, and geometry is important to determine the developmental stage for a glacial valley (Hirano and Aniya, 1988). The developmental

stage in combination with the glaciological and geological context helps to investigate the ice-sheet dynamic history of glaciated and previously glaciated landscapes.

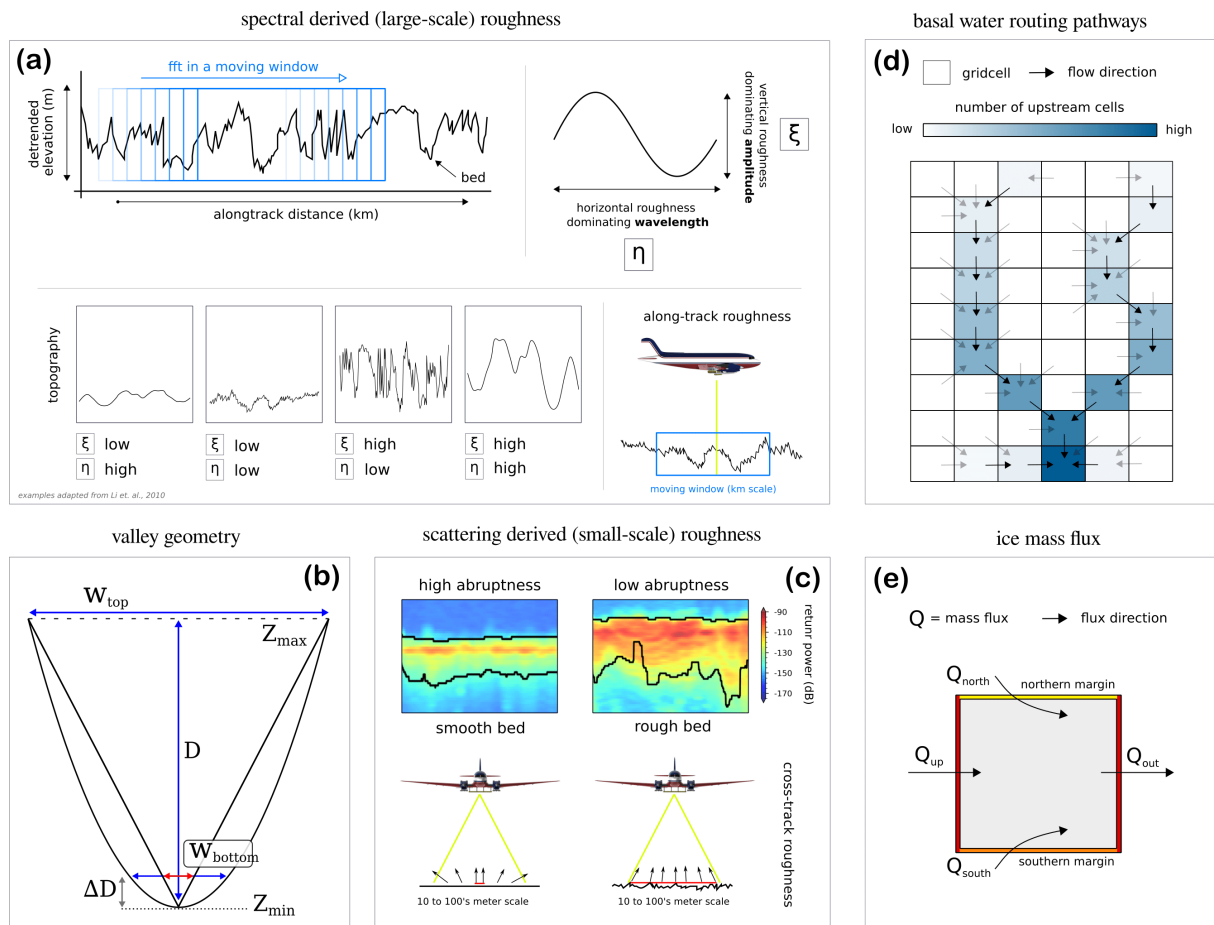


Figure 1.10: Diagram that explains the methods used in this thesis for the analysis of the basal properties. Panel (a) shows the basal roughness derived by the spectral analysis of a detrended bed profile in a moving window. Two parameters characterise the roughness (i) ξ describes the vertical roughness with the dominating amplitude in the MW (moving window), (ii) η provides information about the horizontal roughness with the dominating wavelength. Both parameters are dimensionless and are a relative measures of roughness parallel to the survey line. Examples for different topography settings are shown in the lower part of panel a and are adapted from Li et al. (2010). The sketch in panel (b) indicates the deviation of parameters to describe the geometry of subglacial valleys. Panel (c) shows the waveform scattering derived roughness, which is the ratio between the peak power and integrated power of the bed reflection. High abruptness values indicate a specular reflection, which is interpreted as a smooth bed and low values diffuse scattering, indicating a rough bed. The abruptness parameter is a measure for basal roughness on a finer scale as the spectral roughness approach and provides mainly information for the roughness vertical to the survey line. The principle for basal water routing is shown in (d) and the analysis of mass flux through flux gates at the NEGIS in (e).

2. Analysis of reflection patterns and intensities of the bed

Next to the analysis of the location of the bed elevation, we can obtain valuable information by analysing the waveform characteristics of the bed reflection as well as off-nadir originating signals.

- (A) **Bed return power (BRP)**, which is defined as the reflected (total) energy from the ice–bed interface (Paper II). The analysis of the returned power from the bed can reveal information about the basal conditions (e.g. dry or wet conditions and lithological contrasts). However, retrieving the bed conditions requires the correction of englacial energy losses along the propagation path of the radar wave (Matsuoka et al., 2010).

- (B) **Roughness derived from waveform scattering** (Paper II) describes the relative spread of the bed-echo waveform return (Cooper et al., 2019). The characteristics of the return signal are related to the electromagnetic scattering from the ice–bed interface and therefore provides information about the roughness of the illuminated area (Oswald and Gogineni, 2008; Jordan et al., 2017). Sharp return signals (high abruptness) are in general associated with specular reflections from a smooth interface and diffuse scattered signals (low abruptness) with a rougher interface (see Figure 1.10 c). An important piece of information in this context is the shape of the emitted radar beam. Together with the direction of the roughness of the bed, it is useful to determine the main direction from which we expect scattering reflections.
- (C) **Off-nadir bed reflections** (Paper I). If the shape and width of the radar transmission beam is known, we can use this information to interpret off-nadir reflections. It has to be noted that the direction of signals from along-track will reduce after SAR processing. Hence for the UWB radar system, most off-nadir scatter will arise from cross-track. This information enables us to make further interpretations from, e.g. intersecting radar profiles or continuous off-nadir reflections. Moreover, cross-track off-nadir reflections from the ice-sheet bed can be used to reconstruct strips of ~ 5 km bed topography in high resolution along the flight path. This method is not part of the manuscripts presented here and still under development. An extended description of this method is to be found in Appendix A and B.

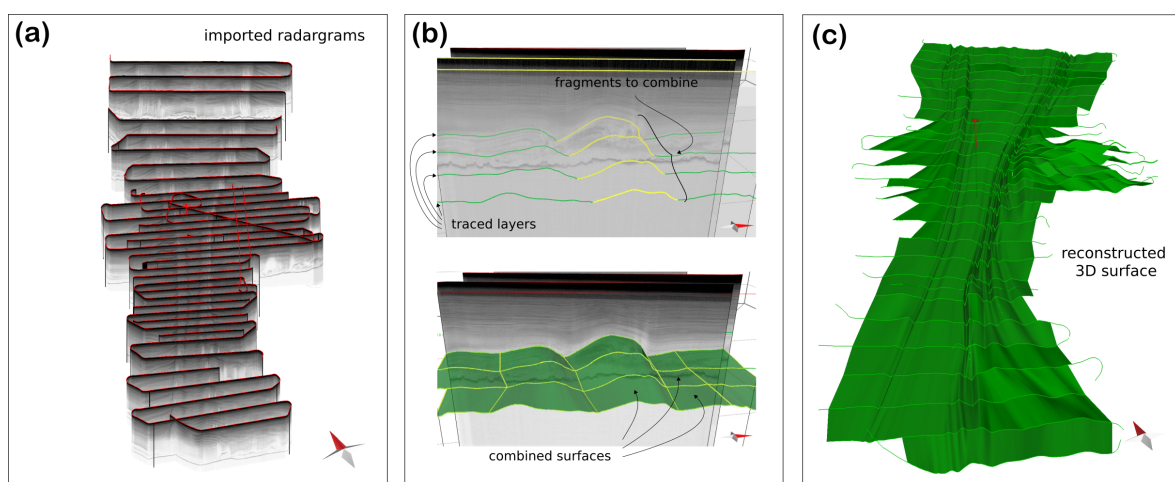


Figure 1.11: Schematic workflow of 3D surface reconstruction from IRHs. (a) shows radargrams transverse to ice flow imported in MOVE. The green lines in the upper part of (b) are traced IRHs of different radargrams and the yellow lines the segments used for interpolation. In the lower part we see the single surfaces created by interpolation. Panel (c) shows the fully reconstructed 3D surface from one layer in the radargrams shown in (a).

3. Analysis of subglacial water transport and ice mass flux

Meltwater is constantly generated beneath the Antarctic and Greenland Ice Sheet and has a strong influence on the resistance at the ice-sheet base (i.e. basal drag) and, thus, speed of ice flow. **Basal water flow routing** (Paper II, IV) indicates where water at the glacier bed would flow according to the gradients of the hydraulic potential, which depends on the bed topography and the overlying ice column. The calculation of the basal water flow routing scheme primarily calculates the upstream accumulation areas (Figure 1.10 d) and is described in detail by, e.g. Le Brocq et al. (2006). Hence, this method does neither represent an observation of the occurrence of

subglacial water, nor does it provide information on quantities of volume or flux. Nonetheless, we can use this information to make extended interpretations of the subglacial environment.

In Paper II we calculate the **ice mass flux** through the trunk and the shear margins of the NEGIS (Figure 1.10 e). The estimation of ice flux through a flow-cross-sectional area (flux gate) depends on the ice surface velocity and an assumption on the vertical ice density and velocity profile. The vertical velocity profile is a valuable parameter and difficult to derive without borehole observations. At the NEGIS, we analyse the thickness evolution of internal layer patches parallel to ice flow and find indications for a decrease of the ice-flow velocity near the ice base, where the bed is rougher (see Figure F.4). Hence, ice flux is not directly a parameter that describes the properties of the bed. However, it relates our findings at the ice base with the ice dynamics of the ice stream. For the ice mass flux calculation, we follow the approach described in Neckel et al. (2012).

4. Two- and three-dimensional analysis of radar stratigraphy

For a three dimensional spatial analysis of internal layers, we apply the method of Bons et al. (2016) and construct 3D surfaces with the model building software MOVETM. Elevation-converted radar data can be imported into MOVE in the SEGY format (Figure 1.11 a). Internal layers, which are visible in all radargrams, can be traced manually and thereafter divided into segments, that show a similar geometry as a segment in an adjacent radargram. The line segments are then interpolated linearly (see Figure 1.11 b). An example of a fully reconstructed 3D surface is shown in Figure 1.11 c. The complete workflow starting with radar data acquisition until the scientific analysis of the 3D surfaces is shown in Figure 1.12. Detailed information on the method and horizons created with this method can be found in Papers VI, VII and VIII.

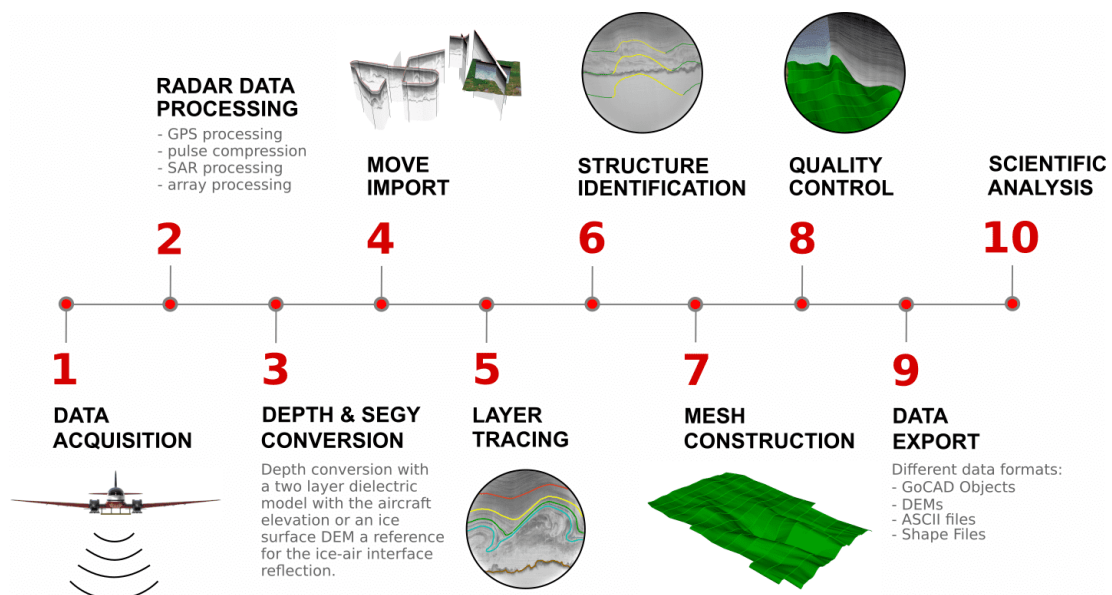


Figure 1.12: Full workflow for 3D surface construction of internal horizons on the basis of radar data (see Papers VI, VII and VIII).

1.6 Study sites and regional overview

The radar data I use in my thesis were obtained from two different regions on the GrIS and one location on the AIS:

1. Upstream region of the 79NG (FINEGIS; Figure 1.13 b). The data in this region are included in Paper VII and VIII.
2. The onset region of the North East Greenland Ice Stream (EGRIP-NOR-2018; Figure 1.13 c). The data of this survey are included in Paper I, II and V – VIII.
3. The onset region of the Jutulstraumen Glacier drainage basin in western Dronning Maud Land, Antarctica (JuRaS; Figure 1.14 b and d). This data set is included in Paper III and IV.

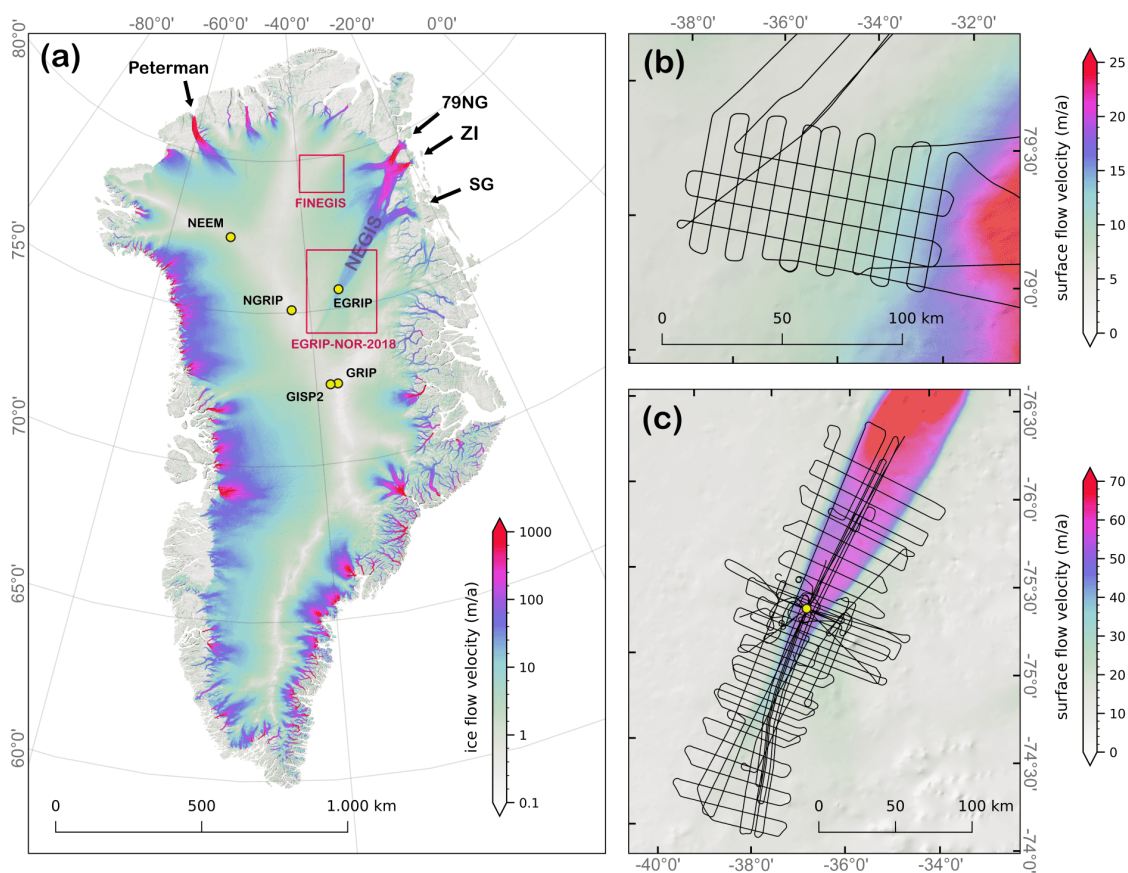


Figure 1.13: Overview of the locations of the two radar survey in Greenland. Panel (a) shows the surface velocity in m a^{-1} on a logarithmic scale (Joughin et al., 2017). The deep drill sites are outlined with yellow circles, the NEGIS and its outled glaciers are indicated with black arrows and the survey area of the (b) FINEGIS survey in northern Greenland and (c) the EGRIP-NOR-2018 survey at the onset of the NEGIS (centred at the EGRIP drill site) are indicated with red rectangles. The ice surface velocities in panel (b) and (c) are shown on a linear scale.

1. Upstream region of the 79NG

The survey region is located in northern Greenland and extends from 79°N to 80°N and from 32°W to 40°W over an area of $\sim 7000 \text{ km}^2$ (Figure 1.13 b). The survey lines are aligned parallel to each other oriented at a bearing angle of 10° (true North) with a spacing of 7.5 km and an average length of $\sim 50\text{--}60 \text{ km}$. Ice thickness in our survey region varies between $\sim 1500 \text{ m}$ to

~ 2250 m, is largest in the Southwest and becomes thinner towards East-Northeast. The bed topography varies between ~ -100 m and 300 m elevation but shows no clear trend in the immediate surrounding of our survey grid. Ice-flow velocity is almost zero in the western part of our survey area at the ice divide and increases up to 15 m a^{-1} in the East (Figure 1.13 b). The horizontal gradient in surface velocity is in general very small and ranges between 0 and 0.1 %.

2. Onset region of the NEGIS

The NEGIS is a prominent feature in northern Greenland and drains $\sim 12\%$ of the ice mass of the GrIS [Rignot and Mouginot \(2012\)](#). The ice stream is more than 600 km long and extends almost up to the ice divide. Ice surface flow velocities range from 10 m a^{-1} at its onset to more than 2000 m a^{-1} at the grounding line of the marine-terminating glaciers ([Mouginot et al., 2017](#)). The ice entering the NEGIS is passing through the well-developed shear margins ([Fahnestock, 2001](#)).

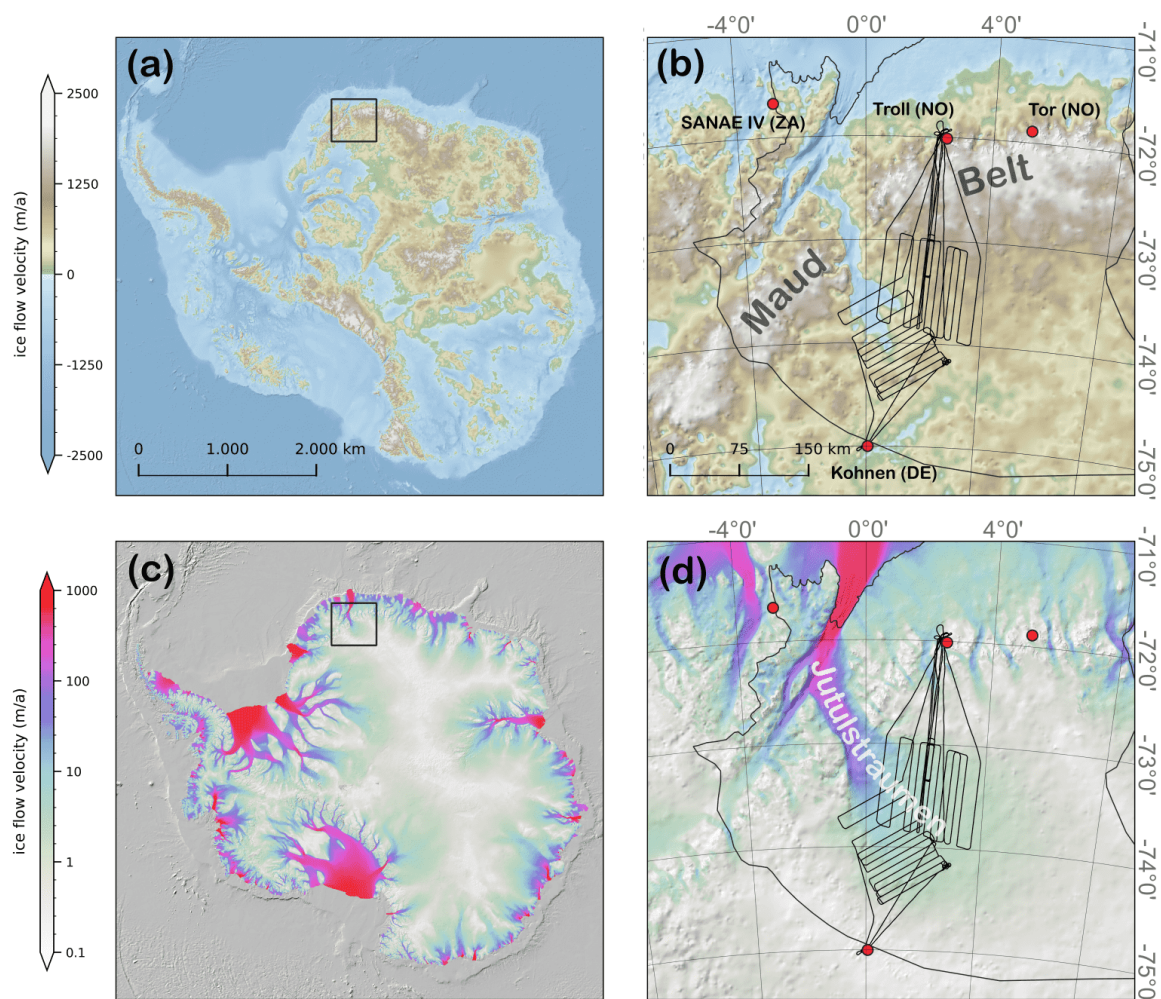


Figure 1.14: Overview of the locations of the two radar survey in Antarctica. Panel (a) and (b) shows the bed topography elevation from [Morlighem et al. \(2019\)](#) and panel (c) and (d) ice-flow velocity from [Mouginot et al. \(2019\)](#).

8 233 km of airborne radar data were recorded on profiles parallel and transverse to the direction of ice flow (Figure 1.13 c). The survey grid is centred at the drill site of the East Greenland Ice-Core Project (EGRIP) and reaches up to 150 km upstream and downstream of the drill site. The survey lines cover the fast-flowing central part of the ice stream, the shear margins as well as the slow-flowing area outside of the ice stream. Survey lines oriented transverse to ice

flow have a spacing of 5 km in the centre of the survey area and 10 km further upstream and downstream. Parallel to flow profiles follow the ice surface flow paths, which were calculated on the basis of the current surface velocity field.

3. Jutulstraumen drainage basin









The Antarctic Jutulstraumen Glacier (JG) is located within a prominent graben system, which separates the geologic provinces of DML. The JG is the largest glacier in DML draining an area of approximately 100 000 km² through the 40–50 km wide Jutulstraumen Graben (Figure 1.14 b). The Graben cuts deep into the Maud Belt through the DML escarpment and reaches down to 1.6 km below present sea level (Fretwell et al., 2013). Ice flow accelerates to up to 760 m a⁻¹ at the grounding line where the JG feeds the Fimbul Ice Shelf (Figure 1.14 d). This part of the DML has been extensively mapped by RES, gravity and magnetic surveys (e.g. Steinhage et al., 2001; Riedel et al., 2012). The survey lines of the UWB survey are located at the onset of JG where ice flow accelerates from 5 to 50 m a⁻¹ (Fig. 1.14 d). The survey lines are divided into two sets and oriented approximately perpendicular to ice flow.

Chapter 2

Summary of scientific contributions

PAPER I

RESEARCH ARTICLE








Franke, S. , Jansen, D. , Binder, T. , Dörr, N. , Helm, V. , Paden, J. , Steinhage D.  and Eisen, O.  (2020). **Bed topography and subglacial landforms in the onset region of the Northeast Greenland Ice Stream.** *Annals of Glaciology*, 61(81) 143-153. <https://doi.org/10.1017/aog.2020.12>

Published online by Cambridge University Press: 18 March 2020

Motivation	The Northeast Greenland Ice Stream (NEGIS) is an integral component of the Greenland Ice Sheet. Ice flow is governed by the geometry and properties of the ice–bed interface, which modulates ice stream dynamics. Hence, the underlying bed topography of the NEGIS is critical to understand and model NEGIS' ice stream dynamics. In this paper, we improve the bed topography at the onset of the NEGIS and investigate the geomorphological structures at the bed with high-resolution airborne radar data.
Conclusion	The data yields a new detailed model of ice-thickness distribution and basal topography. We detect subglacial landforms, which we interpret to be caused by erosional activity of the ice stream, potentially over several glacial–interglacial cycles. Off-nadir reflections from the ice–bed interface in the centre of the ice stream indicate a streamlined bed parallel to ice flow. Our new bed topography model will help to improve the basal boundary conditions of NEGIS prescribed for ice-flow models and thus foster an improved understanding of the ice-dynamic setting.
Own Share 70 %	My own contribution to this paper includes the processing of the radar data from scratch and I traced the bed reflection to calculate ice thickness and bed topography elevation. Moreover, I wrote the paper and took part in the manuscript design. However, I set my own share to 70 %, since the results I used for this paper were preceded by years of preliminary work by Tobias Binder and John Paden, as well as data acquisition in the field by Veit Helm and Daniela Jansen.
Research Questions	This manuscript investigates RQ 1 . We find evidence of how the NEGIS has modified the bed by means of elongated subglacial landforms and local overdeepenings. The subglacial geomorphology exhibits both (i) recent structures that are attributable to the activity of the NEGIS in its present form and (ii) features that would have to have been at least partially entailed in a different ice-sheet configuration. However, we argue that the NEGIS did probably not exist in the current configuration for a very long time (e.g. multiple glacial cycles) due to the absence of an erosional trough.

PAPER II

RESEARCH ARTICLE










Franke, S. , Jansen, D. , Beyer S. , Neckel, N. , Binder, T. , Paden, J.  and Eisen, O.  (2020). **Complex basal conditions and their influence on ice flow at the onset of the Northeast Greenland Ice Stream.** *Journal of Geophysical Research: Earth Surface*, **126**(3), e2020JF005689. <https://doi.org/10.1029/2020JF005689>

Published by the American Geophysical Union: 9 March 2021

Motivation	<p>The motivation for this study is similar to the motivation of Paper I. We pick up on the previous study and focus on the analysis of radar reflections to constrain the ice–bed interface conditions and bulk properties of the subglacial environment. There is still a limited understanding of the spatial variability of subglacial properties in relation to ice flow, in particular to the onset region of the NEGIS. In this paper, we rely on established bed property analysis methods in radioglaciology and apply them on the EGRIP-NOR-2018 radar profiles orientated perpendicular and along ice flow. Finally, we put the bed properties in the context of ice flow and the geometry of the NEGIS and its onset.</p>
Conclusion	<p>Our results indicate a change from a smooth to a rougher bed where the ice stream widens, and a distinct roughness anisotropy, indicating a preferred orientation of subglacial structures. In the upstream region, the excess ice mass flux through the shear margins is balanced by ice-flow acceleration and along-flow stretching of the ice. At the downstream part, the generally rougher bed topography correlates with a decrease in flow acceleration and lateral variations in ice surface velocity. Our findings support the hypothesis that the NEGIS is strongly interconnected to the subglacial water system in its onset region, but also to the subglacial substrate and morphology.</p>
Own Share 80 %	<p>For this paper, I build up on the processing results of Paper I (processed radargrams and bed reflection picks). All results, with the exception of basal water routing pathways and (partly) ice mass flux, were created by myself. I was mainly responsible for the design of the study and entirely for the preparation of the manuscript.</p>
Research Questions	<p>This manuscript investigates mainly RQ 1 and partly RQ 2. We find several indications that the present configuration of the NEGIS in terms of its velocity and extent is related to the properties at the ice–bed interface:</p> <ul style="list-style-type: none"> • The orientation of subglacial landforms, as well as the distribution and anisotropy of basal roughness, is clearly shaped by the activity of the NEGIS. We find a relation between the large-scale roughness at the bed, ice-flow acceleration, mass flux and ice stream width (RQ 1). • A local increase in the basal layer thickness indicates that subglacial roughness as also an effect on the internal radiostratigraphy and has most likely an impact on the vertical velocity profile (RQ 2).

PAPER III

RESEARCH ARTICLE

Franke, S. , Eisermann, H. , Jokat, W. , Eagles, G. , Asseng, J., Miller, H. , Steinhage, D. , Helm, V. , Eisen, O.  and Jansen, D.  (2021). **Pre-Glacial to Present Geomorphological Development of the Jutulstraumen Glacier Basin, Antarctica**¹. **Earth Surface Processes and Landforms**, 1-18. <https://doi.org/10.1002/esp.5203>




Published by John Wiley Sons Ltd.: 14 July 2021.

Motivation	The past ice dynamics of the Antarctic Ice Sheet is poorly constrained because the thick ice cover masks the subglacial environment. Its geomorphological characterization is important because the topography determines where ice builds up, flows and how the ice sheet responds to external forcing. Here, we use an improved radar system to image the bed topography with a fresh eye to investigate the evolution of the subglacial morphology of the Jutulstraumen Glacier drainage system in western Dronning Maud Land, Antarctica.
Conclusion	Our analysis of the bed topography, valley characteristics, and bed roughness leads to the conclusion that much more of the alpine landscape that would have formed prior to the Antarctic ice sheet is preserved than previously anticipated. We identify various geomorphological patterns that can be related to different stages and processes of subglacial erosion. Based on these patterns, we reconstruct the temporal sequence by which ice flow modified the topography since the beginning of the glaciation of Antarctica 34 Ma ago.
Own Share 85 %	I participated in the data acquisition field campaign and processed the radar data. Furthermore, I performed all analysis and results in this study and interpreted the data. The idea for the manuscript was elaborated together with Hannes Eisermann and Wilfried Jokat. All parts of the manuscript, except the geological background were written by myself and discussed and edited by all co-authors.
Research Questions	This manuscript investigates RQ 1 . In contrast to the two previous studies, this manuscript investigates the influence of long-term ice motion since the glaciation of Antarctica. The analysis of subglacial valley geometries reveals how fluvial and glacial erosion have modified the landscape during the last million years. Some of the erosional activity must have taken part during a period of intermediate ice cover. Moreover, we can discriminate presently glaciated regions where ice flow eroded the ice base in the long term and regions where the ice preserved the subglacial environment. Our results are beneficial to validate modelled ice flow and subglacial erosion models.

¹The title of the manuscript changed later during the review process to: "Preserved landscapes underneath the Antarctic Ice Sheet reveal the geomorphological history of Jutulstraumen Basin"

PAPER IV

RESEARCH LETTER

Neckel, N.[†] , Franke, S.[†] , Helm, V. , Drews, R.  and Jansen, D.  (2021). Evidence of cascading subglacial water flow at Jutulstraumen Glacier (Antarctica) derived from DInSAR measurements and ICESat-2 altimetry.














[†] Niklas Neckel and Steven Franke contributed to this paper equally.

In review since 22 May 2021 at: **Geophysical Research Letters**

Motivation	Subglacial lakes and the movement of subglacial water play an important role in the ice dynamics of the Antarctic Ice Sheet. Large quantities of basal meltwater are transported from the interior of the Antarctic Ice Sheet to downstream areas of faster ice flow reducing the frictional resistance at the glacier bed. In this study, we derive short-term vertical ice surface elevation changes by means of differential SAR interferometry in the onset region of the Jutulstraumen Glacier, which we expect to be linked to the subglacial hydrological system.
Conclusion	Our results reveal short-term cascade-like events of subsidence and uplift of the ice surface, which we interpret as a pressure response of drainage and filling of subglacial water basins. This indicates a periodic transport of subglacial water through an interconnected and efficient subglacial drainage system. The water re-location events in this study are first observed in a slow-moving region 225 km upstream of the grounding line. An examination of high-resolution ultra-wideband radar data and the hydropotential gradient reveals that subglacial water is moving downstream along a canyon-like system of local valleys. The water volumes and lake outlines in this study are smaller in comparison to other studies. Furthermore, we observe no horizontal velocity increase correlating with lake filling or drainage events.
Own Share 40 %	The major part of the remote sensing data analysis was performed by Niklas Neckel. Moreover, Veit Helm contributed with ICESat-2 data products. However, the study design, manuscript outline and interpretation of the results were elaborated in equal parts by Niklas Neckel and myself. I participated in the radar data acquisition field campaign and processed the data. All figures were created by myself, and I wrote the manuscript together with Niklas Neckel.
Research Questions	This manuscript investigates RQ 1 . We use the bed reflection signature for multiple reasons to infer the subglacial hydrology system: (i) The improved bed topography provides the constraints on the pathways on subglacial water propagation and confirms that the locations of significant ice surface uplift and subsidence correlate with locally closed topographic depressions. (ii) The intensity of the bed reflection provides no clear evidence for the presence or absence of subglacial water.

PAPER V

DATA DESCRIPTION ARTICLE














Franke, S. , Jansen, D. , Binder, T. , Paden, J. , Dörr N. , Gerber T. , Miller, H. , Dahl-Jensen, D. , Helm V. , Steinhage D. , Weikusat, I. , Wilhelm, F.  and Eisen, O.  (2021). **Airborne ultra-wideband radar sounding over the shear margins and along flow lines at the onset region of the Northeast Greenland Ice Stream.** Earth System Science Data Discussion. <https://doi.org/10.5194/essd-2021-91>

In review since 31 March 2021 at: **Earth System Science Data.**

Motivation	This manuscript is motivated by our interest in making the radar data used in Paper I, II, VI and VII available to the scientific community. We present various data products and describe their characteristics and processing chain in detail. The prospect that parts of the ice core can be rotated back into their correct geographic direction (Westhoff et al., 2020) is a unique possibility for a systematic analysis of ice crystal orientation fabric together with radar data.
Conclusion	This radar data set provides essential observations of internal and bed reflections to determine the spatial distribution of ice thickness, internal layering and reflectivity. These observations constitute boundary conditions and elucidate the properties and processes of the NEGIS.
Own Share 90 %	I developed the outline for the manuscript and wrote the major part with contributions from Nils Dörr and Tamara Gerber. Furthermore, I processed and compiled the data products for publication and created all results and figures. To be transparent, I would like to note that I am not including the data acquisition by Daniela Jansen, John Paden and the Polar6 Team, as well as the years of preparatory work by Tobias Binder in the scope of work here. These were completed for some time, but it has to be acknowledged that the work on this manuscript builds on their efforts.
Research Questions	Due to the fact that this is a data description paper, we do not answer any of the research questions. However, this manuscript presents SAR processed radar data with a wider angular range, which helps to visualize the radar stratigraphy of steeply inclined reflectors. Using this data greatly facilitates answering RQ 2, since more of the internal layers are resolved than in the standard product. Furthermore, the idea behind the manuscript and data release is to answer the research questions in my thesis and more jointly with the scientific community.

PAPER VI

RESEARCH ARTICLE

Jansen, D. , Franke, S. , Bauer, C. C., Binder, T. , Dahl-Jensen, D. , de Riese, T. , Eisen, O. , Llorens, M-G. , Miller, H. , Neckel, N. , Paden, J. D. , Sachau, T. , Weikusat, I. , Zhang, Y. and Bons, P.  (2021). **Interior of the North East Greenland Ice stream reveals that NEGIS-type ice streams may come and go.**

Draft.

Motivation	Localized ice streams drain large portions of the entire Greenland Ice Sheet. It is therefore essential to understand their formation, behaviour, and temporal variability, especially with respect to predicting future sea-level rise. The Northeast Greenland Ice Stream (NEGIS) is by far the longest and largest ice stream in Greenland. Its present ice dynamics are well constrained via remote sensing data. However, it is unclear what processes triggered and control ice flow this far inland. In this study, we present the first 3D analysis of stratigraphic layers from an extensive airborne radar survey at the onset of the NEGIS and show how the deformation history of the ice is recorded in the internal stratigraphy.
Conclusion	The deformation history archived in the ice suggests that the folded layers within the NEGIS system are initiated by convergence and subsequently sheared. By using a novel method for dating folding sequences, we are able to show that the shear margins at the onset of the NEGIS were established ~ 2500 years ago, which marks the timing for the onset of fast flow. Our results lead to the conclusion that, contrary to previous assumptions, the NEGIS has not been stable in its present configuration throughout the Holocene. Our study further shows that ice streams can appear and decay within relatively short periods of time, which has a large impact on ice-sheet stability.
Own Share 25 %	My share in this study includes the processing of radar data from the EGRIP-NOR-2018 campaign (see Paper V) and provided high-resolution radargrams to Paul Bons for the application of the fold-dating scheme. I also created a standardized workflow to efficiently import radar data into the 3D structural geology software MOVE. Furthermore, I traced the stratigraphic layers in the radar data and created the 3D model of the stratigraphic horizons with contributions by Daniela Jansen.
Research Questions	This paper addresses RQ 2 . We use two key aspects of the radar stratigraphy to understand the temporal evolution of the NEGIS: (i) The 3D construction of a stratigraphic horizon. Using this information, we can observe the advection behaviour of existing folds in the NEGIS. (ii) By applying the fold dating method in individual radar profiles, we can estimate when the folds were initially formed and when their growth stopped. From the fact that the folds inside the present shear zone and outside both started to grow at the same time and the folds inside the shear zone stopped growing around 2500 years ago but continued to grow outside the ice stream, we can reconstruct when the NEGIS started to flow in its present configuration.

PAPER VII

RESEARCH ARTICLE

Franke, S. , Bons P. , Westhoff J. , Binder, T. , Streng K., Helm V. , Steinhage D. , Eisen, O. , Paden, J. , Weikusat I. and Jansen, D. (2021). **Indication of ice-stream regime shift in Northeast Greenland.**

Draft.

Motivation	Ice streams are known to exhibit complex spatiotemporal dynamics, which is largely not well understood. A major challenge is the lack of observations on the variability of the temporal dynamics of ice streams of the last thousands of years on contemporary glaciated regions. Here we make use of the geometry of the internal stratigraphy of the Greenland ice sheet, which yields valuable constraints upon its temporal evolution. The stratigraphic record of isochronous layers is shaped by the cumulative deformation sequence of initially surface parallel radar reflectors. Decoding the formation history of these structures offers an excellent possibility to reconstruct past ice movements and draw conclusions about processes on the Earth's surface. Here we use the radiostratigraphic layers from newly acquired and existing radar data in northeastern Greenland to decipher their deformation history.
Conclusion	Our results reveal a deformation sequence pointing to two paleo ice streams reaching far inland into the Greenland ice sheet that nowadays show no ice stream signature in the surface velocity. We propose that (1) a switch from a convergent ice-flow regime to the present surface flow regime with parallel streamlines, including a change in flow direction and (2) a former NEGIS-type ice stream with sharp shear margins, are the most likely scenarios to create the observed structures.
Own Share 70 %	I wrote the main part of the paper and prepared the manuscript with contributions from all co-authors. Furthermore, I processed the ultra-wideband radar data and performed all analyses. All figures in the main document and supplement were generated by myself except for Figure 3, which was generated by Julien Westhoff. I adapted the concept of estimating the timing of the onset of upright fold shearing from Paul Bons and Daniela Jansen and applied it to this data set.
Research Questions	This manuscript addresses RQ 2 . We are able to relate the deformations in the radar stratigraphy of two passive settings to deformation sequences found in two different active ice-dynamic settings: the onset region of the NEGIS, with its sharp shear margins and the convergent ice-flow regime at the onset of the Peterman Glacier. The fold sequences allow further constraints on the approximate time period where changes in the ice-dynamic setting occurred.

PAPER VIII

DATA DESCRIPTION ARTICLE

Franke, S. , Bons P. D. , Mundel F., Sachau, T., Streng K., Weikusat I. , Miller, H. , Binder, T. , Helm V. , Paden, J. , Steinhage D. , Dörr, N. , Eisen, O. , Jansen, D.  (2021). **A 3D view on folded radar stratigraphy in northern Greenland.**

Draft.

Motivation	Englacial stratigraphic layers are interpreted as isochrones (i.e. layers deposited as snow at the same time) and provide insight into the ice-sheet deformation history. During the last decades, continuous progress in the quality and coverage of high-resolution radar data improved the understanding of the englacial stratigraphic architecture of the Greenlandic and Antarctic Ice Sheet. In this manuscript, we publish three data sets of 3D englacial stratigraphic horizons in northern Greenland. The data covers three different ice-dynamic settings in northern Greenland: (i) the onset of the Peterman Glacier (Bons et al., 2016), (ii) a region of deformed stratigraphy close to the ice divide in Northern Greenland (Paper VI) and (iii) the onset of the Northeast Greenland Ice Stream (Paper VII).
Conclusion	Our 3D horizons allow an extended interpretation of fold formation mechanisms, past ice-flow patterns as well as processes at the shear margins of ice streams. We provide an overview of locations and glaciological setting of the 3D stratigraphic horizons, a detailed workflow on how the data were created and data formats.
Own Share 70 %	I created two of the three data sets myself with contributions of Daniela Jansen. The processing includes radar data processing, conversion and import into a structural geology software MOVE, structure identification and 3D horizon construction (see Figure 1.12 and 1.11). The data set at the Peterman Glacier was created by Felicitas Mundel and the team of Paul Bons. I developed the outline of the manuscript, wrote the manuscript and compiled the data set and usage opportunities.
Research Questions	The data presented in this manuscript has been used to analyze RQ 2. A key outcome of this thesis is that a 3D analysis and interpretation of englacial folds in a glaciological context is an important consideration for a comprehensive understanding of present and past ice flow.

Chapter 3

Discussion and outlook

The recent advances in radar data acquisition and processing made it possible to image previously invisible structures in the ice column and in particular details in the near-bed environment of the Greenland and Antarctic Ice Sheet. The studies presented here illustrate the possibilities of how these data can be used to obtain information about the present and paleo ice-flow regimes.

3.1 Ice flow and its imprint in the subglacial environment

The ice sheet bed is difficult to access, yet possibly the most important of all glacier environments. Many decades of research provided an understanding of the main ice-dynamic and subglacial processes responsible for forming the landscape and its relation to erosion and deposition of sediments. In my studies, I use ice-penetrating radar data to obtain information about the subglacial environment and address two key aspects of **RQ 1**: (i) The imprints of ice flow at the onset of the largest ice stream in Greenland (NEGIS) on the ice base and the links between subglacial bed features and ice-flow dynamics of the ice stream. (ii) The modification of the ice base by past ice motion and its reconstruction over several glacial cycles at the Jutulstraumen drainage basin in Antarctica's Dronning Maud Land.

3.1.1 Subglacial geomorphology and its link to the ice dynamics of localised ice flow

Sediments are eroded, transported and deposited beneath ice streams, which creates subglacial landforms (Stokes, 2018). Most of the observations concentrate on nowadays deglaciated regions on- and offshore (e.g. Clark, 1993; Arndt et al., 2020) and only a few on the environment underneath contemporary ice sheets located closely to the glacier terminus (e.g. at the Rutford Ice Stream, Pine Island Glacier or Thwaites Glacier; King et al., 2009; Bingham et al., 2017; Holschuh et al., 2020). In Paper I and II, I find evidence in radar reflections at the ice base that elongated subglacial landforms are present underneath the NEGIS at its onset. Ice-flow velocity in this region is lower in comparison to the previously mentioned studies in Antarctica. Furthermore, they appear almost in the centre of the GrIS more than 600 km upstream of the outlet glaciers. The spatial analysis basal roughness in Paper II shows that streamlining of the bed is restricted to the central part of the NEGIS and is particularly pronounced at moderate ice-flow velocities ($30 - 70 \text{ m a}^{-1}$). Together with the seismic analysis of bed properties performed by Christianson et al. (2014), this leads to the assumption that the subglacial landforms must have been formed by the NEGIS in its present configuration over a longer time period (e.g. hundreds to thousands of years) and that they were formed on a deformable bed. Due to the limited resolution of the bed geometry, it is unfortunately not possible to determine the exact geometry and type (e.g. MSGL, drumlins, crag-and-tails) of the subglacial landforms, as well as estimates of their formation time (Clark, 1993).

A unique feature of the NEGIS is that its onset extends very far towards the interior or the GrIS (Joughin et al., 2001) and its shear zones show no relation to the bed topography in large parts (Morlighem et al., 2017). The analysis of the improved topography of Paper I also shows various large-scale erosion structures. These can be explained by a variable lithology within the ice stream and potentially indicate which regions are covered with sediments. How the location

and type of subglacial landforms is related to the underlying bed properties, is documented by Holschuh et al. (2020) for Thwaites Glacier in Antarctica. If we add to this the finding from Paper II that the roughness in the upstream part of our study area is much smoother than in the downstream part and compare this with the ice-flow velocity and the geometry of the NEGIS, the following ice-dynamic relationship emerges: The upstream part of the NEGIS can accelerate and transport more ice with a smaller width due to its sediment-covered, smooth substrate. In the downstream part, the ice stream becomes wider, which correlates with higher roughness and lower ice thickness. Although it is not clear at this point whether the properties of the bed initiated the NEGIS or the influence of the NEGIS shaped the bed as we find it today, both components are clearly intertwined.

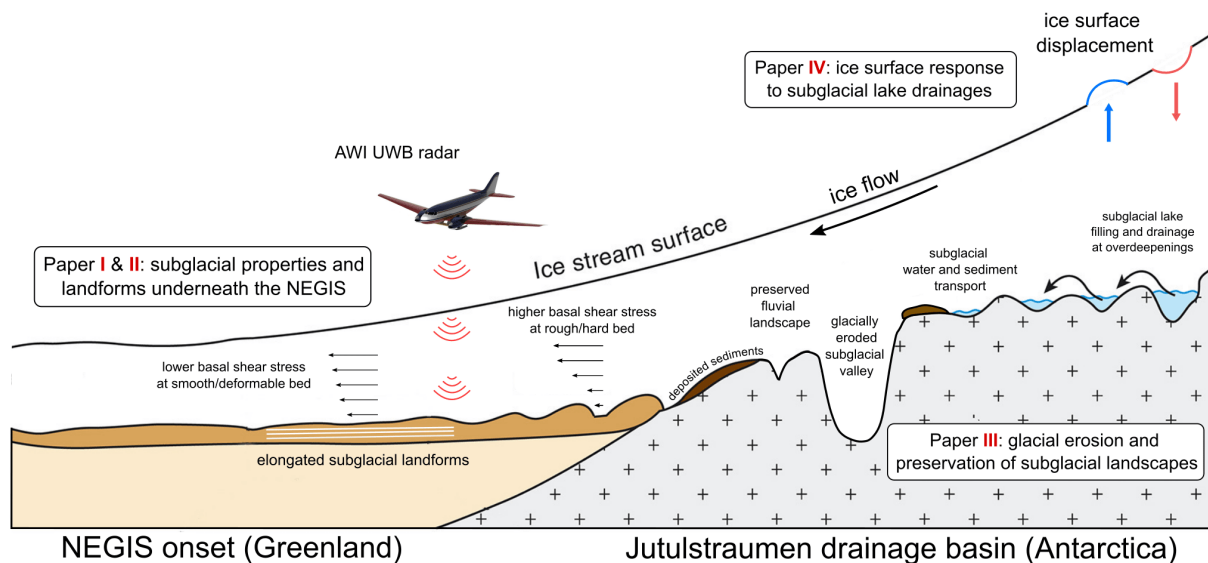


Figure 3.1: Simplified cartoon illustration of radar soundings over the subglacial environments in Greenland and Antarctica. The figure resembles some of the key the subglacial landscapes and processes described in Paper I–IV and how they are connected as a whole in the ice stream system. The original image is from Stokes (2018) and modified.

3.1.2 Reconstruction and modification of the ice base by former ice flow

The history of landscape evolution and pattern of glacial erosion are archived in the subglacial geomorphology (Jamieson et al., 2010). In the second part of studies (III and IV), we will examine how the processes just described at the base of ice streams have left traces in the bed topography over millions of years and how they can be used to reconstruct historical ice movements. The glacial behaviour of the Antarctic Ice Sheet can be investigated by studying the deglaciated regions in the northern hemisphere and alpine glaciers (e.g. Siegert et al., 2005; Taylor et al., 2004). Due to the different stages of ice-sheet growth and decay, we are able to identify erosion patterns of fluvial or alpine regimes in places that are now covered by a thick column of nearly stagnant ice. In Paper III, we investigate the evolution of the subglacial morphology of the Jutulstraumen Glacier drainage system in western Dronning Maud Land (Antarctica). The present ice-flow regime consists of converging ice flow through a single passage towards the ocean. Ice flow at the margins of the drainage system is presently stagnant, but the ice base at these locations reveals subglacial structures are yielding an efficient paleo ice-flow regime. A combination of analysis techniques of the radar bed reflection (e.g. the roughness of the bed, hypsometry, the pre-glacial fluvial system and subglacial valley geometries) allows to systematically categorise regions of particular developmental stages of fluvial and glacial erosion over multiple cycles. For example, we find regions that are fluvially imprinted but have been largely protected from

successive selective glacial erosion or scouring. In another region, we find signs of selective linear erosion, indicating an ice-dynamic regime with much lower ice thickness and different ice-flow direction than today.

My previous work focused exclusively on the analysis of ice-penetrating radar data. However, there is also the possibility to include other remote sensing methods in order to study subglacial processes. In Paper IV, we use differential InSAR to detect vertical displacements of the ice surface. In combination with the information about the bed topography from the radar data, we conclude that the surface motions are caused by a pressure response due to the transport of subglacial meltwater (Gray et al., 2000). From the data, we can infer where the water flows along and that it pools in topographically closed depressions (also referred to as overdeepenings) before being transported further. Subglacial water transport in itself is not necessarily responsible for deep erosion but for the movement of sediments below the ice (Alley et al., 2019). However, a much more interesting aspect emerges when the situation is viewed from a certain distance. The depressions in which the subglacial water collects and causes a particularly strong uplift and subsidence of the ice surface must have been formed by erosional processes at some point in the past. For these specific locations, we can therefore assume that most likely alpine glaciers under a much thinner ice layer have caused these depressions.

The results presented in Paper I–IV provide significant insights for the detection and interpretation of contemporary and paleo ice-flow landforms and their relation to the ice dynamics. I show that landform location, size, shape and distribution are either related to the present ice-flow regime or the consequence of historic ice-flow activity. Investigating ice stream beds at higher resolution is an important step towards developing an understanding of the time scales and what processes generate subglacial landforms.

3.2 Past ice-flow patterns captured in the englacial deformation history

High-resolution radar data do provide not only a detailed image of the glacier base but also insight into the internal layering architecture of an ice sheet. Deformed internal layers are an indicator for past ice-flow activity and reveal large perturbations with no apparent link to the underlying bed geometry (Bons et al., 2016). This section investigates RQ2 and consists of two manuscripts focusing on the derivation and reconstruction of ice-flow patterns in Northeast Greenland (Papers VI and VII) and the implications for the future of the Greenland Ice Sheet. In addition, two further manuscripts are included that publish the data from these and other studies (following the FAIR data principles; Wilkinson et al. 2016) and address both the methods behind the creation of the data sets and their description and value to the scientific community (Papers V and VIII).

Contemporary ice-flow regimes are very well captured by satellite remote sensing data (e.g. Joughin et al., 2017), but less is known about the temporal evolution of ice streams. To reconstruct the former evolution of ice-flow regimes, we consider folded radar isochrones as passive traces for cumulative deformation. The range of studies on the mechanisms that cause large-scale folds in ice sheets has become more abundant in the past decade (Wolovick et al., 2014; Leysinger Vieli et al., 2018; Bons et al., 2016). This is mainly due to the improved coverage and quality of radar data from Operation Ice Bridge by NASA and the Center for Remote Sensing of Ice Sheets (CReSIS) at the University of Kansas (see MacGregor et al.; Leuschen et al., 2010; Li et al., 2013), and is being complemented by data from AWI in the studies presented here. Overall, three basic processes can be hypothesised for the formation of large-scale folds in the ice:

1. **Variations in basal sliding:** The development of large complex stratigraphic folds has

been investigated by [Wolovick et al. \(2014\)](#). According to their simulations, the genesis of large folded and overturned structures in the radar stratigraphy are governed by deformation caused by heterogeneous and time-variable basal sliding.

2. **Basal freeze-on and ice flow:** [Leysinger Vieli et al. \(2018\)](#) simulated the genesis of large plume-like internal structures by basal freeze-on and ice-flow modelling. The authors find a good agreement between their simulations and the radar observations and highlight that the height of the folds is primarily a function of ice-flux and secondarily depends on freeze-on processes.
3. **Convergent ice flow:** [Bons et al. \(2016\)](#) established a conceptual model for the formation processes of cylindrical folds sub-parallel to ice flow. Their modelling shows that these folds can be formed by lateral compression, where mechanical anisotropy plays a major role.

Each of the three mechanisms presented produces folds under a specific glaciological setting and depends on, e.g. the conditions at the glacier bed and ice-flow characteristics. In Paper VII, I discuss all three variants and evaluate the arguments for and against creating the fold structures presented. While [Leysinger Vieli et al. \(2018\)](#) shows that the generation of large plume-like folds is possible with basal freeze-on and ice flow, it seems unlikely that freeze-on would raise the localised areas where we observe the cylindrical anticlines. Moreover, freeze-on cannot explain synclines. However, since freeze-on still can happen, it might be a contributing mechanism for the elevation of anticlines. Therefore, we argue that mechanical folding due to horizontal shortening (due to convergent flow) is the most likely mechanism for initial fold formation (see Figure 3.2 a) for the features shown in Paper VII in northern Greenland.

It has been proven that to have a three-dimensional idea of the location and orientation of the fold axis and the direction of overturning is of particular importance. This information, together with an estimate of the basal conditions and how the ice flow would have been organised over the past thousands of years, was the ultimate reason why we considered that it most likely that convergent flow in the direction of the major outlets in northeast Greenland must have been the cause of the initiation of the folds (Figure 3.2 a).

For the interpretation of deformations in the radar stratigraphy, three different approaches emerge (see Figure 3.2):

- (a) For the case of large overturned folds as in Paper VII, we can divide the deformation process into two subprocesses, assuming the past ice-flow direction is parallel to the fold axis. In the first stage, upright folds are created by convergent flow (e.g. as in the current ice-flow regime at Peterman Glacier; [Bons et al. 2016](#)). A change in the flow regime subsequently shears the radar layers, as long as a component of the flow field is oriented perpendicular to the fold axis (Figure 3.2 a).
- (b) For the second case in Paper VII, I do not use a direct reconstruction based on radar stratigraphy. In principle, I only use the recurring pattern of densely folded radar layers in radargrams and compare them with those of an existing active ice stream (the NEGIS; see findings in Paper VI and Figure 3.2 b).
- (c) For the third approach, we return to the folds in the shear zone, but not to conclude that there was once an ice stream. The approach essentially builds on approach (a) by subsequent shearing of folds initiated by convergent flow due to increasing flow velocity to such an extent that their amplitude does not increase further, but the wavelength is greatly reduced (Figure 3.2 c).

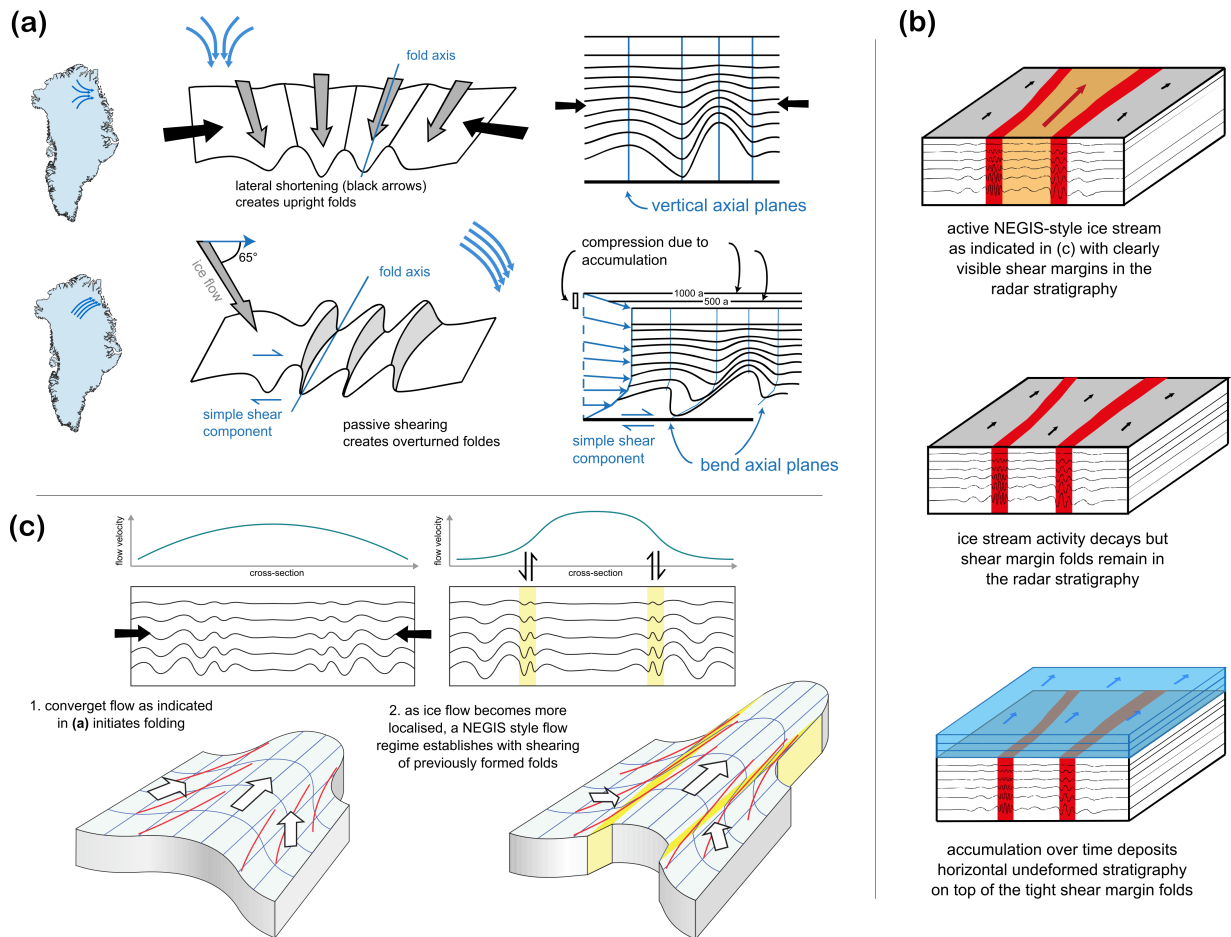


Figure 3.2: Ice-flow reconstruction methods based on radar stratigraphy. Panel (a) and (b) refer to the ice-flow reconstructions presented in Paper VII and panel (c) illustrate the formation of the radar signature in the shear margins of the NEGIS (Paper VI).

The results of Paper VI and VII also have relevant implications for the discussion of the emergence of NEGIS. The hypothesis of Fahnestock (2001) assumes that exceptionally high geothermal heat flux at the onset of the NEGIS is responsible for its formation. This is theoretically possible, as seen in the study by Smith-Johnsen et al. (2019), but the assumptions about the required geothermal heat flow exceed the geologically conceivable processes by a factor of ~ 10 (Bons et al., 2021). The argumentation of an increased geothermal or basal heat flux becomes especially void if we look at the situation further north in Greenland. In Paper VII, we have reconstructed an ancient ice stream similar to NEGIS in its general form with clearly defined shear zones. The possibility that an extreme geothermal heat flow anomaly at the base was also responsible for its formation there can be considered very unlikely.

Both studies indicate that the Greenland Ice Sheet is subject to frequent re-organisation in ice transportation. The observations and conclusions made in Paper VI and VII fit into the argumentation of Stokes et al. (2016), who argues that the location and intensity of the ice stream is linked to the geometry changes of the ice sheet. Hence, ice streams in NE Greenland can appear and decay in relatively short timescales (thousands of years) and were not stable during the Holocene. From here on, it is important to understand the underlying mechanisms of the re-organisation of ice flow in order to make more reliable predictions for the future response of the ice sheets to global warming.

3.3 Perspectives

Rapidly flowing and far-inland reaching ice streams are a key component of the Greenland and Antarctic Ice Sheet. Their importance is increasingly being recognised in the ice-sheet mass balance and their subsequent impacts on sea-level changes (Choi et al., 2021). It has become clear that the internal structure within and the geomorphology beneath ice streams is unique and that their flow characteristics are governed by ice-internal mechanisms and processes at the ice–bed interface (Stokes, 2018; Schoof and Mantelli, 2021). Understanding where, why, and how ice streams and their geomorphology originate and evolve is critical to understanding and comprehensively modelling ice flow.

Although there is a detailed knowledge of the subglacial morphology underneath ice streams and an improved knowledge on the distribution of sediments, basal water and shear stresses, our understanding of the processes at the ice-sheet bed is still limited (Stokes, 2018). Furthermore, there is uncertainty about accurate subglacial erosion rates, which is one of the key processes, which shaped the Earth's surface. Cook et al. (2020) started to establish an empirical relation between glacier sliding and erosion rates from a compilation of 38 glaciers. In this context, we must keep in mind that the possibilities for studying these alpine glaciers are limited. Today they are the laboratories to study fundamental glaciological processes, but soon they will disappear completely, depending on the development of the global climate. As for ice streams, the future usage of much more efficient and high-resolution ice-sheet bed mapping techniques such as via radar swath tomography (see Holschuh et al. (2020) and Appendix B) is a promising method that will greatly improve the resolution at the ice base.

From the findings presented in this thesis, it is clear that radar reflections in ice sheets can be used in a variety of ways to reconstruct and characterize ice flow. In Greenland, although many large-scale folds have been mapped by radar surveys (see Leysinger Vieli et al., 2018), it is unclear for most of them how these structures are related to each other. Further efforts such as those in Paper VI and VII and the work of Bons et al. (2016) and Streng (2019) are the first steps toward a coherent understanding of deformations in Greenland's Ice Sheet. In addition, there is a major effort to model localised ice streams (e.g. Schoof and Mantelli, 2021), which are most likely a major driver of folding (Bons et al., 2016). In this context, the comparison of modelling results and the underlying processes and input parameters with geophysical observations will play a central role. Another important factor will be the integration of these results into the overall Earth system to evaluate how plausible these results are in a different context (see the study of Fahnestock (2001), Smith-Johnsen et al. (2019) and the comment of Bons et al. (2021) regarding the proposed exceptionally high geothermal heat flux).

Bibliography

- Allen, C. R., Kamb, W. B., Meier, M. F., and Sharp, R. P. Structure of the lower blue glacier, Washington. *The Journal of Geology*, 68(6):601–625, 1960. doi: 10.1086/626700. URL <https://doi.org/10.1086/626700>.
- Allen, C. T., Mozaffar, S. N., and Akins, T. L. Suppressing coherent noise in radar applications with long dwell times. *IEEE Geoscience and Remote Sensing Letters*, 2(3): 284–286, July 2005. doi: 10.1109/LGRS.2005.847931. URL <http://dx.doi.org/10.1109/LGRS.2005.847931>.
- Alley, R. B., Cuffey, K. M., and Zoet, L. K. Glacial erosion: status and outlook. *Annals of Glaciology*, 60(80):1–13, 2019. doi: 10.1017/aog.2019.38.
- Allison, I., Alley, R., Fricker, H., Thomas, R., and Warner, R. Ice sheet mass balance and sea level. *Antarctic Science*, 21(5):413–426, 2009. doi: 10.1017/S0954102009990137. URL <https://doi.org/10.1017/S0954102009990137>.
- Anandakrishnan, S. and Alley, R. B. Tidal forcing of basal seismicity of ice stream c, west Antarctica, observed far inland. *Journal of Geophysical Research: Solid Earth*, 102(B7):15183–15196, 1997. doi: <https://doi.org/10.1029/97JB01073>. URL <https://agupubs.onlinelibrary.wiley.com/doi/abs/10.1029/97JB01073>.
- Arndt, J. E., Larter, R. D., Hillenbrand, C.-D., Sørli, S. H., Forwick, M., Smith, J. A., and Wacker, L. Past ice sheet–seabed interactions in the northeastern Weddell Sea embayment, Antarctica. *The Cryosphere*, 14(6):2115–2135, 2020. doi: 10.5194/tc-14-2115-2020. URL <https://tc.copernicus.org/articles/14/2115/2020/>.
- Arnold, E., Leuschen, C., Rodriguez-Morales, F., Li, J., Paden, J., Hale, R., and Keshmiri, S. CReSIS airborne radars and platforms for ice and snow sounding. *Annals of Glaciology*, pages 1–10, Nov 2019. doi: 10.1017/aog.2019.37. URL <https://doi.org/10.1017/aog.2019.37>.
- Aschwanden, A., Fahnestock, M. A., Truffer, M., Brinkerhoff, D. J., Hock, R., Khroulev, C., Mottram, R., and Khan, S. A. Contribution of the Greenland Ice Sheet to sea level over the next millennium. *Science Advances*, 5(6), 2019. doi: 10.1126/sciadv.aav9396. URL <https://advances.sciencemag.org/content/5/6/eaav9396>.
- Bader, H. The Greenland ice sheet. *Hanover, NH, U.S. Army Cold Regions Research and Engineering Laboratory*, (1), 1961. URL <https://erdc-library.erdcdren.mil/jspui/bitstream/11681/2674/1/CRREL-Mono-1-B2.pdf>.
- Bailey, J. T., Evans, S., and Robin, G. d. Q. Radio Echo Sounding of Polar Ice Sheets. *Nature*, 204(4957):420–421, 1964. ISSN 1476-4687. doi: 10.1038/204420a0. URL <https://doi.org/10.1038/204420a0>.
- Bamber, J. L., Vaughan, D. G., and Joughin, I. Widespread complex flow in the interior of the Antarctic ice sheet. *Science*, 287(5456):1248–1250, 2000. ISSN 00368075. doi: 10.1126/science.287.5456.1248. URL <http://dx.doi.org/10.1126/science.287.5456.1248>.
- Bamber, J. L., Layberry, R. L., and Gogineni, S. P. A new ice thickness and bed data set for the Greenland ice sheet: 1. measurement, data reduction, and errors. *Journal of Geophysical Research: Atmospheres*, 106(D24):33773–33780, 2001. doi: <https://doi.org/10.1029/2001JD900054>. URL <https://agupubs.onlinelibrary.wiley.com/doi/abs/10.1029/2001JD900054>.
- Bamber, J. L., Griggs, J. A., Hurkmans, R. T. W. L., Dowdeswell, J. A., Gogineni, S. P., Howat, I., Mouginot, J., Paden, J., Palmer, S., Rignot, E., and Steinhage, D. A new bed elevation dataset for Greenland. *Cryosphere*, 7(2): 499–510, 2013. ISSN 19940416. doi: 10.5194/tc-7-499-2013. URL <http://dx.doi.org/10.5194/tc-7-499-2013>.
- Bell, R. E., Ferraccioli, F., Creyts, T. T., Braaten, D., Corr, H., Das, I., Damaske, D., Frearson, N., Jordan, T., Rose, K., Studinger, M., and Wolovick, M. Widespread Persistent Thickening of the East Antarctic Ice Sheet by Freezing from the Base. *Science*, 331(6024):1592–1595, Mar 2011. doi: 10.1126/science.1200109. URL <https://doi.org/10.1126/science.1200109>.
- Bell, R. E., Tinto, K., Das, I., Wolovick, M., Chu, W., Creyts, T. T., Frearson, N., Abdi, A., and Paden, J. D. Deformation warming and softening of Greenland’s ice by refreezing meltwater. *Nature Geoscience*, 7(7):497–502, Jun 2014. doi: 10.1038/ngeo2179. URL <https://doi.org/10.1038/ngeo2179>.
- Benn, D. and Evans, D. *Glaciers and glaciation*, 2nd edition. *Routledge*, 2010. doi: 10.4324/9780203785010. URL <https://doi.org/10.4324/9780203785010>.
- Bennett, M. R. Ice streams as the arteries of an ice sheet: their mechanics, stability and significance. *Earth-Science Reviews*, 61(3):309–339, 2003. ISSN 0012-8252. doi: 10.1016/S0012-8252(02)00130-7. URL <https://www.sciencedirect.com/science/article/pii/S0012825202001307>.
- Bingham, R. G. and Siegert, M. J. Quantifying subglacial bed roughness in Antarctica: implications for ice-sheet dynamics and history. *Quaternary Science Reviews*, 28(3-4):223–236,

- feb 2009. doi: 10.1016/j.quascirev.2008.10.014. URL <https://doi.org/10.1016%2Fj.quascirev.2008.10.014>.
- Bingham, R. G., King, E. C., Smith, A. M., and Pritchard, H. D. Glacial geomorphology: Towards a convergence of glaciology and geomorphology. *Progress in Physical Geography: Earth and Environment*, 34(3):327–355, 2010. doi: 10.1177/0309133309360631. URL <https://doi.org/10.1177/0309133309360631>.
- Bingham, R. G., Vaughan, D. G., King, E. C., Davies, D., Cornford, S. L., Smith, A. M., Arthern, R. J., Brisbourne, A. M., Rydt, J. D., Graham, A. G. C., Spagnolo, M., Marsh, O. J., and Shean, D. E. Diverse landscapes beneath Pine Island Glacier influence ice flow. *Nature Communications*, 8(1), nov 2017. doi: 10.1038/s41467-017-01597-y. URL <https://doi.org/10.1038%2Fs41467-017-01597-y>.
- Bons, P. D., Jansen, D., Mundel, F., Bauer, C. C., Binder, T., Eisen, O., Jessell, M. W., Llorens, M.-G., Steinbach, F., Steinhage, D., and Weikusat, I. Converging flow and anisotropy cause large-scale folding in Greenland's ice sheet. *Nature Communications*, 7(1), apr 2016. doi: 10.1038/ncomms11427. URL <https://doi.org/10.1038%2Fncomms11427>.
- Bons, P. D., de Riese, T., Franke, S., Llorens, M.-G., Sachau, T., Stoll, N., Weikusat, I., Westhoff, J., and Zhang, Y. Comment on “exceptionally high heat flux needed to sustain the northeast greenland ice stream” by smith-johnsen et al. (2020). *The Cryosphere*, 15(5):2251–2254, 2021. doi: 10.5194/tc-15-2251-2021. URL <https://tc.copernicus.org/articles/15/2251/2021/>.
- Broecker, W. Massive iceberg discharges as triggers for global climate change. *Nature*, 372(6505):421–424, 1994. URL <http://www.nature.com/articles/372421a0%7D0Apapers3://publication/doi/10.1038/372421a0>.
- Cavitte, M. G. P., Blankenship, D. D., Young, D. A., Schroeder, D. M., Parrenin, F., Lemeur, E., MacGregor, J. A., and Siegert, M. J. Deep radiostratigraphy of the east antarctic plateau: connecting the dome c and vostok ice core sites. *Journal of Glaciology*, 62(232):323–334, 2016. doi: 10.1017/jog.2016.11. URL <https://doi.org/10.1017/jog.2016.11>.
- Choi, Y., Morlighem, M., Rignot, E., and Wood, M. Ice dynamics will remain a primary driver of greenland ice sheet mass loss over the next century. *Communications Earth & Environment*, 2(1):26, Feb 2021. ISSN 2662-4435. doi: 10.1038/s43247-021-00092-z. URL <https://doi.org/10.1038/s43247-021-00092-z>.
- Christianson, K., Peters, L. E., Alley, R. B., Anandakrishnan, S., Jacobel, R. W., Riverman, K. L., Muto, A., and Keisling, B. A. Dilatant till facilitates ice-stream flow in northeast Greenland. *Earth and Planetary Science Letters*, 401:57–69, sep 2014. doi: 10.1016/j.epsl.2014.05.060. URL <https://doi.org/10.1016%2Fj.epsl.2014.05.060>.
- Church, J. A. and White, N. J. A 20th century acceleration in global sea-level rise. *Geophysical Research Letters*, 33(1), 2006. doi: <https://doi.org/10.1029/2005GL024826>. URL <https://agupubs.onlinelibrary.wiley.com/doi/abs/10.1029/2005GL024826>.
- Church, J. A., Clark, P., Cazenave, A., Gregory, J., Jevrejeva, S., Levermann, A., Merrifield, M., Milne, G., Nerem, R., Nunn, P., Payne, A., Pfeffer, W., Stammer, D., and Unnikrishnan, A. 2013: Sea level change. In *Climate Change 2013: The Physical Science Basis. Contribution of Working Group I to the Fifth Assessment Report of the Intergovernmental Panel on Climate Change*, pages 1137–1216. 2013. ISBN ISBN 978-1-107-66182-0. doi: 10.1017/CB09781107415315.026. URL <http://dx.doi.org/10.1017/CB09781107415315.026>.
- Clark, C. D. Mega-scale glacial lineations and cross-cutting ice-flow landforms. *Earth Surface Processes and Landforms*, 18(1):1–29, 1993. doi: <https://doi.org/10.1002/esp.3290180102>. URL <https://onlinelibrary.wiley.com/doi/abs/10.1002/esp.3290180102>.
- Clark, P. U., Dyke, A. S., Shakun, J. D., Carlson, A. E., Clark, J., Wohlfarth, B., Mitrovica, J. X., Hostetler, S. W., and McCabe, A. M. The last glacial maximum. *Science*, 325(5941):710–714, 2009. doi: 10.1126/science.1172873. URL <https://science.sciencemag.org/content/325/5941/710>.
- Clarke, G. K. C., Nitsan, U., and Paterson, W. S. B. Strain heating and creep instability in glaciers and ice sheets. *Reviews of Geophysics*, 15(2):235–247, 1977. doi: <https://doi.org/10.1029/RG015i002p00235>. URL <https://agupubs.onlinelibrary.wiley.com/doi/abs/10.1029/RG015i002p00235>.
- Conway, H., Catania, G., Raymond, C. F., Gades, A. M., Scambos, T. A., and Engelhardt, H. Switch of flow direction in an Antarctic ice stream. *Nature*, 419(6906):465–467, oct 2002. ISSN 0028-0836. doi: 10.1038/nature01081. URL <http://www.nature.com/articles/nature01081>.
- Cook, S. J. and Swift, D. A. Subglacial basins: Their origin and importance in glacial systems and landscapes. *Earth-Science Reviews*, 115(4):332 – 372, 2012. ISSN 0012-8252. doi: <https://doi.org/10.1016/j.earscirev.2012.09.009>. URL <http://www.sciencedirect.com/science/article/pii/S0012825212001286>.

- Cook, S. J., Swift, D. A., Kirkbride, M. P., Knight, P. G., and Waller, R. I. The empirical basis for modelling glacial erosion rates. *Nature Communications*, 11(1):759, Feb 2020. ISSN 2041-1723. doi: 10.1038/s41467-020-14583-8. URL <https://doi.org/10.1038/s41467-020-14583-8>.
- Cooper, M. A., Jordan, T. M., Schroeder, D. M., Siegert, M. J., Williams, C. N., and Bamber, J. L. Subglacial roughness of the Greenland Ice Sheet: relationship with contemporary ice velocity and geology. *The Cryosphere*, 13(11): 3093–3115, nov 2019. doi: 10.5194/tc-13-3093-2019. URL <https://doi.org/10.5194/tc-13-3093-2019>.
- CRISIS-Toolbox. J. Paden, URL: https://ops.cresis.ku.edu/wiki/index.php/Main_Page, accessed: 2019-06-01, 2019. URL https://ops.cresis.ku.edu/wiki/index.php/Main_Page.
- Dall, J., Corr, H. F. J., Walker, N., Rommen, B., and Lin, C. Sounding the antarctic ice sheet from space: a feasibility study based on airborne p-band radar data. In *IGARSS 2018 - 2018 IEEE International Geoscience and Remote Sensing Symposium*, pages 4142–4145, 2018. doi: 10.1109/IGARSS.2018.8518826. URL <https://doi.org/10.1109/IGARSS.2018.8518826>.
- Dowdeswell, J. A., Canals, M., Jakobsson, M., Todd, B. J., Dowdeswell, E. K., and Hogan, K. A. The variety and distribution of submarine glacial landforms and implications for ice-sheet reconstruction. *Geological Society, London, Memoirs*, 46(1):519–552, 2016. ISSN 0435-4052. doi: 10.1144/M46.183. URL <https://mem.lyellcollection.org/content/46/1/519>.
- Drews, R., Eisen, O., Weikusat, I., Kipfstuhl, S., Lambrecht, A., Steinhage, D., Wilhelms, F., and Miller, H. Layer disturbances and the radio-echo free zone in ice sheets. *The Cryosphere*, 3(2):195–203, aug 2009. doi: 10.5194/tc-3-195-2009. URL <https://doi.org/10.5194/tc-3-195-2009>.
- Dupont, T. K. and Alley, R. B. Assessment of the importance of ice-shelf buttressing to ice-sheet flow. *Geophysical Research Letters*, 32(4), 2005. doi: <https://doi.org/10.1029/2004GL022024>. URL <https://agupubs.onlinelibrary.wiley.com/doi/abs/10.1029/2004GL022024>.
- Earle. Physical geology - 2nd edition, 2019. URL <https://opentextbc.ca/geology/chapter/16-2-how-glaciers-work/>.
- Edwards, T. L., Nowicki, S., Marzeion, B., Hock, R., Goelzer, H., Seroussi, H., Jourdain, N. C., Slater, D. A., Turner, F. E., Smith, C. J., McKenna, C. M., Simon, E., Abe-Ouchi, A., Gregory, J. M., Larour, E., Lipscomb, W. H., Payne, A. J., Shepherd, A., Agosta, C., Alexander, P., Albrecht, T., Anderson, B., Asay-Davis, X., Aschwanden, A., Barthel, A., Bliss, A., Calov, R., Chambers, C., Champollion, N., Choi, Y., Cullather, R., Cuzzone, J., Dumas, C., Felikson, D., Fettweis, X., Fujita, K., Galton-Fenzi, B. K., Gladstone, R., Golledge, N. R., Greve, R., Hattermann, T., Hoffman, M. J., Humbert, A., Huss, M., Huybrechts, P., Immerzeel, W., Kleiner, T., Kraaijenbrink, P., Le clec'h, S., Lee, V., Leguy, G. R., Little, C. M., Lowry, D. P., Malles, J.-H., Martin, D. F., Maussion, F., Morlighem, M., O'Neill, J. F., Nias, I., Pattyn, F., Pelle, T., Price, S. F., Quiquet, A., Radić, V., Reese, R., Rounce, D. R., Rückamp, M., Sakai, A., Shafer, C., Schlegel, N.-J., Shannon, S., Smith, R. S., Straneo, F., Sun, S., Tarasov, L., Trusel, L. D., Van Breedam, J., van de Wal, R., van den Broeke, M., Winkelmann, R., Zekollari, H., Zhao, C., Zhang, T., and Zwinger, T. Projected land ice contributions to twenty-first-century sea level rise. *Nature*, 593(7857):74–82, 2021. ISSN 0028-0836, 1476-4687. doi: 10.1038/s41586-021-03302-y. URL <http://www.nature.com/articles/s41586-021-03302-y>.
- Fahnestock, M. High Geothermal Heat Flow Basal Melt, and the Origin of Rapid Ice Flow in Central Greenland. *Science*, 294(5550):2338–2342, dec 2001. doi: 10.1126/science.1065370. URL <https://doi.org/10.1126/Science.1065370>.
- Franke, S., Jansen, D., Binder, T., Dörr, N., Helm, V., Paden, J., Steinhage, D., and Eisen, O. Bed topography and subglacial landforms in the onset region of the North-east Greenland Ice Stream. *Annals of Glaciology*, pages 1–11, mar 2020. doi: 10.1017/aog.2020.12. URL <https://doi.org/10.1017/aog.2020.12>.
- Fretwell, P., Pritchard, H. D., Vaughan, D. G., Bamber, J. L., Barrand, N. E., Bell, R., Bianchi, C., Bingham, R. G., Blankenship, D. D., Casassa, G., Catania, G., Callens, D., Conway, H., Cook, A. J., Corr, H. F. J., Damaske, D., Damm, V., Ferraccioli, F., Forsberg, R., Fujita, S., Gim, Y., Gogineni, P., Griggs, J. A., Hindmarsh, R. C. A., Holmlund, P., Holt, J. W., Jacobel, R. W., Jenkins, A., Jokat, W., Jordan, T., King, E. C., Kohler, J., Krabill, W., Riger-Kusk, M., Langley, K. A., Leitchenkov, G., Leuschen, C., Luyendyk, B. P., Matsuoka, K., Mouginot, J., Nitsche, F. O., Nogi, Y., Nost, O. A., Popov, S. V., Rignot, E., Rippin, D. M., Rivera, A., Roberts, J., Ross, N., Siegert, M. J., Smith, A. M., Steinhage, D., Studinger, M., Sun, B., Tinto, B. K., Welch, B. C., Wilson, D., Young, D. A., Xiangbin, C., and Zirizzotti, A. Bedmap2: improved ice bed surface and thickness datasets for Antarctica. *The Cryosphere*, 7(1):375–393, feb 2013. doi: 10.5194/tc-7-375-2013. URL <https://doi.org/10.5194/tc-7-375-2013>.

- Fricker, H. A., Scambos, T., Bindschadler, R., and Padman, L. An active subglacial water system in west antarctica mapped from space. *Science*, 315(5818):1544–1548, 2007. ISSN 0036-8075. doi: 10.1126/science.1136897. URL <https://science.sciencemag.org/content/315/5818/1544>.
- Gagliardini, O., Durand, G., Zwinger, T., Hindmarsh, R. C. A., and Le Meur, E. Coupling of ice-shelf melting and buttressing is a key process in ice-sheets dynamics. *Geophysical Research Letters*, 37(14), 2010. doi: <https://doi.org/10.1029/2010GL043334>. URL <https://agupubs.onlinelibrary.wiley.com/doi/abs/10.1029/2010GL043334>.
- Garbe, J., Albrecht, T., Levermann, A., Donges, J. F., and Winkelmann, R. The hysteresis of the Antarctic Ice Sheet. *Nature*, 585(7826):538–544, 2020. ISSN 14764687. doi: 10.1038/s41586-020-2727-5. URL <http://dx.doi.org/10.1038/s41586-020-2727-5>.
- Glasser, N. F. and Bennett, M. R. Glacial erosional landforms: origins and significance for palaeoglaciology. *Progress in Physical Geography: Earth and Environment*, 28(1):43–75, 2004. doi: 10.1191/0309133304pp401ra. URL <https://doi.org/10.1191/0309133304pp401ra>.
- Gogineni, S., Chuah, T., Allen, C., Jezek, K., and Moore, R. K. An improved coherent radar depth sounder. *Journal of Glaciology*, 44(148):659–669, 1998. doi: 10.3189/S0022143000002161. URL <https://doi.org/10.3189/S0022143000002161>.
- Golledge, N. R., Kowalewski, D. E., Naish, T. R., Levy, R. H., Fogwill, C. J., and Gasson, E. G. The multi-millennial Antarctic commitment to future sea-level rise. *Nature*, 526(7573):421–425, 2015. ISSN 14764687. doi: 10.1038/nature15706. URL <https://www.nature.com/articles/nature15706>.
- Gray, A. L., Mattar, K. E., and Sofko, G. Influence of ionospheric electron density fluctuations on satellite radar interferometry. *Geophysical Research Letters*, 27(10):1451–1454, 2000. ISSN 1944-8007. doi: 10.1029/2000GL000016. URL <http://dx.doi.org/10.1029/2000GL000016>.
- Greenwood, S. L., Clason, C. C., Helanow, C., and Margold, M. Theoretical, contemporary observational and palaeo-perspectives on ice sheet hydrology: Processes and products. *Earth-Science Reviews*, 155:1–27, 2016. ISSN 0012-8252. doi: <https://doi.org/10.1016/j.earscirev.2016.01.010>. URL <https://www.sciencedirect.com/science/article/pii/S0012825216300095>.
- Hale, R., Miller, H., Gogineni, S., Yan, J. B., Leuschen, C., Paden, J., and Li, J. Multi-channel ultra-wideband radar sounder and imager. *2016 IEEE International Geoscience and Remote Sensing Symposium (IGARSS)*, pages 2112–2115, 2016. doi: 10.1109/IGARSS.2016.7729545. URL <http://dx.doi.org/10.1109/IGARSS.2016.7729545>.
- Hambrey, M. J. and Glasser, N. F. The role of folding and foliation development in the genesis of medial moraines: Examples from svalbard glaciers. *The Journal of Geology*, 111(4):471–485, 2003. doi: 10.1086/375281. URL <https://doi.org/10.1086/375281>.
- Helm, V., Humbert, A., and Miller, H. Elevation and elevation change of Greenland and Antarctica derived from CryoSat-2. *Cryosphere*, 8(4):1539–1559, aug 2014. ISSN 19940424. doi: 10.5194/tc-8-1539-2014. URL <https://tc.copernicus.org/articles/8/1539/2014/>.
- Hirano, M. and Aniya, M. A rational explanation of cross-profile morphology for glacial valleys and of glacial valley development. *Earth Surface Processes and Landforms*, 13(8):707–716, 1988. doi: <https://doi.org/10.1002/esp.3290130805>. URL <https://onlinelibrary.wiley.com/doi/abs/10.1002/esp.3290130805>.
- Holland, D. M., Thomas, R. H., De Young, B., Ribergaard, M. H., and Lyberth, B. Acceleration of Jakobshavn Isbr triggered by warm subsurface ocean waters. *Nature Geoscience*, 1(10):659–664, 2008. ISSN 17520894. doi: 10.1038/ngeo316. URL <http://dx.doi.org/>.
- Holschuh, N., Christianson, K., Paden, J., Alley, R., and Anandakrishnan, S. Linking postglacial landscapes to glacier dynamics using swath radar at Thwaites Glacier Antarctica. *Geology*, jan 2020. doi: 10.1130/g46772.1. URL <https://doi.org/10.1130%2Fg46772.1>.
- Hubbard, B., Siegert, M. J., and McCarroll, D. Spectral roughness of glaciated bedrock geomorphic surfaces: Implications for glacier sliding. *Journal of Geophysical Research: Solid Earth*, 105(B9):21295–21303, sep 2000. doi: 10.1029/2000jb900162. URL <https://doi.org/10.1029%2F2000jb900162>.
- Hudleston, P. J. Structures and fabrics in glacial ice: A review, 2015. ISSN 01918141. URL <https://www.sciencedirect.com/science/article/pii/S0191814115300365>.
- IAS. Ias preparation. URL <http://officersiasacademy.blogspot.com/2016/04/landforms-created-by-glacier.html>.
- IPCC 2013. *IPCC, 2013: Climate Change 2013: The Physical Science Basis. Contribution of Working Group I to the Fifth Assessment Report of the Intergovernmental Panel on Climate Change [Stocker, T.F., D. Qin, G.-K. Plattner, M. Tignor, S.K.*

- Allen, J., Boschung, A., Nauels, Y., Xia, V. Bex and P.M. Midgley (eds.). Cambridge University Press, Cambridge, United Kingdom and New York, NY, USA. ISBN 9789291691517.
- Jacobel, R. W. and Hodge, S. M. Radar internal layers from the greenland summit. *Geophysical Research Letters*, 22(5):587–590, 1995. doi: <https://doi.org/10.1029/95GL00110>. URL <https://agupubs.onlinelibrary.wiley.com/doi/abs/10.1029/95GL00110>.
- Jacobson, H. P. and Waddington, E. D. Recumbent folding of divide arches in response to unsteady ice-divide migration. *Journal of Glaciology*, 51(173):201–209, 2005. doi: [10.3189/172756505781829412](https://doi.org/10.3189/172756505781829412). URL <https://doi.org/10.3189/172756505781829412>.
- Jamieson, S. S., Sugden, D. E., and Hulton, N. R. The evolution of the subglacial landscape of Antarctica. *Earth and Planetary Science Letters*, 293(1-2):1–27, 2010. ISSN 0012821X. doi: [10.1016/j.epsl.2010.02.012](https://doi.org/10.1016/j.epsl.2010.02.012). URL <http://dx.doi.org/10.1016/j.epsl.2010.02.012>.
- Jansen, D., Llorens, M.-G., Westhoff, J., Steinbach, F., Kipfstuhl, S., Bons, P. D., Griera, A., and Weikusat, I. Small-scale disturbances in the stratigraphy of the NEEM ice core: observations and numerical model simulations. *The Cryosphere*, 10(1):359–370, feb 2016. doi: [10.5194/tc-10-359-2016](https://doi.org/10.5194/tc-10-359-2016). URL <https://doi.org/10.5194/tc-10-359-2016>.
- Jordan, T. M., Cooper, M. A., Schroeder, D. M., Williams, C. N., Paden, J. D., Siegert, M. J., and Bamber, J. L. Self-affine subglacial roughness: consequences for radar scattering and basal water discrimination in northern Greenland. *The Cryosphere*, 11(3):1247–1264, may 2017. doi: [10.5194/tc-11-1247-2017](https://doi.org/10.5194/tc-11-1247-2017). URL <https://doi.org/10.5194/tc-11-1247-2017>.
- Joughin, I., Fahnestock, M., MacAyeal, D., Bamber, J. L., and Gogineni, P. Observation and analysis of ice flow in the largest Greenland ice stream. *Journal of Geophysical Research: Atmospheres*, 106(D24):34021–34034, dec 2001. doi: [10.1029/2001jd900087](https://doi.org/10.1029/2001jd900087). URL <https://doi.org/10.1029/2001jd900087>.
- Joughin, I., Rignot, E., Rosanova, C. E., Lucchitta, B. K., and Bohlander, J. Timing of recent accelerations of pine island glacier, antarctica. 30(13), 2003. ISSN 1944-8007. doi: <https://doi.org/10.1029/2003GL017609>. URL <https://agupubs.onlinelibrary.wiley.com/doi/abs/10.1029/2003GL017609>.
- Joughin, I., Smith, B. E., Howat, I. M., Scambos, T., and Moon, T. Greenland flow variability from ice-sheet-wide velocity mapping. *Journal of Glaciology*, 56(197):415–430, 2010. ISSN 0022-1430. doi: [10.3189/002214310792447734](https://doi.org/10.3189/002214310792447734). URL <http://dx.doi.org/10.3189/002214310792447734>.
- Joughin, I., Smith, B. E., and Medley, B. Marine ice sheet collapse potentially under way for the thwaites glacier basin, west antarctica. *Science*, 344(6185):735–738, 2014. ISSN 0036-8075. doi: [10.1126/science.1249055](https://doi.org/10.1126/science.1249055). URL <https://science.sciencemag.org/content/344/6185/735>.
- Joughin, I., Smith, B. E., and Howat, I. M. A complete map of Greenland ice velocity derived from satellite data collected over 20 years. *Journal of Glaciology*, 64(243):1–11, nov 2017. doi: [10.1017/jog.2017.73](https://doi.org/10.1017/jog.2017.73). URL <https://doi.org/10.1017/jog.2017.73>.
- Jouzel, J., Masson-Delmotte, V., Cattani, O., Dreyfus, G., Falourd, S., Hoffmann, G., Minster, B., Nouet, J., Barnola, J. M., Chappellaz, J., Fischer, H., Gallet, J. C., Johnsen, S., Leuenberger, M., Loulergue, L., Luethi, D., Oerter, H., Parrenin, F., Raisbeck, G., Raynaud, D., Schilt, A., Schwander, J., Selmo, E., Souchez, R., Spahni, R., Stauffer, B., Steffensen, J. P., Stenni, B., Stocker, T. F., Tison, J. L., Werner, M., and Wolff, E. W. Orbital and millennial antarctic climate variability over the past 800,000 years. *Science*, 317(5839):793–796, 2007. doi: [10.1126/science.1141038](https://doi.org/10.1126/science.1141038). URL <https://science.sciencemag.org/content/317/5839/793>.
- Kaplan, M. R., Hein, A. S., Hubbard, A., and Lax, S. M. Can glacial erosion limit the extent of glaciation? *Geomorphology*, 103(2):172–179, 2009. ISSN 0169-555X. doi: <https://doi.org/10.1016/j.geomorph.2008.04.020>. URL <https://www.sciencedirect.com/science/article/pii/S0169555X08001578>.
- Kessler, M. A., Anderson, R. S., and Briner, J. P. Fjord insertion into continental margins driven by topographic steering of ice. *Nature Geoscience*, 1(6):365–369. ISSN 1752-0908. doi: [10.1038/ngeo201](https://doi.org/10.1038/ngeo201). URL <https://www.nature.com/articles/ngeo201>.
- Khan, S. A., Kjær, K. H., Bevis, M., Bamber, J. L., Wahr, J., Kjeldsen, K. K., Bjørk, A. A., Korsgaard, N. J., Stearns, L. A., Van Den Broeke, M. R., Liu, L., Larsen, N. K., and Muresan, I. S. Sustained mass loss of the northeast Greenland ice sheet triggered by regional warming. *Nature Climate Change*, 4(4):292–299, 2014. ISSN 17586798. doi: [10.1038/nclimate2161](https://doi.org/10.1038/nclimate2161). URL <http://dx.doi.org/10.1038/nclimate2161>.
- Khan, S. A., Aschwanden, A., Bjørk, A. A., Wahr, J., Kjeldsen, K. K., and Kjær, K. H. Greenland ice sheet mass balance: a review. *Reports on Progress in Physics*, 78(4):046801, 2015. doi: [10.1088/0034-4885/78/4/046801](https://doi.org/10.1088/0034-4885/78/4/046801). URL <https://doi.org/10.1088/0034-4885/78/4/046801>.

- King, E. C., Hindmarsh, R. C. A., and Stokes, C. R. Formation of mega-scale glacial lineations observed beneath a West Antarctic ice stream. *Nature Geoscience*, 2(8):585–588, jul 2009. doi: 10.1038/ngeo581. URL <https://doi.org/10.1038%2Fngo581>.
- Lawson, W. J., Sharp, M. J., and Hambrey, M. J. The structural geology of a surge-type glacier. *Journal of Structural Geology*, 16(10):1447–1462, 1994. ISSN 0191-8141. doi: 10.1016/0191-8141(94)90008-6. URL <https://www.sciencedirect.com/science/article/pii/0191814194900086>.
- Le Brocq, A. M., Payne, A. J., and Siegert, M. J. West Antarctic balance calculations: Impact of flux-routing algorithm smoothing algorithm and topography. *Computers & Geosciences*, 32(10):1780–1795, dec 2006. doi: 10.1016/j.cageo.2006.05.003. URL <https://doi.org/10.1016%2Fj.cageo.2006.05.003>.
- Legarsky, J. J., Gogineni, S. P., and Akins, T. L. Focused synthetic aperture radar processing of ice-sounder data collected over the greenland ice sheet. *IEEE Transactions on Geoscience and Remote Sensing*, 39(10):2109–2117, 2001. doi: 10.1109/36.957274. URL <http://dx.doi.org/10.1109/36.957274>.
- Leuschen, C., Gogineni, S., and Tammana, D. SAR processing of radar echo sounder data. pages 2570–2572, 2000. doi: 10.1109/igarss.2000.859643. URL <http://dx.doi.org/10.1109/igarss.2000.859643>.
- Leuschen, C., Gogineni, P. S., Allen, C., Paden, J. D., Hale, R., Rodriguez-Morales, F., Harish, A., Seguin, S., Arnold, E., Blake, W., Byers, K., Crowe, R., Lewis, C., Panzer, B., Patel, A., and Shi, L. The CReSIS Radar Suite for Measurements of the Ice Sheets and Sea Ice during Operation Ice Bridge. In *AGU Fall Meeting Abstracts*, volume 2010, pages C44A–02, Dec. 2010. URL <https://ui.adsabs.harvard.edu/abs/2010AGUFM.C44A..02L>.
- Leysinger Vieli, G. J.-M. C., Martín, C., Hindmarsh, R. C. A., and Lüthi, M. P. Basal freeze-on generates complex ice-sheet stratigraphy. *Nature Communications*, 9(1), nov 2018. doi: 10.1038/s41467-018-07083-3. URL <https://doi.org/10.1038%2Fs41467-018-07083-3>.
- Li, J., Paden, J., Leuschen, C., Rodriguez-Morales, F., Hale, R. D., Arnold, E. J., Crowe, R., Gomez-Garcia, D., and Gogineni, P. High-altitude radar measurements of ice thickness over the antarctic and greenland ice sheets as a part of operation icebridge. *IEEE Transactions on Geoscience and Remote Sensing*, 51(2):742–754, 2013. ISSN 0196-2892. doi: 10.1109/TGRS.2012.2203822.
- Li, X., Sun, B., Siegert, M. J., Bingham, R. G., Tang, X., Zhang, D., Cui, X., and Zhang, X. Characterization of subglacial landscapes by a two-parameter roughness index. *Journal of Glaciology*, 56(199):831–836, 2010. doi: 10.3189/002214310794457326. URL <https://doi.org/10.3189%2F002214310794457326>.
- LIMA. Landsat image mosaic of antarctica (lima). URL <https://lima.usgs.gov/>.
- Lindbäck, K. and Pettersson, R. Spectral roughness and glacial erosion of a land-terminating section of the Greenland Ice Sheet. *Geomorphology*, 238:149–159, jun 2015. doi: 10.1016/j.geomorph.2015.02.027. URL <https://doi.org/10.1016%2Fj.geomorph.2015.02.027>.
- Lisiecki, L. E. and Raymo, M. E. A pliocene-pleistocene stack of 57 globally distributed benthic 18o records. *Paleoceanography*, 20(1), 2005. doi: <https://doi.org/10.1029/2004PA001071>. URL <https://agupubs.onlinelibrary.wiley.com/doi/abs/10.1029/2004PA001071>.
- Lüthi, D., Le Floch, M., Bereiter, B., Blunier, T., Barnola, J.-M., Siegenthaler, U., Raynaud, D., Jouzel, J., Fischer, H., Kawamura, K., and Stocker, T. F. High-resolution carbon dioxide concentration record 650,000–800,000 years before present. *Nature*, 453(7193):379–382, May 2008. doi: 10.1038/nature06949. URL <https://doi.org/10.1038/nature06949>.
- MacGregor, J. A., Boisvert, L. N., Medley, B., Petty, A. A., Harbeck, J. P., Bell, R. E., Blair, J. B., Blanchard-Wrigglesworth, E., Buckley, E. M., Christoffersen, M. S., Cochran, J. R., Csathó, B. M., De Marco, E. L., Dominguez, R. T., Fahnestock, M. A., Farrell, S. L., Gogineni, S. P., Greenbaum, J. S., Hansen, C. M., Hofton, M. A., Holt, J. W., Jezek, K. C., Koenig, L. S., Kurtz, N. T., Kwok, R., Larsen, C. F., Leuschen, C. J., Locke, C. D., Manizade, S. S., Martin, S., Neumann, T. A., Nowicki, S. M., Paden, J. D., Richter-Menge, J. A., Rignot, E. J., Rodriguez-Morales, F., Siegfried, M. R., Smith, B. E., Sonntag, J. G., Studinger, M., Tinto, K. J., Truffer, M., Wagner, T. P., Woods, J. E., Young, D. A., and Yungel, J. K. The scientific legacy of nasa’s operation icebridge. *Reviews of Geophysics*, n/a(n/a):e2020RG000712. doi: <https://doi.org/10.1029/2020RG000712>. URL <https://agupubs.onlinelibrary.wiley.com/doi/abs/10.1029/2020RG000712>.
- MacGregor, J. A., Fahnestock, M. A., Catania, G. A., Paden, J. D., Gogineni, S. P., Young, S. K., Rybarski, S. C., Mabrey, A. N., Wagman, B. M., and Morlighem, M. Radiostatigraphy and age structure of the Greenland Ice Sheet. *Journal of Geophysical Research: Earth Surface*, 120(2):212–241, feb 2015. doi: 10.1002/2014jff003215. URL <https://doi.org/10.1002%2F2014jff003215>.

- Margold, M., Stokes, C. R., and Clark, C. D. Ice streams in the Laurentide Ice Sheet: Identification characteristics and comparison to modern ice sheets. *Earth-Science Reviews*, 143:117–146, apr 2015. doi: 10.1016/j.earscirev.2015.01.011. URL <https://doi.org/10.1016%2Fj.earscirev.2015.01.011>.
- Matsuoka, K., Morse, D., and Raymond, C. F. Estimating englacial radar attenuation using depth profiles of the returned power, central west antarctica. *Journal of Geophysical Research: Earth Surface*, 115(F2), 2010. doi: <https://doi.org/10.1029/2009JF001496>. URL <https://agupubs.onlinelibrary.wiley.com/doi/abs/10.1029/2009JF001496>.
- Meredith, M., Sommerkorn, M., Cassotta, S., Derksen, C., Ekaykin, A., Hollowed, A., Kofinas, G., Mackintosh, A., Melbourne-Thomas, J., Muelbert, M., Ottersen, G., Pritchard, H., , and Schuur, E. Polar regions. *IPCC Special Report on the Ocean and Cryosphere in a Changing Climate* [H.-O. Pörtner, D.C. Roberts, V. Masson-Delmotte, P. Zhai, M. Tignor, E. Poloczanska, K. Mintenbeck, A. Alegría, M. Nicolai, A. Okem, J. Petzold, B. Rama, N.M. Weyer (eds.)]. In press, 2019. URL <https://www.ipcc.ch/srocc/chapter/chapter-3-2/>.
- Michael Oppenheimer. Global warming and the stability of the West Antarctic Ice Sheet. *Nature*, 393:325–332, 1998. doi: 10.1038/30661. URL <https://www.nature.com/articles/30661>.
- Morlighem, M., Williams, C. N., Rignot, E., An, L., Arndt, J. E., Bamber, J. L., Catania, G., Chauché, N., Dowdeswell, J. A., Dorschel, B., Fenty, I., Hogan, K., Howat, I., Hubbard, A., Jakobsson, M., Jordan, T. M., Kjeldsen, K. K., Millan, R., Mayer, L., Mouginot, J., Noël, B. P. Y., O’Cofaigh, C., Palmer, S., Rysgaard, S., Seroussi, H., Siegert, M. J., Slabon, P., Straneo, F., van den Broeke, M. R., Weinrebe, W., Wood, M., and Zinglensen, K. B. BedMachine v3: Complete Bed Topography and Ocean Bathymetry Mapping of Greenland From Multibeam Echo Sounding Combined With Mass Conservation. *Geophysical Research Letters*, 44(21): 11,051–11,061, nov 2017. doi: 10.1002/2017gl074954. URL <https://doi.org/10.1002%2F2017gl074954>.
- Morlighem, M., Rignot, E., Binder, T., Blankenship, D., Drews, R., Eagles, G., Eisen, O., Ferraccioli, F., Forsberg, R., Fretwell, P., Goel, V., Greenbaum, J. S., Gudmundsson, H., Guo, J., Helm, V., Hofstede, C., Howat, I., Humbert, A., Jokat, W., Karlsson, N. B., Lee, W. S., Matsuoka, K., Millan, R., Mouginot, J., Paden, J., Pattyn, F., Roberts, J., Rosier, S., Ruppel, A., Seroussi, H., Smith, E. C., Steinhage, D., Sun, B., van den Broeke, M. R., van Ommen, T. D., van Wessem, M., and Young, D. A. Deep glacial troughs and stabilizing ridges unveiled beneath the margins of the Antarctic ice sheet. *Nature Geoscience*, 13(2): 132–137, dec 2019. doi: 10.1038/s41561-019-0510-8. URL <https://doi.org/10.1038%2Fs41561-019-0510-8>.
- Mouginot, J., Rignot, E., Scheuchl, B., and Millan, R. Comprehensive annual ice sheet velocity mapping using Landsat-8, Sentinel-1, and RADARSAT-2 data. *Remote Sensing*, 9(4), apr 2017. ISSN 20724292. doi: 10.3390/rs9040364. URL <http://dx.doi.org/10.3390/rs9040364>.
- Mouginot, J., Rignot, E., Bjørk, A. A., van den Broeke, M., Millan, R., Morlighem, M., Noël, B., Scheuchl, B., and Wood, M. Forty-six years of Greenland Ice Sheet mass balance from 1972 to 2018. *Proceedings of the National Academy of Sciences*, 116(19):9239–9244, apr 2019. doi: 10.1073/pnas.1904242116. URL <https://doi.org/10.1073%2Fpnas.1904242116>.
- Neckel, N., Drews, R., Rack, W., and Steinhage, D. Basal melting at the Ekström Ice Shelf, Antarctica, estimated from mass flux divergence. *Annals of Glaciology*, 53(60):294–302, 2012. ISSN 0260-3055. doi: 10.3189/2012aog60a167. URL <https://doi.org/10.3189/2012aog60a167>.
- NEEM community members. Eemian interglacial reconstructed from a Greenland folded ice core. *Nature*, 493 (7433):489–494, jan 2013. doi: 10.1038/nature11789. URL <https://doi.org/10.1038%2Fnature11789>.
- Oswald, G. and Gogineni, S. Recovery of subglacial water extent from Greenland radar survey data. *Journal of Glaciology*, 54(184):94–106, 2008. doi: 10.3189/002214308784409107. URL <https://doi.org/10.3189%2F002214308784409107>.
- Panton, C. and Karlsson, N. B. Automated mapping of near bed radio-echo layer disruptions in the Greenland Ice Sheet. *Earth and Planetary Science Letters*, 432:323–331, dec 2015. doi: 10.1016/j.epsl.2015.10.024. URL <https://doi.org/10.1016%2Fj.epsl.2015.10.024>.
- Paren, J. G. and Robin, G. d. Q. Internal reflections in polar ice sheets. *Journal of Glaciology*, 14(71):251–259, 1975. doi: 10.3189/S0022143000021730. URL <https://doi.org/10.3189/S0022143000021730>.
- Raymond, C. F. Deformation in the vicinity of ice divides. *Journal of Glaciology*, 29(103):357–373, 1983. doi: 10.3189/S0022143000030288. URL <https://doi.org/10.3189/S0022143000030288>.
- Reynolds, J. M. An Introduction to Applied and Environmental Geophysics (2nd Edition). *Wiley-Blackwell*, 2011.

- Riedel, S., Jokat, W., and Steinhage, D. Mapping tectonic provinces with airborne gravity and radar data in Dronning Maud Land, East Antarctica. *Geophysical Journal International*, 189(1):414–427, 2012. ISSN 0956540X. doi: 10.1111/j.1365-246X.2012.05363.x. URL <https://doi.org/10.1111/j.1365-246X.2012.05363.x>.
- Rignot, E. and Mouginot, J. Ice flow in Greenland for the International Polar Year 2008–2009. *Geophysical Research Letters*, 39(11):n/a–n/a, jun 2012. ISSN 00948276. doi: 10.1029/2012GL051634. URL <http://doi.wiley.com/10.1029/2012GL051634>.
- Rignot, E., Jacobs, S., Mouginot, J., and Scheuchl, B. Ice-Shelf Melting Around Antarctica. *Science*, 341(6143):266–270, 2013. ISSN 0036-8075. doi: 10.1126/science.1235798. URL <https://science.sciencemag.org/content/341/6143/266>.
- Rippin, D., Bingham, R., Jordan, T., Wright, A., Ross, N., Corr, H., Ferraccioli, F., Brocq, A. L., Rose, K., and Siegert, M. Basal roughness of the Institute and Möller Ice Streams West Antarctica: Process determination and landscape interpretation. *Geomorphology*, 214:139–147, jun 2014. doi: 10.1016/j.geomorph.2014.01.021. URL <https://doi.org/10.1016%2Fj.geomorph.2014.01.021>.
- Ross, N., Corr, H., and Siegert, M. Large-scale englacial folding and deep-ice stratigraphy within the West Antarctic Ice Sheet. *The Cryosphere*, 14(6):2103–2114, jun 2020. doi: 10.5194/tc-14-2103-2020. URL <https://doi.org/10.5194%2Ftc-14-2103-2020>.
- Schoof, C. Basal perturbations under ice streams: form drag and surface expression. *Journal of Glaciology*, 48(162):407–416, 2002. doi: 10.3189/172756502781831269. URL <https://doi.org/10.3189/172756502781831269>.
- Schoof, C. and Mantelli, E. The role of sliding in ice stream formation. *Proceedings of the Royal Society A: Mathematical, Physical and Engineering Sciences*, 477(2248):20200870, 2021. doi: 10.1098/rspa.2020.0870. URL <https://royalsocietypublishing.org/doi/abs/10.1098/rspa.2020.0870>.
- Schroeder, D. M., Bingham, R. G., Blankenship, D. D., Christianson, K., Eisen, O., Flowers, G. E., Karlsson, N. B., Koutnik, M. R., Paden, J. D., Siegert, M. J., and et al. Five decades of radioglaciology. *Annals of Glaciology*, 61(81):1–13, 2020. doi: 10.1017/aog.2020.11. URL <https://doi.org/10.1017/aog.2020.11>.
- Shepherd, A., Ivins, E. R., Geruo, A., Barletta, V. R., Bentley, M. J., Bettadpur, S., Briggs, K. H., Bromwich, D. H., Forsberg, R., Galin, N., Horwath, M., Jacobs, S., Joughin, I., King, M. A., Lenaerts, J. T., Li, J., Ligtenberg, S. R., Luckman, A., Luthcke, S. B., McMillan, M., Meister, R., Milne, G., Mouginot, J., Muir, A., Nicolas, J. P., Paden, J., Payne, A. J., Pritchard, H., Rignot, E., Rott, H., Sørensen, L. S., Scambos, T. A., Scheuchl, B., Schrama, E. J., Smith, B., Sundal, A. V., Van Angelen, J. H., Van De Berg, W. J., Van Den Broeke, M. R., Vaughan, D. G., Velicogna, I., Wahr, J., Whitehouse, P. L., Wingham, D. J., Yi, D., Young, D., and Zwally, H. J. A reconciled estimate of ice-sheet mass balance. *Science*, 338(6111):1183–1189, nov 2012. ISSN 10959203. doi: 10.1126/science.1228102. URL <https://doi.org/10.1126/science.1228102>.
- Shepherd, A., Ivins, E., Rignot, E., Smith, B., Van Den Broeke, M., Velicogna, I., Whitehouse, P., Briggs, K., Joughin, I., Krinner, G., Nowicki, S., Payne, T., Scambos, T., Schlegel, N., Geruo, A., Agosta, C., Ahlstrøm, A., Babonis, G., Barletta, V., Blazquez, A., Bonin, J., Csatho, B., Cullather, R., Felikson, D., Fettweis, X., Forsberg, R., Gallee, H., Gardner, A., Gilbert, L., Groh, A., Gunter, B., Hanna, E., Harig, C., Helm, V., Horwath, A., Horwath, M., Khan, S., Kjeldsen, K. K., Konrad, H., Langen, P., Lecavalier, B., Loomis, B., Luthcke, S., McMillan, M., Melini, D., Mernild, S., Mohajerani, Y., Moore, P., Mouginot, J., Moyano, G., Muir, A., Nagler, T., Nield, G., Nilsson, J., Noël, B., Otosaka, I., Pattle, M. E., Peltier, W. R., Pie, N., Rietbroek, R., Rott, H., Sandberg-Sørensen, L., Sasgen, I., Save, H., Scheuchl, B., Schrama, E., Schröder, L., Seo, K. W., Simonsen, S., Slater, T., Spada, G., Sutterley, T., Talpe, M., Tarasov, L., Van De Berg, W. J., Van Der Wal, W., Van Wessem, M., Vishwakarma, B. D., Wiese, D., and Wouters, B. Mass balance of the Antarctic Ice Sheet from 1992 to 2017. 558(7709):219–222, 2018. doi: 10.1038/s41586-018-0179-y. URL <https://www.nature.com/articles/s41586-018-0179-y>.
- Shepherd, A., Ivins, E., Rignot, E., Smith, B., van den Broeke, M., Velicogna, I., Whitehouse, P., Briggs, K., Joughin, I., Krinner, G., Nowicki, S., Payne, T., Scambos, T., Schlegel, N., A. G., Agosta, C., Ahlstrøm, A., Babonis, G., Barletta, V. R., Bjørk, A. A., Blazquez, A., Bonin, J., Colgan, W., Csatho, B., Cullather, R., Engdahl, M. E., Felikson, D., Fettweis, X., Forsberg, R., Hogg, A. E., Gallee, H., Gardner, A., Gilbert, L., Gourmelen, N., Groh, A., Gunter, B., Hanna, E., Harig, C., Helm, V., Horwath, A., Horwath, M., Khan, S., Kjeldsen, K. K., Konrad, H., Langen, P. L., Lecavalier, B., Loomis, B., Luthcke, S., McMillan, M., Melini, D., Mernild, S., Mohajerani, Y., Moore, P., Mottram, R., Mouginot, J., Moyano, G., Muir, A., Nagler, T., Nield, G., Nilsson, J., Noël, B., Otosaka, I., Pattle, M. E., Peltier, W. R., Pie, N., Rietbroek, R., Rott, H., Sandberg Sørensen, L., Sasgen, I., Save, H., Scheuchl, B., Schrama, E., Schröder, L., Seo, K. W., Simonsen, S. B., Slater, T., Spada, G., Sutterley, T., Talpe, M., Tarasov, L., van de Berg, W. J., van der Wal, W., van Wessem, M.,

- Vishwakarma, B. D., Wiese, D., Wilton, D., Wagner, T., Wouters, B., and Wuite, J. Mass balance of the Greenland Ice Sheet from 1992 to 2018. *Nature*, 579(7798):233–239, 2020. ISSN 14764687. doi: 10.1038/s41586-019-1855-2. URL <https://doi.org/10.1038/s41586-019-1855-2>.
- Siegert, M., Alley, R. B., Rignot, E., Englander, J., and Corell, R. Twenty-first century sea-level rise could exceed ipcc projections for strong-warming futures. *One Earth*, 3(6):691–703, 2020. ISSN 2590-3322. doi: 10.1016/j.oneear.2020.11.002. URL <https://www.sciencedirect.com/science/article/pii/S2590332220305923>.
- Siegert, M. J., Taylor, J., and Payne, A. J. Spectral roughness of subglacial topography and implications for former ice-sheet dynamics in East Antarctica. *Global and Planetary Change*, 45(1-3):249–263, feb 2005. doi: 10.1016/j.gloplacha.2004.09.008. URL <https://doi.org/10.1016%2Fj.gloplacha.2004.09.008>.
- Sigman, D. M., Hain, M. P., and Haug, G. H. The polar ocean and glacial cycles in atmospheric CO₂ concentration. *Nature*, 466(7302):47–55, 2010. ISSN 00280836. doi: 10.1038/nature09149. URL <https://www.nature.com/articles/nature09149>.
- Smith-Johnsen, S., de Fleurian, B., Schlegel, N., Seroussi, H., and Nisancioglu, K. Exceptionally High Geothermal Heat Flux Needed to Sustain the Northeast Greenland Ice Stream. *The Cryosphere*, sep 2019. doi: 10.5194/tc-2019-212. URL <https://doi.org/10.5194%2Ftc-2019-212>.
- Steinhage, D., Nixdorf, U., Meyer, U., and Miller, H. *Annals of Glaciology*. doi: 10.3189/172756499781821409. URL <https://doi.org/10.3189/172756499781821409>.
- Steinhage, D., Nixdorf, U., Meyer, U., and Miller, H. Subglacial topography and internal structure of Central and Western Dronning Maud Land, Antarctica, determined from airborne radio echo sounding. *Journal of Applied Geophysics*, 47(3-4):183–189, jul 2001. ISSN 09269851. doi: 10.1016/S0926-9851(01)00063-5. URL [https://doi.org/10.1016/S0926-9851\(01\)00063-5](https://doi.org/10.1016/S0926-9851(01)00063-5).
- Stephenson, S. N. and Bindschadler, R. A. Observed velocity fluctuations on a major antarctic ice stream. *Nature*, 334: 695–697, 1988. ISSN 1476-4687. doi: 10.1038/334695a0. URL <https://www.nature.com/articles/334695a0>.
- Stokes, C. R. Geomorphology under ice streams: Moving from form to process. *Earth Surface Processes and Landforms*, 43(1):85–123, 2018. doi: <https://doi.org/10.1002/esp.4259>. URL <https://onlinelibrary.wiley.com/doi/abs/10.1002/esp.4259>.
- Stokes, C. R. and Clark, C. D. Palaeo-ice streams. *Quaternary Science Reviews*, 20(13):1437–1457, 2001. ISSN 0277-3791. doi: [https://doi.org/10.1016/S0277-3791\(01\)00003-8](https://doi.org/10.1016/S0277-3791(01)00003-8). URL <https://www.sciencedirect.com/science/article/pii/S0277379101000038>.
- Stokes, C. R., Clark, C. D., Lian, O. B., and Tulaczyk, S. Ice stream sticky spots: A review of their identification and influence beneath contemporary and palaeo-ice streams. *Earth-Science Reviews*, 81(3-4):217–249, apr 2007. doi: 10.1016/j.earscirev.2007.01.002. URL <https://doi.org/10.1016%2Fj.earscirev.2007.01.002>.
- Stokes, C. R., Margold, M., Clark, C. D., and Tarasov, L. Ice stream activity scaled to ice sheet volume during Laurentide Ice Sheet deglaciation. *Nature*, 530(7590):322–326, feb 2016. doi: 10.1038/nature16947. URL <https://doi.org/10.1038%2Fnature16947>.
- Streng, K. Characterisation of folds in the northern greenland ice sheet. *BSc Thesis, Eberhard Karls Universität Tübingen*, 2019.
- Swithinbank, C. W. M. “ice streams”. *Polar Record*, 7(48): 185–186, 1954. doi: 10.1017/S0032247400043746. URL <https://doi.org/10.1017/S0032247400043746>.
- Taylor, J., Siegert, M., Payne, A., Hambrey, M., O’Brien, P., Cooper, A., and Leitchenkov, G. Topographic controls on post-Oligocene changes in ice-sheet dynamics, Prydz Bay region, East Antarctica. *Geology*, 32(3):197–200, 03 2004. ISSN 0091-7613. doi: 10.1130/G20275.1. URL <https://doi.org/10.1130/G20275.1>.
- Ugelvig, S. V., Egholm, D. L., Anderson, R. S., and Iverson, N. R. Glacial erosion driven by variations in meltwater drainage. *Journal of Geophysical Research: Earth Surface*, 123(11):2863–2877, 2018. doi: <https://doi.org/10.1029/2018JF004680>. URL <https://agupubs.onlinelibrary.wiley.com/doi/abs/10.1029/2018JF004680>.
- Westhoff, J. Small scale folding in neem ice core. *BSc Thesis, Eberhard Karls Universität Tübingen*, 2014.
- Westhoff, J., Stoll, N., Franke, S., Weikusat, I., Bons, P., Kerch, J., Jansen, D., Kipfstuhl, S., and Dahl-Jensen, D. A stratigraphy-based method for reconstructing ice core orientation. *Annals of Glaciology*, page 1–12, 2020. doi: 10.1017/aog.2020.76. URL <https://doi.org/10.1017/aog.2020.76>.
- Wilkens, N., Behrens, J., Kleiner, T., Rippin, D., Rückamp, M., and Humbert, A. Thermal structure and basal sliding parametrisation at Pine Island Glacier – a 3-D full-Stokes model study. *The Cryosphere*, 9(2):675–690, apr 2015. doi: 10.5194/tc-9-675-2015. URL <https://doi.org/10.5194%2Ftc-9-675-2015>.

- Wilkinson, M. D., Dumontier, M., Aalbersberg, I. J., Appleton, G., Axton, M., Baak, A., Blomberg, N., Boiten, J.-W., da Silva Santos, L. B., Bourne, P. E., Bouwman, J., Brookes, A. J., Clark, T., Crosas, M., Dillo, I., Dumon, O., Edmunds, S., Evelo, C. T., Finkers, R., Gonzalez-Beltran, A., Gray, A. J., Groth, P., Goble, C., Grethe, J. S., Heringa, J., 't Hoen, P. A., Hooft, R., Kuhn, T., Kok, R., Kok, J., Lusher, S. J., Martone, M. E., Mons, A., Packer, A. L., Persson, B., Rocca-Serra, P., Roos, M., van Schaik, R., Sansone, S.-A., Schultes, E., Sengstag, T., Slater, T., Strawn, G., Swertz, M. A., Thompson, M., van der Lei, J., van Mulligen, E., Velterop, J., Waagmeester, A., Wittenburg, P., Wolstencroft, K., Zhao, J., and Mons, B. The fair guiding principles for scientific data management and stewardship. *Scientific Data*, 3(1):160018, Mar 2016. ISSN 2052-4463. doi: 10.1038/sdata.2016.18. URL <https://doi.org/10.1038/sdata.2016.18>.
- Winsborrow, M. C., Clark, C. D., and Stokes, C. R. What controls the location of ice streams? *Earth-Science Reviews*, 103(1):45–59, 2010. ISSN 0012-8252. doi: <https://doi.org/10.1016/j.earscirev.2010.07.003>. URL <https://www.sciencedirect.com/science/article/pii/S0012825210000838>.
- Wolovick, M. J., Creyts, T. T., Buck, W. R., and Bell, R. E. Traveling slippery patches produce thickness-scale folds in ice sheets. *Geophysical Research Letters*, 41(24):8895–8901, dec 2014. doi: 10.1002/2014gl062248. URL <https://doi.org/10.1002/2014gl062248>.

Appendix A

UWB radar: theoretical background

A.1 Electromagnetic wave propagation

A.1.1 Physical basics

The propagation and reflection of electromagnetic (EM) waves depends on three fundamental properties of a medium where EM waves propagate through:

1. the complex dielectric permittivity (ϵ), where ϵ_r is the real part of the relative permittivity and ϵ_0 the permittivity of free space,
2. the complex magnetic permeability (μ), where μ_r is the complex relative permeability and μ_0 the magnetic permeability of free space,
3. the electric conductivity (σ).

The role of these properties is described by Maxwell's Equations for EM waves in isotropic and homogeneous media (Maxwell, 1865). This leads to the following differential equation for an electric field \vec{E} :

$$\nabla^2 \vec{E} = \mu\sigma \frac{\partial \vec{E}}{\partial t} + \mu\epsilon \frac{\partial^2 \vec{E}}{\partial t^2} \quad (\text{A.1})$$

The dielectric permittivity quantifies how easily material becomes polarized in the presence of an electric field. Split into its real and imaginary part, the complex dielectric permittivity can be formulated as:

$$\epsilon = \epsilon' - i\epsilon'' = \epsilon_r\epsilon_0 - i\frac{\sigma}{\omega}, \quad (\text{A.2})$$

where ω represents the angular frequency of an external electric field. For most non-ferromagnetic materials (including ice) we can approximate $\mu \approx \mu_0$. The values of electric permittivity and magnetic permeability are never zero, even in free space, and can be seen as an analogue for the elastic constants in seismic wave propagation theory. The real part of the electric permittivity ϵ' denotes the ability of a material to store energy in the presence of an external electric field. In contrast, the imaginary part ϵ'' represents the energy loss due to charge motion (Petrenko, 1999).

The relative electric permittivity is a key property for radio-echo sounding (RES) surveys. It controls the

EM wave propagation velocity, the wavelength and thus the resolution of the target (Baker et al., 2007):

$$v = \frac{c}{\sqrt{\epsilon_r}}, \quad (\text{A.3})$$

$$\lambda = \frac{c}{\sqrt{\epsilon_r} f}, \quad (\text{A.4})$$

where v is the propagation velocity, λ the wavelength, c the speed of light and f the frequency.

A.1.2 Propagation and reflection basics

EM wave propagation through a medium is frequency-dependent and only occurs when EM frequencies are above the materials transition frequency f_t (Baker et al., 2007) and depends on both conductivity and relative permittivity:

$$f_t = \frac{\sigma}{2\pi\epsilon_0\epsilon_r}. \quad (\text{A.5})$$

The propagation constant, for a EM field to propagate is approximated as (Baker et al., 2007):

$$\gamma = \sqrt{i\omega\mu(\sigma + i\omega\epsilon)} = \pm(\alpha + i\beta), \quad (\text{A.6})$$

where the real part α represents the attenuation factor and the imaginary part β the phase constant, propagation constant or wave number. For a low-loss medium, such as ice, β can be defined as:

$$\beta = \omega\sqrt{\epsilon\mu}. \quad (\text{A.7})$$

The propagation velocity of the EM wave is dependent on the phase constant and assumed to be non-dispersive for low-loss materials (such as ice):

$$v = \frac{\omega}{\beta} \approx \frac{c}{\sqrt{\epsilon_r}}. \quad (\text{A.8})$$

The phase velocity of EM waves in ice ranges between 168.0–169.5 m μ s⁻¹ (Fujita et al., 2000). The reflection and transmission of EM waves at specular and planar interfaces are determined by changes in the dielectric properties. For signals arriving at normal incidence, the amplitude coefficients for transmission T and reflection

R can be simplified to:

$$R = \frac{\sqrt{\epsilon_1} - \sqrt{\epsilon_2}}{\sqrt{\epsilon_1} + \sqrt{\epsilon_2}}, \quad T = \frac{2\sqrt{\epsilon_2}}{\sqrt{\epsilon_1} + \sqrt{\epsilon_2}}. \quad (\text{A.9})$$

The incidence angle θ_i equals the reflection angle θ_r . The refraction of EM waves can be described by Snell's law, where the transmission angle:

$$\frac{\sin \theta_t}{\sin \theta_i} = \frac{\sqrt{\epsilon_{r1}}}{\sqrt{\epsilon_{r2}}} \quad (\text{A.10})$$

with two different values for the relative electric permittivity ϵ_{r1} and ϵ_{r2} .

The deviation of the paths of EM waves at localized objects with a size less than $1/4$ of the wavelength of the signal is called scattering. Scattering introduces errors in the location of the reflectors, which have to be corrected. Furthermore, reflections at thin horizontal layers (less than $1/4$ of a wavelength) are characterized by constructive and destructive interference from multiple reflections at the top and bottom of the layer (Baker et al., 2007). This interference can cause a time delay and phase shift of the reflected signal. However, this effect is so small for radar reflections in ice that it can be neglected.

A.1.3 Ice crystal related anisotropy

Ice is composed of single ice crystals, which are not oriented uniformly at snow deposition. Their principle axis (C-axis) rotates towards the direction of compression (Figure A.1) in response to directional stress (Alley, 1988). Hence, the C-axis orientation reflects the deformation history and also depicts a physical controlling factor upon ice flow (Gillet-Chaulet et al., 2005). The propagation of EM waves in ice is affected by the anisotropic orientation of the crystal orientation fabric (COF) and the cause for two electromagnetic phenomena (Jordan et al., 2019):

1. birefringent propagation associated with horizontal anisotropy of the COF (Hargreaves, 1978)
2. anisotropic scattering associated with sharp depth transitions in the COF (Fujita et al., 2006)

Birefringence in polar ice is caused by the anisotropy related to the dielectric permittivity of ice crystals affecting the polarization and propagation direction of electromagnetic (radar) waves (Hargreaves, 1978). Radar waves decompose into two orthogonal oriented waves propagating with different velocities. This results in a phase shift rotating the electric field. For a linearly-polarized antenna, this causes a polarization misalignment and subsequently results in a power loss of the recorded amplitude (see Doake, 1981; Young

et al.). By contrast, anisotropic scattering results from direct anisotropic changes in the dielectric properties, such as small-scale bulk COF variations with depth (see Drews et al., 2012; Fujita et al., 2006).

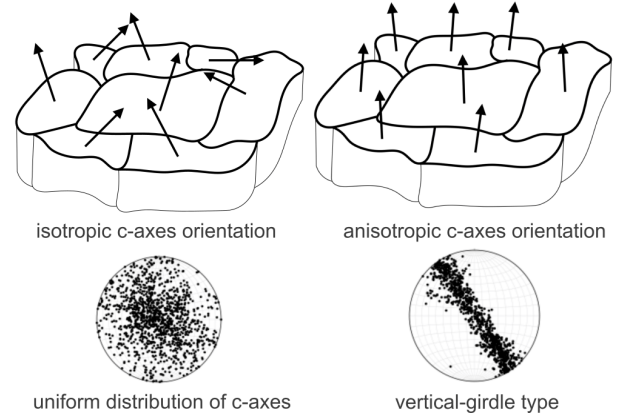


Figure A.1: Illustration of isotropic and anisotropic crystal (C-axis) orientation. Image used with permission from Ole Zeising.

A.1.4 RES reflections in ice sheets

The radar system records the complex reflection signal at interfaces in the ice sheet, which depend on the radar system specifications, the energy losses within the ice and the reflectivity at every interface. The analysis of radar sounding echoes from polar ice sheets provide valuable information to analyze englacial conditions and the subglacial environment. In general, radar reflections consist of both, specularly reflected (representing a smooth interface) and diffusely scattered (representing a rough or inhomogeneous interface) radar waves (Peters et al., 2005).

A.1.4.1 Englacial reflections

Most reflections detected by RES, which are visible in glacial ice, represent layer interfaces of the same age of deposition. Reflections at these so-called internal reflection horizons (IRHs) are caused due to changes in the dielectric properties. The following causes for changes in the dielectric properties in ice sheets have been proposed:

1. density fluctuations (affecting permittivity; Robin et al., 1969)
2. changes in conductivity (Paren and Robin, 1975) due to changes in acid concentrations
3. changes in crystal-orientation fabrics (COF; affecting permittivity; Harrison, 1973)

It has to be noted that for reflections based on density and COF changes the amplitude of the complex coefficient is independent from the radar frequency as well as

ice temperature (Fujita et al., 2000). By contrast, reflections based on changes in conductivity strongly depend on temperature and show an inverse relation between frequency and amplitude. Furthermore, the majority of englacial reflections are considered to be specular reflections with a negligible amount of scattering.

A.1.4.2 Reflections at the ice base

The reflection at the ice base depends solely on the dielectric contrast present at the bed and the radar frequency (Jacobel et al., 2009). If all energy losses between the radar and the bed reflection are taken into account it is possible to estimate the “true” bed reflectivity and infer the basal conditions based on the reflection power (Table A.1).

The reflectivity at the bed is a mixed expression of the variations in the basal materials and geometric (e.g. roughness) properties at the bed (Peters et al., 2005). Although difficult to determine, the analysis of subglacial reflectivity has contributed to the detection of subglacial water (e.g. Jacobel et al., 2009; Peters et al., 2005).

Table A.1: Reflectivity values for subglacial materials (the reflectivity is valid for meteoric ice as the upper medium and defined as the smooth interface power reflection coefficient; adapted from Peters et al. 2005).

Subglacial material	Reflectivity
Seawater	-1 dB
Groundwater	-2 dB
Freshwater	-3 dB
Unfrozen till (40 % groundwater)	-6 dB
Unfrozen bedrock (15 % groundwater)	-13 dB
Frozen till (40 % groundwater ice)	-30 dB
Frozen bedrock (15 % groundwater ice) ratio	-28 dB
Marine ice	-33 dB

A.1.4.3 Return power analysis

The analysis of the return power of an englacial or basal reflection can reveal additional information about ice properties. Retrieving the return power requires to extract the path effects of all overburden ice at the location of the reflection target. The loss in energy between the emission of the radar signal and the reflection is referred to as englacial attenuation and is mainly a function of ice temperature and chemistry (MacGregor et al., 2007). According to Fujita et al. (2000), the chemically related attenuation in the ice sheets is mainly controlled by conductivity (caused by the presence of acidity). Furthermore, the return power within ice depends on the ice characteristics I , the radar instrumentation S as well

as on the loss by spherical spreading G of the radar wave. For the return power the decibel scale of one pathway through ice, we can write (Matsuoka et al., 2010):

$$P_{dB} = S_{dB} + I_{dB} - G_{dB}. \quad (\text{A.11})$$

The spherical spreading loss G can be derived by the range between the radar antenna and the target reflection. The range depends on the antenna height h above the ice surface, the distance from the ice surface to the target in ice z and the relative permittivity of the ice ϵ_r :

$$G_{dB} = 2 \left(h + \frac{z}{\sqrt{\epsilon_r}} \right)_{dB} \quad (\text{A.12})$$

The material properties I are composed of the reflectivity of the target R , the integrated dielectric attenuation L along the radar wave travel path and energy loss caused by COF induced birefringence B (Matsuoka et al., 2010):

$$I_{dB} = R_{dB} - L_{dB} - B_{dB}. \quad (\text{A.13})$$

A.1.4.4 Challenges in retrieving return power

Internal layers Holschuh et al. (2014) noticed a power drop at internal layers in the region of the shear margins of the Northeast Greenland Ice Stream (NEGIS). At the NEGIS, this effect has been particularly observed at steeply inclined internal layers (Keisling et al., 2014). Similar patterns have been observed in radar data acquired over ice streams in West Antarctica. A power loss in IRH affects the interpretation in respect to (i) continuous layer tracing and (ii) the interpretation of dielectric contrasts (Holschuh et al., 2014).

According to Holschuh et al. (2014) the energy loss for inclined internal reflectors is caused by the following mechanisms:

1. destructive interference in trace stacking of adjacent range lines (at data acquisition in the hardware and during processing)
2. energy dispersion through SAR processing
3. off-nadir energy losses

Castelletti et al. (2019) address this issue and present a layer-optimized synthetic aperture radar processing scheme to overcome this problem and estimate slope orientation of internal layers (Figure A.2).

Bed reflection Without an exact knowledge of the physical and chemical conditions of the ice along radar profiles it is not possible to derive the true relative bed reflectivity values. Common methods to correct for

englacial attenuation are based on ice sheet modelling or obtained by empirical methods. The weakness behind both approaches is that they either depend on assumptions or do not capture the horizontal heterogeneity of changes in ice velocity, temperature, and surface roughness at critical glaciological settings, such as ice stream shear margins (Matsuoka et al., 2010; Matsuoka, 2011; Schroeder et al., 2015).

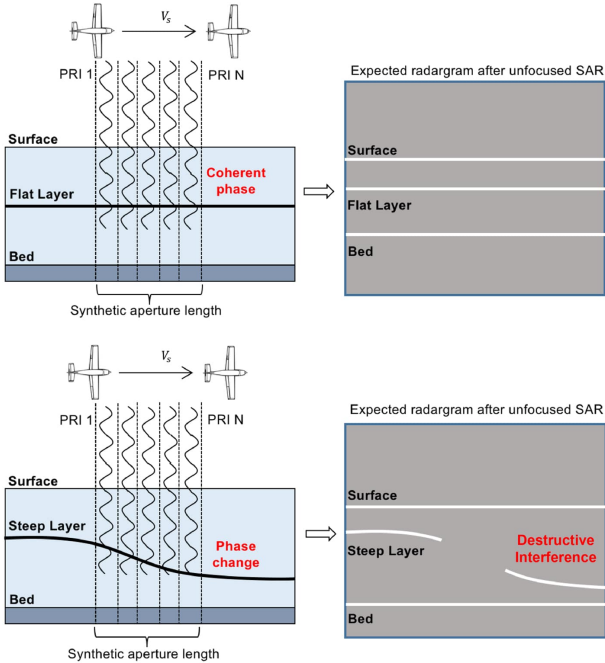


Figure A.2: Sloping layer effect on radar processing. Comparison of radar data processing on flat and sloping internal layers (image obtained from Castelletti et al. (2019)).

A.1.5 Real and synthetic aperture radar

Along-track resolution for traditional radars is determined by the beamwidth of the antenna, which in turn depends on the length of the antenna (so-called real aperture radars; RAR). The along-track resolution is proportional to the aperture length and in this case the antenna dimensions. Hence, obtaining a high along-track resolution requires very long antennas, which is in many cases unfeasible and has the disadvantage to reduce the resolution in range. A synthetic aperture radar (SAR) overcomes this problem by using a small antenna, which is moved while taking the measurement. The recorded data can be combined to obtain a synthesized longer aperture,

A.2 AWI UWB radar system

In my thesis I use radar data from AWI's (Alfred Wegener Institute) ultra-wideband radar (UWB). The

radar was developed at the Center for Remote Sensing of Ice Sheets (CReSIS) at the university of Kansas, is a MCoRDS (Multichannel Coherent Radar Depth Sounder) type radar (Arnold et al., 2019) and designed to image a full vertical profile of the ice column.

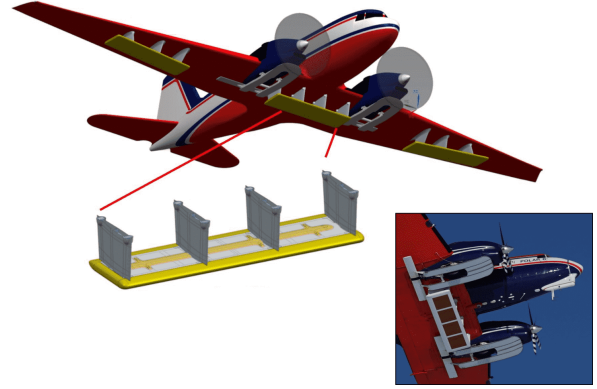


Figure A.3: AWI UWB radar system on Polar6. Schematic illustration and photograph of the antenna arrays. The 3D animation was kindly provided by University of Kansas and the photograph by Sepp Kipfstuhl.

Multi-element antenna arrays in combination with SAR techniques overcome typical limitations in radioglaciology. SAR algorithms improve the azimuth resolution and the usage of beam-steering techniques can reduce surface clutter and allow the detection of off-nadir oriented reflectors. Moreover, an increased bandwidth in combination with pulse compression techniques allow the sounding of thick ice in high resolution. Furthermore, multiple waveforms are emitted to sound different parts of the ice column. After processing the waveform images are combined to increase the overall resolution of the entire ice column. The system can operate in two different modes:

1. **Sounding mode:** The "traditional" 2D acquisition mode of a nadir section of the ice below the radar.
2. **Image mode:** Also referred to as "swath tomography" mode, which uses off-nadir scattering reflections from the ice-base to create a high-resolution DEM of the bed topography for a width of ~ 5 km along the radar transect.

The radar system comprises an eight-element antenna array, which is mounted underneath the fuselage of the AWI Basler BT-67 Polar 6 aircraft and two further eight-antenna arrays, which can be mounted underneath the wings (Hale et al., 2016). The centre array can alternate between transmission and reception, whereas both wing antenna-arrays only represent receivers. The data I used in my thesis were acquired during surveys, where only the centre array has been used.

A.3 UWB radar data acquisition

The radar can operate in a frequency range of 150–600 MHz with a pulse repetition frequency (PRF) of 10 kHz and the sampling frequency 1.6 GHz. The current maximum transmit power is 6 kW. Transmission and recording settings can be programmed in order to create individual acquisition profiles to sound different glaciological settings accordingly.

For fixed-frequency radar systems, the relationship between the minimum resolvable distance between targets in range direction δ_r can be written as:

$$\delta_r = \frac{v\tau}{2} \quad (\text{A.14})$$

with the EM wave propagation velocity v (see Equation A.8) and the pulse length τ . The emitted power is proportional to the pulse duration, which therefore, defines the maximum penetration depth. We note that a long pulse will lead to a large penetration depth but low resolution.

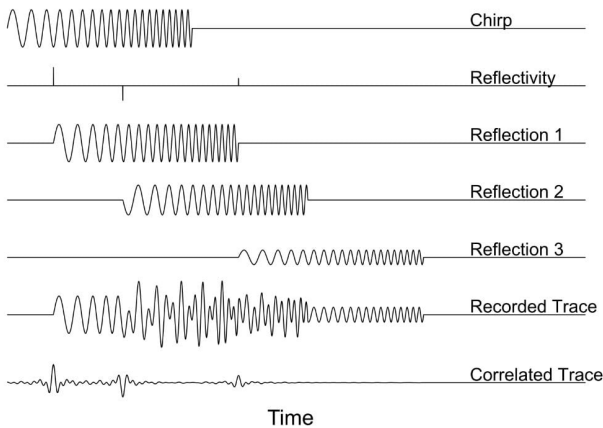


Figure A.4: Schematic illustration of chirped radar waveforms and reflections. The graphic was kindly provided by Nils Dörr (KIT).

The AWI UWB radar transmission signals are linear frequency-modulated chirps in a chosen frequency band and for a chosen pulse length. To overcome the tradeoff between range resolution and penetration depth, the pulse compression method is applied. When a transmitted chirp signal is reflected at interfaces of dielectric contrasts, the reflected trace represents a superposition of all reflections. To identify the first arrivals of the reflections recorded signal is correlated with the transmitted chirp (see Figure A.4). The reference signal can be a replica of the transmitted pulse but can also be a mathematically defined ideal version of the transmitted pulse.

For the selection of the appropriate bandwidth for a survey, we have to keep in mind that the reflection

characteristics of the target will be responsible for the signal-to-noise ratio (SNR). We must first differentiate between point and distributed targets. Point targets (e.g. internal layers, such as isochrones) reflect pixels with one scattering phase centre, whereas distributed targets contain many scattering phase centres. An increase in bandwidth will have no effect on SNR of point targets because the signal power remains at the same location. Distributed targets lose SNR with an increased bandwidth due to the variation of scattering positions. Appendix B provides an overview of different acquisition bandwidths for repeat flights over the same location, where the effects just described here are shown (Figure B.1).

A.3.1 Transmit equalization

SNR can be increased in the resulting data by correcting for phase, amplitude and time delay errors at each receiving antenna (Figure A.5). Adjustments in the individual antenna elements are made prior to the survey to compensate for any mismatches in the channel equalization coefficients on transmission and recording. This processing step is of particular importance for beamforming and the coherent averaging to increase SNR. If possible, the configuration of the individual correction factors are acquired during a test flight over open water or a flat ice surface. Errors in time delay are corrected via a phase shift in the frequency domain. By contrast, amplitude and phase errors are corrected via a scaling factor and phase shift in the time domain (Smith, 2014).

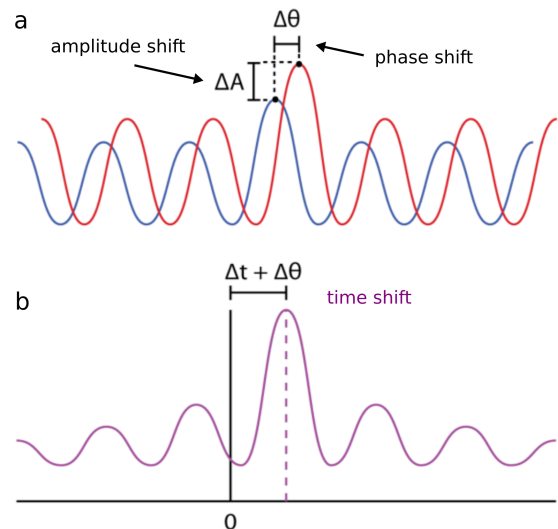


Figure A.5: Amplitude, time and phase correction. The graphic illustrates the corrections, which have to be applied prior to data acquisition to emit and record a coherent radar signal. The graphic was modified and used with permission from Smith (2014).

A.3.2 Presums

During data acquisition, the recorded traces are coherently presummed in the frequency domain with zero-pi modulation in the hardware (Allen et al. (2005)). While this step will increase SNR, it will reduce the effective PRF at the same time. The factors for presumming can be set individually for the respective waveforms.

A.4 UWB radar data processing

Radar data processing for the AWI UWB system is carried out with the CReSIS Toolbox (CReSIS, 2020). The main processing steps include pulse compression in range direction, synthetic aperture radar (SAR) focussing in the along-track dimension and array processing in the cross-track dimension (see Figure A.6). Each processing step is carried out for each waveform and each channel individually. The processing parameters are optimized in a way to create a high-resolution radargram, which is composed of the combination of the information from all channels and all waveforms.

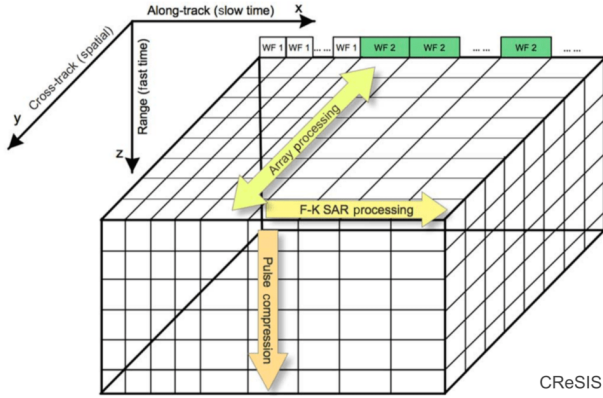


Figure A.6: CReSIS radar data processing. The main processing steps include pulse compression (in range) fk SAR processing (along-track) and array processing (cross-track). The image was obtained and used by courtesy from CReSIS.

A.4.1 Pulse compression

Pulse compression is applied to detect distant targets with high resolution. The long-coded (chirped) transmitted pulse is decoded (dechirped) at acquisition to generate a short pulse for high range resolution (Li et al., 2013). The method introduces range sidelobes on both sides of the main return power with a time window of twice the pulse duration (Tanner et al., 1994). To reduce sidelobes near the main peak of the echoes and to avoid the loss of transmission power, the transmitted and recorded signals are amplitude-tapered with a Tukey window with a taper ratio of 0.08 (Li et al., 2013).

A.4.2 Range resolution

The above mentioned factors and the propagation speed of the radar wave, which depends on the relative permittivity ϵ_r , determines the range resolution:

$$\delta(\epsilon_r) = \frac{k_i c}{2B\sqrt{\epsilon_r}}, \quad (\text{A.15})$$

where B is the bandwidth of the transmitted chirp, k_i the window widening factor as a result of the windows applied to the frequency and time domain and the speed of light in a vacuum c .

A.4.3 Motion compensation

SAR processing algorithms require a uniformly spaced linear trajectory of the antenna along the extent of the SAR aperture. Furthermore, high precision timing, positioning and aircraft orientation parameters are required to achieve the maximum possible SNR and avoid phase errors. For this step it is important to calculate the phase centre of the radar measurements. The spatial positioning is acquired via GPS positioning, which is in general not the location where the phase centre is located. Therefore, the GPS data is corrected according to the positioning of the GPS receivers at the aeroplane relative to the position of the radar antenna (Figure A.7).

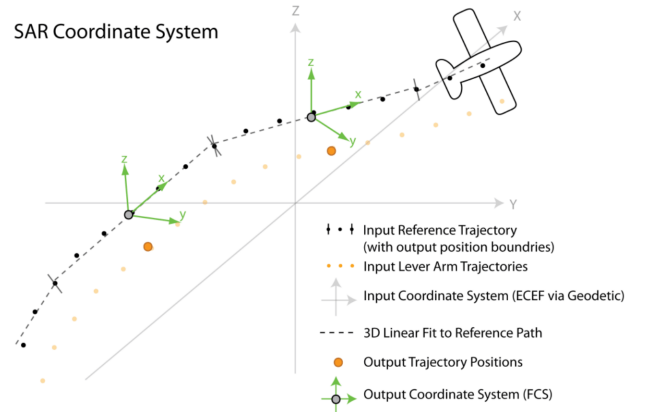


Figure A.7: SAR coordinate system in the CReSIS processing. The graphic was provided and used with permission from Smith (2014).

High precision positioning data are obtained by four NovAtel DL-V3 GPS receivers which are operating at 20 Hz and are mounted at different locations at the acquisition aircraft. The accuracy of the GPS system can be enhanced via post-processing routines. Furthermore, additional INS data is used to correct for aircraft motion. In summary, the following motion compensation steps are carried out before SAR processing (Figure A.7):

1. data re-sampling in along-track using a windowed sinc-interpolation kernel
2. flight path corrections with a time delay
3. correcting due to changes in elevation, roll and pitch along the trajectory

Motion compensation and the creation of a synthetic flight trajectory also eliminates errors in the along-track spacing due to variations in the aircraft velocity.

A.4.4 SAR processing

Synthetic aperture radar (SAR) focusing is used to improve along-track resolution of the radargram. This processing step is particularly important to better resolve internal layers orientation and bed conditions. The synthetic aperture trajectory with a uniform sample space allows to use the frequency-wavenumber (fk) wave field migration technique to re-locate reflection energy back to the location of the target. In the CReSIS Toolbox, this step is summarized as SAR focusing (in along-track direction). Fk-migration is a common technique in seismics for layered media (Gazdag, 1978) and has been adapted for radioglaciology. Several SAR methods exist for focussing RES data (Heister and Scheiber, 2018). Here we use a SAR processor, which relies on a 1-D two-layer velocity model with constant respective permittivity values (Leuschen et al., 2000): $\epsilon_r = 1$ for air and $\epsilon_r = 3.15$ for ice. The boundary between the two layers is the radar reflection at the ice surface and is traced automatically. At the end, the total signal power in the scene is not changed but focused.

The main fk-migration steps in the CReSIS Toolbox are the following (for details see the CReSIS Toolbox Guide, <https://ops.cresis.ku.edu/wiki/index.php>):

1. fast time FFT (fast Fourier transform)
2. acquire motion compensation parameters
3. apply motion compensation corrections
4. data re-sampling in slow time
5. slow time FFT
6. fk migration (SAR processor, see Leuschen et al. 2000)
7. inverse FFT in fast time (range) and slow time (along-track; see Figure A.6)

A.4.5 Channel combination (beamforming)

After SAR processing, we obtain traces of each waveform-channel (wf-adc) pair, which contain the

back-scattered signals from all conceivable directions. These signals may originate from far off-nadir scatterers at the ice surface (e.g. crevasses), from within the ice (e.g. englacial channels or moulins) or from structures at the ice base. These echoes can mask the nadir reflection, which is commonly the information we are interested in. Theoretically, off-nadir scattering can originate from everywhere within the cross-track beam angle of the radar. The angle β_y for the UWB radar is defined by:

$$\beta_y = \arcsin \frac{\lambda_c}{Nd_y}, \quad (\text{A.16})$$

with the centre frequency λ_c , the number of antenna elements $N = 8$ and the antenna spacing $d_y = 0.468$ m.

Off-nadir reflections have a phase shift at the antenna elements. Identification and correction of this phase shift is called beamforming. Several methods in the CReSIS Toolbox are implemented to combine the wf-adc pairs (beamforming) to suppress surface clutter and side reflections and steer the antenna beam towards nadir. However, there are also beamforming algorithms to achieve the opposite, e.g. to calculate the cross-track origin of a scattered signal. The CReSIS Toolbox contains the following beamforming methods:

1. *delay and sum* beamforming with incoherent power multilooking (standard)
2. MVDR (minimum variance distortionless response)
3. MUSIC (multiple signal classification)

The most frequently used beamforming method for 2D nadir steered surveys is called *delay and sum* (Richards, 2005). The antenna array beam is steered toward nadir by coherently summing the data from each channel while accounting for the actual position of each measurement phase centre. The method basically assumes that a wavefront approaches an antenna array at a certain arrival time at each respective antenna element. The data is shifted by a certain time assuming a certain incident angle. Thereafter, the data of the single antennas are stacked subsequently. The idea behind steering the antenna arrivals to a certain angle is to disregard any destructive interfering signals from off-nadir.

MVDR represents a method to reduce the effect of strong interference and noise, such as from surface clutter from basal crevasses (Wang et al., 2016). MUSIC searches for signal peaks for angle-of-arrival estimation. The algorithm provides estimates of the number of incident waveforms, directions of arrivals (which gives information of the reflection location) and the cross-correlation among the incoming waveforms (Schmidt, 1986; Rubsamen and Gershman, 2009).

A comparison of a radar section combined with the *delay and sum* and MVDR method is provided in Figure B.2 c and d in Appendix B. The application and output of the MUSIC processing is addressed in the later section *Ice-Sheet Bed 3D Tomography* and in Figure B.4 in Appendix B.

A.4.6 Waveform combination

The UWB system uses alternating waveforms to increase the dynamic range of the system. A typical recording setup uses: (1) short pulses ($1 \mu\text{s}$) and low-receiver gain of 11 dB to image the glacier surface, and longer pulses (3 - $10 \mu\text{s}$) with higher receiver gain (48 dB) to image internal features and the ice base. The channel combination accounts for all channels in a waveform and produces one individual radargram per waveform. In a last (optional) step, the different waveform images were vertically combined to increase the dynamic range of the result. The advantage is to obtain a better resolution in the upper, middle and lower part of the radargram (see Figure A.8). The TWT at which the radargrams are combined were chosen with regard to the pulse durations of the transmitted waveforms and the surface return in order to avoid saturation of the high gain channels due to the strong surface return. For three waveform collection with pulse durations of $1 \mu\text{s}$, $3 \mu\text{s}$, $10 \mu\text{s}$ nadir waveforms, image 2 is combined with image 1 after $3 \mu\text{s}$ TWT after the surface reflection and image 3 with image 2 $10 \mu\text{s}$ TWT after the surface return. For 3D swath mode surveys, the waveform images can be fused horizontally.

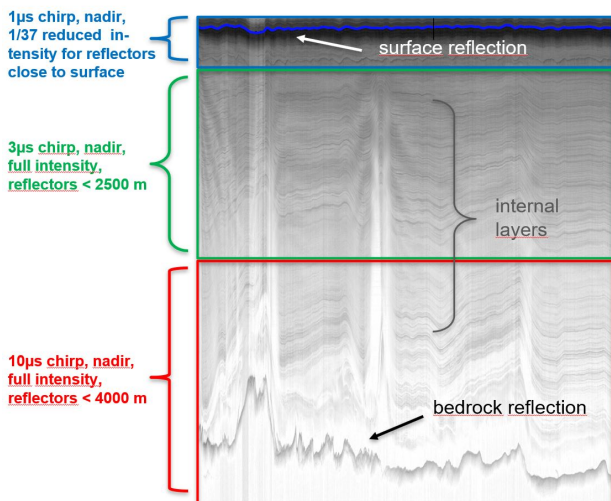


Figure A.8: Illustration of the different waveform images in the CReSIS processing. Image 1 is used to determine the ice surface reflection and uppermost layers, image 2 to record the intermediate part (the first hundreds of meters) of ice thickness and image 3 for the deep stratigraphy and bed reflection.

A.4.7 Ice sheet bed 3D swath tomography (image mode)

Mapping the subglacial topography at high resolution (e.g. King et al., 2009; Bingham et al., 2017) represents a major challenge with conventional 2D radar surveys. While the resolution along-track is high, the cross-track resolution of the bed topography depends on the survey line spacing. Due to the temporal and logistical limitations, researchers need to decide on a survey design, which either covers a large region (with less spatial resolution) or a small region (with higher spatial resolution).

3D swath tomography offers the possibility to extend the cross-track area. Unlike radar-interferometry, this technique uses the absolute phase measured by each antenna element (Jezek et al., 2011). The method has been successfully applied by Paden et al. (2010) and Jezek et al. (2011) to image small areas of the glacier bed in high resolution. Holschuh et al. (2020) analyzed a larger area at Thwaites Glacier in Antarctica and created a high-resolution DEM of the bed topography showing a variety of subglacial landforms and their connection to the subglacial hydrology.

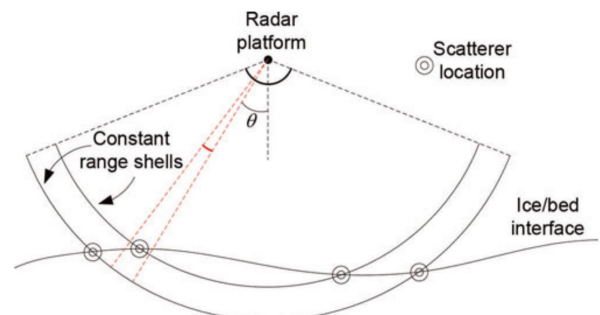


Figure A.9: Principle of 3D swath tomography. The image illustrates the estimation of the arrival angle from scattering reflections of the ice sheet bed (image obtained from Paden et al. (2010)).

The amplitude and phase of each return signal of each receiving antenna are related to the arrival angle and range of the reflection from scattering targets (Figure A.9). Hence, to estimate the bed topography, we have to estimate the direction-of-arrival of the backscattered radar waves. The CReSIS Toolbox makes use of the MUSIC algorithm (Schmidt, 1986) to estimate the direction-of-arrival with the signals from the eight antenna element receiver.

The bed topography surface is generated by tracking the maximum range-bin return for each spatial frequency bin produced by the MUSIC algorithm (Paden et al., 2010). The toolbox uses a maximum likelihood

method to calculate signal amplitude and the direction-of-arrival for the left and right side along the flight trajectory (Jezek et al., 2011). Together with an estimation of the refraction index for ice, the ice thickness and bed topography can be calculated. The approach assumes that there is little or no volume scattering occurring along the EM wave path. Furthermore, it is assumed that scattering at internal layers can be neglected due to the anticipated specular reflectivity of internal layers (Paren and Robin, 1975).

The results from the first bed topography DEM on the basis of AWI UWB swath radar data are shown in Figure B.4 Appendix B in the section *Swath Mode (3D Imaging Mode)*.

Bibliography

- Allen, C. T., Mozaffar, S. N., and Akins, T. L. Suppressing coherent noise in radar applications with long dwell times. *IEEE Geoscience and Remote Sensing Letters*, 2(3):284–286, July 2005. doi: 10.1109/LGRS.2005.847931. URL <http://dx.doi.org/10.1109/LGRS.2005.847931>.
- Alley, R. B. Fabrics in polar ice sheets: Development and prediction. *Science*, 240(4851):493–495, 1988. doi: 10.1126/science.240.4851.493. URL <https://science.sciencemag.org/content/240/4851/493>.
- Arnold, E., Leuschen, C., Rodriguez-Morales, F., Li, J., Paden, J., Hale, R., and Keshmiri, S. CReSIS airborne radars and platforms for ice and snow sounding. *Annals of Glaciology*, pages 1–10, nov 2019. doi: 10.1017/aog.2019.37. URL <https://doi.org/10.1017/2Faog.2019.37>.
- Baker, G. S., Jordan, T. E., and Pardy, J. An introduction to ground penetrating radar (GPR). In *Stratigraphic Analyses Using GPR*. Geological Society of America, 01 2007. ISBN 9780813724324. doi: 10.1130/2007.2432(01). URL [https://doi.org/10.1130/2007.2432\(01\)](https://doi.org/10.1130/2007.2432(01)).
- Bingham, R. G., Vaughan, D. G., King, E. C., Davies, D., Cornford, S. L., Smith, A. M., Arthern, R. J., Brisbourne, A. M., Rydt, J. D., Graham, A. G. C., Spagnolo, M., Marsh, O. J., and Shean, D. E. Diverse landscapes beneath Pine Island Glacier influence ice flow. *Nature Communications*, 8(1), nov 2017. doi: 10.1038/s41467-017-01597-y. URL <https://doi.org/10.1038/2Fs41467-017-01597-y>.
- Castelletti, D., Schroeder, D. M., Mantelli, E., and Hilger, A. Layer optimized sar processing and slope estimation in radar sounder data. *Journal of Glaciology*, 65(254):983–988, 2019. doi: 10.1017/jog.2019.72. URL <https://doi.org/10.1017/jog.2019.72>.
- CReSIS. CReSIS Toolbox [computer software], Lawrence, Kansas, USA. Retrieved from <https://github.com/CReSIS/>, 2020.
- Doake, C. S. M. Polarization of radio waves in ice sheets. *Geophysical Journal International*, 64(2):539–558, 02 1981. ISSN 0956-540X. doi: 10.1111/j.1365-246X.1981.tb02682.x. URL <https://doi.org/10.1111/j.1365-246X.1981.tb02682.x>.
- Drews, R., Eisen, O., Steinhage, D., Weikusat, I., Kipfstuhl, S., and Wilhelms, F. Potential mechanisms for anisotropy in ice-penetrating radar data. *Journal of Glaciology*, 58(209):613–624, sep 2012. ISSN 0022-1430. doi: 10.3189/2012JogG11J114. URL <http://dx.doi.org/>.
- Fujita, S., Matsuoka, T., Ishida, T., Matsuoka, K., and Mae, S. A summary of the complex dielectric permittivity of ice in the megahertz range and its applications for radar sounding of polar ice sheets. *Physics of Ice Core Records*, pages 185–212, 2000. URL <https://eprints.lib.hokudai.ac.jp/dspace/bitstream/2115/32469/1/P185-212.pdf>.
- Fujita, S., Maeno, H., and Matsuoka, K. Radio-wave depolarization and scattering within ice sheets: a matrix-based model to link radar and ice-core measurements and its application. *Journal of Glaciology*, 52(178):407–424, 2006. doi: 10.3189/172756506781828548. URL <https://doi.org/10.3189/172756506781828548>.
- Gazdag, J. Wave equation migration with the phase-shift method. *Geophysics*, 43(7):1342–1351, 1978. ISSN 0016-8033. doi: 10.1190/1.1440899. URL <http://dx.doi.org/10.1190/1.1440899>.
- Gillet-Chaulet, F., Gagliardini, O., Meyssonier, J., Montagnat, M., and Castelnau, O. A user-friendly anisotropic flow law for ice-sheet modeling. *Journal of Glaciology*, 51(172):3–14, 2005. doi: 10.3189/172756505781829584.
- Hale, R., Miller, H., Gogineni, S., Yan, J. B., Rodriguez-Morales, F., Leuschen, C., Paden, J., Li, J., Binder, T., Steinhage, D., Gehrman, M., and Braaten, D. Multi-channel ultra-wideband radar sounder and imager. In *2016 IEEE International Geoscience and Remote Sensing Symposium (IGARSS)*. IEEE, jul 2016. doi: 10.1109/igarss.2016.7729545. URL <https://doi.org/10.1109/2Figarss.2016.7729545>.
- Hargreaves, N. D. The Radio-Frequency Birefringence of Polar Ice. *Journal of Glaciology*, 21(85):301–313, 1978. ISSN 0022-1430. doi: 10.3189/s0022143000033499. URL <https://doi.org/10.3189/s0022143000033499>.
- Harrison, C. H. Radio echo sounding of horizontal layers in ice. *Journal of Glaciology*, 12(66):383–397, 1973. doi: 10.3189/S0022143000031804. URL <https://doi.org/10.3189/S0022143000031804>.
- Heister, A. and Scheiber, R. Coherent large beamwidth processing of radio-echo sounding data. *The Cryosphere*, 12(9):2969–2979, 2018. doi: 10.5194/tc-12-2969-2018. URL <https://tc.copernicus.org/articles/12/2969/2018/>.

- Holschuh, N., Christianson, K., and Anandakrishnan, S. Power loss in dipping internal reflectors imaged using ice-penetrating radar. *Annals of Glaciology*, 55(67):49–56, 2014. doi: 10.3189/2014aog67a005. URL <https://doi.org/10.3189%2F2014aog67a005>.
- Holschuh, N., Christianson, K., Paden, J., Alley, R., and Anandakrishnan, S. Linking postglacial landscapes to glacier dynamics using swath radar at Thwaites Glacier Antarctica. *Geology*, jan 2020. doi: 10.1130/g46772.1. URL <https://doi.org/10.1130%2Fg46772.1>.
- Jacobel, R. W., Welch, B. C., Osterhouse, D., Pettersson, R., and MacGregor, J. A. Spatial variation of radar-derived basal conditions on kamb ice stream, west antarctica. *Annals of Glaciology*, 50(51):10–16, 2009. doi: 10.3189/172756409789097504. URL <https://doi.org/10.3189/172756409789097504>.
- Jezek, K., Wu, X., Gogineni, P., Rodríguez, E., Freeman, A., Rodríguez-Morales, F., and Clark, C. D. Radar images of the bed of the Greenland Ice Sheet. *Geophysical Research Letters*, 38(1):1–5, 2011. ISSN 00948276. doi: 10.1029/2010GL045519. URL <http://dx.doi.org/10.1029/2010GL045519>.
- Jordan, T. M., Schroeder, D. M., Castelletti, D., Li, J., and Dall, J. A polarimetric coherence method to determine ice crystal orientation fabric from radar sounding: Application to the neem ice core region. *IEEE Transactions on Geoscience and Remote Sensing*, 57(11):8641–8657, 2019. doi: 10.1109/TGRS.2019.2921980. URL <https://ieeexplore.ieee.org/document/8755860>.
- Keisling, B. A., Christianson, K., Alley, R. B., Peters, L. E., Christian, J. E., Anandakrishnan, S., Riverman, K. L., Muto, A., and Jacobel, R. W. Basal conditions and ice dynamics inferred from radar-derived internal stratigraphy of the northeast Greenland ice stream. *Annals of Glaciology*, 55(67):127–137, 2014. doi: 10.3189/2014aog67a090. URL <https://doi.org/10.3189%2F2014aog67a090>.
- King, E. C., Hindmarsh, R. C. A., and Stokes, C. R. Formation of mega-scale glacial lineations observed beneath a West Antarctic ice stream. *Nature Geoscience*, 2(8):585–588, jul 2009. doi: 10.1038/ngeo581. URL <https://doi.org/10.1038%2Fngeo581>.
- Leuschen, C., Gogineni, S., and Tammana, D. SAR processing of radar echo sounder data. pages 2570–2572, 2000. doi: 10.1109/igarss.2000.859643. URL <http://dx.doi.org/10.1109/igarss.2000.859643>.
- Li, J., Paden, J., Leuschen, C., Rodríguez-Morales, F., Hale, R. D., Arnold, E. J., Crowe, R., Gomez-Garcia, D., and Gogineni, P. High-altitude radar measurements of ice thickness over the antarctic and greenland ice sheets as a part of operation ice-bridge. *IEEE Transactions on Geoscience and Remote Sensing*, 51(2):742–754, 2013. ISSN 0196-2892. doi: 10.1109/TGRS.2012.2203822.
- MacGregor, J. A., Winebrenner, D. P., Conway, H., Matsuoka, K., Mayewski, P. A., and Clow, G. D. Modeling englacial radar attenuation at siple dome, west antarctica, using ice chemistry and temperature data. *Journal of Geophysical Research: Earth Surface*, 112(F3), 2007. doi: <https://doi.org/10.1029/2006JF000717>. URL <https://agupubs.onlinelibrary.wiley.com/doi/abs/10.1029/2006JF000717>.
- Matsuoka, K. Pitfalls in radar diagnosis of ice-sheet bed conditions: Lessons from englacial attenuation models. *Geophysical Research Letters*, 38(5):n/a–n/a, mar 2011. doi: 10.1029/2010gl046205. URL <https://doi.org/10.1029%2F2010gl046205>.
- Matsuoka, K., Morse, D., and Raymond, C. F. Estimating englacial radar attenuation using depth profiles of the returned power, central west antarctica. *Journal of Geophysical Research: Earth Surface*, 115(F2), 2010. doi: <https://doi.org/10.1029/2009JF001496>. URL <https://agupubs.onlinelibrary.wiley.com/doi/abs/10.1029/2009JF001496>.
- Maxwell, J. C. Viii. a dynamical theory of the electromagnetic field. *Philosophical Transactions of the Royal Society of London*, 155:459–512, 1865. doi: 10.1098/rstl.1865.0008. URL <https://royalsocietypublishing.org/doi/abs/10.1098/rstl.1865.0008>.
- Paden, J., Akins, T., Dunson, D., Allen, C., and Gogineni, P. Ice-sheet bed 3-D tomography. *Journal of Glaciology*, 56(195):3–11, 2010. doi: 10.3189/002214310791190811. URL <https://doi.org/10.3189%2F002214310791190811>.
- Paren, J. G. and Robin, G. d. Q. Internal reflections in polar ice sheets. *Journal of Glaciology*, 14(71):251–259, 1975. doi: 10.3189/S0022143000021730.
- Peters, M. E., Blankenship, D. D., and Morse, D. L. Analysis techniques for coherent airborne radar sounding: Application to west antarctic ice streams. *Journal of Geophysical Research: Solid Earth*, 110(B6), 2005. doi: <https://doi.org/10.1029/2004JB003222>. URL <https://agupubs.onlinelibrary.wiley.com/doi/abs/10.1029/2004JB003222>.
- Petrenko, V. F. und Whitworth, R. W. Physics of ice. *Oxford University Press, Oxford, New York*, 1999.
- Richards, M. Fundamentals of Radar Signal Processing. *Professional Engineering, New York: McGraw-Hill Education*, 2005.

- Robin, G. D. Q., Evans, S., Bailey, J. T., and Bullard, E. C. Interpretation of radio echo sounding in polar ice sheets. *Philosophical Transactions of the Royal Society of London. Series A, Mathematical and Physical Sciences*, 265(1166):437–505, 1969. doi: 10.1098/rsta.1969.0063. URL <https://royalsocietypublishing.org/doi/abs/10.1098/rsta.1969.0063>.
- Rubsamen, M. and Gershman, A. B. Direction-of-arrival estimation for nonuniform sensor arrays: From manifold separation to fourier domain music methods. *IEEE Transactions on Signal Processing*, 57(2):588–599, 2009. doi: 10.1109/TSP.2008.2008560. URL <https://ieeexplore.ieee.org/document/4663945>.
- Schmidt, R. Multiple emitter location and signal parameter estimation. *IEEE Transactions on Antennas and Propagation*, 34(3):276–280, 1986. doi: 10.1109/TAP.1986.1143830. URL <https://ieeexplore.ieee.org/document/1143830>.
- Schroeder, D. M., Grima, C., and Blankenship, D. D. Evidence for variable grounding-zone and shear-margin basal conditions across Thwaites Glacier, West Antarctica. *Geophysics*, 81(1):WA35–WA43, 2015. ISSN 0016-8033. doi: 10.1190/geo2015-0122.1. URL <https://doi.org/10.1190/geo2015-0122.1>.
- Smith, L. Validation of CReSIS synthetic aperture radar processor and optimal processing parameters. *Master's thesis, University of Kansas*, 2014. URL <https://kuscholarworks.ku.edu/handle/1808/18381> (lastaccess:1December2020).
- Tanner, A., Durden, S., Denning, R., Im, E., Li, F., Ricketts, W., and Wilson, W. Pulse compression with very low sidelobes in an airborne rain mapping radar. *IEEE Transactions on Geoscience and Remote Sensing*, 32(1):211–213, 1994. doi: 10.1109/36.285205.
- Wang, Z., Gogineni, S., Rodriguez-Morales, F., Yan, J. B., Paden, J., Leuschen, C., Hale, R. D., Li, J., Carabaja, C. L., Gomez-Garcia, D., Townley, B., Willer, R., Stearns, L., Child, S., and Braaten, D. Multichannel Wideband Synthetic Aperture Radar for Ice Sheet Remote Sensing: Development and the First Deployment in Antarctica. *IEEE Journal of Selected Topics in Applied Earth Observations and Remote Sensing*, 9(3):980–993, 2016. ISSN 21511535. doi: 10.1109/JSTARS.2015.2403611. URL <http://dx.doi.org/10.1109/JSTARS.2015.2403611>.
- Young, T. J., Schroeder, D. M., Jordan, T. M., Christoffersen, P., Tulaczyk, S. M., Culberg, R., and Bienert, N. L. Inferring ice fabric from birefringence loss in airborne radargrams: Application to the eastern shear margin of thwaites glacier, west antarctica. *Journal of Geophysical Research:* *Earth Surface*, n/a(n/a):e2020JF006023. doi: <https://doi.org/10.1029/2020JF006023>. URL <https://agupubs.onlinelibrary.wiley.com/doi/abs/10.1029/2020JF006023>.

Appendix B

UWB radar: acquisition and processing tests

This chapter is devoted to the various recording and processing options for UWB radar data. First, I show how the data quality and resolution differs between different frequency bands at acquisition. Then, I discuss the different processing options that can be adapted depending on the focus of the study. In my work, the main goal was to assess which processing steps produce consistent high-resolution radargrams and should be included in a standardized workflow. In particular, the focus lies on a good resolution of the lower radar stratigraphy and the best possible to achieve resolution of steeply dipping internal layers. In addition to the analyses mentioned so far, which refer to the 2D mode (sounding mode), I also discuss the 3D swath tracking of the bed topography (imaging mode, see Appendix A), which is now fully implemented in the *CReSIS Toolbox*.

B.1 Data acquisition tests

The AWI UWB radar system operates in a frequency range between 150–600 MHz. Several acquisition modes with varying bandwidth at different centre frequencies were tested in the field season 2018/19 in Antarctica. All tests were performed in the sounding mode, which is the regular 2D data acquisition mode. Four different frequency ranges were tested in a repeated flight over the same survey line (Figure B.1): 180–210 MHz, 150–240 MHz (centre frequency = 195 MHz) and 320–350 MHz, 150–520 MHz (centre frequency = 335 MHz). All modes use three chirped pulses (1, 3 and 10 μ s steered towards nadir) on acquisition, which are finally combined to produce the radargram (see Appendix A). Due to the different centre frequencies and bandwidths we obtain different reflection patterns:

1. The 180–210 MHz (Frame 20181230_01_003) mode has a range resolution of $R = 4.31$ m and is thus limited in the resolution of the amount of internal layers. This mode however shows the best resolution for reflections in the deep ice column, in particular in the usually echo-free zone (Figure B.1 a).
2. The 150–240 MHz mode (Frame 20181230_02_004) has the same centre frequency as 180–210 MHz

but a larger bandwidth. This means that the total energy transmitted is spanned over a larger frequency spectrum, which leads to finer range resolution ($R = 1.44$ m). The intensity of reflections in the lower part of the ice as well as the bed reflection is only slightly weaker than the 180–210 MHz mode (Figure B.1 b).

3. The 320–350 MHz mode (Frame 20181230_09_004) has a higher centre frequency as the previous two modes (and as such is subject to higher attenuation; see e.g. Equations A.2 and A.13) but the same bandwidth as the 180–210 MHz mode. Hence, range resolution is equal to the 180–210 MHz mode ($R = 4.31$ m; Figure B.1 c).
4. The 150–520 MHz mode (Frame 20181230_08_003) shows the largest bandwidth and finest resolution of layers ($R = 0.35$ m). The strength of radar reflections from the bed and deep ice is weaker as in comparison to the other modes (Figure B.1 d).

The range resolution R is the minimum difference to distinguish two targets of isolation. It is defined as:

$$R = \frac{k_i c}{2B \sqrt{\epsilon_r}}, \quad (\text{B.1})$$

where B is the bandwidth, $\epsilon_R = 3.15$ is the approximate dielectric of ice, c the speed of light in a vacuum and k_i the window widening factor ($k_i = 1.53$ for 20% Tukey window on transmit and at pulse compression for our settings). Hence, the range resolution is primarily controlled by the bandwidth and not by the centre frequency.

B.2 Data processing tests

A variety of settings can be changed for UWB radar data processing. For this thesis, I focussed on processing optimization to recover:

1. deep ice stratigraphy reflections, such as the low-ermost isochrones or signals which do not represent isochrones but reflect traces of deformation
2. the recovery of steeply dipping englacial layers (e.g. isochrones from folding)

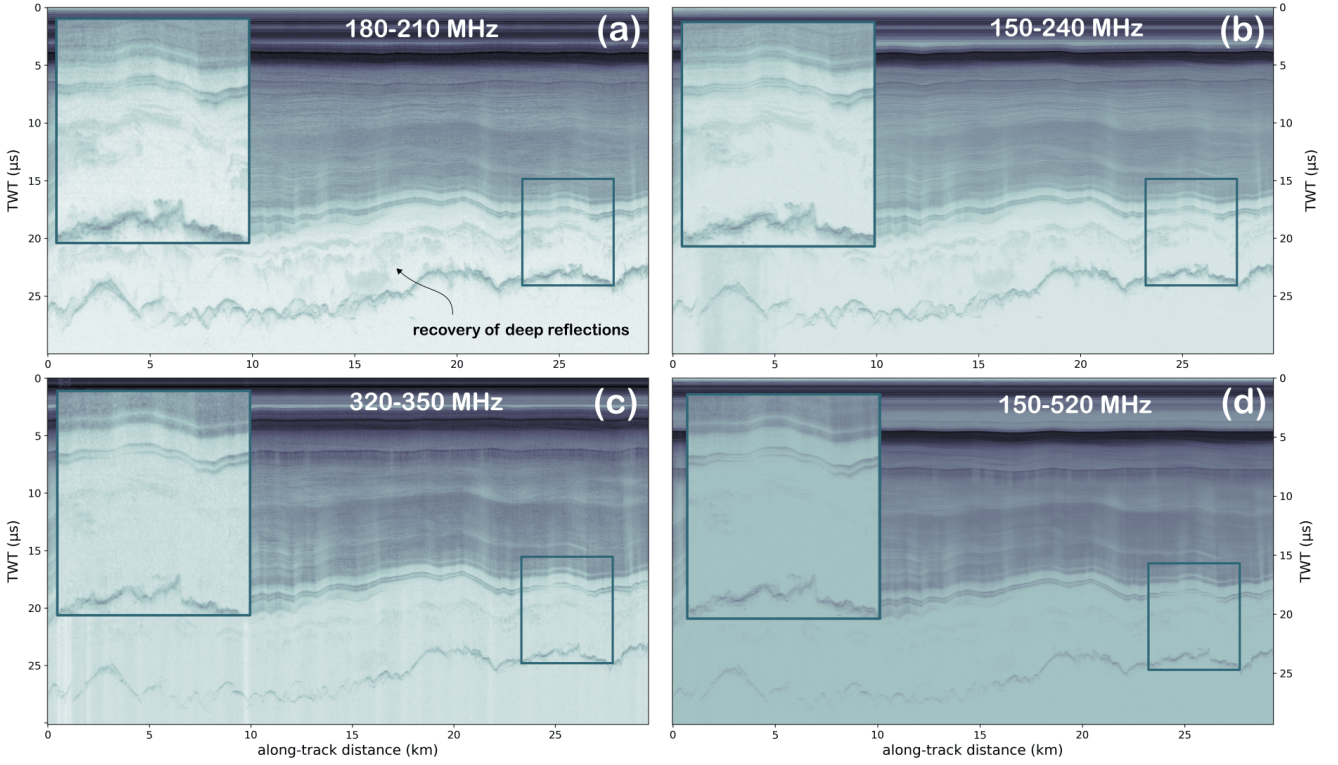


Figure B.1: Radargrams of the same survey line in four different acquisition modes: (a) Frame 20181230_01_003 with 180–210 MHz, (b) Frame 20181230_02_004 with 150–240 MHz, (c) Frame 20181230_09_004 with 320–350 MHz and (d) Frame 20181230_08_003 with 150–520 MHz.

B.2.1 Qlook and SAR processing

Two of the standard data products in the CReSIS processing chain are the so called quicklook (or *qlook*) and SAR focussed (or *standard*) results. Processing distinguishes between unfocussed and focussed SAR. The quicklook product uses unfocussed synthetic aperture radar processing for each channel and assumes that all reflections arrive at the receiver from nadir. The data within each channel are coherently stacked in slow time and no correction for propagation delay changes is applied. Here, no motion compensation is applied. Finally, the signals from all eight channels are averaged incoherently. The SAR focussed data product uses focussed synthetic aperture radar processing (fk migration) on each channel individually (Leuschen et al., 2000). The SAR processing requires a uniformly sampled linear trajectory along the extent of the SAR aperture.

A comparison between the two products reveals the following features (see Figure B.2 a and b):

- Hyperbolas from scattering reflectors are reduced and the energy focussed in the SAR focussed product compared to the quicklooks.
- The SAR focussed product shows a better resolution for internal features in the deep stratigraphy.

- The total power of the whole scene should not differ between the qlook and SAR focussed result. However, from the standpoint of analyzing internal layer reflection power it is simpler to use the qlook product. While the SAR focussed product is better to image inclined layers due to the wider aperture, additional investigations are required to understand its effect on the return power. This generally leads to the fact that the scattering properties of the reflector (in fact, the angular scattering distribution) have to be taken into account here. The answer would be different for isotropic scattering targets as for specular targets.

B.2.2 Array methods

At a certain step in the radar processing chain the along-track focussed or unfocussed single channels of the individual waveform are combined to increase the SNR and to reduce the impact of surface clutter and off-nadir reflections. Here we compare the results of two different algorithms (Figure B.2 c and d): the *delay-and-sum* method (Richards, 2005), which allows beam forming with incoherent power multilooking and MVDR (minimum variance distortionless response; Wang et al. 2016). For further details see Appendix A.

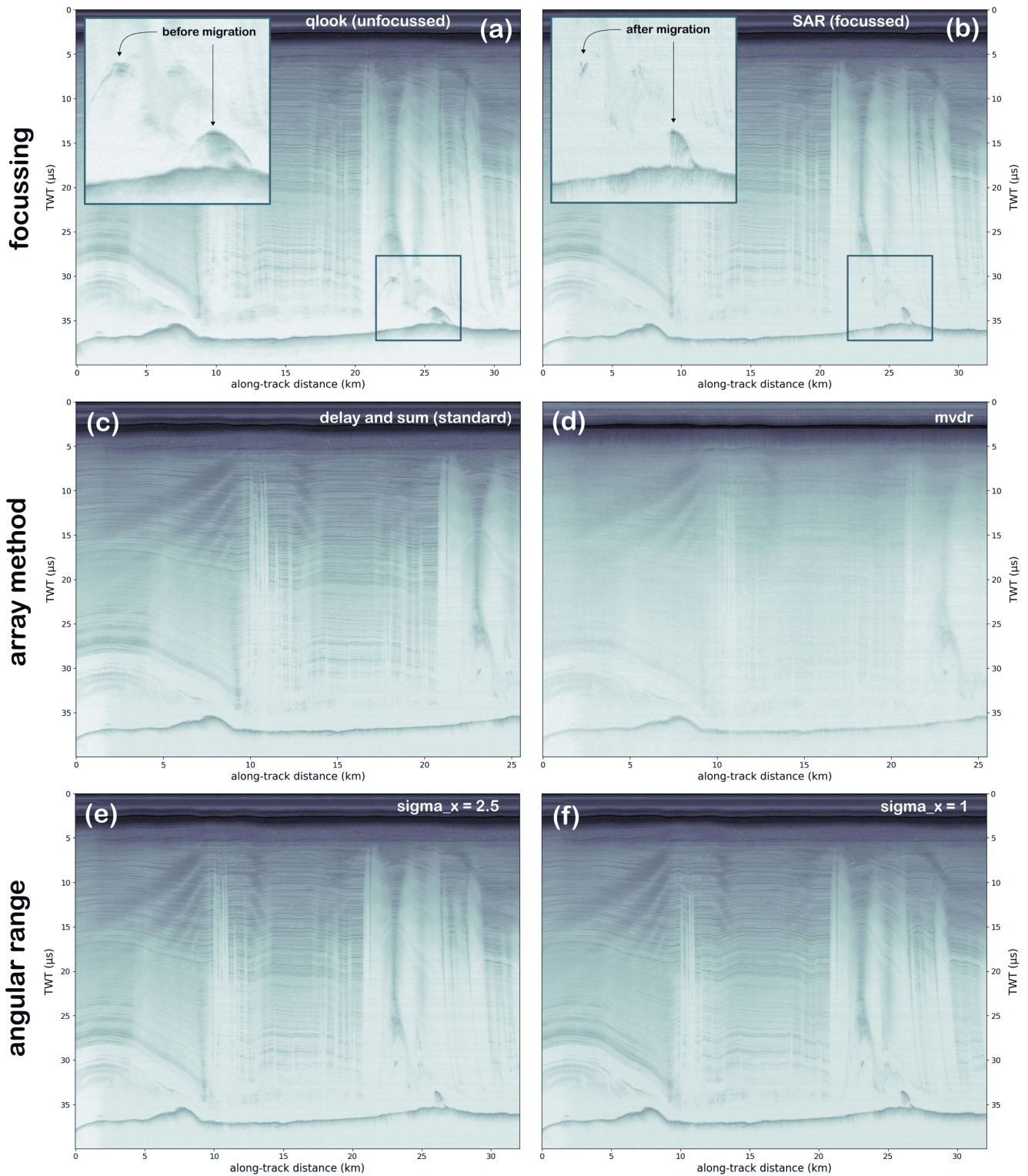


Figure B.2: Comparison between two different processing methods. Panel (a) shows a radargram processed with the qlook algorithm (unmigrated). Panel (b) shows the same radar section processed with the SAR algorithm (fk migrated). Two radargrams showing different array methods are shown in panel (c) the *delay and sum* (standard) array method and (d) the *mvdr* array method. A comparison of different angular range (SAR along-track resolution factors; σ_x) are shown in panel (e) with $\sigma_x = 2.5$ and panel (f) the same radar section with $\sigma_x = 1$. Steeply inclined internal layers are better resolved when σ_x is small.

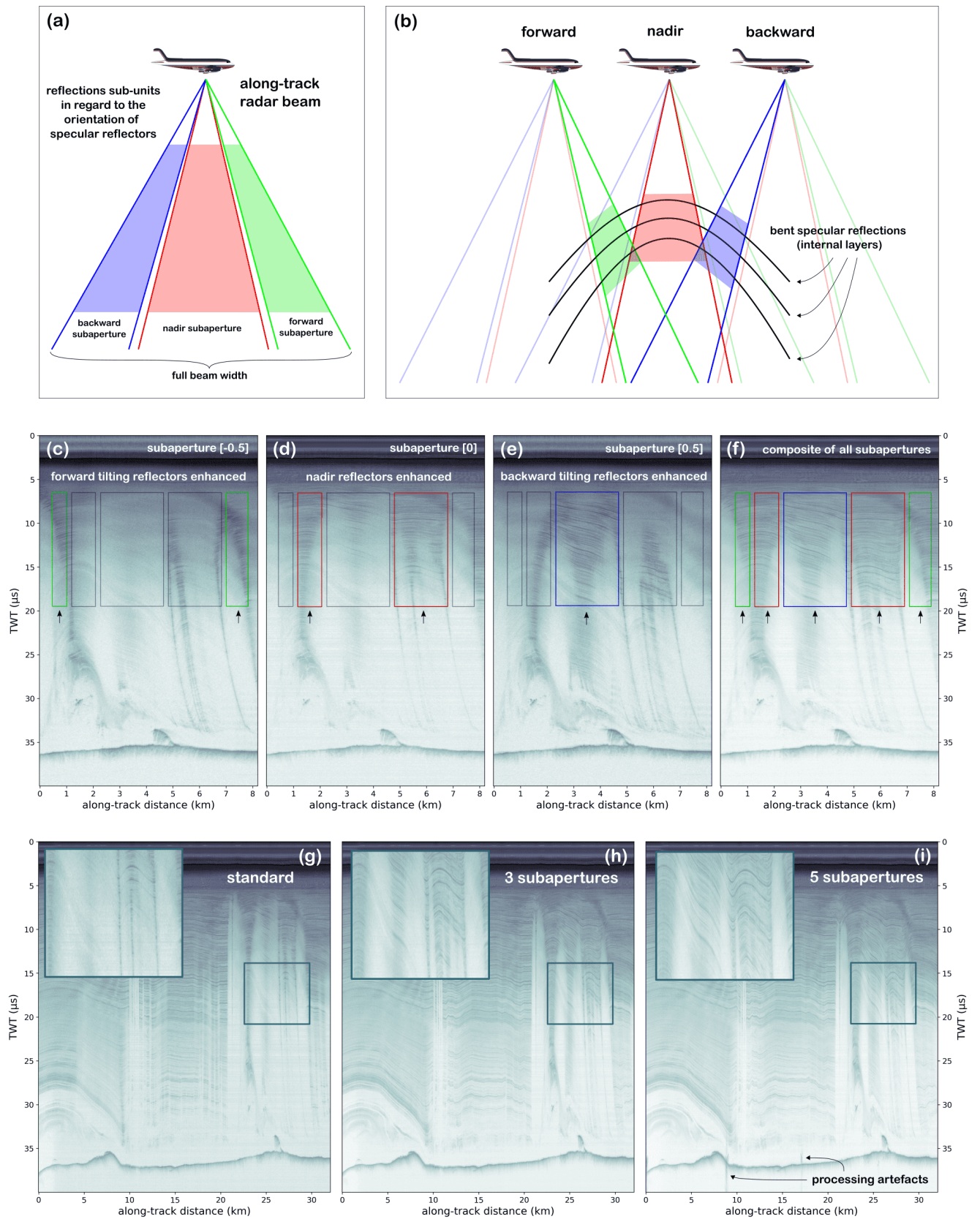


Figure B.3: Sketch and radargrams showing the principle of sub-aperture processing. Panels (a) and (b) illustrate which how the different parts of the radar beam capture the reflections from differently oriented reflectors. The different sub-aperture radargrams (forward, nadir and backward) as well as the combined radargram (uncoherently stacked) are shown in panels (c)–(f). Panels (g)–(i) show the effect of combined radargrams with one (only nadir), three and five sub-apertures.

I compared several radar sections with the *MVDR* and *delay-and-sum* method and I can clearly state that *delay-and-sum* shows always the better results. This can most likely be explained that we did not survey ice where the signal was interfered by severe surface clutter.

B.2.3 SAR with wider angular range

I tested several settings to increase the return power for steeply dipping internal reflections. One possibility offers the parameter σ_x (σ_x), which performs the SAR focussing with a wider angular range. By processing at a finer SAR resolution, the SAR processor uses scattered energy from a wider angular range around nadir to form the image. Since the angle of scattered returns from a specular internal layer is proportional to the internal layer slope, the SAR processor's increased sensitivity to larger angle returns translates to an increased sensitivity to layers with larger slopes. We achieve a better resolution of steeply inclined internal reflectors by changing the along-track resolution before SAR processing to 1 m ($\sigma_x = 1$), whereas the default setting is $\sigma_x = 2.5$. 1 m is not the smallest possible value for processing, but is on the limit to achieve a sufficiently high SNR. The SNR is smaller for larger angles because the range to the target increases for greater angles, which leads to additional signal loss (spherical spreading loss and additional signal attenuation in ice).

Figure B.2e and f show a comparison between the same radar section processed with $\sigma_x = 2.5$ and $\sigma_x = 1$, respectively. The results generated with $\sigma_x = 1$ recover some portion of the steeply dipping internal reflections, particularly in the upper part of the ice column without causing any SNR loss in other parts of the scene. Due to the increase in along-track samples, the data amount increases significantly in comparison to the $\sigma_x = 2.5$ result.

B.2.4 Sub-apertures

Another method to enhance the reflection power of steeply inclined reflectors via sub-aperture processing. Hereby we can create several radargrams of the same scene from defined sub-apertures, which are partial sections of the full aperture (Figure B.3). For regular processing, only the nadir sub-aperture is used. The working principle is shown in Figure B.3c–f. For example, the forward steered sub-aperture will produce a radargram where only signals from internal layers inclined towards the airplane are resolved in the radargram.

One radargram is produced for each sub-aperture. It has been proven to be best to create three, five or nine sub-apertures. Because it is not very useful to work

with a single sub-aperture radargram, we can stack all sub-aperture radargrams to obtain the desired information for the whole scene. However, this step is subject to two issues: (i) the return power and amplitude information is not very useful for further analysis and (ii) the SNR for the whole scene reduces due to the incoherent stacking.

A comparison of a radar scene with (a) the regular nadir sub-aperture, (b) the combination of three and (c) five sub-apertures is presented in Figure B.3g–i. We note the advantage of a better resolution for dipping reflectors but also the disadvantages of a reduced SNR of the nadir reflections and the appearance of processing artefacts.

B.3 Image mode

In addition to the data recorded in the (2D) sounding mode, the EGRIP-NOR-2018 data set also contains two segments recorded in the (3D) image mode. The acquisition settings of these segments are slightly different since the transmission signals are composed of four instead of three pulses: 1 μ s and 3 μ s waveforms with nadir directed transmit beam followed by two 10 μ s waveforms, one with the transmit beam directed to the left and one with it directed to the right (left and right in respect to the flight direction) to increase the imaged swath width at the ice bottom (Figure B.4a). The processing consists of three steps:

1. **Generating 3D images.** In this step, we generate a cross-track snapshot of the off-nadir return signals with an estimate of the data covariance matrix, which depends on the number of off-nadir cross-track multilooks. A high number of looks will reduce the resolution but increase the accuracy. For our 8-channel system, a number of 33 looks usually provides an acceptable trade-off.
2. **3D surface/bed tracking.** In this step, the ice surface and bed topography is automatically tracked (in the direction-of-arrival vs depth diagram; see Figure B.4c). Both surfaces are needed for the processing, but finally the reconstruction of the bed is the ultimate output. The nadir bed reflection can be set as ground truth, which increases the accuracy of the autotracker. Moreover, it is possible to manually fix the surface tracking.
3. **DEM Generation.** Based on the ice surface and bed topography tracking data, a gridded DEM will be produced.

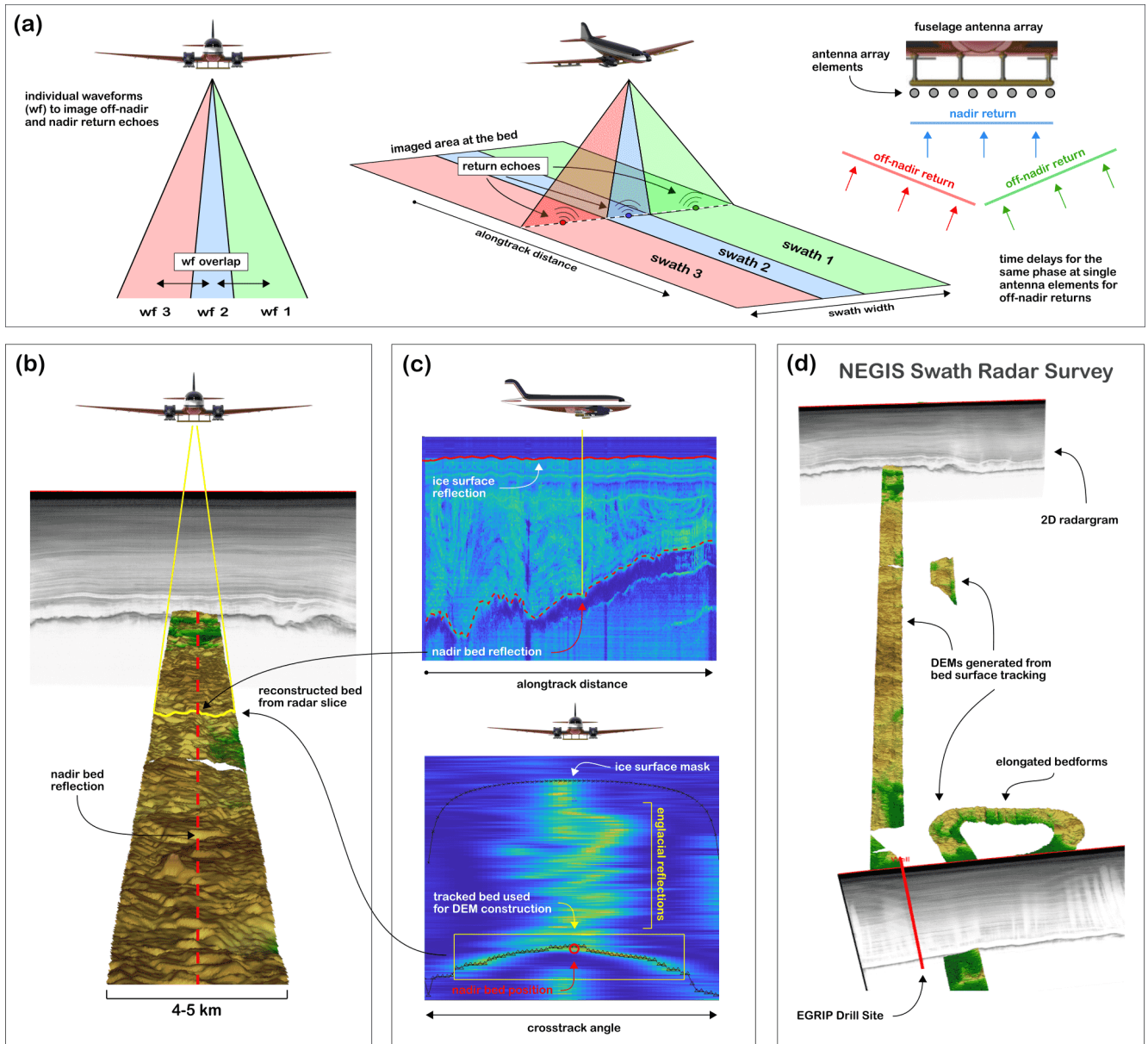


Figure B.4: Bed topography imaging with 3D swath processing. Panel (a) illustrates the emitted radar beams and the direction of arrival of cross-track off-nadir signals at the antenna array. A composite of a processed 2D radargram and a bed DEM generated via 3D processing is illustrated in panel (b). Panel (c) shows the cross-track snapshots along a radar profile, which is the basis for the surface tracking. The upper image shows an along-track radargram, where the yellow line marks the location of the cross-track-direction-of-arrival vs depth plot below. A preliminary result of the bed topography and hints on subglacial structures is shown in panel (d).

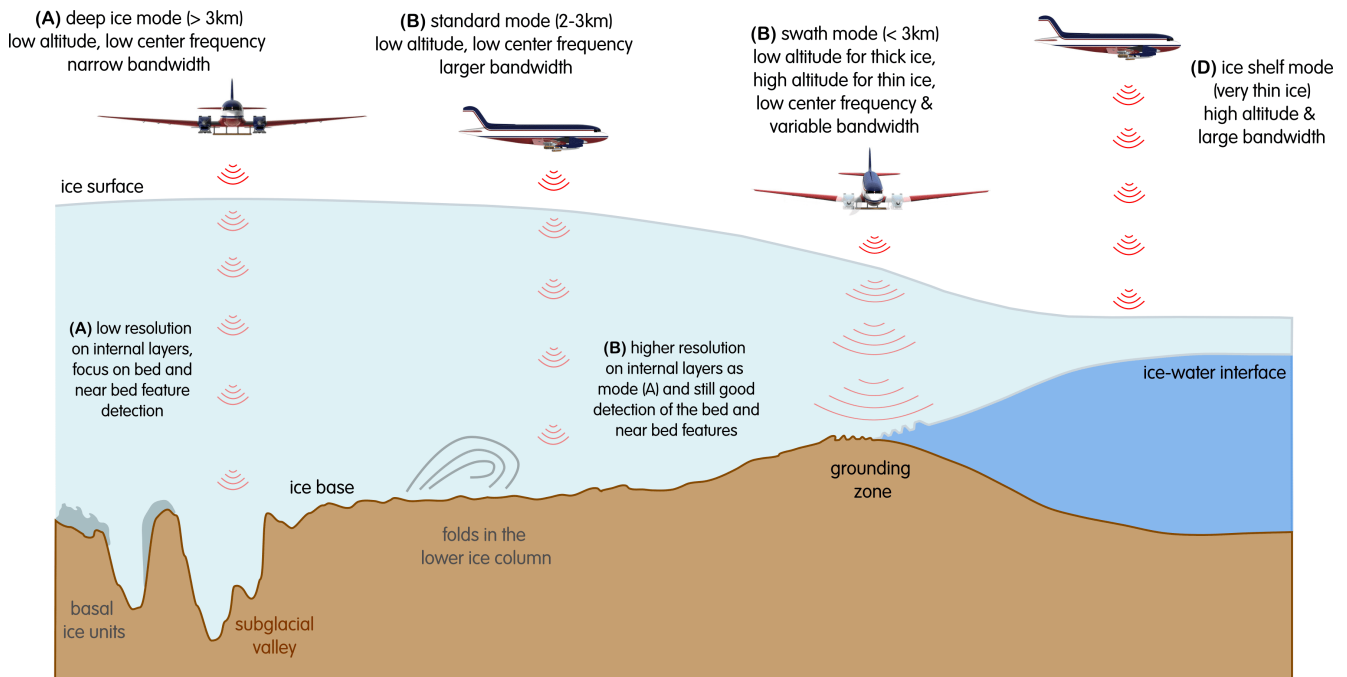


Figure B.5: UWB acquisition modes over different glaciological settings.

B.4 Recommendations

B.4.1 Acquisition

Based on the performance of the AWI UWB Radar soundings in Greenland and Antarctica and the acquisition and processing tests, I propose the following recommendations for specific operations (see Figure B.5):

- (A) Sounding deep (> 3 km thick) or temperate ice with a focus on bed and near-bed feature recovery
- (B) Sounding 2–3 km thick ice and focus on both internal layering and bed recovery
- (C) Image mode (3D bed tomography)
- (D) Sounding very thin ice (e.g. 200–500 m thick ice shelf)

B.4.1.1 A. Sounding deep (> 3 km thick) or temperate ice with a focus on bed and near-bed feature recovery

If the detection of the bed or near-bed ice structures is the priority of the survey, it is recommended to use the 180–210 MHz mode. In Appendix A, I described the effect of the bandwidth on the SNR of point and distributed targets. It can be assumed that the near bed reflections in ice sheets such as shown in the magnified

windows in Figure B.1, mostly represent distributed targets. Hence, a narrow bandwidth is the best choice for a high SNR. Moreover, because englacial attenuation is frequency-dependent, a low centre frequency will penetrate further as lower frequencies (see the comparison of Figure B.1 a and c).

B.4.1.2 B. Sounding 2–3 km thick ice and focus on both internal layering and bed recovery

If the aim of the survey is to image both the internal stratigraphy and the ice base with a reasonable resolution, I suggest to use the 150–240 MHz mode. We note in Figure B.1 that this acquisition mode offers a higher resolution for internal layers as the 180–210 MHz (narrowband) mode. The loss in detail in near-bed structures is comparably small in comparison to Figure B.1 c and d. In comparison to the narrowband mode the increased bandwidth should have almost no change to the SNR for internal layers. In general, an increased bandwidth should cause no loss for point targets (e.g. internal layers). However, distributed targets will lose SNR, when the bandwidth is increased. This is one reason why the 150–520 MHz mode is ideal for internal layer resolution, but not to resolve basal reflections under a thick ice column. Furthermore, there is no advantage to the 320–350 MHz mode for this particular setting and shows the worst characteristics for any other survey type.

B.4.1.3 C. Image mode (3D bed tomography)

Theoretically, any 2D survey could be designed to map the desired 2D features in combination with a 3D swath. However, we have to keep in mind that the best results are most likely obtained with the low-frequency, narrowband mode, which produces the strongest bed returns. While the sounding mode is important, we also have to consider englacial attenuation caused by the ice thickness and the chemical and thermal conditions of the ice. Hence, a setting with thinner ice, or where less englacial attenuation is expected, would allow either to use a larger bandwidth (to increase range resolution) or to fly at a higher altitude (to increase the area of bed topography mapped along the flight profile).

B.4.1.4 D. Sounding very thin ice (e.g. 200 – 500 m thick ice shelf)

For the investigation of very thin ice or ice shelves, the 150–520 MHz mode is the most suitable. On the one hand, it resolves the internal stratigraphy with highest resolution without losing much energy due to the thick ice column. Second, the expected dielectric contrast on the ice-water/ice-bed interface at the ice shelf or near the grounding line is most likely so strong that it can be expected to be clearly detected. The proficiency of this mode has been demonstrated by [Bessette et al. \(2021\)](#) at the large impact crater beneath Hiawatha Glacier, Greenland. For soundings near the grounding line (whether on the grounded or floating ice site, it is certainly also helpful to use the 3D mode. The basal crevasses or basal terraces ([Dutrieux et al., 2014](#)) should be suitable refractors for the 3D mode.

Special attention should be paid to the flight altitude. In particular, if it is likely that the ice surface and also the underlying layers will produce a strong reflection, it should be flown at an elevation that the first multiple reflection of the ice top is located below the bed reflection. One expected advantage of this method is that the footprint of the 3D swath will be larger, i.e. more (bed topography) area can be mapped along the flight profile.

B.4.2 Processing

In addition to the standard processing settings and products (qlook and SAR focussed), it is worth to generate additional standardized data products for particular campaigns. The SAR processed product with a wider angular range (where $\sigma_x = 1$) is useful for most purposes. The only limitation is that much larger data sets are generated. The supaperture processing is probably not suitable for routine processing in my opinion but can be used for certain individual profiles.

Bibliography

- Bessette, J. T., Schroeder, D. M., Jordan, T. M., and MacGregor, J. A. Radar-sounding characterization of the subglacial groundwater table beneath hiawatha glacier, greenland. *Geophysical Research Letters*, 48(10):e2020GL091432, 2021. doi: <https://doi.org/10.1029/2020GL091432>. URL <https://agupubs.onlinelibrary.wiley.com/doi/abs/10.1029/2020GL091432>.
- Dutrieux, P., Stewart, C., Jenkins, A., Nicholls, K. W., Corr, H. F. J., Rignot, E., and Steffen, K. Basal terraces on melting ice shelves. *Geophysical Research Letters*, 41(15):5506–5513, 2014. doi: 10.1002/2014GL060618. URL <https://agupubs.onlinelibrary.wiley.com/doi/abs/10.1002/2014GL060618>.
- Leuschen, C., Gogineni, S., and Tammana, D. SAR processing of radar echo sounder data. pages 2570–2572, 2000. doi: 10.1109/igarss.2000.859643. URL <http://dx.doi.org/10.1109/igarss.2000.859643>.
- Richards, M. Fundamentals of Radar Signal Processing. *Professional Engineering, New York: McGraw-Hill Education*, 2005.
- Wang, Z., Gogineni, S., Rodriguez-Morales, F., Yan, J. B., Paden, J., Leuschen, C., Hale, R. D., Li, J., Carabaja, C. L., Gomez-Garcia, D., Townley, B., Willer, R., Stearns, L., Child, S., and Braaten, D. Multichannel Wideband Synthetic Aperture Radar for Ice Sheet Remote Sensing: Development and the First Deployment in Antarctica. *IEEE Journal of Selected Topics in Applied Earth Observations and Remote Sensing*, 9(3):980–993, 2016. ISSN 21511535. doi: 10.1109/JSTARS.2015.2403611. URL <http://dx.doi.org/10.1109/JSTARS.2015.2403611>.

Appendix C

Software, data and documentation

Software

CReSIS toolbox

I used the *CReSIS Toolbox* for the processing of AWI UWB MCoRDS depth sounder radar data. The toolbox is a collection of software routines, most of them written in Matlab. The toolbox is designed for data processing of raw radar data as well as GPS/INS data (metadata) and produces support files, calibration files, radar image files as well as layer tracking files. The *CReSIS Toolbox* can be downloaded from the following Git repository: <https://github.com/CReSIS/>. A setup guide as well as the full documentation is available via the CReSIS Wiki page: <https://ops.cresis.ku.edu/wiki/index.php>. The contact person for the CReSIS Toolbox is John D. Paden from the University of Kansas: paden@ku.edu.

Python

I used Python3 (<https://www.python.org>), including standard Python Libraries for the major part of the data analysis as well as for data conversion. Moreover, all figures and plots (excluding geographic maps and 3D images) were created with Python. Furthermore, I used the following non-standard libraries:

Data handling: h5py, scipy, obspy

Geo-tools: geopandas, shapely, pyorj, geopy, rasterio, rioxarray, xarray, pygmt, gdal

Data processing: numpy, pandas, obspy, scipy

Visualization: matplotlib, seaborn

GIS

QGIS is a free and open-source geographic information system (GIS) and was used in this thesis to perform numerous spatial calculations, for the general handling of geo-data and geo-data files as well as for the generation of 2D maps. In addition, I used QGIS for data interpretation. QGIS can be downloaded here: <https://www.qgis.org>

SAGA GIS algorithms are implemented within QGIS and I used several algorithms for terrain analysis such

as: flow accumulation, hypsometry as well as raster tools for gridding (<http://www.saga-gis.org>).

GDAL/OGR geo-algorithms were used to for the manipulation and conversion of (geo) raster and vector data (<https://gdal.org/>). GDAL can be used in a stand-alone command-line interface or within QGIS.

ECHOS

Emerson's E&P EchosTM is a commercial software suite for seismic processing. For this work, I used the software to trace the ice surface, internal layers as well as the bed reflection of the radar data. The results were used for instance to calculate ice and individual layer thickness or to perform the roughness analysis of the bed topography. For more information see <https://www.pdgm.com/products/echos/>.

MOVE

I used the 3D model building software MOVETM to construct 3D surfaces of internal stratigraphic horizons in the radar data. Furthermore, many of the 3D figures in this thesis and the manuscripts were created with Move. Further information at <https://www.petex.com/products/move-suite/move/>.

Inkscape

Inkscape is an open-source vector graphics editor to create and modify vector images (<https://inkscape.org>). I used this software to create sketches and to assemble and annotate figures.

GMT

I used several functions of the GMT (Generic Mapping Tools) toolbox for gridding and other geographic data manipulations. GMT is an open-source collection of command-line tools for manipulating geographic data sets (further information at: <https://www.generic-mapping-tools.org/>).

IDL toolbox

A part of the radar data processing routine is performed with an IDL toolbox written by Veit Helm (AWI; veit.helm@awi.de). I used his tools to post-process GPS data and for data conversion. IDL (Interactive Data Language) is commonly used in the scientific community for processing of large amounts of data (<https://www.l3harrisgeospatial.com/Software-Technology/IDL>).

Code

The Python scripts and methods I used to process the data are stored in the **Strata** (Small Toolbox for **R**Adar da**T**a Processing and Analysis) Github repository: <https://github.com/stvnfrnk/Strata.git>.

- Functions for radar data processing are available at: https://github.com/stvnfrnk/uwbradar_library.git
- A collection of scripts is available at: <https://github.com/stvnfrnk/Kangaroo.git>

Data

Ultra-wideband radar data

The data of the UWB system is stored at different locations. The following paragraphs describe where to find acquisition settings, the parameter spreadsheets, raw data (waveform data) and the processing outputs.

MCoRDS acquisition XML files store all relevant information used for data acquisition, e.g. number of waveforms, pulse durations, receiver gains, number of individual presums, etc. Each acquisition setting has an individual name and is divided into one file containing the transmission settings and another file containing the receiver settings. We learned during the 2019 field season in Antarctica (*antr2019*) that the usage of the wrong transmission/receiver files leads to waveform data which cannot be used for analysis. The files for the *arkr2018* campaign are available at: `/hs/gsys/p_radar/arkr2018/CSARP_2018_Greenland_Polar6_rds/waveforms` and for the *antr2019* campaign at: `/hs/gsys/p_radar/arkr2018/CSARP_2018_Greenland_Polar6_rds/waveforms`. Note that both waveform folders have the same file content. To track which setting has been used in a survey, see the parameter spreadsheet.

Parameter spreadsheets (for processing) The so-called *ct_params* parameter spreadsheet controls the processing settings for the CReSIS toolbox. It contains radar and processing settings. A full documentation for is available under: https://ops.cresis.ku.edu/wiki/index.php/Parameter_Spreadsheet_Guide. Parameter spreadsheets for completed campaigns should be added to the *ct_params* Git repository: https://github.com/CReSIS/ct_params.

Raw data In this thesis I used AWI UWB data from the summer 2018 field season in Greenland (FINEGIS and EGRIP-NOR-2018) and austral summer season 2018/19 in Antarctica (JuRaS). The raw data is at the moment (September 27, 2021) stored at the AWI HSM Server in the WORM (Write Once Read Many) file system: `/hs/platforms/WORM/aircraft/polar6/uwbr/exdata/` in the following two campaigns:

- P6-211_RESURV79_2018 (FINEGIS)
- P6-211_EGRIP-NOR_2018 (NEGIS)
- P6-215_UWB_2018 (JuRaS)

Processed data The processing results of the radar data processing, which I created among others for the field season 2018 in Greenland, are also stored on the AWI HSM Server System (last access September 27, 2021):

- `/hs/gsys/p_radar/arkr2018/CSARP_2018_Greenland_Polar6_rds`
- `/hs/gsys/p_radar/antr2019/CSARP_2019_Antarctica_Polar6_rds`

Internal layers

Traced internal layers of the work presented in this thesis are stored in the ECHOS database in the *arkr2018* and *antr2019* project.

Data products generated during my PhD

- Ice thickness in TWT at the onset of the NEGIS (point data)
<https://doi.org/10.1594/PANGAEA.907917>
- Bed topography and ice thickness in meters at the onset of the NEGIS (gridded data)
<https://doi.org/10.1594/PANGAEA.907916>
- Bed return power (BRP) and waveform abruptness of the onset of the NEGIS (point data)
<https://doi.pangaea.de/10.1594/PANGAEA.915135>

- Spectral subglacial bed roughness of the onset of the NEGIS (point data)
<https://doi.pangaea.de/10.1594/PANGAEA.915133>
- Hydropotential and subglacial water routing of the onset of the NEGIS (gridded data)
<https://doi.pangaea.de/10.1594/PANGAEA.915134>
- Ice thickness from the northern catchment region of Greenland's 79 North Glacier (point data)
<https://doi.pangaea.de/10.1594/PANGAEA.913193>
- Locations and outlines of active lakes at the onset of the Jutulstraumen Glacier (Antarctica) derived from DInSAR measurements. (shapefiles)
<https://doi.pangaea.de/10.1594/PANGAEA.927120>
- Ice thickness from Jutulstraumen Glacier recorded with the airborne AWI UWB radar system, Antarctica. (point data)
<https://doi.pangaea.de/10.1594/PANGAEA.911475>
- Ice thickness and bedrock topography of the ice divide, South of Sør Rondane Mountains (DML), Antarctica. (point data)
<https://doi.org/10.1594/PANGAEA.910019>
- Ice thickness from the coast of Dronning Maud Land (Antarctica), recorded 2018/19 with the AWI UWB radar system. (point data)
<https://doi.pangaea.de/10.1594/PANGAEA.911868>
- Ultra-wideband radar data over the shear margins and along flow lines at the onset region of the Northeast Greenland Ice Stream. (radar data)
<https://doi.org/10.1594/PANGAEA.928569>

Documentation

I documented everything I found useful and might be useful to others working with AWI UWB data in the AWI Confluence Wiki: <https://spaces.awi.de/display/Glaziologie/Aero-UWB>. Furthermore, there is information available regarding the radar usage in MOVE and ECHOS. You will find useful information there if you have one of the following questions:

1. Where are the individual raw data and data products stored?
2. How do I import the UWB data to ECHOS?
3. Is there a translation table from UWB Frame IDs to ECHOS Line IDs?
4. How do I import and use the radar data in MOVE?

Appendix D

Further contributions

Co-authored manuscripts

The following manuscripts where I am a co-author are not included in this dissertation:

Westhoff, J., Stoll, N., **Franke, S.**, Weikusat, I., Bons, P., Kerch, J., Jansen, D., Kipfstuhl, S. and Dahl-Jensen (2020). A stratigraphy Based Method for Reconstructing Ice Core Orientation. **Annals of Glaciology**, **61**(83) 1-12. <https://doi.org/10.1017/aog.2020.76>

Bons, P., de Riese, T., **Franke, S.**, Llorens, M-G., Sachau, T., Westhoff, J., Stoll, N., Weikusat, I. and Zhang, Y. (2021). Comment on 'Exceptionally high heat flux needed to sustain the Northeast Greenland Ice Stream' by S. Smith-Johnsen et al., *The Cryosphere*, **14**, 841-854, 2020. **The Cryosphere**, **15**, 2251–2254, <https://doi.org/10.5194/tc-15-2251-2021>

Gerber, T. A., Hvidberg, C., Rasmussen, S. O., **Franke, S.**, Sinnl, G., Grinsted, A., Jansen, D. and Dahl-Jensen, D. (2021; in review). Upstream flow effects revealed in the EastGRIP ice core using a Monte-Carlo inversion of a 2D ice flow model. **The Cryosphere**, **15**, 3655–3679, <https://doi.org/10.5194/tc-15-3655-2021>

Mojtabavi, S., Eisen, O., **Franke, S.**, Jansen, D., Steinhage, D., Paden, J., Dahl-Jensen, D., Weikusat, I., Eichler, J. and Wilhelms, F. (2021; in review). Physical properties of the Greenland Ice Sheet from linking radar surveys to three deep ice cores by synthetic radar modelling. In review for: **Journal of Glaciology**

Conference contributions

I presented my research at the following conferences:

Franke, S., Jansen, D. Beyer, S., Neckel, N., Binder, T., Paden, J., Dörr, N., Helm, V., Steinhage, D. Eisen, O. (2020). Ice flow and the conditions of the ice-bed interface at the onset of the Northeast Greenland Ice Stream. Online iPoster: **AGU Fall Meeting 2020**, Online Everywhere (December 1-17, 2020). <https://epic.awi.de/id/eprint/53403/>

Franke, S., Jansen, D. Beyer, S., Binder, T., Paden, J. Eisen, O. (2020). Radar derived basal conditions at the onset of the Northeast Greenland Ice Stream. Online Presentation: **NEGIS Symposium 2020, EGRIP Online Seminars** (September 13-November 3, 2020). <https://epic.awi.de/id/eprint/53120/>

Franke, S., Jansen, D. Westhoff, J., Weikusat, I., Bons, P., Binder, T. Eisen, O. (2020). Folded ice stratigraphy in North East Greenland: A three dimensional structural analysis. Online Presentation (Video): **ESA 2020 European Polar Science Week**, Virtual Event (October 26-30, 2020).

<https://epic.awi.de/id/eprint/53185/>

Franke, S., Stoll, N., Jansen, D. Koldtoft, I. (2020). Understanding an ice stream in Greenland at the EastGRIP camp: An international-multidisciplinary effort and knowledge transfer among scientists. Online Presentation: **6th annual APECS International Online Conference** (May 19-21, 2020). <https://epic.awi.de/id/eprint/52032/> **Honors: 3rd prize for best Arctic presentation**

Franke, S., Jansen, D., Paden, J. Eisen, O. (2020). Complex basal conditions influence flow at the onset of the North East Greenland Ice Stream. Online Presentation: **EGU General Assembly 2020**, Sharing Geosciences (Vienna, Austria, May 3-9, 2020). <https://doi.org/10.5194/egusphere-egu2020-1173>

Franke, S., Jansen, D., Binder, T., Dörr, N., Helm, V., Paden, J., Steinhage, D. Eisen, O. (2019). Bedrock topography and subglacial landforms of the Northeast Greenland Ice Stream. Oral Presentation: **NEGIS Symposium, EastGRIP Steering Committee Meeting** (Copenhagen, Denmark, November 11-15, 2019). <https://epic.awi.de/id/eprint/50856/>

Franke, S., Jansen, D., Binder, T., Helm, V., Steinhage, D., Dörr, N., Paden, J. Eisen, O. (2019). Ice Thickness and Bed Conditions of the North East Greenland Ice Stream. Poster Presentation: **AWI PhD Days** (Potsdam, Germany, July 4-7, 2019).

Franke, S., Jansen, D., Binder, T., Helm, V., Steinhage, D., Dörr, N., Paden, J., Weikusat, I., Bons, P. Eisen, O. (2019). Detailed bedrock topography in the vicinity of the EGRIP ice-core drill site. Poster Presentation: **IGS Symposium Five Decades of Radioglaciology** (Stanford, USA, July 8-12, 2019). (Presented by Daniela Jansen) <https://epic.awi.de/id/eprint/50861/>

Franke, S., Jansen, D., Binder, T., Helm, V., Steinhage, D., Paden, J., Weikusat, I. Eisen, O. (2018). First results of the AWI-Polar6 airborne radio echo sounding survey around the EGRIP drill site. Oral Presentation: **NEGIS Symposium, EastGRIP Steering Committee Meeting** (Copenhagen, Denmark, November 12-16, 2018). <https://epic.awi.de/id/eprint/49976/>

Appendix E

PAPER I

RESEARCH ARTICLE

Bed topography and subglacial landforms in the onset region of the Northeast Greenland Ice Stream

Steven Franke¹ , Daniela Jansen¹ , Tobias Binder¹ , Nils Dörr¹ , Veit Helm¹ , John Paden² , Daniel Steinhage¹  and Olaf Eisen^{1,3} 

¹ Alfred Wegener Institute, Helmholtz Centre for Polar and Marine Research, Bremerhaven, Germany

² Center for Remote Sensing of Ice Sheets (CReSIS), University of Kansas, Lawrence, KS, USA

³ Department of Geosciences, University of Bremen, Bremen, Germany

Published on 18 March 2020 in *Annals of Glaciology*

<https://doi.org/10.1017/aog.2020.12>

Abstract

The North East Greenland Ice Stream (NEGIS) is an important dynamic component for the total mass balance of the Greenland Ice Sheet, as it reaches up to the central divide and drains 12 % of the ice sheet. The geometric boundary conditions and in particular the nature of the subglacial bed of the NEGIS are essential to understand its ice flow dynamics. We present a record of more than 8,000 km of radar survey lines of multi-channel, ultra-wideband radio echo sounding data covering an area of 24,000 km², centered on the drill site for the East Greenland Ice-core Project (EGRIP), in the upper part of the NEGIS catchment. Our data yield a new detailed model of ice-thickness distribution and basal topography in the region. The enhanced resolution of our bed topography model shows features which we interpret to be caused by erosional activity, potentially over several glacial-interglacial cycles. Off-nadir reflections from the ice–bed interface in the center of the ice stream indicate a streamlined bed with elongated subglacial landforms. Our new bed topography model will help to improve the basal boundary conditions of NEGIS prescribed for ice-flow models and thus foster an improved understanding of the ice-dynamic setting.

Received: 3 October 2019 - Revised 26 February 2020 - Accepted: 27 February 2020

Introduction

The Greenland Ice Sheet (GrIS) is the second largest land ice mass on Earth and one of the largest contributors to global sea-level rise (Khan et al., 2014a; Gardner et al., 2013; Rignot et al., 2011). Observations indicate that its contribution increased from 0.09 mm a⁻¹ for the period 1992–2001 to 0.68 mm a⁻¹ for 2012–2016 (IPCC, 2019, Section 4.2.2). Apart from a negative surface mass balance due to melting, this contribution to sea level rise is driven by speed-up and retreat of marine-terminating glaciers, leading to ice thinning (Howat et al., 2007; Rignot et al., 2011; Gillet-Chaulet et al., 2012; IPCC, 2019). Of particular importance for sea-level predictions are observations of ice streams that transport ice from the interior of the ice sheet to the margin, where it either melts or calves into icebergs. Dynamic processes of ice sheets in Greenland and Antarctica have been progressively included in numerical models to project sea-level changes (Robinson

et al., 2012; Church et al., 2013; Rückamp et al., 2020; Goelzer et al., 2020). To simulate present ice stream flow and determine its contribution to the mass balance of ice sheets, we have to understand the natural variability of ice stream dynamics on time scales of tens to thousands of years (Robel et al., 2013). For an accurate assessment of the dynamic component of mass loss, ice-sheet flow requires high-resolution observations of the kinematic properties and the geometry conditions.

Ice stream characteristics vary in their geographical settings and thus boundary conditions, for instance ice thickness, subglacial topography, resistive properties of the underlying substrate, subglacial hydrology, as well as atmospheric and oceanic forcing (Aschwanden et al., 2016; Khan et al., 2014b; Robel et al., 2013). In contrast to flow of outlet glaciers, which often drain ice through bedrock channels or valleys, the high flow velocities of ice streams extend further into

the interior of the ice sheet. In some cases their location is not controlled by the bed topography and their boundaries are characterized by narrow shear zones (Truffer and Echelmeyer, 2003). Basal properties of ice streams in Greenland have been mostly investigated at the (now sub-marine) ice sheet margins of paleo glacier beds with multi-beam bathymetry and marine sediment cores (e. g. Dowdeswell et al., 2014; Hogan et al., 2016; Newton et al., 2017). The beds of paleo ice streams can be hard or soft and often show a large number of streamlined bedforms, mostly parallel to ice flow (Roberts et al., 2010). Streamlined bedforms underneath contemporary ice streams in Antarctica have been analyzed by King et al. (2009) and Bingham et al. (2017) and classified as mega-scale glacial lineations (MSGSL) (Stokes and Clark, 2002). As subglacial structures may have formed over multiple glaciations, their interpretation is often challenging (Roberts and Long, 2005). Little is known about the current conditions of ice stream beds in the central regions of the GrIS, at the onset of streaming ice flow, because data acquisition as well as determination of the geometry and composition of the bed is much more difficult to elaborate than on the continental shelf. For central Greenland it was generally assumed until recently that the ice sheet is underlain by lithified sediment or a crystalline basement. However, a detailed study of Christianson et al. (2014) identifies deformable and water saturated sediment several meters thick at the onset zone of the North East Greenland Ice Stream (NEGIS), which indicates that deformation of the basal substrate could influence sliding at the ice-bed interface and probably also limit subglacial erosion. Furthermore, Jezek et al. (2011) detect elongated landforms probably formed by erosion at the base of the southern flank of the Jakobshavn ice stream. Both interpretations indicate a more complex interplay of basal conditions and ice dynamics than present in the case of a simply hard-based ice sheet in Greenland's interior.

The NEGIS is one of the most prominent features of the GrIS. With a length of ~ 600 km it drains $\sim 12\%$ of the Greenland ice sheet via fast-flowing marine-terminating glaciers (Rignot and Mouginot, 2012). Surface ice flow velocities vary from 10 m a^{-1} at the onset to more than 2000 m a^{-1} at the grounding line of the outlet glaciers (Mouginot et al., 2017). The NEGIS differs from all other marine-terminating glaciers in Greenland with its catchment of fast streaming ice flow almost reaching the central ice divide (Joughin et al., 2018). This configuration provides a possible mechanism to transmit forcing from the marine area far inland (Christianson et al., 2014) and several studies have assessed potential changes in the stability of the NEGIS and the ice dynamics in North-East Greenland (Joughin et al., 2010; Fahnestock et al., 2001; Bamber et al., 2013; Khan et al., 2014a).

To fully understand the dominating processes and basal boundary conditions driving NEGIS ice flow, in particular in its onset region, on-site measurements are most useful. So far, geophysical surveys investigating the upstream part of the NEGIS concentrated on the immediate surroundings of the EGRIP drill site (Figure E.1 b), where the ice stream widens (Vallelonga et al., 2014; Keisling et al., 2014). High basal melt rates caused by higher continental geothermal heat flux close to the ice divide, as a remnant of the passing of the Icelandic hot spot, are assumed to cause the onset of the ice stream (Fahnestock et al., 2001; Rogozhina et al., 2016; Martos et al., 2018). Further downstream, acceleration is likely caused by subglacial water routing and the presence of high porosity, water-saturated deformable subglacial till, which lubricates the ice stream (Christianson et al., 2014). The geophysical data of Christianson et al. (2014) suggest that subglacial till is distributed in the center of our survey region, across the entire ice stream, and is dilatant in the fast-flowing part of the ice stream. The source and routing of till is not yet fully understood. The presence of unconsolidated sediment inside and outside of the NEGIS suggest that sediments are funnelled into the NEGIS from the upstream catchment (Christianson et al., 2014). Overall it is difficult to assess which processes dominate the different regions of the ice stream and how they interact (Schlegel et al., 2015).

The most important factors controlling ice streams are their basal properties, ice thickness and bed topography, especially as studies of subglacial hydrology are dependent upon bed and surface slope and thus the variation in ice thickness on a local to regional scale (Wright et al., 2008). Without a sufficient spatial data coverage also at the onset of ice streams, it is not possible to assess the nature of the ice stream bed and its properties. Over the last five decades, most radio-echo sounding campaigns have concentrated on ice divides, domes or fast flowing outlet glaciers (Bamber et al., 2013; Fretwell et al., 2013). To date, several bed elevation models for Greenland exist (e. g. Bamber et al., 2013; Morlighem et al., 2017) with variable resolution and data coverage. Furthermore, modelling studies reveal that an interpretation of isochrones of ice streams is challenging without a detailed knowledge of the bed topography (Leysinger Vieli et al., 2007). These existing limitations motivated the acquisition of new high resolution ice thickness data to improve available bed topographies around NEGIS, in order to help interpret basal structures and thereby determine ice-substrate interaction within NEGIS and in its vicinity (Vallelonga et al., 2014; Keisling et al., 2014).

In this paper, we use airborne radio-echo sounding data to extend previous geophysical surveys of ice thickness and internal layering around the EGRIP drill site. We provide a new high-resolution bed topography

map and discuss the overall glaciological setting in the context of NEGIS' ice dynamics. Furthermore, we interpret radar returns from subglacial structures, which are not visible in our bed topography DEM, to deduce bed properties and complement simple interpretations based on ice thickness only.

Data and methods

Survey area

The radar data were recorded in the vicinity of the EGRIP drill site in May 2018. A total area of $\sim 24,000 \text{ km}^2$ was mapped with 8,233 km of profiles sub parallel and perpendicular to ice flow direction (Figure E.1 b). The central part of the survey area, in direct vicinity to the EGRIP drill site, was covered with a profile spacing of 5 km, further up- and downstream the spacing is 10 km. The area reaches from 150 km upstream to 150 km downstream of the EGRIP drilling site and covers, both, shear margins and parts of the slow flowing areas outside and adjacent to the ice stream. The shear margins, as boundaries of the ice stream, are mapped over a distance of more than 250 km. The survey lines also cover the transition zone of two north-western shear margins, located southwest of the EGRIP drill site. Several profiles follow flow paths of a point on the ice surface that has passed through the shear margin.

Radar system

Since 2016 the Alfred Wegener Institute, Helmholtz Centre for Polar and Marine Research (AWI) has been operating a multi-channel ultra-wideband (UWB) airborne radar sounder and imager for sounding ice thickness and imaging internal layering and the basal interface of polar ice sheets. The Multichannel Coherent Radar Depth Sounder (MCoRDS) was developed at the Center for Remote Sensing of Ice Sheets (CReSIS) at the University of Kansas in 1993 and has been continuously improved (Gogineni et al., 2001; Shi et al., 2010). This radar system is designed to operate with multiple antenna elements to increase the power radiated to the target and to compensate for unwanted signals from side echoes and surface clutter by multi-looking and steering a beam to a desired orientation. A comprehensive description of AWI's UWB radar system is given by Hale et al. (2016); Rodriguez-Morales et al. (2014) and Wang et al. (2014). Its full capabilities were demonstrated by Kjær et al. (2018). The radar system is installed on the fuselage of the AWI Polar6 Basler BT-67 aircraft and comprises eight transmit channels to transmit and receive radar signals, with a high power transmit and receiver module with fast switching speed. All antenna elements were oriented in

along-track (HH) polarization. The radar system is able to alternate between different pulse duration stages and different receiver gains for each stage to increase the dynamic range. Global Positioning System (GPS) data were acquired by four geodetic NovAtel DL-V3 GNSS receivers operating at 20 Hz. After processing we achieve a positioning accuracy of 3–4 cm in horizontal space and 10 cm in elevation for the aircraft.

Table E.1: Acquisition parameters of AWI's UWB radar campaign in Greenland 2018.

Parameter	Value
Radar System	MCoRDS5
Frequency Range ^a	180-210 MHz
Waveform Signal	$1\mu\text{s}$, $3\mu\text{s}$, $10\mu\text{s}$ chirp
Waveform Presums ^b	2, 4, 32
Pulse Repetition Frequency	10 kHz
Sampling Frequency	1600 MHz
Tukey Window taper ratio	0.08
Transmit Channels	8
Receiving Channels	8
Aircraft Altitude	$\sim 360 \text{ m}$
Aircraft Velocity	$\sim 260 \text{ km/h}$

^aFrequency Range from 180 to 210 MHz is referred to Narrow Band mode (NB)

^bPresums are set for each waveform individually.

Data acquisition

Signals were transferred in three stages with different pulse durations and gains (see Table I.1). The transmitted waveforms are amplitude-tapered with a Tukey window with a taper ratio of 0.08 to reduce range side-lobes caused by the sudden transitions of the envelope in a standard chirped pulse without losing much transmit power (Li et al., 2013). To reduce the data rate and writing speed and to increase signal to noise ratio (SNR), coherent integrations (presums) with zero-pi modulation (Allen et al., 2005) are performed for each waveform depending on the acquisition mode. The aircraft altitude on all survey flights was $\sim 365 \text{ m}$ above ground level and the data were acquired at a pulse repetition frequency (PRF) of 10 kHz. With an aircraft speed of $\sim 260 \text{ km/h}$ this results in an initial horizontal transmitting interval of about 0.7 cm. All profiles were recorded in our narrow band (NB) mode with a frequency range of 180–210 MHz.

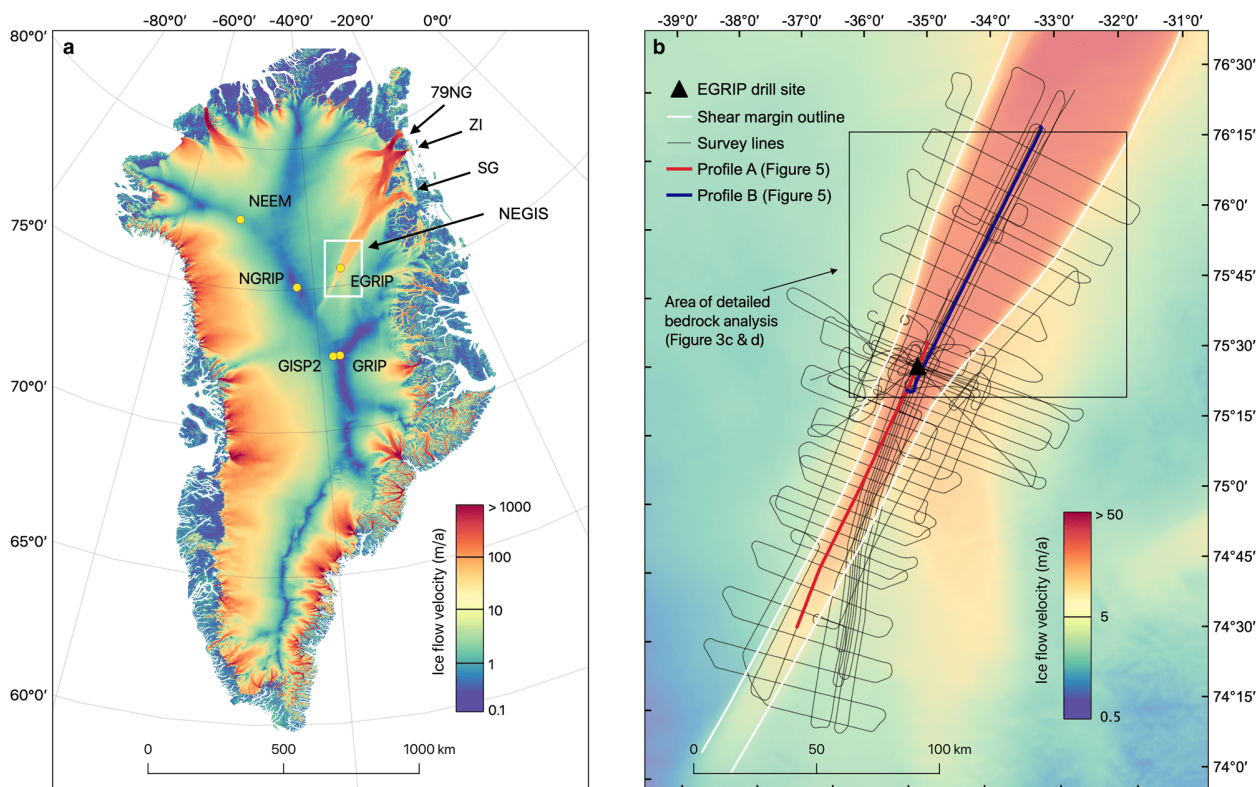


Figure E.1: Overview of the survey area. Surface velocity map of the Greenland Ice Sheet (a), highlighting the NEGIS and its marine terminating outlets (79NG, Zachariae Isbrae (ZI) and Storstrømmen Glacier (SG)). The survey area (b) is marked with a white outline. (b) Ice flow velocity field of the survey area. The schematic outline of the shear margin was derived from Landsat images. Both maps are displayed in WGS 84 / NSIDC Sea Ice Polar Stereographic North (EPSG:3413) and show velocity data of Joughin et al. (2018).

Data processing

For processing, we use the CReSIS Toolbox algorithms for all three spatial domains: vertical range (pulse compression), along-track (fk migration) and cross track (array processing) (see CReSIS-Toolbox (2019)). Further detailed description of the radar data processing is given in the Appendix.

Surface and bed detection

Radar data are recorded in the time domain in two-way travel time (TWT). To convert from radar time to depth, we use the same dielectric constant of 3.15 for depth-conversion as used for SAR processing. No compensation was done for a firn layer because the spatial variability of firn properties in dynamic regimes can vary on a scale of a few kilometres (Dutrieux et al., 2013). The detection of the ice surface is performed automatically by applying a threshold filter searching for the first maximum in a given time window. This window depends on the flight altitude of the aircraft over ground. The location of the surface reflection has been verified using the seismic processing and interpretation software Paradigm by Emerson E&P.

At several locations, the range detection of the bed reflector was not clear. Off-nadir reflections offered multiple horizons for bed picks in regions with rough bed topography, where scattered off-nadir reflections and the nadir bed are simultaneously present. In most cases, we selected the strongest reflection, because the nadir return signal is usually stronger than off-nadir scattered signals. However, this was not always the case, especially in areas of strong internal deformation, where englacial layers of high reflectivity reduce the energy and mask the the bed return.

Nested bed topography model

We computed an ice thickness and bed elevation model based on our observed ice thickness. We integrate them into the existing data set of Morlighem et al. (2017), Bed-Machine v3 (BMv3), in order to get a better overview of the regional topographic setting. We create a buffer of 5 km around our flight lines, use our ice thickness inside this buffer and BMv3 data outside of it. To prevent a strong gradient at the edges of the buffer, we apply a block mean filter on our output grid. The ice thickness data are subtracted from the digital elevation model (DEM) of the Greenland Ice Mapping Project (GIMP)

ice surface (Howat et al., 2014). This particular DEM was used in order to compare our bed topography with the BMv3 bed, which also uses GIMP as a reference surface. The grid has been created with the adjustable tension continuous curvature splines method. We also use a tension factor of 0.5 to suppress undesired oscillations and a convergence factor of 0.15 % of our gradient in input data. The output grid has a cell size of 500 m and elevations are referenced to mean sea-level using the geoid EIGEN-6C4 (Förste et al., 2014). For all bed elevation maps we used the Polar Stereographic North (70°N, 45°W) projection, which corresponds to ESPG 3413.

Uncertainty analysis

We take the root mean square (RMS) error of the range resolution and add the RMS error of the dielectric constant (CReSIS-Toolbox, 2019). This analysis requires an exact detection of the ice surface, which is well constrained for our data. To determine range resolution variability, we performed a crossover analysis of bed picks at 1449 profile intersections and calculated the mean deviation h_c . For the dielectric constant, we consider an error on the order of 1 % for typical dry ice (Bohleber et al., 2012),

$$\sigma_r = \sqrt{(h_c)^2 + \left(\frac{-t}{2} 0.01\right)^2}, \quad (\text{E.1})$$

with the radar wave travel time t and a mean value for crossover deviation, h_c , of 8.03 m. For ice thickness ranging from 2000–3000 m our error, σ_r , ranges from 13 to 17 m.

Results

Ice thickness and bed topography model

The mean ice thickness of our survey area is 2748 m and varies from 2059 m (± 13 m) to 3092 m (± 17 m). We observe a gradual decrease of ice thickness from the onset of the NEGIS close to the ice divide towards northeast (Figure E.2). Upstream of the EGRIP drill site we observe an increase in the spatial variability of ice thickness. The variation in ice thickness is mainly dominated by basal topography because the ice surface shows only small changes in surface deviation and slope. We present our bed elevation model (EGRIP-NOR-18) as a nested bed elevation model in Figure E.3. The data agree overall with recent Greenland bed topography models of Bamber et al. (2013) and Morlighem et al. (2017). Bed elevation in our study region ranges from -293 m (± 17 m) to 606 m (± 13 m). The area of

lowest bed elevation in our survey region is located southwest of the EGRIP drill site. Bed topography is generally lower and shows less spatial variability upstream of EGRIP. The topography downstream shows higher mean elevation and also more variability of a few hundred meters elevation change over a distance of 5–10 km.

In comparison to the BMv3 bed the most prominent differences of our bed topography appear at different locations and show five main features:

1. Figure E.2 b and Figure E.3 a and b show a location with elevation differences as large as 367 m. This isolated hill in the southeast of our survey area (indicated with a black arrow in Figure E.3 a and b) shows a higher basal elevation and larger surface area in the EGRIP-NOR-2018 topography in comparison to BMv3.
2. A hill in the central southeast of our survey area, which is visible in the BMv3 bed topography (Figure E.2 b and marked with a blue arrow in Figure E.3 a and b) and roughly 20 km away from the eastern shear margin, is not present in our bed topography. At this position, we find no significant change in ice surface topography but a strong internal reflection above the bed (Figure E.4). The highest elevation of BMv3 at this point is 697 m higher than our bed elevation. Three survey lines cover this feature and reveal strongly folded isochrones in our echograms. An internal anticline extending up to 15 km along the track exhibits elevation differences of isochrones of more than 900 m (Figure E.4). Furthermore, this radargram shows a strong power return of a similar amplitude as the bottom reflector in the proximity of the anticline. This reflection is irregularly shaped with interruptions, steeply dipping flanks and shows multiple layering. Underneath this anticline, we observe a weaker reflection, which we interpret as the real bed echo.
3. A longitudinal ridge in the center of the ice stream 35 to 90 km downstream of the EGRIP drill site is located 300–500 m higher than the surrounding bed. In contrast to BMv3, this topographic high is now represented as being more isolated from the high elevated area in the east, that coincides with the position of the eastern shear margin on its western edge. The ridge is oriented only a few degrees off from the direction of the surface ice flow of the NEGIS.
4. Southeast of the ridge (3), we find a trough. The transition is marked by a high elevation gradient of up to 500 m over a distance of 2–5 km. The

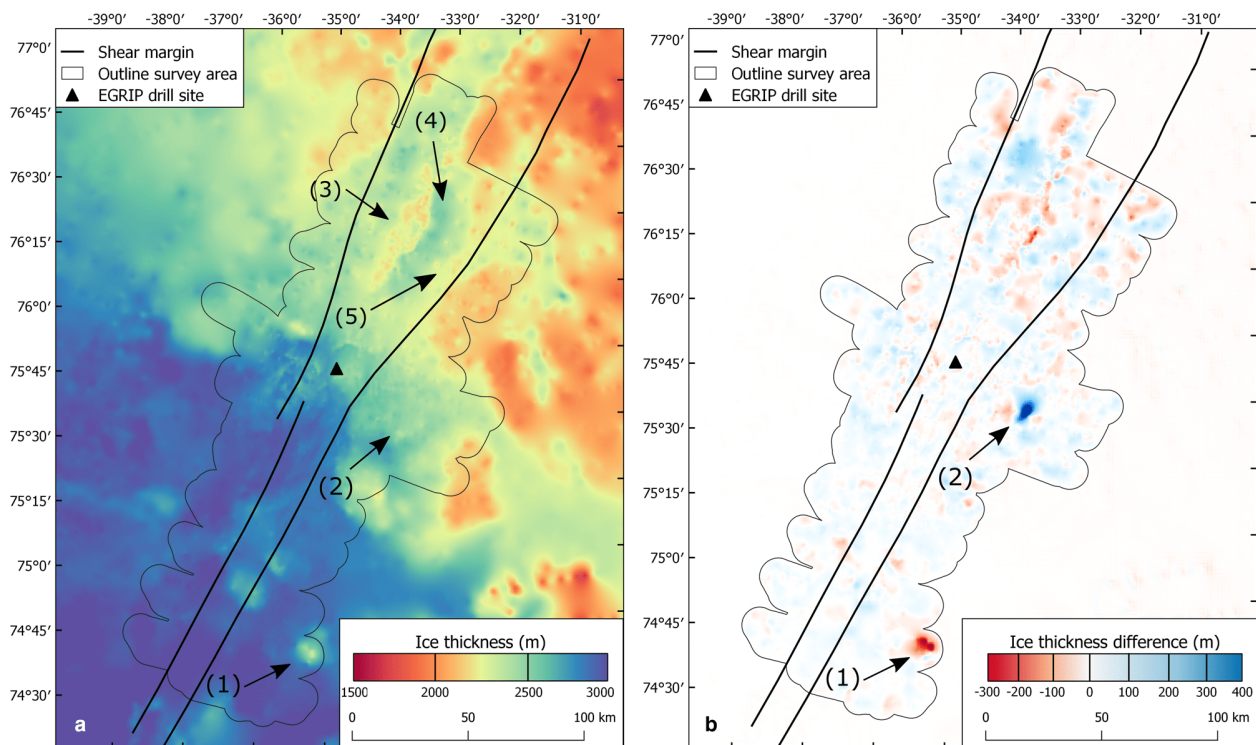


Figure E.2: Map of ice thickness distribution based on the data of the AWI radar survey 2018, termed EGRIP-NOR-2018. EGRIP-NOR-2018 ice thickness minus BMv3 ice thickness is shown in the right image recommendations. Blue colors represent higher and red colors lower ice thickness in our data set, respectively. The numbers 1–5 indicate the locations of the main features.

trough shows an increasing depth in the along-flow direction and ends abruptly with a 300 m elevation increase over a distance of 3 km.

5. Further east of the trough our radar lines show isolated bed undulations, which are aligned in the ice flow direction and bend downstream towards the western shear margin. The shape of this alignment is similar to the eastern and western slope of the trough to the West.

Discussion

Large scale bed structures

The EGRIP-NOR-18 bed topography shows several structures which are not present in previous bed elevation models. This is mainly due to our increased density in line spacing than in former surveys. Previous radar survey lines by AWI and Operation IceBridge (OIB) only covered parts of our survey area. At feature (1) in Figure E.3 a and b, only the edge of the bed feature was covered by one former survey line. However, the profile lines of other surveys indicate that this structure does not extend further than 10 km to the East. Feature (2) in Figure E.3 a is an ice bottom tracking error resulting from a strong reflection that does not represent the ice-bed interface (see Figure E.4).

Except for these larger scale differences between previously available data sets, the new nested bed elevation model mainly differs by more definition and steeper topographic gradients afforded by the increased spatial resolution of our data. The steeper gradients stand out in the region downstream of the EGRIP drill site, where a ridge in the center of the ice stream and an adjacent trough towards the east are delineated by a 300 m drop in bed elevation over 2 km. These structures are oriented almost parallel to ice flow (labelled with 3 and 4 in Figure E.3 d). Further towards the east, the trough is bordered by a chain of bed undulations, which very likely form a connected ridge (Figure E.3 d, features labelled 3, 4 and 5), also orientated roughly along ice flow. However, due to the lack of flow-parallel survey lines in this region this remains speculative. The trough shows the characteristics of an elongated, closed topographic depression: an overdeepening. These are common features in formally glaciated landscapes, and have been also documented underneath existing ice sheets and glaciers (e.g. Patton et al., 2016; Cook and Swift, 2012). A section of the bed along a flow line shows the typical profile of an overdeepening over two terraces, with the deeper part shifted towards the head (upstream) and a gentler upward slope downstream in each part of the basin. This indicates ongoing erosion by quarrying on the upstream end, leading to further deepening (Cook and Swift, 2012). This geomorphology is usually more common towards the margins of

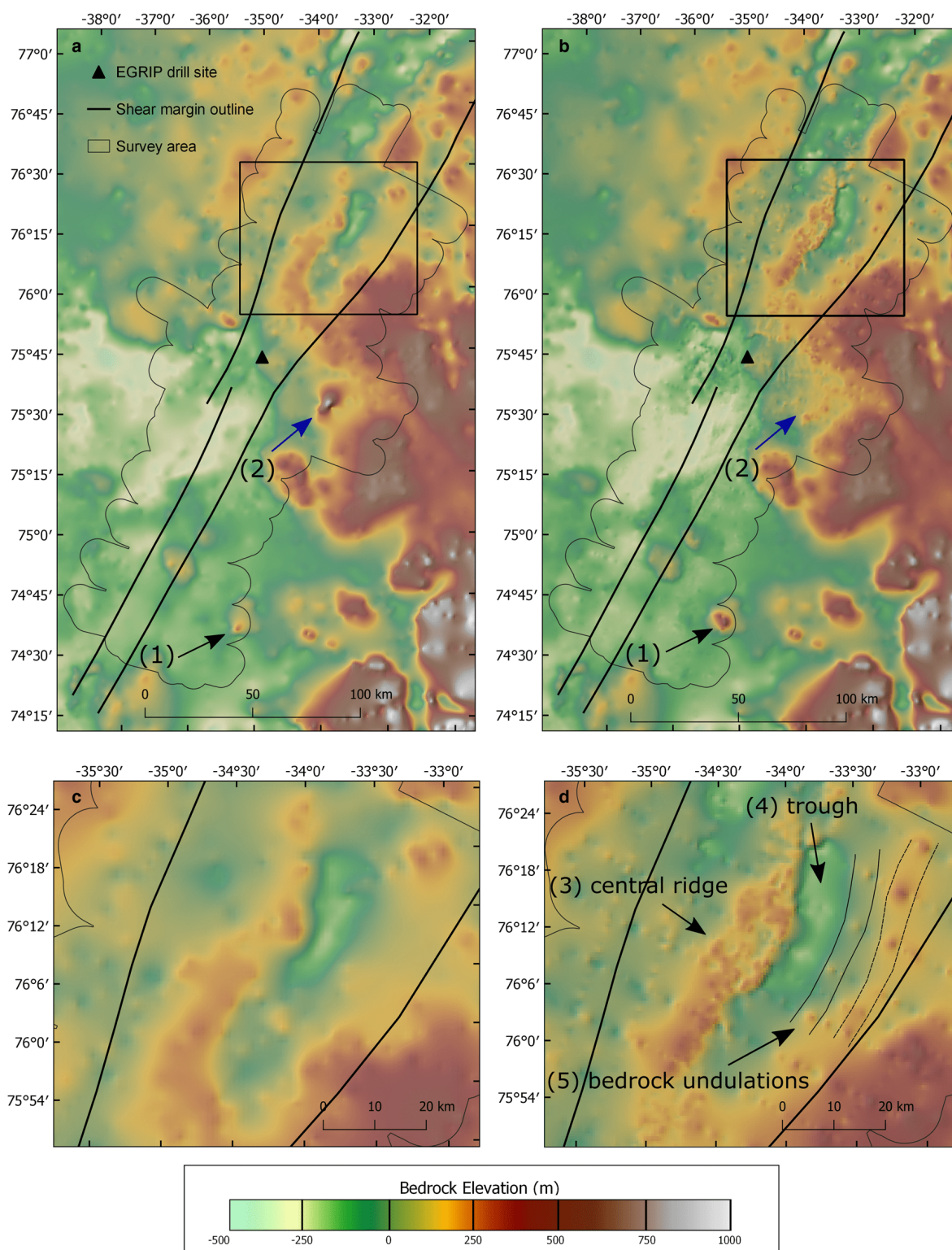


Figure E.3: Bed topography of a) BedMachine v3 (Morigheim et al. (2017)) and b) the EGRIP-NOR-2018 bed topography derived from our ice thickness data. A magnified view for the area upstream of the EGRIP drill site for both models (a) and (b) is shown on the two lower images (c) and (d), respectively). Two locations with strong elevation differences are marked with a blue arrow. In the magnified sections, (c) and (d), we show the location of features 3–5.

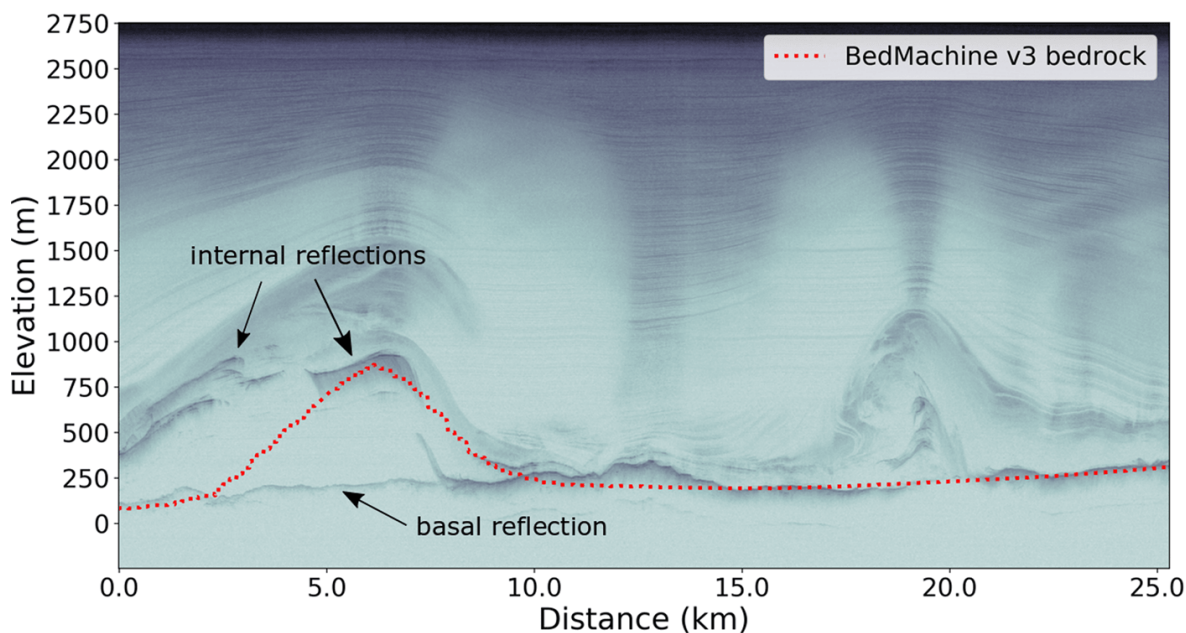


Figure E.4: Echogram from profile 20180508_06_003 along the point of our largest deviation in ice thickness (blue mark on Figure E.2). The dashed red line represents the bed elevation as used in BedMachine v3 (Morlighem et al., 2017). The high peak at 6 km distance along the profile and ~ 750 m elevation correlates with a high energy internal reflection located in an area of folded internal layers. Underneath that undulation a fainter laterally straight and coherent reflection with a lower amplitude is visible, which we interpret as the basal reflection.

the ice sheet, where large, fast flowing outlet glaciers drain through confined valleys. Patton et al. (2016) suggested that the overdeepening structures found in their analysis of the bed topography beneath the central part of the Antarctic and Greenlandic ice sheets might have been initiated in a period with a thinner ice layer, when the ice flow was more defined by the basal topography. The unusually high surface velocities of NEGIS, at least for the central region of the ice sheet, appear to facilitate ongoing erosion of the previously existing bed morphology. Patton et al. (2016) also suggest that sedimentation of eroded material at the downstream end of the overdeepening would lead to a stabilization of the structure, preventing erosion downstream due to the softness of the sediment layer and thus, protecting the bed. This would then also result in the flattening of the surface profile. In case of the NEGIS there is a distinct step in the surface elevation at the downstream boundary of the basin, which might be interpreted as the erosion material being effectively flushed away.

As noted before by Christianson et al. (2014), the position and shape of the ice stream cannot be directly linked to the bed topography. The widening of the ice stream from a narrow channel with a width of 15 km upstream of the EGRIP Camp to a more than 50 km wide stream at the downstream end of our survey area is coincident with a 300 to 500 m step in the topography aligned perpendicular to the flow direction .

Interpretation of off-nadir reflections

For the major part of the survey area, the bed shows a clear reflection signature. Survey lines oriented transverse to ice flow show a variable bed topography with frequent elevation changes. Radargrams parallel to ice flow show a smooth and straight basal reflection. Elevation changes appear as elongated steps rather than a pattern of ridges and troughs. Several of the along-flow radargrams show off-nadir events underneath the initial bed reflection (Figure E.5). These events are only found in survey lines from within the ice stream. We interpret them to likely be caused by side reflections off-nadir, i. e. by elevation changes in the across-track dimension. Figure E.6 shows a sketch of what kind of structures along the flight direction could generate these reflections in the radargrams. In some cases, we detect reflections in the form of straight lines, almost parallel and very similar to the shape of the primary bed reflection (Subfigures 1, 2 and 3 in Figure E.5). These features are too close to the primary bed event to represent multiple reflections. We argue that the topography in these areas shows elongated ridges oriented parallel to ice flow, which are not visible in the large-scale topography of Figure E.3 because of a lack of adequate spatial coverage and data point density. Considering the geometry of the radar beam and the footprint at the base of the ice sheet, the multiple reflectors could be generated by ridges with a height difference of tens of meters, and a ridge-to-ridge distance in the range of a hundred meters. However, on

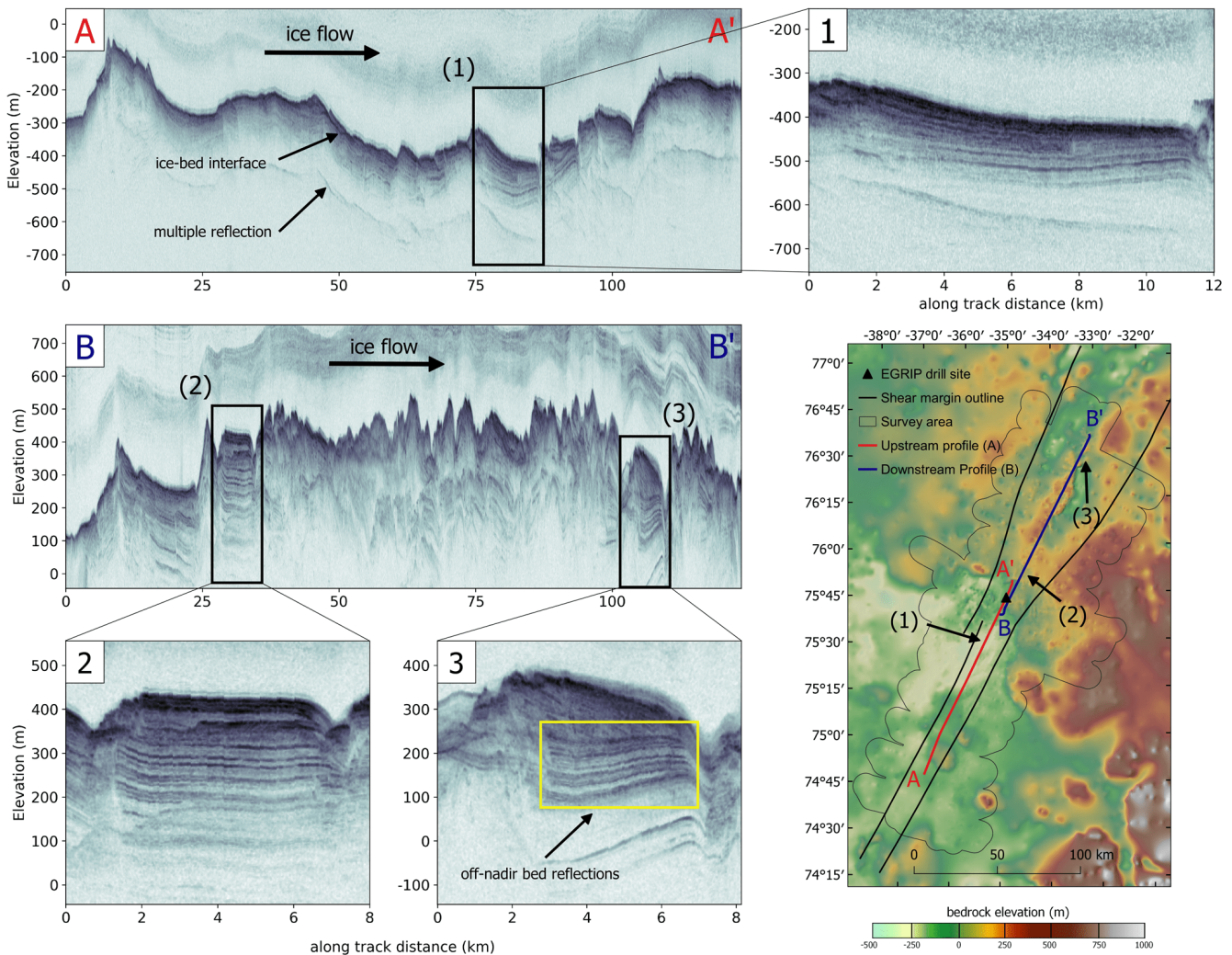


Figure E.5: A set of radargrams from the: upstream (A) and downstream part (B) of the survey area oriented parallel to ice flow. The data were recorded with an increased radar cross-track beam angle. Subsections of the radargrams indicating the location of off-nadir reflections are shown in the radargrams 1, 2 and 3. An example of the off-nadir bed reflection pattern in the radargram 3 with the yellow outline. The position and the orientation of the radargrams (A to A' in red and B to B' in blue) as well as the location of the off-nadir reflection patterns 1, 2 and 3 are indicated in the map in the lower right corner.

the basis of our data, this can only be evaluated qualitatively. These off-nadir reflection signatures are absent at the upstream end of our survey area, where ice-sheet velocity is below 30 m a^{-1} . They become more pronounced with increasing velocity in the downstream area, approximately around the EGRIP camp, where the ice stream begins to widen. They appear in the western trough as well as on the central ridge. Unfortunately, there are no flow-parallel survey lines along the overdeepening in the east, so we cannot determine their presence. The structures have a length of up to 10 km (feature (1) in Figure E.5 A). It is possible that the ridges extend even further, as the flight trajectory might not be exactly parallel to the orientation of the structures, which would cause a fading of the reflections in the radar data and thus interruptions in their appearance. In most cases the main bed reflection along these features is very smooth, at constant depth

or with a very gentle slope, while at the downstream end of the multiple reflections a significant change in the bed slope can be detected (Figure 5 A & B). This indicates that the flight line here is cutting the grooved bed at a small angle. Thus, it is not possible to derive the exact along-flow extension of these features from the airborne data, but we can only provide a lower estimate.

The small-scale subglacial elongated landforms, which we deduce from the interpretation of side reflections, are probably a result of the flow activity of NEGIS in its current configuration, as they are parallel to the direction of observed surface ice flow. Elongated ridges at the ice-bed interface of a similar scale have been mapped underneath active ice streams before. Holschuh et al. (2020) used swath radar data at Thwaites Glacier in Antarctica and mapped subglacial

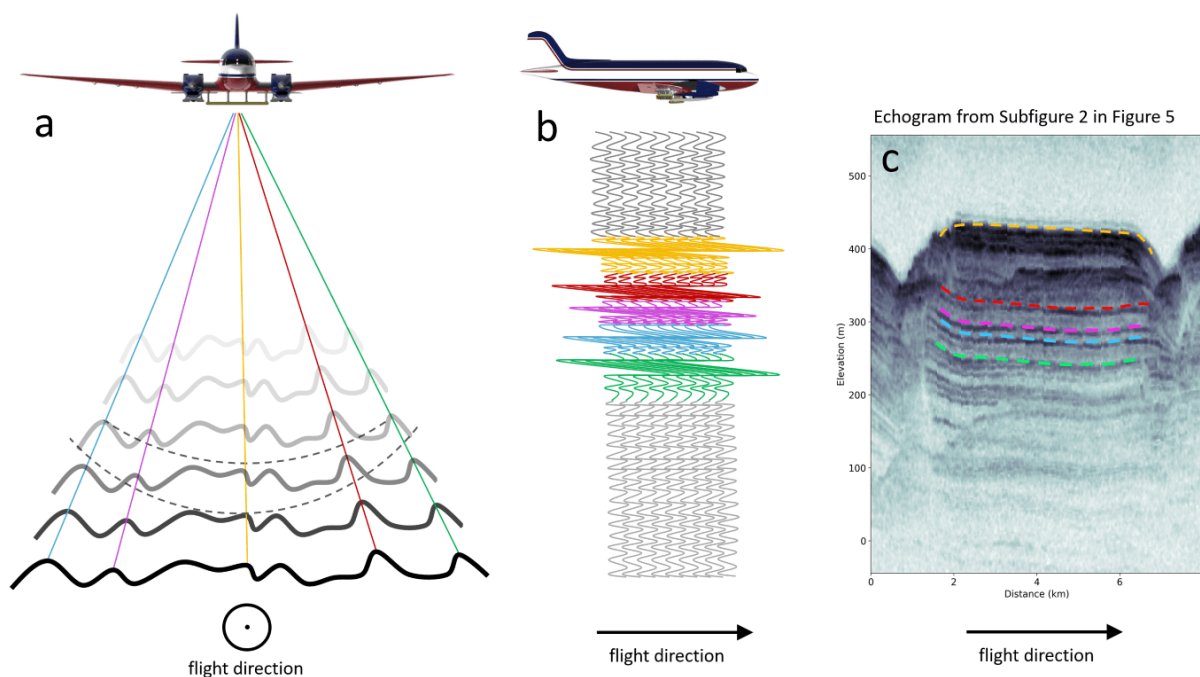


Figure E.6: Sketch showing how the bed structures of our interpretation of basal off-nadir reflections can look like. **(a)** Side reflections are scattered towards the receiver from elongated landforms aligned parallel to the flight trajectory. The black lines represent the bed reflector at different positions along the flight path. The different off-nadir reflections, which are most likely caused by scattered reflections by the elongated structures, are shown here in five different colours. **(b)** If the structure is parallel to the flight direction, a similar reflection pattern is recorded in the traces along the flight trajectory. **(c)** In the example echogram section of the profile 20180515_01_007, the recorded signal could potentially look as indicated by the coloured dashed layers. Plane model by curtsey University of Kansas, Department of Engineering (2015).

landforms which show a clear link between bedform orientation and ice flow. Jezek et al. (2011) interpreted ridges underneath parts of the Jakobshavn Isbræ as linear erosion of a hard bed, a landform which is also known from previously glaciated areas (Bradwell et al., 2008). To create these structures high flow velocities and a significant sliding between ice and bed is required. However, data from a seismic survey close to the EGRIP Camp indicates a layer of soft, water saturated sediments beneath the main trunk of the ice stream. Saturated deformable sediments are one facilitator of fast flowing ice streams (Winsborrow et al., 2010) which can produce elongated bedforms, such as mega-scale glacial lineations (MSGs) (Stokes and Clark, 2002). Apart from areas with relict MSGs, they have also been documented beneath active ice streams, e.g. in West Antarctica below the Rutford Ice Stream by King et al. (2009), as well as below Pine Island Glacier Bingham et al. (2017). MSGs may be produced by either rapid ice flow over a short time, or slower ice flow over a longer duration (Stokes and Clark, 2002). We observe our features in areas of slow to moderate ice surface flow velocities of 30 to 80 m a⁻¹ (based on surface velocities provided by Joughin et al. (2018)). This would indicate that these subglacial features can either form at lower flow velocities or that ice flow in this region has persisted for a long time or at higher velocities than at

present, and that dilatant till is present over a wide area beneath the ice stream. It is also possible that there are transitions between hard-bedded eroded streamlined landforms to soft-bedded landforms caused by different basal lithologies or a changing dynamic activity over several glacial cycles. Without further evidence about the nature of the ice–bed interface this remains speculative.

Conclusion

A new high resolution ice thickness data set has been computed on the basis of airborne radar data. We derived a bed elevation model and analysed topography related structures in the area of the NEGIS in the vicinity of the EGRIP drill site. Basal topography is resolved in greater detail than in current bed elevation models of Greenland and covers a greater area than previous investigations and identified several misinterpretations of earlier ice thickness and thus bed elevation data. The enhanced resolution and more accurate geometry of the bed topography influences estimates of hydropotential and basal water routing. We observe an elongated topographic overdeepening, which indicates long term erosion, potentially even over multiple glacial cycles. Small-scale elongated subglacial landforms in the center of the ice stream oriented parallel ice flow probably

cause off-nadir reflections in our radargrams. Due to the survey line spacing and without additional geophysical data, the nature and geomorphology of these structures cannot be determined further. Either these landforms are formed by erosion in hard bed or by depositional processes, in which case they could represent MSGs. The latter would also be consistent with the observations of [Christianson et al. \(2014\)](#), who found a metre thick layer of sediment across the ice stream located in the vicinity to the locations where we identify these features. Another set of seismic profiles and a higher resolution of the bed topography in regions where we interpret our basal radar return as subglacial landforms would be helpful to evaluate our hypothesis in terms of the composition and structure of elongated bedforms and the existence of sediments. However, a full 3D bed elevation model is basically a requirement to more comprehensively interpret areas where we find evidence for the types and formation subglacial landforms. Nevertheless, our current analysis significantly improves previous bed elevation data set in terms of coverage and accuracy, thus fostering more reliable ice-flow model applications to investigate driving ice-dynamic process of NEGIS.

Data availability

The gridded ice thickness and bed topography data as well as the TWTs of the ice thickness along the radar profiles will be available at the Data Publisher for Earth & Environmental Science (PANGAEA: <https://doi.pangaea.de/10.1594/PANGAEA.907918>).

Author contributions

Steven Franke wrote the manuscript and conducted the main part of the data processing and analysis. Olaf Eisen and Daniela Jansen were PI and Co-I of the campaign and designed the study. Daniela Jansen coordinated and conducted the field work together with Tobias Binder and John Paden. Veit Helm processed GPS data and assisted with further data processing together with Daniel Steinhage. John Paden and Nils Dörr contributed to the radar data processing with the CReSIS Toolbox and implemented the set-up for the nested bed elevation model. Daniela Jansen, Steven Franke and Olaf Eisen interpreted the radar and bed topography data. All co-authors discussed and commented on the manuscript.

Acknowledgements

We thank the crew of the research aircraft Polar 6. Logistical support in the field was provided by the East

Greenland Ice-Core Project. EGRIP is directed and organized by the Center of Ice and Climate at the Niels Bohr Institute. It is supported by funding agencies and institutions in Denmark (A. P. Møller Foundation, University of Copenhagen), USA (U.S. National Science Foundation, Office of Polar Programs), Germany (Alfred Wegener Institute, Helmholtz Centre for Polar and Marine Research), Japan (National Institute of Polar Research and Arctic Challenge for Sustainability), Norway (University of Bergen and Bergen Research Foundation), Switzerland (Swiss National Science Foundation), France (French Polar Institute Paul-Emile Victor, Institute for Geosciences and Environmental research), and China (Chinese Academy of Sciences and Beijing Normal University). We acknowledge the use of software from CReSIS generated with support from the State of Kansas, NASA Operation IceBridge grant NNX16AH54G, and NSF grant ACI-1443054. The authors would like to thank Emerson E&P Software, Emerson Automation Solutions, for providing licenses in the scope of the Emerson Academic Program. We thank Martin Siegert and two anonymous reviewer for comments that improved the quality and readability of this manuscript.

Appendix

Radar data processing

As a preliminary result, which is also generated in the field, we produce a quick look echogram with pre-summed unmigrated data. This output is used to automatically determine the ice surface location by using a maximum power layer tracker. CReSIS SAR processing algorithms use the surface location to model the ice as a layered media for fk migration ([Leuschen et al., 2000](#)). A simple dielectric half-space is used for representing the layered media with an ice dielectric permittivity of 3.15. Recorded radar signals of each channel are processed individually and stacked coherently, equivalent to beamforming towards nadir. Depending on the number and pulse duration of the transmitted waveforms, different receiver gains are applied to increase the dynamic range. Radargrams with low and high gain are combined into a single image. The low gain echogram is used for the upper part of the image and the high gain echogram is used for the lower part of the image.

Pulse compression in the frequency domain is used to improve range resolution and SNR. As a result of this processing step, range sidelobes appear on both sides of the main return with a time window of twice the pulse duration ([Li et al., 2013](#)). A Hanning window is applied in the frequency domain to suppress range sidelobes and both the transmit signal and the matched filter are tapered with a Tukey window in the time domain. Range resolution depends on the propagation

speed of the radar wave, and thus on the real part of the relative permittivity ϵ_r , the bandwidth of the transmitted chirp B and a factor for window widening due to the frequency and time domain windows, k_i , according to

$$\delta(r) = \frac{k_i c}{2B\sqrt{\epsilon_r}}. \quad (\text{E.2})$$

For the NB bandwidth of 30 MHz, the theoretical range resolution in ice with $\epsilon_r = 3.15$ and $k_i = 1.53$ is 4.31 m.

Transmit equalization

Prior to the data acquisition, transmit equalization of the emitted radar signals were performed on open water on the transit to Greenland. Adjustment of coefficients for amplitude, phase and time delay for each transmitter and each receiver helps to compensate any mismatches caused by the hardware. This adjustment is of particular importance for beam-focusing and array processing to increase SNR. The coefficients are determined during a test flight prior to the actual data acquisition.

Motion compensation

Fourier-based processing algorithms for SAR processing require a uniformly sampled linear trajectory of the receivers along the extent of the SAR aperture and high precision timing information. Any deviation from a straight line reduces the maximum possible SNR of the received signal and induces phase errors, which degrade the target focusing (Legarsky et al., 2001). Velocity variations, for instance, alter the along-track sampling and create an irregular sample spacing. High precision processed GPS and INS data from the aircraft are used to correct these effects. Before SAR processing, we 1) resampled the data in along-track using a windowed sinc interpolation kernel and 2) corrected any flight path deviations with a time delay.

SAR processing

The energy of radar wave reflectors spreads over a hyperbola in the along-track dimension produced by off-nadir reflections. The straight trajectory over the synthetic aperture length with uniform sampling points allows us to use frequency-wavenumber (fk) migration to locate reflection energy back to the target location. The technique is based on the fk -migration for seismic data (Gazdag, 1978) and was adapted for radioglaciology (Leuschen et al., 2000). The processing uses signal information from adjacent traces and the result is

based on the dielectric model of the subsurface to determine the radar wave propagation speed (Legarsky et al., 2001). For the migration we use a layered velocity model with two constant permittivity values ($\epsilon = 1$ for air and $\epsilon_{ice} = 3.15$ for ice). The air–ice interface is determined with an automatic surface tracker on unmigrated data. Time delays occurring due to changes of the aircraft trajectory and altitude are also corrected during this step (Rodriguez-Morales et al., 2014). The SAR aperture length at each pixel is chosen to create a fixed along-track resolution of 2.5 m.

Array processing

Coherent combination of return signals in the cross-track dimension is applied to increase SNR and to reduce surface clutter. For our processing, the antenna array beam is steered towards nadir. Since surface clutter due to crevasses is not prominent in our data, we applied the ‘delay and sum’ method for channel combination. This algorithm uses multi-looking of ambient pixels of the image pixel that is combined followed by along-track decimation (Jezek et al., 2013). To multilook, the array processed output is power detected and then averaged with neighbouring pixels. In this case, the averaging window is 5 range lines before and 5 range lines after the current range line, resulting in reduced signal variance or fading and a coarser resolution of $2.5 \text{ m} \times 11 = 27.5 \text{ m}$ along track. An output is generated every 6 range lines so that the sampling or posting in the final image is $2.5 \text{ m} \times 6 = 15 \text{ m}$.

For our bed return, we consider a cross-track resolution for a typical rough surface σ_y , which is constrained by the pulse-limited footprint and is dependent on Haning and Tukey window factors,

$$\sigma_y = 2\sqrt{\frac{H_a}{\sqrt{\epsilon_r}} \frac{ck_i}{B}}, \quad (\text{E.3})$$

where H_a is the height of the aircraft over the ice surface. Our flights were all performed at an elevation of $\sim 365 \text{ m}$ above ground, which corresponds to a cross-track footprint of 300–350 m for an ice column of 2000–3000 m in our survey region. The bed return, however, is in some cases characterized by layover signals from off-nadir due to topography. In this case, cross-track resolution depends on the full beam width, β_y , of the antenna array,

$$\beta_y = \arcsin \frac{\lambda_c}{Nd_y}, \quad (\text{E.4})$$

where λ_c is the wavelength at the center frequency, N is the number of array elements and d_y is the element

spacing of 46.8 cm. Cross-track resolution can now be calculated as

$$\sigma_y = 2 \frac{H_a + T}{\sqrt{\varepsilon}} \tan \frac{\beta_y k_t}{2}. \quad (\text{E.5})$$

Considering Equation (1.5) with a beam angle of $\sim 21^\circ$ corresponds to a cross-track resolution for the bed layer of 800 m to 1100 m for an ice thickness range of 2000–3000 m.

Bibliography

- Allen, C. T., Mozaffar, S. N., and Akins, T. L. Suppressing coherent noise in radar applications with long dwell times. *IEEE Geoscience and Remote Sensing Letters*, 2(3): 284–286, July 2005. doi: 10.1109/LGRS.2005.847931. URL <http://dx.doi.org/10.1109/LGRS.2005.847931>.
- Aschwanden, A., Fahnstock, M. A., and Truffer, M. Complex Greenland outlet glacier flow captured. *Nature Communications*, 7(May 2015):1–8, 2016. ISSN 20411723. doi: 10.1038/ncomms10524. URL <http://dx.doi.org/10.1038/ncomms10524>.
- Bamber, J. L., Griggs, J. A., Hurkmans, R. T. W. L., Dowdeswell, J. A., Gogineni, S. P., Howat, I., Mouginot, J., Paden, J., Palmer, S., Rignot, E., and Steinhage, D. A new bed elevation dataset for Greenland. *Cryosphere*, 7(2): 499–510, 2013. ISSN 19940416. doi: 10.5194/tc-7-499-2013. URL <http://dx.doi.org/10.5194/tc-7-499-2013>.
- Bingham, R. G., Vaughan, D. G., King, E. C., Davies, D., Cornford, S. L., Smith, A. M., Arthern, R. J., Brisbourne, A. M., De Rydt, J., Graham, A. G. C., Spagnolo, M., Marsh, O. J., and Shean, D. E. Diverse landscapes beneath Pine Island Glacier influence ice flow. *Nature Communications*, 8(1):1618, dec 2017. ISSN 2041-1723. doi: 10.1038/s41467-017-01597-y. URL <http://www.nature.com/articles/s41467-017-01597-y>.
- Bohleber, P., Wagner, N., and Eisen, O. Permittivity of ice at radio frequencies: Part II. Artificial and natural polycrystalline ice. *Cold Regions Science and Technology*, 83-84:13–19, dec 2012. ISSN 0165-232X. doi: 10.1016/J.COLDREGIONS.2012.05.010. URL <https://www.sciencedirect.com/science/article/pii/S0165232X12001103>.
- Bradwell, T., Stoker, M., and Krabbendam, M. Megagrooves and streamlined bedrock in NW Scotland: The role of ice streams in landscape evolution. *Geomorphology*, 97(1-2):135–156, 2008. ISSN 0169555X. doi: 10.1016/j.geomorph.2007.02.040. URL <http://dx.doi.org/10.1016/j.geomorph.2007.02.040>.
- Christianson, K., Peters, L. E., Alley, R. B., Anandakrishnan, S., Jacobel, R. W., Riverman, K. L., Muto, A., and Keisling, B. A. Dilatant till facilitates ice-stream flow in northeast Greenland. *Earth and Planetary Science Letters*, 401:57–69, 2014. ISSN 0012821X. doi: 10.1016/j.epsl.2014.05.060. URL <http://dx.doi.org/10.1016/j.epsl.2014.05.060>.
- Church, J. A., Clark, P., Cazenave, A., Gregory, J., Jevrejeva, S., Levermann, A., Merrifield, M., Milne, G., Nerem, R., Nunn, P., Payne, A., Pfeffer, W., Stammer, D., and Unnikrishnan, A. 2013: Sea level change. In *Climate Change 2013: The Physical Science Basis. Contribution of Working Group I to the Fifth Assessment Report of the Intergovernmental Panel on Climate Change*, pages 1137–1216. 2013. ISBN ISBN 978-1-107-66182-0. doi: 10.1017/CB09781107415315.026. URL <http://dx.doi.org/10.1017/CB09781107415315.026>.
- Cook, S. J. and Swift, D. A. Subglacial basins: Their origin and importance in glacial systems and landscapes. *Earth-Science Reviews*, 115(4):332 – 372, 2012. ISSN 0012-8252. doi: <https://doi.org/10.1016/j.earscirev.2012.09.009>. URL <http://www.sciencedirect.com/science/article/pii/S0012825212001286>.
- CRISIS-Toolbox. J Paden, URL: https://ops.cresis.ku.edu/wiki/index.php/Main_Page, accessed: 2019-06-01, 2019. URL https://ops.cresis.ku.edu/wiki/index.php/Main_Page.
- Dowdeswell, J. A., Hogan, K. A., Ó Cofaigh, C., Fugelli, E. M., Evans, J., and Noormets, R. Late Quaternary ice flow in a West Greenland fjord and cross-shelf trough system: Submarine landforms from Rink Isbrae to Uummannaq shelf and slope. *Quaternary Science Reviews*, 2014. ISSN 02773791. doi: 10.1016/j.quascirev.2013.09.007. URL <http://dx.doi.org/10.1016/j.quascirev.2013.09.007>.
- Dutrieux, P., Vaughan, D. G., Corr, H. F. J., Jenkins, A., Holland, P. R., Joughin, I., and Fleming, A. H. Pine Island glacier ice shelf melt distributed at kilometre scales. *The Cryosphere*, 7(5):1543–1555, 2013. ISSN 19940416. doi: 10.5194/tc-7-1543-2013. URL <http://dx.doi.org/10.5194/tc-7-1543-2013>.
- Fahnstock, M., Abdalati, W., Joughin, I., Brozena, J., and Gogineni, P. High geothermal heat flow, basal melt, and the origin of rapid ice flow in central Greenland. *Science*, 294(5550):2338–2342, 2001. ISSN 00368075. doi: 10.1126/science.1065370. URL <http://dx.doi.org/10.1126/science.1065370>.
- Förste, C., Bruinsma, S., Abrikosov, O., Flechtner, F., Marty, J.-C., Lemoine, J.-M., Dahle, C., Neumayer, H., Barthelmes, F., König, R., and Biancale, R. EIGEN-6C4 - The latest combined global gravity field model including GOCE data up to degree and order 1949 of GFZ Potsdam and GRGS Toulouse. *EGU General Assembly 2014, held 27 April - 2 May, 2014 in Vienna, Austria, id.3707*, 16, 2014. URL <http://adsabs.harvard.edu/abs/2014EGUGA..16.3707F>.
- Fretwell, P., Pritchard, H. D., Vaughan, D. G., Bamber, J. L., Barrand, N. E., Bell, R., Bianchi, C., Bingham, R. G., Blankenship, D. D., Casassa, G., Catania, G., Callens, D., Conway, H., Cook, A. J., Corr, H. F. J., Damaske, D., Damm, V., Ferraccioli, F., Forsberg, R., Fujita, S., Gim, Y., Gogineni, P., Griggs, J. A., Hindmarsh, R. C. A., Holmlund, P., Holt, J. W., Jacobel, R. W., Jenkins, A., Jokat, W., Jordan, T., King, E. C., Kohler, J., Krabill, W., Riger-Kusk, M., Langley, K. A., Leitchenkov, G., Leuschen, C., Luyendyk, B. P., Matsuoka, K., Mouginot, J., Nitsche, F. O., Nogi, Y., Nost, O. A., Popov, S. V., Rignot, E., Rippin, D. M., Rivera, A., Roberts, J., Ross, N., Siegert, M. J., Smith, A. M., Steinhage, D., Studinger, M., Sun, B., Tinto, B. K., Welch, B. C., Wilson, D., Young, D. A., Xiangbin, C., and Zirizzotti, A. Bedmap2: improved ice bed, surface and thickness datasets for Antarctica. *The Cryosphere*, 7(1):375–393, feb 2013. ISSN 1994-0424. doi: 10.5194/tc-7-375-2013. URL <https://www.the-cryosphere.net/7/375/2013/>.

- Gardner, A. S., Moholdt J.G., G., Wouters, B., Arendt, A. A., Wahr, J., Berthier, E., Hock, R., Pfeffer, W. T., Kaser, G., Ligtenberg, S. R. M., Bolch, T., Sharp, M. J., Hagen, J. O., van den Broeke, M. R., and Paul, F. A Reconciled Estimate of Glacier Contributions to Sea Level Rise: 2003 to 2009. *Science*, 340(May):852–857, 2013. doi: 10.1126/science.1234532. URL <http://dx.doi.org/10.1126/science.1234532>.
- Gazdag, J. Wave equation migration with the phase-shift method. *Geophysics*, 43(7):1342–1351, 1978. ISSN 0016-8033. doi: 10.1190/1.1440899. URL <http://dx.doi.org/10.1190/1.1440899>.
- Gillet-Chaulet, F., Gagliardini, O., Seddik, H., Nodet, M., Durand, G., Ritz, C., Zwinger, T., and Greve, R. The Cryosphere Greenland ice sheet contribution to sea-level rise from a new-generation ice-sheet model. *The Cryosphere*, 6(6):1561–1576, 2012. doi: 10.5194/tc-6-1561-2012. URL <http://dx.doi.org/10.5194/tc-6-1561-2012>.
- Goelzer, H., Nowicki, S., Payne, A., Larour, E., Seroussi, H., Lipscomb, W. H., Gregory, J., Abe-Ouchi, A., Shepherd, A., Simon, E., Agosta, C., Alexander, P., Aschwanden, A., Barthel, A., Calov, R., Chambers, C., Choi, Y., Cuzzzone, J., Dumas, C., Edwards, T., Felikson, D., Fettweis, X., Golledge, N. R., Greve, R., Humbert, A., Huybrechts, P., Le clec'h, S., Lee, V., Leguy, G., Little, C., Lowry, D. P., Morlighem, M., Nias, I., Quiquet, A., Rückamp, M., Schlegel, N.-J., Slater, D., Smith, R., Straneo, F., Tarasov, L., van de Wal, R., and van den Broeke, M. The future sea-level contribution of the greenland ice sheet: a multi-model ensemble study of ismip6. *The Cryosphere Discussions*, 2020:1–43, 2020. doi: 10.5194/tc-2019-319. URL <https://www.the-cryosphere-discuss.net/tc-2019-319/>.
- Gogineni, S., Tammana, D., Braaten, D., Leuschen, C., Akins, T., Legarsky, J., Kanagaratnam, P., Stiles, J., Allen, C., and Jezek, K. Coherent radar ice thickness measurements over the Greenland ice sheet. *Journal of Geophysical Research*, 106(D24):33,761–33,772, 2001. ISSN 0148-0227. doi: 10.1029/2001JD900183. URL <http://dx.doi.org/10.1029/2001JD900183>.
- Hale, R., Miller, H., Gogineni, S., Yan, J. B., Leuschen, C., Paden, J., and Li, J. Multi-channel ultra-wideband radar sounder and imager. *2016 IEEE International Geoscience and Remote Sensing Symposium (IGARSS)*, pages 2112–2115, 2016. doi: 10.1109/IGARSS.2016.7729545. URL <http://dx.doi.org/10.1109/IGARSS.2016.7729545>.
- Hogan, K. A., Ó Cofaigh, C., Jennings, A. E., Dowdeswell, J. A., and Hiemstra, J. F. Deglaciation of a major palaeo-ice stream in Disko Trough, West Greenland. *Quaternary Science Reviews*, 2016. ISSN 02773791. doi: 10.1016/j.quascirev.2016.01.018. URL <http://dx.doi.org/10.1016/j.quascirev.2016.01.018>.
- Holschuh, N., Christianson, K., Paden, J., Alley, R., and Anandakrishnan, S. Linking postglacial landscapes to glacier dynamics using swath radar at Thwaites Glacier, Antarctica. *Geology*, jan 2020. ISSN 0091-7613. doi: 10.1130/g46772.1. URL <http://dx.doi.org/10.1130/g46772.1>.
- Howat, I. M., Joughin, I., and Scambos, T. A. Rapid Changes in Ice Discharge from. *Science*, 315(5818):1559–1561, 2007. doi: 10.1126/science.1138478. URL <http://dx.doi.org/10.1126/science.1138478>.
- Howat, I. M., Negrete, A., and Smith, B. E. The Greenland Ice Mapping Project (GIMP) land classification and surface elevation data sets. *Cryosphere*, 8(4):1509–1518, 2014. ISSN 19940424. doi: 10.5194/tc-8-1509-2014. URL <http://dx.doi.org/10.5194/tc-8-1509-2014>.
- IPCC. IPCC Special Report on the Ocean and Cryosphere in a Changing Climate [H.-O. Pörtner, Roberts, D. C., Masson-Delmotte, V., Zhai, P., Tignor, M., Poloczanska, E., Mintenbeck, K., Nicolai, M., Okem, A., Petzold, J., Rama, B. Weyer, N. (eds.)]. Technical report, 2019. URL <https://www.ipcc.ch/srocc/chapter/technical-summary/>.
- Jezek, K., Wu, X., Gogineni, P., Rodríguez, E., Freeman, A., Rodríguez-Morales, F., and Clark, C. D. Radar images of the bed of the Greenland Ice Sheet. *Geophysical Research Letters*, 38(1):1–5, 2011. ISSN 00948276. doi: 10.1029/2010GL045519. URL <http://dx.doi.org/10.1029/2010GL045519>.
- Jezek, K., Wu, X., Paden, J., and Leuschen, C. Radar mapping of isunnguata Sermia, Greenland. *Journal of Glaciology*, 59(218):1135–1146, 2013. ISSN 00221430. doi: 10.3189/2013JoG12J248. URL <http://dx.doi.org/10.3189/2013JoG12J248>.
- Joughin, I., Smith, B. E., Howat, I. M., Scambos, T., and Moon, T. Greenland flow variability from ice-sheet-wide velocity mapping. *Journal of Glaciology*, 56(197):415–430, 2010. ISSN 0022-1430. doi: 10.3189/002214310792447734. URL <http://dx.doi.org/10.3189/002214310792447734>.
- Joughin, I., Smith, B. E., and Howat, I. M. A complete map of Greenland ice velocity derived from satellite data collected over 20 years. *Journal of Glaciology*, 64(243):1–11, feb 2018. ISSN 0022-1430. doi: 10.1017/jog.2017.73. URL <https://www.cambridge.org/core/product/identifier/S0022143017000739/type/journal{ }article>.
- Keisling, B. A., Christianson, K., Alley, R. B., Peters, L. E., Christian, J. E., Anandakrishnan, S., Riverman, K. L., Muto, A., and Jacobel, R. W. Basal conditions and ice dynamics inferred from radar-derived internal stratigraphy of the northeast Greenland ice stream. *Annals of Glaciology*, 55(67):127–137, 2014. ISSN 02603055. doi: 10.3189/2014AoG67A090. URL <http://dx.doi.org/10.3189/2014AoG67A090>.
- Khan, S. A., Kjær, K. H., Bevis, M., Bamber, J. L., Wahr, J., Kjeldsen, K. K., Bjørk, A. A., Korsgaard, N. J., Stearns, L. A., Van Den Broeke, M. R., Liu, L., Larsen, N. K., and Muresan, I. S. Sustained mass loss of the northeast Greenland ice sheet triggered by regional warming. *Nature Climate Change*, 4(4):292–299, 2014a. ISSN 17586798. doi: 10.1038/nclimate2161. URL <http://dx.doi.org/10.1038/nclimate2161>.

- Khan, S. A., Kjeldsen, K. K., Kjær, K. H., Bevan, S., Luckman, A., Bjørk, A. A., Korsgaard, N. J., Box, J. E., Van Den Broeke, M., Van Dam, T. M., and Fitzner, A. Glacier dynamics at Helheim and Kangerdlugssuaq glaciers, southeast Greenland, since the Little Ice Age. *Cryosphere*, 8(4):1497–1507, 2014b. ISSN 19940424. doi: 10.5194/tc-8-1497-2014. URL <http://dx.doi.org/10.5194/tc-8-1497-2014>.
- King, E. C., Hindmarsh, R. C. A., and Stokes, C. R. Formation of mega-scale glacial lineations observed beneath a West Antarctic ice stream. *Nature Geoscience*, 2(8):585–588, aug 2009. ISSN 1752-0894. doi: 10.1038/ngeo581. URL <http://www.nature.com/articles/ngeo581>.
- Kjær, K. H., Larsen, N. K., Binder, T., Bjørk, A. A., Eisen, O., Fahnestock, M. A., Funder, S., Garde, A. A., Haack, H., Helm, V., Houmark-Nielsen, M., Kjeldsen, K. K., Khan, S. A., Machguth, H., McDonald, I., Morlighem, M., Mouginot, J., Paden, J. D., Waight, T. E., Weikusat, C., Willerslev, E., and MacGregor, J. A. A large impact crater beneath Hiawatha Glacier in northwest Greenland. *Science Advances*, 4(11):eaar8173, nov 2018. ISSN 2375-2548. doi: 10.1126/sciadv.aar8173. URL <http://advances.sciencemag.org/lookup/doi/10.1126/sciadv.aar8173>.
- Legarsky, J. J., Gogineni, S. P., and Akins, T. L. Focused synthetic aperture radar processing of ice-sounder data collected over the greenland ice sheet. *IEEE Transactions on Geoscience and Remote Sensing*, 39(10):2109–2117, 2001. doi: 10.1109/36.957274. URL <http://dx.doi.org/10.1109/36.957274>.
- Leuschen, C., Gogineni, S., and Tammana, D. SAR processing of radar echo sounder data. pages 2570–2572, 2000. doi: 10.1109/igarss.2000.859643. URL <http://dx.doi.org/10.1109/igarss.2000.859643>.
- Laysinger Vieli, G.-M., Hindmarsh, R. C. a., and Siegert, M. J. Three-dimensional flow influences on radar layers stratigraphy. *Annals of Glaciology*, pages 22–28, 2007. doi: 10.3189/172756407782871729. URL <http://dx.doi.org/10.3189/172756407782871729>.
- Li, J., Paden, J., Leuschen, C., Rodriguez-Morales, F., Hale, R. D., Arnold, E. J., Crowe, R., Gomez-Garcia, D., and Gogineni, P. High-altitude radar measurements of ice thickness over the antarctic and greenland ice sheets as a part of operation icebridge. *IEEE Transactions on Geoscience and Remote Sensing*, 51(2):742–754, 2013. ISSN 0196-2892. doi: 10.1109/TGRS.2012.2203822.
- Martos, Y. M., Jordan, T. A., Catalán, M., Jordan, T. M., Bamber, J. L., and Vaughan, D. G. Geothermal Heat Flux Reveals the Iceland Hotspot Track Underneath Greenland. *Geophysical Research Letters*, 45(16):8214–8222, aug 2018. ISSN 0094-8276. doi: 10.1029/2018GL078289. URL <https://onlinelibrary.wiley.com/doi/abs/10.1029/2018GL078289>.
- Morlighem, M., Williams, C. N., Rignot, E., An, L., Arndt, J. E., Bamber, J. L., Catania, G., Chauché, N., Dowdeswell, J. A., Dorschel, B., Fenty, I., Hogan, K., Howat, I., Hubbard, A., Jakobsson, M., Jordan, T. M., Kjeldsen, K. K., Millan, R., Mayer, L., Mouginot, J., Noël, B. P., O’Cofaigh, C., Palmer, S., Rysgaard, S., Seroussi, H., Siegert, M. J., Slabon, P., Straneo, F., van den Broeke, M. R., Weinrebe, W., Wood, M., and Zinglensen, K. B. BedMachine v3: Complete Bed Topography and Ocean Bathymetry Mapping of Greenland From Multibeam Echo Sounding Combined With Mass Conservation. *Geophysical Research Letters*, 44(21):11,051–11,061, 2017. ISSN 19448007. doi: 10.1002/2017GL074954. URL <http://dx.doi.org/10.1002/2017GL074954>.
- Mouginot, J., Rignot, E., Scheuchl, B., and Millan, R. Comprehensive annual ice sheet velocity mapping using Landsat-8, Sentinel-1, and RADARSAT-2 data. *Remote Sensing*, 9(4), apr 2017. ISSN 20724292. doi: 10.3390/rs9040364. URL <http://dx.doi.org/10.3390/rs9040364>.
- Newton, A. M. W., Knutz, P. C., Huuse, M., Gannon, P., Brocklehurst, S. H., Clausen, O. R., and Gong, Y. Ice stream reorganization and glacial retreat on the northwest Greenland shelf. *Geophysical Research Letters*, 44(15):7826–7835, aug 2017. ISSN 00948276. doi: 10.1002/2017GL073690. URL <http://doi.wiley.com/10.1002/2017GL073690>.
- Patton, H., Swift, D. A., Clark, C. D., Livingstone, S. J., and Cook, S. J. Distribution and characteristics of overdeepenings beneath the Greenland and Antarctic ice sheets: Implications for overdeepening origin and evolution. *Quaternary Science Reviews*, 2016. ISSN 02773791. doi: 10.1016/j.quascirev.2016.07.012. URL <http://dx.doi.org/10.1016/j.quascirev.2016.07.012>.
- Rignot, E. and Mouginot, J. Ice flow in Greenland for the International Polar Year 2008–2009. *Geophysical Research Letters*, 39(11):n/a–n/a, jun 2012. ISSN 00948276. doi: 10.1029/2012GL051634. URL <http://doi.wiley.com/10.1029/2012GL051634>.
- Rignot, E., Velicogna, I., Van Den Broeke, M. R., Monaghan, A., and Lenaerts, J. Acceleration of the contribution of the Greenland and Antarctic ice sheets to sea level rise. *Geophysical Research Letters*, 38(5):1–5, 2011. ISSN 00948276. doi: 10.1029/2011GL046583. URL <http://dx.doi.org/10.1029/2011GL046583>.
- Robel, A. A., Degiuli, E., Schoof, C., and Tziperman, E. Dynamics of ice stream temporal variability: Modes, scales, and hysteresis. *Journal of Geophysical Research: Earth Surface*, 118(2):925–936, 2013. ISSN 21699011. doi: 10.1002/jgrf.20072. URL <http://dx.doi.org/10.1002/jgrf.20072>.
- Roberts, D. H. and Long, A. J. Streamlined bedrock terrain and fast ice flow, Jakobshavns Isbrae, West Greenland: implications for ice stream and ice sheet dynamics. *Boreas*, 34(1):25–42, jun 2005. doi: 10.1111/j.1502-3885.2005.tb01002.x. URL <http://doi.wiley.com/10.1111/j.1502-3885.2005.tb01002.x>.
- Roberts, D. H., Long, A. J., Davies, B. J., Simpson, M. J. R., and Schnabel, C. Ice stream influence on West Greenland Ice Sheet dynamics during the Last Glacial Maximum. *Journal of Quaternary Science*, 25(6):850–864, sep 2010. ISSN 02678179. doi: 10.1002/jqs.1354. URL <http://doi.wiley.com/10.1002/jqs.1354>.

- Robinson, A., Calov, R., and Ganopolski, A. Multistability and critical thresholds of the Greenland ice sheet. *Nature Climate Change*, 2(6):429–432, 2012. ISSN 1758678X. doi: 10.1038/nclimate1449. URL <http://dx.doi.org/10.1038/nclimate1449>.
- Rodriguez-Morales, F., Gogineni, S., Leuschen, C. J., Paden, J. D., Li, J., Lewis, C. C., Panzer, B., Gomez-Garcia Alvestegui, D., Patel, A., Byers, K., Crowe, R., Player, K., Hale, R. D., Arnold, E. J., Smith, L., Gifford, C. M., Braaten, D., and Panton, C. Advanced multifrequency radar instrumentation for polar Research. *IEEE Transactions on Geoscience and Remote Sensing*, 52(5):2824–2842, 2014. ISSN 01962892. doi: 10.1109/TGRS.2013.2266415. URL <http://dx.doi.org/10.1109/TGRS.2013.2266415>.
- Rogozhina, I., Petrunin, A. G., Vaughan, A. P., Steinberger, B., Johnson, J. V., Kaban, M. K., Calov, R., Rickers, F., Thomas, M., and Koulakov, I. Melting at the base of the Greenland ice sheet explained by Iceland hotspot history. *Nature Geoscience*, 9(5):366–369, 2016. ISSN 17520908. doi: 10.1038/ngeo2689. URL <http://dx.doi.org/10.1038/ngeo2689>.
- Rückamp, M., Goelzer, H., and Humbert, A. Sensitivity of greenland ice sheet projections to spatial resolution in higher-order simulations: the awi contribution to ismip6-greenland using issm. *The Cryosphere Discussions*, 2020: 1–26, 2020. doi: 10.5194/tc-2019-329. URL <https://www.the-cryosphere-discuss.net/tc-2019-329/>.
- Schlegel, N. J., Larour, E., Seroussi, H., Morlighem, M., and Box, J. E. Ice discharge uncertainties in Northeast Greenland from boundary conditions and climate forcing of an ice flow model. *Journal of Geophysical Research: Earth Surface*, 120(1):29–54, 2015. ISSN 21699011. doi: 10.1002/2014JF003359. URL <http://dx.doi.org/10.1002/2014JF003359>.
- Shi, L., Allen, C. T., Ledford, J. R., Rodriguez-Morales, F., Blake, W. A., Panzer, B. G., Prokopiack, S. C., Leuschen, C. J., and Gogineni, S. Multichannel coherent radar depth sounder for NASA operation ice bridge. *International Geoscience and Remote Sensing Symposium (IGARSS)*, pages 1729–1732, 2010. doi: 10.1109/IGARSS.2010.5649518. URL <http://dx.doi.org/10.1109/IGARSS.2010.5649518>.
- Stokes, C. R. and Clark, C. D. Are long subglacial bedforms indicative of fast ice flow? *Boreas*, 31(3): 239–249, 2002. doi: 10.1111/j.1502-3885.2002.tb01070.x. URL <https://onlinelibrary.wiley.com/doi/abs/10.1111/j.1502-3885.2002.tb01070.x>.
- Truffer, M. and Echelmeyer, K. A. Of isbræ and ice streams. *Annals of Glaciology*, 36:66–72, 2003. ISSN 02603055. doi: 10.3189/172756403781816347. URL <http://dx.doi.org/10.3189/172756403781816347>.
- Vallelonga, P., Christianson, K., Alley, R. B., Anandakrishnan, S., Christian, J. E., Dahl-Jensen, D., Gkinis, V., Holme, C., Jacobel, R. W., Karlsson, N. B., Keisling, B. A., Kipfstuhl, S., Kjær, H. A., Kristensen, M. E., Muto, A., Peters, L. E., Popp, T., Riverman, K. L., Svensson, A. M., Tibuleac, C., Vinther, B. M., Weng, Y., and Winstrup, M. Initial results from geophysical surveys and shallow coring of the Northeast Greenland Ice Stream (NEGIS). *Cryosphere*, 8(4):1275–1287, 2014. ISSN 19940424. doi: 10.5194/tc-8-1275-2014. URL <http://dx.doi.org/10.5194/tc-8-1275-2014>.
- Wang, Z., Gogineni, S., Rodriguez-Morales, F., Yan, J. B., Hale, R., Paden, J., Leuschen, C., Carabajal, C., Gomez-Garcia, D., Townley, B., Willer, R., Stearns, L., Child, S., and Braaten, D. Wideband imaging radar for cryospheric remote sensing. *International Geoscience and Remote Sensing Symposium (IGARSS)*, pages 4026–4029, 2014. doi: 10.1109/IGARSS.2014.6947369. URL <http://dx.doi.org/10.1109/IGARSS.2014.6947369>.
- Winsborrow, M. C., Clark, C. D., and Stokes, C. R. What controls the location of ice streams? *Earth-Science Reviews*, 103(1-2):45–59, 2010. ISSN 00128252. doi: 10.1016/j.earscirev.2010.07.003. URL <http://dx.doi.org/10.1016/j.earscirev.2010.07.003>.
- Wright, A. P., Siegert, M. J., Le Brocq, A. M., and Gore, D. B. High sensitivity of subglacial hydrological pathways in Antarctica to small ice-sheet changes. *Geophysical Research Letters*, 35(17):L17504, sep 2008. ISSN 0094-8276. doi: 10.1029/2008GL034937. URL <http://doi.wiley.com/10.1029/2008GL034937>.

Appendix F

PAPER II

RESEARCH ARTICLE

Complex basal conditions and their influence on ice flow at the onset of the Northeast Greenland Ice Stream

Steven Franke¹ , Daniela Jansen¹ , Sebastian Beyer^{1,2} , Niklas Neckel¹ , Tobias Binder¹ , John D. Paden³  and Olaf Eisen^{1,4} 

¹ Alfred Wegener Institute, Helmholtz Centre for Polar and Marine Research, Bremerhaven, Germany

² MARUM - Center for Marine Environmental Sciences, University of Bremen, Bremen, Germany

³ Center for Remote Sensing of Ice Sheets (CReSIS), University of Kansas, Lawrence, KS, USA

⁴ Department of Geosciences, University of Bremen, Bremen, Germany

Published on 9 March 2021 in JGR: Earth Surface

<https://doi.org/10.1029/2020JF005689>

Abstract

The ice stream geometry and large ice surface velocities at the onset region of the Northeast Greenland Ice Stream (NEGIS) are not yet well reproduced by ice sheet models. The quantification of basal sliding and a parametrisation of basal conditions remains a major gap. In this study, we assess the basal conditions of the onset region of the NEGIS in a systematic analysis of airborne ultra-wideband radar data. We evaluate basal roughness and basal return echoes in the context of the current ice stream geometry and ice surface velocity. We observe a change from a smooth to a rougher bed where the ice stream widens, and a distinct roughness anisotropy, indicating a preferred orientation of subglacial structures. In the upstream region, the excess ice mass flux through the shear margins is evacuated by ice flow acceleration and along-flow stretching of the ice. At the downstream part, the generally rougher bed topography correlates with a decrease in flow acceleration and lateral variations in ice surface velocity. Together with basal water routing pathways, this hints to two different zones in this part of the NEGIS: the upstream region collecting water, with a reduced basal traction and downstream, where the ice stream is slowing down and is widening on a rougher bed, with a distribution of basal water towards the shear margins. Our findings support the hypothesis that the NEGIS is strongly interconnected to the subglacial water system in its onset region, but also to the subglacial substrate and morphology.

Received: 14 May 2020 - Revised 5 December 2020 - Accepted: 8 December 2020

Plain Language Summary

The Northeast Greenland Ice Stream (NEGIS) transports a large amount of ice mass from the interior of the Greenland Ice Sheet (GrIS) towards the ocean. The extent and geometry of the NEGIS are difficult to reproduce in current ice sheet models because many boundary conditions, such as the properties of the ice base, are not well known. In this study, we present new characteristics of the ice base from the onset region of the NEGIS derived by airborne radio-echo sounding data. Our data yield a smooth and increasingly lubricated bed in the upstream part of our survey area, which enables the ice to accelerate. Our results confirm the hypothesis that the position of the ice stream boundaries are coupled to the subglacial hydrology system.

Introduction

The lack of high-resolution bed topography and knowledge about the subglacial conditions in Greenland and Antarctica is one of the largest sources of uncertainty in present ice sheet projections (Morlighem et al., 2019) and higher resolution bed topography is needed to improve the accuracy of ice sheet models (Durand et al., 2011). The subglacial environment of the Antarctic and Greenland Ice Sheet (AIS, GrIS) is only poorly known from direct observations. The technical and logistical efforts for an analysis of the base underneath ice, often several kilometres thick, is much more challenging than observations on paleo-glaciated areas on land or the seafloor through remote sensing techniques (e.g. Stokes et al. (2013); Clark and Meehan (2001)) or marine swath bathymetry (e.g. Arndt et al. (2020); Dowdeswell et al. (2004)). Most of the knowledge about the ice covered bathymetry, bed topography and basal properties are deduced from the analysis and interpretation of indirect observations like radio-echo sounding (Fretwell et al., 2013; Humbert et al., 2018; Morlighem et al., 2017, 2019; Schroeder et al., 2020, 2019; Winter et al., 2017), seismic (Brisbourne et al., 2014; Dow et al., 2013; Hofstede et al., 2018; Kulesa et al., 2017; Rosier et al., 2018; Smith et al., 2020) as well as magnetic and gravimetric surveys combined with modelling approaches (An et al., 2019; Cochran and Bell, 2012; Muto et al., 2013; Eisermann et al., 2020).

In the central regions of the AIS and GrIS, little is known about the distribution and properties of bedrock, lithified and unlithified sediments, liquid water quantity, hydromechanical processes and the thermal and mechanical properties of ice (Clarke, 2005). Variations of these parameters over time can influence the spatial and temporal behaviour of the ice sheets and their streams, by altering the fast flow dynamics or the mobilisation of subglacial sediments. It is assumed that parts of the base of the GrIS are covered by mechanically weak sediments, which facilitate basal sliding (Christianson et al., 2014; Dow et al., 2013). Furthermore, an analysis of the thermal state of the base reveals large areas of a thawed bed and high melt rates at the interior of the GrIS (Fahnestock, 2001; MacGregor et al., 2016; Jordan et al., 2018). However, the response of changes at the glacier base to the ice surface dynamics can vary on several time scales (Ryser et al., 2014).

In Greenland, one feature causing the most significant discrepancies between numerically modelled and observed ice surface velocities is the Northeast Greenland Ice Stream (NEGIS) (Aschwanden et al., 2016), which therefore represents one of the largest uncertainties for ice flow predictions. Several studies assessed the genesis as well as the positioning and geometry of the NEGIS in its onset region close to the ice divide (Fahnestock, 2001; Fahnestock et al., 1993; Joughin et al.,

2001). The ice stream is constrained by its 400-km-long shear margins, and their locations at its onset region show no apparent indications for a topographic control (Holschuh et al., 2019; Franke et al., 2020b). Christianson et al. (2014) established an extended hypothesis on the initiation and development of the NEGIS based on these studies and an analysis of data from an extensive geophysical survey at the onset of the ice stream, centred at the drill site of the EGRIP ice core where the ice stream widens (Vallelonga et al., 2014). The ice stream is most likely initiated by anomalous high geothermal heat flux (GHF) close to the ice divide (Fahnestock, 2001). The GHF is the primary control on the generation of basal meltwater and the sensitivity of the hydrology system (Smith-Johnsen et al., 2020). In the absence of cross-marginal ice flow, acceleration along the trunk of NEGIS should lead to the development of a surface trough. However, the lack of an observed trough must mean acceleration is compensated by an influx of ice through the shear margins (Christianson et al., 2014). The increasing ice flow velocity of the onset of the NEGIS in its current geometry would lead to the development a surface trough, which is not consistent with observations.

In present ice-sheet models, the NEGIS is reproduced through estimating basal-shear stress from inverse methods informed by surface velocities (Larour et al., 2014; Smith-Johnsen et al., 2019). Estimates of basal resistance are not accurate enough to sufficiently reproduce geometry and surface velocities of ice streams by ice-flow models, as our understanding of processes and conditions is still very limited. In this regard, the analysis of the basal roughness has become important for glacial geomorphological research and is an increasingly accepted attribute to describe subglacial conditions and to derive a controlling factor for the dynamics of ice-sheets (Smith et al., 2013). Basal roughness parameters can thus help us to discriminate whether the ice is underlain by softer sediments or harder rock, to reveal traces of former ice dynamics, to constrain the thermal regime and identify potential processes of subglacial erosion and deposition of sediments (Bingham and Siegert, 2009). They are key parameters for the ice-bed coupling (Hughes et al., 2011), to model basal sliding (Wilkens et al., 2015) as well as a parameter for subglacial hydrology studies Meyer et al. (2018). At present, the roughness of the bed topography is typically analyzed by spectral analysis of vertical and horizontal topography variations, based on the approaches of Shepard et al. (2001); Taylor et al. (2004) and Li et al. (2010). In many studies, basal roughness shows a clear correlation to basal drag and ice sheet velocity (Smith et al., 2013). In radio-echo sounding measurements, the roughness of the subglacial topography on different scales also influences the scattering of reflected radar waves (Jordan et al., 2017) and thus, the

reflectivity of the bed (Jacobel et al., 2010). Furthermore, the intensity and reflection pattern of the bed return informs us about the reflection properties of the base, thus complementing inferences made by the roughness parameter. Jordan et al. (2017), for example, analyze the radar scattering in combination with the topographically derived roughness to evaluate the relationship between basal roughness and the basal thermal state. The study concludes that frozen regions are relatively smooth and many thawed regions are relatively rough.

The majority of subglacial roughness studies in Antarctica focus on outlet glaciers (Bingham and Siegert, 2007, 2009; Diez et al., 2018; MacGregor et al., 2013; Rippin et al., 2006, 2011, 2014; Taylor et al., 2004) with only a few studies extending over large areas (e.g. Eisen et al. (2020) in East Antarctica). In a study to model the surface flow field of Pine Island Glacier, Wilkens et al. (2015) related basal sliding to a bed roughness parameter and were able to reproduce some essential flow features, like the location of the fast-flowing central stream and various tributaries. One of the first studies of basal roughness in Greenland was conducted by Layberry and Bamber (2001) using the residual bed elevation deviation to quantify basal roughness. An estimate of the basal roughness distribution based on a spectral approach for those part of GrIS covered by radio-echo sounding data was given by Rippin (2013). A recent study by Cooper et al. (2019) indicates different relationships between ice flow and basal roughness parameters. They conclude that in certain regions of slow ice flow, coinciding with low vertical roughness (i.e. smooth topography), a mechanism other than basal sliding must control ice flow. The relation between basal traction and sliding is still under debate and varies for different glaciological settings. For example, the study of Stearns and van der Veen (2018), observed that bed friction, which should control basal sliding, does not control the rapid flow of a large number of glaciers in Greenland. (For a full account of the discussion also see the subsequent replies to the study (Minchew et al., 2019; Stearns and van der Veen, 2019).) Furthermore, the inverse correlation between basal roughness and ice-sheet flow velocity (slow-flowing areas are mostly smooth, while increased ice flow shows rougher beds) encouraged the authors of more recent studies to rethink the influence of basal roughness to basal traction (Rippin, 2013). Possible mechanisms that control basal traction could be the thermal state at the base, subglacial hydrology and the rates of erosion and deformation of sediments.

In this paper, we use airborne radar data from AWI's ultra-wideband radar system to analyze the basal conditions of the onset of the NEGIS. We perform a spectral roughness analysis to characterize the pattern of the bed return signals and investigate the subglacial roughness parallel and perpendicular to ice flow. For

the basal roughness analysis on finer spatial scales, we analyze the scattering pattern of the bed return echoes. Based on an improved bed elevation model, we investigate subglacial water pathways. We then combine these data with an analysis of ice mass flux at the ice stream. This should ultimately give a consistent picture of the processes at the base, which control ice flow dynamics. Finally, we use our larger-scale data set to discuss the extended hypothesis of Christianson et al. (2014) of the initiation and development of the NEGIS as well as the positioning of the shear margins in its onset region.

Our results reveal a regional change in basal roughness and the pattern and intensity of the basal return echo from the upstream towards the downstream part in our study area on the NEGIS (Figure F.2). Furthermore, we detect a bed roughness anisotropy concerning the ice flow direction, indicating streamlining parallel to ice flow. The analysis of water flow paths on the basis of a better resolved bed topography confirms the hypothesis that the subglacial hydrology and the position of the shear margins are tightly coupled.

Data and methods

Survey area and data acquisition

We use airborne radar data of the EGRIP-NOR-2018 survey in the onset area of the NEGIS (Figure F.1). The data were collected with the AWI multi-channel ultra-wideband (UWB) airborne radar sounder (for details see Hale et al. (2016); Arnold et al. (2019); Franke et al. (2020b)) and recorded at a centre frequency of 195 MHz and a bandwidth of 30 MHz. The transmit signals are chirp waveforms transmitted at three stages with different pulse durations and gains to obtain high signal-to-noise ratio (SNR) in all parts of the radargrams. Radar data processing comprises pulse compression, along-track SAR processing (fk-migration) and cross-track array processing. A complete methodological description of the radar data processing and uncertainty estimation is described in Franke et al. (2020b). In the study area, the NEGIS accelerates from ~ 10 to 80 m/a over a distance of roughly 300 km and widens from ~ 20 km in the upstream boundary of our survey area to ~ 65 km further downstream (Figure F.1). More than 8000 km of survey profiles are distributed over an area of more than 250 km along ice flow direction and 50 to 100 km across, covering the interior of the ice stream, the shear margins and the slow-flowing area in the vicinity of the NEGIS (Figure F.1). The profile spacing of across-flow profiles is 5 km in the central part of the survey area, near the drill site of the East Greenland Ice-core Project (EGRIP; <http://eastgrip.org>), and 10 km further upstream and downstream. Along-flow profiles are mostly aligned along calculated pathways of ice

flow based on the velocity field of Joughin et al. (2017). For the rest of this paper, we will refer to upstream and downstream as the regions upstream and downstream of the EGRIP drill site, respectively.

Basal roughness calculation

We define basal roughness as the relative vertical and horizontal variation of the topography of the ice-bed interface. In our analysis we calculate two parameters (ζ and η), which are commonly used to characterize basal roughness (Li et al., 2010; Gudlaugsson et al., 2013; Rippin et al., 2014; Cooper et al., 2019):

- ζ reflects the vertical irregularity of the bed and provides information about the dominating vertical amplitudes. This roughness parameter is defined as the integral of the wavenumber spectrum over the range of a moving window (MW). Values close to 0 reflect the dominance of smaller amplitudes and a smoother topography.
- Li et al. (2010) introduced the frequency roughness parameter η which is calculated by dividing the vertical roughness ζ by the roughness of the bed slope ζ_{sl} . This parameter reflects the horizontal variation pointing out the dominance of a particular wavelength. High values represent the dominance of longer wavelength and smaller values the dominance of shorter wavelength.

We use the bed picks of the EGRIP-NOR-18 data set (Franke et al., 2019, 2020b) for basal roughness calculation. The roughness analysis in this paper is based on the approaches of Hubbard et al. (2000) and Taylor et al. (2004) and uses a Fast Fourier Transform (FFT) to analyze the wavenumber spectra of variations in topography (Gudlaugsson et al., 2013). This requires a uniform sampling interval of data points on the bed elevation profiles. Synthetic Aperture Radar processing of our radar data already includes the creation of a new coordinate system with a constant spatial sampling interval for the focused radar data. The average spacing between data points is 14.78 m. For each data point on a linearly detrended profile, we calculate the wavenumber spectrum over a MW of 2^N data points. We test two different MW for our analysis: (i) ~ 400 meters, which corresponds to 32 data points ($N=5$) and (ii) ~ 2000 m, which corresponds to 128 data points ($N=7$). For the 32-data point MW, one data point covers the roughness at a resolution which is finer than the cell size of 500 m used for the bed elevation data sets of Morlighem et al. (2017) for Greenland and the NEGIS onset region by Franke et al. (2020b). To make sure that this small MW does not suppress long-wave structures, we compared the result of the 500 m MW with the results obtained for

the ~ 2000 m MW. The comparison shows that significant changes are represented in both MWs. Because we focus on regions where clusters of high or low roughness values or trends appear, we use the larger ($N=7$) MW for further analysis. For this manuscript, we will refer to this kind of basal roughness as *large-scale* roughness.

Because the interpretation of roughness parameters is highly directionally dependent and the dominating factor influencing bed formations is the direction of ice flow as shown by Falcini et al. (2018); Gudlaugsson et al. (2013) and Rippin et al. (2014), we separately analyze along- and across-flow profiles. We present roughness values on a logarithmic scale to emphasize the range of up to four orders of magnitude.

Ice mass flux

In order to calculate the ice mass flux in the survey area we employed 20 flux gates orientated perpendicular to the ice flow direction. These are limited by 19 additional flux gates along each shear margin forming 19 closed boxes. Following Neckel et al. (2012) the ice flux through each gate is calculated by

$$F = \sum_{i=2}^{i=N-1} v_i (\phi'_i) H_i d_i \quad (\text{F.1})$$

with N being the number of pixels in the flux gate and ϕ'_i the normal angle to the flux gate at position i . The ice flow velocity, ice thickness and pixel spacing are indicated by v_i , H_i and d_i respectively. In order to translate volume flux into mass flux we employed an ice density of 910 kg m^{-3} .

We consider the full ice column for the analysis of the flux gate balance and calculate the ice fluxes as if there is no basal drag (plug flow). As input data we use the ice surface velocity data from Joughin et al. (2017) and the ice thickness data from Franke et al. (2020b). Because we make only a large-scale interpretation of the mass flux in our survey region, we neglect surface and basal mass balance.

Basal return power

We use the intensity of the return echoes from the basal interface as an additional parameter to analyze the basal conditions at the onset region of the NEGS. We follow the approach of Jordan et al. (2016) and Jordan et al. (2017), which is based on the method developed by Oswald and Gogineni (2008) and Oswald and Gogineni (2012). The return power is calculated from an along-track average of the basal return echo and is defined as the integral over a window of samples that represent the reflected energy from the bed (equation

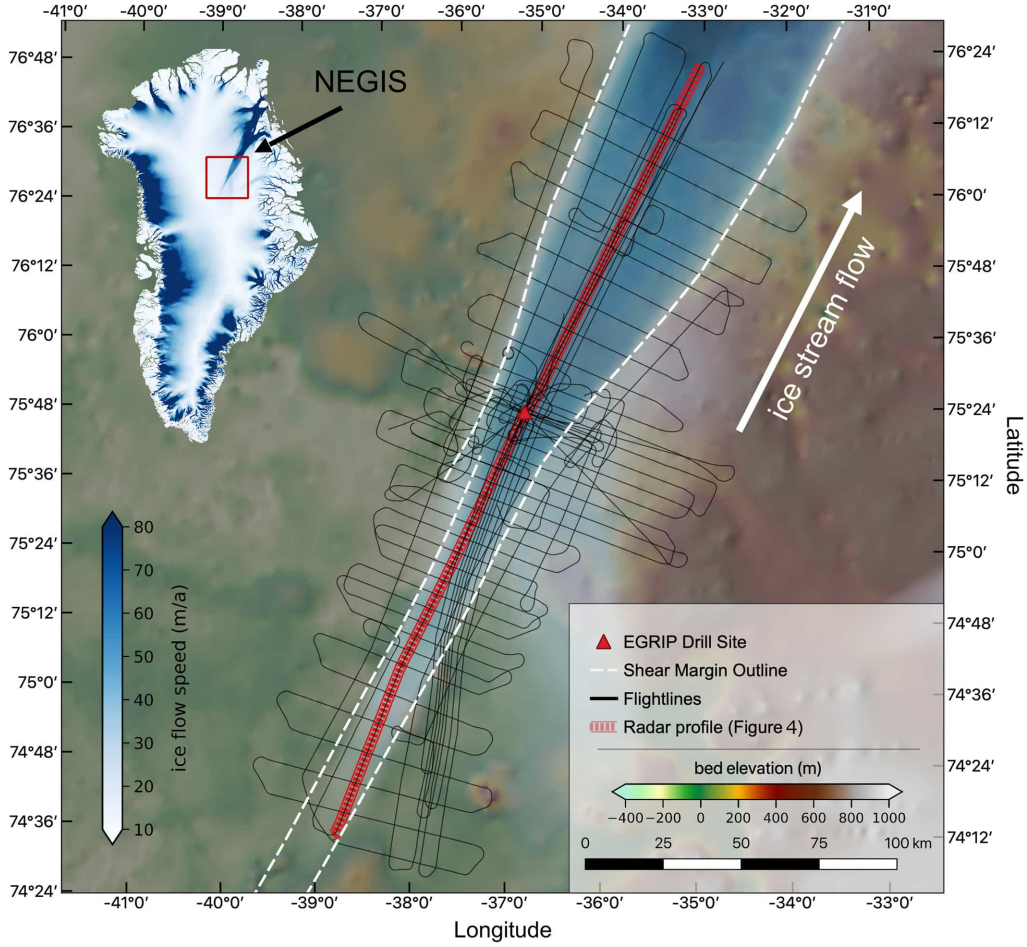


Figure F.1: Overview of the survey area in the interior of the Greenland Ice Sheet at the onset of fast flow of the NEGIS. The black lines, which are centred at the EGRIP drill site, represent the survey profiles of the EGRIP-NOR-2018 airborne UWB radar survey (Franke et al., 2020b). The white dashed lines show the outline of the shear margins (determined from satellite imagery) and the dashed red line the radar profile shown in Figure F.4. Bed elevation is referenced to mean sea level (EIGEN-6C4 geoid (Förste et al., 2007), this reference applies to all other maps showing the bed elevation) and ice flow velocity is based on the data set of Joughin et al. (2017) and is shown in blue colour code for velocities larger than 10 m/a. The projection of this map and all following maps are shown in the coordinate system EPSG 3413 (WGS84 / NSIDC Sea Ice Polar Stereographic North).

1). Before arithmetically averaging along-track, we use the bed picks of Franke et al. (2020b) to shift the bed reflection to a single level. The arithmetical averages are phase-incoherent, but help to reduce fading effects and to smooth power fluctuations (Oswald and Gogineni, 2008). We tested different values for along-track averaging and chose a value of 50 (two times 25 adjacent traces). With this value the power fluctuations are small enough to analyze as many tracks as possible, but also not too low, so that the signal is not smoothed too much. The size of the range window is kept variable and is set for a threshold above 3.5% the noise floor for a section above the bed reflection. The upper boundary is defined where the signal starts to be above the threshold and the lower boundary where the signal drops for the first time below this threshold (for further details, see Figure 3 in Jordan et al. (2016)). We follow

Jordan et al. (2016) and define the integrated power P_{int} , referred to as the bed return power (BRP), by

$$P_{int} = \int_{L_{upper}}^{L_{lower}} P(L_i), \quad (\text{F.2})$$

with the upper and lower limit of the integration window threshold L_{upper} and L_{lower} , the return power of a sample P and the depth range index L_i . The full waveform of the basal return in the integration window represents an overlay of the specularly reflected energy from nadir and scattered energy from along- and cross-track off-nadir (Young et al., 2016). The majority of the scatter from off-nadir will arise from across-track reflections because SAR post-processing reduces the footprint of return signals in along-track (Raney, 1998). Similar to the approaches of Jordan et al. (2016) and

Jordan et al. (2018), we implement additional quality control rules. Traces where the window for the integration of depth-range bins was smaller than five range bins were abnormally thin and abrupt reflections associated with clutter and were removed. The maximum size of the integration window is set to 40 range bins to limit the amount of far off-nadir layover signals.

The radar wave bed return power is corrected for spherical spreading and therefore depends mainly on the properties of the ice-bed interface, scattering properties of the bed, anisotropy in the ice fabric and dielectric attenuation within the ice column. The largest energy loss is related to dielectric attenuation, which depends on ice temperature, chemistry and other impurities in the ice column (Corr et al., 1993; Matsuoka, 2011). If dielectric attenuation varies significantly, the distinction between basal water and dry sediment is difficult because the effect of englacial attenuation can be much more significant than the contrast in reflectivity between a wet and dry base (Matsuoka, 2011).

No ice sheet models exist so far to accurately reproduce ice flow and englacial temperature in the rather complicated region of the NEGIS ice stream with its distinct shear margins. Therefore, we apply a simple linear fit between bed power and ice thickness to obtain the average attenuation rate. Based on this fit, we correct for englacial attenuation with a constant value of 8 dB per km ice thickness. However, this correction will only remove the depth-correlated component of the bed reflection power.

The correction factor depends mainly on ice temperature, which in turn depends on the geothermal heat flux (GHF), the mean annual air temperature, surface accumulation rates and frictional heating at the glacier bed and from internal ice deformation. Estimates on GHF vary significantly and are associated with large uncertainties (Rogozhina et al., 2012). Other radar studies investigating BRP at the NEGIS find different values to correct for englacial attenuation. Christianson et al. (2014) found attenuation rates from a linear fit between bed power and ice thickness at the onset of the NEGIS of 8 dB/km. Attenuation rates at the NEGIS onset in the Greenland wide study of MacGregor et al. (2015) are larger than 12 dB/km, but show an increasing uncertainty towards the ice sheet margin. The overall resulting depth-averaged attenuation rate of the common midpoint survey of Holschuh et al. (2016) are up to 3 times higher than the attenuation rates found in the previous studies (27 dB/km).

Waveform abruptness

The intensity of the integrated bed return echo as well as the length of the integration window is sensitive to small-scale variations in basal roughness (Cooper et al.,

2019), which are not resolved in the radar measurements and depend on the size of the Fresnel zone. The diameter of the Fresnel Zone for a bandwidth of 180–210 MHz and an ice thickness range of 2–3 km is ~ 60 m. Ice-bed interface roughness and the wavelength of the radar signal determines the nature of the electromagnetic scattering. However, rough subglacial terrain can produce side reflections, which are difficult to separate from the nadir bed echo return. In this case, the footprint of the radar signal and consequently the area of the basal backscatter is larger than the Fresnel zone and determined by the beam angle of the transmitted signal. To characterize the basal scattering, we follow the approach of Oswald and Gogineni (2008) which has been adapted and extensively used in Greenland by Cooper et al. (2019); Jordan et al. (2016, 2017) and Jordan et al. (2018) analysing the waveform abruptness of the bed reflection. We follow Cooper et al. (2019) and define the abruptness parameter A by

$$A = \frac{P_{max}}{P_{agg}}, \quad (\text{F.3})$$

where P_{max} is the maximum amplitude of the basal return echo in the integration window and P_{agg} the integrated basal return power (Oswald and Gogineni, 2008). A large P_{max} in a small integration window will result in a large value of A . If the reflected energy is distributed over a larger integration window, it will decrease the maximum amplitude and result in a small value of A (for details see Figure 4 in Cooper et al. (2019)). High values indicate an abrupt return (i.e., along-track focusing was sufficient to recover energy to the nadir reflection point), whereas low values indicate a broad return (likely due to energy recovered from a range of cross-track angles, which could not be focused due to the narrow antenna array in the cross-track direction). We will refer to this scattering-derived roughness as *small-scale* roughness because it represents roughness of a different scale and type than the spectral *large-scale* roughness.

Basal water routing

We compute (potential) subglacial water pathways from the hydrological potential F . We assume that the water flow depends on the elevation potential and the water pressure r_w (Shreve, 1972). Under the assumption of equilibrium between water pressure and ice overburden pressure we can write

$$\Phi = \rho_w g b + \rho_i g H, \quad (\text{F.4})$$

where ρ_w is the density of water, g is the acceleration due to gravity, b is the height of the ice base and

H the ice thickness (Le Brocq et al., 2009; Livingstone et al., 2013). We apply a simple flux routing scheme as described by Le Brocq et al. (2006) to successively compute the number of upstream cells (cells that potentially contribute water to this cell) for each grid cell. The equilibrium assumption in equation 3 is only valid at large scales (km) and makes the potential especially sensitive to the ice surface gradient. Hence, this method cannot account for localised water flow, such as flow through channels (more details on our implementation can be found in Calov et al., 2018). We make use of bed topography and ice thickness data of the EGRIP-NOR-2018 bed elevation model from Franke et al. (2020b) as well as the BedMachine v3 topography (Morlighem et al. (2017); BMv3). We use both models as input fields to analyze the sensitivity of subglacial water routing to the bed topography. While this method allows for using basal melt rates as input to quantify transported water volumes, we chose to simply count the number of upstream cells as a measure for potential water pathways. Basal melt rates are poorly constrained for this area, in particular, because the spatial variations in geothermal heat flux are subject to considerable uncertainties (Dow et al., 2018; Jordan et al., 2018; Smith-Johnsen et al., 2019). Nevertheless, we can use the water pathways to estimate the distribution of basal water, particularly for areas where we can infer a thawed base and the generation of meltwater by other methods. Several studies have detected or modelled water at the base of the Greenland Ice Sheet, but the amount of basal water is uncertain and difficult to measure (Fahnestock, 2001; MacGregor et al., 2016; Jordan et al., 2018).

Results

Spatial distribution of spectral basal roughness

We analyzed $\sim 370,000$ data points for vertical and horizontal roughness with a spectral analysis approach and present our result as the dominating vertical amplitude (ζ) and horizontal wavelength (η) over a 2000 m MW in along-flow and across-flow profiles in Figure F.2. We observe that high ζ , in general, correlate with higher η values. Also, the correlation of ζ and η shows higher vertical roughness values for the same horizontal roughness in cross-flow profiles compared to along-flow profiles. On the linear scale, vertical roughness values vary on the order of four magnitudes and horizontal roughness in the order of 2.5. Basal roughness values show distinctly different spatial patterns, independent of flight-line orientation, in two areas: upstream and downstream of the EGRIP drill site (Figure F.2). We will refer to these two regions as R_{up} (upstream) and R_{down} (downstream), respectively, and will present their particular characteristics in the following.

Region R_{up} shows low vertical and horizontal roughness values for profiles along- and across-flow. On average, ζ and η are small for profiles along-flow in the ice stream, while we observe an increase of ζ for profiles perpendicular to flow when moving from the upstream end in the south-west towards the EGRIP drill site. Across-flow profiles show distinctly different roughness values within and outside of the ice stream. Outside of the south-eastern shear margin, η is higher than inside the ice stream. Along-flow profiles that are located outside of the ice stream show similar horizontal and vertical roughness values as along-flow profiles in the ice stream. The statistical distribution of roughness values for both, ζ and η , for across-flow profiles is much wider. However, it has to be noted that the profiles also extend further to the South-East and North-West here than further upstream.

The bed elevation in the transition area rises about 500 m in flow direction and the average ice thickness decreases 400 m compared to the region R_{up} . The transition zone between regions R_{up} and R_{down} is characterized by a dominance of lower vertical amplitudes (ζ) and shorter horizontal wavelengths (η). Both the vertical and horizontal roughness values are, on average, higher for along and across flow profiles in the downstream region R_{down} in comparison to the upstream region R_{up} . Along-flow profiles show a strong increase in ζ and η , and both remain high in value with little variability. Along profiles perpendicular to ice flow, ζ shows a trend towards increasing values downstream and at the upstream end of region R_{down} . The horizontal roughness η shows two different domains for across-flow profiles. Low values of horizontal roughness dominate in the south-eastern part of region R_{down} , which we will refer to as region R_{east} , and high values in the north-western region R_{west} (Figure F.2 d). The transition from high to low values between these two sub-regions, which we will refer to as R_{trough} (Figure F.2 c), coincides with the steep eastern flank of a central ridge as well as with a local topographic low (Franke et al., 2020b). In the region R_{trough} we observe low vertical roughness values in the centre and higher roughness values at the edges of the region. For region R_{down} , along-flow profiles located outside of the ice stream, show a similar development in both, ζ and η (Figure F.2 a and b). For the parts of across-flow profiles, which are located outside of the shear margin, we detect the same trend of increasing vertical roughness from upstream to downstream (Figure F.2 c), but not in the horizontal roughness which is highly variable on across-flow profiles outside the shear margins.

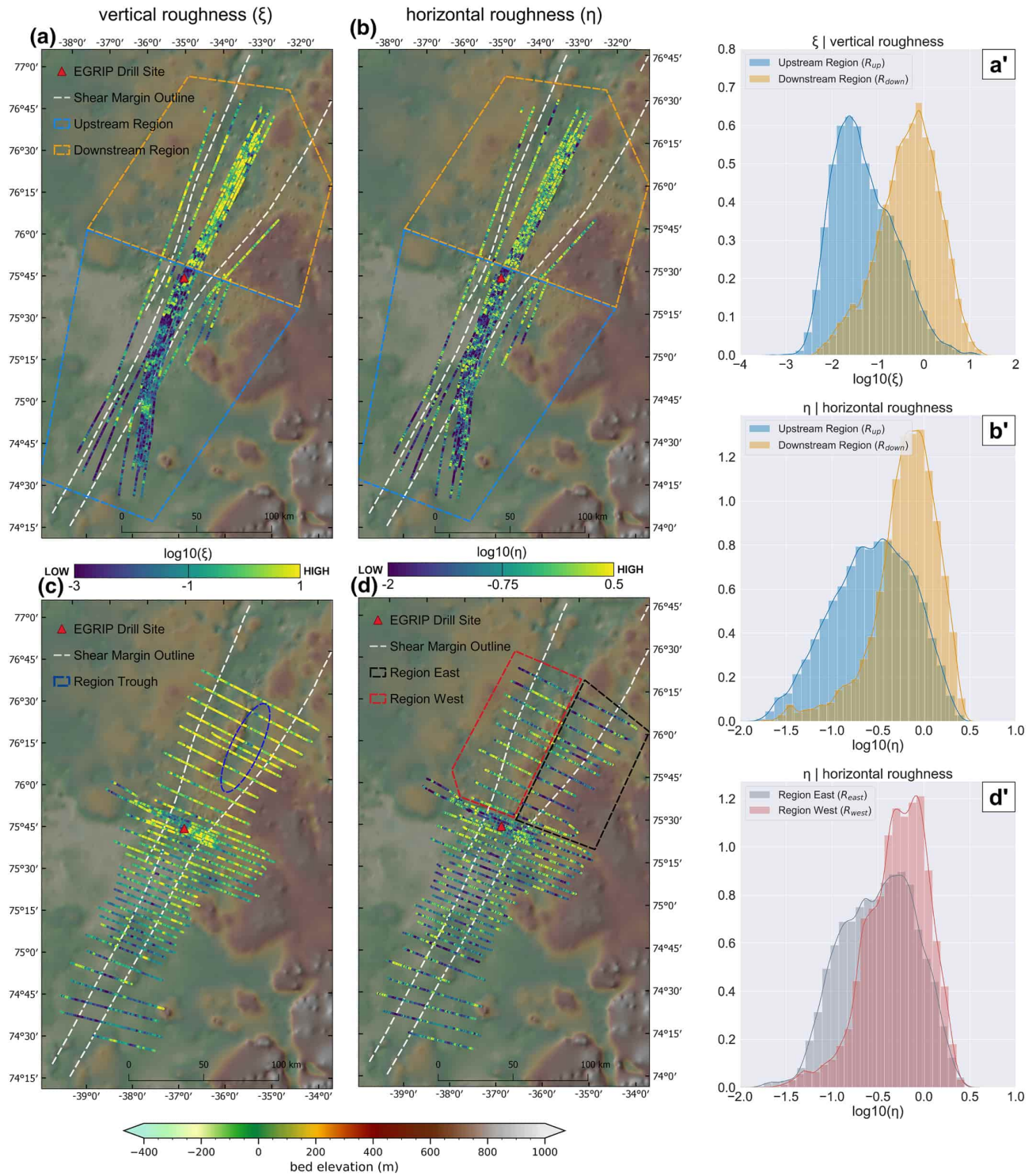


Figure F.2: Survey area at the NEGIS showing (a) along- and (c) cross-flow profiles of the vertical roughness parameter ξ and the horizontal roughness parameter η in (b) along and (d) cross-flow profiles respectively. Both parameters are shown on a logarithmic scale. The background map represents the EGRIP-NOR-2018 bed topography of Franke et al. (2020b) in meters, referenced to mean sea-level (EIGEN-6C4 geoid). Histograms a' and b' show the distribution of ξ and η for the along-flow profiles for the upstream and downstream region, respectively (orange and blue outline in a and b). The distribution of η in the western and eastern part of the downstream region (red and black outline in d) are shown in a histogram d'.

Development of ice stream flux in a kinematic-geometrical context

For an interpretation of subglacial properties and ice stream development, we consider a flux balance, a development of englacial units along ice flow and the change of width and lateral surface velocity along the ice stream.

The flux gate analysis focuses on (i) the comparison of the mass flux through a central gate (Q_{out}) to the sum of mass flux of the upstream gate and the respective shear margin gates ($Q_{up} + Q_{south} + Q_{north}$; shown schematically in Figure F.3 b/c) as well as (ii) the cumulative mass flux through the shear margins, which shows the following features:

1. Upstream of the EGRIP drill site (gates 1-8) the ice stream has a constant width and ice mass flux increases and we observe an acceleration of the ice surface speed. The initial mass flux at gate 1 is relatively small and Figure F.3 c indicates that most of the additional mass flux is provided through the southern shear margin.
2. Between gate 8 and 15 the ice stream widens. Total mass flux increases constantly, with a small step due to the shift northward of the northern shear margin. The widths of the central gates increase, and thus, provides the ice stream with additional mass flux through the shear margins.
3. After gate 15, the widening rate of the ice stream decreases but the flux gates indicate no change in the rate of mass flux.

We use two isochrones in a central radar profile as boundaries to define two englacial units. Figure F.4 a shows this radar profile, which is oriented along-flow at the location indicated in Figure F.1 and F.5 with a red line. This radar section is composed of two profiles and was concatenated at the location of the EGRIP drill site. The profile from 0 to 160 km will be referred to as the upstream section and the profile from 160 to 280 km as the downstream section. There is an offset between the two profiles of 1 km across-flow. For both sections, we tracked two internal reflection horizons, which have a respective age of ~ 30 and 52 ka, respectively, which we transferred from dating of radar reflections at the location of the NGRIP ice core (Vallelonga et al., 2014). We will refer to the thickness of these two layers as the basal unit between the 52 ka horizon and the bed reflection; and the internal unit between the 30 ka horizon and the 52 ka horizon, respectively. The upstream section shows an increase of ice surface velocity (Figure F.4 b) from 12 to 58 m/a over a distance of 150 km. Vertical and horizontal roughness (Figure F.4 c and d) are on average low but vary over two to three orders of

magnitude. Furthermore, the thickness of the internal and basal unit remains nearly constant in the upstream section (Figure F.4 e). In the downstream section, between 150 and 175 km, we observe a decrease of the internal unit thickness of ~ 125 m, whereas the basal unit thickness remains constant downstream to 240 km. The surface velocity in the downstream section shows a small decrease between 175 and 210 km and increases thereafter to ~ 80 m/a. Vertical and horizontal roughness in the downstream section is higher on average than in the upstream section. The increase in roughness correlates with a decrease in ice surface velocity and also with a decrease in the thickness of the ice column. The internal unit becomes thinner while the thickness of the basal unit remains constant.

Figure F.5 shows the downstream section and the spatial distribution of ice surface velocity, flow lines indicating the flow path (Figure F.5 a) of a point on the ice surface, as well as vertical and horizontal roughness (Figure F.5 b and c respectively). Surface flow velocity is about 5-8 m/a higher in the eastern part of the section than in the western part. The area of increased ice surface velocity correlates with the location of the basal topographic depression (R_{trough}) and is also characterized by lower vertical and horizontal roughness. Flowlines in Figure F.5 a show that ice surface flow in the eastern part of the region (yellow flow line in Figure F.5 a) deviates slightly towards south-east (orographic right) as it flows around the central ridge trough the topographic depression, whereas a flowline located north-west to the ridge bend less towards the trough (green flow line in Figure F.5 a).

Basal return power and waveform abruptness

In Figure F.6 we present the BRP of the basal reflection in (dB) for profiles aligned along-flow (a) and across-flow (b). The BRP, which is corrected for spherical spreading and englacial attenuation (constant value of 8 dB per km ice thickness), varies in a range of -25 to 25 dB. The BRP for the area around the EGRIP drill site agrees with the data of Christianson et al. (2014) and Holschuh et al. (2019). These two studies analyzed the BRP in the immediate surrounding of the EGRIP drill site, which they characterized as high return power in the centre of the ice stream, low return power in the area of the shear margins and again higher return power outside of the shear margins. In general, the BRP on along- and across-flow profiles within the ice stream is higher than outside. Highest BRP values on across-flow profiles are concentrated within a ~ 10 km corridor in the center of the ice stream, and decrease towards the shear margins. Along-flow profiles in the upstream part, which are located inside of the ice stream, show a stronger BRP than profiles located outside of the ice

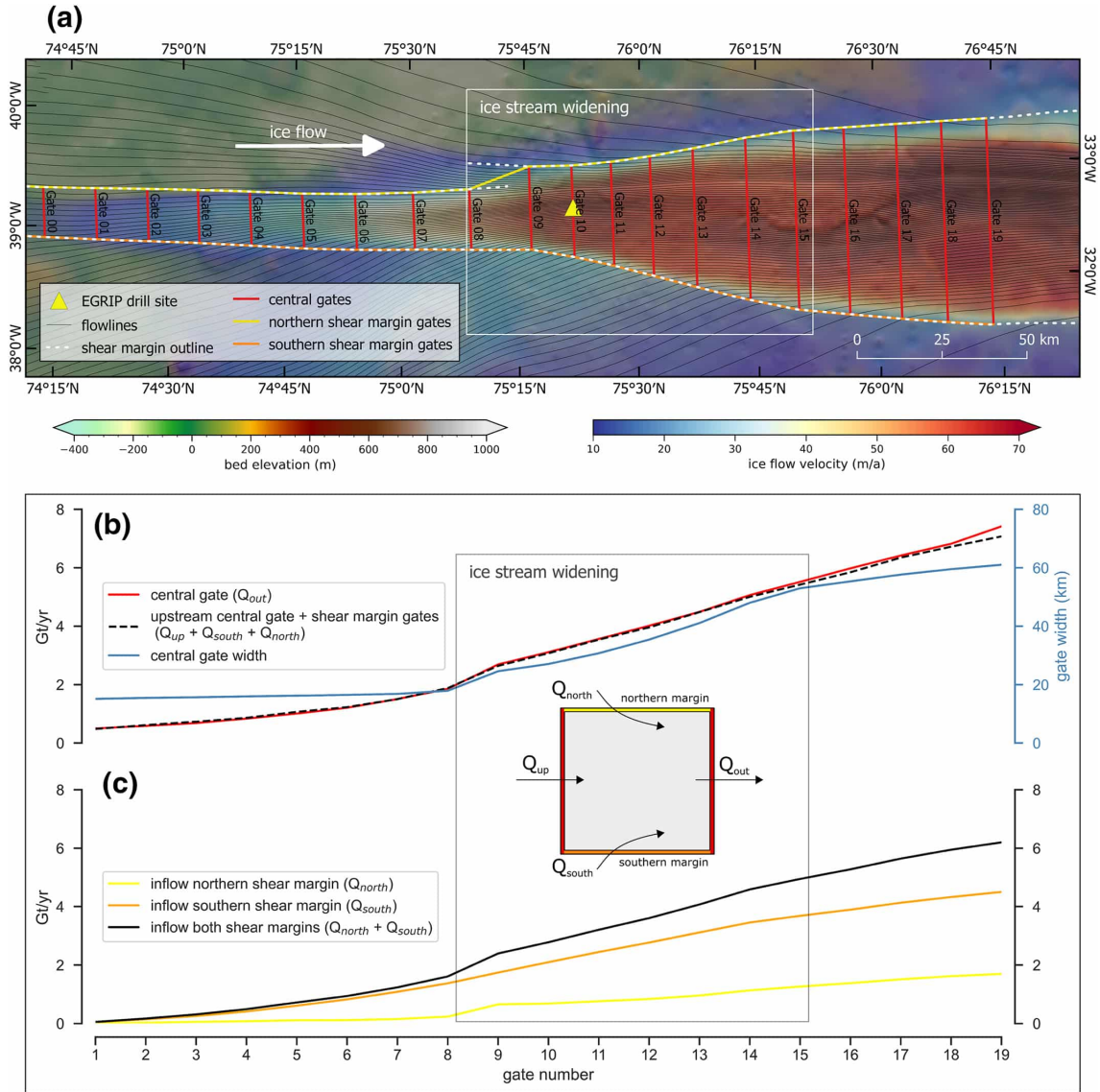


Figure F.3: Flux gate analysis of the onset of the NEGIS. Panel (a) shows the position of central flux gates (red) and flux gates at the shear margins (yellow and orange, respectively). The location where the ice stream widens is marked with a white outline. Panel (b) shows the mass flux (in Gt/yr) through the central gates (Q_{out} ; red line) in comparison to the sum of the respective upstream central gate (Q_{up}) and the corresponding shear margin gates ($Q_{south} + Q_{north}$; black dashed line). The blue line represents the width of the central gates. The cumulative mass flux through the northern and southern shear margin (as well as the sum of both) is shown in panel (c).

stream. Downstream of the EGRIP drill site, where the ice stream is widening, high return power values of across-flow profiles are not constrained to the centre of the ice stream. Further downstream, BRP in across-flow profiles is highest in the region of the topographic depression (R_{trough}), is lower on the central ridge and decreases towards the margins. The strongest drop of BRP in profiles parallel to flow profiles coincides with the location of the central ridge (ridge indicated in Figure F.5 a). However, because we use a constant correction factor for englacial attenuation, some of the variations in BRP might be introduced by this correction. It is very likely that the large heterogeneity in BRP

is a result from this simple correction scheme.

Figure F.6 c and d show the spatial distribution of the waveform abruptness for along- and across-flow profiles, respectively. Abruptness values range from 0.03 to 0.6, where smaller values are associated with a dominance of diffuse scattering (e.g. off-nadir reflections from cross-track) and higher values with more specular reflections. Along-flow profiles show significantly lower average abruptness values than profiles oriented perpendicular to ice flow in both, the upstream and downstream region. Furthermore, along-flow profiles in the upstream region show slightly higher abruptness values than the downstream region. Across-flow

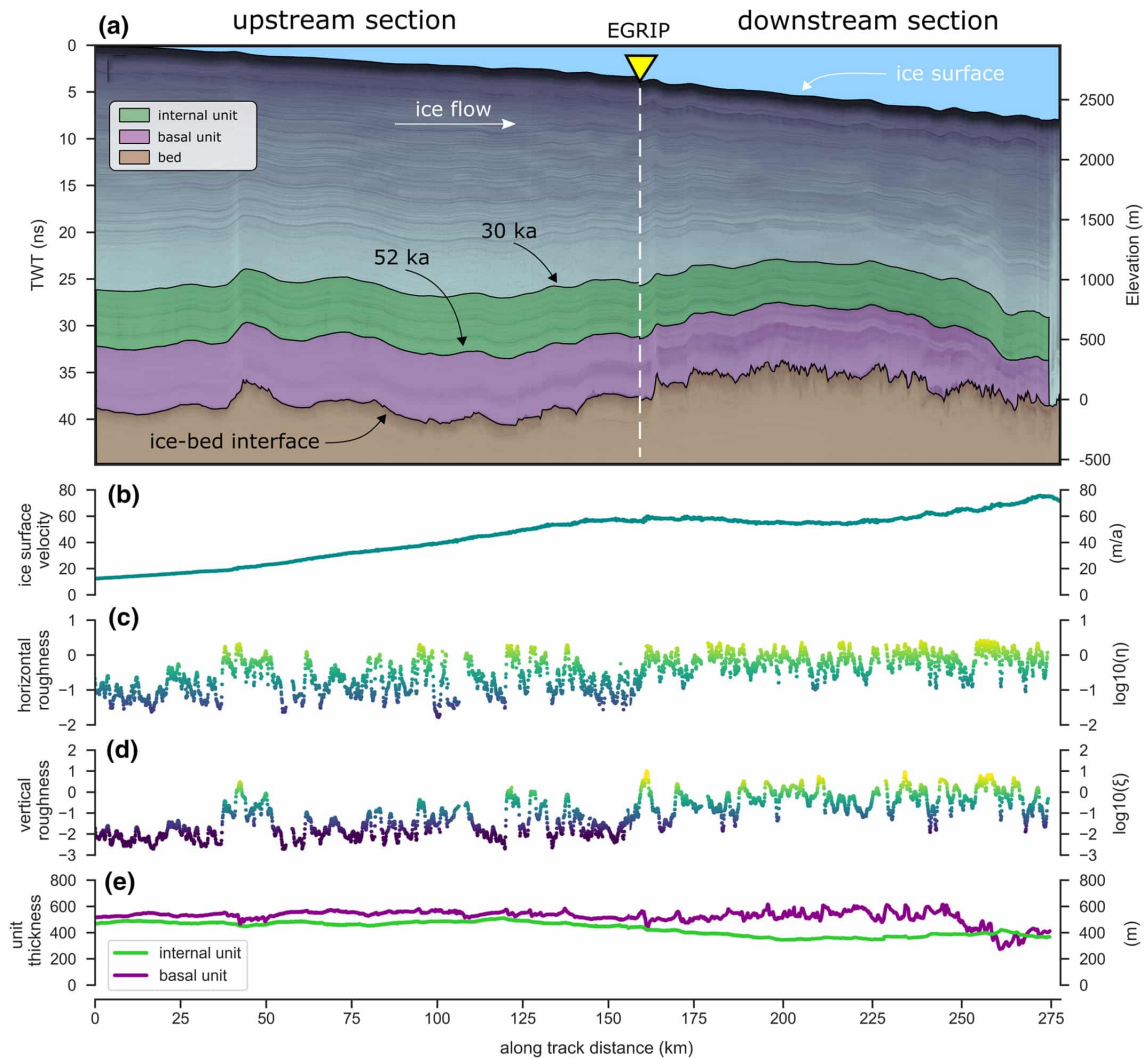


Figure F.4: Evolution of several basal and englacial properties in ice flow direction, extending from far upstream to the downstream end of our survey area (red line in Figure F.1 and F.5). Because there is no continuous survey profile, the downstream part (right part of the dashed line) is offset ~ 1 km to the South-East (transverse to along-flow profile orientation) relative to the upstream profile (left of the dashed line). The transition between the two profiles marks the position of the EGRIP drill site (yellow triangle). Ice flow direction is from left to right. (a) along-flow radargrams with continuously tracked surface (white), two internal ice units (basal unit in purple and internal unit in green) and bed reflection (red dashed line); (b) ice surface flow velocity; (c) horizontal roughness η and (d) vertical roughness ζ , both with the same colour code and scaling as in Figure F.2; and (e) the thickness of the internal and basal unit.

profiles in Figure F.6 d show the highest values in the upstream survey area, which are concentrated in the centre of the ice stream. This patch of high abruptness values has a similar extent as the patch of high basal return power in Figure F.6 b. Lower abruptness values in the upstream area are aligned in a zone extending 2-5 km from the shear margin to the ice stream centre and outside of the shear margins. In the downstream area, high abruptness values are located in a zone of a localised topographic depression (R_{trough}) as well as in the immediate surrounding of the EGRIP drill site. Abruptness values in the downstream region, outside of these two areas are significantly lower. Values of BRP and waveform abruptness show a strong correlation in

across-flow profiles but not as clear in along-flow profiles (high abruptness values with high BRP and low abruptness values with low BRP).

Two representative radargrams for the upstream and downstream region with their corresponding bed return power and abruptness are shown in Figure F.7. Profile 6a shows high bed return power and high abruptness in the centre of the ice stream (outlined with the black dashed line) and outside of the ice stream close to the shear margin (white and grey dashed line). The along-flow profile F.7 b in the center of the stream shows on average a constant high basal return power. Its waveform abruptness is on average higher between 0-12 km along-track and decreases thereafter.

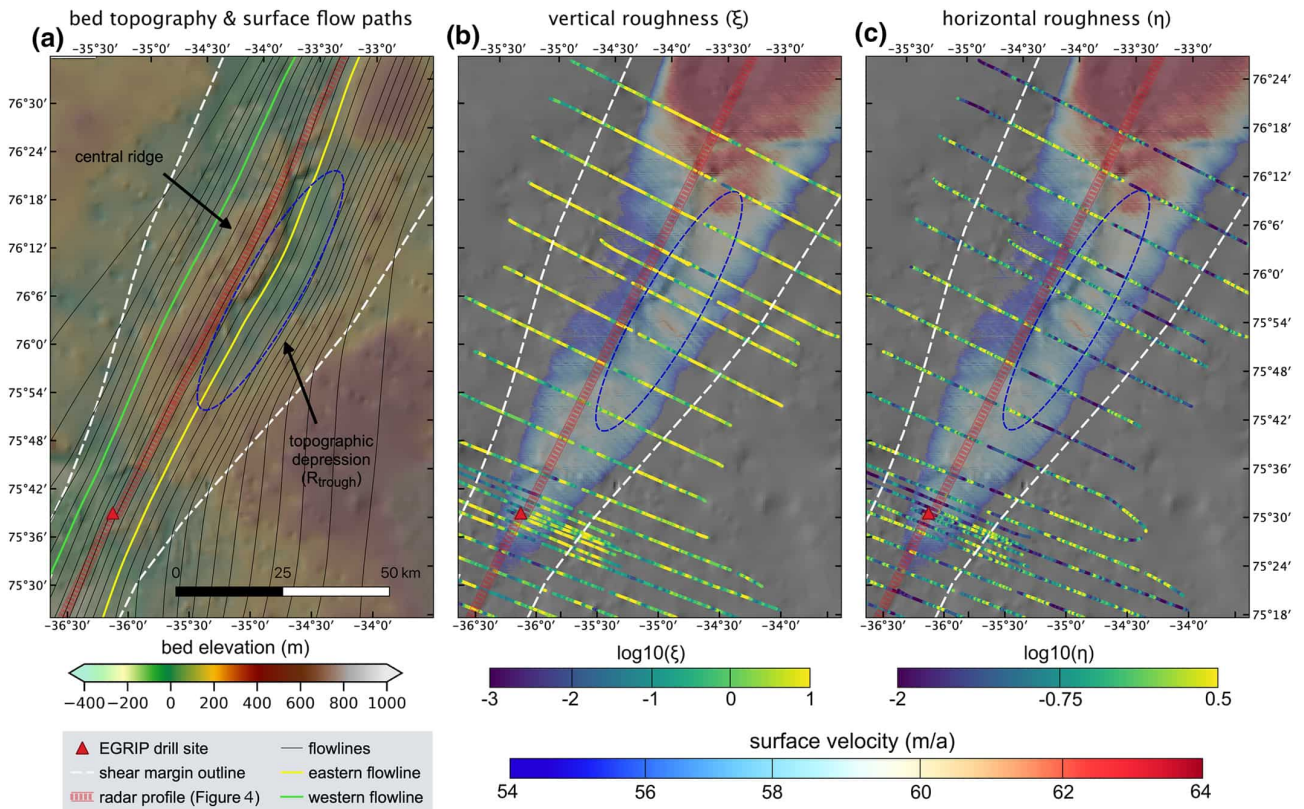


Figure F.5: Bed and flow properties in the downstream survey region, North-East of the EGRIP drill site (red triangle). Panel (a) shows the bed topography and flowlines of the ice surface (ice flow direction is towards North-East as indicated in Figure F.1). Panel (b) shows the vertical roughness parameter ξ as well as the ice surface velocity (Joughin et al., 2017) in a range of 54 to 64 m/a (velocity values lower than 54 m/a are transparent). Panel (c) shows the same velocity map together with the horizontal roughness η . Both roughness maps (b and c) show the hillshade of the bed elevation in the background. The red line on all three maps represents the location of the radar profile in Figure F.4.

This change correlates with a step in the bed elevation, which marks a general change of the topographic regime.

Basal water routing

The subglacial water flux follows the gradient of the hydraulic potential. The direction of the water pathways is in general oriented towards the direction of ice flow and decreasing ice thickness (Figure F.8). We compared subglacial water routing derived by the EGRIP-NOR-2018 bed elevation model and the BMv3 bed elevation model (blue and red lines in Figure 7 respectively). The general pattern is the same: In the upstream region, pathways that drain the largest area lead into the ice stream and flow around bed obstacles. About 20 km upstream of the EGRIP drill site, the main water pathways lead through the shear margins into the ice stream towards the point of lowest bed elevation. The pathway with the highest number of upstream routing cells is entering the ice stream from the South-East. About 10 km upstream of the EGRIP drill site the routing inside of the ice stream follows the south-eastern shear margin

and propagates downstream. Pathways entering the ice stream at the north-western shear margin propagate along the shear margin downstream. At the location of the drill site, the ice stream widens from ~ 25 km to ~ 60 km at the downstream end of our survey area and two dominant pathways develop in the ice stream: One on the south-eastern side of the ice stream with a higher number of upstream cells, and a second on the western side of the NEGIS. About 40 km downstream of EGRIP, the south-eastern path changes its location from the eastern shear margin to the local trough (our subregion R_{trough}), continuing in ice-flow direction and then switching its location back to the shear margin after another 40 km. The north-western pathway stays more or less in the area of the shear margin. Summarizing, the water routing in the downstream area seems to predominantly follow the location of the shear margins and local troughs in the bed topography in the ice stream.

We identify three locations where the routing pathways deviate significantly for the two topographies (features 1-3 in Figure F.8). At all three features, the

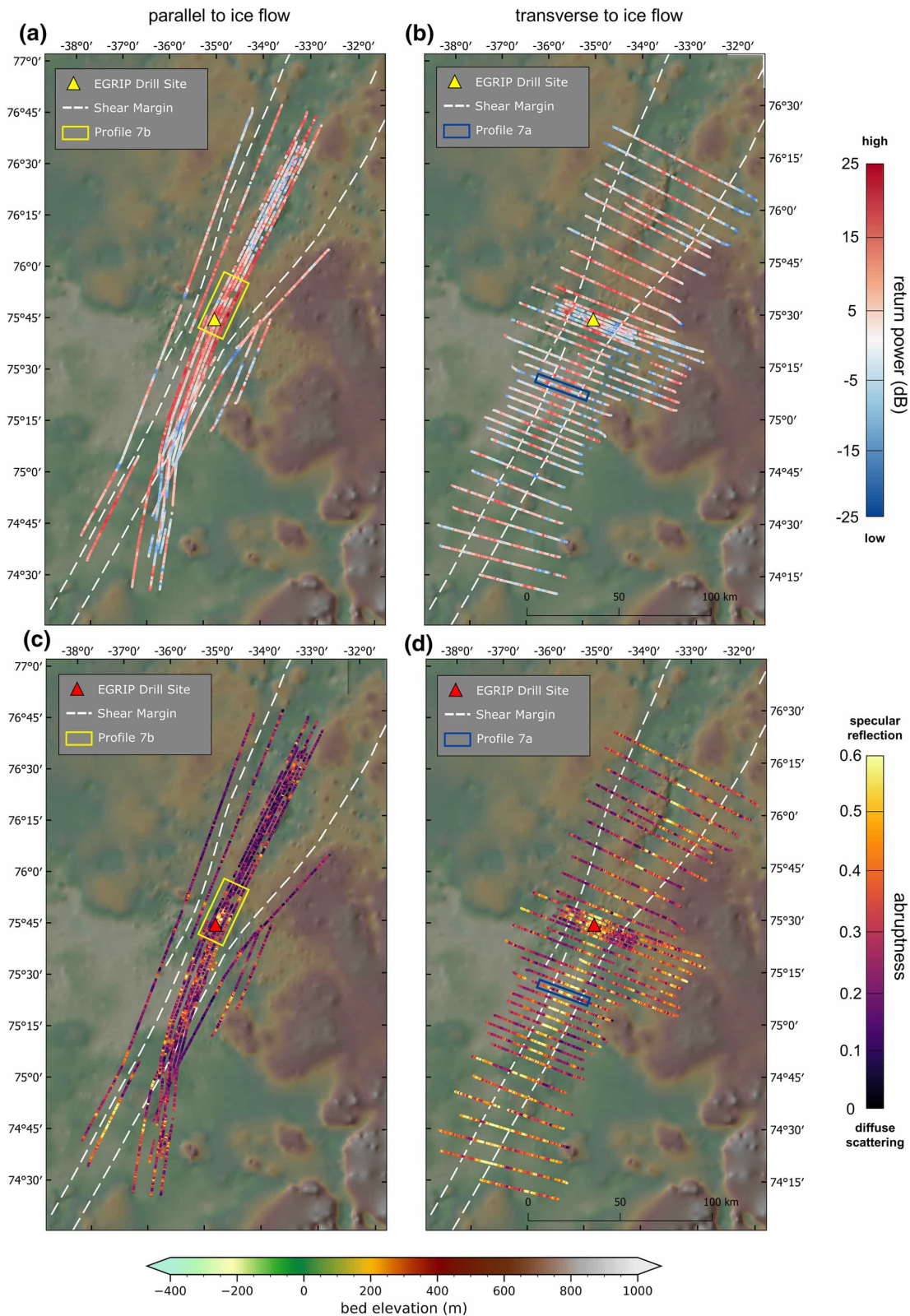


Figure F.6: Bed echo characteristics for: (a and b) basal return power and (c and d) waveform abruptness for profiles oriented along-flow (a and c) and across-flow (b and d), respectively. Basal return power is corrected for spherical spreading as well as englacial attenuation losses (8 dB/km ice thickness) and displayed in decibel (dB with respect to unity). Waveform abruptness is expressed as the ratio between the maximum BRP and the integrated bed return power and is thus unitless. High values (yellow) represent the dominance of specular reflection and low values (dark purple) the dominance of diffuse scattering of the base. The yellow and blue rectangular outlines indicate the position of the radargrams in Figure F.7. The interpretation of bed permittivity from the BRP data presented here is limited due to the simple correction scheme for englacial attenuation applied here. A large part of the spatial heterogeneity in BRP probably results due to an inaccurate englacial attenuation correction, which cannot be overcome due to an uncertainty in englacial temperature distribution.

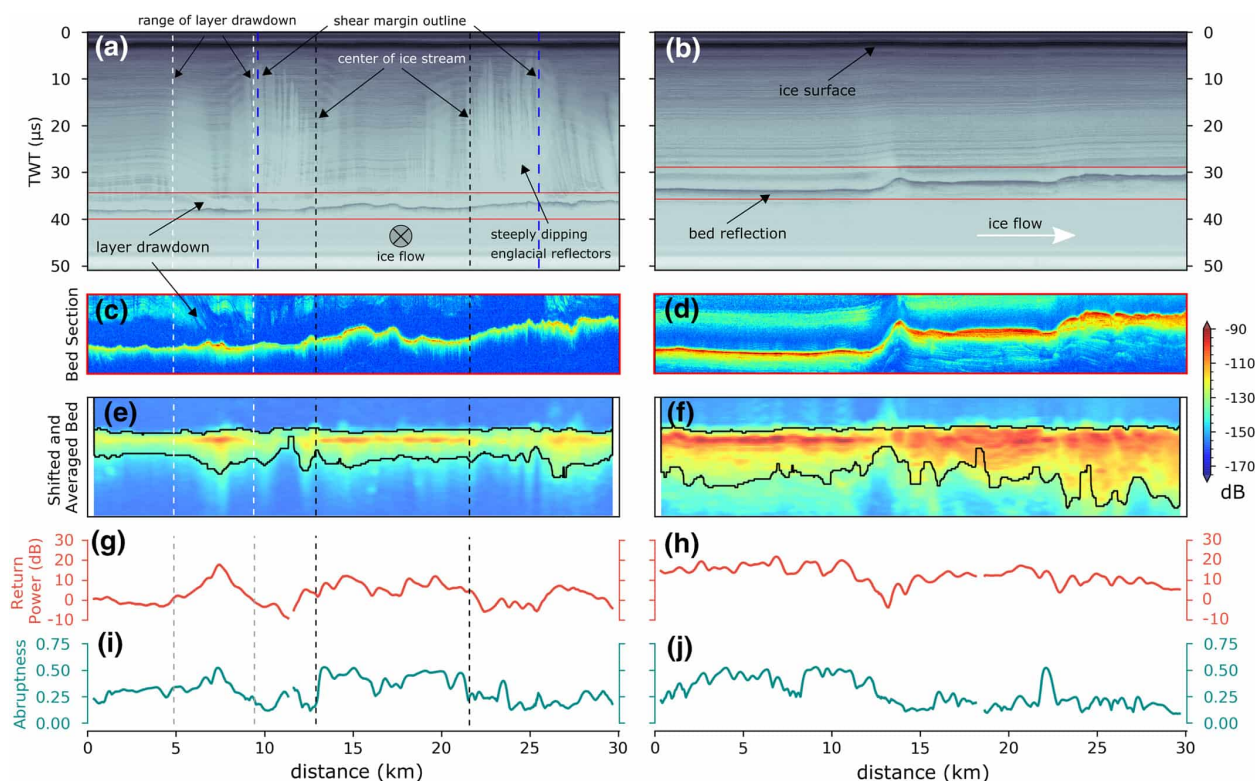


Figure F.7: Radar cross-sections with BRP and waveform abruptness. Two radar sections (two-way travel time (TWT) on the y-axis) and basal return echo properties from (a) an across-flow profile (location is indicated in Figure F.6 b and d with the blue outline) and (b) an along-flow profile (location is indicated in Figure F.6 a and c with the yellow outline). Panels (c) and (d) represent the analysis window of the ice-bed interface of the corresponding radargrams (indicated with the red lines in the radargrams) and their amplitude in dB. Panels (e) and (f) show the elevation-levelled basal reflectors and the corresponding BRP after along-track averaging. The black outline represents the window of integration for basal return power. The radargrams in panels a–f are neither corrected for spherical spreading nor englacial attenuation. Panels (g) and (h) show BRP corrected for spherical spreading as well as englacial attenuation (8 dB per km ice thickness) and (i and j) the waveform abruptness. The blue dashed lines in (a) show the position of the shear margins, the white dashed lines the region of layer drawdown outside of the shear margins and the black dashed lines the central part of the ice stream.

blue EGRIP-NOR-2018 water routing follows preferably the location of the shear margin outline, whereas the BMv3 routing deviates and flows towards the centre of the ice stream.

Discussion

The analysis and interpretation of the conditions of the ice base inferred by airborne radar sounding data are subject to several uncertainties resulting from radar data processing, the energy loss in the ice column as well as the interpretation of basal roughness parameters. We address these uncertainties in detail in the appendix. The uncertainties from each method affects the robustness of our interpretations with different significance. For example, the potential uncertainty of BRP due to the unknown variations in englacial temperature in our survey region has a much larger effect on the interpretation than the uncertainty of BRP caused by the roughness of the bed.

Interpretation of large-scale basal conditions

The observation of higher *large-scale* vertical roughness values in the faster-flowing area of our study region does not conform with the results of other subglacial roughness studies in West Antarctica (Bingham and Siegert, 2009; Diez et al., 2018; Rippin et al., 2014; Siegert et al., 2005, 2016). These studies conclude that fast ice flow is mostly topographically controlled and associated with a smooth bed, while slow-flowing areas are characterized by a rougher bed and the absence of a trough. Rippin et al. (2011) suggest that a smooth bed hints to a decrease of basal drag, favouring high ice-flow velocities. In contrast to our study, those study areas were concentrated mostly on the terminating part of glaciers. Therefore, we cannot directly relate to the interpretations from studies investigating outlet glaciers and ice streams. However, Holschuh et al. (2020) investigated Thwaites glacier several hundred kilometres of the grounding line and find the area of lowest basal drag in the region of extremely rough bed topography.

The generally higher values of vertical roughness in across-flow profiles in comparison to along-flow profiles of ζ and η (Figure F.9 a and b) is an indication that the bed has been modified by ice flow. In the upstream region R_{up} , we find a trend towards higher vertical roughness in across-flow profiles inside and outside of the ice stream. A higher ζ in across-flow profiles could be an indication for streamlining of the bed in ice flow direction. The formation of elongated subglacial landforms with increasing ice flow velocities cannot be interpreted by our large-scale roughness values alone but is supported by the observations of Franke et al. (2020b), who interpret off-nadir side reflections as an indication for the presence of elongated subglacial landforms oriented parallel to ice flow.

Further downstream the ice stream slows down on its northern side due to a step in the bed topography and a general change of the terrain, which might be due to a change in bedrock type, and thus a higher mean vertical roughness, which is probably not related to ice flow. The analysis of flux gates shows that the additional incoming ice mass through the shear margins is evacuated by two different mechanisms. In the upstream regime we observe that flowlines converge (Figure F.3), which is compensated by along-flow stretching due to ice stream acceleration. Downstream of flux gate 8, ice flow acceleration decreases, the ice stream widens and flowlines do neither converge or diverge. Hence, the widening of the ice stream has two interdependent effects: (i) excess ice mass can be evacuated without ice stream acceleration but also (ii) more ice is added to the system on a shorter distance due to the widening. Disregarding the initial cause for ice stream widening we observe a strong interdependence between the roughness of the bed, ice surface flow velocity and the geometry of the ice stream.

In contrast to the large-scale roughness, the small-scale roughness is defined by the reflection pattern and energy distribution of the bed echo. The resolution of a single point can range from ~ 60 m, which is the footprint of the Fresnel zone, to several 100s of meters if off-nadir side reflections interfere with the nadir return signal. For the analysis of the small-scale roughness, it is assumed that the energy reflected from a diffuse reflector in a large integration window should be proportional to the reflected energy of a specular target in a small window. The waveform abruptness is a measure for bed roughness in the across-track dimension of a radar profile. Low abruptness values indicate a rather diffuse reflection and high values a rather specular reflection transverse to the flight trajectory. If an intersection of two profiles shows a high value of A in an across-flow profile and a low A on an along-flow profile, we can infer a geomorphologic anisotropy, that indicates streamlining in ice flow direction (Figure F.9 c). This anisotropy is significant in the centre of the ice

stream in the upstream region (Figure F.6 c and d) and supports the hypothesis of a streamlined bed.

Unlike the pattern in the waveform abruptness, we find no significant directional anisotropy in basal return power (Figure F.9 d). The basal return power can be influenced either by the scattering characteristics of the base, englacial energy loss due to folded internal layers or scattering, the thermal state of the ice as well as the availability and amount of liquid water at the base or a combination of these factors.

Englacial attenuation should be higher in the ice stream than in the surrounding ice (Matsuoka et al., 2012) and probably highest at the shear margin due to an increase in ice temperature by internal shear. It is likely that elevated temperatures in the margins do affect the BRP (see Holschuh et al. 2019). However, we have no evidence in our data to state if the increase in temperature is substantial to indicate temperate ice or the production of basal melt water. The existence of temperate ice in some regions would agree with a subglacial hydrology modelling study by Riverman et al. (2019). They suggested that subglacial bedforms in the shear margins are created by melt out of sediment within the ice column. The phenomenon described by Keisling et al. (2014) and Holschuh et al. (2014) of weak internal reflections at steeply dipping englacial reflectors in the shear margin area, as indicated in Figure F.7 a, does most likely have no effect on the BRP.

We find several indications that the BRP is influenced by the roughness of the bed. Within the ice stream area, we find higher BRP associated with high abruptness values in across-track profiles (see Figure F.6 b and d) as well as with low vertical roughness values (see Figure F.2 c). Low BRP on the central ridge in the downstream area is associated with low abruptness and high vertical roughness values in both along- and across-flow profiles. From this relationship we can interpret that the bed roughness can explain many of the changes in BRP inside of the ice stream. This interconnection was also observed by MacGregor et al. (2013) at the eastern shear margin at Thwaites Glacier.

The high BRP and low large- and small-scale roughness values in across-flow profiles in the centre of region R_{up} could be interpreted as an indication for weak, porous, water saturated sediment, following similar interpretations of Rippin et al. (2011). As the modeled subglacial water routes suggest, it is possible that water is continuously channelled towards the ice stream and weakens the subglacial sediments, which could have a potential stabilising effect on the ice flow (Bougamont et al., 2014). Our routing paths indicate that basal water does not leave the ice stream. Consequently, the base could become increasingly lubricated, reducing basal shear stress and facilitating basal slip.

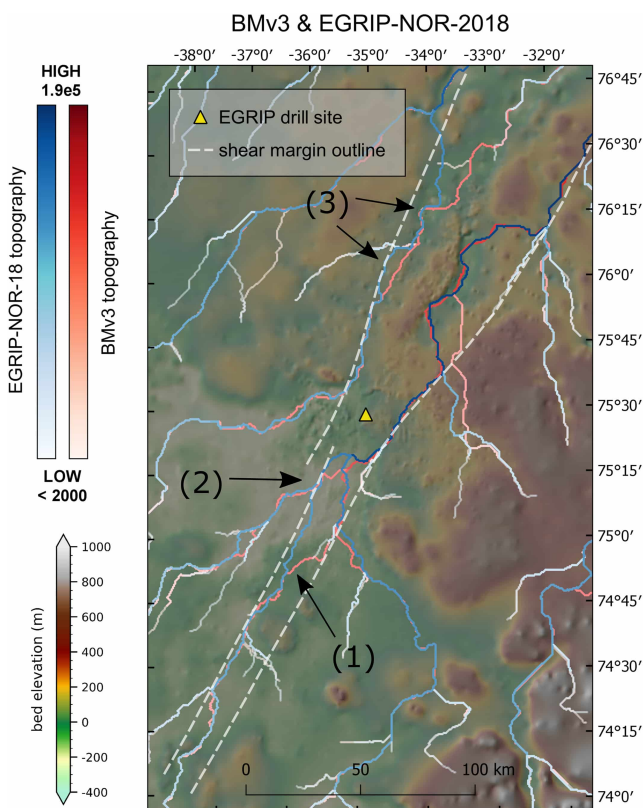


Figure F.8: Basal water routing pathways calculated based on EGRIP-NOR-2018 bed elevation (Franke et al. (2020b); in blue) as well as pathways calculated with the bed elevation model BMv3 (Morlighem et al. (2017); in red). The basal water routing colour saturation represents the number of accumulated upstream cells. Pixels containing less than 2000 upstream cells are transparent. High values and dark colours represent pathways that transport larger amounts of upstream cells. Features (1)–(3) present locations where the routing pathways from the two bed elevation models show the largest deviations. The background map represents the bed elevation of the EGRIP-NOR-18 data.

The analysis of basal water routing shows that in the downstream region the water is distributed towards the shear margins. This pattern is much more consistent in the routing scheme calculated with the new high-resolution EGRIP-NOR-2018 bed topography than with BMv3. The additional radar data and the design of the EGRIP-NOR-2018 survey provide more details in the bed topography at the shear margins and inside of the ice stream than in previous models (Franke et al., 2020b). This highlights the importance of high-resolution bed elevation models to determine the subglacial water routing accurately and supports the hypothesis that the geometry of the NEGIS is strongly connected to the subglacial hydrology system (Perol et al., 2015).

Only a few regions in our survey area would be candidates for a topographically controlled positioning of the shear margins. Routing pathways indicate that basal water is distributed to both shear margins and propagates downstream directly along or in the vicinity

of the position of the shear margins. If the position of the shear margins is particularly sensitive to the subglacial water pathways, it could facilitate the change of the location and the geometry of the NEGIS.

As the shear margins in the upstream regions of NEGIS appear not to be constrained by the bed topography or the basal substrate, their location might be fluctuating over time, allowing a more sensitive reaction to large-scale changes in the entire catchment area. Temporal variations in the surface slope of the ice sheet in Northeast Greenland, caused by changes in accumulation, distribution of surface melt or ocean forcing, can influence the subglacial water pathways (Karlsson and Dahl-Jensen, 2015). Hence, a warming climate with changes in the surface mass balance and characteristics in central Northeast Greenland may also influence the positioning of the shear margins of the NEGIS, or ice streaming in general.

Localised geomorphological and geological features

The abrupt increase of ζ and η in region R_{down} is probably associated with a change in lithology because the roughness change coincides with a general change of topographic terrain properties. Downstream of the EGRIP drill site, the bed elevation is higher and the topography much more variable than upstream. A difference in horizontal roughness of the eastern (R_{east}) and the western region (R_{west}) of the downstream area (Figure F.2 d) as well as the local variations of vertical roughness in region R_{trough} (Figure F.2 c), could be explained by a different geomorphological setting. In this area, the interpretation scheme of Li et al. (2010) would explain the roughness distribution well. R_{east} shows a topographic depression and faster ice flow, low η and ζ could indicate material which is easier to erode. The geomorphic interpretation for the western region R_{west} , showing higher η and ζ could be a mountainous setting with minor erosion and deposition of sediments and slower ice flow (Li et al., 2010). A setting similar to the downstream area of our survey region can be found in Antarctic ice streams: a central ridge oriented along-flow (Figure F.5 a), showing evidence for elongated subglacial landforms and indicating long term ice flow, and a several meters thick sediment. This has been reported for the Rutford ice stream (King et al., 2009) as well as Pine Island Glacier (Bingham et al., 2017; Brisbourne et al., 2017).

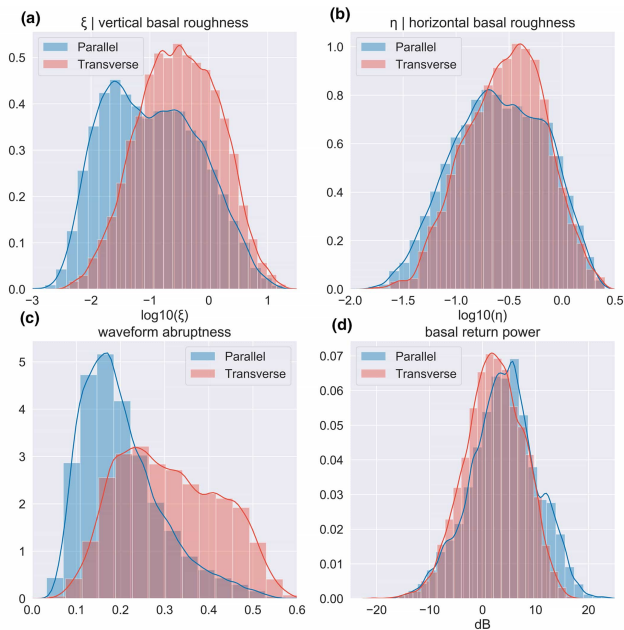


Figure F.9: Histograms presenting the distribution of (a) vertical basal roughness, (b) horizontal basal roughness, (c) waveform abruptness and (d) BRP for profiles oriented along- and across-flow for the location inside of the ice stream. The interpretation of anisotropy of BRP is limited due to the simple correction scheme for englacial attenuation. Blue bins represent along- and red bins across-flow profiles. The y-axis shows the kernel density estimation.

The increase of ξ along ice flow, the anisotropy of basal roughness, as well as the high waveform abruptness values in across-flow profiles within the ice stream in the upstream region R_{up} , indicate the development of elongated subglacial landforms inside of the ice stream. This is consistent with other observations (Christianson et al., 2014; Franke et al., 2020b). In several along-flow profiles on the central ridge in the downstream region R_{down} , we observe a side reflection pattern beneath the bed reflection, indicating side reflections of along-flow oriented structures (for details see Franke et al. (2020b)). Streamlined elongated bedforms in most cases consist of unconsolidated glacial sediments, were formed by fast streaming flow and are, thus, a record of former ice flow (Stokes and Clark, 2002). The pattern is similar to the bed striations found by Arnold et al. (2019), which are probably caused by glacier flow and suggest that elongated subglacial landforms are also present in this part of the survey area.

The appearance of elongated subglacial landforms can also occur at the shear margins of NEGIS. By analysing seismic and radar data and modelling subglacial water flow, Riverman et al. (2019) find flow parallel features composed of saturated, soft, high-porosity till. Elongated subglacial landforms like mega-scale glacial lineation can form on soft beds, but also on hardbeds, although the generation of hard bed streamlining

probably takes more time and/or higher ice flow velocities (Krabbendam et al., 2016). Because the ice surface velocities at the location where we interpret elongated subglacial landforms are comparably low, we argue that these landforms were probably generated on a soft and deformable bed. This interpretation is also in agreement with the findings of unconsolidated sediments of Christianson et al. (2014) inside and outside of the ice stream at the position where the ice stream widens. In the upstream region basal roughness patterns in along-flow profiles outside and inside the ice stream (Figure F.2 a and b) are similar, which indicates that the basal properties, and thus potentially basal substrate do not vary across the shear margins. Vallelonga et al. (2014) showed that sediments around the EGRIP drill site are present outside of the shear margin and suggested based on these findings, that the location of the shear margin could shift its location and maybe respond to a re-routing of basal water.

In the downstream region we observe a decrease in velocity of the ice stream. Higher average vertical roughness contributes to an increase basal resistance and a slope in the bed topography decreases the local driving stress in this region. Around the location of the EGRIP Camp, the ice stream is widening and the ice thickness is reducing by ~ 700 m. The thinning appears not to be uniform over the entire ice column, as the lowermost ice layer, until 200 m above bedrock, does not change its thickness (Figure F.4 a and e). Our flux analysis shows that the flux in the NEGIS ice stream is balanced by inflow through the shear margins. A vertically different response in flux indicates a change in the vertical velocity distribution. This could be interpreted as a transition in the stress regime from pure to simple shear at the base of the ice and thus less basal sliding. Indeed, a decrease in ice flow velocity can be observed at this location, which could be caused by a decrease in basal sliding. The basal unit retains its thickness for more than 100 km further along flow, which could be explained by decreased longitudinal stretching. This process would indicate an increased rate of internal deformation (Bons et al., 2018). An increase of internal shear and deformation within the ice column redistributes the shear strain from the ice-bed interface to within the ice column. Depending on the localized basal shear stress and the basal flow velocity, which we are not able to quantify in this study, the basal ice temperature can be increased and eventually produce basal melt water.

The increase in BRP at locations where we also observe a drawdown of internal layers at the outer edges of the shear margins (e.g. Figure F.7 a and c) could be explained by two different mechanisms. Either, basal melting, and thus a wet base, which produces the drawdown of layers in the first place, increases BRP. However, we observe that deep layers outside of the ice

stream appear at a higher elevation after they passed through the shear margin, which would contradict the mechanism of basal melting. It is also possible that the drawdown of internal layers moves colder ice masses downwards, which reduces the temperature of the ice close to the base and decreases englacial attenuation, potentially masking true changes in the BRP (Holschuh et al., 2019). High-resolution ice flow models and better estimates or measurements of the GHF are necessary to obtain a more reliable estimate of temperature distribution in the ice to correctly determine attenuation.

Synopsis of NEGIS characteristics

A summary of the key findings and interpretations for the basal conditions of the NEGIS in the onset region are presented in Figure F.10. Our results support the hypothesis and mechanisms proposed by Christianson et al. (2014). The predominant amount of ice mass flows into the ice stream through the shear margins. In the onset region of NEGIS, available meltwater and the presence of a soft, deformable bed provide lower resistance for sliding and facilitate accelerated ice flow. Given increasing velocities in the upstream region, the soft bed is most likely strongly deformable, leading to longitudinal geomorphological bedforms. In the upstream part, hydraulic pathways indicate that water is routed into the ice stream from neighbouring areas. Further downstream, where the ice stream widens, basal water is pushed towards and beyond the shear margin, partly because of the local topography and lithological properties but also partly because of surface slopes of the ice surface. This leads to less resistant basal properties at the margins and enables a widening of the ice stream. Inside of the ice stream in the downstream area, high vertical roughness coincides with lower ice surface velocity and smooth areas with higher ice surface velocities. Both characteristics as well as the different thinning of internal layers are strong indications that basal shear stress is on average higher where the bed is rough. This could explain the non-uniform lateral ice surface velocities (feature 3 and 4 in the downstream region of Figure F.10) and an increase in the rate of internal deformation of the basal ice unit (Figure F.4 a and e).

Conclusions

We characterized the basal properties of the onset region of NEGIS and discussed involved physical processes. The analysis of spectral basal roughness and basal return echoes shows a distinct change of basal conditions at the position where the ice stream widens. We conclude that a smooth, deformable and lubricated

base helps to initiate or at least favour ice flow acceleration at the onset of the NEGIS. The positioning of the shear margins and the pathways of subglacial water flow shows an immediate relationship between the ice stream extent and the subglacial hydrology system. Ice surface velocity, shear margin positioning and the pattern and intensity of the bed reflection are influenced by different scales of basal roughness. Regionally extending our interpretation, the involved processes could have a significant impact on the ice dynamics and ice stream catchments of Greenland in a warming climate. Changes in the surface mass balance in the upstream catchment, which is currently relatively small, could reorganize the location of the shear margins. It is possible that this could either initiate faster ice flow even further upstream, and/or take up a larger catchment area and, thus, increase the amount of ice discharge of the GrIS.

The drilling of the East Greenland Ice Core down to the bed will provide further insights into NEGIS' characteristics and dynamical processes, especially into fabric distribution, thermal structure, sediment properties and geothermal heat flux. As shown by our analyzes, useful additional information to constrain the basal conditions can be provided by spatially extensive and closely-spaced geophysical surveys. Considerable insights could be obtained by seismic soundings further upstream and downstream and borehole drillings to the base. However, these are time-consuming and expensive to acquire over a large area. To fully constrain the basal boundary conditions for ice flow models, a sufficient coverage of the middle and lower sections of NEGIS are needed.

Data availability

All relevant datasets for this research are available from the PANGAEA repository: EGRIP-NOR-2018 bed topography (Franke et al. (2019); <https://doi.pangaea.de/10.1594/PANGAEA.907918>) and radar-derived basal conditions data (Franke et al., 2020a), which contains spectral basal roughness data (<https://doi.pangaea.de/10.1594/PANGAEA.915133>), bed return power and scattering derived abruptness waveform data (<https://doi.pangaea.de/10.1594/PANGAEA.915135>) as well as basal water routing (<https://doi.pangaea.de/10.1594/PANGAEA.915134>). The BedMachine v3 bed elevation data set is available at the National Snow and Ice Data Center (NSIDC): <https://doi.org/10.5067/2CIX82HUV88Y>. The MEaSURES Greenland Ice Sheet Velocity Map from InSAR Data, Version 2 is available from <https://doi.org/10.5067/OC7B04ZM9G6Q>.

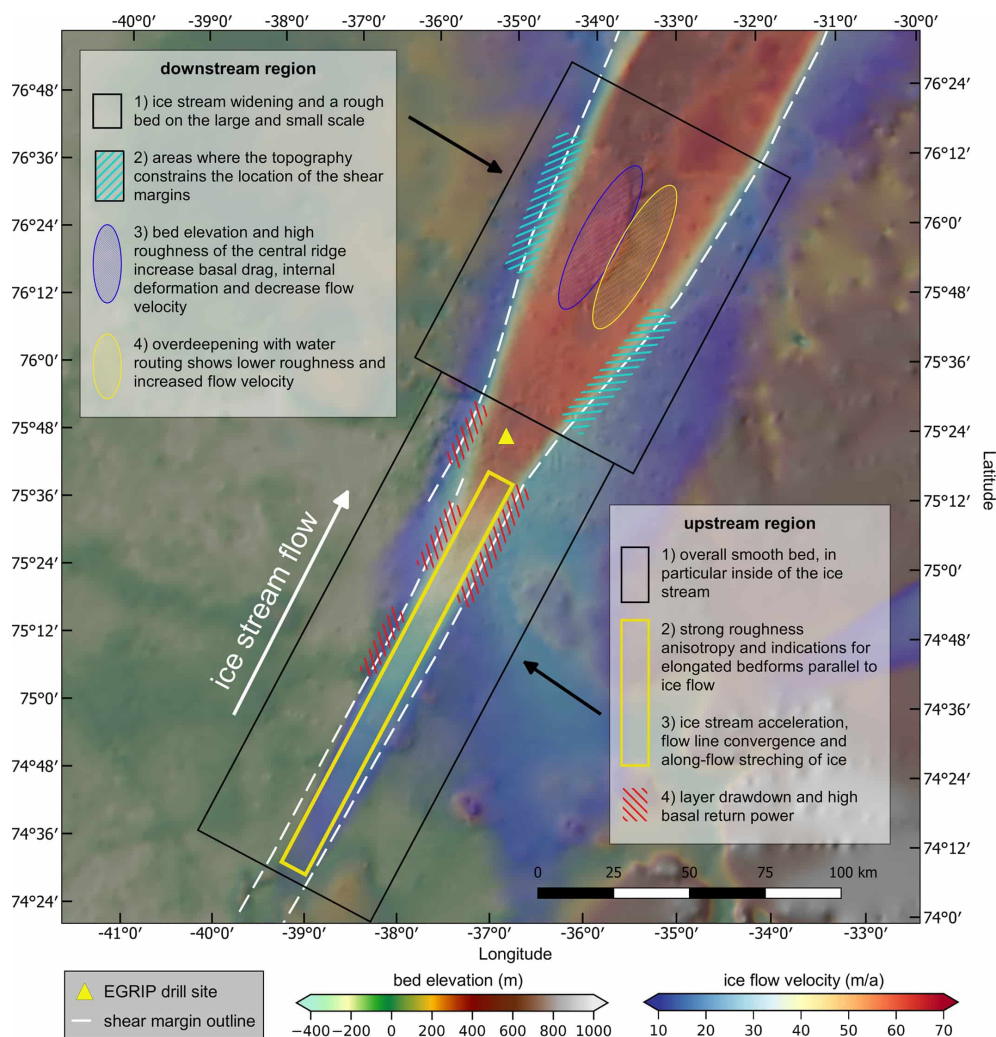


Figure F.10: Summary of the basal properties of the upstream and the downstream survey region.

Acknowledgements

We thank the Ken Borek crew and AWI's aeroplane technical staff of the research aircraft Polar 6. Logistical support in the field was provided by the East Greenland Ice-Core Project (EGRIP). EGRIP is directed and organised by the Center of Ice and Climate at the Niels Bohr Institute. It is supported by funding agencies and institutions in Denmark (A. P. Møller Foundation, University of Copenhagen), USA (US National Science Foundation, Office of Polar Programs), Germany (Alfred Wegener Institute, Helmholtz Centre for Polar and Marine Research), Japan (National Institute of Polar Research and Arctic Challenge for Sustainability), Norway (University of Bergen and Bergen Research Foundation), Switzerland (Swiss National Science Foundation), France (French Polar Institute Paul-Emile Victor, Institute for Geosciences and Environmental research) and

China (Chinese Academy of Sciences and Beijing Normal University). We acknowledge the use of the CRE-SIS toolbox from CRE-SIS generated with support from the University of Kansas, NASA Operation IceBridge grant NNX16AH54G, and NSF grants ACI-1443054, OPP-1739003, and IIS-1838230. The analysis of spectral basal roughness parameters builds on the work by Franz-Fabian Bellot and Eythor Gudlaugsson under the supervision of Angelika Humbert. We acknowledge the discussion with Thomas Kleiner, which helped to develop and improve the manuscript. Furthermore, we thank Giulia Sinnl and Enrico Pochini. They performed a first initial analysis of the spectral basal roughness during the Karthaus Summer School 2019 organised by the the Institute for Marine and Atmospheric research Utrecht (IMAU).

Author contributions

Steven Franke designed and wrote the manuscript, conducted the radar data processing, performed the main part of the data analysis and created all figures. Olaf Eisen and Daniela Jansen were PI and Co-I of the airborne radar campaign and designed the study. Sebastian Beyer computed the hydraulic potential and basal water pathways. Niklas Neckel and Steven Franke calculated ice mass flux. Tobias Binder acquired the airborne radar data together with Daniela Jansen and John Paden. Tobias Binder contributed to the radar data processing and John Paden to the analysis of bed return echoes. Daniela Jansen, Steven Franke, Niklas Neckel, Sebastian Beyer and Olaf Eisen interpreted the data. All co-authors discussed and commented on the manuscript.

Appendix

Uncertainties

Several uncertainties can influence the results and interpretation of the spectral bed roughness parameters. This accounts in particular for small values of ζ in conjunction with η . A major uncertainty arises from missing or ambiguous bed reflections and how continuous the tracking of the basal event is applied. In rough terrains, automatic trackers, e.g. of reflection power, often create zigzag or step patterns whereas manual picking is often characterized by straight lines. A combination of both methods may represent the best possible way to pick the bed geometry efficiently. Still, it will have an impact on both vertical and horizontal roughness values, in particular when ζ is small. The uncertainty decreases if larger vertical amplitudes come into play. Li et al. (2010) introduced schematic interpretations for geomorphic settings based on the combination of ζ and η , which we will refer to as cases in the following. For example, low ζ and high η (case 1) can refer to a marine setting with intensive deposition of sediments. Low ζ and low η (case 2) could imply a continental setting after intensive erosion. For minimal values of ζ , this categorisation is accompanied with a high uncertainty based on the radar data or bed topography product and the method of the ice-bed interface detection. For example, automatic or semiautomatic picking with a maximum power tracker might lead to a high-frequency zigzag pattern leading to case 2 (erosion). Manual picking at locations where a tracker is not useful can smooth the surface and would favour case 1 (deposition). Therefore, we argue that an interpretation of subglacial landscapes with low ζ are difficult to interpret in combination with η , even though the bed reflection is quality checked and picked very accurately. A robust interpretation of small ζ , regardless of high or

low η , is that the base is smooth. Without additional data like radar wave scattering properties, seismic information about the basal substrate's lithology, or an indication for the presence of water at the base, further interpretations have low confidence. Another source of uncertainty are off-nadir/side reflections that are difficult to distinguish from nadir reflections. Only coherent and phase-sensitive radar depth sounders with multiple cross-track antenna elements and appropriate 3D processing algorithms can compute the direction angle of the reflected signal (Paden et al., 2010). A better estimate of the effect of cross-track roughness is the scattering-derived waveform abruptness (Oswald and Gogineni, 2008; Jordan et al., 2017; Cooper et al., 2019). However, this method does not consider side reflections from far off-nadir angles.

Several uncertainties in the BRP result from the mostly unobserved physical bulk properties of the ice column and their lateral variation, mainly across the ice stream. We anticipate an effect of ice crystal anisotropy on the basal return signal due to a different expected preferred orientation in the crystal fabric in the ice stream, outside of the ice stream and in the area of the shear margins. However, overall we consider it as a negligible effect on the BRP Matsuoka (2011), given the magnitude of other uncertainties. The most significant uncertainty will arise from the unknown dielectric attenuation of the ice column from impurity loading and temperature, which is difficult to estimate for an ice stream. It is challenging to estimate the effect of englacial attenuation in our survey area because ice temperature has not been sufficiently constrained yet. For an ice stream, we have to consider three different lateral domains, with unknown dielectric attenuation: the fast-flowing central part of streaming ice, the slow-flowing part outside of the ice stream and the shear margins. Finally, in general, a layer of temperate ice of finite thickness might be present above the bed (Humbert et al., 2018). As we cannot constrain its presence further because of missing measurements, we do not consider it in our evaluation. An additional feature, influencing the bed return intensity can be internal layers of altered ice or containing entrainments of basal material which reduce the return energy of the bed. We find areas of large folds south-west of the EGRIP drill site outside of the ice stream. Therefore, we excluded this region because the strong internal deformation and bed entrainments appear to disturb the reflection power of the base significantly.

Further uncertainties are related to data acquisition and processing. Another source of uncertainty for the BRP can arise during SAR processing of the radar data. Focusing of scattered signals effectively shifts energy from multiple unfocused pixels into a single pixel. As a consequence, poor focusing due to position errors or directional scattering may cause the return power to

deviate from the ideal case. Furthermore, the steeply dipping reflectors due to englacial layer folding in the vicinity of the shear margins will most likely reduce the reflected energy from the ice-basal interface underneath this zone. The energy loss probably occurs due to destructive interference in trace stacking, energy dispersion through SAR processing and off-nadir ray path losses (see [Holschuh et al. 2014](#) for details).

Bibliography

- An, L., Rignot, E., Chauche, N., Holland, D. M., Holland, D., Jakobsson, M., Kane, E., Wood, M., Klauke, I., Morlighem, M., Velicogna, I., Weinrebe, W., and Willis, J. K. Bathymetry of Southeast Greenland From Oceans Melting Greenland (OMG) Data. *Geophysical Research Letters*, 46(20):11197–11205, oct 2019. doi: 10.1029/2019gl083953. URL <https://doi.org/10.1029%2F2019gl083953>.
- Arndt, J. E., Larter, R. D., Hillenbrand, C.-D., Sørli, S. H., Forwick, M., Smith, J. A., and Wacker, L. Past ice sheet–seabed interactions in the northeastern weddell sea embayment, antarctica. *The Cryosphere*, 14(6):2115–2135, 2020. doi: 10.5194/tc-14-2115-2020. URL <https://tc.copernicus.org/articles/14/2115/2020/>.
- Arnold, E., Leuschen, C., Rodriguez-Morales, F., Li, J., Paden, J., Hale, R., and Keshmiri, S. CReSIS airborne radars and platforms for ice and snow sounding. *Annals of Glaciology*, pages 1–10, nov 2019. doi: 10.1017/aog.2019.37. URL <https://doi.org/10.1017%2Faog.2019.37>.
- Aschwanden, A., Fahnestock, M. A., and Truffer, M. Complex Greenland outlet glacier flow captured. *Nature Communications*, 7(1), feb 2016. doi: 10.1038/ncomms10524. URL <https://doi.org/10.1038%2Fncmms10524>.
- Bingham, R. G. and Siegert, M. J. Radar-derived bed roughness characterization of Institute and Möller ice streams West Antarctica, and comparison with Siple Coast ice streams. *Geophysical Research Letters*, 34(21), nov 2007. doi: 10.1029/2007gl031483. URL <https://doi.org/10.1029%2F2007gl031483>.
- Bingham, R. G. and Siegert, M. J. Quantifying subglacial bed roughness in Antarctica: implications for ice-sheet dynamics and history. *Quaternary Science Reviews*, 28(3-4):223–236, feb 2009. doi: 10.1016/j.quascirev.2008.10.014. URL <https://doi.org/10.1016%2Fj.quascirev.2008.10.014>.
- Bingham, R. G., Vaughan, D. G., King, E. C., Davies, D., Cornford, S. L., Smith, A. M., Arthern, R. J., Brisbourne, A. M., Rydt, J. D., Graham, A. G. C., Spagnolo, M., Marsh, O. J., and Shean, D. E. Diverse landscapes beneath Pine Island Glacier influence ice flow. *Nature Communications*, 8(1), nov 2017. doi: 10.1038/s41467-017-01597-y. URL <https://doi.org/10.1038%2Fs41467-017-01597-y>.
- Bons, P. D., Kleiner, T., Llorens, M.-G., Prior, D. J., Sachau, T., Weikusat, I., and Jansen, D. Greenland Ice Sheet: Higher Nonlinearity of Ice Flow Significantly Reduces Estimated Basal Motion. *Geophysical Research Letters*, 45(13): 6542–6548, jul 2018. doi: 10.1029/2018gl078356. URL <https://doi.org/10.1029%2F2018gl078356>.
- Bougamont, M., Christoffersen, P., Hubbard, A. L., Fitzpatrick, A. A., Doyle, S. H., and Carter, S. P. Sensitive response of the Greenland Ice Sheet to surface melt drainage over a soft bed. *Nature Communications*, 5(1), sep 2014. doi: 10.1038/ncomms6052. URL <https://doi.org/10.1038%2Fncmms6052>.
- Brisbourne, A. M., Smith, A. M., King, E. C., Nicholls, K. W., Holland, P. R., and Makinson, K. Seabed topography beneath Larsen C Ice Shelf from seismic soundings. *The Cryosphere*, 8(1):1–13, jan 2014. doi: 10.5194/tc-8-1-2014. URL <https://doi.org/10.5194%2Ftc-8-1-2014>.
- Brisbourne, A. M., Smith, A. M., Vaughan, D. G., King, E. C., Davies, D., Bingham, R. G., Smith, E. C., Nias, I. J., and Rosier, S. H. R. Bed conditions of Pine Island Glacier West Antarctica. *Journal of Geophysical Research: Earth Surface*, 122(1):419–433, jan 2017. doi: 10.1002/2016j004033. URL <https://doi.org/10.1002%2F2016j004033>.
- Calov, R., Beyer, S., Greve, R., Beckmann, J., Willeit, M., Kleiner, T., Rückamp, M., Humbert, A., and Ganopolski, A. Simulation of the future sea level contribution of Greenland with a new glacial system model. *The Cryosphere*, 12(10):3097–3121, oct 2018. doi: 10.5194/tc-12-3097-2018. URL <https://doi.org/10.5194%2Ftc-12-3097-2018>.
- Christianson, K., Peters, L. E., Alley, R. B., Anandakrishnan, S., Jacobel, R. W., Riverman, K. L., Muto, A., and Keisling, B. A. Dilatant till facilitates ice-stream flow in north-east Greenland. *Earth and Planetary Science Letters*, 401: 57–69, sep 2014. doi: 10.1016/j.epsl.2014.05.060. URL <https://doi.org/10.1016%2Fj.epsl.2014.05.060>.
- Clark, C. D. and Meehan, R. T. Subglacial bedform geomorphology of the Irish Ice Sheet reveals major configuration changes during growth and decay. *Journal of Quaternary Science*, 16(5):483–496, 2001. doi: 10.1002/jqs.627. URL <https://doi.org/10.1002%2Fjqs.627>.
- Clarke, G. K. SUBGLACIAL PROCESSES. *Annual Review of Earth and Planetary Sciences*, 33(1):247–276, may 2005. doi: 10.1146/annurev.earth.33.092203.122621. URL <https://doi.org/10.1146%2Fannurev.earth.33.092203.122621>.
- Cochran, J. R. and Bell, R. E. Inversion of IceBridge gravity data for continental shelf bathymetry beneath the Larsen Ice Shelf Antarctica. *Journal of Glaciology*, 58(209): 540–552, 2012. doi: 10.3189/2012jog11j033. URL <https://doi.org/10.3189%2F2012jog11j033>.
- Cooper, M. A., Jordan, T. M., Schroeder, D. M., Siegert, M. J., Williams, C. N., and Bamber, J. L. Subglacial roughness of the Greenland Ice Sheet: relationship with contemporary ice velocity and geology. *The Cryosphere*, 13(11): 3093–3115, nov 2019. doi: 10.5194/tc-13-3093-2019. URL <https://doi.org/10.5194%2Ftc-13-3093-2019>.
- Corr, H., Moore, J. C., and Nicholls, K. W. Radar absorption due to impurities in Antarctic ice. *Geophysical Research Letters*, 20(11):1071–1074, jun 1993. doi: 10.1029/93gl01395. URL <https://doi.org/10.1029%2F93gl01395>.
- Diez, A., Matsuoka, K., Ferraccioli, F., Jordan, T. A., Corr, H. F., Kohler, J., Olesen, A. V., and Forsberg, R. Basal Settings Control Fast Ice Flow in the Recovery/Slessor/Bailey Region East Antarctica. *Geophysical Research Letters*, 45(6):

- 2706–2715, mar 2018. doi: 10.1002/2017gl076601. URL <https://doi.org/10.1002/2F2017gl076601>.
- Dow, C., Hubbard, A., Booth, A., Doyle, S., Gusmeroli, A., and Kulesa, B. Seismic evidence of mechanically weak sediments underlying Russell Glacier West Greenland. *Annals of Glaciology*, 54(64):135–141, 2013. doi: 10.3189/2013aog64a032. URL <https://doi.org/10.3189/2F2013aog64a032>.
- Dow, C. F., Werder, M. A., Babonis, G., Nowicki, S., Walker, R. T., Csatho, B., and Morlighem, M. Dynamics of Active Subglacial Lakes in Recovery Ice Stream. *Journal of Geophysical Research: Earth Surface*, 123(4):837–850, 2018. doi: <https://doi.org/10.1002/2017JF004409>. URL <https://agupubs.onlinelibrary.wiley.com/doi/abs/10.1002/2017JF004409>.
- Dowdeswell, J. A., Cofaigh, C. Ó., and Pudsey, C. J. Thickness and extent of the subglacial till layer beneath an Antarctic paleo-ice stream. *Geology*, 32(1):13, 2004. doi: 10.1130/g19864.1. URL <https://doi.org/10.1130/2Fg19864.1>.
- Durand, G., Gagliardini, O., Favier, L., Zwinger, T., and le Meur, E. Impact of bedrock description on modeling ice sheet dynamics. *Geophysical Research Letters*, 38(20):n/a–n/a, oct 2011. doi: 10.1029/2011gl048892. URL <https://doi.org/10.1029/2F2011gl048892>.
- Eisen, O., Winter, A., Steinhage, D., Kleiner, T., and Humbert, A. Basal roughness of the east antarctic ice sheet in relation to flow speed and basal thermal state. *Annals of Glaciology*, 61(81):162–175, 2020. doi: 10.1017/aog.2020.47. URL <https://doi.org/10.1017/aog.2020.47>.
- Eisermann, H., Eagles, G., Ruppel, A., Smith, E. C., and Jokat, W. Bathymetry beneath ice shelves of western dronning maud land, east antarctica, and implications on ice shelf stability. *Geophysical Research Letters*, 47(12):e2019GL086724, 2020. doi: <https://doi.org/10.1029/2019GL086724>. URL <https://agupubs.onlinelibrary.wiley.com/doi/abs/10.1029/2019GL086724>.
- Fahnestock, M. High Geothermal Heat Flow Basal Melt, and the Origin of Rapid Ice Flow in Central Greenland. *Science*, 294(5550):2338–2342, dec 2001. doi: 10.1126/science.1065370. URL <https://doi.org/10.1126/2Fscience.1065370>.
- Fahnestock, M., Bindschadler, R., Kwok, R., and Jezek, K. Greenland Ice Sheet Surface Properties and Ice Dynamics from ERS-1 SAR Imagery. *Science*, 262(5139):1530–1534, dec 1993. doi: 10.1126/science.262.5139.1530. URL <https://doi.org/10.1126/2Fscience.262.5139.1530>.
- Falcini, F. A., Rippin, D. M., Krabbendam, M., and Selby, K. A. Quantifying bed roughness beneath contemporary and palaeo-ice streams. *Journal of Glaciology*, 64(247):822–834, sep 2018. doi: 10.1017/jog.2018.71. URL <https://doi.org/10.1017/2Fjog.2018.71>.
- Franke, S., Jansen, D., Binder, T., Dörr, N., Paden, J., Helm, V., Steinhage, D., and Eisen, O. Bedrock topography and ice thickness in the onset region of the Northeast Greenland Ice Stream recorded with the airborne AWI Ultra-Wideband radar (UWB) in 2018, 2019. URL <https://doi.pangaea.de/10.1594/PANGAEA.907918>.
- Franke, S., Jansen, D., Beyer, S., Paden, J., and Eisen, O. Basal conditions of the onset zone of the Northeast Greenland Ice Stream derived from airborne ultra-wideband radar data. *PANGAEA*, 2020a. doi: 10.1594/PANGAEA.915136. URL <https://doi.org/10.1594/PANGAEA.915136>.
- Franke, S., Jansen, D., Binder, T., Dörr, N., Helm, V., Paden, J., Steinhage, D., and Eisen, O. Bed topography and subglacial landforms in the onset region of the Northeast Greenland Ice Stream. *Annals of Glaciology*, pages 1–11, mar 2020b. doi: 10.1017/aog.2020.12. URL <https://doi.org/10.1017/2Faog.2020.12>.
- Fretwell, P., Pritchard, H. D., Vaughan, D. G., Bamber, J. L., Barrand, N. E., Bell, R., Bianchi, C., Bingham, R. G., Blankenship, D. D., Casassa, G., Catania, G., Callens, D., Conway, H., Cook, A. J., Corr, H. F. J., Damaske, D., Damm, V., Ferraccioli, F., Forsberg, R., Fujita, S., Gim, Y., Gogineni, P., Griggs, J. A., Hindmarsh, R. C. A., Holmlund, P., Holt, J. W., Jacobel, R. W., Jenkins, A., Jokat, W., Jordan, T., King, E. C., Kohler, J., Krabill, W., Riger-Kusk, M., Langley, K. A., Leitchenkov, G., Leuschen, C., Luyendyk, B. P., Matsuoka, K., Mouginot, J., Nitsche, F. O., Nogi, Y., Nost, O. A., Popov, S. V., Rignot, E., Rippin, D. M., Rivera, A., Roberts, J., Ross, N., Siegert, M. J., Smith, A. M., Steinhage, D., Studinger, M., Sun, B., Tinto, B. K., Welch, B. C., Wilson, D., Young, D. A., Xiangbin, C., and Zirizzotti, A. Bedmap2: improved ice bed surface and thickness datasets for Antarctica. *The Cryosphere*, 7(1):375–393, feb 2013. doi: 10.5194/tc-7-375-2013. URL <https://doi.org/10.5194/2Ftc-7-375-2013>.
- Förste, C., Schmidt, R., Stubenvoll, R., Flechtner, F., Meyer, U., König, R., Neumayer, H., Biancale, R., Lemoine, J.-M., Bruinsma, S., Loyer, S., Barthelmes, F., and Esselborn, S. The GeoForschungsZentrum Potsdam/Groupe de Recherche de Gèodésie Spatiale satellite-only and combined gravity field models: EIGEN-GL04S1 and EIGEN-GL04C. *Journal of Geodesy*, 82(6):331–346, oct 2007. doi: 10.1007/s00190-007-0183-8. URL <https://doi.org/10.1007/2Fs00190-007-0183-8>.
- Gudlaugsson, E., Humbert, A., Winsborrow, M., and Andreassen, K. Subglacial roughness of the former Barents Sea ice sheet. *Journal of Geophysical Research: Earth Surface*, 118(4):2546–2556, dec 2013. doi: 10.1002/2013jf002714. URL <https://doi.org/10.1002/2F2013jf002714>.
- Hale, R., Miller, H., Gogineni, S., Yan, J. B., Rodriguez-Morales, F., Leuschen, C., Paden, J., Li, J., Binder, T., Steinhage, D., Gehrmann, M., and Braaten, D. Multi-channel ultra-wideband radar sounder and imager. In *2016 IEEE International Geoscience and Remote Sensing Symposium (IGARSS)*. IEEE, jul 2016. doi: 10.1109/igarss.2016.7729545. URL <https://doi.org/10.1109/2Figarss.2016.7729545>.
- Hofstede, C., Christoffersen, P., Hubbard, B., Doyle, S. H., Young, T. J., Diez, A., Eisen, O., and Hubbard, A. Physical Conditions of Fast Glacier Flow: 2. Variable Extent

- of Anisotropic Ice and Soft Basal Sediment From Seismic Reflection Data Acquired on Store Glacier West Greenland. *Journal of Geophysical Research: Earth Surface*, 123(2):349–362, feb 2018. doi: 10.1002/2017jf004297. URL <https://doi.org/10.1002/2F2017jf004297>.
- Holschuh, N., Christianson, K., and Anandakrishnan, S. Power loss in dipping internal reflectors imaged using ice-penetrating radar. *Annals of Glaciology*, 55(67):49–56, 2014. doi: 10.3189/2014aog67a005. URL <https://doi.org/10.3189/2F2014aog67a005>.
- Holschuh, N., Christianson, K., Anandakrishnan, S., Alley, R. B., and Jacobel, R. W. Constraining attenuation uncertainty in common midpoint radar surveys of ice sheets. *Journal of Geophysical Research: Earth Surface*, 121(10):1876–1890, oct 2016. ISSN 21699011. doi: 10.1002/2016JF003942. URL <http://doi.wiley.com/10.1002/2016JF003942>.
- Holschuh, N., Lilien, D., and Christianson, K. Thermal Weakening, Convergent Flow, and Vertical Heat Transport in the Northeast Greenland Ice Stream Shear Margins. *Geophysical Research Letters*, 46:8184–8193, 2019. doi: 10.1029/2019GL083436. URL <https://doi.org/10.1029/2019GL083436>.
- Holschuh, N., Christianson, K., Paden, J., Alley, R., and Anandakrishnan, S. Linking postglacial landscapes to glacier dynamics using swath radar at Thwaites Glacier Antarctica. *Geology*, jan 2020. doi: 10.1130/g46772.1. URL <https://doi.org/10.1130/2Fg46772.1>.
- Hubbard, B., Siegert, M. J., and McCarroll, D. Spectral roughness of glaciated bedrock geomorphic surfaces: Implications for glacier sliding. *Journal of Geophysical Research: Solid Earth*, 105(B9):21295–21303, sep 2000. doi: 10.1029/2000jb900162. URL <https://doi.org/10.1029/2F2000jb900162>.
- Hughes, T., Sargent, A., and Fastook, J. Ice-bed coupling beneath and beyond ice streams: Byrd Glacier Antarctica. *Journal of Geophysical Research*, 116(F3), jul 2011. doi: 10.1029/2010jf001896. URL <https://doi.org/10.1029/2F2010jf001896>.
- Humbert, A., Steinhage, D., Helm, V., Beyer, S., and Kleiner, T. Missing Evidence of Widespread Subglacial Lakes at Recovery Glacier Antarctica. *Journal of Geophysical Research: Earth Surface*, 123(11):2802–2826, nov 2018. doi: 10.1029/2017jf004591. URL <https://doi.org/10.1029/2F2017jf004591>.
- Jacobel, R. W., Lapo, K. E., Stamp, J. R., Youngblood, B. W., Welch, B. C., and Bamber, J. L. A comparison of basal reflectivity and ice velocity in East Antarctica. *The Cryosphere*, 4(4):447–452, oct 2010. doi: 10.5194/tc-4-447-2010. URL <https://doi.org/10.5194/2Ftc-4-447-2010>.
- Jordan, T. M., Bamber, J. L., Williams, C. N., Paden, J. D., Siegert, M. J., Huybrechts, P., Gagliardini, O., and Gillet-Chaulet, F. An ice-sheet-wide framework for englacial attenuation from ice-penetrating radar data. *The Cryosphere*, 10(4):1547–1570, jul 2016. doi: 10.5194/tc-10-1547-2016. URL <https://doi.org/10.5194/2Ftc-10-1547-2016>.
- Jordan, T. M., Cooper, M. A., Schroeder, D. M., Williams, C. N., Paden, J. D., Siegert, M. J., and Bamber, J. L. Self-affine subglacial roughness: consequences for radar scattering and basal water discrimination in northern Greenland. *The Cryosphere*, 11(3):1247–1264, may 2017. doi: 10.5194/tc-11-1247-2017. URL <https://doi.org/10.5194/2Ftc-11-1247-2017>.
- Jordan, T. M., Williams, C. N., Schroeder, D. M., Martos, Y. M., Cooper, M. A., Siegert, M. J., Paden, J. D., Huybrechts, P., and Bamber, J. L. A constraint upon the basal water distribution and thermal state of the Greenland Ice Sheet from radar bed echoes. *The Cryosphere*, 12(9):2831–2854, sep 2018. doi: 10.5194/tc-12-2831-2018. URL <https://doi.org/10.5194/2Ftc-12-2831-2018>.
- Joughin, I., Fahnestock, M., MacAyeal, D., Bamber, J. L., and Gogineni, P. Observation and analysis of ice flow in the largest Greenland ice stream. *Journal of Geophysical Research: Atmospheres*, 106(D24):34021–34034, dec 2001. doi: 10.1029/2001jd900087. URL <https://doi.org/10.1029/2F2001jd900087>.
- Joughin, I., Smith, B. E., and Howat, I. M. A complete map of Greenland ice velocity derived from satellite data collected over 20 years. *Journal of Glaciology*, 64(243):1–11, nov 2017. doi: 10.1017/jog.2017.73. URL <https://doi.org/10.1017/2Fjog.2017.73>.
- Karlsson, N. B. and Dahl-Jensen, D. Response of the large-scale subglacial drainage system of Northeast Greenland to surface elevation changes. *The Cryosphere*, 9(4):1465–1479, aug 2015. doi: 10.5194/tc-9-1465-2015. URL <https://doi.org/10.5194/2Ftc-9-1465-2015>.
- Keisling, B. A., Christianson, K., Alley, R. B., Peters, L. E., Christian, J. E., Anandakrishnan, S., Riverman, K. L., Muto, A., and Jacobel, R. W. Basal conditions and ice dynamics inferred from radar-derived internal stratigraphy of the northeast Greenland ice stream. *Annals of Glaciology*, 55(67):127–137, 2014. doi: 10.3189/2014aog67a090. URL <https://doi.org/10.3189/2F2014aog67a090>.
- King, E. C., Hindmarsh, R. C. A., and Stokes, C. R. Formation of mega-scale glacial lineations observed beneath a West Antarctic ice stream. *Nature Geoscience*, 2(8):585–588, jul 2009. doi: 10.1038/ngeo581. URL <https://doi.org/10.1038/2Fng581>.
- Krabbendam, M., Eyles, N., Putkinen, N., Bradwell, T., and Arbelaez-Moreno, L. Streamlined hard beds formed by palaeo-ice streams: A review. *Sedimentary Geology*, 338:24–50, jun 2016. doi: 10.1016/j.sedgeo.2015.12.007. URL <https://doi.org/10.1016/2Fj.sedgeo.2015.12.007>.
- Kulesa, B., Hubbard, A. L., Booth, A. D., Bougamont, M., Dow, C. F., Doyle, S. H., Christoffersen, P., Lindbäck, K., Pettersson, R., Fitzpatrick, A. A. W., and Jones, G. A. Seismic evidence for complex sedimentary control of Greenland Ice Sheet flow. *Science Advances*, 3(8):e1603071, aug 2017. doi: 10.1126/sciadv.1603071. URL <https://doi.org/10.1126/2Fsciadv.1603071>.

- Larour, E., Utke, J., Csatho, B., Schenk, A., Seroussi, H., Morlighem, M., Rignot, E., Schlegel, N., and Khazendar, A. Inferred basal friction and surface mass balance of the Northeast Greenland Ice Stream using data assimilation of ICESat (Ice Cloud and land Elevation Satellite) surface altimetry and ISSM (Ice Sheet System Model). *The Cryosphere*, 8(6):2335–2351, dec 2014. doi: 10.5194/tc-8-2335-2014. URL <https://doi.org/10.5194%2Ftc-8-2335-2014>.
- Layberry, R. L. and Bamber, J. L. A new ice thickness and bed data set for the Greenland ice sheet: 2. Relationship between dynamics and basal topography. *Journal of Geophysical Research: Atmospheres*, 106(D24):33781–33788, dec 2001. doi: 10.1029/2001jd900053. URL <https://doi.org/10.1029%2F2001jd900053>.
- Le Brocq, A. M., Payne, A. J., and Siegert, M. J. West Antarctic balance calculations: Impact of flux-routing algorithm smoothing algorithm and topography. *Computers & Geosciences*, 32(10):1780–1795, dec 2006. doi: 10.1016/j.cageo.2006.05.003. URL <https://doi.org/10.1016%2Fj.cageo.2006.05.003>.
- Le Brocq, A. M., Payne, A., Siegert, M., and Alley, R. A subglacial water-flow model for West Antarctica. *Journal of Glaciology*, 55(193):879–888, 2009. doi: 10.3189/002214309790152564. URL <https://doi.org/10.3189%2F002214309790152564>.
- Li, X., Sun, B., Siegert, M. J., Bingham, R. G., Tang, X., Zhang, D., Cui, X., and Zhang, X. Characterization of subglacial landscapes by a two-parameter roughness index. *Journal of Glaciology*, 56(199):831–836, 2010. doi: 10.3189/002214310794457326. URL <https://doi.org/10.3189%2F002214310794457326>.
- Livingstone, S. J., Clark, C. D., Woodward, J., and Kingslake, J. Potential subglacial lake locations and meltwater drainage pathways beneath the Antarctic and Greenland ice sheets. *The Cryosphere*, 7(6):1721–1740, nov 2013. doi: 10.5194/tc-7-1721-2013. URL <https://doi.org/10.5194%2Ftc-7-1721-2013>.
- MacGregor, J. A., Catania, G. A., Conway, H., Schroeder, D. M., Joughin, I., Young, D. A., Kempf, S. D., and Blankenship, D. D. Weak bed control of the eastern shear margin of Thwaites Glacier West Antarctica. *Journal of Glaciology*, 59(217):900–912, 2013. doi: 10.3189/2013jog13j050. URL <https://doi.org/10.3189%2F2013jog13j050>.
- MacGregor, J. A., Fahnestock, M. A., Catania, G. A., Paden, J. D., Gogineni, S. P., Young, S. K., Rybarski, S. C., Mabrey, A. N., Wagman, B. M., and Morlighem, M. Radiostereography and age structure of the Greenland Ice Sheet. *Journal of Geophysical Research: Earth Surface*, 120(2):212–241, feb 2015. doi: 10.1002/2014jf003215. URL <https://doi.org/10.1002%2F2014jf003215>.
- MacGregor, J. A., Fahnestock, M. A., Catania, G. A., Aschwanden, A., Clow, G. D., Colgan, W. T., Gogineni, S. P., Morlighem, M., Nowicki, S. M. J., Paden, J. D., Price, S. F., and Seroussi, H. A synthesis of the basal thermal state of the Greenland Ice Sheet. *Journal of Geophysical Research: Earth Surface*, 121(7):1328–1350, jul 2016. doi: 10.1002/2015jf003803. URL <https://doi.org/10.1002%2F2015jf003803>.
- Matsuoka, K. Pitfalls in radar diagnosis of ice-sheet bed conditions: Lessons from englacial attenuation models. *Geophysical Research Letters*, 38(5):n/a–n/a, mar 2011. doi: 10.1029/2010gl046205. URL <https://doi.org/10.1029%2F2010gl046205>.
- Matsuoka, K., Pattyn, F., Callens, D., and Conway, H. Radar characterization of the basal interface across the grounding zone of an ice-rise promontory in East Antarctica. *Annals of Glaciology*, 53(60):29–34, 2012. doi: 10.3189/2012aog60a106. URL <https://doi.org/10.3189%2F2012aog60a106>.
- Meyer, C. R., Yehya, A., Minchew, B., and Rice, J. R. A Model for the Downstream Evolution of Temperate Ice and Subglacial Hydrology Along Ice Stream Shear Margins. *Journal of Geophysical Research: Earth Surface*, 123(8):1682–1698, aug 2018. doi: 10.1029/2018jf004669. URL <https://doi.org/10.1029%2F2018jf004669>.
- Minchew, B. M., Meyer, C. R., Pegler, S. S., Lipovsky, B. P., Rempel, A. W., Gudmundsson, G. H., and Iverson, N. R. Comment on “friction at the bed does not control fast glacier flow”. *Science*, 363(6427), 2019. ISSN 0036-8075. doi: 10.1126/science.aau6055. URL <https://science.sciencemag.org/content/363/6427/eaau6055>.
- Morlighem, M., Williams, C. N., Rignot, E., An, L., Arndt, J. E., Bamber, J. L., Catania, G., Chauché, N., Dowdeswell, J. A., Dorschel, B., Fenty, I., Hogan, K., Howat, I., Hubbard, A., Jakobsson, M., Jordan, T. M., Kjeldsen, K. K., Millan, R., Mayer, L., Mouginot, J., Noël, B. P. Y., O’Cofaigh, C., Palmer, S., Rysgaard, S., Seroussi, H., Siegert, M. J., Slabon, P., Straneo, F., van den Broeke, M. R., Weinrebe, W., Wood, M., and Zinglensen, K. B. BedMachine v3: Complete Bed Topography and Ocean Bathymetry Mapping of Greenland From Multibeam Echo Sounding Combined With Mass Conservation. *Geophysical Research Letters*, 44(21):11,051–11,061, nov 2017. doi: 10.1002/2017gl074954. URL <https://doi.org/10.1002%2F2017gl074954>.
- Morlighem, M., Rignot, E., Binder, T., Blankenship, D., Drews, R., Eagles, G., Eisen, O., Ferraccioli, F., Forsberg, R., Fretwell, P., Goel, V., Greenbaum, J. S., Gudmundsson, H., Guo, J., Helm, V., Hofstede, C., Howat, I., Humbert, A., Jokat, W., Karlsson, N. B., Lee, W. S., Matsuoka, K., Millan, R., Mouginot, J., Paden, J., Pattyn, F., Roberts, J., Rosier, S., Ruppel, A., Seroussi, H., Smith, E. C., Steinhage, D., Sun, B., van den Broeke, M. R., van Ommen, T. D., van Wessem, M., and Young, D. A. Deep glacial troughs and stabilizing ridges unveiled beneath the margins of the Antarctic ice sheet. *Nature Geoscience*, 13(2):132–137, dec 2019. doi: 10.1038/s41561-019-0510-8. URL <https://doi.org/10.1038%2Fs41561-019-0510-8>.
- Muto, A., Anandakrishnan, S., and Alley, R. B. Subglacial bathymetry and sediment layer distribution beneath the Pine Island Glacier ice shelf West Antarctica, modeled using aerogravity and autonomous underwater vehicle data. *Annals of Glaciology*, 54(64):27–32, 2013. doi: 10.

- 3189/2013aog64a110. URL <https://doi.org/10.3189%2F2013aog64a110>.
- Neckel, N., Drews, R., Rack, W., and Steinhage, D. Basal melting at the Ekström Ice Shelf, Antarctica, estimated from mass flux divergence. *Annals of Glaciology*, 53(60):294–302, 2012. ISSN 0260-3055. doi: 10.3189/2012aog60a167. URL <https://doi.org/10.3189/2012aog60a167>.
- Oswald, G. and Gogineni, S. Recovery of subglacial water extent from Greenland radar survey data. *Journal of Glaciology*, 54(184):94–106, 2008. doi: 10.3189/002214308784409107. URL <https://doi.org/10.3189%2F002214308784409107>.
- Oswald, G. K. A. and Gogineni, S. P. Mapping Basal Melt Under the Northern Greenland Ice Sheet. *IEEE Transactions on Geoscience and Remote Sensing*, 50(2):585–592, feb 2012. doi: 10.1109/tgrs.2011.2162072. URL <https://doi.org/10.1109%2Ftgrs.2011.2162072>.
- Paden, J., Akins, T., Dunson, D., Allen, C., and Gogineni, P. Ice-sheet bed 3-D tomography. *Journal of Glaciology*, 56(195):3–11, 2010. doi: 10.3189/002214310791190811. URL <https://doi.org/10.3189%2F002214310791190811>.
- Perol, T., Rice, J. R., Platt, J. D., and Suckale, J. Subglacial hydrology and ice stream margin locations. *Journal of Geophysical Research: Earth Surface*, 120(7):1352–1368, jul 2015. doi: 10.1002/2015jf003542. URL <https://doi.org/10.1002%2F2015jf003542>.
- Raney, R. The delay/Doppler radar altimeter. *IEEE Transactions on Geoscience and Remote Sensing*, 36(5):1578–1588, 1998. doi: 10.1109/36.718861. URL <https://doi.org/10.1109%2F36.718861>.
- Rippin, D., Bamber, J., Siegert, M., Vaughan, D., and Corr, H. Basal conditions beneath enhanced-flow tributaries of Slessor Glacier East Antarctica. *Journal of Glaciology*, 52(179):481–490, 2006. doi: 10.3189/172756506781828467. URL <https://doi.org/10.3189%2F172756506781828467>.
- Rippin, D., Vaughan, D., and Corr, H. The basal roughness of Pine Island Glacier West Antarctica. *Journal of Glaciology*, 57(201):67–76, 2011. doi: 10.3189/002214311795306574. URL <https://doi.org/10.3189%2F002214311795306574>.
- Rippin, D., Bingham, R., Jordan, T., Wright, A., Ross, N., Corr, H., Ferraccioli, F., Brocq, A. L., Rose, K., and Siegert, M. Basal roughness of the Institute and Möller Ice Streams West Antarctica: Process determination and landscape interpretation. *Geomorphology*, 214:139–147, jun 2014. doi: 10.1016/j.geomorph.2014.01.021. URL <https://doi.org/10.1016%2Fj.geomorph.2014.01.021>.
- Rippin, D. M. Bed roughness beneath the Greenland ice sheet. *Journal of Glaciology*, 59(216):724–732, 2013. doi: 10.3189/2013jog12j212. URL <https://doi.org/10.3189%2F2013jog12j212>.
- Riverman, K. L., Anandakrishnan, S., Alley, R. B., Holschuh, N., Dow, C. F., Muto, A., Parizek, B. R., Christianson, K., and Peters, L. E. Wet subglacial bedforms of the NE Greenland Ice Stream shear margins. *Annals of Glaciology*, 60(80):91–99, dec 2019. doi: 10.1017/aog.2019.43. URL <https://doi.org/10.1017%2Faog.2019.43>.
- Rogozhina, I., Hagedoorn, J. M., Martinec, Z., Fleming, K., Soucek, O., Greve, R., and Thomas, M. Effects of uncertainties in the geothermal heat flux distribution on the greenland ice sheet: An assessment of existing heat flow models. *Journal of Geophysical Research: Earth Surface*, 117(F2), 2012. doi: 10.1029/2011JF002098. URL <https://agupubs.onlinelibrary.wiley.com/doi/abs/10.1029/2011JF002098>.
- Rosier, S. H. R., Hofstede, C., Brisbourne, A. M., Hattermann, T., Nicholls, K. W., Davis, P. E. D., Anker, P. G. D., Hillenbrand, C.-D., Smith, A. M., and Corr, H. F. J. A New Bathymetry for the Southeastern Filchner-Ronne Ice Shelf: Implications for Modern Oceanographic Processes and Glacial History. *Journal of Geophysical Research: Oceans*, 123(7):4610–4623, jul 2018. doi: 10.1029/2018jc013982. URL <https://doi.org/10.1029%2F2018jc013982>.
- Ryser, C., Lüthi, M. P., Andrews, L. C., Catania, G. A., Funk, M., Hawley, R., Hoffman, M., and Neumann, T. A. Caterpillar-like ice motion in the ablation zone of the Greenland ice sheet. *Journal of Geophysical Research: Earth Surface*, 119(10):2258–2271, oct 2014. doi: 10.1002/2013jf003067. URL <https://doi.org/10.1002%2F2013jf003067>.
- Schroeder, D. M., Dowdeswell, J. A., Siegert, M. J., Bingham, R. G., Chu, W., MacKie, E. J., Siegfried, M. R., Vega, K. I., Emmons, J. R., and Winstein, K. Multidecadal observations of the Antarctic ice sheet from restored analog radar records. *Proceedings of the National Academy of Sciences*, 116(38):18867–18873, sep 2019. doi: 10.1073/pnas.1821646116. URL <https://doi.org/10.1073%2Fpnas.1821646116>.
- Schroeder, D. M., Bingham, R. G., Blankenship, D. D., Christianson, K., Eisen, O., Flowers, G. E., Karlsson, N. B., Koutnik, M. R., Paden, J. D., and Siegert, M. J. Five decades of radioglaciology. *Annals of Glaciology*, pages 1–13, mar 2020. doi: 10.1017/aog.2020.11. URL <https://doi.org/10.1017%2Faog.2020.11>.
- Shepard, M. K., Campbell, B. A., Bulmer, M. H., Farr, T. G., Gaddis, L. R., and Plaut, J. J. The roughness of natural terrain: A planetary and remote sensing perspective. *Journal of Geophysical Research: Planets*, 106(E12):32777–32795, dec 2001. doi: 10.1029/2000je001429. URL <https://doi.org/10.1029%2F2000je001429>.
- Shreve, R. L. Movement of Water in Glaciers. *Journal of Glaciology*, 11(62):205–214, 1972. doi: 10.3189/s002214300002219x. URL <https://doi.org/10.3189%2Fs002214300002219x>.
- Siegert, M. J., Taylor, J., and Payne, A. J. Spectral roughness of subglacial topography and implications for former ice-sheet dynamics in East Antarctica. *Global and Planetary Change*, 45(1-3):249–263, feb 2005. doi: 10.1016/j.

- gloplacha.2004.09.008. URL <https://doi.org/10.1016%2Fj.gloplacha.2004.09.008>.
- Siegert, M. J., Ross, N., Li, J., Schroeder, D. M., Rippin, D., Ashmore, D., Bingham, R., and Gogineni, P. Subglacial controls on the flow of Institute Ice Stream West Antarctica. *Annals of Glaciology*, 57(73):19–24, may 2016. doi: 10.1017/aog.2016.17. URL <https://doi.org/10.1017%2Faog.2016.17>.
- Smith, A. M., Jordan, T. A., Ferraccioli, F., and Bingham, R. G. Influence of subglacial conditions on ice stream dynamics: Seismic and potential field data from Pine Island Glacier West Antarctica. *Journal of Geophysical Research: Solid Earth*, 118(4):1471–1482, apr 2013. doi: 10.1029/2012jb009582. URL <https://doi.org/10.1029%2F2012jb009582>.
- Smith, E. C., Hattermann, T., Kuhn, G., Gaedicke, C., Berger, S., Drews, R., Ehlers, T. A., Franke, D., Gromig, R., Hofstede, C., Lambrecht, A., Läufer, A., Mayer, C., Tiedemann, R., Wilhelms, F., and Eisen, O. Detailed seismic bathymetry beneath ekström ice shelf, antarctica: Implications for glacial history and ice-ocean interaction. *Geophysical Research Letters*, 47(10): e2019GL086187, 2020. doi: 10.1029/2019GL086187. URL <https://agupubs.onlinelibrary.wiley.com/doi/abs/10.1029/2019GL086187>. e2019GL086187 10.1029/2019GL086187.
- Smith-Johnsen, S., de Fleurian, B., Schlegel, N., Seroussi, H., and Nisancioglu, K. Exceptionally High Geothermal Heat Flux Needed to Sustain the Northeast Greenland Ice Stream. *The Cryosphere*, sep 2019. doi: 10.5194/tc-2019-212. URL <https://doi.org/10.5194%2Ftc-2019-212>.
- Smith-Johnsen, S., Schlegel, N.-J., Fleurian, B., and Nisancioglu, K. H. Sensitivity of the Northeast Greenland Ice Stream to Geothermal Heat. *Journal of Geophysical Research: Earth Surface*, 125(1), jan 2020. doi: 10.1029/2019jf005252. URL <https://doi.org/10.1029%2F2019jf005252>.
- Stearns, L. A. and van der Veen, C. Response to comment on “friction at the bed does not control fast glacier flow”. *Science*, 363(6427), 2019. ISSN 0036-8075. doi: 10.1126/science.aau8375. URL <https://science.sciencemag.org/content/363/6427/eaau8375>.
- Stearns, L. A. and van der Veen, C. J. Friction at the bed does not control fast glacier flow. *Science*, 361(6399): 273–277, jun 2018. doi: 10.1126/science.aat2217. URL <https://doi.org/10.1126%2Fscience.aat2217>.
- Stokes, C., Spagnolo, M., Clark, C., Cofaigh, C. Ó., Lian, O., and Dunstone, R. Formation of mega-scale glacial lineations on the Dubawnt Lake Ice Stream bed: 1. size shape and spacing from a large remote sensing dataset. *Quaternary Science Reviews*, 77:190–209, oct 2013. doi: 10.1016/j.quascirev.2013.06.003. URL <https://doi.org/10.1016%2Fj.quascirev.2013.06.003>.
- Stokes, C. R. and Clark, C. D. Are long subglacial bedforms indicative of fast ice flow? *Boreas*, 31(3): 239–249, 2002. doi: 10.1111/j.1502-3885.2002.tb01070.x. URL <https://onlinelibrary.wiley.com/doi/abs/10.1111/j.1502-3885.2002.tb01070.x>.
- Taylor, J., Siegert, M., Payne, A., Hambrey, M., O’Brien, P., Cooper, A., and Leitchenkov, G. Topographic controls on post-Oligocene changes in ice-sheet dynamics, Prydz Bay region, East Antarctica. *Geology*, 32(3):197–200, 03 2004. ISSN 0091-7613. doi: 10.1130/G20275.1. URL <https://doi.org/10.1130/G20275.1>.
- Vallalonga, P., Christianson, K., Alley, R. B., Anandakrishnan, S., Christian, J. E. M., Dahl-Jensen, D., Gkinis, V., Holme, C., Jacobel, R. W., Karlsson, N. B., Keisling, B. A., Kipfstuhl, S., Kjær, H. A., Kristensen, M. E. L., Muto, A., Peters, L. E., Popp, T., Riverman, K. L., Svensson, A. M., Tibuleac, C., Vinther, B. M., Weng, Y., and Winstrup, M. Initial results from geophysical surveys and shallow coring of the Northeast Greenland Ice Stream (NEGIS). *The Cryosphere*, 8(4): 1275–1287, jul 2014. doi: 10.5194/tc-8-1275-2014. URL <https://doi.org/10.5194%2Ftc-8-1275-2014>.
- Wilkins, N., Behrens, J., Kleiner, T., Rippin, D., Rückamp, M., and Humbert, A. Thermal structure and basal sliding parametrisation at Pine Island Glacier – a 3-D full-Stokes model study. *The Cryosphere*, 9(2):675–690, apr 2015. doi: 10.5194/tc-9-675-2015. URL <https://doi.org/10.5194%2Ftc-9-675-2015>.
- Winter, A., Steinhage, D., Arnold, E. J., Blankenship, D. D., Cavitte, M. G. P., Corr, H. F. J., Paden, J. D., Urbini, S., Young, D. A., and Eisen, O. Comparison of measurements from different radio-echo sounding systems and synchronization with the ice core at Dome C Antarctica. *The Cryosphere*, 11(1):653–668, mar 2017. doi: 10.5194/tc-11-653-2017. URL <https://doi.org/10.5194%2Ftc-11-653-2017>.
- Young, D. A., Schroeder, D. M., Blankenship, D. D., Kempf, S. D., and Quartini, E. The distribution of basal water between Antarctic subglacial lakes from radar sounding. *Philosophical Transactions of the Royal Society A: Mathematical Physical and Engineering Sciences*, 374(2059):20140297, jan 2016. doi: 10.1098/rsta.2014.0297. URL <https://doi.org/10.1098%2Frsta.2014.0297>.

Appendix G

PAPER III

RESEARCH ARTICLE

Pre-glacial to present geomorphological development of the Jutulstraumen glacier basin, Antarctica

Steven Franke¹ , Hannes Eisermann¹ , Wilfried Jokat^{1,2} , Graeme Eagles¹ , Jölund Asseng¹, Heinrich Miller¹ , Daniel Steinhage¹ , Veit Helm¹ , Olaf Eisen^{1,2}  and Daniela Jansen¹ 

¹ Alfred Wegener Institute, Helmholtz Centre for Polar and Marine Research, Bremerhaven, Germany

² Department of Geosciences, University of Bremen, Bremen, Germany

Published on 14 July 2021 in ESPL

<https://doi.org/10.1002/esp.5203>

Abstract

This paper investigates the evolution of the subglacial morphology of the Jutulstraumen Glacier drainage system in western Dronning Maud Land. The Jutulstraumen Glacier reaches the ocean via the Jutul-Penck Trough and Jutulstraumen graben. These two deep subglacial valleys are the only significant passages for draining the East Antarctic Ice Sheet through the western part of the Dronning Maud Land mountain chain. We acquired new bed topography data during an airborne radar campaign in the region upstream of the Jutulstraumen Graben to characterise the source area of the Jutulstraumen Glacier. The new data show deep relief to be generally under-represented in available bed topography compilations. Our analysis of the bed topography, valley characteristics and bed roughness leads to the conclusion that much more of the alpine landscape that would have formed prior to the Antarctic Ice Sheet is preserved than previously anticipated. We identify various geomorphological patterns that can be related to different stages and processes of subglacial erosion. Based on these patterns, we reconstruct the temporal sequence by which ice flow modified the topography since the beginning of the glaciation of Antarctica.

Received: 11 March 2021 - Revised: 25 June 2021 - Accepted: 27 June 2021

Introduction

The bedrock topography beneath the Antarctic Ice Sheet (AIS) has been modified by extensive glacial and subglacial erosion on continental, regional and local scales (Jamieson et al., 2010). *In situ* observations of the bedrock and basal properties of the AIS have only been made at a handful of locations, due to the difficulties involved in accessing the bed. In addition, airborne radio-echo sounding (RES) data can be used to describe subglacial geomorphology over much larger areas, on which basis inferences can be made about present and former ice stream activity and ice sheet configurations (Siegert et al., 2005). This can, and must, be done at high spatial resolution Sugden and John (1976).

To study the behaviour of the AIS, we depend on an understanding of the relationship between pre-glacial landscapes and the processes by which ice flow can

modify them (Sugden and Jamieson, 2018). This is necessary and important if we are to understand past and future ice sheet behaviour (Oerlemans, 2010; Jamieson et al., 2010). In particular, constraints on ice sheet and landscape development are key boundary conditions for numerical simulations of geomorphological development of the landscape beneath the AIS (Jamieson et al., 2010).

In this study, we use existing and new high-resolution airborne radar data to improve our understanding of the bed topography and landscape evolution in the source region of the Jutulstraumen Glacier (JG) in western Dronning Maud Land (DML). JG is the largest and most important outlet glacier in DML. The glacial history of central DML is engraved in its bed topography, which has been continuously shaped by erosion and deposition under the region's ice sheet since its formation over 30 million years ago. We present and discuss various geomorphological structures at the

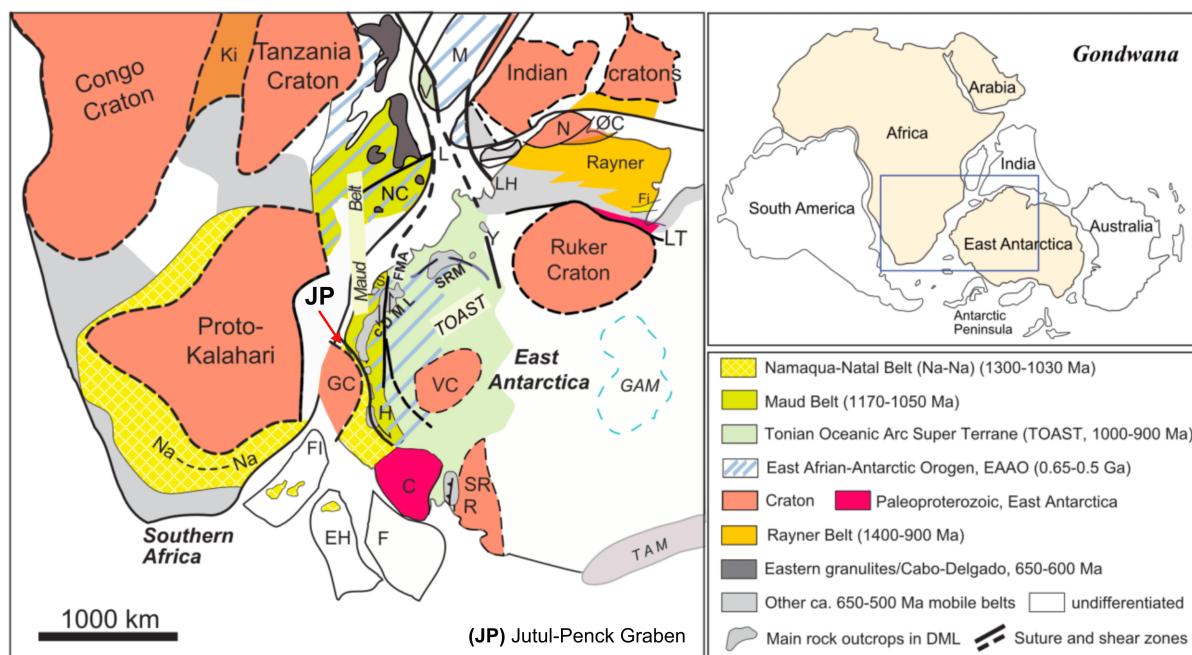


Figure G.1: Distribution of geological units within Gondwana during Proterozoic and earliest Paleozoic times [Figure modified after Wang et al., 2020; Jacobs et al., 2017; Gray et al., 2008]: Position of DML, East Antarctica, relative to Africa and India. DML terrane boundaries interpreted from scattered outcrops and interpolated on the basis of regional aeromagnetic data (Jacobs et al., 2017; Mieth and Jokat, 2014). Abbreviations: C, Coats Land; cDML, central Dronning Maud Land; EH, Ellsworth-Haag block; F, Filchner block; FI, Falkland Islands; Fi, Fisher Terrane; FMA, Forster Magnetic Anomaly; GAM, Gamburtsev Mountains; GC, Grunehogna Craton; H, Heimefrontfjella; Ki, Kibaran; L, Lurio Belt; LH, Lützow-Holm Bay; LT, Lambert Terrane; M, Madagascar; N, Napier Complex; NC, Nampula Complex; Na-Na, Namaqua-Natal Belt; ØC, Øygarden Complex; R, Read Block; S, Schirmacher Oasis; SR, Shackleton Range; SRM, Sør Rondane Mountains; TAM, Transantarctic Mountains; V, Vohibori Terrane; VC, Valkyrie Craton; Y, Yamato Mountains.

glacier bed, and interpret them in terms of the region's erosional history. Our results give insight into the effects of past and present ice dynamics on the glacier bed and into landscape development in glaciated areas in general.

Regional setting

The JG is located within a prominent graben system, which separates the complex geology of DML. A thick ice sheet however prevents a detailed understanding of its geological history since Precambrian times. Only the combination of geological sampling of the sparse outcrops/nuntaks (Jacobs et al., 1998, 2017) combined with aerogeophysical data (Mieth and Jokat, 2014) made it possible to retrieve some first-order information of the regional geology (Figure G.1).

Geoscientific research shows that Antarctica was part of the large supercontinent Rodinia at approximately 1090 million years ago (McLelland et al., 2010), which subsequently underwent rifting and broke apart between 800-750 million years ago (Cawood et al., 2016). Numerous geological affinities between DML and South Africa show that both fragments re-collided between 650 and 500 million years ago (Jacobs and Thomas, 2004) along the East Africa-Antarctic Orogen

to form a new southern supercontinent named Gondwana. Gondwana was geologically stable for around 300 million years before the arrival of a mantle plume caused the dispersal of this vast continent. Massive volcanism started around 180 million years ago both off East Africa and in DML (Elliot, 1992), which finally led to the fragmentation of Gondwana. At first, East Africa and South America separated in Jurassic times (Jokat et al., 2003; Leinweber and Jokat, 2012; Mueller and Jokat, 2019) followed by India, Australia and New Zealand in the Cretaceous.

As a consequence of geological events, the Jutul-Penck Graben formed. It represents a deep trough which cuts through the otherwise-continuous Dronning Maud Land mountains extending for 1500 km from 15°W to 30°E (Jacobs, 1991; Jacobs et al., 1992). This mountain chain includes the Heimefrontfjella in the west, the Borg- and Wohlthatmassifs that form the flanks of the Jutul-Penck Graben, and the Sør Rondane Mountains (Steinhage et al.; Riedel et al., 2012; Mieth and Jokat, 2014) in the east. Since the graben system runs along several geological units of different ages it is still debated, if the trough is a feature which formed along geological weakness zones representing a failed rift formed prior to the Gondwana break up (Ferraccioli et al., 2005) or has a different origin.

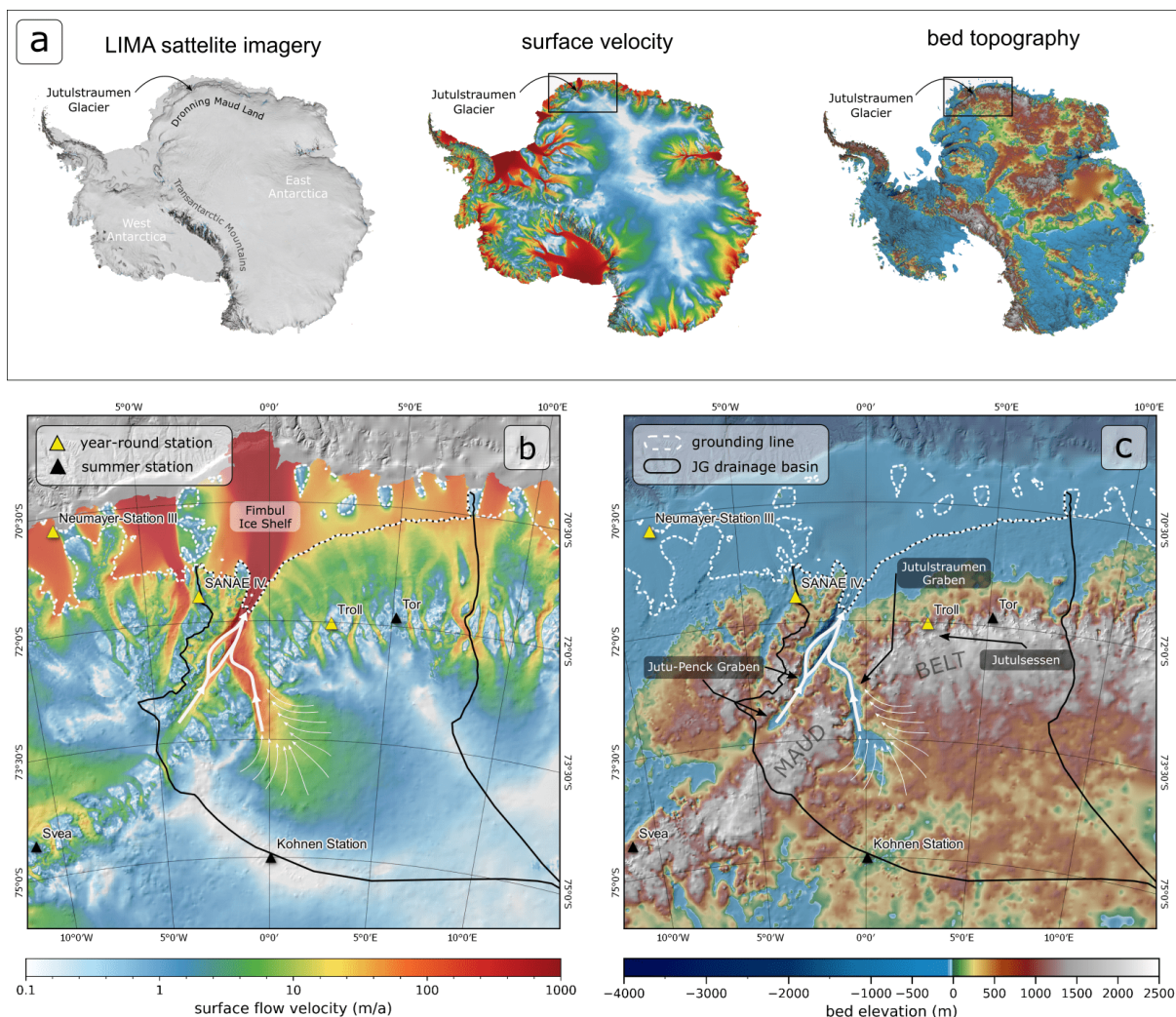


Figure G.2: Overview of the geographical and glaciological setting of the JG drainage basin. Panel (a) shows three maps of the LIMA Landsat image mosaic (Bindschadler et al., 2008), the ice surface velocity (Mouginot et al., 2019) and BedMachine Antarctica (BMA) bed topography (Morlighem et al., 2019). Panels (b) and (c) zoom in on the ice flow velocity and bed topography maps for the study region. White arrows schematically indicate the convergent ice flow upstream of the Jutulstraumen graben. The black outline represents the JG drainage system boundary after Rignot et al. (2013).

The JG and its tributary the Penck Trough ice stream, mainly follow the tectonic lineament (Figure G.2b and c), which provides a northward oriented draining system for the East Antarctic Ice Sheet. With a catchment area extend of 100,000 km², the JG is the largest glacier in DML (Rignot et al., 2013). At the seaward termination of the graben, the JG feeds DML's largest ice shelf, the Fimbul Ice Shelf (Figure G.2b).

Towards the south, DML hosts a complex subglacial landscape. Näslund (2001) proposes a step-by-step genesis, starting with the development of relief by subaerial weathering and erosion by mountain glaciers and river systems, resulting in an alpine landscape, and ending with erosion of the mountain range by large ice streams following the growth of the East Antarctic ice sheet in mid-Miocene times (Shevenell et al., 2004; Holbourn

et al., 2005). Further east, between the ice streams that flow around the Sør Rondane Mountains, the plateau inland of the escarpment has been interpreted to preserve features of a pre-existing fluvial landscape by Eagles et al. (2018).

Data and methods

Previous radar surveys

Näslund (2001) presented helicopter-based RES data collected from a small area around Jutulsessen Nunatak in the 1990s, using it for an interpretation of long-term landscape development in western and central DML. His interpretation started with continental breakup in Jurassic times and continued over the multiple glacial

cycles of Neogene times. Around the same time, the Alfred Wegener Institute for Polar and Marine Research (AWI) gathered more than 50 000 km of airborne RES data in DML as part of the pre-site survey for the European Project for Ice Coring in Antarctica (EPICA) (Steinhage et al., 2001). Subsequently, additional geophysical data sets were acquired by the British Antarctic Survey in the Jutulstraumen region (Ferraccioli et al., 2005) and by the AWI in western DML (Riedel et al., 2012; Mieth and Jokar, 2014).

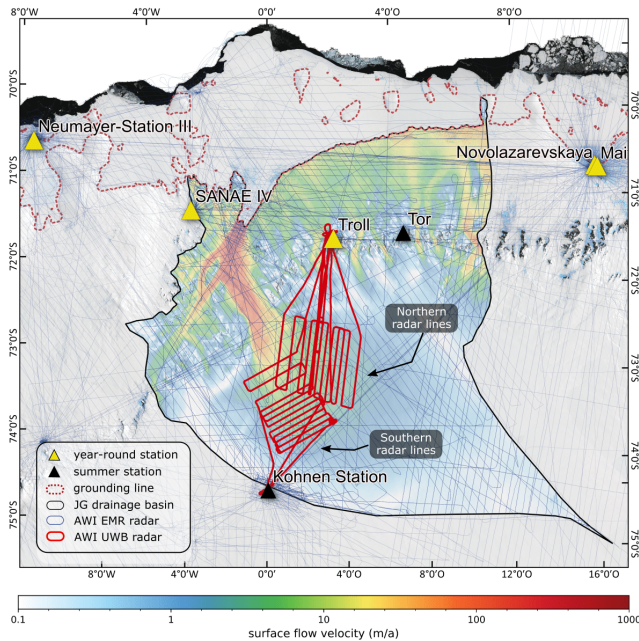


Figure G.3: Flight tracks with new AWI UWB JURAS-2018 (red) airborne radar data in the Jutulstraumen drainage system (black outline). Previous airborne AWI EMR tracks (Steinhage et al., 2001) are highlighted blue and ice surface velocity field of Mougnot et al. (2019). The EPSG projection code for this and all following maps is epsg:3031

These data have supported detailed interpretations of the geological history of central and western DML, compilations of continental-scale bed topography and subglacial lake distributions (Huybrechts et al., 2000; Fretwell et al., 2013; Morlighem et al., 2019; Goeller et al., 2016), and targeted studies of bathymetry beneath DML's ice shelves (Goeller et al., 2016; Eisermann et al., 2020). To date, however, they have not been used for a regional-scale interpretation of subglacial landscape-forming processes that would complement and update the early interpretations of Näslund (2001).

Ice thickness and radar data

AWI's airborne JURAS-2018 survey in the Antarctic austral summer season of 2018/19 used the multichannel ultra-wideband (UWB) radar. The UWB system

is the improved version 5 of the Multichannel Coherent Radar Depth Sounder (MCoRDS) developed at the University of Kansas, Center for Remote Sensing of ice sheets (CReSIS) (Rodriguez-Morales et al., 2014). The radar system comprises an array of eight antenna elements, which is installed on AWI's *Polar 6* BT-67 aircraft. A detailed description of the instrument is given by Hale et al. (2016) and Rodriguez-Morales et al. (2014).

All JURAS-2018 radar profiles were recorded in a frequency range of 180-210 MHz and at a flight altitude equivalent to 365 m above ground. For radar data processing, we use the CReSIS Toolbox (CReSIS, 2020). The processing comprises algorithms for pulse compression, Synthetic Aperture Radar (SAR) processing via *fk* migration and array processing. Our SAR-processed radargrams have a trace interval of 15 m and a range resolution of 4.3 m. Franke et al. (2020a) give a detailed description of the radar acquisition and processing. The uncertainty of ice thickness estimation is defined by the RMS of the sum of the crossover mean at 62 intersections (24.7 m), which also includes a 1% error of the dielectric permittivity (for further details see Franke et al. 2020a).

The UWB radar data were acquired at the onset of streaming flow, as defined by ice surface velocities of 5 to 100 m a⁻¹, between the Troll (Norway) and Kohnen (Germany) stations (red lines in Figure G.3). In the south, the survey covers an area within which ice flow of the JG accelerates. The southern survey lines are oriented perpendicular to the direction of ice flow. The northern survey lines are oriented at ~60° to the southern survey lines. They cover parts of the eastern trough leading to the Jutulstraumen graben, which also correspond to an area of accelerating surface velocities and parts of the higher elevated topography to the east of it.

Complementary ice thickness radar data acquired with the AWI EMR system (Nixdorf et al., 1999) and depicted in Figure G.3 (blue lines) were gathered over the last three decades throughout DML (Steinhage et al., 2001; Riedel et al., 2012).

UWB radar ice thickness and bed topography

Ice thickness (z_{ice}) can be determined by converting the two way travel time (TWT) of the radar wave between the ice surface and bed reflection to depth. To do this, we use the depth-dependent electromagnetic wave speed in firn and ice,

$$c_{ice}(z) = \frac{c_0}{\sqrt{\epsilon'(z)}}, \quad (\text{G.1})$$

with the vacuum wave speed c_0 and the real part ϵ' of

the complex relative dielectric permittivity. Now we can convert the TWT t between ice surface and bed reflection:

$$z_{ice} = \frac{c_{ice} t}{2} + z_f, \quad (\text{G.2})$$

with a constant electromagnetic wave speed $c_{ice} = 1.685 \pm 8 \text{ m s}^{-1}$ and a firm correction factor $z_f = 10 \text{ m}$.

The bed topography is calculated by subtracting the ice thickness from an ice surface digital elevation model (REMA DEM; Howat et al. (2019)). For the creation of an improved bed topography, we use the SAGA GIS multi-level B-spline interpolation module (Conrad et al., 2015) where line coverage is dense and ordinary kriging where line coverage is sparse.

Valley morphology

Knowledge of the morphology, distribution and spatial orientation of subglacial landforms is important for investigating the ice sheet dynamic history of glaciated and previously-glaciated landscapes. For this study, we analyse the geometry of single valleys along the JURAS-2018 radar transects to determine the developmental stage for a glacial valley (Hirano and Aniya, 1988). We derive three geometrical parameters to categorise the valley type (see Figure G.4): (i) the valley depth D ($D = Z_{max} - Z_{min}$), (ii) the valley ratio, defined as the ratio between the valley depth D and the width at the valley top W_{top} ($R = D/W_{top}$), and (iii) the valley shape, which is defined as the ratio between the W_{top} and the width at the deepest 5% ($\Delta D = 5\% D$) of the valley.

Next to the trivial parameter D , we use the parameters R and R_w to obtain information about the geometry of the valley. The valley ratio factor R informs whether the valley is wide or narrow, whereas the valley shape factor R_w ($R_w = W_{top}/W_{bottom}$) helps to discriminate between U-shaped and V-shaped valleys. Here, we bear in mind that R_w is a relative measure, that is, a high R_w value states that the valley is more V-shaped than a valley with a low R_w and vice versa. Because valley shapes are sometimes not symmetrical, the elevation Z_{max} refers to the elevation of the lower shoulder.

Basal roughness

Topographic roughness is an indicator of subglacial conditions during past ice flow activity and a potential control on current ice sheet dynamics (Rippin et al., 2014; Franke et al., 2021). Here, we consider a spectral method (Li et al., 2010; Cooper et al., 2019) in combination with the root-mean-square (RMS) height (Shepard et al., 2001) to quantify subglacial roughness.

Spectrally-derived roughness is the relative vertical and horizontal variation of the ice-bed interface derived from the nadir bed reflection. We distinguish between two parameters: ζ , which reflects the vertical irregularity of the bed and provides information about the dominating vertical amplitudes; and η , which describes the dominating horizontal wavelength. For the calculation of these two parameters, we follow Franke et al. (2021). For this study, we use a moving window length of 512 samples, which corresponds to an approximate ground distance of 7.5 km.

In addition, we make use of the RMS height. The RMS height χ (or the standard deviation of heights about the mean) is defined by:

$$\chi = \left[\frac{1}{n-1} \sum_{i=1}^n (z(x_i) - \bar{z})^2 \right]^{\frac{1}{2}} \quad (\text{G.3})$$

where n represents the number of sample points, $z(x_i)$ the height of the bed at position x_i , and \bar{z} the mean height of the detrended profile.

Here, we perform a bed roughness analysis using the JURAS-2018 radar data. The combination of spectral vertical and horizontal roughness estimates enables us to infer the general appearance of the structure at the bed surface, whilst the RMS height provides information about the absolute elevation differences. The three methods require a uniform sample spacing, which is 15 m in the JURAS-2018 radar data.

Isostatic adjustment

We follow the simple approach of Rose et al. (2015) to simulate the isostatic rebound in order to get an idea of the ice-free paleotopography. Here, we only simulate the bed elevation prior to the start of glaciation of Antarctica (34 million years ago). The Airy–Heiskanen model (Airy, 1855) predicts that different topographic heights are fully compensated by variations in crustal thickness. We use this model to predict the elevation change the overburden ice will cause on the bed topography. For the calculation, we use densities of 915 kg m^{-3} for ice (ρ_i) 2750 kg m^{-3} for the crust (ρ_c) and 3330 kg m^{-3} for the mantle (ρ_m). For a single location or grid cell, we can calculate the uplift response h_r using:

$$h_r = \frac{\rho_c - \rho_i}{\rho_m - \rho_c}. \quad (\text{G.4})$$

This approach does not account for the entire complexity of processes involved in isostatic rebound after overburden ice removal (Rose et al., 2015). Furthermore, it is possible that the isostatically rebounded topography is underestimated and the original surface may

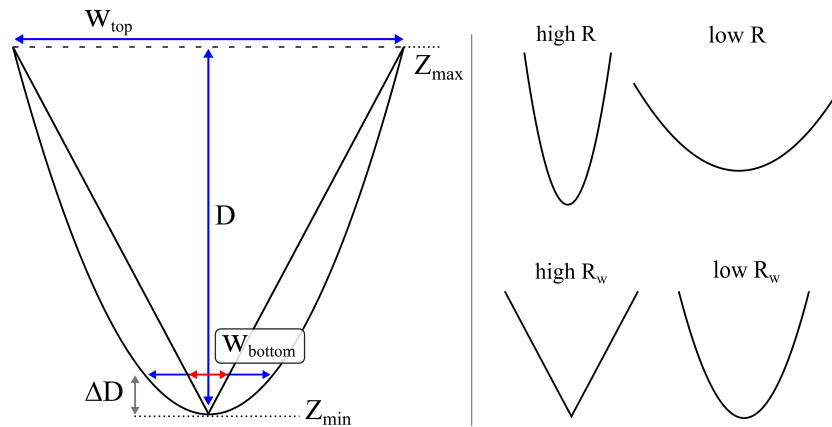


Figure G.4: Sketch indicating the deviations of parameters used to describe the geometries of valleys.

have formed at a higher elevation (Sugden et al., 1995). Nonetheless, we obtain a rough idea about the paleotopography and are able to use simple statistical methods to infer the characteristics of the landscape.

Hypsometry

An isostatically corrected bed topography allows us to analyse the frequency distribution of elevations (hypsometry) to characterise the landscape morphology (Brozović et al., 1997). The aim of this method is to generate indications of whether or not the landscape has a fluvially- or a glacially imprinted character. A widespread approach to hypsometry is to create a simple histogram of the frequencies in different elevation bins from a topographic DEM.

In this context, Brocklehurst and Whipple (2004) argue that hypsometry of large arbitrary regions potentially masks the detail in topographic variation in comparison to smaller regions. In addition, hypsometric analyses are sensitive to the resolution of the DEMs on which they are based. The method is most often applied for ice-free alpine regions where the topography is resolved with a grid cell resolution of 30–50 m (Brocklehurst and Whipple, 2004). By contrast, continental-scale bed topography DEMs of ice-covered areas in Antarctica have a resolution of 1 km (e.g. Fretwell et al., 2013) and are interpolated over large distances (up to tens to hundreds of kilometres).

To overcome some of these drawbacks, we follow Creyts et al. (2014) and apply hypsometry on the radar-derived ice thickness data of the AWI UWB survey after applying an isostatic correction (Eq. G.4). For this study, we use the results of a hypsometric analysis to compare different landscapes and to (i) infer the degree of glaciation (Brocklehurst and Whipple, 2004), (ii) discriminate between fluvial and glacial landscapes (Sternai et al., 2011) and, (iii) discuss modes of glacial landscape evolution (Sugden and John, 1976; Jamieson

et al., 2014).

Water flow routing

We apply a simple water flux scheme to simulate the general water flow network, assuming a completely ice-free isostatically compensated topography. By doing so, we aim to approximate features of the paleo-fluvial system in our survey region. We make use of the following SAGA GIS algorithms (Conrad et al., 2015): (i) the *fill sinks* module, to fill surface depressions with a minimum angle of 0.1° and (ii) the *catchment area* algorithm, to calculate the flow accumulation, which represents the number of accumulated cells.

Results

Radar data and bed topography

The profiles of the JURAS-2018 survey were designed to map the ice-bed interface at high resolution whilst also filling substantial gaps in the existing RES data. Most of these data gaps occur over deep topographic depressions in which the bed could not be detected by older radar systems (see Figure G.5 b). In the upstream region, data gaps occur in regions with comparable or thinner ice cover than in downstream regions with continuous bed reflections (Figure G.6). This indicates that higher englacial attenuation is causing the signal loss or that the bed reflection itself is weaker. Figure G.6 shows four JURAS-2018 radar profiles located: (a) where the main valley beneath the JG is widest, and probably deepest, (b) east of the valleys, and (c and d) upstream of the main trough (profile locations indicated in Figure G.5 a). Our radar data reveal that the two troughs in the upstream part of radar section D (Figure G.6 d), merge into the main trough (Figure G.6 c). Generally, the bed topography west of the main trunk of the JG shows a deeper relief in comparison to the area to the east.

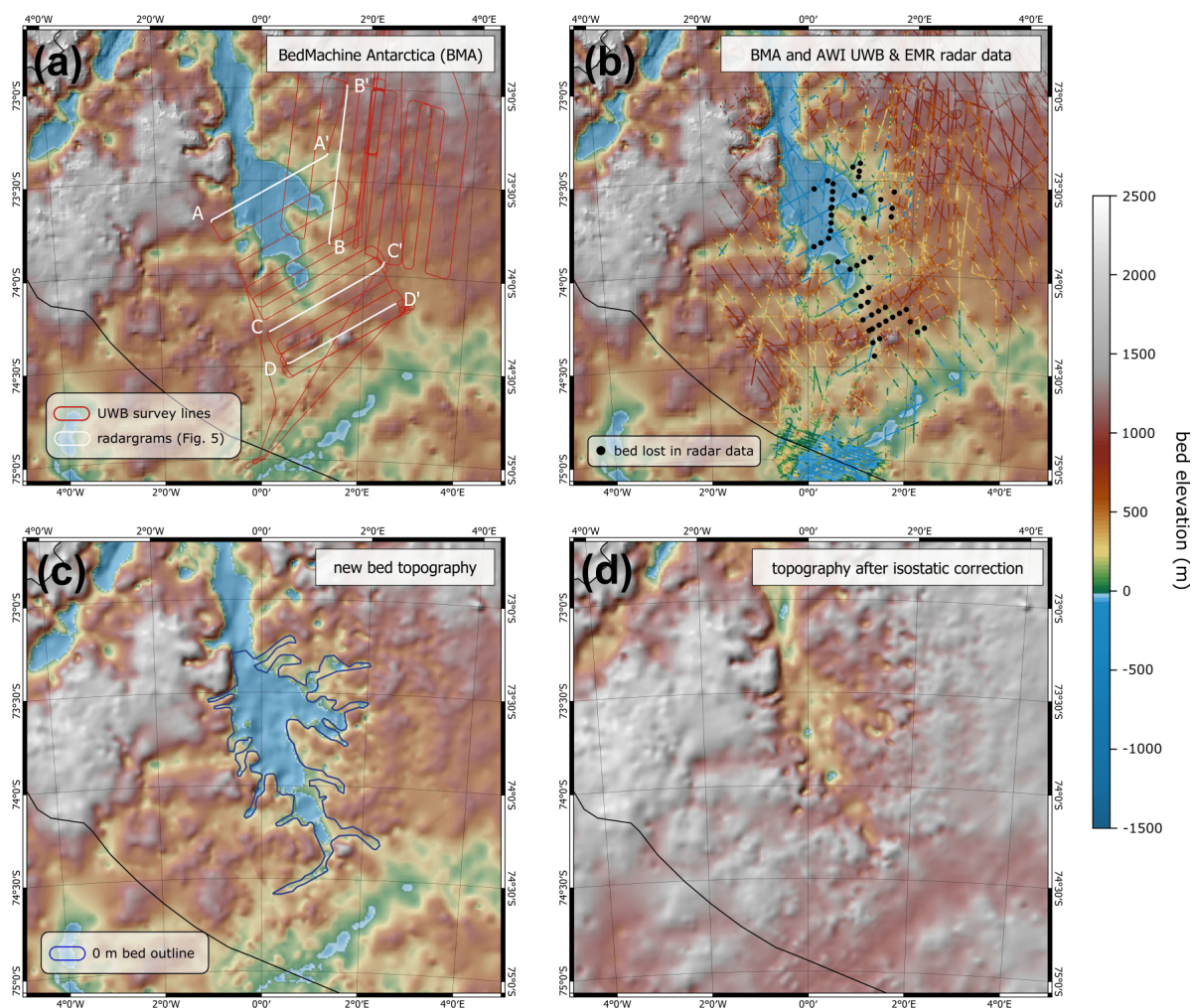


Figure G.5: Bed topography in survey area: Panel (a) shows the location of the JURAS-2018 survey lines (red lines) and selected radargrams of Figure G.6 (white lines) with BMA in background. Bed elevation data of the AWI EMR data in (b) correspond to data included in BMA, additional bed topography data of the AWI UWB and AWI EMR radar surveys, and the locations of UWB data gaps. Panel (c) depicts the new interpolated bed as well as an outline highlighting the extents of the trough network that lie below sea level. Panel (d) shows the bed topography after isostatic correction.

The JURAS-2018 data show regions where the position of the bed is either not interpretable at all or where bottom reflections are too faint for reliable imaging of the full valley geometry (see white outlines in Figure 4c and the radargrams in Figure G.6). Despite these difficulties, it is still possible to estimate these valleys' general topographies on the basis of the shape of the adjacent bed and internal layering. We use this information in conjunction with the new ice thickness data to create an outline of the trough network associated with the Jutulstraumen graben (see Figure G.5 c). A comparison between existing bed topography and new AWI UWB ice thickness data with a subsequent interpretation of the aforementioned data gaps enables the following observations:

1. Gaps occur in both the old and new radar data over pronounced topographic depressions, where no bed reflection could be detected. For

some of these regions, the new UWB data added new information.

2. A comparison of JURAS-2018 radar data and the BMA bed shows that BMA generally underestimates ice thicknesses in the JG region, and smooths over the relief of crests and troughs.
3. A network of very fine channels runs perpendicular to the ice flow direction. These channels merge with the Jutulstraumen graben. The network continues further southwards where it connects to the adjacent inland basin.

Valley morphology

The bed topography in the southern set of radar profiles shows generally different characteristic valley depths (D), valley ratios (R) and valley shapes (R_w) than in the northern set of radar profiles (Figure G.7 a–c). Valleys

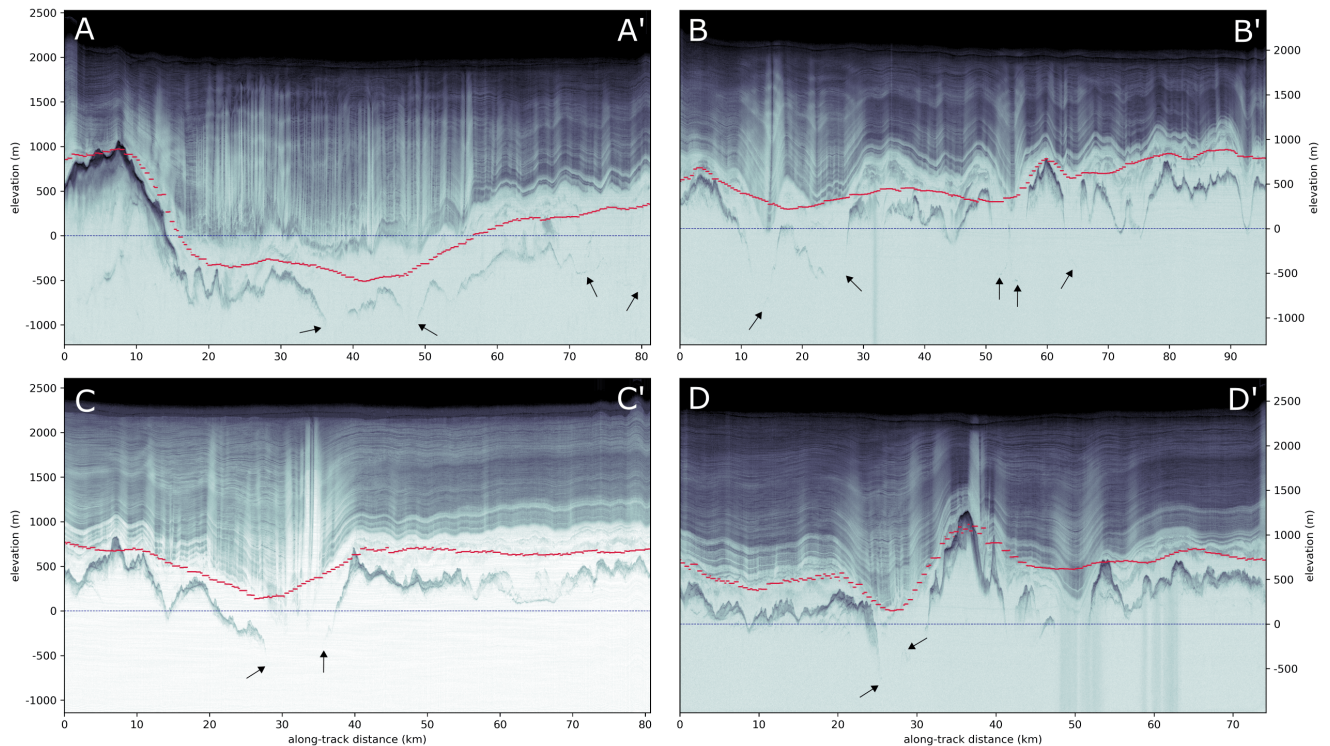


Figure G.6: JURAS-2018 radargrams showing internal ice layering and bed topography in the onset region of the JG. Profile locations are indicated in Figure G.5 a. The red dashed line represents the BMA bed topography elevation, while the blue line represents present sea level. Deep and faint bed reflections are indicated with black arrows.

located in the southern set are deeper (high D), wider (low R), and relatively more U-shaped (high R_w) than their northern counterparts. Although data gaps prevented the calculation of statistics for crossings of the main JG valleys, it is clear from those reflections that are available that they, too, class as deep, wide, U-shaped valleys (see Figures G.6 a, c and d).

We observe that the valleys far upstream in the southern radar set (red outline in Figure G.7 d) are shallower (low D) than valleys in the rest of the region. Based on the spatial distribution of the valley parameters, we define three regions with characteristic parameter combinations:

1. A region of wide and deep U-shaped valleys (black outline in Figure G.7 d). The main trunk of the JG represents the largest valley structure in this region. This area shows the lowest bed elevation on average, up to several hundred meters below present sea level (see Figure G.6 a).
2. A region of wide and shallow U-shaped valleys (red outline in Figure G.7 d). A representative radargram for this region is shown in Figure G.7 V₂. This region shows a bed elevation range around 0 to 1000 m above sea level.

3. A region of shallow and narrow V- and U-shaped valleys (blue outline in Figure G.7 d). The radargram in Figure G.7 V₁ illustrates the characteristic valley geometries for this region. We also note that this area shows the highest overall bed topography, with elevations of around 500 to 2000 m.

The radargram in Figure G.7 V₃ shows a mix between the characteristics of the black and blue outlined regions in Figure G.7 d. Deeper sections of the bed topography are incised by deep U-shaped valleys. The central section with higher elevation shows smaller V- and U-shaped valley depths.

Basal roughness

The analysis of valley geometries is somewhat subjective because it relies on a starting interpretation to select the set of features to analyse as valleys. To complement it, we use the analysis of basal roughness to quantify the bed topography in a systematic way. Figure G.8 shows the three roughness parameters (the spectral vertical and horizontal roughnesses, ζ and η , as well as RMS height, χ) and their relationship to the topographic setting and ice surface flow velocity. The majority of radar

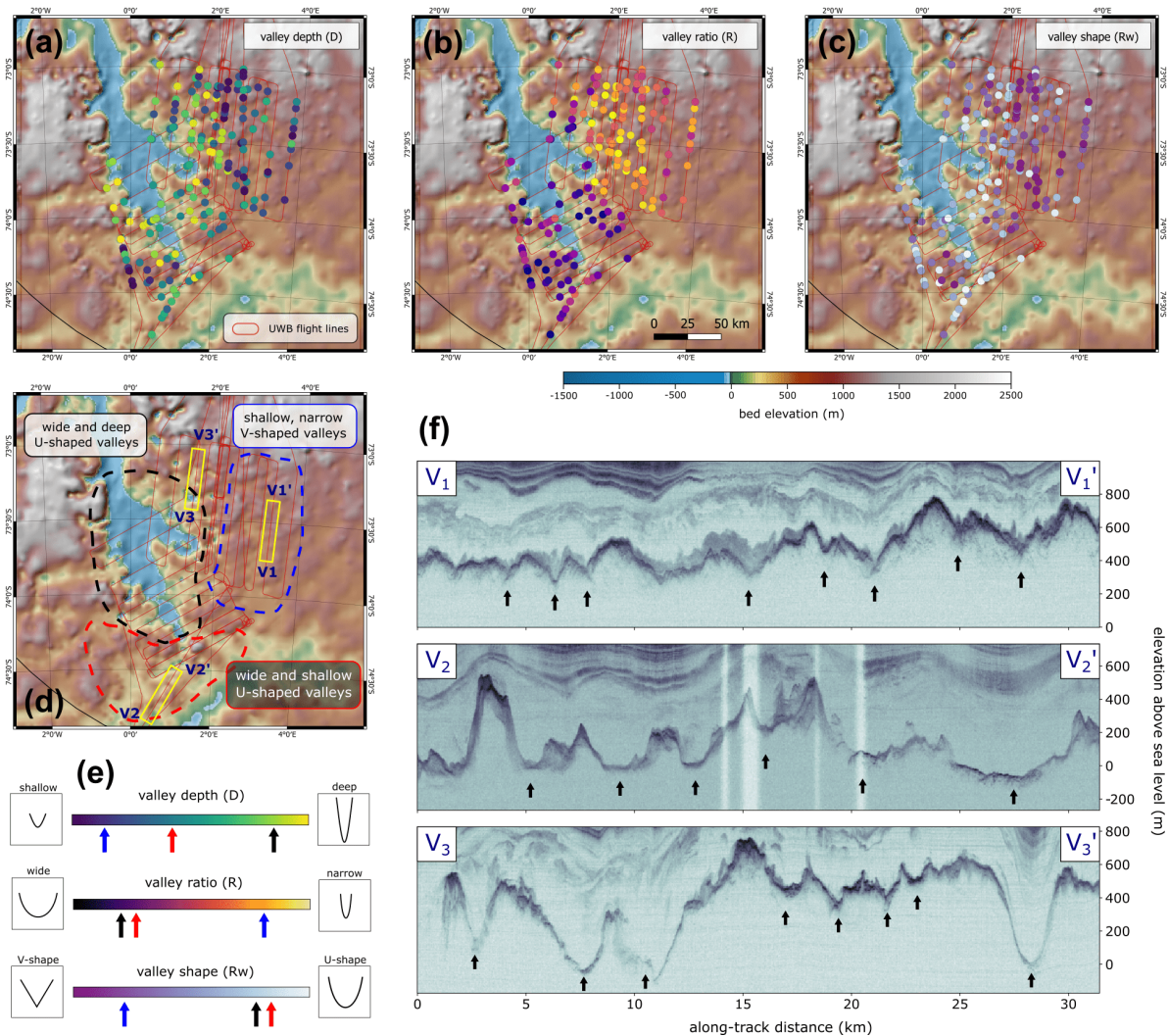


Figure G.7: Panels (a), (b) and (c) show the analysis of valley geometries (valley depth D , valley ratio R and valley shape R_w , respectively). In (d) we define three regions characterised by contrasting valley statistics. The average characteristics for each region are indicated with the black, blue and red arrows in panel (e) and summarized by idealized sketches next to the colour bars. Panel (f) represents three radar profiles ($V_{1,2,3}$) showing the contrasting ice bed morphologies in the three regions. Black arrows mark valleys that we considered for our analysis (see Figure G.4). Profile locations are indicated in (d) inside yellow boxes.

lines are oriented parallel to each other and approximately perpendicular to ice flow. This alignment promotes a more robust comparison of roughness values than would be possible with a random survey layout.

The highest vertical roughness values in the surveyed region tend to be concentrated below and around the main trunk of the JG in a region that we refer to as *Zone a* (white dashed outline in Figure G.8). *Zone a* hosts the largest valleys and the highest overall RMS height values, which peak well in excess of 400 m. The distribution of RMS height varies systematically with the distribution of deep and shallow valleys. *Zone a* also hosts all those data gaps in which the bed could not be detected, and in which higher vertical roughness values and longer wavelengths are expected.

Zone b (marked with a black dashed outline east of *Zone a*) shows a distinctive pattern of low vertical roughness and low RMS height. Here, the ice flow velocity is slightly lower than in *Zone a*, while bed topography is more elevated than in the west. Furthermore, we detect a small difference in horizontal roughness between *Zone a* and *Zone b*. Shorter wavelengths are more dominant in the eastern part of the northern radar set than in the western part.

Hypsometry

Analysis of the elevations derived from JURAS-2018 radar data reveals that, in addition to their contrasting basal roughnesses, zones *a* and *b* are hypsometrically distinct (Figure G.8d). In *Zone a*, bed elevation values scatter within a range of 1700 m with a maximum

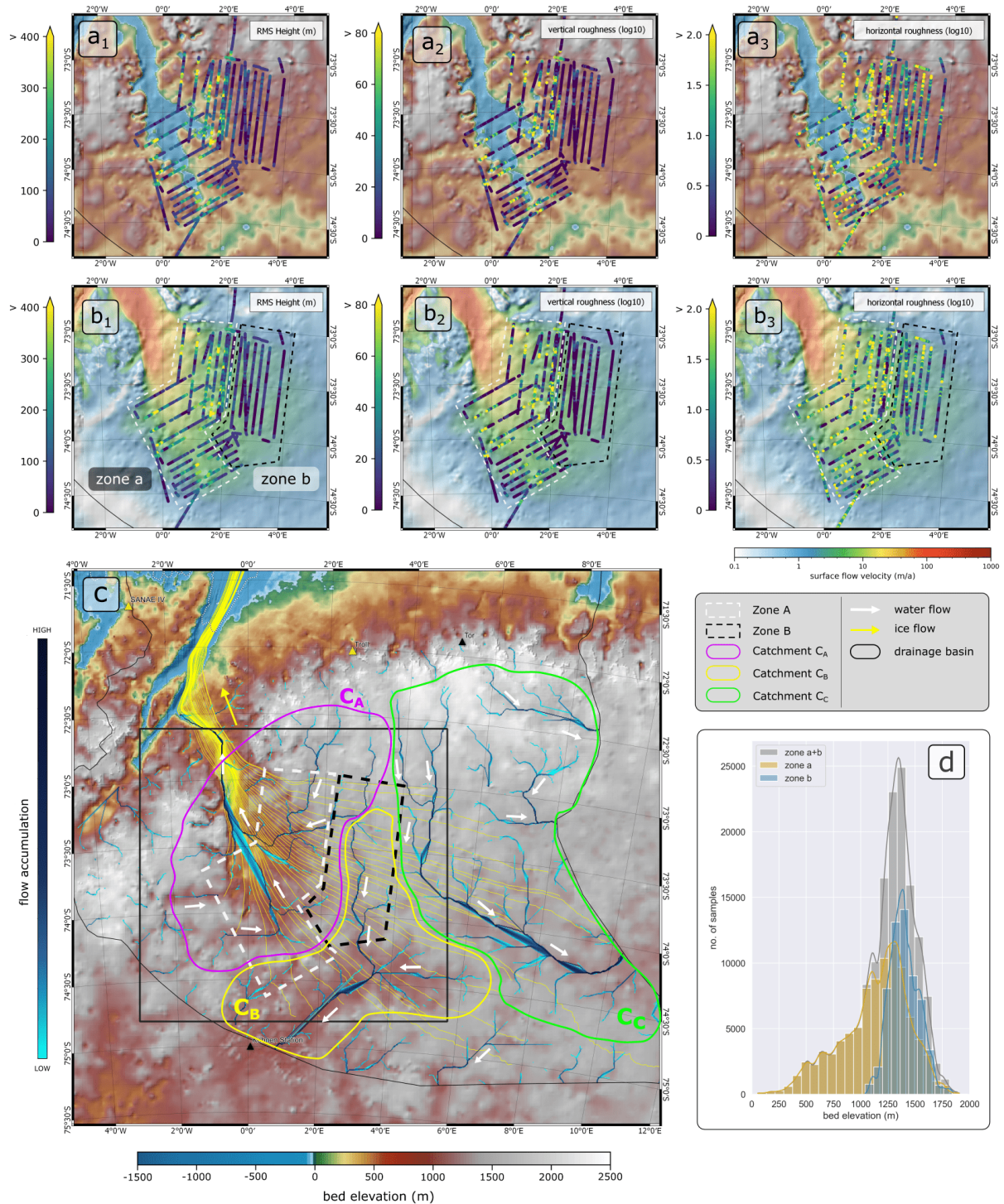


Figure G.8: Results of basal roughness, water flow routing and hypsometric analyses. Panels a_{1,2,3} and b_{1,2,3} show the parameters for RMS height, spectral vertical roughness and horizontal roughness plotted over the BMA bed topography and ice flow velocity, respectively. In panel (b) we divide the radar lines into two zones of distinctly differing basal roughness. Panel (c) shows the water flow routing on the isostatically-compensated bed elevation for a simulated ice-free region. The flow accumulation color code represents the number of accumulated (upstream) cells. Yellow lines indicate the present ice flow trajectories. The extent of the maps in panels (a) and (b) is indicated with a black outline. The general water flow direction is indicated by white arrows. We divide the water flow routing into three main catchments (C_{A,B,C}). The result of the hypsometric analyses of Zones A and B is presented in panel (d).

at 1000–1400 m elevation. Hence, the data are asymmetrically concentrated towards high elevations. This distribution does not include those low elevations that would have been encountered over gaps in the UWB data. The distribution of bed elevations in *Zone b* is narrower and, on average, higher. Its shape is approximately normal, with a slightly higher concentration of counts on its low-elevation flank. Analysis of combined elevations from both zones shows a similar pattern overall to that in *Zone a*.

Water flow routing

The water flow routing analysis aims to simulate the potential pre-glacial surface hydrology of the paleo-fluvial landscape. The calculations of water flow routing and the analysis of the hydrologic system was performed over the isostatically-compensated bed topography. In this study, we only show the water routing for the drainage basin of the JG. Most of the water originates from high-elevation regions within the DML mountain chain and is distributed towards three main catchments (Figure G.8 c):

1. Catchment C_A leads into the main trough below what is now the JG and covers the north-eastern part of the present-day ice drainage basin. Most of the routing pathways of this catchment are located within *Zone a*.
2. The second catchment, C_B , leads towards a topographic depression in the south of the present-day ice drainage basin. Most of the radar survey lines of *Zone b* are located in this catchment. Furthermore, the EPICA ice core is located at the south-western tip of this catchment.
3. Catchment C_C is located in the eastern part of the drainage basin where ice flow velocity is lowest. The flow routing indicates a flow direction towards the east.

The water routing pathways of catchment C_A correspond approximately to the present-day ice flow direction and propagation of subglacial water. The flow directions of C_B and C_C , however, lead towards regions of higher present-day ice thicknesses and therefore in the opposite direction to that of present ice flow. Thus, the direction of water flow may in part correspond to the current subglacial hydrology (Livingstone et al., 2013) which is not parallel to the direction of present ice flow.

Interpretation and discussion

Bed topography and valley morphology

Bed topography construction via simple interpolation techniques such as those used to generate Bedmap2 (Fretwell et al., 2013) relies for its resolution on the spatial data density of ice thickness measurements alone. Hence, the deep bed relief at the onset of the main trunk of the JG, where the bed could not be detected with radar techniques, is biased to shallower values in Bedmap2.

U-shaped valleys are distinctive features that suggest selective linear erosion on a local to regional scale, and thus an indication for the presence of warm based ice at the time of erosion (Sugden and John, 1976). The deepest troughs in the JG drainage area are located where present-day ice flow velocity and acceleration are highest. This suggests the region (black outline in Figure G.7 d) has experienced erosion over a long period. The wide but shallow U-shaped valleys in the upstream region (red outline in Figure G.7 d) are located close to the ice divide, where the ice column is thickest and current ice flow velocities are low. This indicates that the troughs of these valleys were probably not eroded under the present ice sheet configuration. The locations, shapes and sizes of these valleys suggest they most likely formed in regions of tectonic or lithologic weakness, or by the exploitation of valleys in a pre-existing fluvial network (e.g. Jordan et al., 2013; Baroni et al., 2005; Rose et al., 2015).

As an ice sheet grows to an intermediate size over a pre-existing fluvial landscape, selective linear erosion will deepen existing river valleys whilst sparing their flanks (Sugden, 1968, 1978). Ongoing ice sheet growth may lead to the development of a cold base, concomitant with a reduction of sliding and increase in ice-bed coupling (Jamieson et al., 2010). As a consequence, ice flow will be dominated by internal deformation and ice flow velocity will reduce (Creyts et al., 2014). At the base of the ice sheet, the consequence of all this may be a change from an erosive alpine environment to a passive setting, in which the bed undergoes little further modification. This kind of evolution may have occurred rapidly over the upstream part of the northern radar data set (blue outline in Figure G.7 d), which reflects the lowest degree of glacial erosion in its average high elevation and the dominance of shallow, V-shaped valleys.

The relative orientation of the radar line to the valley pathways is the largest source of uncertainty in the valley geometry analysis. Oblique crossings will make valleys appear artefactually too wide (a potential candidate could be the rightmost valley in Figure

G.7V₂). Artefacts like this will affect the determinations of valley ratio (R) and valley shape (R_w) but not of valley depth (D). Therefore, narrow and V-shaped valleys could potentially be underrepresented in Figures G.7b–c. The potential discrepancy between valley pathway and optimum radar line orientation mainly depends on the ice flow direction at the time of valley formation. Following this assumption, we can hypothesise under which scenarios the valleys have been most likely formed and can constrain the potential impact of the radar survey layout on the valley geometry calculations.

Basal roughness

Eisen et al. (2020) analysed basal roughness parameters for AWI EMR radar data on a continental scale in Antarctica. They observed low vertical roughness in the region east of our northern survey grid. This is consistent with low vertical roughness in *Zone b* (Figure G.8) and indicates that similar low vertical roughness values are to be expected further east. Eisen et al. (2020) show that basal roughness in this region is on average anisotropic in respect to the orientation of the radar lines to the direction of ice flow. The interpretation of basal roughness is thus limited and restricted to profiles perpendicular to ice flow. Similar to Rose et al. (2015), we note that the interpretation of low vertical roughness regions as indicative of fast ice flow and underlying marine sediments (e.g. Bingham and Siegert, 2007) is not valid in this area. In our study area, ice flow is fastest at the locations close to deeply incised troughs.

Most importantly, the analysis of spectral vertical roughness and RMS height confirms and supports the results of the valley geometry analysis, increasing the robustness of their interpretation. The spatial clusters of deep valleys correlate with high vertical roughness and RMS height, whereas the locations of shallow valleys correlate with low vertical roughness and RMS height. Furthermore, we observe that in *Zone b* the combination of narrow, V-shaped valleys is consistent with the dominance of short horizontal wavelengths.

Hypsometry

The main differences in the hypsometric curves for *Zone a* and *Zone b* (Figure G.8d) are in the location of the peak and the absolute distributions of bed elevations. Jamieson et al. (2014) relate hypsometric patterns to the topographic classifications of Sugden and John (1976). According to Jamieson et al. (2014), the broad distribution of bed elevation values and the maximum towards higher values (as we observe in *Zone a*) is characteristic of a landscape formed under selective linear erosion. The high mean bed elevation values in *Zone b*, in contrast, most likely point to a mainly alpine setting that

has been slightly modified by erosion. The relatively high mean elevations of both zones also suggest that the survey area has not been subject to areal scour or long-term denudation.

Brocklehurst and Whipple (2004) analysed different ice-free mountain regimes and found a relationship between the degree of glaciation and their hypsometric curves. Their analysis shows that hypsometric curves with maxima near higher elevations are indicative of fully glaciated landscapes, whereas maxima at lower elevations tend to characterise curves for non-glaciated landscapes. In this context, *Zone a*, which shows a total range of 0–2000 m elevation and a maximum towards higher elevations (1000–1500 m), can be interpreted as a more fully glaciated landscape than *Zone b*, which shows a slight trend towards a lower-elevation maximum (1400 m) with a total elevation range of 1000–1800 m (Figure G.8).

Landscape classification

Using the isostatically corrected bed topography (Figure G.5d) as an approximation of the pre-glacial surface, we note that the deepest and widest U-shaped valleys extend down to present sea level (Figure G.5d). The Jutulstraumen graben is of tectonic origin, dating back to the ice-free Jurassic, and so must have been subject to a long period of fluvial erosion after its formation (Näslund, 2001). This suggests that the bed in *Zone a* would have been subsequently modified by selective linear glacial erosion (Sugden and John, 1976). The subglacial troughs in *Zone a* are likely candidates for pre-glacial fluvial activity and subsequent selective erosion after the onset of glaciation (Sugden and John, 1976). Hence, the U-shaped valleys of *Zone a* are likely to follow the pre-existing fluvial system. It is likely that, regardless of the regional evolution in the extent and thickness of ice and the location of ice divides, some portion of the region's ice has always flowed through the Jutulstraumen graben towards the margin. Such longevity could explain the deeply-incised relief.

The analysis of basal roughness and hypsometry for the area east of the main trunk of the JG (*Zone b* in Figure G.8) points towards a largely preserved fluvial landscape whose origin precedes extensive glaciation. This is supported by the predominant appearance of shallow and narrow valleys at the glacier bed and the less variable and generally more elevated topography (and the resulting hypsometry). The mix of V- and U-shaped valleys suggests that the bed has been locally modified by glacial erosion at some point in the past, but that the degree of modification was probably limited due to the slow-flowing environment, such as a cold ice base (Sugden and John, 1976). Erosion under cold-based ice is several orders of magnitude slower than under temperate ice (Cuffey and Paterson, 2010).

Jacobs et al. (1995) suggest that intensive denudation by weathering and fluvial erosion were important landforming processes in western DML during the uplift that followed continental breakup in the middle and late Mesozoic. The fluvial landscape preserved east of the JG may have originated in this period. The flow regime calculated for that landscape, in catchments C_B and C_C , does not correlate with that of the drainage basin of the modern-day JG (Figure G.8 d). Today, the mountains of DML prevent the ice from flowing directly towards the margin, whilst the thicker inland ice in the interior of the AIS prevents southwards flow.

The present ice sheet configuration likely causes only selective linear erosion in the deep troughs connected to the Jutulstraumen graben and Jutulsessen Nunatak, where basal temperatures are probably above the pressure melting point. Elevated basal ice temperatures would increase englacial attenuation, consistent with the fact that the locations where we are unable to detect a bed reflection all lie in the deepest parts of the deepest troughs with fastest-flowing ice.

Basal thermal regime

Geothermal heat flow (GHF) at the base of the Antarctic Ice Sheet is a parameter which is subject to substantial uncertainty because it is difficult to measure *in situ* whilst geophysical models diverge greatly. Van Liefferinge et al. (2018) compare existing GHF data sets (Shapiro and Ritzwoller, 2004; Maule et al., 2005; An et al., 2015; Martos et al., 2017) to predict the probable distribution of basal ice that has been frozen over the last 1.5 million years. Their modelled area includes the ice divides at the upstream part of the JG drainage basin. Based on the individual GHF data sets, their modelling reveals it to be likely that the ice base has reached the pressure melting point at least once over the last 1.5 million years. Moreover, it has been shown that measured GHF in eastern DML is locally much higher than predicted by geophysical methods (Talalay et al., 2020), consistent with evidence for temperate bed conditions from subglacial water (Wilhelms et al., 2014; Weikusat et al., 2017).

Modelling results and borehole observations indicate that large parts of the JG drainage basin's ice bed are likely to be temperate. In combination with ice flow, this should lead to subglacial erosion. What remains open to question is exactly how temperate conditions affect processes at the glacier bed under slow flow velocities and near the ice divides. In view of the apparent preservation of fluvial landscapes in the basin, it can be suggested that erosion in such settings may be limited to subglacial fluvial action with relatively limited consequences for landscapes.

Landscape erosion and preservation

The bed morphology of the JG drainage system shows patterns of three successive and/or separate stages of landscape modification (Figure G.9). We regionally extend our interpretation of the structures we have classified in our study and define the following interpretation for landscape erosion and preservation: (1) a pre-glacial landscape shaped by fluvial erosion, minimal glacial erosion and preserved thereafter, (2) a fluvial landscape, which was more strongly modified by selective linear erosion at some time in the past, and (3) an intensively selectively-eroded trough system, in which the erosion has been long-lived and is still ongoing.

The glacial landscape close to the trough system of the JG and further upstream (black and red outlines in Figure G.9) was probably formed by a local alpine-like glacier system during a period when Antarctica was influenced by a warmer climate than present (Holmlund and Näslund, 1994; Young et al., 2011). A former ice divide may have separated the two regions during this period (yellow dashed line in Figure G.9). At some point, as ice coverage increased (Holmlund and Näslund, 1994), erosion terminated in the U-shaped valleys in the south and west (red dashed arrows in Figure G.9), but continued further north where ice surface velocities are still fast today (black dashed arrows in Figure G.9). At locations where the ice sheet grows beyond a critical size, we expect basal melting and the development of a subglacial water network (Creys et al., 2014). In the study area, this might explain the increased erosion rates that locally formed exceptionally deep valleys. Erosion mechanisms, such as plucking and abrasion, are mainly controlled by basal sliding, which requires in turn a lubricated bed (Hallet, 1996). By contrast, re-freezing of subglacial water in cold-based areas with a thinner ice thickness (Creys et al., 2014) is probably also a factor in the preservation of the fluvial landscape in the east.

Jamieson et al. (2010) use an ice sheet and erosion model to investigate the subglacial landscape evolution of Antarctica since the Oligocene (34 million years ago). Those authors use three different stages for their simulations (see Table 1 in Jamieson et al. (2010)) where: (a) ice sheets grow and shrink at similar scales to northern hemisphere Pleistocene ice sheets (34–14 million years before present), (b) cooling shifts the system towards development of a continental polar ice sheet (14–13.6 million years ago) and (c) the continental polar ice sheet stabilises and subsequently experiences only minor changes (13.6 million years ago to present). In order to establish a rough timing for the landscape evolution in the JG drainage system, we compare the erosion rates modelled by Jamieson et al. (2010) with our landscape classification. For the comparison, we mainly rely on the results shown in Figure 6 in Jamieson

et al. (2010).

The model predicts that high erosion rates at the Jutulstraumen graben developed at the end of stage (a) and persisted there ever since. We note that, at the beginning of stage (a), high erosion rates were restricted to the high-elevation areas of the DML mountains. The fluctuating regional ice caps may not have seen the development of a stable ice divide around the JG drainage basin like today's. Instead, they may have drained via ice streams running both northwards through the Jutulstraumen graben and towards the southwest. We find that modelled erosion rates in the lower-elevation regions (e.g. in the Jutulstraumen graben and further upstream) must have been higher than in the highlands. This is consistent with the evidence for the lesser degree of erosion in *Zone b* than in *Zone a*. We note that the erosion rates in our survey region during stages (b) and (c) correspond to those of today's ice-dynamic setting. That is, constant high erosion rates are to be found only in the Jutulstraumen graben.

Considering the modelling of Jamieson et al. (2010), we can estimate that the bed in *Zone b* was most likely modified in the early stages of glaciation of Antarctica (34–14 million years ago) during ice coverage minima when erosion was most intense at high altitudes. By contrast, we consider the U-shaped valleys upstream of the main trunk of JG were formed during a cycle of greater ice extent in stage (a), while more and faster ice was streaming towards the south-west. Erosion in both these settings probably ceased with the onset of continental-scale glaciation of Antarctica in stage (b; 14–13.6 million years ago). Hence, we conclude that the modelling results of Jamieson et al. (2010) are a plausible explanation for the morphological structures identified in our study.

Summary and conclusions

We extend the radar data inventory for central DML, and in particular for the immediate surrounding of the JG onset region. We use the existing bed topography data in combination with new high-resolution UWB radar data to analyse the morphology of the bed in the JG drainage system. For our analysis, we rely on the distribution of bed elevations (hypsometry), parameterisations of the roughness of the bed, estimates of subglacial valley types, and analyses of their slopes and connectivity for characterisation of a pre-glacial fluvial system.

The glacial landscape in the JG drainage system can be divided into three different regimes:

1. The area of contemporary high ice flow velocities

marking the JG, which represents an alpine landscape that has been extensively modified by selective linear (glacial) erosion. The deep U-shaped valleys in this area were probably initiated by fluvial erosion and subsequently modified by long-term glacial erosion.

2. The area upstream of the JG in the south and west of the drainage system, where fluvial valleys were modified by a short period of glacial erosion before ice drainage in them ceased. The resulting U-shaped valleys are relatively small in comparison to the large valleys in the vicinity of the main trunk of JG. This area is close to the present-day ice divide, and ice flow velocities are consequently slow with less than 5 m a^{-1} .
3. The high-elevation region east of the JG, where the ice is immobile under the present ice sheet configuration. The abundance of small-scale V- and U-shaped valleys indicates the activity of an ancient alpine fluvial network which has been only locally and slightly modified by glacial erosion.

The transformation to the current ice sheet configuration around 14 million years ago has limited basal erosion everywhere except in the direct vicinity of the JG, where long-term ice stream activity has excavated several kilometres deep subglacial valleys. This applies in particular to the high-elevation area in the east, where the ice sheet is trapped between the DML mountains in the north and the much thicker ice further south, resulting in the preservation of the pre-glacial fluvial landscape at the ice sheet base. The Jutulstraumen graben is presently the only passage for ice to flow towards the ice sheet margin. This setting must have been a different one to create the U-shaped valleys, which reach up almost to the ice divide in the South-West of the survey area. The high probability that the ice base of our survey region is at pressure melting point leads to the assumption that the potential for erosion in this area is limited as long as ice flow velocities are low. The landscape evolution established in this study is in good agreement with modelled erosion rates in Antarctica over the last 34 million years by Jamieson et al. (2010).

Acknowledgements

We thank the Ken Borek crew as well as Martin Gehrmann and Sebastian Spelz of AWI's technical staff of the research aircraft Polar 6. John Paden (University of Kansas) assisted remotely during the field campaign. We would like to thank Tobias Binder for the implementation of the AWI UWB radar as well as an acquisition backup system. Without his work, it would

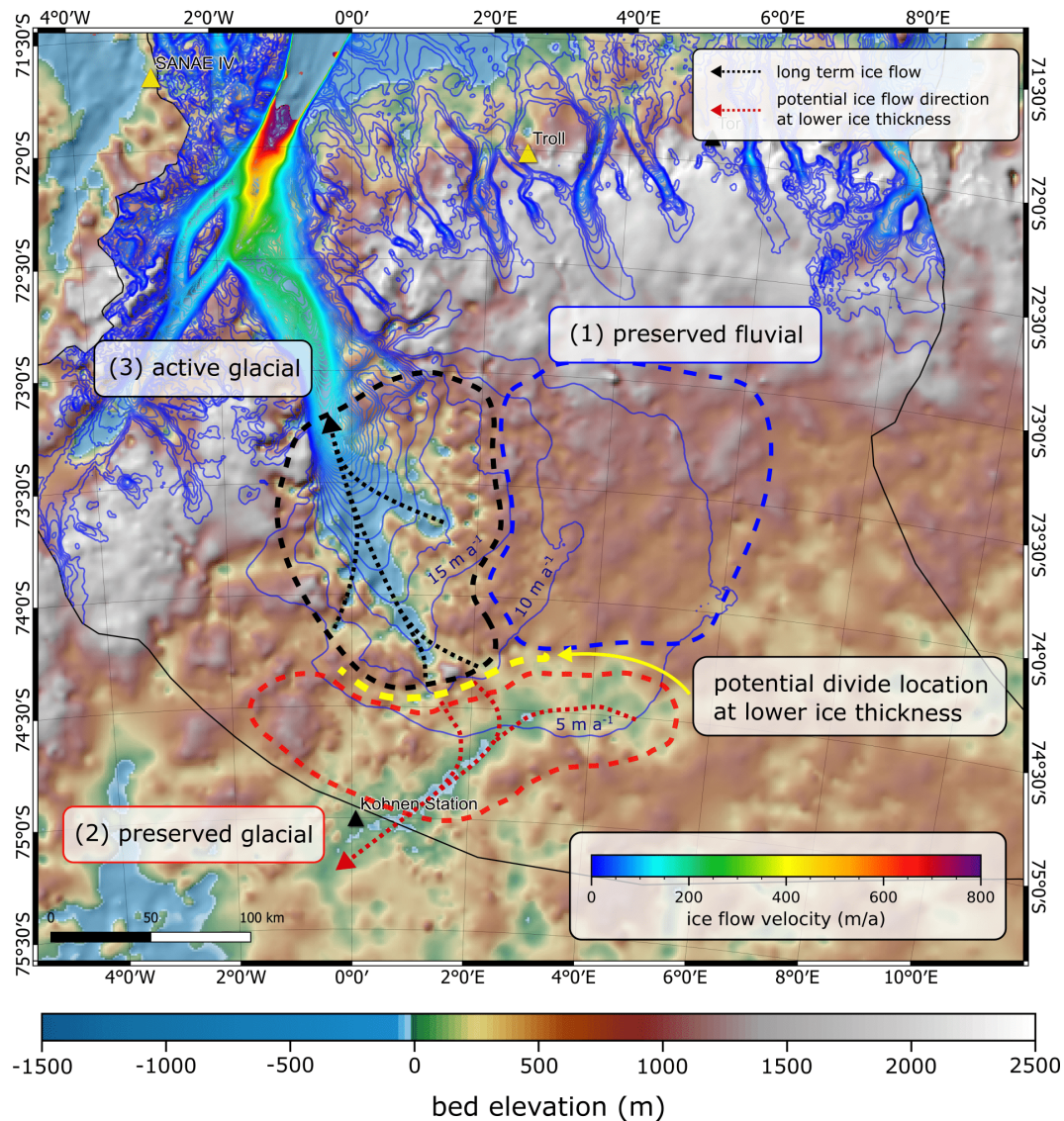


Figure G.9: Summary of our landscape interpretation for the JG drainage system. The active glacial system (black dashed outline) is located in the immediate surroundings of the JG main trunk where the ice flow accelerates to join it. The preserved fluvial system (red dashed outline) is located to the East and the preserved inactive glacial system (red dashed outline) to the West and South of the JG main trunk. The respective outlines do not represent physically-fixed boundaries but instead areas of dominant landscape characteristics. Ice flow velocity is indicated with contour lines in a 5 m a^{-1} interval.

not have been possible to realize the campaign. Logistical support in Antarctica was provided at Troll Station (Norway), Novolazarewskaja-Station (Russia) and Kohlen Station (Germany). The authors would like to thank Emerson E&P Software, Emerson Automation Solutions, for providing licenses in the scope of the Emerson Academic Program.

Data availability

Ice thickness data from the complete JURAS-2018 AWI UWB radar survey (Franke et al., 2020b) are available at <https://doi.pangaea.de/10.1594/PANGAEA.911475>. Ice surface velocities from Mougnot et al.

(2019) are available at the National Snow and Ice Data Center (NSIDC), <https://doi.org/10.7280/D10D4Z>. The drainage system boundaries (Rignot et al., 2013) can be obtained here: <https://doi.org/10.5067/AXE4121732AD>. The Landsat Image Mosaic of Antarctica (LIMA; Bindenschadler et al. (2008)) can be downloaded at <http://lima.usgs.gov>. The BedMachine Antarctica V01 data set from Morlighem et al. (2019) is available at <https://nsidc.org/data/nsidc-0756>. The locations of Antarctic research facilities were obtained from the Quantarctica3 package (<https://www.npolar.no/quantarctica/>).

Author contributions

Steven Franke, Hannes Eisermann, Daniela Jansen and Wilfried Jokat designed the study with contributions of Heinz Miller and Olaf Eisen. Steven Franke and Hannes Eisermann wrote the manuscript. Daniela Jansen designed the JURAS-2018 radar survey and acquired the data together with Steven Franke. Steven Franke performed the data processing and generated the results with contributions from Daniela Jansen, Veit Helm and Daniel Steinhage and Jölund Asseng. All authors discussed and commented the manuscript.

Bibliography

- Airy, G. B. III. On the computation of the effect of the attraction of mountain-masses, as disturbing the apparent astronomical latitude of stations in geodetic surveys. *Philosophical Transactions of the Royal Society of London*, 145:101–104, 1855. doi: 10.1098/rstl.1855.0003. URL <https://royalsocietypublishing.org/doi/abs/10.1098/rstl.1855.0003>.
- An, M., Wiens, D. A., Zhao, Y., Feng, M., Nyblade, A., Kanao, M., Li, Y., Maggi, A., and L  v  que, J.-J. Temperature, lithosphere-asthenosphere boundary, and heat flux beneath the Antarctic Plate inferred from seismic velocities. *Journal of Geophysical Research: Solid Earth*, 120(12):8720–8742, 2015. doi: <https://doi.org/10.1002/2015JB011917>. URL <https://agupubs.onlinelibrary.wiley.com/doi/abs/10.1002/2015JB011917>.
- Baroni, C., Noti, V., Ciccacci, S., Righini, G., and Salvatore, M. C. Fluvial origin of the valley system in northern Victoria Land (Antarctica) from quantitative geomorphic analysis. *Bulletin of the Geological Society of America*, 117(1-2):212–228, 2005. ISSN 00167606. doi: 10.1130/B25529.1. URL <https://pubs.geoscienceworld.org/gsabulletin/article-lookup/117/1-2/212>.
- Bindschadler, R., Vornberger, P., Fleming, A., Fox, A., Mullins, J., Binnie, D., Paulsen, S. J., Granneman, B., and Gorodetzky, D. The Landsat Image Mosaic of Antarctica. *Remote Sensing of Environment*, 112(12):4214 – 4226, 2008. ISSN 0034-4257. doi: <https://doi.org/10.1016/j.rse.2008.07.006>. URL <http://www.sciencedirect.com/science/article/pii/S003442570800223X>.
- Bingham, R. G. and Siegert, M. J. Radar-derived bed roughness characterization of Institute and M  ller ice streams West Antarctica, and comparison with Siple Coast ice streams. *Geophysical Research Letters*, 34(21), nov 2007. doi: 10.1029/2007gl031483. URL <https://doi.org/10.1029/2007gl031483>.
- Brocklehurst, S. H. and Whipple, K. X. Hypsometry of glaciated landscapes. *Earth Surface Processes and Landforms*, 29(7):907–926, 2004. ISSN 01979337. doi: 10.1002/esp.1083. URL <https://doi.org/10.1002/esp.1083>.
- Brozovi  c, N., Burbank, D. W., and Meigs, A. J. Climatic limits on landscape development in the northwestern Himalaya. *Science*, 276(5312):571–574, 1997. ISSN 00368075. doi: 10.1126/science.276.5312.571. URL <https://science.sciencemag.org/content/276/5312/571.abstract>.
- Cawood, P. A., Strachan, R. A., Pisarevsky, S. A., Gladkochub, D. P., and Murphy, J. B. Linking collisional and accretionary orogens during rodinia assembly and breakup: Implications for models of supercontinent cycles. *Earth and Planetary Science Letters*, 449:118–126, 2016. ISSN 0012-821X. doi: <https://doi.org/10.1016/j.epsl.2016.05.049>. URL <https://www.sciencedirect.com/science/article/pii/S0012821X16302746>.
- Conrad, O., Bechtel, B., Bock, M., Dietrich, H., Fischer, E., Gerlitz, L., Wehberg, J., Wichmann, V., and B  hner, J. System for Automated Geoscientific Analyses (SAGA) v. 2.1.4. *Geoscientific Model Development*, 8(7):1991–2007, 2015. doi: 10.5194/gmd-8-1991-2015. URL <https://gmd.copernicus.org/articles/8/1991/2015/>.
- Cooper, M. A., Jordan, T. M., Schroeder, D. M., Siegert, M. J., Williams, C. N., and Bamber, J. L. Subglacial roughness of the Greenland Ice Sheet: relationship with contemporary ice velocity and geology. *The Cryosphere*, 13(11): 3093–3115, nov 2019. doi: 10.5194/tc-13-3093-2019. URL <https://doi.org/10.5194/2Ftc-13-3093-2019>.
- CRISIS. CRISIS Toolbox [computer software], Lawrence, Kansas, USA. Retrieved from <https://github.com/CRISIS>, 2020. URL https://ops.cresis.ku.edu/wiki/index.php/Main_Page.
- Creyts, T. T., Ferraccioli, F., Bell, R. E., Wolovick, M., Corr, H., Rose, K. C., Frearson, N., Damaske, D., Jordan, T., Braaten, D., and Finn, C. Freezing of ridges and water networks preserves the Gamburtsev Subglacial Mountains for millions of years. *Geophysical Research Letters*, 41(22): 8114–8122, nov 2014. doi: 10.1002/2014gl061491. URL <https://doi.org/10.1002/2014gl061491>.
- Cuffey, K. and Paterson, W. S. B. The Physics of Glaciers 4th Edition. *Elsivier, Academic Press*, 2010.
- Eagles, G., Karlsson, N. B., Ruppel, A., Steinhage, D., Jokat, W., and L  ufer, A. Erosion at extended continental margins: Insights from new aerogeophysical data in eastern Dronning Maud Land. *Gondwana Research*, 63:105–116, 2018. ISSN 1342-937X. doi: <https://doi.org/10.1016/j.gr.2018.05.011>. URL <https://www.sciencedirect.com/science/article/pii/S1342937X18301655>.
- Eisen, O., Winter, A., Steinhage, D., Kleiner, T., and Humbert, A. Basal roughness of the East Antarctic Ice Sheet in relation to flow speed and basal thermal state. *Annals of Glaciology*, 61(81):162–175, apr 2020. ISSN 0260-3055. doi: 10.1017/aog.2020.47.
- Eisermann, H., Eagles, G., Ruppel, A., Smith, E. C., and Jokat, W. Bathymetry beneath ice shelves of western Dronning Maud Land, East Antarctica, and implications on ice shelf stability. *Geophysical Research Letters*, 47(12):e2019GL086724, 2020. doi: <https://doi.org/10.1029/2019GL086724>. URL <https://agupubs.onlinelibrary.wiley.com/doi/abs/10.1029/2019GL086724>.
- Elliot, D. H. Jurassic magmatism and tectonism associated with Gondwanaland break-up: an Antarctic perspective. *Geological Society, London, Special Publications*, 68(1): 165–184, 1992. doi: 10.1144/GSL.SP.1992.068.01.11. URL <https://doi.org/10.1144/GSL.SP.1992.068.01.11>.
- Ferraccioli, F., Jones, P. C., Curtis, M. L., and Leat, P. T. Subglacial imprints of early Gondwana break-up as identified from high resolution aerogeophysical data over western Dronning Maud Land, East Antarctica. *Terra Nova*, 17(6):573–579, dec 2005. ISSN 09544879. doi: 10.1111/j.1365-3121.2005.00651.x. URL <https://doi.org/10.1111/j.1365-3121.2005.00651.x>.

- Franke, S., Jansen, D., Binder, T., Dörr, N., Helm, V., Paden, J., Steinhage, D., and Eisen, O. Bed topography and subglacial landforms in the onset region of the Northeast Greenland Ice Stream. *Annals of Glaciology*, pages 1–11, mar 2020a. doi: 10.1017/aog.2020.12. URL <https://doi.org/10.1017/aog.2020.12>.
- Franke, S., Jansen, D., and Helm, V. Ice Thickness from Jutulstraumen Glacier recorded with the airborne AWI UWB radar system, Antarctica. 2020b. doi: 10.1594/PANGAEA.911475. URL <https://doi.pangaea.de/10.1594/PANGAEA.911475>.
- Franke, S., Jansen, D., Beyer, S., Neckel, N., Binder, T., Paden, J., and Eisen, O. Complex basal conditions and their influence on ice flow at the onset of the northeast Greenland ice stream. *Journal of Geophysical Research: Earth Surface*, 126(3):e2020JF005689, 2021. doi: 10.1029/2020JF005689. URL <https://agupubs.onlinelibrary.wiley.com/doi/abs/10.1029/2020JF005689>.
- Fretwell, P., Pritchard, H. D., Vaughan, D. G., Bamber, J. L., Barrand, N. E., Bell, R., Bianchi, C., Bingham, R. G., Blankenship, D. D., Casassa, G., Catania, G., Callens, D., Conway, H., Cook, A. J., Corr, H. F. J., Damaske, D., Damm, V., Ferraccioli, F., Forsberg, R., Fujita, S., Gim, Y., Gogineni, P., Griggs, J. A., Hindmarsh, R. C. A., Holmlund, P., Holt, J. W., Jacobel, R. W., Jenkins, A., Jokat, W., Jordan, T., King, E. C., Kohler, J., Krabill, W., Riger-Kusk, M., Langley, K. A., Leitchenkov, G., Leuschen, C., Luyendyk, B. P., Matsuoka, K., Mouginot, J., Nitsche, F. O., Nogi, Y., Nost, O. A., Popov, S. V., Rignot, E., Rippin, D. M., Rivera, A., Roberts, J., Ross, N., Siegert, M. J., Smith, A. M., Steinhage, D., Studinger, M., Sun, B., Tinto, B. K., Welch, B. C., Wilson, D., Young, D. A., Xiangbin, C., and Zirizzotti, A. Bedmap2: improved ice bed surface and thickness datasets for Antarctica. *The Cryosphere*, 7(1):375–393, feb 2013. doi: 10.5194/tc-7-375-2013. URL <https://doi.org/10.5194/tc-7-375-2013>.
- Goeller, S., Steinhage, D., Thoma, M., and Grosfeld, K. Assessing the subglacial lake coverage of Antarctica. *Annals of Glaciology*, 57(72):109–117, jul 2016. ISSN 02603055. doi: 10.1017/aog.2016.23. URL <http://creativecommons.org/licenses/by/4.0/>.
- Hale, R., Miller, H., Gogineni, S., Yan, J. B., Rodriguez-Morales, F., Leuschen, C., Paden, J., Li, J., Binder, T., Steinhage, D., Gehrmann, M., and Braaten, D. Multi-channel ultra-wideband radar sounder and imager. In *2016 IEEE International Geoscience and Remote Sensing Symposium (IGARSS)*. IEEE, jul 2016. doi: 10.1109/igarss.2016.7729545. URL <https://doi.org/10.1109/igarss.2016.7729545>.
- Hallet, B. Glacial quarrying: a simple theoretical model. *Annals of Glaciology*, 22:1–8, 1996. doi: 10.3189/1996Aog22-1-1-8.
- Hirano, M. and Aniya, M. A rational explanation of cross-profile morphology for glacial valleys and of glacial valley development. *Earth Surface Processes and Landforms*, 13(8):707–716, 1988. doi: <https://doi.org/10.1002/esp.3290130805>. URL <https://onlinelibrary.wiley.com/doi/abs/10.1002/esp.3290130805>.
- Holbourn, A., Kuhnt, W., Schulz, M., and Erlenkeuser, H. Impacts of orbital forcing and atmospheric carbon dioxide on Miocene ice-sheet expansion. *Nature*, 438(7067):483–487, 2005. doi: 10.1038/nature04123. URL <https://www.nature.com/articles/nature04123>.
- Holmlund, P. and Näslund, J.-O. Antarctica, formed by wet-based mountain glaciation and not by the present ice sheet. *Boreas*, 23:139–148, 1994. ISSN 0300-9483. doi: 10.1111/j.1502-3885.1994.tb00594.x. URL <https://doi.org/10.1111/j.1502-3885.1994.tb00594.x>.
- Howat, I. M., Porter, C., Smith, B. E., Noh, M.-J., and Morin, P. The Reference Elevation Model of Antarctica. *The Cryosphere*, 13(2):665–674, feb 2019. ISSN 1994-0424. doi: 10.5194/tc-13-665-2019. URL <https://www.the-cryosphere.net/13/665/2019/>.
- Huybrechts, P., Steinhage, D., Wilhelms, F., and Bamber, J. Balance velocities and measured properties of the Antarctic ice sheet from a new compilation of gridded data for modelling. *Annals of Glaciology*, 30(1996):52–60, 2000. ISSN 02603055. doi: 10.3189/172756400781820778. URL <https://doi.org/10.3189/172756400781820778>.
- Jacobs, J. Strukturelle Entwicklung und Abkühlungsgeschichte der Heimefrontfjella (Westliches Dronning Maud Land/Antarktika) = Structural evolution and cooling history of the Heimefrontfjella (western Dronning Maud Land/Antarctica). *Berichte zur Polarforschung (Reports on Polar Research)*, 97, 1991. URL <https://epic.awi.de/id/eprint/26274/1/BerPolarforsch199197.pdf>.
- Jacobs, J. and Thomas, R. J. Himalayan-type indenter-escape tectonics model for the southern part of the late Neoproterozoic–early Paleozoic East African–Antarctic orogen. *Geology*, 32(8):721–724, 2004. doi: 10.1130/G20516.1. URL <https://doi.org/10.1130/G20516.1>.
- Jacobs, J., Hejl, E., Wagner, G., and Weber, K. Apatite fission track evidence for contrasting thermal and uplift histories of metamorphic basement blocks in western Dronning Maud Land. *Recent Progress in Antarctic Earth Science, Terapub, Tokyo*, pages 323–330, 1992.
- Jacobs, J., Ahrendt, H., Kreutzer, H., and Weber, K. K-Ar ⁴⁰Ar-¹⁹Ar and apatite fission-track evidence for Neoproterozoic and Mesozoic basement rejuvenation event in the Heimefrontfjella and Mannefallknäusane (East Antarctica). *Precambrian Research*, 75:251–262, 1995. doi: 10.1016/0301-9268(95)80009-7. URL [https://doi.org/10.1016/0301-9268\(95\)80009-7](https://doi.org/10.1016/0301-9268(95)80009-7).
- Jacobs, J., Fanning, C. M., Henjes-Kunst, F., Olesch, M., and Paech, H.-J. Continuation of the Mozambique Belt into East Antarctica: Grenville-age metamorphism and polyphase Pan-African high-grade events in central Dronning Maud Land. *The Journal of Geology*, 106(4):385–406, 1998.
- Jacobs, J., Opås, B., Elburg, M., Läufer, A., Estrada, S., Ksienzyk, A. K., Damaske, D., and Hofmann, M. Cryptic sub-ice geology revealed by a U-Pb zircon study of glacial till in Dronning Maud Land, East Antarctica. *Precambrian Research*, 294:1–14, 2017. doi: 10.1016/j.precamres.2017.03.012.

- URL <https://doi.org/10.1016/j.precamres.2017.03.012>.
- Jamieson, S. S., Sugden, D. E., and Hulton, N. R. The evolution of the subglacial landscape of Antarctica. *Earth and Planetary Science Letters*, 293(1-2):1–27, 2010. ISSN 0012821X. doi: 10.1016/j.epsl.2010.02.012. URL <http://dx.doi.org/10.1016/j.epsl.2010.02.012>.
- Jamieson, S. S., Stokes, C. R., Ross, N., Rippin, D. M., Bingham, R. G., Wilson, D. S., Margold, M., and Bentley, M. J. The glacial geomorphology of the Antarctic ice sheet bed. *Antarctic Science*, 26(6):724–741, 2014. doi: 10.1017/S0954102014000212. URL <https://doi.org/10.1017/S0954102014000212>.
- Jokat, W., Boebel, T., König, M., and Meyer, U. Timing and geometry of early Gondwana breakup. *Journal of Geophysical Research: Solid Earth*, 108(B9), 2003. doi: 10.1029/2002JB001802. URL <https://doi.org/10.1029/2002JB001802>.
- Jordan, T. A., Ferraccioli, F., Ross, N., Corr, H. F., Leat, P. T., Bingham, R. G., Rippin, D. M., le Brocq, A., and Siegert, M. J. Inland extent of the Weddell Sea Rift imaged by new aerogeophysical data. *Tectonophysics*, 585:137–160, 2013. ISSN 0040-1951. doi: <https://doi.org/10.1016/j.tecto.2012.09.010>. URL <http://www.sciencedirect.com/science/article/pii/S0040195112005689>.
- Leinweber, V. T. and Jokat, W. The Jurassic history of the Africa–Antarctica corridor—new constraints from magnetic data on the conjugate continental margins. *Tectonophysics*, 530:87–101, 2012. doi: 10.1016/j.tecto.2011.11.008. URL <https://doi.org/10.1016/j.tecto.2011.11.008>.
- Li, X., Sun, B., Siegert, M. J., Bingham, R. G., Tang, X., Zhang, D., Cui, X., and Zhang, X. Characterization of subglacial landscapes by a two-parameter roughness index. *Journal of Glaciology*, 56(199):831–836, 2010. doi: 10.3189/002214310794457326. URL <https://doi.org/10.3189/002214310794457326>.
- Livingstone, S. J., Clark, C. D., Woodward, J., and Kingslake, J. Potential subglacial lake locations and meltwater drainage pathways beneath the Antarctic and Greenland ice sheets. *The Cryosphere*, 7(6):1721–1740, nov 2013. doi: 10.5194/tc-7-1721-2013. URL <https://doi.org/10.5194/tc-7-1721-2013>.
- Martos, Y. M., Catalán, M., Jordan, T. A., Golynsky, A., Golynsky, D., Eagles, G., and Vaughan, D. G. Heat Flux Distribution of Antarctica Unveiled. *Geophysical Research Letters*, 44(22):11,417–11,426, 2017. doi: <https://doi.org/10.1002/2017GL075609>. URL <https://agupubs.onlinelibrary.wiley.com/doi/abs/10.1002/2017GL075609>.
- Maule, C. F., Purucker, M. E., Olsen, N., and Mosegaard, K. Heat Flux Anomalies in Antarctica Revealed by Satellite Magnetic Data. *Science*, 309(5733):464–467, 2005. ISSN 0036-8075. doi: 10.1126/science.1106888. URL <https://science.sciencemag.org/content/309/5733/464>.
- McLelland, J. M., Selleck, B. W., Bickford, M., Tollo, R., Bartholomew, M., Hibbard, J., and Karabinos, P. Review of the Proterozoic evolution of the Grenville Province, its Adirondack outlier, and the Mesoproterozoic inliers of the Appalachians. *From Rodinia to Pangea: The Lithotectonic Record of the Appalachian Region: Geological Society of America Memoir*, 206:21–49, 2010.
- Mieth, M. and Jokat, W. New aeromagnetic view of the geological fabric of southern Dronning Maud Land and Coats Land, East Antarctica. *Gondwana Research*, 25(1):358–367, 2014. ISSN 1342-937X. doi: <https://doi.org/10.1016/j.gr.2013.04.003>. URL <http://www.sciencedirect.com/science/article/pii/S1342937X13001226>.
- Morlighem, M., Rignot, E., Binder, T., Blankenship, D., Drews, R., Eagles, G., Eisen, O., Ferraccioli, F., Forsberg, R., Fretwell, P., Goel, V., Greenbaum, J. S., Gudmundsson, H., Guo, J., Helm, V., Hofstede, C., Howat, I., Humbert, A., Jokat, W., Karlsson, N. B., Lee, W. S., Matsuoka, K., Millan, R., Mouginot, J., Paden, J., Pattyn, F., Roberts, J., Rosier, S., Ruppel, A., Seroussi, H., Smith, E. C., Steinhage, D., Sun, B., van den Broeke, M. R., van Ommen, T. D., van Wessem, M., and Young, D. A. Deep glacial troughs and stabilizing ridges unveiled beneath the margins of the Antarctic ice sheet. *Nature Geoscience*, 13(2):132–137, dec 2019. doi: 10.1038/s41561-019-0510-8. URL <https://doi.org/10.1038/s41561-019-0510-8>.
- Mouginot, J., Rignot, E., Björk, A. A., van den Broeke, M., Millan, R., Morlighem, M., Noël, B., Scheuchl, B., and Wood, M. Forty-six years of Greenland Ice Sheet mass balance from 1972 to 2018. *Proceedings of the National Academy of Sciences*, 116(19):9239–9244, apr 2019. doi: 10.1073/pnas.1904242116. URL <https://doi.org/10.1073/pnas.1904242116>.
- Mueller, C. O. and Jokat, W. The initial Gondwana breakup: a synthesis based on new potential field data of the Africa–Antarctica Corridor. *Tectonophysics*, 750:301–328, 2019. doi: 10.1016/j.tecto.2018.11.008. URL <https://doi.org/10.1016/j.tecto.2018.11.008>.
- Näslund, J. O. Landscape development in western and central Dronning Maud Land, East Antarctica. *Antarctic Science*, 13(3):302–311, 2001. ISSN 09541020. doi: 10.1017/S0954102001000438. URL <https://doi.org/10.1017/S0954102001000438>.
- Nixdorf, U., Steinhage, D., Meyer, U., Hempel, L., Jenett, M., Wachs, P., and Miller, H. The newly developed airborne radio-echo sounding system of the AWI as a glaciological tool. *Annals of Glaciology*, 29:231–238, 1999. doi: 10.3189/172756499781821346. URL <https://doi.org/10.3189/172756499781821346>.
- Oerlemans, J. Numerical Experiments on Large Scale Glacial Erosion. *Zeitschrift für Gletscherkunde und Glaziologie*, 20:107–126, 2010. URL https://dspace.library.uu.nl/bitstream/handle/1874/21026/oerlemans_84_numericalexperimentonglacialerosion.pdf.

- Riedel, S., Jokat, W., and Steinhage, D. Mapping tectonic provinces with airborne gravity and radar data in Dronning Maud Land, East Antarctica. *Geophysical Journal International*, 189(1):414–427, 2012. ISSN 0956540X. doi: 10.1111/j.1365-246X.2012.05363.x. URL <https://doi.org/10.1111/j.1365-246X.2012.05363.x>.
- Rignot, E., Jacobs, S., Mouginot, J., and Scheuchl, B. Ice-Shelf Melting Around Antarctica. *Science*, 341(6143):266–270, 2013. ISSN 0036-8075. doi: 10.1126/science.1235798. URL <https://science.sciencemag.org/content/341/6143/266>.
- Rippin, D., Bingham, R., Jordan, T., Wright, A., Ross, N., Corr, H., Ferraccioli, F., Brocq, A. L., Rose, K., and Siegert, M. Basal roughness of the Institute and Möller Ice Streams West Antarctica: Process determination and landscape interpretation. *Geomorphology*, 214:139–147, jun 2014. doi: 10.1016/j.geomorph.2014.01.021. URL <https://doi.org/10.1016%2Fj.geomorph.2014.01.021>.
- Rodriguez-Morales, F., Gogineni, S., Leuschen, C. J., Paden, J. D., Li, J., Lewis, C. C., Panzer, B., Gomez-Garcia Alvestegui, D., Patel, A., Byers, K., Crowe, R., Player, K., Hale, R. D., Arnold, E. J., Smith, L., Gifford, C. M., Braaten, D., and Panton, C. Advanced multifrequency radar instrumentation for polar Research. *IEEE Transactions on Geoscience and Remote Sensing*, 52(5):2824–2842, 2014. ISSN 01962892. doi: 10.1109/TGRS.2013.2266415. URL <https://doi.org/10.1109/TGRS.2013.2266415>.
- Rose, K. C., Ross, N., Jordan, T. A., Bingham, R. G., Corr, H. F. J., Ferraccioli, F., Le Brocq, A. M., Rippin, D. M., and Siegert, M. J. Ancient pre-glacial erosion surfaces preserved beneath the West Antarctic Ice Sheet. *Earth Surface Dynamics*, 3(1):139–152, 2015. doi: 10.5194/esurf-3-139-2015. URL <https://esurf.copernicus.org/articles/3/139/2015/>.
- Shapiro, N. M. and Ritzwoller, M. H. Inferring surface heat flux distributions guided by a global seismic model: particular application to antarctica. *Earth and Planetary Science Letters*, 223(1):213 – 224, 2004. ISSN 0012-821X. doi: <https://doi.org/10.1016/j.epsl.2004.04.011>. URL <http://www.sciencedirect.com/science/article/pii/S0012821X0400247X>.
- Shepard, M. K., Campbell, B. A., Bulmer, M. H., Farr, T. G., Gaddis, L. R., and Plaut, J. J. The roughness of natural terrain: A planetary and remote sensing perspective. *Journal of Geophysical Research: Planets*, 106(E12): 32777–32795, dec 2001. doi: 10.1029/2000je001429. URL <https://doi.org/10.1029%2F2000je001429>.
- Shevenell, A. E., Kennett, J. P., and Lea, D. W. Middle Miocene southern ocean cooling and Antarctic cryosphere expansion. *Science*, 305(5691):1766–1770, 2004.
- Siegert, M. J., Taylor, J., and Payne, A. J. Spectral roughness of subglacial topography and implications for former ice-sheet dynamics in East Antarctica. *Global and Planetary Change*, 45(1-3):249–263, feb 2005. doi: 10.1016/j.gloplacha.2004.09.008. URL <https://doi.org/10.1016%2Fj.gloplacha.2004.09.008>.
- Steinhage, D., Nixdorf, U., Meyer, U., and Miller, H. *Annals of Glaciology*. doi: 10.3189/172756499781821409. URL <https://doi.org/10.3189/172756499781821409>.
- Steinhage, D., Nixdorf, U., Meyer, U., and Miller, H. Subglacial topography and internal structure of Central and Western Dronning Maud Land, Antarctica, determined from airborne radio echo sounding. *Journal of Applied Geophysics*, 47(3-4):183–189, jul 2001. ISSN 09269851. doi: 10.1016/S0926-9851(01)00063-5. URL [https://doi.org/10.1016/S0926-9851\(01\)00063-5](https://doi.org/10.1016/S0926-9851(01)00063-5).
- Sternai, P., Herman, F., Fox, M. R., and Castelltort, S. Hypsometric analysis to identify spatially variable glacial erosion. *Journal of Geophysical Research: Earth Surface*, 116(F3), 2011. doi: <https://doi.org/10.1029/2010JF001823>. URL <https://agupubs.onlinelibrary.wiley.com/doi/abs/10.1029/2010JF001823>.
- Sugden, D. E. The Selectivity of Glacial Erosion in the Cairngorm Mountains, Scotland. *Transactions of the Institute of British Geographers*, 45:79–92, 1968. ISSN 00202754, 14755661. URL <http://www.jstor.org/stable/621394>.
- Sugden, D. E. Glacial Erosion by the Laurentide Ice Sheet. *Journal of Glaciology*, 20(83):367–391, 1978. doi: 10.3189/S0022143000013915.
- Sugden, D. E. and Jamieson, S. S. R. The pre-glacial landscape of Antarctica. *Scottish Geographical Journal*, 134(3-4): 203–223, 2018. doi: 10.1080/14702541.2018.1535090. URL <https://doi.org/10.1080/14702541.2018.1535090>.
- Sugden, D. E. and John, B. S. Glaciers and Landscape: A Geomorphological Approach. *Edward Arnold, A member of the Hodder Headline Group*, 1976.
- Sugden, D. E., Denton, G. H., and Marchant, D. R. Landscape evolution of the Dry Valleys, Transantarctic Mountains: Tectonic implications. *Journal of Geophysical Research: Solid Earth*, 100(B6):9949–9967, 1995. doi: <https://doi.org/10.1029/94JB02895>. URL <https://agupubs.onlinelibrary.wiley.com/doi/abs/10.1029/94JB02895>.
- Talalay, P., Li, Y., Augustin, L., Clow, G. D., Hong, J., Lefebvre, E., Markov, A., Motoyama, H., and Ritz, C. Geothermal heat flux from measured temperature profiles in deep ice boreholes in Antarctica. *The Cryosphere*, 14(11):4021–4037, 2020. doi: 10.5194/tc-14-4021-2020. URL <https://tc.copernicus.org/articles/14/4021/2020/>.
- Van Liefferinge, B., Pattyn, F., Cavitte, M. G. P., Karlsson, N. B., Young, D. A., Sutter, J., and Eisen, O. Promising Oldest Ice sites in East Antarctica based on thermodynamical modelling. *The Cryosphere*, 12(8):2773–2787, 2018. doi: 10.5194/tc-12-2773-2018. URL <https://tc.copernicus.org/articles/12/2773/2018/>.
- Weikusat, I., Jansen, D., Binder, T., Eichler, J., Faria, S. H., Wilhelms, F., Kipfstuhl, S., Sheldon, S., Miller, H., Dahl-Jensen, D., and Kleiner, T. Physical analysis of an Antarctic ice core towards an integration of micro- and macrodynamics of polar ice*. *Philosophical Transactions of the Royal Society A: Mathematical, Physical and Engineering*

- Sciences*, 375(2086):20150347, 2017. doi: 10.1098/rsta.2015.0347. URL <https://royalsocietypublishing.org/doi/abs/10.1098/rsta.2015.0347>.
- Wilhelms, F., Miller, H., Gerasimoff, M. D., Drücker, C., Frenzel, A., Fritzsche, D., Grobe, H., Hansen, S. B., Hilmarsson, S., Hoffmann, G., and et al. The EPICA Dronning Maud Land deep drilling operation. *Annals of Glaciology*, 55(68):355–366, 2014. doi: 10.3189/2014AoG68A189. URL <https://doi.org/10.3189/2014AoG68A189>.
- Young, D. A., Wright, A. P., Roberts, J. L., Warner, R. C., Young, N. W., Greenbaum, J. S., Schroeder, D. M., Holt, J. W., Sugden, D. E., Blankenship, D. D., Van Ommen, T. D., and Siegert, M. J. A dynamic early East Antarctic Ice Sheet suggested by ice-covered fjord landscapes. *Nature*, 474(7349): 72–75, 2011. ISSN 00280836. doi: 10.1038/nature10114. URL <https://doi.org/10.1038/nature10114>.

Appendix H

PAPER IV

RESEARCH LETTER

Evidence of cascading subglacial water flow at Jutulstraumen Glacier (Antarctica) derived from Sentinel-1 and ICESat-2 measurements

Niklas Neckel^{1,†} , Steven Franke^{1,†} , Veit Helm¹ , Reinhard Drews² , Daniela Jansen¹ 

[†] Steven Franke and Niklas Neckel contributed equally to this work.

¹ Alfred Wegener Institute, Helmholtz Centre for Polar and Marine Research, Bremerhaven, Germany

² Department of Geosciences, Eberhard Karls University Tübingen, Germany

In revision since 22 May 2021 at Geophysical Research Letters

Abstract

Migration of subglacial water underneath thick Antarctic ice is difficult to observe, but is known to influence the dynamics of ice flow. Here we analyse a six-year time series of displacement maps from differential Sentinel-1 SAR interferometry (DInSAR) in the upstream region of Dronning Maud Land's Jutulstraumen Glacier. Our results reveal significant short-term (<2 month) interconnected subsidence- and uplift events of the ice surface, which we interpret as a pressure response to the drainage and filling of subglacial water pockets. This indicates an episodic cascade-like water transport with longer quiescent phases. Abrupt events appear in the DInSAR time series and are confirmed by repeat-track analysis of ICESat-2 data. The events can be traced for a one-year period along a ~175 km flow path. We are able to observe the migration of subglacial water with unprecedented spatial and temporal resolution, providing a new observational baseline to further develop subglacial hydrological models.

Received: 22 May 2021

Plain Language Summary

Subglacial lakes and the movement of subglacial water play an important role in the way how ice flows in the Antarctic Ice Sheet. The drainage and filling of subglacial lakes is reflected in subsidence and uplift at the ice surface, which can be monitored by satellite based elevation measurements. In this study we detect these elevation changes of the ice surface at the onset of Dronning Maud Land's largest glacier (Jutulstraumen Glacier, Antarctica). We register a number of connected events which show us where and when subglacial water moves downstream. We find that the water flows similarly to a self-tipping swimming pool bucket: water beneath the ice is localized and abruptly moves from one place to another after some time has passed. Using a number of echolocation techniques we find that the water flows along preferential flowpaths in the subglacial topography. These are the first confirmed subglacial water movements in central Dronning Maud Land, an area where no subglacial water flow has been observed previously. The episodic nature of water flow is a new observation that will help us to understand how the subglacial water forms its own plumbing system beneath these large glaciers.

Introduction

Large quantities of basal meltwater are transported from the interior of the Antarctic Ice Sheet to downstream areas of faster ice flow, reducing the frictional resistance at the glacier bed (Siegfried and Fricker, 2018; Joughin et al., 2004). Subglacial water is known to travel hundreds of kilometers along such well-defined pathways (Wingham et al., 2006; Fricker et al., 2014). Indirect evidence of subglacial water movement was first detected by analyzing localized surface elevation changes of mountain glaciers (Iken et al., 1983; Fat; Capps et al., 2010). More recently, similar processes were also reported for the Greenland (Howat et al., 2015; Willis et al., 2015; Bowling et al., 2019) and Antarctic Ice Sheets (Spikes et al., 2003; Gray et al., 2005; Fricker et al., 2007; Joughin et al., 2016). Furthermore, it has been postulated that such events cannot be treated as isolated phenomena, but are interconnected through subglacial drainage networks (e.g. Fricker et al., 2007; Ashmore and Bingham, 2014).

Most observations of ice-surface uplift and subsidence are derived from satellite altimetry (e.g. Fricker et al., 2007; Siegfried and Fricker, 2018), while a few studies also use Synthetic Aperture Radar (SAR) interferometry (e.g. Gray et al., 2005; Milillo et al., 2017), SAR speckle tracking (e.g. Joughin et al., 2016; Hoffman et al., 2020) or DEM differencing (Flament et al., 2014; Smith et al., 2017). Subglacial lakes detected with these methods are often referred to as active lakes, in contrast to lakes solely detected using radio-echo sounding (RES), which may or may not show temporal variations at the ice surface (Ashmore and Bingham, 2014). However, the detection of active lakes requires observation periods of months to years to coherently map ice surface elevation changes (Siegfried and Fricker, 2018). First studies indicate that the majority of active lakes are located beneath fast flowing ice streams in Antarctica (Siegfried and Fricker, 2018; Smith et al., 2017; Fricker et al., 2014; Gray et al., 2005; Wingham et al., 2006; Malczyk et al., 2020). Goeller et al. (2016) found evidence for possible subglacial lake locations in Dronning Maud Land (DML) in RES data. However, no active lakes have been reported for central DML so far. Consequently, little is known about the subglacial hydrology, water transport and the impact on local ice dynamics (Thoma et al., 2012).

In this study we derive short-term changes in ice surface displacement by means of differential SAR interferometry (DInSAR) on Sentinel-1 data. These displacement anomalies reveal a cascade-like pattern starting in the onset region of Jutulstraumen Glacier (JG, Fig. H.1). Additional ICESat-2 repeat-track measurements capture more gradual elevation changes at the same locations. However, when integrating the DInSAR displacements over the repeat period of ICESat-2 we find

similar results for both datasets. This indicates vertical movement of the ice surface, which we interpret as filling and drainage of subglacial water pockets. We further use a dense grid of ultra-wideband (UWB) RES data to obtain detailed information of the bed topography. The combination of these datasets indicates that the subglacial water transport follows the hydraulic gradient and migrates downstream in a localized trough system.

Study site

JG is the largest ice draining glacier in DML. Ice flows from the polar plateau to the lower coastal section of the East Antarctic Ice Sheet (EAIS) and follows the bearing of the Jutulstraumen graben through the DML escarpment (Andersen et al., 2020). The JG trough is 40–50 km wide, 1.6 km below present sea level (Fretwell et al., 2013) at its deepest location, and ice flow velocity accelerates to 760 m a^{-1} at the grounding line (Mouginot et al., 2019). Our survey area is located at the onset of JG where ice flow is convergent and accelerating from 5 to 100 m a^{-1} (Fig. H.1 c). Possible locations for subglacial lakes have been reported in central DML by Goeller et al. (2016). However, their analysis is solely based on radio-echo sounding (RES) surveys and the potential lake locations are restricted to the margins of the JG drainage basin. Ice thickness and bed topography have been extensively mapped in this region (Steinhage et al., 2001; Ferraccioli et al., 2005; Riedel et al., 2012) and indicate a spatially variable alpine landscape, which has been most likely generated by relief-controlled glacial erosion, sub-aerial weathering and fluvial erosion from mountain glaciers (Näslund, 2001).

Material and methods

We applied Synthetic Aperture Radar Interferometry (InSAR) on Sentinel-1 Interferometric Wide (IW) swath mode data to detect small-scale surface displacements in the satellite's Line Of Sight (LOS). We hypothesize that only minor variations in horizontal ice movement occur on short time scales, as is commonly assumed (e.g. Rignot et al., 2011; Joughin et al., 2016; Friedl et al., 2020). We computed 247 double-differential interferograms between 2015-05 and 2020-09, covering large parts of our study region (Fig. H.1 b). However, only a few double differential interferograms show a distinct bull's-eye fringe pattern likely related to subsidence or uplift (Fig. H.1 d–f), while the majority show close to zero LOS displacements, adding support to the assumption that horizontal ice flow remain constant over the 12-day repeat pass period of Sentinel-1. Steady horizontal displacements were removed from the time series by

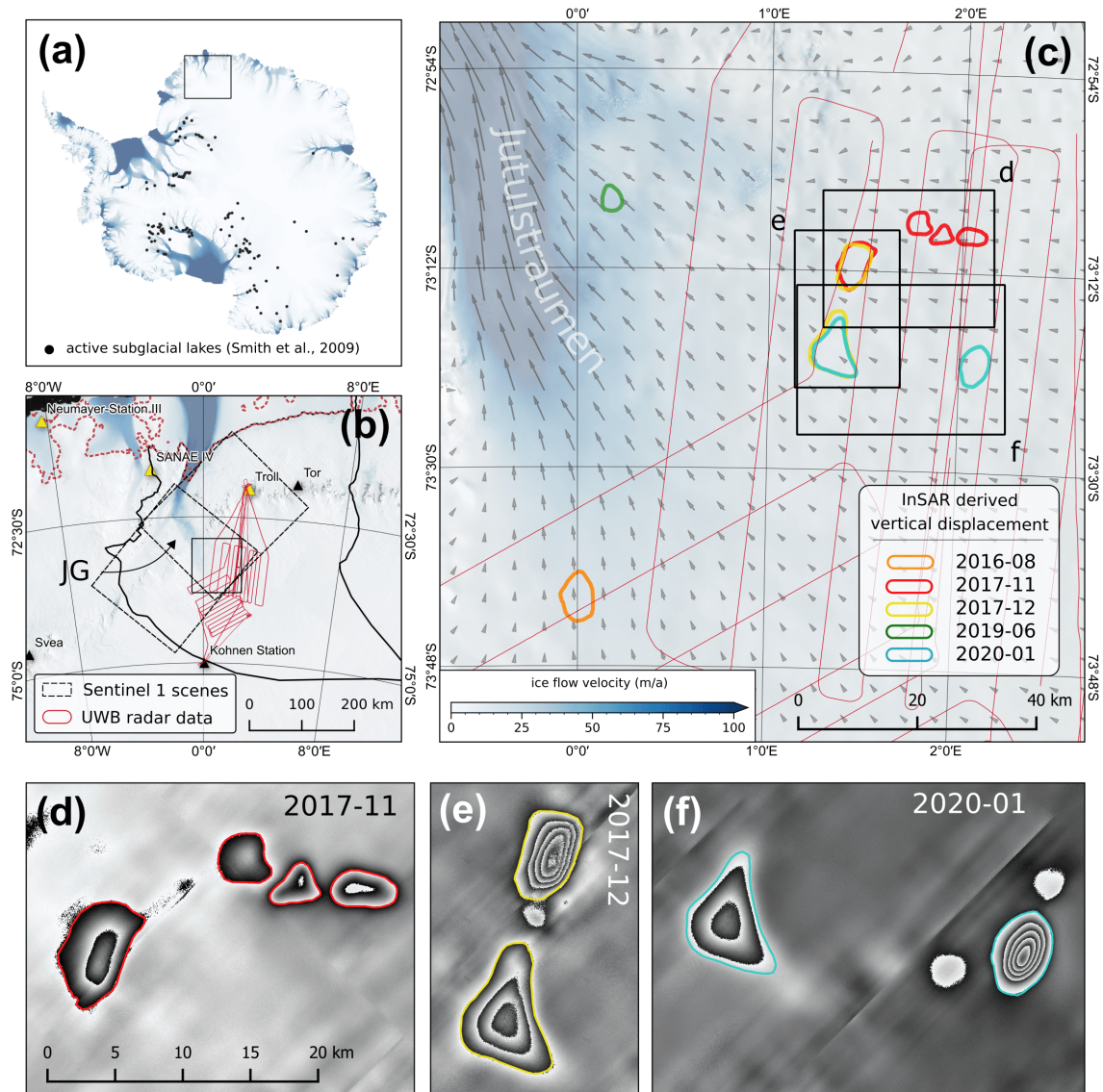


Figure H.1: Survey region overview of: (a) the locations of active subglacial lakes in Antarctica, (b) central/western DML with the drainage basin of Jutulstraumen Glacier (JG), (c) locations of DInSAR detected displacement anomalies of the ice surface at the onset of JG and (d, e and f) differential interferograms of three events indicating coupled displacement of the ice surface. In (a) and (b) we show the subglacial lake inventory derived from ICESat laser altimetry from [Smith et al. \(2009\)](#). Ice surface velocities in (a–c) are obtained from [Mouginot et al. \(2019\)](#) and the boundaries of the drainage system in (b) from [Rignot et al. \(2013\)](#); [Mouginot and Rignot \(2017\)](#).

a) subtracting two interferograms from a short temporal baseline and b) calculating the anomaly with respect to a long-term-average interferogram (Text S1 and Fig S1). As the majority of the interferograms show no bull's-eye fringe pattern, method b) is more suitable for isolating the vertical displacement and better constrains the timing of the events. Hence, all displacement values throughout this manuscript are based on the long-term displacement anomaly with unwrapped results projected from LOS to vertical (e.g. Fig. H.2 d–f).

In addition, we use data from the Advanced Topographic Laser Altimeter System carried on board the Ice, Cloud and land Elevation Satellite-2 (ICESat-2)

to find elevation anomalies over the DInSAR-detected events. We employed level 3A Land Ice Height (ATL06) Version 3 data which are available for the time period starting on 14 October 2018 ([Smith et al., 2020](#)). We modified the repeat-track analysis approach introduced by [Fricker et al. \(2014\)](#) to address the data acquisition characteristics specific to ICESat-2 (six beams instead of one nadir beam; Text S2). Based on this analysis we are able to estimate elevation changes over the locations of the DInSAR-detected bull's-eye fringe patterns (Fig. H.2 g and h).

The DInSAR-detected bull's-eye fringe patterns

in Figure H.1 d–f are also covered by multiple airborne radar data profiles. The data were acquired at the onset region of JG during the austral summer of 2018/19, using a multichannel ultra-wide band (UWB) radar system operated by the Alfred Wegener Institute, Helmholtz Centre for Polar and Marine Research (AWI; Fig. H.1 b and c). The radar system comprises an array of eight antenna elements, which is installed underneath the fuselage of AWI's Polar6 BT-67 aircraft. All radar profiles were recorded at a center frequency of 195 MHz and a bandwidth of 30 MHz (180–210 MHz). A detailed description of the instrument is given by Hale et al. (2016) and Rodriguez-Morales et al. (2014). For further details on radar data acquisition see also the supplementary Text S3. The radar data covers areas that were previously interpolated in Antarctic-wide ice thickness and bed topography maps (Fretwell et al., 2013; Morlighem et al., 2020).

For mapping preferential water flow paths, we use the improved bed topography and the Reference Elevation Model of Antarctica (REMA, Howat et al., 2019) to estimate the glaciological hydraulic potential in our study area (e.g. Shreve, 1972; Smith et al., 2017). A flow accumulation grid is generated using the algorithm proposed by Tarboton (1997) (Text S4). In this approach, flow direction is defined from the steepest downward slope in the hydraulic potential of each pixel's eight triangular facets. The output is displayed as the number of up-slope grid cells (Fig. H.2 d–f).

Results

From our time series of 247 double-differential interferograms we find at least three time periods of significant LOS surface displacement within spatially limited regions (Fig. H.1 d–f). These events are labeled as event *D* in November 2017 (Fig. H.1 d), event *E* in December 2017 (Fig. H.1 e) and event *F* in January 2020 (Fig. H.1 f). All events are clustered in an area of approx. 1 000 km² and are located 225 km upstream the grounding line of JG. The individual areas of these bull's-eye-shaped events range from 17 to 93 km² (Table S1). We find a spatial overlap of event *D* and *E*, as well as *E* and *F*. Volumes were calculated from the displacement anomaly and range between $-2.72 \cdot 10^7 \text{ m}^3$ (D_1) and $-1.20 \cdot 10^7 \text{ m}^3$ (E_1) for subsidence, and between $8.11 \cdot 10^7 \text{ m}^3$ (D_2) and $2.98 \cdot 10^8 \text{ m}^3$ (E_2) for uplift events (Fig. H.2 and Table S1).

In addition to the three main events described above, we detected several smaller displacement events with magnitudes between ~ 2 and 6 cm (Figs. S2 and S3). These smaller events occur close to the region of the main events *D*, *E* and *F* and can be observed during two time periods: 2017-09 to 2018-08 (Fig. S2) and 2019-09 to 2020-03 (Fig. S3). Unwrapping clearly

distinguishes subsidence from uplift allowing the spatial and temporal links between individual events to become apparent (Fig. H.2, Video S1). The first additional event appeared in 2017-09 and is located ~ 50 km northeast of event E_1 . Subsequent events (including *D* and *E*) occur increasingly downstream [as time progresses] (Fig. H.3). A synthesis of all events results in a ~ 175 km-long chain along which successive subsidence and uplift occurs throughout the time series. The second period between 2019-11 and 2020-02 is characterized by a similar pattern but is more restricted to the upstream area (Fig. S3).

The temporal availability of ICESat-2 data restricts our investigation to elevation anomalies along repeated ground tracks intersecting the outlines of event F_1 and F_2 (Fig. H.2 f). Here we find spatial overlaps for the time period between 2019-02 and 2020-06. We observe ice surface elevation changes for two ICESat-2 tracks (see Fig. H.2 g and h). Track ICE_a (Fig. H.2 g) shows constant subsidence adding up to more than 0.7 m between 2019-02-14 and 2020-08-12 in the region F_1 . The elevation changes from track ICE_b (Fig. H.2 h) also indicate gradual ice surface subsidence between 2019-06-18 and 2019-12-16 in the region F_2 . Thereafter, we observe an uplift until 2020-06-15, when the mean elevation level is reached again. The maximum elevation anomaly is found in the center of the target regions F_1 and F_2 . This applies for both positive and negative values. The elevation anomalies approach zero towards the area margins.

To integrate our DInSAR results with the ICESat-2 analysis we show the cumulative sum of the DInSAR time series within the respective repeat pass periods along the ICESat-2 tracks ICE_a and ICE_b (Fig. H.2 g and h). We selected two time periods from our DInSAR time series which closely match the ICESat-2 repeat passes (indicated by the arrows in Figure H.2 g and h) and find a good agreement between ICESat-2 and the cumulative DInSAR displacement.

Figure H.2 shows the subglacial water routing pathways together with the individual events of the DInSAR-derived vertical elevation changes. All identified areas of subsidence or uplift spatially coincide with [interconnected] subglacial water routing pathways. The improved bed topography reveals that the areas of ice uplift and subsidence are mostly related to topographic depressions (Fig. H.3). The bed topography depressions associated with events D_2/E_1 and E_2/F_1 also coincide with sinks in the hydraulic potential (Fig. S8a). Most events are located over V-shaped valleys, the depth of which constantly increases from (hydrologically) upstream to downstream.

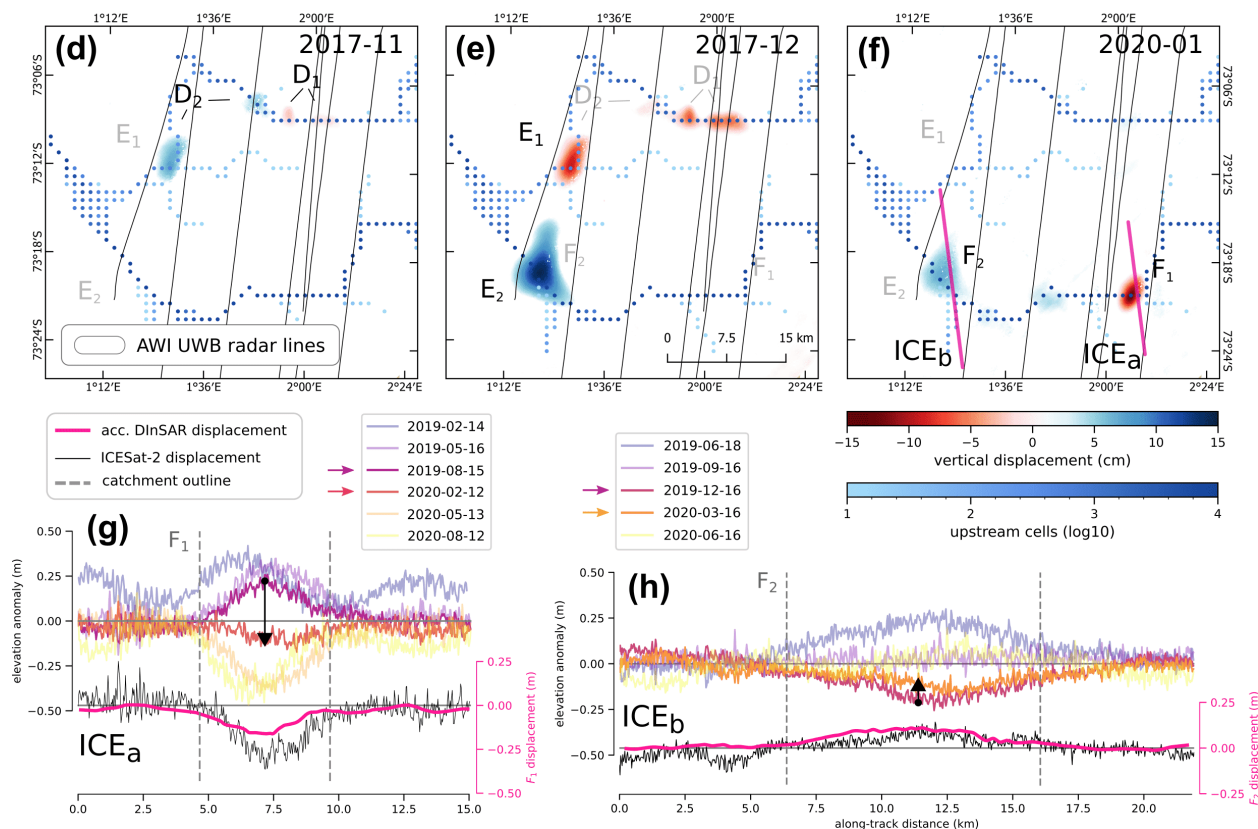


Figure H.2: Vertical displacement of the ice surface derived from DInSAR and ICESat-2 repeat track elevation changes. Panels (d)–(f) show the events D, E and F, which are computed from the anomaly to a long-term average interferogram. The blue dots represent the subglacial water routing pathways based on the number of upstream cells. The grey lines show the locations of the AWI UWB radar lines. Panel (f) shows the locations of the ICESat-2 tracks shown in (g) and (h). Elevation anomalies for multiple ICESat-2 repeat passes are shown in (g) and (h). The cumulated DInSAR anomalies between the time periods indicated by the arrows are shown in the lower part of (g) and (h) together with the difference of the timely consistent ICESat-2 anomalies (black curve).

Discussion

Compared to previous large-scale studies based on satellite altimetry (e.g. Fricker et al., 2007; Siegfried and Fricker, 2018), the combination of Sentinel-1 and ICESat-2 measurements offer new insights into the inter-connectivity of subglacial lake drainage events. Here we present a highly resolved chain-like pattern stretching from the onset of JG towards the grounding line (Fig. 3a and b, Video S1). The setting of JG is such that the subglacial water generated in the large upstream catchment must be funneled through a comparatively narrow constriction starting at the ice-stream onset. This favours the development of efficient channelized drainage systems similar to what has been observed at other ice streams (e.g. at Recovery Ice Stream, Dow et al., 2018). Our observations indicate that this drainage is not steady but contains episodic events of locally increased water storage resulting in negative effective pressure manifested in localized surface uplift. After sufficient build-up, the pressure then abruptly changes in a way that facilitates more downstream

transport of water to a different low in the hydraulic potential where this process is then reiterated (Fig. H.3b and c). These observations are in line with previous modelling based assertions (Dow et al., 2018) and observational studies at Recovery (Fricker et al., 2014) and Thwaites Glacier (Smith et al., 2017; Hoffman et al., 2020).

The proposed mechanism indicates that water is efficiently transported via transient channels. Whether these channels are R othlisberger channels that melt into the ice (Dow et al., 2018) or subglacial canals incised into the sediments (Carter et al., 2017) remains open to discussion. The idea of a channelized drainage system with efficient water transport is further supported by the observed lack of large-scale changes in ice dynamics after each drainage event (Fig. S4). Instead of following the prevailing ice flow direction, the chain of interconnected DInSAR anomalies largely follows the hydraulic gradient (Fig. H.3 a). Small deviations from the hydraulic gradient can be attributed to two main reasons: (1) the assumption that basal water pressure equals the ice overburden pressure might not hold true in all places and (2) interpolation artifacts in the

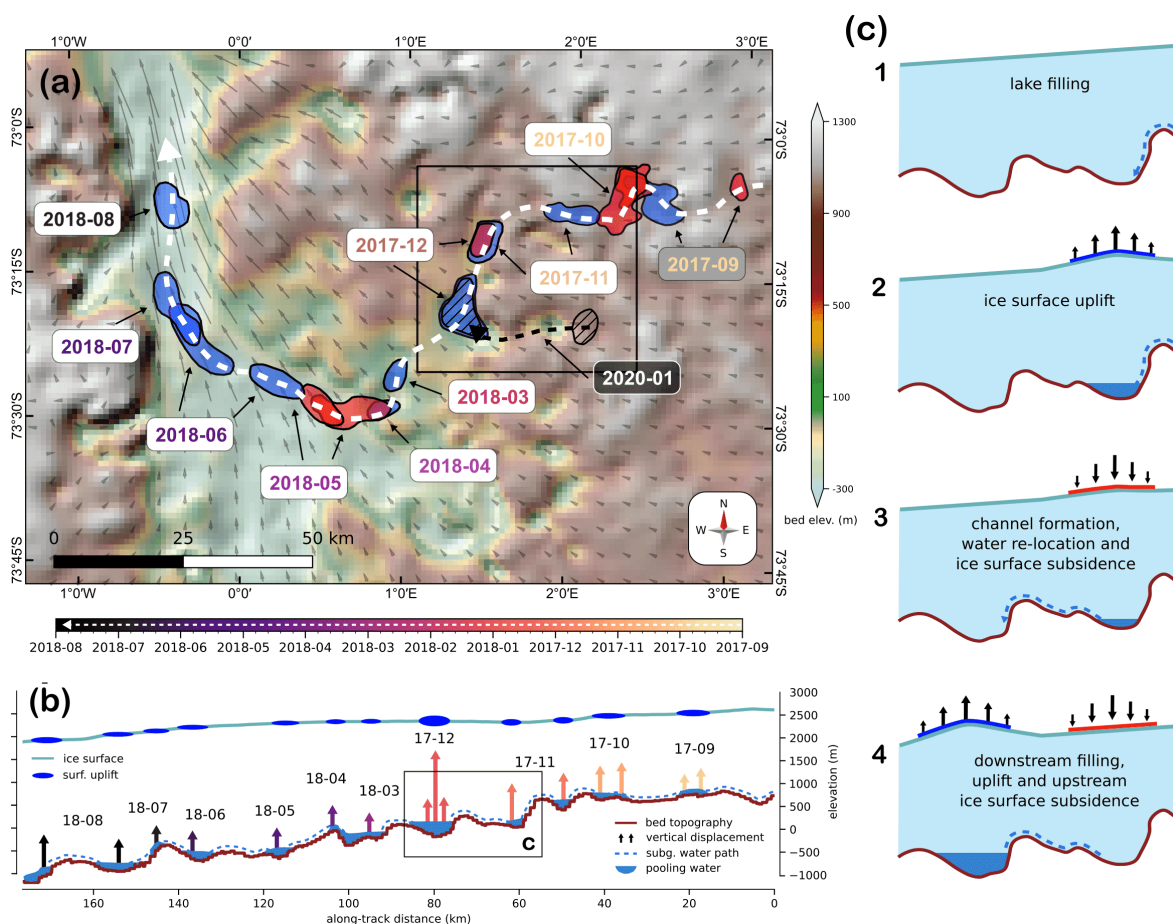


Figure H.3: Spatio-temporal propagation of ice surface uplift and subsidence events. Panel (a) shows selected areas of uplift (blue) and subsidence (red) for each month between 2017-09 and 2018-08. The complete time series is available in Figure S2 and Video S1. Panel (b) shows the initial uplift events for each location. The propagation of subglacial water along the bed is indicated with a blue dashed line as well as the filling of local sinks. The pressure-related uplift is indicated with upright arrows with the respective color for the timing. The length of the arrow is proportional to the maximum uplift. The DInSAR-detected uplift at the ice surface is indicated with a blue outline. Panel (c) indicates the temporal sequence of filling and drainage of two adjacent sinks and the respective response at the ice surface.

input datasets can influence the accuracy of the derived hydraulic potential.

Many locations where active subglacial lakes have been identified using satellite altimetry have also been surveyed by airborne RES campaigns (e.g. Christianson et al., 2012; Humbert et al., 2018; Siegert et al., 2014; Wright et al., 2012), which did not identify any characteristic [strong, flat and specular] bed reflection at the lake sites (Carter et al., 2007). Such reflections are also absent in our study region, which may be due to several factors such as high englacial attenuation rates, which reduce the receiving signal power. Since englacial attenuation is a function of temperature, it is possible that warm ice in the troughs underneath our active lake catchments or a temperate layer of basal ice might be the cause for the reduction in, and in some cases total absence of, basal reflectivity (Humbert et al., 2018; Siegert et al., 2014). Christianson et al. (2012) and Siegert et al. (2014) argue that, in order to create

a dielectric contrast of 10-20 dB higher than the surrounding material, a minimum water table of several meters' thickness is required. However, our centimeter-scale elevation changes combined with the odds of a radar survey coinciding with a filled lake (Siegert et al., 2014), strongly indicate that RES-based detection of subglacial water is very unlikely in our survey area. This agrees with the lack of evidence for a deep water lake at JG. Nonetheless, it may still be possible that larger-than-anticipated amounts of subglacial water are being transported. Carter et al. (2017) showed that subglacial lakes in Antarctica could drain through sediment-floored canals, which might serve as a further explanation for the missing evidence in the RES data.

In comparison to the lakes found in our study, most active lakes so far detected in Antarctica have been found in regions of elevated ice flow velocity (Smith et al., 2009; Siegfried and Fricker, 2018) and are subject to larger lake volume changes (assuming that the water

volume change is proportional to the subsidence and uplift volume; Smith et al. 2009). To our knowledge, this is the first study which finds active lakes in central DML. However, this might be attributed to the fact that compared to the altimetry measurements of previous studies, InSAR is not restricted to sparse repeat tracks and is capable of detecting surface elevation changes at the wavelength scale of the sensor. When we consider the history of subglacial lake identification in Antarctica since the 1960s (Wright et al., 2012) it becomes clear that many lake locations could be identified due to the increasing availability of space-borne data products and analysis techniques. The lake areas and the surface displacement magnitudes in this study are relatively small and could only be confirmed using a combination of remote sensing methods, which have been continuously developed in recent years. Hence, it is very likely that many more small lakes with short-term drainage and filling events will be identified in the future.

Conclusions

We identified a subglacial hydrologic network at Jutulstraumen Glacier in which subglacial water is periodically trapped and released. We are able to trace the propagation of subglacial water over a distance of ~175 km within one year using a combination of different remote sensing methods. DInSAR estimates from Sentinel-1 data reveal abrupt, localized events occurring between 12 days and two month. Individual events are interconnected in a cascade-like pattern of short-term surface uplift and subsidence following lows in the hydraulic potential indicating episodic transport of excess water across subglacial lakes. ICESat-2 repeat-tracks capture the long-term lake drainage patterns and match with the cumulated DInSAR displacements, but undersample the short term dynamics. Additional airborne radar data constrains the hydraulic potential and shows that the inter-connected chain of subsidence and uplift events occurs along projected pathways of subglacial water flux. The subglacial water is not apparent in the bed reflection amplitudes either because of the transient nature or because of a lack in system sensitivity. Despite the widely discussed influence of subglacial water on local ice flow variability, we find no evidence of changes in downstream ice velocities in connection with the detected drainage events.

Acknowledgements

We thank the Ken Borek crew as well as Martin Gehrman and Sebastian Spelz of AWI's technical staff of the research aircraft Polar 6. John Paden (University of Kansas) assisted remotely during the field campaign.

We would like to thank Tobias Binder for the implementation of an entire backup system for UWB radar data acquisition. Without his work we would not have been able to realize the campaign. We acknowledge fruitful discussions with Angelika Humbert. Furthermore, logistical support in Antarctica was provided at Troll Station (Norway), Novolazarewskaja-Station (Russia) and Kohnen Station (Germany). Steven Franke and Daniela Jansen were funded by the AWI strategy fund. R. Drews was supported by an Emmy Noether Grant of the Deutsche Forschungsgemeinschaft (DR 822/3-1).

Data availability

Sentinel-1 SAR data are freely available from <https://scihub.copernicus.eu>. ICESat-2 level 3A land ice height data are freely available from <https://nsidc.org/data/at106/versions/3>. The center coordinates of active lake locations derived in this study are available in the Supplementary Material. The outlines of the lakes will be made available at the PANGAEA repository. Ice thickness from the complete AWI UWB radar survey (Franke et al., 2020) is available at <https://doi.pangaea.de/10.1594/PANGAEA.911475>. Ice surface velocities from Mougnot et al. (2019) are available at the National Snow and Ice Data Center (NSIDC), <https://doi.org/10.7280/D10D4Z>. The REMA ice surface DEM (Howat et al., 2019) is available from the U.S. Polar Geospatial Center at <https://www.pgc.umn.edu/data/rema/>. The drainage system boundaries (Rignot et al., 2013) can be obtained here: <https://doi.org/10.5067/AXE4121732AD>.

Author contributions

Niklas Neckel and Steven Franke wrote the manuscript and designed the study. Veit Helm processed ICESat-2 laser altimetry data. Daniela Jansen was PI of the UWB radar campaign and acquired the radar data together with Steven Franke. Niklas Neckel performed the DInSAR processing of Sentinel-1 SAR data and derived the hydraulic parameters. Steven Franke processed UWB radar data and calculated the ice thickness and bed topography elevation. All authors discussed and commented the manuscript.

Bibliography

- Insar observations of the 1993–95 bering glacier (alaska, u.s.a.) surge and a surge hypothesis. 48. doi: 10.3189/172756502781831296. URL <https://doi.org/10.3189/172756502781831296>.
- Andersen, J., Newall, J., Blomdin, R., Sams, S., Fabel, D., Koester, A., Lifton, N., Fredin, O., Caffee, M., Glasser, N. F., Rogozhina, I., Suganuma, Y., Harbor, J., and Stroeven, A. Ice surface changes during recent glacial cycles along the Jutulstraumen and Penck Trough ice streams in western Dronning Maud Land, East Antarctica. *Quaternary Science Reviews*, 249:106636, 2020. ISSN 0277-3791. doi: <https://doi.org/10.1016/j.quascirev.2020.106636>. URL <http://www.sciencedirect.com/science/article/pii/S0277379120305989>.
- Ashmore, D. and Bingham, R. G. Antarctic subglacial hydrology: Current knowledge and future challenges. *Antarctic Science*, 26:758–773, 12 2014. doi: 10.1017/S0954102014000546. URL <https://doi.org/10.1017/S0954102014000546>.
- Bowling, J. S., Livingstone, S. J., Sole, A. J., and Chu, W. Distribution and dynamics of Greenland subglacial lakes. *Nature Communications*, 10(1):2810, June 2019. ISSN 2041-1723. URL <https://doi.org/10.1038/s41467-019-10821-w>.
- Capps, D. M., Rabus, B., Clague, J. J., and Shugar, D. H. Identification and characterization of alpine subglacial lakes using interferometric synthetic aperture radar (InSAR): Brady Glacier, Alaska, USA. *Journal of Glaciology*, 56(199): 861–870, 2010. doi: 10.3189/002214310794457254. URL <https://doi.org/10.3189/002214310794457254>.
- Carter, S. P., Blankenship, D. D., Peters, M. E., Young, D. A., Holt, J. W., and Morse, D. L. Radar-based subglacial lake classification in antarctica. *Geochemistry, Geophysics, Geosystems*, 8(3):1–20, 2007. doi: <https://doi.org/10.1029/2006GC001408>. URL <https://agupubs.onlinelibrary.wiley.com/doi/abs/10.1029/2006GC001408>.
- Carter, S. P., Fricker, H. A., and Siegfried, M. R. Antarctic subglacial lakes drain through sediment-floored canals: theory and model testing on real and idealized domains. *The Cryosphere*, 11(1):381–405, 2017. doi: 10.5194/tc-11-381-2017. URL <https://tc.copernicus.org/articles/11/381/2017/>.
- Christianson, K., Jacobel, R. W., Horgan, H. J., Anandakrishnan, S., and Alley, R. B. Subglacial lake whillans — ice-penetrating radar and gps observations of a shallow active reservoir beneath a west antarctic ice stream. *Earth and Planetary Science Letters*, 331-332:237 – 245, 2012. ISSN 0012-821X. doi: <https://doi.org/10.1016/j.epsl.2012.03.013>. URL <http://www.sciencedirect.com/science/article/pii/S0012821X12001276>.
- Dow, C. F., Werder, M. A., Babonis, G., Nowicki, S., Walker, R. T., Csatho, B., and Morlighem, M. Dynamics of Active Subglacial Lakes in Recovery Ice Stream. *Journal of Geophysical Research: Earth Surface*, 123(4):837–850, 2018. doi: <https://doi.org/10.1002/2017JF004409>. URL <https://agupubs.onlinelibrary.wiley.com/doi/abs/10.1002/2017JF004409>.
- Ferraccioli, F., Jones, P. C., Curtis, M. L., and Leat, P. T. Subglacial imprints of early Gondwana break-up as identified from high resolution aerogeophysical data over western Dronning Maud Land, East Antarctica. *Terra Nova*, 17(6):573–579, dec 2005. ISSN 09544879. doi: 10.1111/j.1365-3121.2005.00651.x. URL <https://doi.org/10.1111/j.1365-3121.2005.00651.x>.
- Flament, T., Berthier, E., and Rémy, F. Cascading water underneath Wilkes Land, East Antarctic ice sheet, observed using altimetry and digital elevation models. *The Cryosphere*, 8(2):673–687, 2014. doi: 10.5194/tc-8-673-2014. URL <https://tc.copernicus.org/articles/8/673/2014/>.
- Franke, S., Jansen, D., and Helm, V. Ice Thickness from Jutulstraumen Glacier recorded with the airborne AWI UWB radar system, Antarctica. 2020. doi: 10.1594/PANGAEA.911475. URL <https://doi.pangaea.de/10.1594/PANGAEA.911475>.
- Fretwell, P., Pritchard, H. D., Vaughan, D. G., Bamber, J. L., Barrand, N. E., Bell, R., Bianchi, C., Bingham, R. G., Blankenship, D. D., Casassa, G., Catania, G., Callens, D., Conway, H., Cook, A. J., Corr, H. F. J., Damaske, D., Damm, V., Ferraccioli, F., Forsberg, R., Fujita, S., Gim, Y., Gogineni, P., Griggs, J. A., Hindmarsh, R. C. A., Holmlund, P., Holt, J. W., Jacobel, R. W., Jenkins, A., Jokat, W., Jordan, T., King, E. C., Kohler, J., Krabill, W., Riger-Kusk, M., Langley, K. A., Leitchenkov, G., Leuschen, C., Luyendyk, B. P., Matsuoka, K., Mouginot, J., Nitsche, F. O., Nogi, Y., Nost, O. A., Popov, S. V., Rignot, E., Rippin, D. M., Rivera, A., Roberts, J., Ross, N., Siegert, M. J., Smith, A. M., Steinhage, D., Studinger, M., Sun, B., Tinto, B. K., Welch, B. C., Wilson, D., Young, D. A., Xiangbin, C., and Zirizzotti, A. Bedmap2: improved ice bed surface and thickness datasets for Antarctica. *The Cryosphere*, 7(1):375–393, feb 2013. doi: 10.5194/tc-7-375-2013. URL <https://doi.org/10.5194/2Ftc-7-375-2013>.
- Fricker, H. A., Scambos, T., Bindschadler, R., and Padman, L. An active subglacial water system in west antarctica mapped from space. *Science*, 315(5818):1544–1548, 2007. ISSN 0036-8075. doi: 10.1126/science.1136897. URL <https://science.sciencemag.org/content/315/5818/1544>.
- Fricker, H. A., Carter, S. P., Bell, R. E., and Scambos, T. Active lakes of recovery ice stream, east antarctica: a bedrock-controlled subglacial hydrological system. *Journal of Glaciology*, 60(223):1015–1030, 2014. doi: 10.3189/2014JoG14J063. URL <https://doi.org/10.3189/2014JoG14J063>.
- Friedl, P., Weiser, F., Fluhrer, A., and Braun, M. H. Remote sensing of glacier and ice sheet grounding lines: A review. *Earth-Science Reviews*, 201:102948, 2020. ISSN 0012-8252. doi: <https://doi.org/10.1016/j.earscirev.2019>.

102948. URL <http://www.sciencedirect.com/science/article/pii/S0012825219300832>.
- Goeller, S., Steinhage, D., Thoma, M., and Grosfeld, K. Assessing the subglacial lake coverage of Antarctica. *Annals of Glaciology*, 57(72):109–117, jul 2016. ISSN 02603055. doi: 10.1017/aog.2016.23. URL <http://creativecommons.org/licenses/by/4.0/>.
- Gray, L., Joughin, I., Tulaczyk, S., Spikes, V. B., Bindschadler, R., and Jezek, K. Evidence for subglacial water transport in the West Antarctic Ice Sheet through three-dimensional satellite radar interferometry. *Geophysical Research Letters*, 32(3):1–4, feb 2005. ISSN 00948276. doi: 10.1029/2004GL021387. URL <https://agupubs.onlinelibrary.wiley.com/doi/abs/10.1029/2004GL021387>.
- Hale, R., Miller, H., Gogineni, S., Yan, J. B., Rodriguez-Morales, F., Leuschen, C., Paden, J., Li, J., Binder, T., Steinhage, D., Gehrman, M., and Braaten, D. Multi-channel ultra-wideband radar sounder and imager. In *2016 IEEE International Geoscience and Remote Sensing Symposium (IGARSS)*. IEEE, jul 2016. doi: 10.1109/igarss.2016.7729545. URL <https://doi.org/10.1109%2Figarss.2016.7729545>.
- Hoffman, A. O., Christianson, K., Shapero, D., Smith, B. E., and Joughin, I. Brief communication: Heterogenous thinning and subglacial lake activity on Thwaites Glacier, West Antarctica. *The Cryosphere*, 14(12):4603–4609, 2020. doi: 10.5194/tc-14-4603-2020. URL <https://tc.copernicus.org/articles/14/4603/2020/>.
- Howat, I. M., Porter, C., Noh, M. J., Smith, B. E., and Jeong, S. Brief Communication: Sudden drainage of a subglacial lake beneath the Greenland Ice Sheet. *The Cryosphere*, 9(1):103–108, 2015. doi: 10.5194/tc-9-103-2015. URL <https://tc.copernicus.org/articles/9/103/2015/>.
- Howat, I. M., Porter, C., Smith, B. E., Noh, M.-J., and Morin, P. The Reference Elevation Model of Antarctica. *The Cryosphere*, 13(2):665–674, 2019. doi: 10.5194/tc-13-665-2019. URL <https://tc.copernicus.org/articles/13/665/2019/>.
- Humbert, A., Steinhage, D., Helm, V., Beyer, S., and Kleiner, T. Missing evidence of widespread subglacial lakes at recovery glacier, antarctica. *Journal of Geophysical Research: Earth Surface*, 123(11):2802–2826, 2018. doi: <https://doi.org/10.1029/2017JF004591>. URL <https://agupubs.onlinelibrary.wiley.com/doi/abs/10.1029/2017JF004591>.
- Iken, A., Röthlisberger, H., Flotron, A., and Haeberli, W. The uplift of unteraargletscher at the beginning of the melt season—a consequence of water storage at the bed? *Journal of Glaciology*, 29(101):28–47, 1983. doi: 10.3189/S0022143000005128. URL <https://doi.org/10.3189/S0022143000005128>.
- Joughin, I., Tulaczyk, S., MacAyeal, D. R., and Engelhardt, H. Melting and freezing beneath the ross ice streams, antarctica. *Journal of Glaciology*, 50(168):96–108, 2004. doi: 10.3189/172756504781830295. URL <https://doi.org/10.3189/172756504781830295>.
- Joughin, I., Shean, D. E., Smith, B. E., and Dutrieux, P. Grounding line variability and subglacial lake drainage on Pine Island Glacier, Antarctica. *Geophysical Research Letters*, 43(17):9093–9102, Sep 2016. ISSN 0094-8276. doi: 10.1002/2016gl070259. URL <http://dx.doi.org/10.1002/2016GL070259>.
- Malczyk, G., Gourmelen, N., Goldberg, D., Wuite, J., and Nagler, T. Repeat subglacial lake drainage and filling beneath thwaites glacier. *Geophysical Research Letters*, 47(23):e2020GL089658, 2020. doi: <https://doi.org/10.1029/2020GL089658>. URL <https://agupubs.onlinelibrary.wiley.com/doi/abs/10.1029/2020GL089658>. e2020GL089658 2020GL089658.
- Milillo, P., Rignot, E., Mouginot, J., Scheuchl, B., Morlighem, M., Li, X., and Salzer, J. T. On the Short-term Grounding Zone Dynamics of Pine Island Glacier, West Antarctica, Observed With COSMO-SkyMed Interferometric Data. *Geophysical Research Letters*, 44(20):10,436–10,444, 2017. doi: <https://doi.org/10.1002/2017GL074320>. URL <https://agupubs.onlinelibrary.wiley.com/doi/abs/10.1002/2017GL074320>.
- Morlighem, M., Rignot, E., Binder, T., Blankenship, D., Drews, R., Eagles, G., Eisen, O., Ferraccioli, F., Forsberg, R., Fretwell, P., Goel, V., Greenbaum, J. S., Gudmundsson, H., Guo, J., Helm, V., Hofstede, C., Howat, I., Humbert, A., Jokat, W., Karlsson, N. B., Lee, W. S., Matsuoka, K., Millan, R., Mouginot, J., Paden, J., Pattyn, F., Roberts, J., Rosier, S., Ruppel, A., Seroussi, H., Smith, E. C., Steinhage, D., Sun, B., Broeke, M. R. v. d., Ommen, T. D. v., Wessem, M. v., and Young, D. A. Deep glacial troughs and stabilizing ridges unveiled beneath the margins of the Antarctic ice sheet. *Nature Geoscience*, 13(2):132–137, 2020. ISSN 1752-0908. URL <https://doi.org/10.1038/s41561-019-0510-8>.
- Mouginot, J., B. S. and Rignot, E. MEaSUREs Antarctic Boundaries for IPY 2007-2009 from Satellite Radar, Version 2. 2017. doi: 10.5067/AXE4121732AD. URL <https://doi.org/10.5067/AXE4121732AD>.
- Mouginot, J., Rignot, E., and Scheuchl, B. Continent-Wide, Interferometric SAR Phase, Mapping of Antarctic Ice Velocity. *Geophysical Research Letters*, 46(16):9710–9718, 2019. doi: 10.1029/2019GL083826. URL <https://agupubs.onlinelibrary.wiley.com/doi/abs/10.1029/2019GL083826>.
- Näslund, J. O. Landscape development in western and central Dronning Maud Land, East Antarctica. *Antarctic Science*, 13(3):302–311, 2001. ISSN 09541020. doi: 10.1017/S0954102001000438. URL <https://doi.org/10.1017/S0954102001000438>.
- Riedel, S., Jokat, W., and Steinhage, D. Mapping tectonic provinces with airborne gravity and radar data in Dronning Maud Land, East Antarctica. *Geophysical Journal International*, 189(1):414–427, 2012. ISSN 0956540X. doi: 10.1111/j.1365-246X.2012.05363.x. URL <https://doi.org/10.1111/j.1365-246X.2012.05363.x>.

- Rignot, E., Velicogna, I., Van Den Broeke, M. R., Monaghan, A., and Lenaerts, J. Acceleration of the contribution of the Greenland and Antarctic ice sheets to sea level rise. *Geophysical Research Letters*, 38(5):1–5, 2011. ISSN 00948276. doi: 10.1029/2011GL046583. URL <http://dx.doi.org/10.1029/2011GL046583>.
- Rignot, E., Jacobs, S., Mouginot, J., and Scheuchl, B. Ice-Shelf Melting Around Antarctica. *Science*, 341(6143):266–270, 2013. ISSN 0036-8075. doi: 10.1126/science.1235798. URL <https://science.sciencemag.org/content/341/6143/266>.
- Rodriguez-Morales, F., Gogineni, S., Leuschen, C. J., Paden, J. D., Li, J., Lewis, C. C., Panzer, B., Gomez-Garcia Alvestegui, D., Patel, A., Byers, K., Crowe, R., Player, K., Hale, R. D., Arnold, E. J., Smith, L., Gifford, C. M., Braaten, D., and Panton, C. Advanced multifrequency radar instrumentation for polar Research. *IEEE Transactions on Geoscience and Remote Sensing*, 52(5):2824–2842, 2014. ISSN 01962892. doi: 10.1109/TGRS.2013.2266415. URL <https://doi.org/10.1109/TGRS.2013.2266415>.
- Shreve, R. L. Movement of Water in Glaciers. *Journal of Glaciology*, 11(62):205–214, 1972. doi: 10.3189/S002214300002219X. URL <https://doi.org/10.3189/S002214300002219X>.
- Siegert, M. J., Ross, N., Corr, H., Smith, B., Jordan, T., Bingham, R. G., Ferraccioli, F., Rippin, D. M., and Le Brocq, A. Boundary conditions of an active west antarctic subglacial lake: implications for storage of water beneath the ice sheet. *The Cryosphere*, 8(1):15–24, 2014. doi: 10.5194/tc-8-15-2014. URL <https://tc.copernicus.org/articles/8/15/2014/>.
- Siegfried, M. R. and Fricker, H. A. Thirteen years of subglacial lake activity in antarctica from multi-mission satellite altimetry. *Annals of Glaciology*, 59(76pt1):42–55, 2018. doi: 10.1017/aog.2017.36. URL <https://doi.org/10.1017/aog.2017.36>.
- Smith, B., Fricker, H., Gardner, A., Siegfried, M., S., A., Csathó, B., Holschuh, N., Nilsson, J., Paolo, F., and the ICESat-2 Science Team. ATLAS/ICESat-2 L3A Land Ice Height, Version 3. Boulder, Colorado USA. NASA National Snow and Ice Data Center Distributed Active Archive Center. 2020. doi: 10.5067/ATLAS/ATL06.003. URL <https://doi.org/10.5067/ATLAS/ATL06.003>.
- Smith, B. E., Fricker, H. A., Joughin, I. R., and Tulaczyk, S. An inventory of active subglacial lakes in antarctica detected by icesat (2003–2008). *Journal of Glaciology*, 55(192):573–595, 2009. doi: 10.3189/002214309789470879. URL <https://doi.org/10.3189/002214309789470879>.
- Smith, B. E., Gourmelen, N., Huth, A., and Joughin, I. Connected subglacial lake drainage beneath thwaites glacier, west antarctica. *The Cryosphere*, 11(1):451–467, 2017. doi: 10.5194/tc-11-451-2017. URL <https://tc.copernicus.org/articles/11/451/2017/>.
- Spikes, V. B., Csatho, B. M., Hamilton, G. S., and Whillans, I. M. Thickness changes on whillans ice stream and ice stream c, west antarctica, derived from laser altimeter measurements. *Journal of Glaciology*, 49(165):223–230, 2003. doi: 10.3189/172756503781830683. URL <https://doi.org/10.3189/172756503781830683>.
- Steinhage, D., Nixdorf, U., Meyer, U., and Miller, H. *Annals of Glaciology*. doi: 10.3189/172756499781821409. URL <https://doi.org/10.3189/172756499781821409>.
- Steinhage, D., Nixdorf, U., Meyer, U., and Miller, H. Subglacial topography and internal structure of Central and Western Dronning Maud Land, Antarctica, determined from airborne radio echo sounding. *Journal of Applied Geophysics*, 47(3-4):183–189, jul 2001. ISSN 09269851. doi: 10.1016/S0926-9851(01)00063-5. URL [https://doi.org/10.1016/S0926-9851\(01\)00063-5](https://doi.org/10.1016/S0926-9851(01)00063-5).
- Tarboton, D. G. A new method for the determination of flow directions and upslope areas in grid digital elevation models. *Water Resources Research*, 33(2):309–319, 1997. doi: <https://doi.org/10.1029/96WR03137>. URL <https://agupubs.onlinelibrary.wiley.com/doi/abs/10.1029/96WR03137>.
- Thoma, M., Grosfeld, K., Mayer, C., and Pattyn, F. Ice-flow sensitivity to boundary processes: a coupled model study in the vostok subglacial lake area, antarctica. *Annals of Glaciology*, 53(60):173–180, 2012. doi: 10.3189/2012AoG60A009. URL <https://doi.org/10.3189/2012AoG60A009>.
- Willis, M. J., Herried, B. G., Bevis, M. G., and Bell, R. E. Recharge of a subglacial lake by surface meltwater in northeast Greenland. *Nature*, 518(7538):223–227, Feb. 2015. ISSN 1476-4687. URL <https://doi.org/10.1038/nature14116>.
- Wingham, D. J., Siegert, M. J., Shepherd, A., and Muir, A. S. Rapid discharge connects Antarctic subglacial lakes. *Nature*, 440(7087):1033–1036, 2006. ISSN 14764687. doi: 10.1038/nature04660. URL <https://www.nature.com/articles/nature04660>.
- Wright, A. P., Young, D. A., Roberts, J. L., Schroeder, D. M., Bamber, J. L., Dowdeswell, J. A., Young, N. W., Le Brocq, A. M., Warner, R. C., Payne, A. J., Blankenship, D. D., van Ommen, T. D., and Siegert, M. J. Evidence of a hydrological connection between the ice divide and ice sheet margin in the aurora subglacial basin, east antarctica. *Journal of Geophysical Research: Earth Surface*, 117(F1), 2012. doi: 10.1029/2011JF002066. URL <https://agupubs.onlinelibrary.wiley.com/doi/abs/10.1029/2011JF002066>.

PAPER IV**SUPPLEMENTARY INFORMATION****Supplementary Information:**

Evidence of cascading subglacial water flow at Jutulstraumen Glacier (Antarctica) derived from Sentinel-1 and ICESat-2 measurements

Niklas Neckel^{1,†} , Steven Franke^{1,†} , Veit Helm¹ , Reinhard Drews² , Daniela Jansen¹ 

[†] Steven Franke and Niklas Neckel contributed equally to this work.

¹ Alfred Wegener Institute, Helmholtz Centre for Polar and Marine Research, Bremerhaven, Germany

² Department of Geosciences, Eberhard Karls University Tübingen, Germany

The supplementary information for Paper IV is provided on the USB stick submitted alongside the thesis as well as in a private online repository (see below).

Supplementary Information of Paper IV:

1. Text S1 – S4, Table S1 and Figures S1 – S8 (pdf):

<https://storage.luckycloud.de/f/07ca816931cf45ed9d94/>

2. Video S1 (mp4): <https://storage.luckycloud.de/f/ab445e7af39b48ffa87f/>

Appendix I

PAPER V

DATA DESCRIPTION ARTICLE

Airborne ultra-wideband radar sounding over the shear margins and along flow lines at the onset region of the Northeast Greenland Ice Stream

Steven Franke¹ , Daniela Jansen¹ , Tobias Binder^{1,*} , John D. Paden² , Nils Dörr^{1,3} , Tamara A. Gerber⁴ , Heinrich Miller¹ , Dorte Dahl-Jensen^{4,5} , Veit Helm¹ , Daniel Steinhage¹ , Ilka Weikusat^{1,6} , Frank Wilhelm^{1,7}  and Olaf Eisen^{1,8} 

¹ Alfred Wegener Institute, Helmholtz Centre for Polar and Marine Research, Bremerhaven, Germany

² Centre for Remote Sensing of Ice Sheets (CReSIS), University of Kansas, Lawrence, KS, USA

³ Institute of Photogrammetry and Remote Sensing, Karlsruhe Institute of Technology, Karlsruhe, Germany

⁴ Physics of Ice, Climate, and Earth, Niels Bohr Institute, University of Copenhagen, Denmark

⁵ Centre for Earth Observation Science, University of Manitoba, Winnipeg, Canada

⁶ Department of Geosciences, Eberhard Karls University Tübingen, Germany

⁷ Department of Crystallography, Geoscience Centre, University of Göttingen, Germany

⁸ Department of Geosciences, University of Bremen, Bremen, Germany

* now at Ibeo Automotive Systems, Hamburg, Germany

In review since 31 March 2021 at Earth System Science Data. <https://doi.org/10.5194/essd-2021-91>

Abstract

We present a high-resolution airborne radar data set (EGRIP-NOR-2018) for the onset region of the Northeast Greenland Ice Stream (NEGIS). The radar data were acquired in May 2018 with Alfred Wegener Institute's multichannel ultra-wideband (UWB) radar mounted on the Polar6 aircraft. Radar profiles cover an area of ~24 000 km² and extend over the well-defined shear margins of the NEGIS. The survey area is centred at the location of the drill site of the East Greenland Ice-Core Project (EastGRIP) and several radar lines intersect at this location. The survey layout was designed to: (i) map the stratigraphic signature of the shear margins with radar profiles aligned perpendicular to ice flow, (ii) trace the radar stratigraphy along several flow lines and (iii) provide spatial coverage of ice thickness and basal properties. While we are able to resolve radar reflections in the deep stratigraphy, we can not fully resolve the steeply inclined reflections at the tightly folded shear margins in the lower part of the ice column. The NEGIS is causing the most significant discrepancies between numerically modelled and observed ice surface velocities. Given the high likelihood of future climate and ocean warming, this extensive data set of new high-resolution radar data in combination with the EastGRIP ice core will be a key contribution to understand the past and future dynamics of the NEGIS. The EGRIP-NOR-2018 radar data products can be obtained at the PANGAEA Data Publisher (<https://doi.pangaea.de/10.1594/PANGAEA.928569>; Franke et al. 2021a).

Received: 17 Mar 2021 – Accepted for review: 31 Mar 2021 – Discussion started: 6 Apr 2021

Introduction

The Northeast Greenland Ice Stream (NEGIS) efficiently drains a large area of the Greenland Ice Sheet and is a crucial component of the ice sheet mass balance (Fahnestock et al., 1993; Rignot and Mouginot, 2012). It extends from the central ice divide over more than 600 km towards the northeastern coast, where it

discharges ice through the three marine-terminating glaciers (79 N Glacier, Zachariae Isbræ and Storstrømmen Glacier). The currently prevailing hypothesis is that an anomaly of elevated geothermal heat flux (GHF) leads to extensive basal melting (Fahnestock et al., 2001) and induces ice flow.

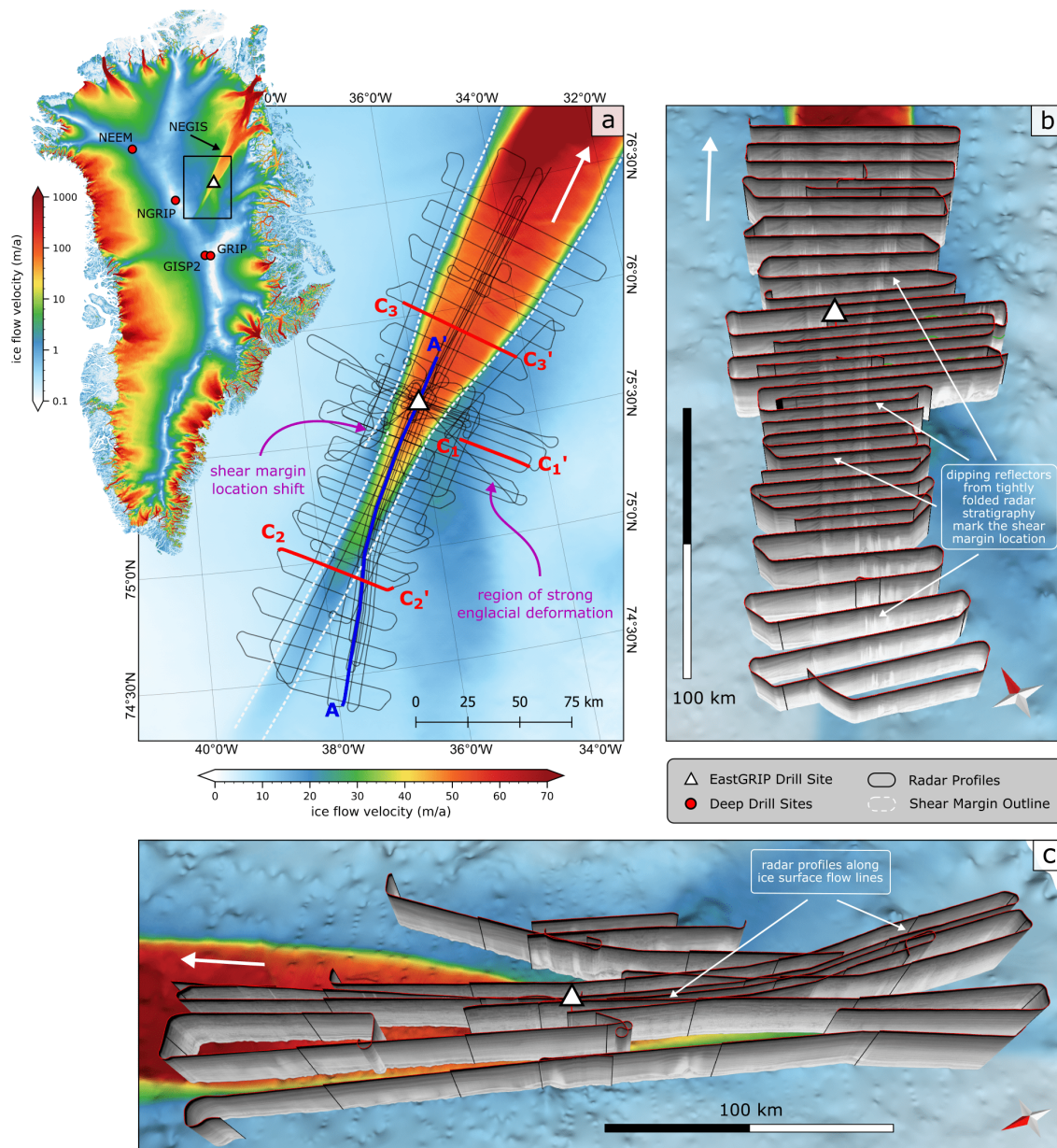


Figure I.1: Location of the EGRIP-NOR-2018 survey area in Northeast Greenland with the MEaSUREs ice surface velocity from Joughin et al. (2017) in the background. (a) The radar survey lines are centred at the EastGRIP drill site (white triangle) and extend up to 150 km upstream and downstream of the NEGIS. The locations of one along-flow radar section (Figure I.2; blue) and three cross-flow radar sections (Figure I.3; red) are shown in panel (a). The ice flow direction of the ice stream is indicated with a white arrow. 3D images of the cross-flow profiles and along-flow profiles are shown in (b) and (c), respectively. The radar sections are shown with a vertical exaggeration factor of $z = 10$. The ice surface velocity (Joughin et al., 2017) is shown on a logarithmic scale (\log_{10}) for entire Greenland (upper left image) and on a linear scale for panels (a), (b) and (c). For panel (b) and (c) the ice surface velocity is projected on top of the bed topography model from Franke et al. (2020). The projection for all maps is: WGS 84 / NSIDC Sea Ice Polar Stereographic North (EPSG:3413).

The GHF at the onset of NEGIS is the most important and, at the same time, most uncertain parameter in the representation of basal melt and the subglacial hydrology in ice flow models (Smith-Johnsen et al., 2020). However, the large gap between observed and modelled basal melt rates (Gerber et al., 2021; Zeising and Humbert, 2021; Bucharadt and Dahl-Jensen, 2007; MacGregor et al., 2016) inside the ice stream and in the

broader surrounding of the NEGIS onset, raise questions about the real thermal state at the bed. The exceptionally high GHF proposed by Fahnestock et al. (2001) would be non-compatible with known geological processes (Joh; Blackwell and Richards, 2004). Therefore, Bons et al. (2020) raise the question of how fast flow at the NEGIS onset is possible without an extraordinary high basal heat flux and meltrates.

Unlike other ice streams in Greenland, the NEGIS lacks an extensive overdeepened bed, and thus lateral topographic constraints (Joughin et al., 2001b; Franke et al., 2020). The ice stream more or less symmetrically broadens along flow, as more ice is dragged through the shear margins (Fahnestock et al., 2001; Joughin et al., 2001a). Subglacial water routing in combination with subglacial till deformation seems to be a further controlling mechanism of ice flow at the onset of the NEGIS (Keisling et al., 2014; Christianson et al., 2014). The outlet area is characterised by an overdeepened basin covered with unconsolidated sediments (Joughin et al., 2001a; Bamber et al., 2013). Ice thinning as a consequence of increasing oceanic water temperatures around Greenland, could thus potentially be transmitted far upstream (Christianson et al., 2014), and changes in the hydropotential might have significant effects on the ice stream geometry. The high susceptibility of NEGIS to marine-triggered discharge and the expected increase in ocean water temperatures in the years to come (Yin et al., 2011; Straneo et al., 2012) raises questions about the future ice stream stability and its effect on the Greenland Ice Sheet mass balance.

Large scale ice flow models are essential tools to predict the future behaviour of glaciers and ice sheets and are necessary to estimate future sea-level rise. Until today, these models fail to successfully simulate the NEGIS due to insufficient understanding of the key processes responsible for ice flow dynamics (Mottram et al., 2019; Shepherd et al., 2020), limiting the prediction accuracy. The East Greenland Ice-Core project (EastGRIP; <https://eastgrip.org>) aims to drill a deep ice core in the upstream area of the NEGIS, providing valuable insights into the climate record, basal properties and ice flow history at the drill site. Ice cores provide *in situ* information on physical and chemical properties at high resolution but are limited as being a spatial point measurement. Hence, further geophysical techniques are required to extrapolate this information to obtain a complete picture of the ice dynamic properties.

Radio-echo sounding (RES) has long become a standard method in glaciology. The polar ice sheets as well as low-latitude glaciers and ice caps have extensively been covered by airborne (e.g. Steinhage et al.; Schroeder et al., 2020) or ground-based (e.g. Pälli et al., 2002) RES surveys. The transmitted electromagnetic waves are sensitive to changes in dielectric permittivity and electrical conductivity and get reflected, scattered or refracted at interfaces of dielectric contrasts in the medium they propagate (Fujita et al., 1999). The most common glaciological application is the sounding of ice thickness and bedrock topography (e.g. Hempel and Thyssen, 1992; Dahl-Jensen et al., 1997; Steinhage et al., 1999; Nixdorf and Göktas, 2001; Kanagaratnam et al., 2001). Reflections within the ice column, or so-called internal reflection horizons (IRH), are often

caused by impurity layers of volcanic origin representing isochronous horizons (Millar, 1981). These provide valuable information on the ice flow regime and strain history (Vaughan et al., 1999; Jacobel et al., 1993; Hodgkins et al.) and can be used to reconstruct past accumulation rates (e.g. Richardson et al., 1997; Nereson et al., 2000; Siegert and Hodgkins, 2000; Pälli et al., 2002; Nereson and Raymond, 2001), to match ice cores from different locations (e.g. Jacobel and Hodge, 1995; Siegert et al., 1998; Hempel et al., 2000) and to validate numerical ice flow models (e.g. Huybrechts et al., 2000; Baldwin et al., 2003). Further applications of RES include the detection of crevasses (e.g. Zamora et al., 2007; Eder et al., 2008; Williams et al., 2014), mapping of subglacial lakes and basal hydrology (e.g. Carter et al., 2007; Palmer et al., 2013; Young et al., 2016), identifying thermal regimes (e.g. Murray et al., 2000; Copland and Sharp, 2001), determining snow and firn genesis (e.g. Frezzotti et al.) and obtaining information on the crystal orientation fabric (e.g. Matsuoka et al., 2003; Eisen et al., 2007; Jordan et al., 2020).

We present unique airborne radar data of the onset region of NEGIS recorded in 2018 by a multichannel ultra-wideband radar system. The data set consists of profiles oriented parallel and perpendicular to the ice flow direction. The high along-track and range resolution allows consistent isochrone tracing, providing insights into the three-dimensional structure of the ice stream. In combination with the EastGRIP ice core, this dataset contributes to a better understanding of ice flow dynamics of the NEGIS. In our manuscript, we introduce the study site and survey design. Furthermore, we describe the radar data processing and the respective data products. The data are freely available at the PANGAEA data publisher (<https://doi.pangaea.de/10.1594/PANGAEA.928569>).

Survey region and previous work

In May 2018, we recorded radar data in the vicinity of the drill site of the EastGRIP ice core. An area of $\sim 24,000$ km² was mapped with 7494 km of radar profiles along flow lines and perpendicular to ice flow (Figure 1). The survey region extends ~ 150 km upstream and downstream of the EastGRIP drill site and ranges from the central part of the ice stream up to 50 km beyond the shear margins. In our survey region, the ice stream accelerates from ~ 10 to more than 80 m a⁻¹ and widens from ~ 15 to ~ 55 km. The radar data also covers the transition in the position of the shear margin as well as strongly folded internal stratigraphy outside of the ice stream (see Figure 1). Figure 1b and c show the locations of radar profiles in relation to the ice surface velocity. Profiles extending perpendicular to ice flow have a spacing of 5 km in the region close

to the drill site and 10 km further up- and downstream. Along-flow profiles either follow flowlines, which in some cases pass through the shear margins, or are constantly located inside the ice stream. Other profiles are oriented parallel to ice flow of the NEGIS but are located outside of the ice stream.

The ice thickness in our survey region ranges from 2059 m to 3092 m and shows, on average, a gradual decrease in thickness from the upstream to the downstream part (Franke et al., 2020, 2019). An analysis of the bed topography, basal roughness and bed return echoes by Franke et al. (2021b) shows that our survey area can be divided into two different morphological regimes. The upstream part (upstream of EastGRIP) is characterised by a narrow ice stream width with accelerating ice flow velocity, a smooth bed with elongated flow-parallel subglacial landforms and a soft till layer at the base (Christianson et al., 2014). Downstream of EastGRIP, the ice stream widens, and we note an overall change to a rougher and more variable bed geomorphology. The ice stream widens up to 57 km and ice flow velocity keeps constant and decreases locally (Franke et al., 2021b).

In the 2012 summer field season, a scientific consortium collected ground-based geophysical data (RES and seismic survey) as well as a shallow ice core (Vallelonga et al., 2014). Christianson et al. (2014) examined the ice-bed interface by means of radar and seismic data analysis. They found high-porosity, water-saturated till, which lubricates the ice stream base and most likely facilitates ice stream flow. Keisling et al. (2014) used the same radar data to analyse the internal radar stratigraphy and suggest that the basal hydrology controls the upstream portion of the NEGIS. By contrast, the downstream part is rather confined by the bed topography. Riverman et al. (2019) and ? analysed the shear margins in particular and observed an increased accumulation and enhanced firn densification in the upper ice column as well as wet elongated subglacial landforms at the bed. Furthermore Holschuh et al. (2019) use RES data to evaluate 3-D thermomechanical models of the NEGIS. The authors highlight the complexity of the stagnant to streaming ice flow transition and provide insights into the englacial heat transport. Finally, a comprehensive chemical analysis of a 67 m deep firn core was conducted by Vallelonga et al. (2014). The results demonstrated that a deep ice core at this location has the potential to retrieve a reliable record of the Holocene and last-glacial cycle.

Methods

Radar data acquisition

The ultra-wideband (UWB) airborne radar is a Multichannel Coherent Radar Depth Sounder (MCoRDS, version 5) which was developed at the centre for Remote Sensing of Ice Sheets (CReSIS) at the University of Kansas (Hale et al., 2016). It has an improved hardware design compared to predecessor radar depth sounders by CReSIS (Gogineni et al., 1998; Wang et al., 2016). The radar configuration deployed in 2018 consists of an eight-element radar array mounted under the Polar 6 Basler BT-67 aircraft's fuselage. The eight antenna elements function as transmit and receive channels using a transmit-receive switch. The total transmit power is 6 kW, the radar can be operated within the frequency band of 150 – 600 MHz. The pulse repetition frequency (PRF) is 10 kHz, and the sampling frequency is 1.6 GHz. The characteristics of the transmitted waveform as well as the recording settings can be manually adjusted. We refer to the combined transmission/reception settings as *waveforms* in the following.

Table I.1: Acquisition parameters of the EGRIP-NOR-2018 radar campaign.

Parameter	Value
Radar system	MCoRDS5
Frequency range	180-210 MHz
Waveform signal	1, 3, 10 μ s chirp
Waveform presums ^a	2, 4, 32
Pulse Repetition Frequency	10 kHz
Sampling frequency	1600 MHz
Tukey window taper ratio	0.08
Transmit channels	8
Receiving channels	8
Aircraft altitude above ground	~ 360 m
Aircraft velocity	~ 260 km h ⁻¹

^aPresums are set for each waveform individually.

All profiles were recorded using linear frequency-modulated chirps in the frequency band of 180-210 MHz, antenna elements oriented with the E-plane aligned with the along-track (HH polarisation), and the transmit antenna beam pointed toward nadir. We used three alternating waveforms to increase the dynamic range of the system (see Table I.1). Short pulses (1 μ s) and low receiver gain of 11 dB to image the glacier surface, and longer pulses (3-10 μ s) with higher receiver gain (48 dB) to image internal features and the ice base.

Recorded traces were coherently presumed with zero-pi modulation in the hardware (Allen et al., 2005) to reduce the data rate and to increase signal-to-noise ratio (SNR), leading to a reduced effective PRF. The presumed factors were selected with regard to the pulse length of the respective waveform. To reduce range sidelobes without losing much signal power, the transmitted and the pulse compression filter were amplitude-tapered using a Tukey window with a taper ratio of 0.08 (Li et al., 2013).

Before the data acquisition, the amplitude, phase and time delay of the antenna elements were equalized during a test flight over open water during the transit to Greenland. During data acquisition, the position of the aircraft was determined by four NovAtel DL-V3 GPS receivers, which are sampling at 20 Hz. The GPS system operates with dual-frequency tracking so that the position accuracy can be enhanced during post-processing.

Radar data processing

The acquired data comprised 24 total radargrams, one from each pairwise combination of 8 receivers and 3 waveforms. The post-flight processing goal was to create single radargrams of the profiles covering the ice sheet from surface to bed with high SNR, fine resolution and high dynamic range. The main processing included pulse compression in the range dimension, synthetic aperture radar focusing in the along-track dimension and array processing in the cross-track/elevation-angle dimension. Lastly, we vertically concatenated the radargrams of the three waveforms. The post-processing tools are implemented in the CReSIS Toolbox (CReSIS, 2020b).

At first, the recorded traces were pulse compressed using a Tukey time domain weighting on the pulse and frequency domain matched filtering with a Hanning window to reduce sidelobes. For this purpose, the matched filter duplicates the transmitted waveforms based on the radar transmit settings.

SAR processing was carried out to focus the SAR radargrams in the along-track direction. The SAR processing is based on the *fk*-migration technique for layered media (Gazdag, 1978), which was adapted for radioglaciology (Leuschen et al., 2000). We used a two-layered velocity model with constant permittivity values for air ($\epsilon_r = 1$) and ice ($\epsilon_r = 3.15$). The air-ice interface was tracked using quicklook imagery, which is generated using 20 coherent averages followed by five incoherent averages by an automated threshold tracker. Platform motion compensation is applied during averaging. The SAR aperture length at each pixel was chosen to create a fixed along-track resolution of 2.5 m. A requirement for the *fk*-migration is a uniformly

sampled linear trajectory of the receivers along the SAR aperture extent. Changes in aircraft elevation, roll, pitch and heading lead to phase errors in the migrated data, thus to decreased SNR and blurring. Processed GPS and INS data in high precision from the aircraft were used to correct these effects. The motion compensation consisted of (1) uniform resampling the data in along-track using a windowed sinc interpolation, (2) fitting lines to the resampled trajectory with the length of the SAR aperture and (3) correcting any flight path deviations from the straight lines with phase shifts in the frequency domain.

After the along-track focusing, the channels were combined to increase the SNR and reduce the impact of surface clutter and off-nadir reflections. The delay-and-sum method allows for steering the antenna array beam. The antenna array beam is steered toward nadir by coherently summing the data from each channel while accounting for the actual position of each measurement phase centre. Eleven along-track averages (multilooking) are then performed to reduce speckle in the imagery.

Finally, the different waveform images were vertically combined to increase the dynamic range of the result. The TWT at which the radargrams are combined were chosen with regard to the pulse durations of the transmitted waveforms and the surface return in order to avoid saturation of the high gain channels due to the strong surface return. For 3 waveform collection with 1 μ s, 3 μ s, 10 μ s nadir waveforms, image 2 is combined with image 1 after 3e-6 s after the surface reflection and image 3 with image 2 10e-6 s after the surface return (see Figure I.5).

Resolution and uncertainty analysis

Range resolution

The theoretical range resolution after pulse compression is

$$\delta r = \frac{kc}{2B\sqrt{\epsilon_r}}, \quad (\text{I.1})$$

where c denotes the speed-of-light in a vacuum, ϵ_r the real part of the ordinary relative permittivity, B the bandwidth of the transmitted chirp and k the windowing factor due to the frequency and time domain windows. For the bandwidth of 30 MHz, the theoretical range resolution in ice with $\epsilon_r = 3.15$ and $k = 1.53$ is 4.31 m.

In addition, to estimate the accuracy of a specific target (internal layer or bed return), we have to consider the RMS error of the dielectric constant (CReSIS, 2020a). Here we depend on the exact detection of the

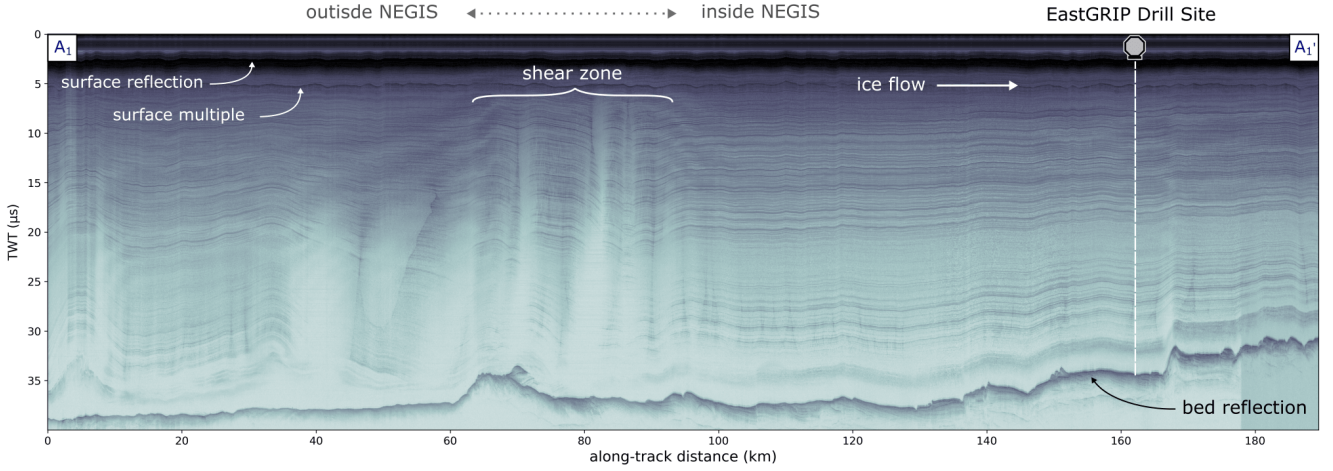


Figure I.2: Flow-parallel radar profile A composed of three frames: 20180512_01_001-004. The location is indicated in Figure I.1 a and covers the area outside of the ice stream, the shear zone and the ice stream's trunk. The position of the EastGRIP drill site is labeled and indicated with a white dashed vertical line.

Table I.2: Data record properties.

Parameter	Value
Covered area	25 000 km ²
Total profile distance	7494 km
Along-track resolution	~ 27 - 30 m (<i>qlook</i>) / ~ 15 m (<i>SAR</i> ₁) / ~ 3 m (<i>SAR</i> ₂)
Range resolution	4.31 m
Data amount	4.5 GB (<i>qlook</i>) / 9.5 GB (<i>SAR</i> ₁) / 25.6 GB (<i>SAR</i> ₂)

ice surface reflection, which is well constrained for our data.

To determine range resolution variability for the bed reflection for the radar data, we performed a crossover analysis of bed pick intersections (see Franke et al., 2020) and calculated the mean deviation h_c . We consider an error on the order of 1% for the dielectric constant for typical dry ice (Bohleber et al., 2012),

$$\sigma_r = \sqrt{(h_c)^2 + \left(\frac{T}{2} 0.01\right)^2}, \quad (\text{I.2})$$

with the ice thickness T and a mean value for crossover deviation, h_c . The full analysis of the range resolution of the bed reflection is documented in Franke et al. (2020) and shows a variability from 13 to 17 m.

Bed return resolution

A further parameter is the size of the area illuminated by the radar wave in the bed reflection signal. Here we consider a cross-track resolution for a typical rough

surface σ_y . It is constrained by the pulse-limited footprint and depends on the Tukey and Hanning window parameters,

$$\sigma_y = 2\sqrt{\frac{H}{\sqrt{\epsilon_r}} ck_i \frac{1}{B}}, \quad (\text{I.3})$$

where H is the elevation of the aircraft over the ice surface. All EGRIP-NOR-2018 flights were performed at an aircraft elevation of ~ 365 m above ground. When off-nadir clutter is visible in the radargrams, the cross-track resolution depends on the full beam width, β_y , of the antenna array,

$$\beta_y = \arcsin \frac{\lambda_c}{Nd_y}, \quad (\text{I.4})$$

where λ_c is the wavelength at the centre frequency, N is the number of array elements and d_y the element spacing of the antennas. The cross-track resolution is

now defined as

$$\sigma_y = 2 \frac{H + T}{\sqrt{\varepsilon}} \tan \frac{\beta_y k_t}{2}. \quad (\text{I.5})$$

For areas without signal-layover, the cross-track footprint ranges between 300–350 m for an ice column of 2000–3000 m in our survey region (Franke et al., 2020). Where layover occurs, we have to consider Equation (I.5) with a beam angle of $\sim 21^\circ$. Here the cross-track resolution ranges between 800 m to 1100 m.

Results

The design of the EGRIP-NOR-2018 radar survey enables a detailed analysis of the bed and englacial stratigraphy: (i) along radar profiles which are parallel to the ice flow (Figure I.1 c) and (ii) along radar profiles perpendicular to the ice flow, crossing the shear margins (Figure I.1 b). In addition, several radar lines cover the location where the northern shear margin shifts its location (Figure I.1 a) and an area South-West of EastGRIP where we observe patterns of strong internal ice deformation (location indicated in Figure I.1 a).

In flow-parallel profiles, we observe three regimes showing different characteristics in the radar stratigraphy. Figure I.2 shows a ~ 200 km long flow-parallel radargram extending from the far upstream end outside of the NEGIS up to 30 km downstream of EastGRIP. The area outside of the ice stream in a distance of 0–60 km shows slightly folded internal layers, which have no connection to the local basal topography. Steeply dipping internal layers are characterised by a decrease in reflectivity with depth. The part of the profile, which is crossing the shear zone (in 60–90 km distance) is characterised by tight folds in the internal layers, which extend almost up to the ice surface. The folds' apparent wavelength in profile direction depends on the intersection angle with respect to the shear margin orientation. Folds are tightest in profiles oriented $\sim 90^\circ$ to the shear margin fold axis. We observe the best resolution of internal layers inside the ice stream, particularly in the lower part of the ice column. All distortions in the internal stratigraphy inside the ice stream seem to be related to the underlying bed.

Radar profiles oriented perpendicular to ice flow show a strong imprint of NEGIS' dynamics. The most striking features are tight folds in the area of the shear margins. Bright stripes characterise them in the radargrams (e.g. Figure I.3), which represent a loss in return power due to steeply inclined internal reflectors (Holschuh et al., 2014). The onset of this kind of folding starts at the shear zone's outer boundary (marked by yellow triangles in Figure I.3 c and d). Depending on the ice stream's location and width, these folds can be

traced towards the ice stream centre for up to tens of kilometres, also towards locations where no shearing at the ice surface is observed. This becomes evident by comparing the upstream and further downstream radargram in Figure I.3 c and d.

At several locations in flow-perpendicular radargrams we observe a drawdown of the radar stratigraphy towards the shear zone's outer margin (see Figure I.3 c). In general, the stratigraphy of internal layers North-West of the NEGIS differs from the stratigraphy South-East of the NEGIS. The North-West is much more undisturbed than the South-East. A distinct example is shown in Figure I.3 a and b. The stratigraphy is marked by long-wavelength anticlines and synclines with elevation differences of almost half of the ice column. In the anticlines' cores, we find strong englacial reflections, which have been misinterpreted before as bedrock (Franke et al., 2020). We note that some of the englacial reflections appear to be attached to the basal reflection (Figure I.3 a). Figure I.3 b shows that the deformations patterns in the anticline cores are very complex.

Data products

We offer three different data products of the EGRIP-NOR-2018 radar survey: (i) quick-looks (qlook), (ii) SAR focused (SAR₁) and (iii) SAR focused with a large aperture (SAR₂). Detailed documentation can be found in the CReSIS MCoRDS documentation (<https://data.cresis.ku.edu/>) and on the CReSIS Wiki Website (https://ops.cresis.ku.edu/wiki/index.php/Main_Page). In Figure I.4 we provide an overview of the differences between these three data products of the radargrams.

Qlook

This product uses unfocused synthetic aperture radar processing for each channel and assumes that all reflections arrive at the receiver from nadir. The data are coherently stacked in slow time and no correction for propagation delay changes is applied. Here, no motion compensation is applied. Finally, the signals from all eight channels are averaged incoherently. The range resolution is the same as for all other products. The trace spacing is ~ 27 –30 m.

SAR with default settings (SAR₁)

This data product uses focused synthetic aperture radar processing (fk migration) on each channel individually. The SAR processing requires a uniformly sampled linear trajectory along the extent of the SAR aperture. Motion compensation is applied using high precision

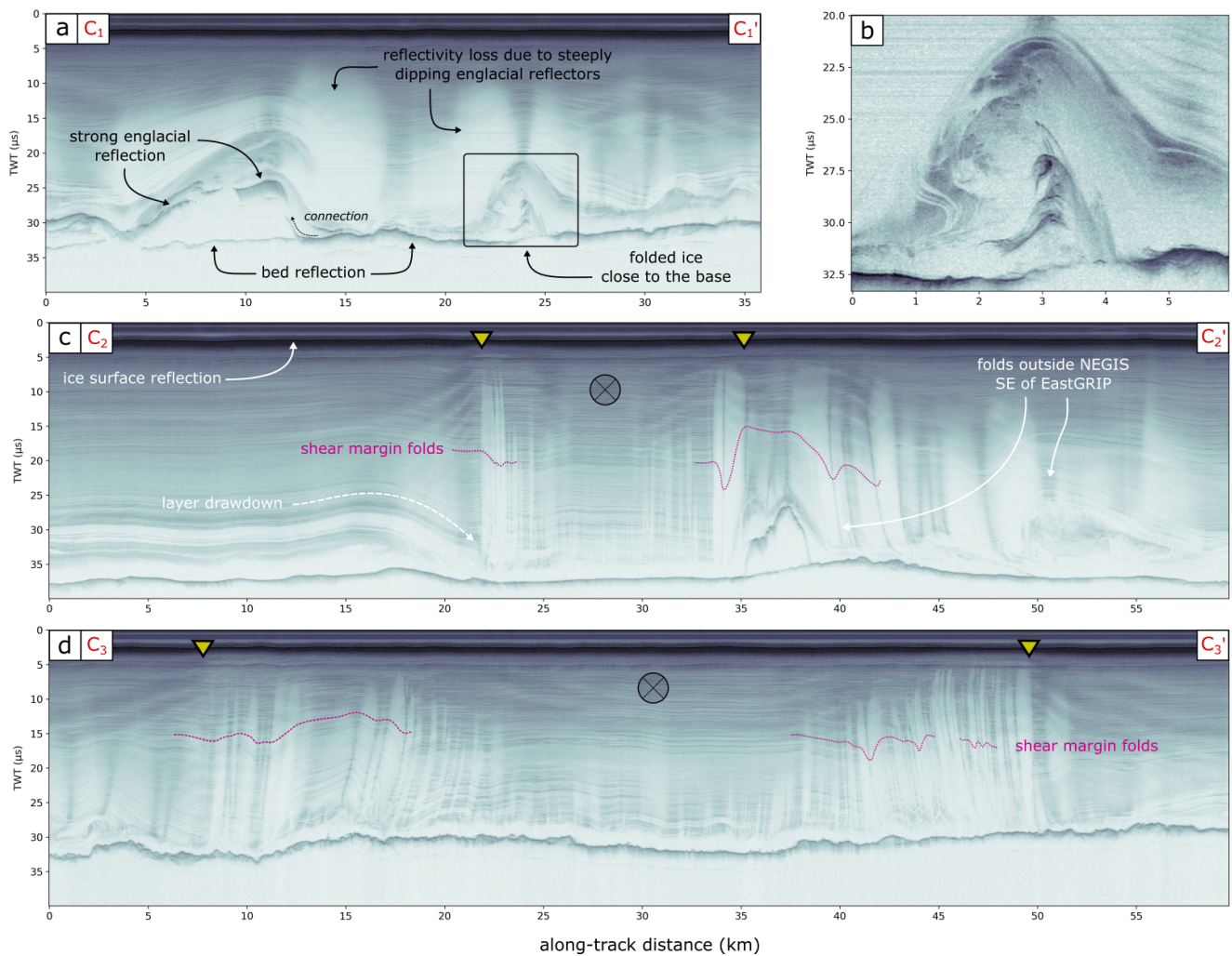


Figure I.3: Radar profiles $C_{1,2,3}$ (frames 20180508_06_003, 20180511_01_007 and 20180514_01_011-012, respectively). The corresponding locations are shown in Figure I.1 a. Panel (a) shows a profile located outside of the NEGIS, SE of EastGRIP. A close up of an anticline and other patterns of deformation are shown in panel (b), resembling the skeleton of a dead penguin. A slice through the ice stream in the upstream region is shown in panel (c) and a radar section further downstream in (d). The position of the shear margins (the maximum in the surface velocity gradient) are indicated with a yellow triangle and the folds in the shear margin areas with purple lines. The ice flow direction is out of the page.

processed GPS and INS data from the aircraft. The direction of arrival is estimated by delay-and-sum beamforming to combine the channels. A Hanning window is applied in the frequency domain to suppress sidelobes. This product is comparable to the CRISIS standard data product. The trace spacing is ~ 15 m.

SAR with wider angular range (SAR₂)

By processing at a finer SAR resolution, the SAR processor uses scattered energy from a wider angular range around nadir to form the image. Since the angle of scattered returns from a specular internal layer is proportional to the internal layer slope, the SAR processor's increased sensitivity to larger angle returns translates to an increased sensitivity to layers with larger slopes. We

achieve a better resolution of steeply inclined internal reflectors by changing the along-track resolution before SAR processing to 1 m ($\approx \sigma_x = 1$, whereas the default setting is $\sigma_x = 2.5$). 1 m is not the smallest possible value for processing, but is on the limit to achieve a sufficiently high SNR. The SNR is smaller for larger angles because the range to the target increases for greater angles, which leads to additional signal loss (spherical spreading loss and additional signal attenuation in ice). The differences between radargrams processed with $\sigma_x = 1$ and 2.5 are shown in Figure I.4. The final trace spacing is ~ 3 m.

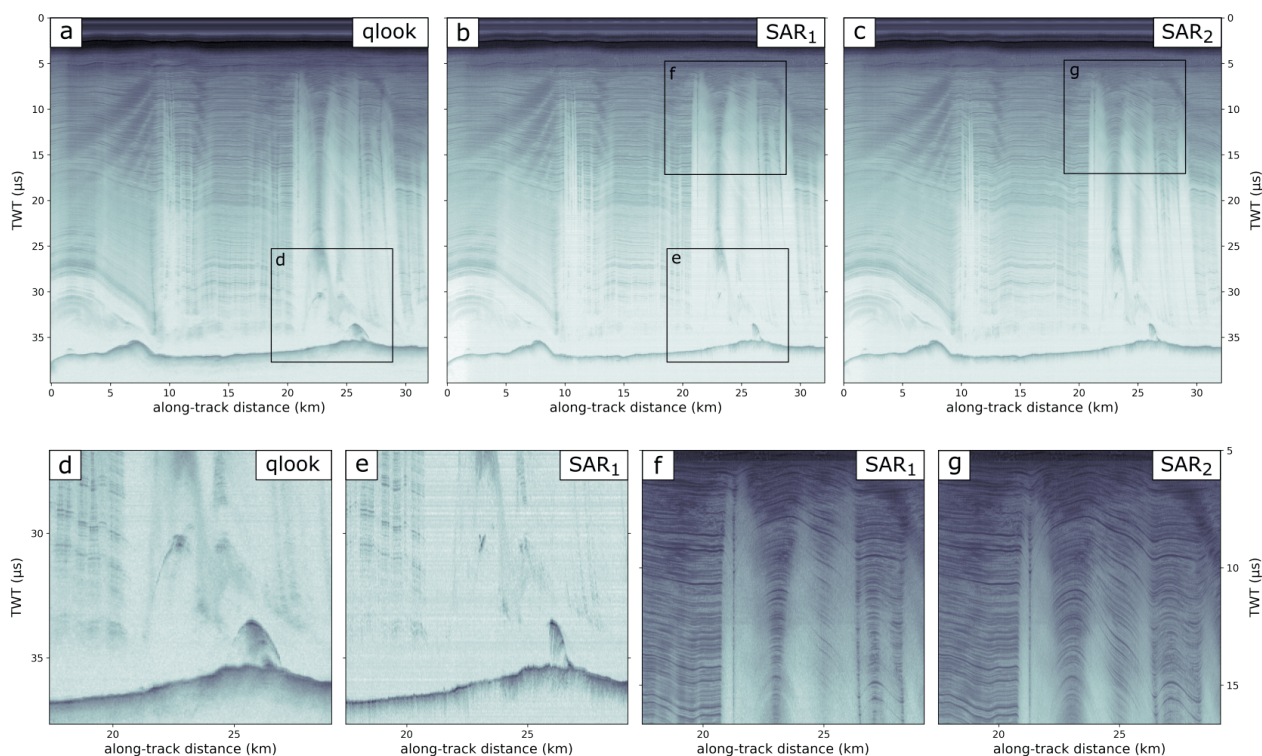


Figure I.4: Radargrams of a flow-perpendicular radar profile showing the three different data products: (a) quick-look (qlook) processed, (b) SAR focused (SAR_1) and (c) SAR focused with a larger aperture (SAR_2). The main difference between qlook and SAR_1 is the focusing of signals via fk migration (panel d and e). In contrast do the default SAR focusing (panel f) a larger aperture enables a better resolution of steeply inclined internal layers (panel g).

Individual waveforms

The combination of the three waveform images will increase the dynamic range of the whole radargram. However, specific analyses may require only a single waveform. Therefore, we provide the respective echogram data for each waveform separately (see Figure I.5). The files are labelled with *img_01*, *img_02* and *img_03* for image 1, 2 and 3, respectively.

Image mode flights

In addition to the data recorded in the so-called sounding mode, the data set also contains two segments (20180510_02 and 20180515_01) recorded in the image mode (see Table I.3). The acquisition settings of these segments are slightly different since the transmission signals are composed of four instead of three pulses: 1 μ s and 3 μ s waveforms with nadir directed transmit beam followed by two 10 μ s waveforms, one with the transmit beam directed to the left and one with it directed to the right to increase the imaged swath width at the ice bottom. We processed the data in a way that the 10 μ s left and 10 μ s right signal are steered towards nadir during data processing. This is possible because both waveforms contain nadir information since the

beams overlap at nadir. However, the reflection power from nadir is reduced because the two side looking transmit beams have reduced gain by about 3-4 dB relative to when the beam is pointed directly at nadir. The third waveform (see Figure I.5 c and d) in the combined image for the two particular segments has been computed from the coherent combination of both, the 10 μ s left and 10 μ s right return signals.

Data formats

We provide the main radar data and auxiliary data in the following formats:

1. The radar data containing a matrix of the echogram and the corresponding GPS information, such as coordinates, aircraft elevation, and timing of every trace, are stored as *matfiles* (HDF-5 based format). The echograms are provided for the combined waveform product as well as for the individual waveforms. Furthermore, these files contain cell arrays with information about all processing parameters used.
2. A set of figures for each profile, showing the radargram and its respective location in the EGRIP-NOR-2018 survey.

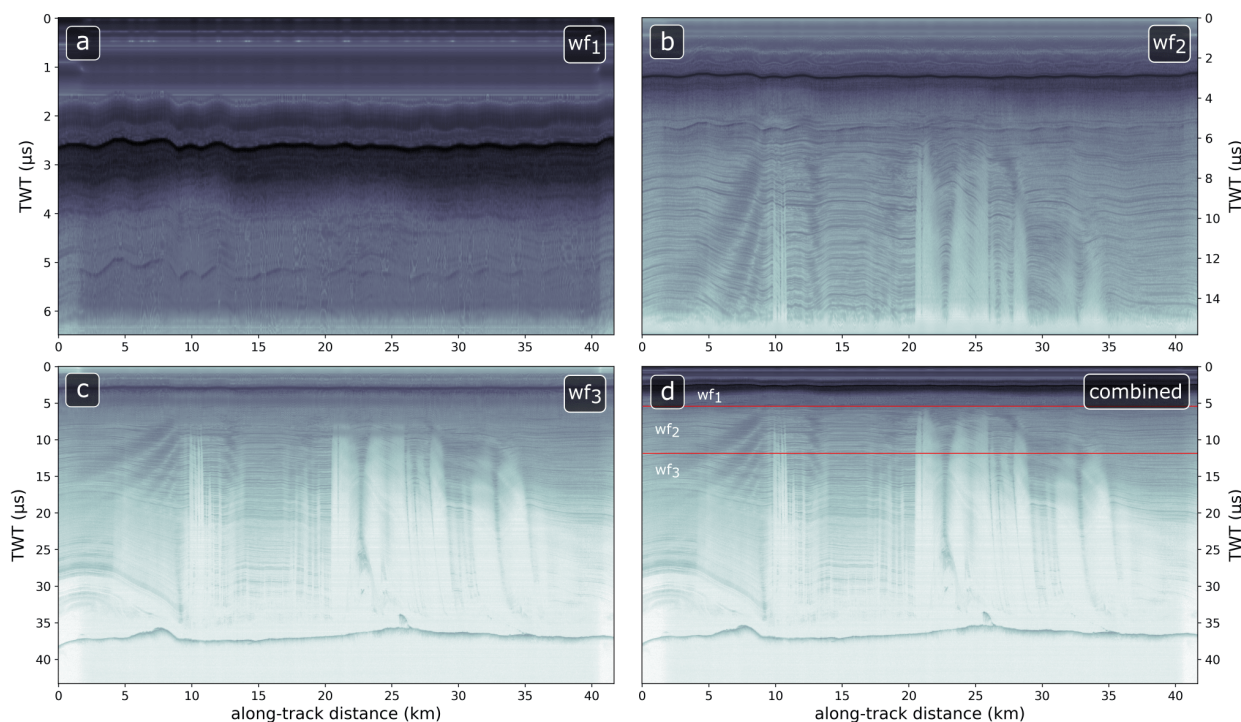


Figure I.5: Radargrams of the frame 20180517_01_008 subdivided into: (a) waveform 1, (b) waveform 2, (c) waveform 3 and (d) the radargram composed of all three waveforms in combination. The locations, where the different waveforms are concatenated, are indicated with red lines in (d). Waveform 1 and 2 are plotted at full range. Note the different resolution of the near-surface stratigraphy in waveforms 1 to 3.

3. A set of shapefiles (lines) containing the location of every frame.
4. An Excel Spreadsheet which contains all parameter settings applied during radar data processing.

In the Appendix we describe the data architecture and how the data is stored in the PANGAEA repository.

Relevance of the data set

This radar data set provides essential observations of internal and bed reflections to determine spatial distribution of ice thickness, internal layering and reflectivity. These observables constitute boundary conditions and elucidate properties and processes of the NEGIS. The data comprises ~7500 km high-resolution radar data to the scientific community. In contrast to previous surveys in this area, the data presented here were specifically recorded over a broad spatial extent to understand the history of the NEGIS and our general understanding about ice streams. The tightly spaced radar profiles perpendicular to ice flow allow a 3D interpretation of the ice-internal stratigraphic architecture. Because most radar lines are directly or indirectly spatially connected to the location of the drill site of the EastGRIP ice core, these data are significant for various objectives regarding the ice-dynamic understanding of NEGIS as well

as interpretation of the climate proxy record retrievable from the ice core. With this data set the scientific community will be able to upscale the findings of the EastGRIP project from the location of the ice core to the immediate surrounding of the upstream part of the NEGIS. The prospect that parts of the ice core can be rotated back into their correct geographic direction (Westhoff et al., 2020) also allows a systematic analysis of ice crystal orientation fabric together with the radar data. Furthermore, the data presented here can be combined with the radar data acquired during Operation Ice Bridge (OIB) to extend the large-scale understanding of glaciological properties in the Greenland Ice Sheet.

Conclusions

We present a high-resolution ice-penetrating radar data set at the onset region of the NEGIS. The EGRIP-NOR-2018 radar data reveal the internal stratigraphy and bed topography of the upstream part of the NEGIS in high vertical and horizontal resolution, given the dense coverage. Several survey lines intersect at the EastGRIP drill site location, enabling a combination of both data sets. Ultimately, this data set will improve our understanding of the NEGIS in its present form and also contributes to our understanding of its genesis and evolution. Radar and auxiliary data will be provided

Table I.3: EGRIP-NOR-2018 segment specifications.

Segment	Frames	Frequency Range	Waveforms (pulse length and direction)	Segment Length
20180508_02	2	180–210 MHz	3 (1 μ s, 3 μ s, 10 μ s nadir)	72 km
20180508_06	4	180–210 MHz	3 (1 μ s, 3 μ s, 10 μ s nadir)	189 km
20180509_01	18	180–210 MHz	3 (1 μ s, 3 μ s, 10 μ s nadir)	852 km
20180510_01	15	180–210 MHz	3 (1 μ s, 3 μ s, 10 μ s nadir)	726 km
20180510_02 ^a	15	180–210 MHz	4 (1 μ s and 3 μ s nadir, 10 μ s left, 10 μ s right)	675 km
20180511_01	13	180–210 MHz	3 (1 μ s, 3 μ s, 10 μ s nadir)	721 km
20180512_01	15	180–210 MHz	3 (1 μ s, 3 μ s, 10 μ s nadir)	635 km
20180512_02	14	180–210 MHz	3 (1 μ s, 3 μ s, 10 μ s nadir)	645 km
20180514_01	19	180–210 MHz	3 (1 μ s, 3 μ s, 10 μ s nadir)	750 km
20180514_03	12	180–210 MHz	3 (1 μ s, 3 μ s, 10 μ s nadir)	740 km
20180515_01 ^a	16	180–210 MHz	4 (1 μ s and 3 μ s nadir, 10 μ s left, 10 μ s right)	733 km
20180517_01	20	180–210 MHz	3 (1 μ s, 3 μ s, 10 μ s nadir)	753 km

^aThe nadir part of all four waveforms was used for image combination

as *matfiles* for the combined echograms as well as for the individual waveforms. The radar data products comprise unfocused data (qlook), SAR focused data (SAR₁) and SAR focused data with a wider angular range (SAR₂)

Code and data availability

The EGRIP-NOR-2018 radar data products are available at the PANGAEA Data Publisher (<https://doi.pangaea.de/10.1594/PANGAEA.928569>; Franke et al. 2021a). The EGRIP-NOR-2018 bed topography (Franke et al. (2019) is available under <https://doi.pangaea.de/10.1594/PANGAEA.907918>). The CReSIS-toolbox is available under <https://github.com/CReSIS/> and the main documentation can be found at <https://ops.cresis.ku.edu/wiki/>. The MEaSUREs Greenland Ice Sheet Velocity Map from InSAR Data, Version 2 from Joughin et al. (2017) is available from <https://doi.org/10.5067/OC7B04ZM9G6Q>.

Author contributions

Steven Franke, Nils Dörr and Tamara Gerber wrote the manuscript. Tobias Binder, Daniela Jansen and John Paden acquired the radar data in the field. Olaf Eisen and Daniela Jansen were PI and co-PI of the radar campaign. Tobias Binder and Steven Franke processed the radar data with the support of John Paden, Daniela Jansen, Veit Helm and Daniel Steinhage. All authors discussed and revised the manuscript.

Acknowledgements

We thank the AWI and Ken Borek crew of the research aircraft Polar6. Logistical support in the field was provided by the East Greenland Ice-Core Project. EastGRIP is directed and organized by the centre of Ice and Climate at the Niels Bohr Institute. It is supported by funding agencies and institutions in Denmark (A. P. Møller Foundation, University of Copenhagen), USA (U.S. National Science Foundation, Office of Polar Programs), Germany (Alfred Wegener Institute, Helmholtz Centre for Polar and Marine Research), Japan (National Institute of Polar Research and Arctic Challenge for Sustainability), Norway (University of Bergen and Bergen Research Foundation), Switzerland (Swiss National Science Foundation), France (French Polar Institute Paul-Emile Victor, Institute for Geosciences and Environmental research) and China (Chinese Academy of Sciences and Beijing Normal University). We acknowledge the use of the CReSIS toolbox from CReSIS generated with support from the University of Kansas, NASA Operation IceBridge grant NNX16AH54G, and NSF grants ACI-1443054, OPP-1739003, and IIS-1838230.

Appendix

Additional information for the segments

The data are stored in *zip* archives for each segment and processing product, respectively. For details on the specifications of each segment and their respective coverage, see Table I.3 and Figure I.6. The filenames of the archives are composed of the segment

and the data product (e.g. 20180508_02_qlook.zip, 20180508_02_sar1.zip and 20180508_02_sar2.zip for the quick-look, SAR with default settings (SAR₁) and SAR with larger angular range data product (SAR₂), respectively). Each *zip* archive contains the individual frames in the *matfile* format.

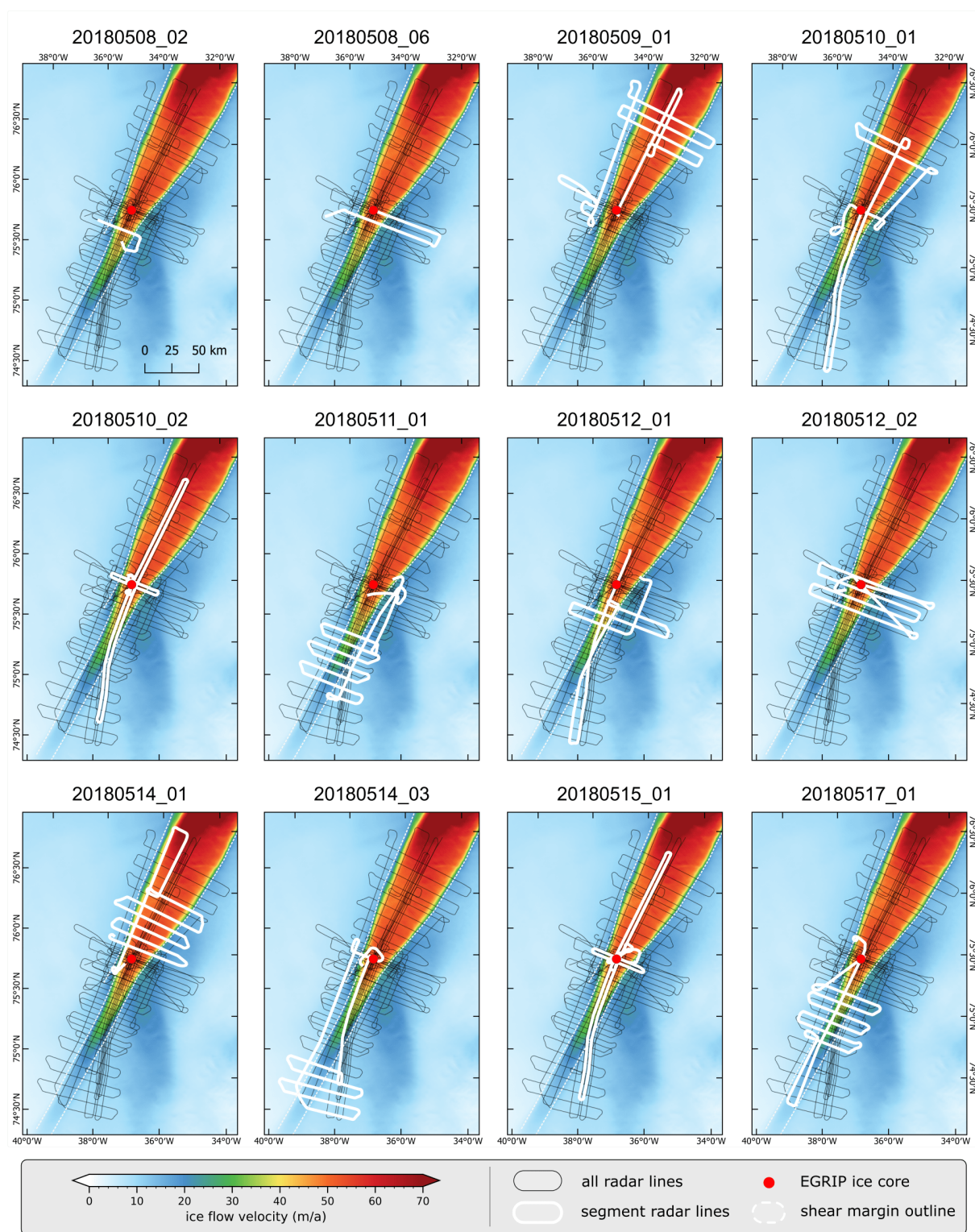


Figure I.6: Radar profiles locations of the 12 segments shown in Table I.3 of the EGRIP-NOR-2018 data set. The respective segments are highlighted with a white line and the radar profiles of the complete survey with a finer black line. The background map represents ice surface velocity from Joughin et al. (2017). The shear margin is indicated with a white dashed outline and the location of EastGRIP with a red dot.

Bibliography

- Non-surface mass balance of glaciers in iceland. 66. doi: 10.1017/jog.2020.37. URL <https://doi.org/10.1017/jog.2020.37>.
- Allen, C. T., Mozaffar, S. N., and Akins, T. L. Suppressing coherent noise in radar applications with long dwell times. *IEEE Geoscience and Remote Sensing Letters*, 2(3): 284–286, July 2005. doi: 10.1109/LGRS.2005.847931. URL <http://dx.doi.org/10.1109/LGRS.2005.847931>.
- Baldwin, D. J., Bamber, J. L., Payne, A. J., and Layberry, R. L. Using internal layers from the Greenland ice sheet, identified from radio-echo sounding data, with numerical models. *Annals of Glaciology*, 37:325–330, 2003. ISSN 02603055. doi: 10.3189/172756403781815438.
- Bamber, J. L., Griggs, J. A., Hurkmans, R. T. W. L., Dowdeswell, J. A., Gogineni, S. P., Howat, I., Mouginot, J., Paden, J., Palmer, S., Rignot, E., and Steinhage, D. A new bed elevation dataset for Greenland. *Cryosphere*, 7(2): 499–510, 2013. ISSN 19940416. doi: 10.5194/tc-7-499-2013. URL <http://dx.doi.org/10.5194/tc-7-499-2013>.
- Blackwell, D. and Richards, M. Geothermal map of north america, aapg map, scale 1:6,500,000, 2004.
- Bohleber, P., Wagner, N., and Eisen, O. Permittivity of ice at radio frequencies: Part ii. artificial and natural polycrystalline ice. *Cold Regions Science and Technology*, 83-84:13–19, 2012. ISSN 0165-232X. doi: <https://doi.org/10.1016/j.coldregions.2012.05.010>. URL <https://www.sciencedirect.com/science/article/pii/S0165232X12001103>.
- Bons, P. D., de Riese, T., Franke, S., Llorens, M.-G., Sachau, T., Stoll, N., Weikusat, I., and Zhang, Y. Comment on “exceptionally high heat flux needed to sustain the north-east greenland ice stream” by s. smith-johnson et al., the cryosphere, 14, 841–854, 2020. *The Cryosphere Discussions*, 2020:1–5, 2020. doi: 10.5194/tc-2020-339. URL <https://tc.copernicus.org/preprints/tc-2020-339/>.
- Buchardt, S. L. and Dahl-Jensen, D. Estimating the basal melt rate at northgrip using a monte carlo technique. *Annals of Glaciology*, 45:137–142, 2007. doi: 10.3189/172756407782282435. URL <https://doi.org/10.3189/172756407782282435>.
- Carter, S. P., Blankenship, D. D., Peters, M. E., Young, D. A., Holt, J. W., and Morse, D. L. Radar-based subglacial lake classification in Antarctica. *Geochemistry, Geophysics, Geosystems*, 8(3), 2007. ISSN 15252027. doi: 10.1029/2006GC001408. URL <https://doi.org/10.1029/2006GC001408>.
- Christianson, K., Peters, L. E., Alley, R. B., Anandakrishnan, S., Jacobel, R. W., Riverman, K. L., Muto, A., and Keisling, B. A. Dilatant till facilitates ice-stream flow in north-east Greenland. *Earth and Planetary Science Letters*, 401: 57–69, sep 2014. doi: 10.1016/j.epsl.2014.05.060. URL <https://doi.org/10.1016%2Fj.epsl.2014.05.060>.
- Copland, L. and Sharp, M. Mapping thermal and hydrological conditions beneath a polythermal glacier with radio-echo sounding. *Journal of Glaciology*, 47(157):232–242, 2001. ISSN 00221430. doi: 10.3189/172756501781832377.
- CReSIS. CReSIS rds documentation., 2020a. URL https://data.cresis.ku.edu/data/rds/rds_readme.pdf.
- CReSIS. CReSIS Toolbox [computer software], Lawrence, Kansas, USA. Retrieved from <https://github.com/CReSIS>, 2020b. URL https://ops.cresis.ku.edu/wiki/index.php/Main_Page.
- Dahl-Jensen, D., Thorsteinsson, T., Alley, R., and Shoji, H. Flow properties of the ice from the Greenland Ice Core Project ice core: The reason for folds? *Journal of Geophysical Research: Oceans*, 102(C12):26831–26840, 1997. ISSN 21699291. doi: 10.1029/97JC01266. URL <https://doi.org/10.1029/97JC01266>.
- Eder, K., Reidler, C., Mayer, C., and Leopold, M. Crevasse detection in alpine areas using ground penetrating radar as a component for a mountain guide system. *International Archives of the Photogrammetry, Remote Sensing and Spatial Information Sciences - ISPRS Archives*, 37:837–842, 2008. ISSN 1682-1750.
- Eisen, O., Hamann, I., Kipfstuhl, S., Steinhage, D., and Wilhelm, F. Direct evidence for radar reflector originating from changes in crystal-orientation fabric. *The Cryosphere Discussions*, 1(1):1–16, jun 2007. doi: 10.5194/tcd-1-1-2007. URL <https://doi.org/10.5194%2Ftcd-1-1-2007>.
- Fahnestock, M., Bindschadler, R., Kwok, R., and Jezek, K. Greenland Ice Sheet Surface Properties and Ice Dynamics from ERS-1 SAR Imagery. *Science*, 262(5139):1530–1534, dec 1993. doi: 10.1126/science.262.5139.1530. URL <https://doi.org/10.1126%2Fscience.262.5139.1530>.
- Fahnestock, M., Abdalati, W., Joughin, I., Brozena, J., and Gogineni, P. High geothermal heat flow, basal melt, and the origin of rapid ice flow in central Greenland. *Science*, 294(5550):2338–2342, 2001. ISSN 00368075. doi: 10.1126/science.1065370. URL <http://dx.doi.org/10.1126/science.1065370>.
- Franke, S., Jansen, D., Binder, T., Dörr, N., Paden, J., Helm, V., Steinhage, D., and Eisen, O. Bedrock topography and ice thickness in the onset region of the Northeast Greenland Ice Stream recorded with the airborne AWI Ultra-Wideband radar (UWB) in 2018, 2019. URL <https://doi.pangaea.de/10.1594/PANGAEA.907918>.
- Franke, S., Jansen, D., Binder, T., Dörr, N., Helm, V., Paden, J., Steinhage, D., and Eisen, O. Bed topography and subglacial landforms in the onset region of the Northeast Greenland Ice Stream. *Annals of Glaciology*, 61(81): 143–153, mar 2020. doi: 10.1017/aog.2020.12. URL <https://doi.org/10.1017%2Faog.2020.12>.

- Franke, S., Binder, T., Jansen, D., Paden, J. D., Dörr, N., Gerber, T., Miller, H., Dahl-Jensen, D., Helm, V., Steinhage, D., Weikusat, I., Wilhelms, F., and Eisen, O. [DATASET] Ultra-wideband radar data over the shear margins and along flow lines at the onset region of the Northeast Greenland Ice Stream (NEGIS), 2021a. URL <https://doi.pangaea.de/10.1594/PANGAEA.928569>.
- Franke, S., Jansen, D., Beyer, S., Neckel, N., Binder, T., Paden, J., and Eisen, O. Complex basal conditions and their influence on ice flow at the onset of the northeast greenland ice stream. *Journal of Geophysical Research: Earth Surface*, 126(3):e2020JF005689, 2021b. doi: 10.1029/2020JF005689. URL <https://agupubs.onlinelibrary.wiley.com/doi/abs/10.1029/2020JF005689>.
- Frezzotti, M., Gandolfi, S., and Urbini, S. doi: 10.1029/2001JD000673. URL <https://doi.org/10.1029/2001JD000673>.
- Fujita, S., Maeno, H., Uratsuka, S., Furukawa, T., Mae, S., Fujii, Y., and Watanabe, O. Nature of radio echo layering in the Antarctic Ice Sheet detected by a two-frequency experiment. *Journal of Geophysical Research: Solid Earth*, 104(B6):13013–13024, jun 1999. doi: 10.1029/1999jb900034. URL <https://doi.org/10.1029/1999jb900034>.
- Gazdag, J. Wave equation migration with the phase-shift method. *Geophysics*, 43(7):1342–1351, 1978. ISSN 0016-8033. doi: 10.1190/1.1440899. URL <http://dx.doi.org/10.1190/1.1440899>.
- Gerber, T. A., Hvidberg, C. S., Rasmussen, S. O., Franke, S., Sinnl, G., Grinsted, A., Jansen, D., and Dahl-Jensen, D. Upstream flow effects revealed in the eastgrip ice core using a monte carlo inversion of a two-dimensional ice-flow model. *The Cryosphere Discussions*, 2021:1–32, 2021. doi: 10.5194/tc-2021-63. URL <https://tc.copernicus.org/preprints/tc-2021-63/>.
- Gogineni, S., Chuah, T., Allen, C., Jezek, K., and Moore, R. K. An improved coherent radar depth sounder. *Journal of Glaciology*, 44(148):659–669, 1998. doi: 10.3189/S002214300002161. URL <https://doi.org/10.3189/S002214300002161>.
- Hale, R., Miller, H., Gogineni, S., Yan, J. B., Leuschen, C., Paden, J., and Li, J. Multi-channel ultra-wideband radar sounder and imager. *2016 IEEE International Geoscience and Remote Sensing Symposium (IGARSS)*, pages 2112–2115, 2016. doi: 10.1109/IGARSS.2016.7729545. URL <http://dx.doi.org/10.1109/IGARSS.2016.7729545>.
- Hempel, L. and Thyssen, F. Deep radio echo soundings in the vicinity of GRIP and GISP2 drill sites, Greenland. *Polarforschung*, 62(1):11–16, 1992. ISSN 00322490. URL <https://epic.awi.de/id/eprint/28321/>.
- Hempel, L., Thyssen, F., Gundestrup, N., Clausen, H. B., and Miller, H. A comparison of radio-echo sounding data and electrical conductivity of the GRIP ice core. *Journal of Glaciology*, 46(154):369–374, 2000. ISSN 00221430. doi: 10.3189/172756500781833070. URL <https://doi.org/10.3189/172756500781833070>.
- Hodgkins, R., Siegert, M. J., and Dowdeswell, J. A. doi: 10.3189/172756500781833223. URL <https://doi.org/10.3189/172756500781833223>.
- Holschuh, N., Christianson, K., and Anandakrishnan, S. Power loss in dipping internal reflectors imaged using ice-penetrating radar. *Annals of Glaciology*, 55(67):49–56, 2014. doi: 10.3189/2014aog67a005. URL <https://doi.org/10.3189/2F2014aog67a005>.
- Holschuh, N., Lilien, D., and Christianson, K. Thermal Weakening, Convergent Flow, and Vertical Heat Transport in the Northeast Greenland Ice Stream Shear Margins. *Geophysical Research Letters*, 46:8184–8193, 2019. doi: 10.1029/2019GL083436. URL <https://doi.org/10.1029/2019GL083436>.
- Huybrechts, P., Steinhage, D., Wilhelms, F., and Bamber, J. Balance velocities and measured properties of the Antarctic ice sheet from a new compilation of gridded data for modelling. *Annals of Glaciology*, 30(1996):52–60, 2000. ISSN 02603055. doi: 10.3189/172756400781820778. URL <https://doi.org/10.3189/172756400781820778>.
- Jacobel, R. W. and Hodge, S. M. Radar internal layers from the greenland summit. *Geophysical Research Letters*, 22(5):587–590, 1995. doi: <https://doi.org/10.1029/95GL00110>. URL <https://agupubs.onlinelibrary.wiley.com/doi/abs/10.1029/95GL00110>.
- Jacobel, R. W., Gades, A. M., Gottschling, D. L., Hodge, S. M., and Wright, D. L. Interpretation of radar-detected internal layer folding in West Antarctic ice streams. *Journal of Glaciology*, 39(133):528–537, 1993. ISSN 00221430. doi: 10.1017/s0022143000016427. URL <https://doi.org/10.1017/s0022143000016427>.
- Jordan, T. M., Schroeder, D. M., Elsworth, C. W., and Siegfried, M. R. Estimation of ice fabric within Whillans Ice Stream using polarimetric phase-sensitive radar sounding. *Annals of Glaciology*, 61(81):74–83, 2020. ISSN 02603055. doi: 10.1017/aog.2020.6. URL <https://doi.org/10.1017/aog.2020.6>.
- Joughin, I., Fahnestock, M., MacAyeal, D., Bamber, J. L., and Gogineni, P. Observation and analysis of ice flow in the largest Greenland ice stream. *Journal of Geophysical Research Atmospheres*, 106(D24):34021–34034, 2001a. ISSN 01480227. doi: 10.1029/2001JD900087.
- Joughin, I., Fahnestock, M., MacAyeal, D., Bamber, J. L., and Gogineni, P. Observation and analysis of ice flow in the largest Greenland ice stream. *Journal of Geophysical Research: Atmospheres*, 106(D24):34021–34034, dec 2001b. doi: 10.1029/2001jd900087. URL <https://doi.org/10.1029/2F2001jd900087>.
- Joughin, I., Smith, B. E., and Howat, I. M. A complete map of Greenland ice velocity derived from satellite data collected over 20 years. *Journal of Glaciology*, 64(243):1–11, nov 2017. doi: 10.1017/jog.2017.73. URL <https://doi.org/10.1017/2Fjog.2017.73>.

- Kanagaratnam, P., Gogineni, S. P., Gundestrup, N., and Larsen, L. High-resolution radar mapping of internal layers at the North Greenland Ice Core Project. *Journal of Geophysical Research Atmospheres*, 106(D24):33799–33811, 2001. ISSN 01480227. doi: 10.1029/2001JD900191. URL <https://doi.org/10.1029/2001JD900191>.
- Keisling, B. A., Christianson, K., Alley, R. B., Peters, L. E., Christian, J. E., Anandakrishnan, S., Riverman, K. L., Muto, A., and Jacobel, R. W. Basal conditions and ice dynamics inferred from radar-derived internal stratigraphy of the northeast Greenland ice stream. *Annals of Glaciology*, 55(67):127–137, 2014. doi: 10.3189/2014aog67a090. URL <https://doi.org/10.3189/2014aog67a090>.
- Leuschen, C., Gogineni, S., and Tammana, D. SAR processing of radar echo sounder data. pages 2570–2572, 2000. doi: 10.1109/igarss.2000.859643. URL <http://dx.doi.org/10.1109/igarss.2000.859643>.
- Li, J., Paden, J., Leuschen, C., Rodriguez-Morales, F., Hale, R. D., Arnold, E. J., Crowe, R., Gomez-Garcia, D., and Gogineni, P. High-altitude radar measurements of ice thickness over the antarctic and greenland ice sheets as a part of operation icebridge. *IEEE Transactions on Geoscience and Remote Sensing*, 51(2):742–754, 2013. ISSN 0196-2892. doi: 10.1109/TGRS.2012.2203822.
- MacGregor, J. A., Fahnestock, M. A., Catania, G. A., Aschwanden, A., Clow, G. D., Colgan, W. T., Gogineni, S. P., Morlighem, M., Nowicki, S. M. J., Paden, J. D., Price, S. F., and Seroussi, H. A synthesis of the basal thermal state of the Greenland Ice Sheet. *Journal of Geophysical Research: Earth Surface*, 121(7):1328–1350, jul 2016. doi: 10.1002/2015jf003803. URL <https://doi.org/10.1002/2015jf003803>.
- Matsuoka, K., Furukawa, T., Fujita, S., Maeno, H., Uratsuka, S., Naruse, R., and Watanabe, O. Crystal orientation fabrics within the Antarctic ice sheet revealed by a multipolarization plane and dual-frequency radar survey. *Journal of Geophysical Research: Solid Earth*, 108(B10), 2003. ISSN 0148-0227. doi: 10.1029/2003jb002425. URL <https://doi.org/10.1029/2003jb002425>.
- Millar, D. H. Radio-echo layering in polar ice sheets and past volcanic activity. *Nature*, 292(5822):441–443, 1981. ISSN 00280836. doi: 10.1038/292441a0. URL <https://www.nature.com/articles/292441a0>.
- Mottram, R., Simonsen, S. B., Svendsen, S. H., Barletta, V. R., Sørensen, L. S., Nagler, T., Wuite, J., Groh, A., Horwath, M., Rosier, J., Solgaard, A., Hvidberg, C. S., and Forsberg, R. An integrated view of greenland ice sheet mass changes based on models and satellite observations. *Remote Sensing*, 11(12):1–26, 2019. ISSN 20724292. doi: 10.3390/rs11121407. URL <https://doi.org/10.3390/rs11121407>.
- Murray, T., Stuart, G. W., Miller, P. J., Woodward, J., Smith, A. M., Porter, P. R., and Jiskoot, H. Glacier surge propagation by thermal evolution at the bed. *Journal of Geophysical Research: Solid Earth*, 105(B6):13491–13507, 2000. ISSN 21699356. doi: 10.1029/2000jb900066. URL <https://doi.org/10.1029/2000jb900066>.
- Nereson, N. A. and Raymond, C. F. The elevation history of ice streams and the spatial accumulation pattern along the Siple Coast of West Antarctica inferred from ground-based radar data from three inter-ice-stream ridges. *Journal of Glaciology*, 47(157):303–313, 2001. ISSN 00221430. doi: 10.3189/172756501781832197. URL <https://doi.org/10.3189/172756501781832197>.
- Nereson, N. A., Raymond, C. F., Jacobel, R. W., and Waddington, E. D. The accumulation pattern across Siple Dome, West Antarctica, inferred from radar-detected internal layers. *Journal of Glaciology*, 46(152):75–87, 2000. ISSN 00221430. doi: 10.3189/172756500781833449. URL <https://doi.org/10.3189/172756500781833449>.
- Nixdorf, U. and Göktas, F. Spatial depth distribution of the subglacial bed and internal layers in the ice around NGRIP, Greenland, derived with airborne RES. *Journal of Applied Geophysics*, 47(3-4):175–182, 2001. ISSN 09269851. doi: 10.1016/S0926-9851(01)00062-3. URL [https://doi.org/10.1016/S0926-9851\(01\)00062-3](https://doi.org/10.1016/S0926-9851(01)00062-3).
- Pälli, A., Kohler, J. C., Isaksson, E., Moore, J. C., Pinglot, J. F., Pohjola, V. A., and Samuelsson, H. Spatial and temporal variability of snow accumulation using ground-penetrating radar and ice cores on a Svalbard glacier. *Journal of Glaciology*, 48(162):417–424, 2002. ISSN 00221430. doi: 10.3189/172756502781831205. URL <https://doi.org/10.3189/172756502781831205>.
- Palmer, S. J., Dowdeswell, J. A., Christoffersen, P., Young, D. A., Blankenship, D. D., Greenbaum, J. S., Benham, T., Bamber, J., and Siegert, M. J. Greenland subglacial lakes detected by radar. *Geophysical Research Letters*, 40(23):6154–6159, 2013. ISSN 00948276. doi: 10.1002/2013GL058383. URL <https://doi.org/10.1002/2013GL058383>.
- Richardson, C., Aarholt, E., Hamran, S.-E., Holmlund, P., and Isaksson, E. Spatial distribution of snow in western Dronning Maud Land, East Antarctica, mapped by a ground-based snow radar. *Journal of Geophysical Research*, 102(B9):20343–20353, 1997. doi: 10.1029/97JB01441. URL <https://doi.org/10.1029/97JB01441>.
- Rignot, E. and Mouginot, J. Ice flow in Greenland for the International Polar Year 2008–2009. *Geophysical Research Letters*, 39(11):n/a–n/a, jun 2012. ISSN 00948276. doi: 10.1029/2012GL051634. URL <http://doi.wiley.com/10.1029/2012GL051634>.
- Riverman, K. L., Alley, R. B., Anandakrishnan, S., Christianson, K., Holschuh, N. D., Medley, B., Muto, A., and Peters, L. E. Enhanced Firn Densification in High-Accumulation Shear Margins of the NE Greenland Ice Stream. *Journal of Geophysical Research: Earth Surface*, 124(2):365–382, feb 2019. ISSN 2169-9003. doi: 10.1029/2017JF004604. URL <https://onlinelibrary.wiley.com/doi/abs/10.1029/2017JF004604>.
- Schroeder, D. M., Bingham, R. G., Blankenship, D. D., Christianson, K., Eisen, O., Flowers, G. E., Karlsson, N. B., Koutnik, M. R., Paden, J. D., and Siegert, M. J. Five decades of radioglaciology. *Annals of Glaciology*, pages

- 1–13, mar 2020. doi: 10.1017/aog.2020.11. URL <https://doi.org/10.1017%2Faog.2020.11>.
- Shepherd, A., Ivins, E., Rignot, E., Smith, B., van den Broeke, M., Velicogna, I., Whitehouse, P., Briggs, K., Joughin, I., Krinner, G., Nowicki, S., Payne, T., Scambos, T., Schlegel, N., A. G., Agosta, C., Ahlstrøm, A., Babonis, G., Barletta, V. R., Bjørk, A. A., Blazquez, A., Bonin, J., Colgan, W., Csatho, B., Cullather, R., Engdahl, M. E., Felikson, D., Fettweis, X., Forsberg, R., Hogg, A. E., Gallee, H., Gardner, A., Gilbert, L., Gourmelen, N., Groh, A., Gunter, B., Hanna, E., Harig, C., Helm, V., Horvath, A., Horwath, M., Khan, S., Kjeldsen, K. K., Konrad, H., Langen, P. L., Lecavalier, B., Loomis, B., Luthcke, S., McMillan, M., Melini, D., Mernild, S., Mohajerani, Y., Moore, P., Mottram, R., Mouginot, J., Moyano, G., Muir, A., Nagler, T., Nield, G., Nilsson, J., Noël, B., Otsuka, I., Pattle, M. E., Peltier, W. R., Pie, N., Rietbroek, R., Rott, H., Sandberg Sørensen, L., Sasgen, I., Save, H., Scheuchl, B., Schrama, E., Schröder, L., Seo, K. W., Simonsen, S. B., Slater, T., Spada, G., Sutterley, T., Talpe, M., Tarasov, L., van de Berg, W. J., van der Wal, W., van Wessem, M., Vishwakarma, B. D., Wiese, D., Wilton, D., Wagner, T., Wouters, B., and Wuite, J. Mass balance of the Greenland Ice Sheet from 1992 to 2018. *Nature*, 579(7798):233–239, 2020. ISSN 14764687. doi: 10.1038/s41586-019-1855-2. URL <https://doi.org/10.1038/s41586-019-1855-2>.
- Siegert, M. J. and Hodgkins, R. A stratigraphic link across 1100 km of the antarctic ice sheet between the Vostok ice core site and Titan Dome (near South Pole). *Geophysical Research Letters*, 27(14):2133–2136, 2000. ISSN 00948276. doi: 10.1029/2000GL008479. URL <https://doi.org/10.1029/2000GL008479>.
- Siegert, M. J., Hodgkins, R., and Dowdeswell, J. A. A chronology for the Dome C deep ice-core site through radio-echo layer correlation with the Vostok ice core, Antarctica. *Geophysical Research Letters*, 25(7):1019–1022, 1998. ISSN 00948276. doi: 10.1029/98GL00718.
- Smith-Johnsen, S., Schlegel, N.-J., de Fleurian, B., and Nisançioğlu, K. H. Sensitivity of the northeast greenland ice stream to geothermal heat. *Journal of Geophysical Research: Earth Surface*, 125(1):e2019JF005252, 2020. doi: 10.1029/2019JF005252. URL <https://agupubs.onlinelibrary.wiley.com/doi/abs/10.1029/2019JF005252>.
- Steinhage, D., Nixdorf, U., Meyer, U., and Miller, H. *Annals of Glaciology*. doi: 10.3189/172756499781821409. URL <https://doi.org/10.3189/172756499781821409>.
- Steinhage, D., Nixdorf, U., Meyer, U., and Miller, H. New maps of the ice thickness and subglacial topography in Dronning Maud Land, Antarctica, determined by means of airborne radio-echo sounding. *Annals of Glaciology*, 29:267–272, 1999. ISSN 02603055. doi: 10.3189/172756499781821409.
- Straneo, F., Sutherland, D. A., Holland, D., Gladish, C., Hamilton, G. S., Johnson, H. L., Rignot, E., Xu, Y., and Koppes, M. Characteristics of ocean waters reaching Greenland’s glaciers. *Annals of Glaciology*, 53(60):202–210, 2012. ISSN 02603055. doi: 10.3189/2012AoG60A059. URL <https://doi.org/10.3189/2012AoG60A059>.
- Vallelonga, P., Christianson, K., Alley, R. B., Anandakrishnan, S., Christian, J. E. M., Dahl-Jensen, D., Gkinis, V., Holme, C., Jacobel, R. W., Karlsson, N. B., Keisling, B. A., Kipfstuhl, S., Kjær, H. A., Kristensen, M. E. L., Muto, A., Peters, L. E., Popp, T., Riverman, K. L., Svensson, A. M., Tibuleac, C., Vinther, B. M., Weng, Y., and Winstrup, M. Initial results from geophysical surveys and shallow coring of the Northeast Greenland Ice Stream (NEGIS). *The Cryosphere*, 8(4): 1275–1287, jul 2014. doi: 10.5194/tc-8-1275-2014. URL <https://doi.org/10.5194%2Ftc-8-1275-2014>.
- Vaughan, D. G., Corr, H. F., Doake, C. S., and Waddington, E. D. Distortion of isochronous layers in ice revealed by ground-penetrating radar. *Nature*, 398(6725): 323–326, 1999. ISSN 00280836. doi: 10.1038/18653. URL <https://www.nature.com/articles/18653>.
- Wang, Z., Gogineni, S., Rodriguez-Morales, F., Yan, J. B., Paden, J., Leuschen, C., Hale, R. D., Li, J., Carabajal, C. L., Gomez-Garcia, D., Townley, B., Willer, R., Stearns, L., Child, S., and Braaten, D. Multichannel Wideband Synthetic Aperture Radar for Ice Sheet Remote Sensing: Development and the First Deployment in Antarctica. *IEEE Journal of Selected Topics in Applied Earth Observations and Remote Sensing*, 9(3):980–993, 2016. ISSN 21511535. doi: 10.1109/JSTARS.2015.2403611. URL <http://dx.doi.org/10.1109/JSTARS.2015.2403611>.
- Westhoff, J., Stoll, N., Franke, S., Weikusat, I., Bons, P., Kerch, J., Jansen, D., Kipfstuhl, S., and Dahl-Jensen, D. A stratigraphy-based method for reconstructing ice core orientation. *Annals of Glaciology*, page 1–12, 2020. doi: 10.1017/aog.2020.76. URL <https://doi.org/10.1017/aog.2020.76>.
- Williams, R. M., Ray, L. E., Lever, J. H., and Burzynski, A. M. Crevasse detection in ice sheets using ground penetrating radar and machine learning. *IEEE Journal of Selected Topics in Applied Earth Observations and Remote Sensing*, 7(12):4836–4848, 2014. ISSN 21511535. doi: 10.1109/JSTARS.2014.2332872. URL <https://doi.org/10.1109/JSTARS.2014.2332872>.
- Yin, J., Overpeck, J. T., Griffies, S. M., Hu, A., Russell, J. L., and Stouffer, R. J. Different magnitudes of projected subsurface ocean warming around Greenland and Antarctica. *Nature Geoscience*, 4:524–528, 2011. ISSN 17452481. doi: 10.1038/nphys1189. URL <http://dx.doi.org/10.1038/nphys1189>.
- Young, D. A., Schroeder, D. M., Blankenship, D. D., Kempf, S. D., and Quartini, E. The distribution of basal water between Antarctic subglacial lakes from radar sounding. *Philosophical Transactions of the Royal Society A: Mathematical, Physical and Engineering Sciences*, 374(2059), 2016. ISSN 1364503X. doi: 10.1098/rsta.2014.0297. URL <https://royalsocietypublishing.org/doi/abs/10.1098/rsta.2014.0297>.
- Zamora, R., Casassa, G., Rivera, A., Ordenes, F., Neira, G., Araya, L., Mella, R., and Bunster, C.

Crevasse detection in glaciers of southern Chile and Antarctica by means of ground penetrating radar. (318):153–162, 2007. ISSN 01447815. URL <http://citeseerx.ist.psu.edu/viewdoc/download?doi=10.1.1.544.8213&rep=rep1&type=pdf>.














Zeising, O. and Humbert, A. Indication of high basal melting at eastgrip drill site on the northeast greenland ice stream. *The Cryosphere Discussions*, 2021:1–15, 2021. doi: 10.5194/tc-2021-37. URL <https://tc.copernicus.org/preprints/tc-2021-37/>.

Appendix J

PAPER VI

ARTICLE

Interior of the North East Greenland Ice stream reveals that NEGIS-type ice streams may come and go

Daniela Jansen¹ , Steven Franke¹ , Catherine C. Bauer², Tobias Binder^{1,†} , Dorthe Dahl-Jensen^{3,4} , Tamara de Riese² , Olaf Eisen^{1,5} , Maria-Gema Llorens⁶ , Heinrich Miller¹ , Niklas Neckel¹ , John D. Paden⁷ , Till Sachau² , Ilka Weikusat^{1,2} , Yu Zhang² and Paul D. Bons^{2,8} 

¹ Alfred Wegener Institute, Helmholtz Centre for Polar and Marine Research, Bremerhaven, Germany

² Department of Geosciences, Eberhard Karls University Tübingen, Germany

³ Physics of Ice, Climate, and Earth, Niels Bohr Institute, University of Copenhagen, Denmark

⁴ Centre for Earth Observation Science, University of Manitoba, Winnipeg, Canada

⁵ Department of Geosciences, University of Bremen, Bremen, Germany

⁶ Institute of Earth Sciences Jaume Almera, Barcelona, Spain

⁷ Center for Remote Sensing of Ice Sheets (CReSIS), University of Kansas, Lawrence, KS, USA

⁸ China University of Geosciences, Beijing, China

[†] now at Ibeo Automotive Systems, Hamburg, Germany

Abstract

The outflow of ice from the Greenland (GrIS) Ice Sheet is strongly localized, with only few ice streams draining large proportions of the entire ice sheet. Thus, understanding ice stream behaviour and their temporal variability is crucially important to predict the rates of sea-level change. The > 500 km long North-East Greenland Ice Stream (NEGIS) is by far the largest ice stream in Greenland and is remarkable for the lack of any clear bedrock channel to explain its presence (Fahnestock, 2001). Its current dynamics are well constrained by remote sensing data (Hvidberg et al., 2020; Joughin et al., 2017), but the trigger for the onset of streaming close to the divide and its temporal development in its upstream region remain unknown. We present the first 3-dimensional analysis of stratigraphic layers from airborne radar survey in a large ice stream, NEGIS, showing how the deformation history of the ice is recorded in the stratigraphy by folding and advection. The layers folded by convergence (Bons et al., 2016) and subsequently sheared into the actual stream indicate a shift in the velocity distribution over time. With a novel method for dating the folding events, we show that the NEGIS shear margins in the survey area were established at ca. 2000–2500 a BP, which provides a timing for the onset of fast flow. Our results contradict the assumption that NEGIS has been stable throughout the Holocene in its current form (Keisling et al., 2014), and show that NEGIS-type ice streams can appear suddenly and have a large impact on ice sheet discharge and geometry on short time scales. This is a major concern, as global warming changes the boundary conditions of our ice sheets, which may trigger the appearance of new ice streams in the future.

Introduction

Predicting the amount and rate of future sea-level rise as a result of mass loss of polar ice sheets is one of the major challenges related to climate change. A significant percentage of discharge of ice into the oceans takes place by solid ice discharge via ice streams (Choi et al., 2021). These are river-like zones where ice flow is significantly faster than in their surroundings, assumed to be triggered by either bedrock properties or

shape, by enhanced sliding, and/or by deformation mechanisms leading to shear localization (Schoof and Mantelli, 2021). The most conspicuous one in the Greenland Ice Sheet (GrIS) is the North-East Greenland Ice Stream (NEGIS), which extends about 500 km inland from its outlets in the NE of the GrIS, and its catchment area covers 17.2 % of the ice sheet area (Krieger et al., 2020).

The NEGIS cuts into the Greenland ice sheet all

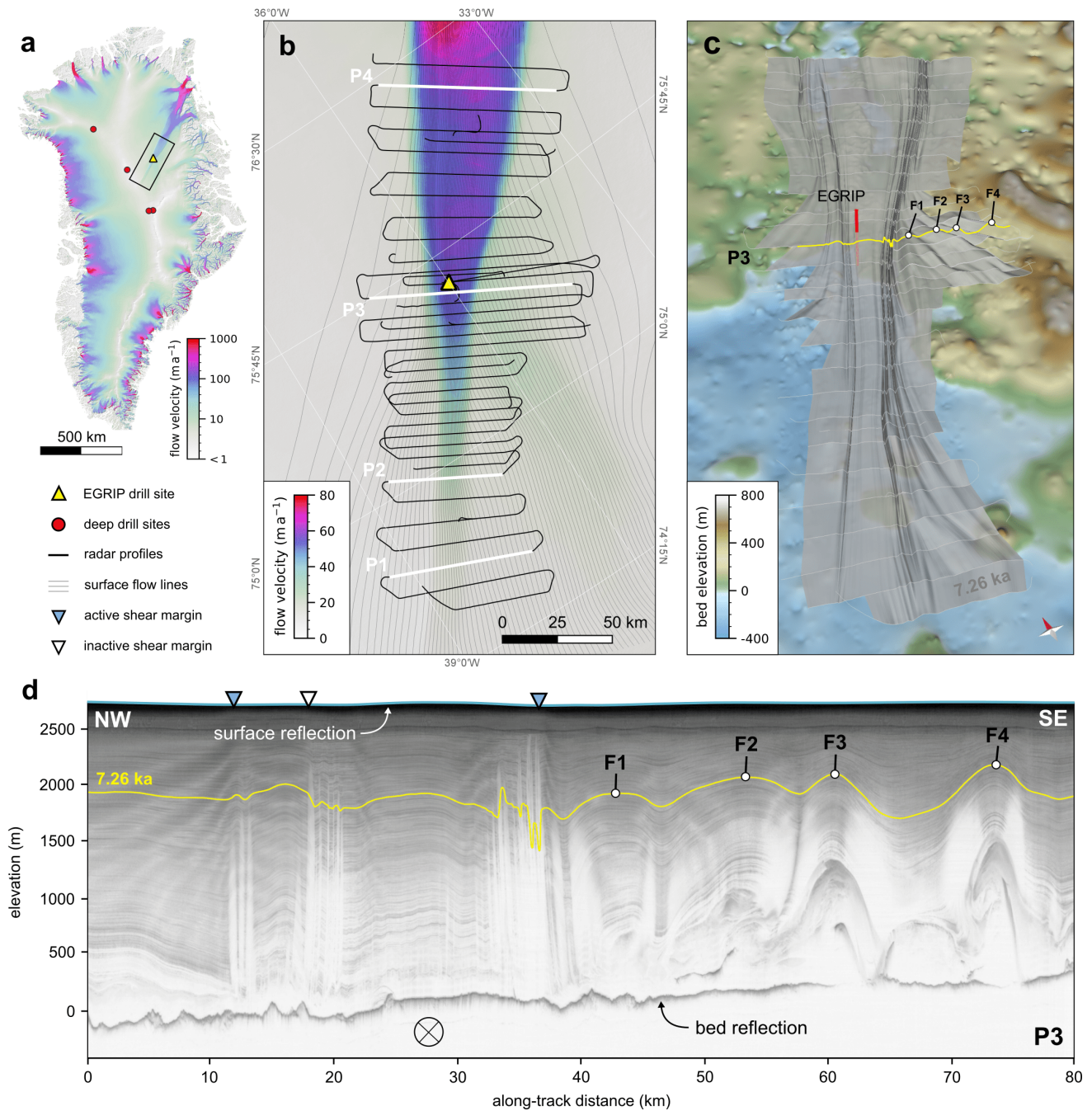


Figure J.1: Overview map of survey area and radar lines with ice flow velocity (panel (a); Joughin et al. 2017). EGRIP camp is represented by the yellow triangle. (b) Close view on the survey area. the black lines show the positions of the radar profiles evaluated for this study. Radar profile P3 is shown in panel (d), P1–2 and P4 are shown in the supplementary Figure S4 and S5. (c) 3D-visualization of the 7260 years BP isochrone horizon as a shaded relief of the elevation derived from picking the radar isochrone dated as a shaded relief plot of the elevation above the bedrock (the visualization is 10 times exaggerated in the vertical). F1–F4 indicate the location of fold anticlines also highlighted in the radar profile P3 in panel (d). The location of P3 is indicated by a yellow line. (d) Airborne radar profile P3 across NEGIS from the centre of the survey area. The grey triangles on the surface indicate the location of the shear margins on either side of the stream, while the blue triangle shows the position of an area which is no longer subject to shear. The flow is into the page. F1–F4 indicate the anticlines highlighted in panel (c).

the way up to the central ice divide (Fahnestock, 2001), where its influence manifests itself in the stratigraphy derived by radar profiles along the divide as an area with drawdown of layers due to the enhanced outflow (Vallelonga et al., 2014). While the gates in the coastal

mountain range in the north East of Greenland clearly determines the location of the coastal outlet, its course in the interior of the ice sheet appears not to be constrained by bed topography (Franke et al., 2020). The

flow velocity increases from about 3 m a^{-1} in the region of its upstream end at the divide, to 55 m a^{-1} at the EGRIP Drilling camp (Hvidberg et al., 2020), which is the center of the airborne radar survey used in this study (Fig. J.1 a, b). In the upper part the stream is about 15 km wide, but around the EGRIP camp the stream begins to widen and eventually reaches a width of about 50 km, defining its characteristic “bottleneck shape”. The widening is coincident with a reduction in ice thickness due to a rise of the bedrock (Franke et al., 2021). The present-day shape and surface velocity and shape of the NEGIS is very well constrained by satellite remote sensing products (Hvidberg et al., 2020; Joughin et al., 2017). Much less is known about the spatial and temporal evolution of the stream. To reveal this we use radar stratigraphy, where we consider the radar reflections as isochrones that provide us with 3-dimensional passive tracers of the past flow field.

Folds in ice, and what they tell about deformation

Disturbances, such as folds, in radar isochrones have been conclusive to constrain temporal shifts in ice stream flow regimes in Antarctica (Catania et al., 2006; Winter, K., J. Woodward, N. Ross, S. A. Dunning, R. G. Bingham, H. F. J. Corr, 2015), studies which based their analysis on disruptions in the reflections. New radar systems significantly improved the data quality in recent years (Schroeder et al., 2020; MacGregor et al., 2015), which now makes it possible to have a closer look at the processes influencing the shape of the isochrones to a greater detail. Bons et al. (2016) illustrated the importance of a high resolution, 3D-visualisation of deformed passive tracer planes as a necessary base for analyses and interpretation.

To analyze the overall structure of the distortion of the radar isochrones, we visualized selected reflections as 3D-horizons (see Methods). We chose one of the deepest layers in the upper half of the ice column, deposited approximately 7260 a ago (EGRIP-core dating; Mojtabavi et al. 2020), that could be traced continuously and reliably over the entire survey area. The plot of the complete 7260 a-layer (Figure J.1 c) reveals that the ice stream has left a significant imprint on the layer shape over the entire survey area, with complexity and intensity of folding increasing downstream in its complexity and number of folds. In the upstream area of the survey, the layers form a wave-like anticline / syncline folding structure within a band around the shear margins with partly more than 300 m amplitude A , the difference in height between anticlinal crest and synclinal troughs or valleys for the 7260 a-layer (Figure J.1 c and supplementary Figure S1). The development of these folds along flow shows that they become laterally more constricted

and develop a characteristic zig/zag pattern (z-folds).

The radar profiles in the SE of NEGIS show longer wavelength open folding outside of the ice stream. The 3-D visualization clearly shows how the folds' characteristic change progressively from widely open (long wavelength) folds outside of the southern shear margin towards isoclinal (more “closed”, shorter wavelength) folds towards and into the SE shear margin. The characteristic of the folds changes when they are affected by the South East shear margin, where the shearing deformation regime is consistent with a shortening of the wavelength without further growth of the amplitude. Bons et al. (2016) argued that the folds with their fold axes converging on the Peterman Ice Stream along flow resulted from lateral flow convergence and thus shortening of the layers with a strong mechanical anisotropy. The latter results from the alignment of the easy-glide crystallographic basal planes towards parallelism with the bedrock surface. The tapering shape of fold axes outside NEGIS is likewise consistent with folding due to convergence, which also fits the geometry of the NEGIS catchment area (Supplementary Figure S3).

What is the timescale of fold formation?

So far, none of the numerous publications (e.g. Wolovick et al., 2014; Bell et al., 2014) on the mechanism of folding in ice sheets addressed the timing and duration of fold formation. Dating of the active folding process is not only essential to constrain fold formation, but also to determine the age of the flow perturbations that lead to fold growth, in this case the formation of NEGIS. Here we address this issue by presenting the results of a novel method to date the folding events. Irrespective of the folding mechanism, folding of originally essentially flat, horizontal layers implies laterally varying vertical velocities on top of the overall bedrock-parallel flow field. Synclines form in zones of downward displacement, while anticlines form where layers move up. However, the vertical displacements are not equal within the whole ice sheet column. Clearly, they are zero at the ice-bedrock interface. Folds in ice sheets show no or only minor surface-elevation perturbations, in the order of a few tens of metres at the very most. At deeper levels fold amplitudes A (the difference in height between anticlinal crest and synclinal trough) may reach $> 1000 \text{ m}$ (Leysinger Vieli et al., 2018; Franke et al., 2020). This gradient of vertical displacement can be interpreted as strain applied to the ice layers over the whole column by a vertical displacement applied at depth, while the vertical displacement at the surface remains approximately zero. Following the Dansgaard-Johnson model (Dansgaard and Johnsen, 1969) we assume that this vertical strain is constant with depth at

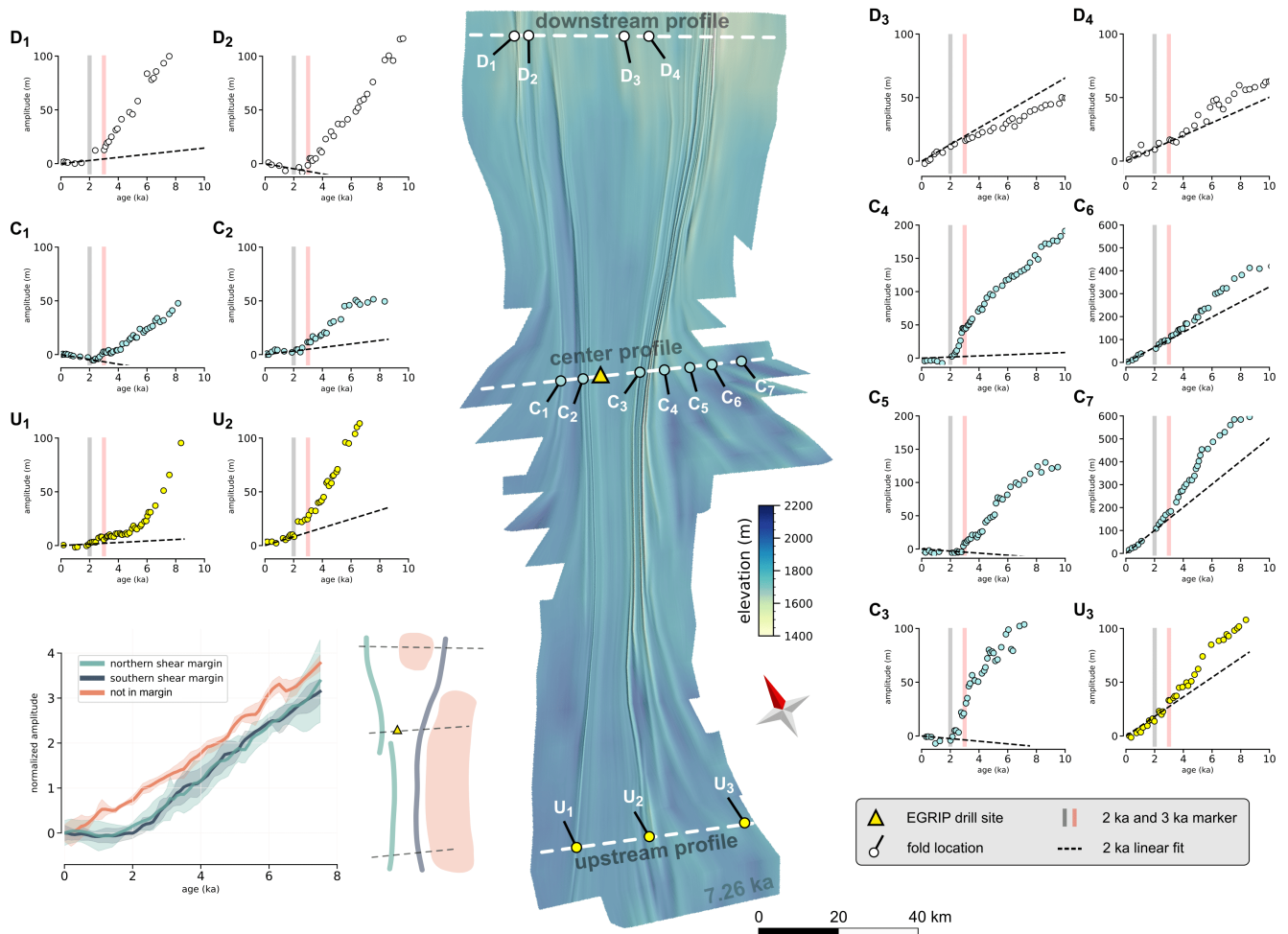


Figure J.2: Fold amplitude vs depth for three selected radar profiles. Black dotted lines represent a linear fit to the data points from 2 ka BP until today. Letters U, C, and D (Upstream, Central and Downstream) and numbers (increasing from left to right) indicate folds and their locations. The grey and red vertical lines indicate 2 ka and 3 ka BP for orientation. The centre of the Figure shows the 3D-visualization of the 7260 years BP isochrone horizontal. The graph on the lower left shows the mean normalized fold amplitudes vs depth for the two margins and the outside of NEGIS with shaded standard deviation. The sketch to the right shows the origin area of the mean amplitude values.

one point in time, at least for the upper ~ 80 % of an ice sheet. If two adjacent columns of ice experience a different vertical strain, the different vertical displacement shows as a shift in depth for the same isochrone. The resulting amplitude of the emerging fold will increase linearly with depth (see supplements for a detailed derivation). This strain affects all layers that are already present at the time of folding t_1 , and thus are older than t_1 . Layers younger than the t_1 folding event cannot have experienced the strain and will, therefore, not show the same linear increase in amplitude with depth. Any subsequent folding event will add another increment of strain to all layers that exist at that time t_2 . It follows that (i) folding events can be detected by changes in the slope of the amplitude-depth curve and that (ii) the intensity of folding is determined by that slope (Supplementary Figure S1).

Figure J.2 summarizes fold-amplitude analyses using 14 individual anticline-syncline structures from two

radargrams perpendicular to NEGIS, one at the East-GRIP site and one 130 km upstream. We chose 3 profiles representative for the upstream area (U), the central part around the EGRIP Camp (C), and the downstream end of the survey area (D). For a detailed example of a radargram with the picked layers for amplitude analysis see supplementary Figure S1. The folds all show a major kink in the Amplitude-age curve at ca 2–2.5 ka BP, corresponding to a depth of about 300 m. Amplitudes of folds inside the shear margins are close to zero for younger layers. Amplitudes in older layers rapidly increase with age, reaching values in the order of 50–100 m in 8 ka BP old layers at about a kilometre in depth. Amplitudes keep increasing below, but cannot be measured accurately as folding becomes too intense. A linear increase of amplitude with depth starts with layers about 3.5–4 ka BP in age. Amplitude-depth curves in the intermediate layers are variable.

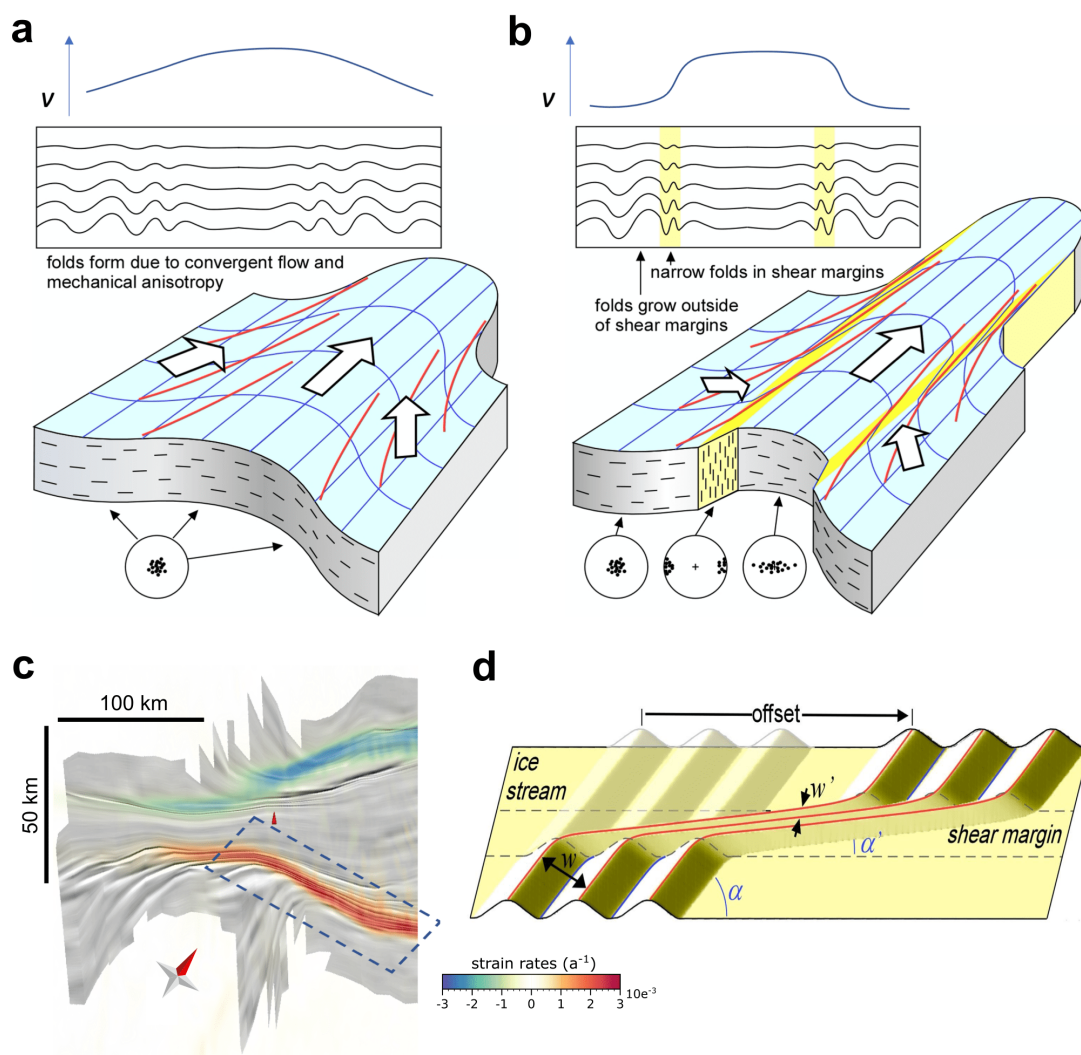


Figure J.3: (a) Situation before localisation of strain in distinct shear zones. Red lines indicate fold hinges, white arrows indicate direction of flow (b) after the establishment of shear zones (highlighted in yellow): Inside of the stream the fold hinges are rotated towards the shear margins due to the velocity gradient. (c) Folded layer with shear strain rates, the blue frame highlights the area which is described in panel (d). The image is distorted to exaggerate the angles relative to the shear zones, which are very small. (d) Sketch to illustrate the development of an apparent shorter wavelength of folds within the shear zone.

What can the folds reveal about the history of NEGIS?

Bons et al. (2016) argued that the folds with their fold axes converging on the Peterman Ice Stream along flow resulted from lateral flow convergence and thus shortening of the layers with a strong mechanical anisotropy. The tapering shape of fold axes outside NEGIS is likewise consistent with folding due to convergence, which also fits the geometry of the NEGIS catchment area (Figure S3). This type of folding can occur without strong localisation of shear and a distributed compressive regime throughout the catchment area.

A conceptual model for the development of the structures in NEGIS that we see today in our radar horizon is summarized in Figure J.3: in the upstream region

of NEGIS convergent folding occurred as a "first deformation phase" (time period t1) due to the mechanical anisotropy typical in flowing ice (Bons et al., 2016). The strong localization of shear deformation in the margins, that is today apparent in the observed surface velocity field, has not yet developed. Thus, the strike of the fold hinges was orientated roughly towards the outlet gate (Figure J.3 a). Due to enhanced drawdown of ice along the evolving stream, probably triggered at the outlet of NEGIS, the shear margins then intensified. To compensate the local mass loss caused by this drawdown, the ice stream has two ways how to provide the material without substantial thinning of the stream area: by widening or elongating. As the formation of shear zones quickly results in reorientation of the mechanical anisotropy (vertical to horizontal CPO), the shear zones' lateral position and thus the width of the

stream is pinned/fixed and thus shear zones are likely to travelled upwards, a behavior which is common in rock deformation. The fold trains which then were cut by a new shear margin experienced a “secondary deformation phase” (time period t2), due to the strong lateral velocity gradient in the shear margin. This leads to a rotation of the fold hinges towards the margins of the stream, as the ice in the center is moving faster, which is apparent in the isochrone horizon shown in fig. 1c and center panel of fig. 2, but becomes even more obvious when the horizon is shortened along the flow direction (Fig. J.3c). The rotation of the hinges is connected to a shortening of the wavelengths of the folds (Fig. J.3c, d), but not to further growth of the amplitudes as it would be expected for the geometry of a simply progressing first deformation phase. The stagnation of amplitude growth within the shear margin is also consistent with the expected change in CPO in strong horizontal shearing, which very likely produces a horizontal single maximum. Thus, the horizontal shortening is effectively resolved by glide along the basal planes and rotation.

In the mapped layers folding relicts are visible inside the stream, which must have been part of convergent fold structures which formed in the area before the establishment of the shear margins happened (Figure J.3c). The connection of these fold hinges to their counterpart on the outside of the stream provides a means to estimate the duration of the current “secondary” deformation phase by calculating the angle of rotation assuming today's shearing, and also by evaluating the distance between the “breaking points” of the inner and outer folds. From this, our first estimate of the timing of shear zone establishment is approximately 2.3 ka BP (see supplementary material for details).

This age estimation from the offset of the folds disrupted by the shear margin is consistent with the evaluation of the amplitude-age graphs of the picked folds. The graph in Figure J.2 on the lower left shows normalized fold amplitudes for the three different regions, both shear margins and the outside of the stream. A noticeable difference between folds in the shear margins and those outside NEGIS is that the outside folds amplitudes are distinctly non-zero in the youngest layers as well. This means that these folds were still growing until recently, possibly up to the present day. Kinks in the amplitude-age curves are also present at ca 2–2.5 ka and/or 3.5–4 ka BP.

The constructed isochrone surfaces show that folds outside and inside the shear margins are the same folds initiated during t1, with the latter ones being sheared into the margins during t2. A common feature is that they all show bends in their amplitude-age curves at about 3.5–4 ka BP, below which the curves tend to

straighten. This strongly suggests that all folds initiated around that time (t1). Sections of the folds that were caught in the strong shearing at the margins essentially stopped growing at 2–2.5 ka BP, while sections outside NEGIS did not. The intensification of folding in a two-stage process could be interpreted as a result of increasing discharge from the NEGIS catchment area. The first stage, around 3.5 to 4 ka BP, is coincident with the end of the ice sheet re-advance during the Holocene.

Larsen et al. (2018) summarized geological evidence from the north east Greenland coast and showed that the three major outlets of NEGIS, the Nioghalvfjerdingsfjord Gletscher (NG), the Zachariae Isstrom (ZI), and the Storstrommen Gletscher (SG) have been retreating beyond their current extent and re-advancing again at least twice during the last 45 ka. In the Holocene Thermal Maximum (HTM) in the early to middle Holocene, temperatures in the Arctic were higher than today, caused by orbital forcing, which resulted in a change of insolation, and thus mainly influenced the summer temperature (Miller et al., 2010). This had a large effect on the sea ice conditions and also on Greenland ice volume and frontal positions of outlet glaciers (Axford et al., 2021). The onset and ending of this warm period was regionally different, and there is evidence from geological data that in the area of the three major outlets of the NEGIS, warming started around 8 000 years ago, and ended approximately 4 000 years ago (Miller et al., 2010). Accordingly, NG was smaller than today in its extension at least until 4.6 ka ago (Bennike and Weidick, 2001).

Our observed intensification of folding in the upstream NEGIS area in a two-stage process could be interpreted as a result of increasing discharge from the NEGIS catchment area following the readvance of the ice front after the HTM. This would fit into the line of argument of Stokes et al. (2016), who concluded, that ice stream activity is linked to the geometry changes of the ice sheet, with increasing intensity of streaming for higher ice volume. The first stage, around 3.5 to 4 ka BP, could be a consequence of a still distributed increase of the outflow, leading to a drawdown of ice from the flanks and a confluent flow regime due to the geometry of the catchment and the bedrock. The localization effect of shear in narrow shear margin as we see them today is, if similar to processes in other geologic materials, initiated closer to the margin of the ice sheet and travelling upwards in time, thus reaching our survey area at a significantly later time around 2 300 BP. Our results thus indicate how and on which time scales changes at the front are translated into the inner ice sheet, and that processes at the calving front of NEGIS are much more likely to trigger formation and intensification of streaming than local heatflow anomalies (Bons et al., 2021).

Methods

Airborne Radar

The data presented in this study have been derived from an airborne radar survey in May 2018 using an ultra-wide-band radar system (AWI UWB, detailed description see [Rodríguez-Morales et al. 2014](#); [Franke et al. 2020](#)) with an array of 8 transmitters and receivers mounted beneath the fuselage of the AWI aircraft Polar 6. The layout of the survey was designed for mapping radar stratigraphy and bedrock properties in the vicinity of the EGRIP drilling camp, with an area stretching along flow from 150 km upstream of the camp to 150 km downstream. The profiles used in this study were recorded in narrow-band mode, with the Frequency range set to 180–210 MHz. Due to the focus on stratigraphy, the radar lines are mostly perpendicular to ice flow in order to best reproduce the deformation pattern in the shear margins. Here we only use data from across-flow profiles (Figure J.1 b). The distance between the profiles is 5 km in the central part of the survey region, in the outer area the distance is 10 km. Bedrock reflections from this data set have been used to produce a high-resolution bedrock data set in the vicinity of EGRIP camp ([Franke et al., 2020](#)), as well as for bed properties and roughness ([Franke et al., 2021](#)).

Move 3D

In order to assess the distortion of the radar isochrones in terms of their deformation history to determine the dynamic setting of the ice stream, the 2-dimensional profiles have to be combined to produce a 3-dimensional model of the folded isochrone surfaces ([Bons et al., 2016](#)). For this purpose, we picked selected internal reflections, which are detectable throughout most of the survey area. To ensure spatial continuity, we restrict our analysis to reflections from the upper half of the ice column. By manually assigning profile sections from two neighboring lines to each other, a surface can be generated in a half-automated way. For this step of the analysis, we used the software MOVETM, a tool for structural analysis and 3-D visualization in geosciences. The isochrones are dated by tying them in the depth domain to the age dating of the EGRIP ice core ([Mojtabavi et al., 2020](#)) and transferring age in a particular depth to the respective isochrone at that depth. The absolute age and its uncertainty is of minor importance in our study, as we focus on the overall deformation of the initial flat shape of the considered isochrones.

Dating of folding events

To determine the amplitude-depth curves, as many layers in a radargram as possible are manually traced for anticline-syncline pairs. Axial planes are constructed as lines that connect the fold hinges. Near the ice surface folds may die out upwards, in which case the axial planes are extended vertically towards the surface. Depth (z) of a stratigraphic layer is now defined as the vertical distance between a hinge of that layer and the height of the ice surface at the point where it is intersected by the axial planes. For each anticline-syncline pair, referred to as a fold, this results in a set of $z_{anti}(i)$ and $z_{syn}(i)$ data for each layer (i) that was deposited at $a(i)$. The fold amplitude is now defined as $A(i) = z_{syn}(i) - z_{anti}(i)$, with associated depth $z(i) = (z_{syn}(i) + z_{anti}(i)) / 2$. Ages of layers are derived from tracing or correlating of layers with known ages from the EastGRIP drill site. This results in a set of layers with known depositional ages. Over half of the traceable layers within one fold cannot be traced all the way to the drill site or can be recognised in the radargram at that site. Their ages are estimated by interpolating between nearest layers above and below the layer of unknown age, assuming that within the age window the relation between height of the layer above the bedrock (h) and age (a) is given by: $h = H - z = \exp(k \cdot a)$. Details on error analysis and reduction are provided in supplementary information.

Strain rates

In order to describe the overall dynamic setting of the survey area, we used two different velocity products. The velocity data from the Measures Project ([Joughin et al. 2017](#), Figure J.1) with a resolution of 250 m was used to characterize the present-day surface velocity magnitude and flow direction, which we also used to calculate advection and distortion of stratigraphic features. As the picked isochrones are located in the upper half of the ice column throughout our survey area, we assume that the surface velocity field is still a valid approximation at the depth of the horizon. This velocity field has been also used to calculate principal strain rates and strain rates in flow and across the flow direction for each pixel. For this purpose, the data was filtered with a Lee filter over a window of 10×10 pixels to reduce the noise. A high-resolution velocity product based on TerraSAR-X data is available in a limited area around the EastGRIP camp ([Hvidberg et al., 2020](#)). Although this data set shows significantly less noise than Measures, we also deployed a Lee filter with a 5×5 pixel window before calculating strain rates. Strain rates and projections were calculated following Paterson (the textbook).

Acknowledgements

We thank the Ken Borek crew of the research aircraft Polar 6 and system engineer Lukas Kandora. Logistical support in the field was provided by the East Greenland Ice-Core Project (EGRIP). EGRIP is directed and organized by the Center of Ice and Climate at the Niels Bohr Institute. It is supported by funding agencies and institutions in Denmark (A. P. Møller Foundation, University of Copenhagen), USA (US National Science Foundation, Office of Polar Programs), Germany (Alfred Wegener Institute, Helmholtz Centre for Polar and Marine Research), Japan (National Institute of Polar Research and Arctic Challenge for Sustainability), Norway (University of Bergen and Bergen Research Foundation), Switzerland (Swiss National Science Foundation), France (French Polar Institute Paul-Emile Victor, Institute for Geosciences and Environmental research) and China (Chinese Academy of Sciences and Beijing Normal University). We acknowledge the use of the CRE-SIS toolbox from CRE-SIS generated with support from the University of Kansas, NASA Operation IceBridge grant NNX16AH54G, and NSF grants ACI-1443054, OPP-1739003, and IIS-1838230. The advection of the folds have been calculated with the tool Grd2Stream developed by Thomas Kleiner. Steven Franke was funded by the AWI Strategy fund, Daniela Jansen was funded by the AWI Strategy funds and the Helmholtz Young investigator group HGF YIG VH-NG-802.

Bibliography

- Axford, Y., de Vernal, A., and Osterberg, E. C. Past warmth and its impacts during the holocene thermal maximum in greenland. *Annual Review of Earth and Planetary Sciences*, 49(1):null, 2021. doi: 10.1146/annurev-earth-081420-063858. URL <https://doi.org/10.1146/annurev-earth-081420-063858>.
- Bell, R. E., Tinto, K., Das, I., Wolovick, M., Chu, W., Creyts, T. T., Frearson, N., Abdi, A., and Paden, J. D. Deformation warming and softening of Greenland's ice by refreezing meltwater. *Nature Geoscience*, 7(7):497–502, jun 2014. doi: 10.1038/ngeo2179. URL <https://doi.org/10.1038/2Fng2179>.
- Bennike, O. and Weidick, A. Late quaternary history around nioghalvfjerdingsfjorden and jøkelbugten, north-east greenland. *Boreas*, 30(3):205–227, 2001. doi: <https://doi.org/10.1111/j.1502-3885.2001.tb01223.x>. URL <https://onlinelibrary.wiley.com/doi/abs/10.1111/j.1502-3885.2001.tb01223.x>.
- Bons, P. D., Jansen, D., Mundel, F., Bauer, C. C., Binder, T., Eisen, O., Jessell, M. W., Llorens, M.-G., Steinbach, F., Steinhage, D., and Weikusat, I. Converging flow and anisotropy cause large-scale folding in Greenland's ice sheet. *Nature Communications*, 7(1), apr 2016. doi: 10.1038/ncomms11427. URL <https://doi.org/10.1038/2Fncomms11427>.
- Bons, P. D., de Riese, T., Franke, S., Llorens, M.-G., Sachau, T., Stoll, N., Weikusat, I., Westhoff, J., and Zhang, Y. Comment on “exceptionally high heat flux needed to sustain the northeast greenland ice stream” by smith-johnsen et al. (2020). *The Cryosphere*, 15(5):2251–2254, 2021. doi: 10.5194/tc-15-2251-2021. URL <https://tc.copernicus.org/articles/15/2251/2021/>.
- Catania, G. A., Scambos, T. A., Conway, H., and Raymond, C. F. Sequential stagnation of kamb ice stream, west antarctica. *Geophysical Research Letters*, 33(14), 2006. doi: <https://doi.org/10.1029/2006GL026430>. URL <https://agupubs.onlinelibrary.wiley.com/doi/abs/10.1029/2006GL026430>.
- Choi, Y., Morlighem, M., Rignot, E., and Wood, M. Ice dynamics will remain a primary driver of greenland ice sheet mass loss over the next century. *Communications Earth & Environment*, 2(1):26, Feb 2021. ISSN 2662-4435. doi: 10.1038/s43247-021-00092-z. URL <https://doi.org/10.1038/s43247-021-00092-z>.
- Dansgaard, W. and Johnsen, S. J. A flow model and a time scale for the ice core from camp century, greenland. *Journal of Glaciology*, 8(53):215–223, 1969. doi: 10.3189/S0022143000031208.
- Fahnestock, M. High Geothermal Heat Flow Basal Melt, and the Origin of Rapid Ice Flow in Central Greenland. *Science*, 294(5550):2338–2342, dec 2001. doi: 10.1126/science.1065370. URL <https://doi.org/10.1126/2Fscience.1065370>.
- Franke, S., Jansen, D., Binder, T., Dörr, N., Helm, V., Paden, J., Steinhage, D., and Eisen, O. Bed topography and subglacial landforms in the onset region of the Northeast Greenland Ice Stream. *Annals of Glaciology*, pages 1–11, mar 2020. doi: 10.1017/aog.2020.12. URL <https://doi.org/10.1017/2Faog.2020.12>.
- Franke, S., Jansen, D., Beyer, S., Neckel, N., Binder, T., Paden, J., and Eisen, O. Complex basal conditions and their influence on ice flow at the onset of the northeast greenland ice stream. *Journal of Geophysical Research: Earth Surface*, 126(3):e2020JF005689, 2021. doi: 10.1029/2020JF005689. URL <https://agupubs.onlinelibrary.wiley.com/doi/abs/10.1029/2020JF005689>.
- Hvidberg, C. S., Grinsted, A., Dahl-Jensen, D., Khan, S. A., Kusk, A., Andersen, J. K., Neckel, N., Solgaard, A., Karlsson, N. B., Kjær, H. A., and Vallelonga, P. Surface velocity of the northeast greenland ice stream (negis): assessment of interior velocities derived from satellite data by gps. *The Cryosphere*, 14(10):3487–3502, 2020. doi: 10.5194/tc-14-3487-2020. URL <https://tc.copernicus.org/articles/14/3487/2020/>.
- Joughin, I., Smith, B. E., and Howat, I. M. A complete map of Greenland ice velocity derived from satellite data collected over 20 years. *Journal of Glaciology*, 64(243): 1–11, nov 2017. doi: 10.1017/jog.2017.73. URL <https://doi.org/10.1017/2Fjog.2017.73>.
- Keisling, B. A., Christianson, K., Alley, R. B., Peters, L. E., Christian, J. E., Anandakrishnan, S., Riverman, K. L., Muto, A., and Jacobel, R. W. Basal conditions and ice dynamics inferred from radar-derived internal stratigraphy of the northeast Greenland ice stream. *Annals of Glaciology*, 55(67):127–137, 2014. doi: 10.3189/2014aog67a090. URL <https://doi.org/10.3189/2F2014aog67a090>.
- Krieger, L., Floricioiu, D., and Neckel, N. Drainage basin delineation for outlet glaciers of Northeast Greenland based on Sentinel-1 ice velocities and TanDEM-X elevations. *Remote Sensing of Environment*, 237:111483, 2020. ISSN 0034-4257. doi: <https://doi.org/10.1016/j.rse.2019.111483>. URL <http://www.sciencedirect.com/science/article/pii/S0034425719305024>.
- Larsen, N. K., Levy, L. B., Carlson, A. E., Buizert, C., Olsen, J., Strunk, A., Bjørk, A. A., and Skov, D. S. Instability of the Northeast Greenland Ice Stream over the last 45,000 years. *Nature Communications*, 9(1):3–10, 2018. ISSN 20411723. doi: 10.1038/s41467-018-04312-7. URL <http://dx.doi.org/10.1038/s41467-018-04312-7>.
- Leysinger Vieli, G. J.-M. C., Martín, C., Hindmarsh, R. C. A., and Lüthi, M. P. Basal freeze-on generates complex ice-sheet stratigraphy. *Nature Communications*, 9(1), nov 2018. doi: 10.1038/s41467-018-07083-3. URL <https://doi.org/10.1038/2Fs41467-018-07083-3>.
- MacGregor, J. A., Fahnestock, M. A., Catania, G. A., Paden, J. D., Gogineni, S. P., Young, S. K., Rybarski, S. C., Mabrey,














- A. N., Wagman, B. M., and Morlighem, M. Radios-tratigraphy and age structure of the Greenland Ice Sheet. *Journal of Geophysical Research: Earth Surface*, 120(2):212–241, feb 2015. doi: 10.1002/2014jg003215. URL <https://doi.org/10.1002/2F2014jg003215>.
- Miller, G., Brigham-Grette, J., Alley, R., Anderson, L., Bauch, H., Douglas, M., Edwards, M., Elias, S., Finney, B., Fitzpatrick, J., Funder, S., Herbert, T., Hinzman, L., Kaufman, D., MacDonald, G., Polyak, L., Robock, A., Serreze, M., Smol, J., Spielhagen, R., White, J., Wolfe, A., and Wolff, E. Temperature and precipitation history of the arctic. *Quaternary Science Reviews*, 29(15):1679–1715, 2010. doi: <https://doi.org/10.1016/j.quascirev.2010.03.001>. URL <https://www.sciencedirect.com/science/article/pii/S0277379110000673>.
- Mojtabavi, S., Wilhelms, F., Cook, E., Davies, S. M., Sinnl, G., Skov Jensen, M., Dahl-Jensen, D., Svensson, A., Vinther, B. M., Kipfstuhl, S., Jones, G., Karlsson, N. B., Faria, S. H., Gkinis, V., Kjær, H. A., Erhardt, T., Berben, S. M. P., Nisancioglu, K. H., Koldtoft, I., and Rasmussen, S. O. A first chronology for the east greenland ice-core project (egrip) over the holocene and last glacial termination. *Climate of the Past*, 16(6):2359–2380, 2020. doi: 10.5194/cp-16-2359-2020. URL <https://cp.copernicus.org/articles/16/2359/2020/>.
- Rodriguez-Morales, F., Byers, K., Crowe, R., Player, K., Hale, R. D., Arnold, E. J., Smith, L., Gifford, C. M., Braaten, D., Panton, C., Gogineni, S., Leuschen, C. J., Paden, J. D., Li, J., Lewis, C. C., Panzer, B., Alvestegui, D. G.-G., and Patel, A. Advanced Multifrequency Radar Instrumentation for Polar Research. *IEEE Transactions on Geoscience and Remote Sensing*, 52(5):2824–2842, may 2014. doi: 10.1109/tgrs.2013.2266415. URL <https://doi.org/10.1109/2Ftgrs.2013.2266415>.
- Schoof, C. and Mantelli, E. The role of sliding in ice stream formation. *Proceedings of the Royal Society A: Mathematical, Physical and Engineering Sciences*, 477(2248):20200870, 2021. doi: 10.1098/rspa.2020.0870. URL <https://royalsocietypublishing.org/doi/abs/10.1098/rspa.2020.0870>.
- Schroeder, D. M., Bingham, R. G., Blankenship, D. D., Christianson, K., Eisen, O., Flowers, G. E., Karlsson, N. B., Koutnik, M. R., Paden, J. D., and Siegert, M. J. Five decades of radioglaciology. *Annals of Glaciology*, pages 1–13, mar 2020. doi: 10.1017/aog.2020.11. URL <https://doi.org/10.1017/2Faog.2020.11>.
- Stokes, C. R., Margold, M., Clark, C. D., and Tarasov, L. Ice stream activity scaled to ice sheet volume during Laurentide Ice Sheet deglaciation. *Nature*, 530(7590):322–326, feb 2016. doi: 10.1038/nature16947. URL <https://doi.org/10.1038/2Fnature16947>.
- Vallelonga, P., Christianson, K., Alley, R. B., Anandakrishnan, S., Christian, J. E. M., Dahl-Jensen, D., Gkinis, V., Holme, C., Jacobel, R. W., Karlsson, N. B., Keisling, B. A., Kipfstuhl, S., Kjær, H. A., Kristensen, M. E. L., Muto, A., Peters, L. E., Popp, T., Riverman, K. L., Svensson, A. M., Tibuleac, C., Vinther, B. M., Weng, Y., and Winstrup, M. Initial results from geophysical surveys and shallow coring of the Northeast Greenland Ice Stream (NEGIS). *The Cryosphere*, 8(4):1275–1287, jul 2014. doi: 10.5194/tc-8-1275-2014. URL <https://doi.org/10.5194/2Ftc-8-1275-2014>.
- Winter, K., J. Woodward, N. Ross, S. A. Dunning, R. G. Bingham, H. F. J. Corr, a. J. S. Airborne radar evidence for tributary flow switching in Institute Ice Stream, West Antarctica: Implications for ice sheet configuration and dynamics. *Journal of Geophysical Research: Earth Surface*, 120(9):2498–2528, 2015. doi: 10.1002/2015JF003518. URL <https://agupubs.onlinelibrary.wiley.com/doi/full/10.1002/2015JF003518>.
- Wolovick, M. J., Creyts, T. T., Buck, W. R., and Bell, R. E. Traveling slippery patches produce thickness-scale folds in ice sheets. *Geophysical Research Letters*, 41(24):8895–8901, dec 2014. doi: 10.1002/2014gl062248. URL <https://doi.org/10.1002/2F2014gl062248>.

PAPER VI

SUPPLEMENTARY INFORMATION

Supplementary Information:

Interior of the North East Greenland Ice stream reveals that NEGIS-type ice streams may come and go

Daniela Jansen¹ , Steven Franke¹ , Catherine C. Bauer², Tobias Binder^{1,†} , Dorthe Dahl-Jensen^{3,4} , Tamara de Riese² , Olaf Eisen^{1,5} , Maria-Gema Llorens⁶ , Heinrich Miller¹ , Niklas Neckel¹ , John D. Paden⁷ , Till Sachau² , Ilka Weikusat^{1,2} , Yu Zhang² and Paul D. Bons^{2,8} 

¹ Alfred Wegener Institute, Helmholtz Centre for Polar and Marine Research, Bremerhaven, Germany

² Department of Geosciences, Eberhard Karls University Tübingen, Germany

³ Physics of Ice, Climate, and Earth, Niels Bohr Institute, University of Copenhagen, Denmark

⁴ Centre for Earth Observation Science, University of Manitoba, Winnipeg, Canada

⁵ Department of Geosciences, University of Bremen, Bremen, Germany

⁶ Institute of Earth Sciences Jaume Almera, Barcelona, Spain

⁷ Center for Remote Sensing of Ice Sheets (CReSIS), University of Kansas, Lawrence, KS, USA

⁸ China University of Geosciences, Beijing, China

[†] now at Ibeo Automotive Systems, Hamburg, Germany

The supplementary information for Paper VI is provided on the USB stick submitted alongside the thesis as well as in a private online repository (see below).

Supplementary Information of Paper VI:

1. Figures S1 – S5 and Equations S1 – S9 (pdf):











<https://storage.luckycloud.de/f/ec67a445dad54ed98e4b/>

Appendix K

PAPER VII

RESEARCH ARTICLE

Indication of ice-stream regime shift in Northeast Greenland

Steven Franke¹ , Paul Bons^{2,3} , Julien Westhoff⁴ , Tobias Binder^{1,†} , Kyra Streng², Veit Helm¹ , Daniel Steinhage¹ , Olaf Eisen^{1,5} , John Paden⁶ , Ilka Weikusat^{1,2}  and Daniela Jansen¹ 

¹ Alfred Wegener Institute, Helmholtz Centre for Polar and Marine Research, Bremerhaven, Germany

² Department of Geosciences, Eberhard Karls University Tübingen, Germany

³ China University of Geosciences, Beijing, China

⁴ Physics of Ice, Climate, and Earth, Niels Bohr Institute, University of Copenhagen, Denmark

⁵ Department of Geosciences, University of Bremen, Bremen, Germany

⁶ Centre for Remote Sensing of Ice Sheets (CReSIS), University of Kansas, Lawrence, KS, USA

[†] now at Ibeo Automotive Systems, Hamburg, Germany

Abstract

Ice penetrating radar reveals the geometry of internal stratigraphy of the Greenland Ice Sheet and thus constrains its evolution. The record of radar reflectors is shaped by the cumulative deformation of initially surface-parallel isochronous stratigraphic layers. Decoding the deformation history of these structures offers an excellent possibility to reconstruct past ice movements and draw conclusions about processes on the Earth's surface. Here we use the radiostratigraphic layers from newly acquired and older radar data from northeastern Greenland to decipher their deformation history. We apply a three-dimensional construction of isochronous surfaces and connect recurring patterns in the radar signature. Our results reveal a deformation sequence pointing to two former ice streams reaching far inland in the northeastern Greenland Ice Sheet that nowadays show no trace in the surface velocity. We propose that the observed fold geometries are best explained by (1) the former presence of a Peterman-type ice stream with convergent flow that subsequently changed to the present-day surface flow field and (2) a ceased former localized NEGIS-type ice stream with sharp shear margins.

Introduction

Despite the continuous increase in *in-situ* and remote sensing data of the polar ice sheets, we find a large gap of observations that are necessary to reconstruct past ice motion. Satellite observations of ice surface flow of the Greenland (GrIS) and Antarctic (AIS) reach back to the 1970s (Rosenau et al., 2015; Rignot et al., 2019; Mouginot et al., 2019). The reconstruction of ice stream activity at formerly glaciated regions is limited to the end of the last glacial (Margold et al., 2015; Stokes et al., 2016) but shows that ice streams operated at different times during deglaciation of the (22 ka–7 ka ago) and were activated and deactivated in different locations and periods. A way to close this observational gap is provided by high-quality radio-echo sounding (RES) data (Rodriguez-Morales et al., 2014; Gogineni et al., 2001; MacGregor et al., 2015; Bell et al., 2014) that show details of the sometimes disturbed or folded englacial

stratigraphic architecture of internal reflection horizons (IRHs) of the GrIS and AIS. Most IRHs are assumed to be isochrones (Fujita et al., 1999), representing the horizons of buried former ice-sheet surfaces (Siegert, 1999). Englacial deformation can disturb the conformity and continuity of IRHs and lead to a non-monotonically increasing age distribution with depth, which is a challenge for ice-core analysis (Waddington et al., 2001).

Disturbances of different types and magnitudes of internal layers were found in Greenland (MacGregor et al., 2015; Leysinger Vieli et al., 2018; Panton and Karlsson, 2015; Bell et al., 2014) and Antarctica (Drews et al., 2009; Bell et al., 2011; Wrona et al., 2018). They range from small folds on a centimetre-scale found in ice cores (e.g. Dahl-Jensen et al., 2013; Westhoff et al., 2020; Jansen et al., 2016) to tight folds that extend almost over the entire ice column with a fold axis oriented parallel to the shear margins of ice streams (e.g.

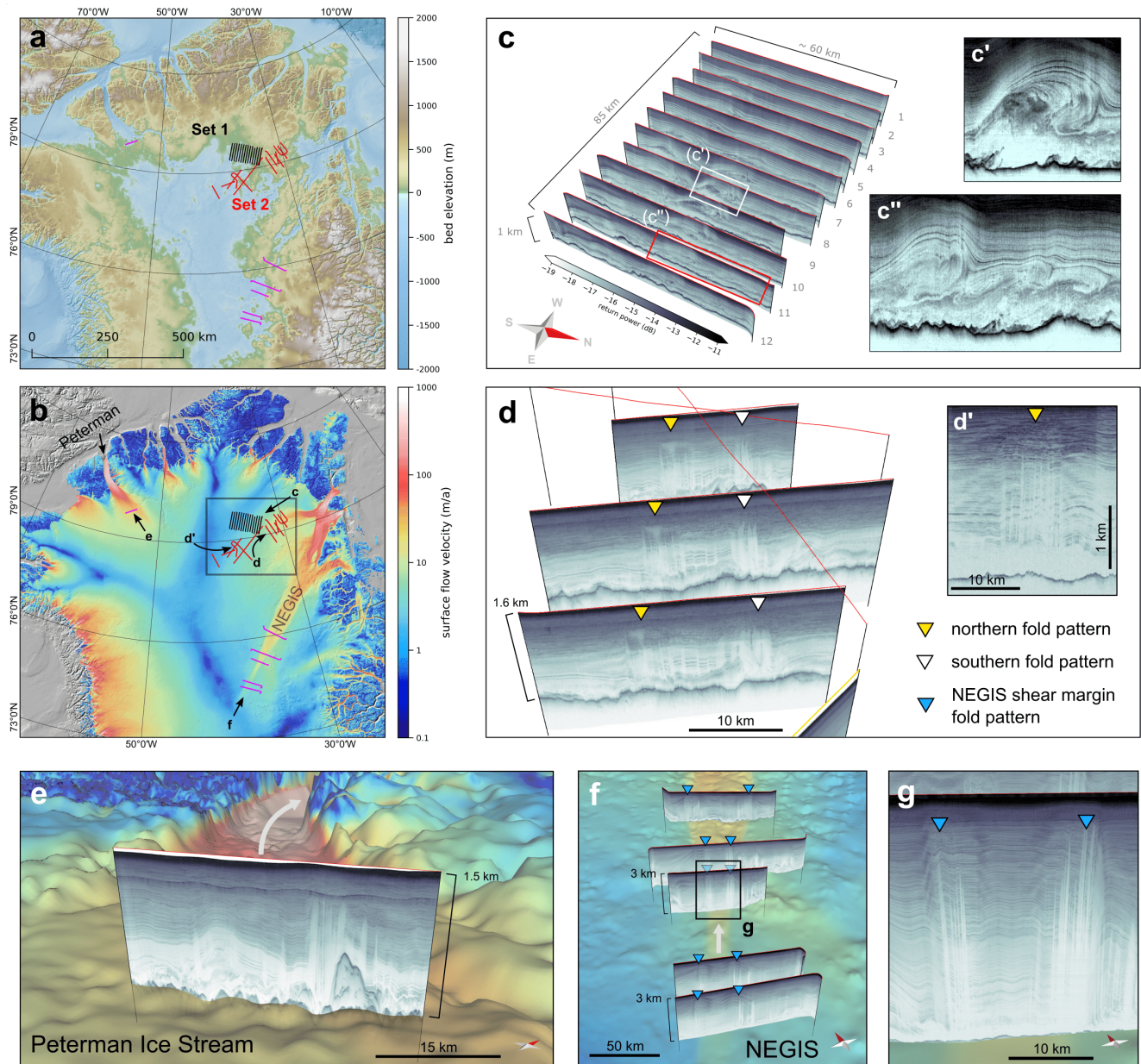


Figure K.1: Study site overview and key radar observations. Panels (a) and (b) show northern Greenland bed topography (a) and ice surface velocity (b; Joughin et al. 2017) with the location of two sets of radar profile lines (Set 1 in black and Set 2 in red). The black rectangle indicates the map outline of Figures K.2.d and e. Selected radar profiles of Set 1 are shown in panel (c) and radar profiles of Set 2 in (d). Panel e shows a radargram from the onset of the Peterman Glacier and panel (f) and (g) radargrams at the onset of the NEGIS. The white arrow in (e) and (f) indicates today's general ice flow direction.

Franke et al., 2020, 2021), and overturned and sheath folds, as well as plume-like structures associated with large units of disrupted stratigraphy at the ice base (e.g. MacGregor et al., 2015; Bell et al., 2014; Bons et al., 2016; Leysinger Vieli et al., 2018). Explanations for fold genesis range from basal freeze-on (Leysinger Vieli et al., 2018; Bell et al., 2014, 2011; Creyts et al., 2014), over differences in the ice rheology (Dahl-Jensen et al., 2013), changes in the basal resistance (Wolovick et al., 2014; Wolovick and Creyts, 2016) to convergent flow regimes (Bons et al., 2016).

Here, we combine recently acquired and older existing radar data from northeast Greenland to reconstruct the deformation sequence of the radiostratigraphy. Our findings indicate that two former ice streams were active far upstream close to the location of the current ice divide in Northeast Greenland.

Radiostratigraphic patterns

We consider radar profiles in Northeast Greenland upstream of the 79° N Glacier (Figure K.1 a–d) acquired during Operation Ice Bridge (OIB) and by the Alfred Wegener Institute, Helmholtz Centre for Polar and Marine Research (AWI). The radar profiles in Figure K.1 c (Set 1, black profiles in Figure K.1 a and b) were acquired with AWI's multi-channel ultra-wideband (UWB) radar system in 2018. The survey layout is designed to map two large cylindrical fold units at a bearing angle of 10° true North, perpendicular to their fold axis. Ice surface velocity is almost zero in the west close to the ice divide and increases up to 15 m a⁻¹ towards the east (Figure S1). The survey was designed to investigate a roughly 100°-striking set of folds detected in earlier surveys. Twelve radar profiles were flown, 7.5 km apart, perpendicular to the 100° strike. The mapped cylindrical folds show the highest amplitude in the centre of the radar profiles and are not in conformity with the underlying bed topography (Figures S2, S3, S16 and S17). Similar folds have been observed at multiple locations in the GrIS (Leysinger Vieli et al., 2018; MacGregor et al., 2015; Bell et al., 2014) among them at the convergent flow region of the Peterman Glacier (Bons et al., 2016) (Figure K.1 e).

The radar profiles of Set 2 (Figure K.1 a, b and d; red profiles) are composed of OIB and AWI profiles recorded with different acquisition systems. They extend from the central divide eastwards towards the northern catchment of the 79° N Glacier. The radargrams reveal a recurring signature of vertical low reflectivity stripes visible in the lower 70 % of the ice column (yellow markers in Figure K.1 d and S19–S25). The radar pattern of the features as well as their appearance in multiple radargrams (Figure K.1 d) bear a strong resemblance to the radar signature in the shear margins at the Northeast Greenland Ice Stream (NEGIS; Figure K.1 f and S27–S30; see Keisling et al. 2014; Franke et al. 2021).

Overtaken Cylindrical folds

We analysed the englacial stratigraphy of the 12 parallel radar sections of Set 1 (Figure S2–S14). The vertical radiostratigraphy can be divided into four units (units 1–4 in Figure S15 A–D), where the uppermost unit consists of undisturbed meteoric ice underlain by a unit of radar reflectors, which are visible in all radargrams but are disrupted where folds overturn (Figure S15 B and C). The unit underneath is located above the echo-free zone and shows non-continuous radar reflection. We note that the radargrams close to the ice divide show horizontally layered strata and the least degree of layer deformation of all profiles (Figure S15 A). The central

sections show two large overturned folds (anticline-syncline pairs) with amplitudes increasing downwards in the ice column. Fold intensities increase downstream where maximum amplitudes reach 500–600 m (e.g. Figure S15 D). Folds are upright in the upper part of the ice column and become increasingly recumbent downwards, indicating bedrock-parallel shearing.

We trace three radar layers in the lower part of the ice column, which are continuously visible in all radargrams (Figure K.2). We estimate the respective age of the layers to 45, 52 and 60 ka (ages transferred from ???QUELLE???). We construct 3D surfaces from these traces that represent the best estimate of the shape of the three stratigraphic horizons, revealing two parallel cylindrical anticline-syncline pairs (Figure K.2 b and c). Furthermore, we reconstruct the axial traces and fold axial surfaces of the southern anticlines and their adjacent two synclines (Figure K.2 a). The folds strike E–W are asymmetrically sheared top-to-the-North (see Figure K.2 c).

Inactive Shear Margins

We find a characteristic reflection signature in the radar stratigraphy in Set 2 extending almost from the ice divide to the northern catchment of the 79° N Glacier (Figure K.1 a and d and Figure K.2 d and e). The recurring radar pattern is evident from the supplementary Figures S19–S25 and resembles two sequences of tightly folded isochrones separated by a sequence of almost undisturbed radar stratigraphy. In particular, in the downstream portion of the radar data, we find a remarkable resemblance to the radar signature at the shear margins of flow-perpendicular radargrams at the NEGIS (Figures 1c, d and S28–S32). At the NEGIS we observe the onset of tightly folded radar stratigraphy at the location of the highest ice surface velocity gradient. The number of folds and the wavelengths increases from up- to downstream. In addition to the shear margin radar signature, we find further similarities, such as downward-sloping internal layers at the outer margins of the fold sequences, kink-folds in the region between them (Figure S29) and in radar profiles oriented obliquely to the folds (Figure S30). The folds at NEGIS's shear margins are found almost up to the ice surface. The location of fold sequences in the radar data coincides with a faint signature in the gradient of the ice surface velocity (Figure K.2 e). While we are able to track the northern fold sequence far upstream along with the surface velocity gradient feature, the southern folds are less pronounced and far upstream we only find single large folds (including one, which has been misinterpreted as bedrock) along with the velocity gradient feature (Supplementary Figures S26 and S27).

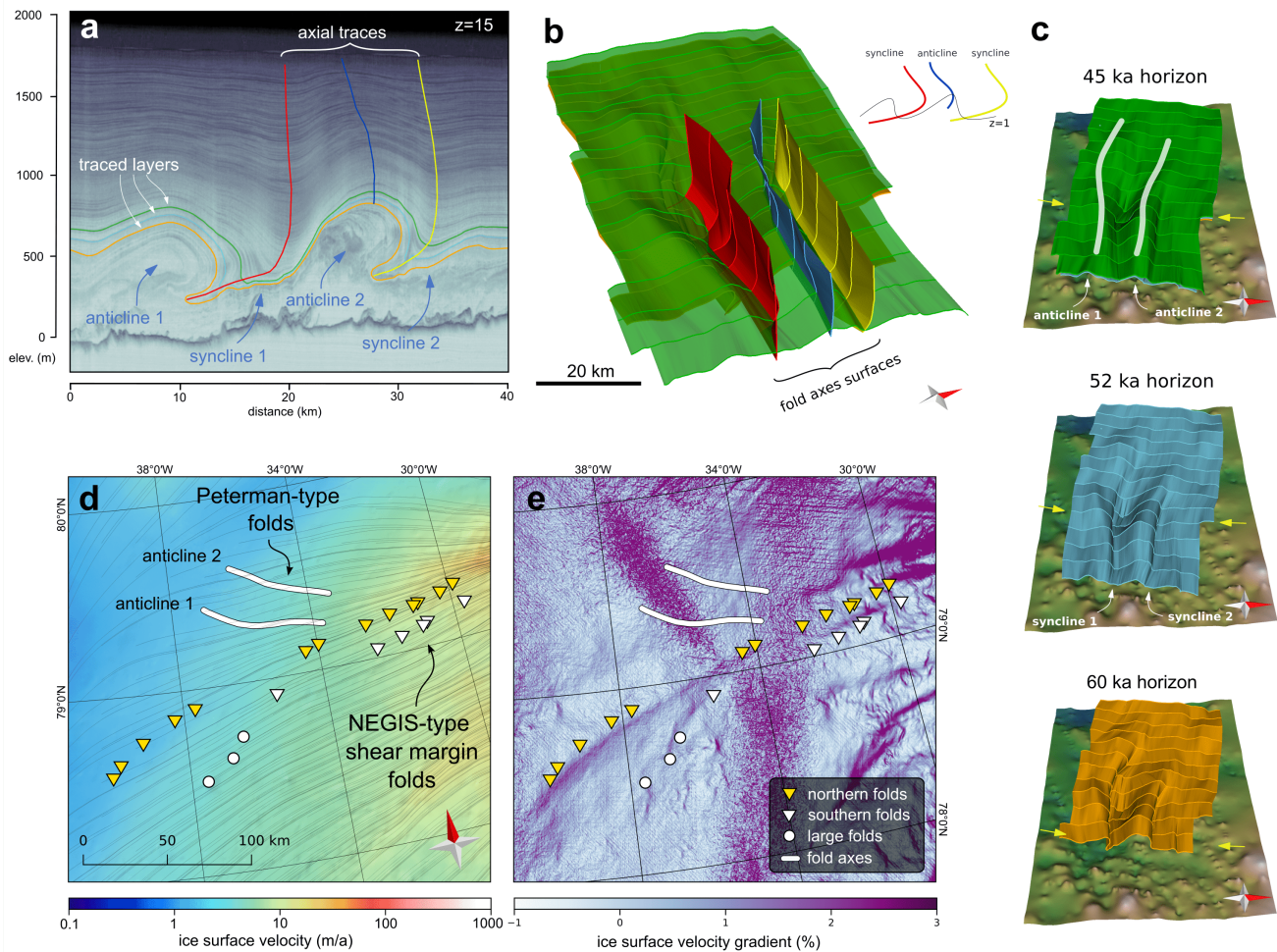


Figure K.2: Locations of folded radiostratigraphy patterns in NE Greenland. Panel (a) shows a radargram of Set 1 with three traced internal layers (45 ka, 52 ka and 60 ka old) and axial traces of two synclines and one anticline. The 3D horizons and axial surfaces constructed from the traced radar layers and axial traces are shown in (b) and the respective horizons in (c). Panels (d) and (e) provide an overview of the locations of the Peterman-type folds (two cylindrical anticlines of Set 1) and the NEGIS-type shear margin folds (tight fold sequences). The background map in (d) shows the ice surface velocity of Joughin et al. (2017) and in (e) the velocity gradient on a logarithmic scale (\log_{10}).

Folding sequences and ice flow

We consider the following mechanisms for fold formation and growth in the radargrams in Set 1: basal freeze-on (Leysinger Vieli et al., 2018), changes in the basal resistance or slippery patches (Wolovick et al., 2014), and convergent ice flow (Bons et al., 2016). The generation of large folds via basal freeze-on and slippery patches relies on long-term ice flow perpendicular to the fold axis. Both cylindrical folds show a direction of overturning towards north. However, this does not correlate with the present flow field, hence ice flow must have been towards northern Greenland in the past to create folds via freeze-on or slippery patches. We consider this to be unlikely for two reasons: (1) the location and orientation of ice divides and thus the configuration of the entire Greenland Ice Sheet, must have been very different to the present setting and (2) there are no

indications for a large outlet area north of the folds producing the required flow field (Figure K.1 a and S1 and S17 a). With respect to the likelihood of basal freeze-on, we analyze the freeze-on index (Leysinger Vieli et al., 2018) and radar-based basal water detection (Jordan et al., 2018) and find no indications for the availability of liquid water in the surrounding or that the ice would freeze at the base at the particular location of the folds (Figure S17 d). Furthermore, the folds consist of anticlines where the layers are raised, but also of synclines where they are lowered, which would require alternating strips of basal freeze-on and melt. The initial formation of upright folds as described for the Petermann Glacier (Bons et al., 2016) is not consistent with the present flow field, as ice flow does not converge, nor does it explain fold overturning towards the north. Both observations indicate that the folds were not created at the current flow regime.

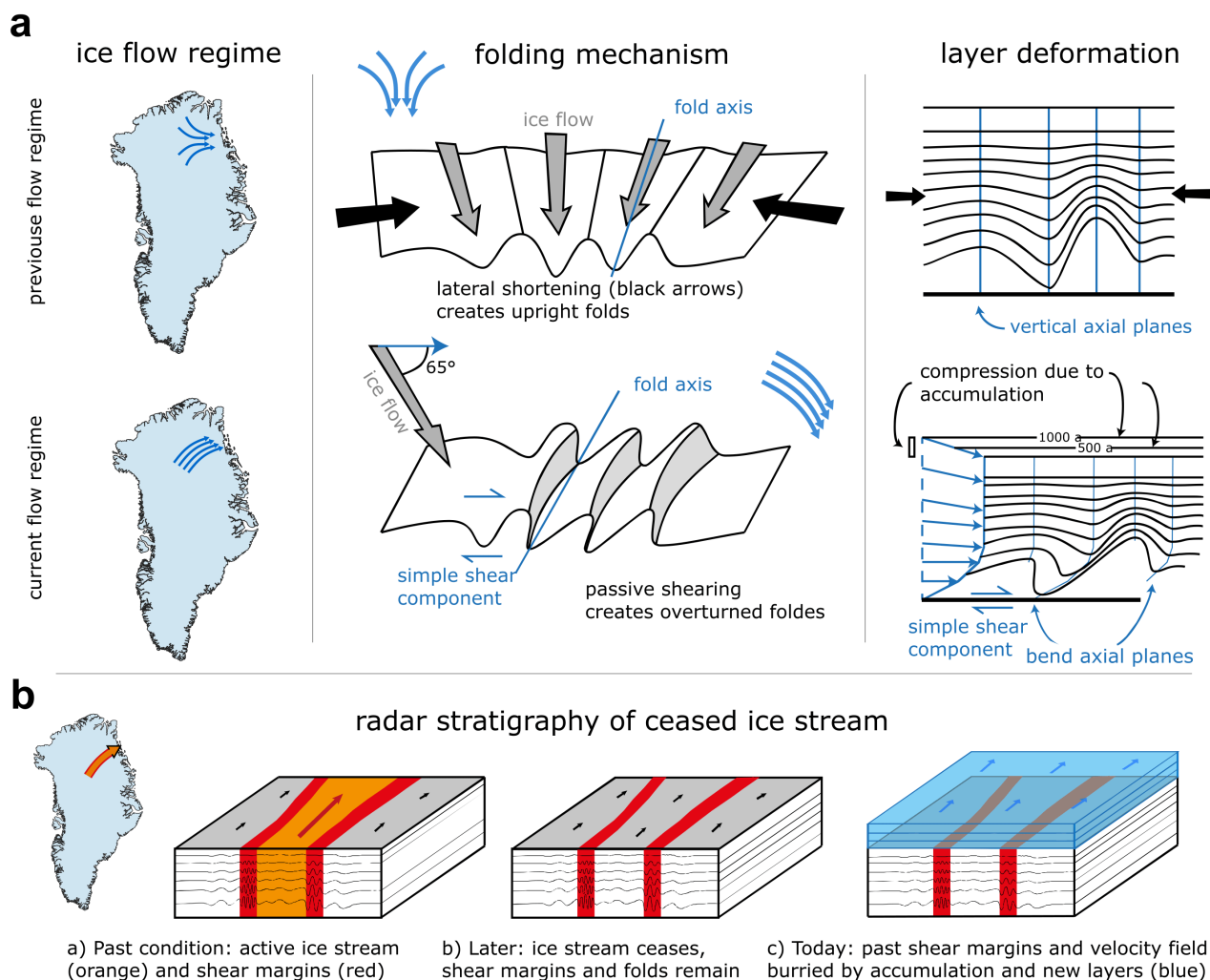


Figure K.3: Ice-dynamic reconstruction of fold patterns. Panel (a) shows the formation overturned cylindrical folds of Set 1. The upper row illustrates the formation of upright folds due to a paleo convergent flow regime. The row below indicates a change from the paleo flow regime to the present flow regime, which passively shears of the upright folds. The schematic ice flow regime is indicated in the left column, the folding mechanisms on a 3D horizon in the middle column and the schematic layer deformation in a radargram in the right column. Panel (b) illustrates the reconstructed sequence of flow regimes producing the observed radar stratigraphy patterns in Set 2. An active NEGIS-type ice stream with localized ice flow (orange) created the tight folds at its shear margins (red). Later, ice flow ceased and subsequent accumulation buried deposited horizontal layers on top of folded layers (blue).

Based on available theories for fold formation, the 3D geometry, the glaciological setting and orientation of the folds, we consider the following scenario as the most likely to explain initial fold formation and subsequent modification (Figure K.3 a): (i) A convergent flow regime similar to the one at the Petermann Glacier onset created large upright folds. The required flow regime would create folds with fold axes aligned towards the outlet, which is consistent with the position of the large outlets in NE Greenland (Figure 4 purple). The intensity of folding increases downstream due to the increase in horizontal shortening. (ii) The flow regime changed to the present one, in which the flow is oblique to the earlier one, resulting in the shearing of the existing folds. Accumulation without further fold growth compressed

the folds. Along-flow stretching and shearing has affected the downstream portion more due to the higher ice flow velocities here.

The similarities of the radar signatures in Set 2 with the NEGIS radargrams suggest the remnants of the shear margins of an inactive former ice stream (see Figure K.3 b and the Supplementary Section 2). While the radar data coverage and profile orientation is denser in the downstream section, it remains unclear how far exactly the shear margins can be traced towards the ice divide. Similar to the NEGIS, the northern folds sequence is narrower compared to the southern folds and the number of folds increases from up to downstream. Similar to the region southeast outside of the NEGIS, we find large folds in the vicinity of the shear margins

of the inactive ice stream. The fold locations coincide with the small signature in the velocity gradient (Figure K.2 e and S26). Whether the folds mark the location of the former shear margin or not is unclear. A further similarity is that (if the folds mark the shear margin location) the ice stream is wider at its very onset as further downstream. An analysis of the isochrones in the upper part of the ice column shows that the imprint of the downstream folds in Set 2 reaches almost up to the ice surface (~ 90 %), similar to the signature in the NEGIS. By contrast the fold imprint in the upstream isochrones in Set 2 is lost at ~ 70 % of the ice column.

All this points to the fact that the fold sequences in Set 2 were created by a former ice-flow regime similar to the present one at the upstream part of the NEGIS. The downstream portion most likely persisted longer and is not buried by long-term accumulation in contrast to the upstream portion. Since we find only a marginal indication of the required flow regime in the surface velocity gradient, we argue that a paleo ice-flow regime, similar to the present one at the onset of the NEGIS, but different to the present one created these structures (Figure 4 red).

Ice streams come and go

Numerical modelling results for the flow field of the recent Greenland Ice Sheet poorly represent the strong localisation of ice drawdown from the central ice sheet by the NEGIS. Results from [Aschwanden et al. \(2019\)](#) show a more distributed outflow within the catchment north eastern catchment area, towards the three main outlets, the Nioghalvfjærdsfjord Gletscher (79° N Glacier), the Zachariae Isstrom (ZI), and the Storstrommen Gletscher (SG). Our findings suggest that the activity of ice streams or flow regimes in this catchment has been shifting over time, and possibly faster than previously anticipated. Changes in past flow regimes were so far detected at Antarctic ice streams closely to the outlets (e.g. [Conway et al., 2002](#); [Anandkrishnan and Alley, 1997](#); [Jacobel et al., 1996](#); [Payne and Dongelmans, 1997](#)) as a result to localized thinning in the drainage system and formerly glaciated regions (e.g. [Dowdeswell et al., 2006](#)) due to long-term modifications of glacial erosion and deposition of sediments over multiple glacial cycles. For the outlets of NEGIS there is geological evidence that at least their extent also varied in the past as a reaction to the varying climate conditions during the Holocene Thermal maximum.

For Antarctica, [Payne and Dongelmans \(1997\)](#) propose that the cause for the switching behaviour appears to arise from a competition of ice discharge between the adjacent drainage basins. The authors suggest that localized thickening might be responsible for the initiation of a new ice stream at a different location. A

similar line of Argument is followed by [Stokes et al. \(2016\)](#), who describe the ice stream activity in the Laurentide ice stream in relation to its volume. They suggest that streaming is triggered if ice volume is large, but could also cease rapidly if volume is reduced. Thus, ice streams are much more likely to be initiated at the beginning of deglaciation, and might be less important later on. For Greenland, geologic evidence (e.g. [Larsen et al., 2018](#)), and also modelling studies ([Lecavalier et al., 2014](#)) indicate that the geometry and elevation of the ice sheet has changed significantly during the Holocene. We earlier showed in Paper VI ([Jansen et al., 2021](#); in prep.) the upstream part of NEGIS as it is today has very likely been activated around 3 500 years ago, following the onset of the re-advance of the front of the 79° N Glacier. We suggest that after the HTM retreat, the geometry of the catchment area and especially the elevation did not support streaming any more in its northern part, which then shifted further south to the position of the current NEGIS. It also has to be noted that a shift in the ice divide following the opening of the Nares Straight around 8k a ago ([England, 1999](#)) could be one possible explanation for the shift.

The fact that a NEGIS-type ice stream was active at another location in the Greenland ice sheet again raises the fundamental question of how such ice streams are formed. It is questionable whether the theory of [Fahnestock \(2001\)](#), that an extremely high geothermal heat flux (GHF) determines the location and formation of the NEGIS, was also responsible for this ice stream further north in the past. That such a high GHF is geologically realistic and is responsible for the formation and continuation of the NEGIS is widely discussed (see [Smith et al. 2019](#) and the comment of [Bons et al. 2021](#)) and suggests that a combination of various ice-dynamic and the conditions at the glacier base determine the appearance of this ice stream type. Another striking feature of the location of the past NEGIS-type ice stream is that its relics lie in an area where ice is still draining rapidly today. Furthermore, as we show, the downstream portion of this ice stream was active longer as the upstream portion. We take that as an indication that the ice flow regime changed gradually from a far-inland reaching localized ice stream to the present flow regime. The modeling of [Schoof and Mantelli \(2021\)](#) shows that ice streams with highly localized shear zones can simply be created by self-reinforcing processes. This mechanism fits our observations and suggests that past stronger runoff led to strong localization and rapid ice flow and weakened over time.

Methods

AWI UWB Radar Data Profiles

In April and April and May 2018, we collected radar data upstream of the 79° N Glacier and at the onset of the Northeast Greenland Ice Stream (NEGIS) with the multi-channel ultra-wideband (UWB) airborne radar sounder of the Alfred Wegener Institute, Helmholtz Centre for Polar and Marine Research (AWI; black lines of Set 1 and purple lines at the NEGIS in Figure K.1 a, b, c and f). The system comprises an antenna array with eight channels (HH polarization), and the data were recorded at a frequency range of 180- 210 MHz. For a comprehensive description of AWI's UWB radar system and the survey design of the NEGIS survey (see Franke et al., 2020, 2021; Hale et al., 2016; Rodriguez-Morales et al., 2014). We used the CReSIS Toolbox (CReSIS, 2020) for radar data processing, which includes synthetic aperture radar (SAR) and array processing (for further details see the appendix in Franke et al. (2020, 2021). For the geometrical analysis of the IRHs we translate the two-way travel time (TWT) radar data into an elevation domain with a two dimensional dielectric constant (ϵ) model for air with $\epsilon = 1$ and ice with $\epsilon = 3.15$. The boundary between the two dielectric constants is the ice surface radar reflection.

3D Horizon Construction

For a three-dimensional analysis of the IRHs, we build up on the approach of Bons et al. (2016) and use the 3D model building software MOVETM (MOVE Core Application, Version 2019). The elevation-converted radargrams were converted to the SEG-Y format with the ObsPy Python toolbox (Beyreuther et al., 2010) and imported in MOVE. Internal layers, which could be clearly identified in all radar sections, were traced manually. The traced layers were split into fragments which show a similar geometry (e.g. anticlines and synclines) as a fragment of the same IRH in the adjacent radargram. Supplementary Figure S35a shows how the line fragments are interpolated between two radargrams.

Fold axial surfaces

We construct three axial surfaces (one anticline and two synclines) of the northern cylindrical folds upstream of the 79° N Glacier (Figure K.1 c and 2. The method is analogous to the construction of the 3D horizons (see Figure K.2 a, Y and SX). We trace the points of maximum curvature in the radargrams for two synclines and the anticline of the cylindrical fold to create a line segment and interpolate between the lines of each radargram.

Ice flow reconstruction from axial traces

Due to the curvature of the fold axial traces, we define a minimum and a maximum distance for a measure of the displacement of the ice column (dS_{min} and dS_{max}) for five profiles for syncline 1 and 2, respectively. At each position we use the absolute ice flow velocity (v_S) to calculate the velocity component parallel to the direction of shearing with the offset angle α : $v_y = v_S \cos(\alpha)$ (see Figure S36). We assume that the ice flow velocity does not change over time and only changes very little in space. Then we calculate the time needed for the displacement of the upper ice column t_S assuming that the deepest end of the axial trace is immobile: $t_S = dS$. The vector components of the velocity field are shown in supplementary Figure S36a.

Acknowledgements

We thank the crew of the research aircraft Polar 6. We acknowledge the use of radar data from CReSIS generated with support from the University of Kansas, NASA Operation IceBridge grant NNX16AH54G, NSF grants ACI-1443054, OPP-1739003, and IIS-1838230, Lilly Endowment Incorporated, and Indiana METACyt Initiative. Steven Franke and Daniela Jansen were funded by the AWI strategy fund.

Data Availability

The CReSIS radio-echo sounding data used in this study are available under CReSIS data products <https://data.cresis.ku.edu/data/rds/>. The list of profiles is provided in the supplementary material. AWI UWB ice thickness data from Jansen et al. (2020) are available at the PANGAEA data publisher <https://doi.pangaea.de/10.1594/PANGAEA.913193>.

Author Contributions

SF wrote the manuscript, processed the radar data, constructed the 3D horizons, and performed all calculations and analyses. DJ designed the study and developed the scientific idea with contributions of PB, IW and SF. DJ was PI on the airborne radar survey and TB and VH collected the data. DS provided additional ice thickness data and VH assisted with GPS post processing. JW developed the idea for the visualization for the fold deformation stages and developed the folding hypothesis together with PB, DJ, IW, KS and SF. OE, DS, VH and IW provided detailed feedback on the analyses. All authors discussed and reviewed the manuscript.

Bibliography

- Anandakrishnan, S. and Alley, R. B. Tidal forcing of basal seismicity of ice stream c, west antarctica, observed far inland. *Journal of Geophysical Research: Solid Earth*, 102(B7):15183–15196, 1997. doi: <https://doi.org/10.1029/97JB01073>. URL <https://agupubs.onlinelibrary.wiley.com/doi/abs/10.1029/97JB01073>.
- Aschwanden, A., Fahnestock, M. A., Truffer, M., Brinkerhoff, D. J., Hock, R., Khroulev, C., Mottram, R., and Khan, S. A. Contribution of the Greenland Ice Sheet to sea level over the next millennium. *Science Advances*, 5(6), 2019. doi: 10.1126/sciadv.aav9396. URL <https://advances.sciencemag.org/content/5/6/eaav9396>.
- Bell, R. E., Ferraccioli, F., Creyts, T. T., Braaten, D., Corr, H., Das, I., Damaske, D., Frearson, N., Jordan, T., Rose, K., Studinger, M., and Wolovick, M. Widespread Persistent Thickening of the East Antarctic Ice Sheet by Freezing from the Base. *Science*, 331(6024):1592–1595, mar 2011. doi: 10.1126/science.1200109. URL <https://doi.org/10.1126%2Fscience.1200109>.
- Bell, R. E., Tinto, K., Das, I., Wolovick, M., Chu, W., Creyts, T. T., Frearson, N., Abdi, A., and Paden, J. D. Deformation warming and softening of Greenland's ice by refreezing meltwater. *Nature Geoscience*, 7(7):497–502, jun 2014. doi: 10.1038/ngeo2179. URL <https://doi.org/10.1038%2Fng2179>.
- Beyreuther, M., Barsch, R., Krischer, L., Megies, T., Behr, Y., and Wassermann, J. ObsPy: A Python Toolbox for Seismology. *Seismological Research Letters*, 81(3):530–533, may 2010. doi: 10.1785/gssrl.81.3.530. URL <https://doi.org/10.1785%2Fgssrl.81.3.530>.
- Bons, P. D., Jansen, D., Mundel, F., Bauer, C. C., Binder, T., Eisen, O., Jessell, M. W., Llorens, M.-G., Steinbach, F., Steinhage, D., and Weikusat, I. Converging flow and anisotropy cause large-scale folding in Greenland's ice sheet. *Nature Communications*, 7(1), apr 2016. doi: 10.1038/ncomms11427. URL <https://doi.org/10.1038%2Fncomms11427>.
- Bons, P. D., de Riese, T., Franke, S., Llorens, M.-G., Sachau, T., Stoll, N., Weikusat, I., Westhoff, J., and Zhang, Y. Comment on “exceptionally high heat flux needed to sustain the northeast greenland ice stream” by smith-johnsen et al. (2020). *The Cryosphere*, 15(5):2251–2254, 2021. doi: 10.5194/tc-15-2251-2021. URL <https://tc.copernicus.org/articles/15/2251/2021/>.
- Conway, H., Catania, G., Raymond, C. F., Gades, A. M., Scambos, T. A., and Engelhardt, H. Switch of flow direction in an Antarctic ice stream. *Nature*, 419(6906):465–467, oct 2002. ISSN 0028-0836. doi: 10.1038/nature01081. URL <http://www.nature.com/articles/nature01081>.
- CRISIS. CRISIS Toolbox [computer software], Lawrence, Kansas, USA. Retrieved from <https://github.com/CRISIS>, 2020. URL https://ops.cresis.ku.edu/wiki/index.php/Main_Page.
- Creyts, T. T., Ferraccioli, F., Bell, R. E., Wolovick, M., Corr, H., Rose, K. C., Frearson, N., Damaske, D., Jordan, T., Braaten, D., and Finn, C. Freezing of ridges and water networks preserves the Gamburtsev Subglacial Mountains for millions of years. *Geophysical Research Letters*, 41(22): 8114–8122, nov 2014. doi: 10.1002/2014gl061491. URL <https://doi.org/10.1002%2F2014gl061491>.
- Dahl-Jensen, D., Albert, M. R., Aldahan, A., Azuma, N., Balslev-Clausen, D., Baumgartner, M., Berggren, A. M., Bigler, M., Binder, T., Blunier, T., Bourgeois, J. C., Brook, E. J., Buchardt, S. L., Buizert, C., Capron, E., Chappellaz, J., Chung, J., Clausen, H. B., Cvijanovic, I., Davies, S. M., Ditlevsen, P., Eicher, O., Fischer, H., Fisher, D. A., Fleet, L. G., Gfeller, G., Gkinis, V., Gogineni, S., Goto-Azuma, K., Grinsted, A., Gudlaugsdottir, H., Guillevic, M., Hansen, S. B., Hansson, M., Hirabayashi, M., Hong, S., Hur, S. D., Huybrechts, P., Hvidberg, C. S., Iizuka, Y., Jenk, T., Johnsen, S. J., Jones, T. R., Jouzel, J., Karlsson, N. B., Kawamura, K., Keegan, K., Kettner, E., Kipfstuhl, S., Kjær, H. A., Koutnik, M., Kuramoto, T., Köhler, P., Laepple, T., Landais, A., Langen, P. L., Larsen, L. B., Leuenberger, D., Leuenberger, M., Leuschen, C., Li, J., Lipenkov, V., Martinerie, P., Maselli, O. J., Masson-Delmotte, V., McConnell, J. R., Miller, H., Mini, O., Miyamoto, A., Montagnat-Rentier, M., Mulvaney, R., Muscheler, R., Orsi, A. J., Paden, J., Panton, C., Pattyn, F., Petit, J. R., Pol, K., Popp, T., Possnert, G., Prié, F., Prokopiou, M., Quiquet, A., Rasmussen, S. O., Raynaud, D., Ren, J., Reutenauer, C., Ritz, C., Röckmann, T., Rosen, J. L., Rubino, M., Rybak, O., Samyn, D., Sapart, C. J., Schilt, A., Schmidt, A. M., Schwander, J., Schüpbach, S., Seierstad, I., Severinghaus, J. P., Sheldon, S., Simonsen, S. B., Sjolte, J., Solgaard, A. M., Sowers, T., Sperlich, P., Steen-Larsen, H. C., Steffen, K., Steffensen, J. P., Steinhage, D., Stocker, T. F., Stowasser, C., Sturevik, A. S., Sturges, W. T., Sveinbjörnsdottir, A., Svensson, A., Tison, J. L., Uetake, J., Vallelonga, P., Van De Wal, R. S., Van Der Wel, G., Vaughn, B. H., Vinther, B., Waddington, E., Wegner, A., Weikusat, I., White, J. W., Wilhelms, F., Winstrup, M., Witrant, E., Wolff, E. W., Xiao, C., and Zheng, J. Eemian interglacial reconstructed from a Greenland folded ice core. *Nature*, 493(7433):489–494, 2013. ISSN 00280836. doi: 10.1038/nature11789. URL <http://dx.doi.org/10.1038/nature11789>.
- Dowdeswell, J. A., Ottesen, D., and Rise, L. Flow switching and large-scale deposition by ice streams draining former ice sheets. *Geology*, 34(4):313–316, 2006. doi: 10.1130/G22253.1. URL <https://doi.org/10.1130/G22253.1>.
- Drews, R., Eisen, O., Weikusat, I., Kipfstuhl, S., Lambrecht, A., Steinhage, D., Wilhelms, F., and Miller, H. Layer disturbances and the radio-echo free zone in ice sheets. *The Cryosphere*, 3(2):195–203, aug 2009. doi: 10.5194/tc-3-195-2009. URL <https://doi.org/10.5194%2Ftc-3-195-2009>.
- England, J. Coalescent greenland and inuitian ice during the last glacial maximum: revising the quaternary of the canadian high arctic. *Quaternary Science Reviews*, 18(3):

- 421–456, 1999. doi: 10.1016/S0277-3791(98)00070-5. URL <https://www.sciencedirect.com/science/article/pii/S0277379198000705>.
- Fahnestock, M. High Geothermal Heat Flow Basal Melt, and the Origin of Rapid Ice Flow in Central Greenland. *Science*, 294(5550):2338–2342, dec 2001. doi: 10.1126/science.1065370. URL <https://doi.org/10.1126/2Fscience.1065370>.
- Franke, S., Jansen, D., Binder, T., Dörr, N., Helm, V., Paden, J., Steinhage, D., and Eisen, O. Bed topography and subglacial landforms in the onset region of the Northeast Greenland Ice Stream. *Annals of Glaciology*, pages 1–11, mar 2020. doi: 10.1017/aog.2020.12. URL <https://doi.org/10.1017/2F2020.12>.
- Franke, S., Jansen, D., Binder, T., Paden, J. D., Dörr, N., Gerber, T., Miller, H., Dahl-Jensen, D., Helm, V., Steinhage, D., Weikusat, I., Wilhelms, F., and Eisen, O. Airborne ultra-wideband radar sounding over the shear margins and along flow lines at the onset region of the northeast Greenland ice stream. *Earth System Science Data Discussions*, 2021:1–24, 2021. doi: 10.5194/essd-2021-91. URL <https://essd.copernicus.org/preprints/essd-2021-91/>.
- Fujita, S., Maeno, H., Uratsuka, S., Furukawa, T., Mae, S., Fujii, Y., and Watanabe, O. Nature of radio echo layering in the Antarctic Ice Sheet detected by a two-frequency experiment. *Journal of Geophysical Research: Solid Earth*, 104(B6): 13013–13024, jun 1999. doi: 10.1029/1999jb900034. URL <https://doi.org/10.1029/2F1999jb900034>.
- Gogineni, S., Tammana, D., Braaten, D., Leuschen, C., Akins, T., Legarsky, J., Kanagaratnam, P., Stiles, J., Allen, C., and Jezek, K. Coherent radar ice thickness measurements over the Greenland ice sheet. *Journal of Geophysical Research: Atmospheres*, 106(D24):33761–33772, dec 2001. doi: 10.1029/2001jd900183. URL <https://doi.org/10.1029/2F2001jd900183>.
- Hale, R., Miller, H., Gogineni, S., Yan, J. B., Rodriguez-Morales, F., Leuschen, C., Paden, J., Li, J., Binder, T., Steinhage, D., Gehrmann, M., and Braaten, D. Multi-channel ultra-wideband radar sounder and imager. In *2016 IEEE International Geoscience and Remote Sensing Symposium (IGARSS)*. IEEE, jul 2016. doi: 10.1109/igarss.2016.7729545. URL <https://doi.org/10.1109/2F2016.7729545>.
- Jacobel, R. W., Scambos, T. A., Raymond, C. F., and Gades, A. M. Changes in the configuration of ice stream flow from the west antarctic ice sheet. *Journal of Geophysical Research: Solid Earth*, 101(B3):5499–5504, 1996. doi: <https://doi.org/10.1029/95JB03735>. URL <https://agupubs.onlinelibrary.wiley.com/doi/abs/10.1029/95JB03735>.
- Jansen, D., Llorens, M.-G., Westhoff, J., Steinbach, F., Kipfstuhl, S., Bons, P. D., Griera, A., and Weikusat, I. Small-scale disturbances in the stratigraphy of the NEEM ice core: observations and numerical model simulations. *The Cryosphere*, 10(1):359–370, feb 2016. doi: 10.5194/tc-10-359-2016. URL <https://doi.org/10.5194/2Ftc-10-359-2016>.
- Jansen, D., Franke, S., Binder, T., Helm, V., and Paden, J. D. Ice thickness from the northern catchment region of Greenland's 79 North Glacier, recorded with the airborne AWI UWB radar system [DATA SET], 2020. URL <https://doi.org/10.1594/PANGAEA.913193>.
- Jordan, T. M., Williams, C. N., Schroeder, D. M., Martos, Y. M., Cooper, M. A., Siegert, M. J., Paden, J. D., Huybrechts, P., and Bamber, J. L. A constraint upon the basal water distribution and thermal state of the Greenland Ice Sheet from radar bed echoes. *The Cryosphere*, 12(9): 2831–2854, sep 2018. doi: 10.5194/tc-12-2831-2018. URL <https://doi.org/10.5194/2Ftc-12-2831-2018>.
- Joughin, I., Smith, B. E., and Howat, I. M. A complete map of Greenland ice velocity derived from satellite data collected over 20 years. *Journal of Glaciology*, 64(243): 1–11, nov 2017. doi: 10.1017/jog.2017.73. URL <https://doi.org/10.1017/2Fjog.2017.73>.
- Keisling, B. A., Christianson, K., Alley, R. B., Peters, L. E., Christian, J. E., Anandakrishnan, S., Riverman, K. L., Muto, A., and Jacobel, R. W. Basal conditions and ice dynamics inferred from radar-derived internal stratigraphy of the northeast Greenland ice stream. *Annals of Glaciology*, 55 (67):127–137, 2014. doi: 10.3189/2014aog67a090. URL <https://doi.org/10.3189/2F2014aog67a090>.
- Larsen, N. K., Levy, L. B., Carlson, A. E., Buizert, C., Olsen, J., Strunk, A., Bjørk, A. A., and Skov, D. S. Instability of the Northeast Greenland Ice Stream over the last 45,000 years. *Nature Communications*, 9(1):3–10, 2018. ISSN 20411723. doi: 10.1038/s41467-018-04312-7. URL <http://dx.doi.org/10.1038/s41467-018-04312-7>.
- Lecavalier, B. S., Milne, G. A., Simpson, M. J., Wake, L., Huybrechts, P., Tarasov, L., Kjeldsen, K. K., Funder, S., Long, A. J., Woodroffe, S., Dyke, A. S., and Larsen, N. K. A model of Greenland ice sheet deglaciation constrained by observations of relative sea level and ice extent. *Quaternary Science Reviews*, 102:54–84, 2014. ISSN 0277-3791. doi: 10.1016/j.quascirev.2014.07.018. URL <https://www.sciencedirect.com/science/article/pii/S0277379114003011>.
- Leysinger Vieli, G. J.-M. C., Martín, C., Hindmarsh, R. C. A., and Lüthi, M. P. Basal freeze-on generates complex ice-sheet stratigraphy. *Nature Communications*, 9(1), nov 2018. doi: 10.1038/s41467-018-07083-3. URL <https://doi.org/10.1038/2Fs41467-018-07083-3>.
- MacGregor, J. A., Fahnestock, M. A., Catania, G. A., Paden, J. D., Gogineni, S. P., Young, S. K., Rybarski, S. C., Mabrey, A. N., Wagman, B. M., and Morlighem, M. Radiostратigraphy and age structure of the Greenland Ice Sheet. *Journal of Geophysical Research: Earth Surface*, 120(2):212–241, feb 2015. doi: 10.1002/2014jff003215. URL <https://doi.org/10.1002/2F2014jff003215>.
- Margold, M., Stokes, C. R., and Clark, C. D. Ice streams in the Laurentide Ice Sheet: Identification characteristics











- and comparison to modern ice sheets. *Earth-Science Reviews*, 143:117–146, apr 2015. doi: 10.1016/j.earscirev.2015.01.011. URL <https://doi.org/10.1016%2Fj.earscirev.2015.01.011>.
- Mouginot, J., Rignot, E., Bjørk, A. A., van den Broeke, M., Millan, R., Morlighem, M., Noël, B., Scheuchl, B., and Wood, M. Forty-six years of Greenland Ice Sheet mass balance from 1972 to 2018. *Proceedings of the National Academy of Sciences*, 116(19):9239–9244, apr 2019. doi: 10.1073/pnas.1904242116. URL <https://doi.org/10.1073%2Fpnas.1904242116>.
- Payne, A. J. and Dongelmans, P. W. Self-organization in the thermomechanical flow of ice sheets. *Journal of Geophysical Research: Solid Earth*, 102(B6):12219–12233, 1997. doi: <https://doi.org/10.1029/97JB00513>. URL <https://agupubs.onlinelibrary.wiley.com/doi/abs/10.1029/97JB00513>.
- Rignot, E., Mouginot, J., Scheuchl, B., van den Broeke, M., van Wessem, M. J., and Morlighem, M. Four decades of Antarctic Ice Sheet mass balance from 1979–2017. *Proceedings of the National Academy of Sciences*, 116(4):1095–1103, jan 2019. doi: 10.1073/pnas.1812883116. URL <https://doi.org/10.1073%2Fpnas.1812883116>.
- Rodriguez-Morales, F., Byers, K., Crowe, R., Player, K., Hale, R. D., Arnold, E. J., Smith, L., Gifford, C. M., Braaten, D., Pantou, C., Gogineni, S., Leuschen, C. J., Paden, J. D., Li, J., Lewis, C. C., Panzer, B., Alvestegui, D. G.-G., and Patel, A. Advanced Multifrequency Radar Instrumentation for Polar Research. *IEEE Transactions on Geoscience and Remote Sensing*, 52(5):2824–2842, may 2014. doi: 10.1109/tgrs.2013.2266415. URL <https://doi.org/10.1109%2Ftgrs.2013.2266415>.
- Rosenau, R., Scheinert, M., and Dietrich, R. A processing system to monitor Greenland outlet glacier velocity variations at decadal and seasonal time scales utilizing the Landsat imagery. *Remote Sensing of Environment*, 169:1–19, nov 2015. doi: 10.1016/j.rse.2015.07.012. URL <https://doi.org/10.1016%2Fj.rse.2015.07.012>.
- Schoof, C. and Mantelli, E. The role of sliding in ice stream formation. *Proceedings of the Royal Society A: Mathematical, Physical and Engineering Sciences*, 477(2248):20200870, 2021. doi: 10.1098/rspa.2020.0870. URL <https://royalsocietypublishing.org/doi/abs/10.1098/rspa.2020.0870>.
- Siegert, M. On the origin nature and uses of Antarctic ice-sheet radio-echo layering. *Progress in Physical Geography*, 23(2):159–179, jun 1999. doi: 10.1191/030913399671124903. URL <https://doi.org/10.1191%2F030913399671124903>.
- Smith, E. C., Hattermann, T., Kuhn, G., Gaedicke, C., Berger, S., Drews, R., Ehlers, T. A., Franke, D., Gromig, R., Hofstede, C., Lambrecht, A., Läufer, A., Mayer, C., Tiedemann, R., Wilhelms, F., and Eisen, O. Detailed seismic bathymetry beneath Ekstroem Ice Shelf Antarctica: Implications for glacial history and ice-ocean interaction. nov 2019. doi: 10.1002/essoar.10501125.1. URL <https://doi.org/10.1002%2Fessoar.10501125.1>.
- Stokes, C. R., Margold, M., Clark, C. D., and Tarasov, L. Ice stream activity scaled to ice sheet volume during Laurentide Ice Sheet deglaciation. *Nature*, 530(7590):322–326, feb 2016. doi: 10.1038/nature16947. URL <https://doi.org/10.1038%2Fnature16947>.
- Waddington, E. D., Bolzan, J. F., and Alley, R. B. Potential for stratigraphic folding near ice-sheet centers. *Journal of Glaciology*, 47(159):639–648, 2001. doi: 10.3189/172756501781831756. URL <https://doi.org/10.3189%2F172756501781831756>.
- Westhoff, J., Stoll, N., Franke, S., Weikusat, I., Bons, P., Kerch, J., Jansen, D., Kipfstuhl, S., and Dahl-Jensen, D. A stratigraphy-based method for reconstructing ice core orientation. *Annals of Glaciology*, page 1–12, 2020. doi: 10.1017/aog.2020.76. URL <https://doi.org/10.1017/aog.2020.76>.
- Wolovick, M. J. and Creyts, T. T. Overturned folds in ice sheets: Insights from a kinematic model of traveling sticky patches and comparisons with observations. *Journal of Geophysical Research: Earth Surface*, 121(5):1065–1083, may 2016. doi: 10.1002/2015jf003698. URL <https://doi.org/10.1002%2F2015jf003698>.
- Wolovick, M. J., Creyts, T. T., Buck, W. R., and Bell, R. E. Traveling slippery patches produce thickness-scale folds in ice sheets. *Geophysical Research Letters*, 41(24):8895–8901, dec 2014. doi: 10.1002/2014gl062248. URL <https://doi.org/10.1002%2F2014gl062248>.
- Wrona, T., Wolovick, M. J., Ferraccioli, F., Corr, H., Jordan, T., and Siegert, M. J. Position and variability of complex structures in the central east antarctic ice sheet. *Geological Society, London, Special Publications*, 461(1):113–129, 2018. ISSN 0305-8719. doi: 10.1144/SP461.12. URL <https://sp.lyellcollection.org/content/461/1/113>.

PAPER VII

SUPPLEMENTARY INFORMATION

Supplementary Information:

Indication of ice-stream regime shift in Northeast Greenland

Steven Franke¹ , Paul Bons^{2,3} , Julien Westhoff⁴ , Tobias Binder^{1,†} , Kyra Streng², Veit Helm¹ , Daniel Steinhage¹ , Olaf Eisen^{1,5} , John Paden⁶ , Ilka Weikusat^{1,2}  and Daniela Jansen¹ 

¹ Alfred Wegener Institute, Helmholtz Centre for Polar and Marine Research, Bremerhaven, Germany

² Department of Geosciences, Eberhard Karls University Tübingen, Germany

³ China University of Geosciences, Beijing, China

⁴ Physics of Ice, Climate, and Earth, Niels Bohr Institute, University of Copenhagen, Denmark

⁵ Department of Geosciences, University of Bremen, Bremen, Germany

⁶ Centre for Remote Sensing of Ice Sheets (CReSIS), University of Kansas, Lawrence, KS, USA

[†] now at Ibeo Automotive Systems, Hamburg, Germany

The supplementary information for Paper VII is provided on the USB stick submitted alongside the thesis as well as in a private online repository (see below).

Supplementary Information of Paper VII:

1. Figures S1 – S36 and Tables S1 – S2 (pdf):












<https://storage.luckycloud.de/f/b4b3bc2457a740a68e3c/>

Appendix L

PAPER VIII

DATA DESCRIPTION ARTICLE

A 3D view on folded radar stratigraphy in northern Greenland

Steven Franke¹ , Paul D. Bons^{2,3} , Felicitas Mundel², Till Sachau², Kyra Streng², Ilka Weikusat^{1,2} , Heinrich Miller¹ , Tobias Binder^{1,*} , Veit Helm¹ , John D. Paden⁴ , Daniel Steinhage¹ , Nils Dörr^{1,5} , Olaf Eisen^{1,6} , Daniela Jansen¹ 

¹ Alfred Wegener Institute, Helmholtz Centre for Polar and Marine Research, Bremerhaven, Germany

² Department of Geosciences, Eberhard Karls University Tübingen, Germany

³ China University of Geosciences, Beijing, China

⁴ Centre for Remote Sensing of Ice Sheets (CRISIS), University of Kansas, Lawrence, KS, USA

⁵ Institute of Photogrammetry and Remote Sensing, Karlsruhe Institute of Technology, Karlsruhe, Germany

⁶ Department of Geosciences, University of Bremen, Bremen, Germany

* now at Ibeo Automotive Systems, Hamburg, Germany

Draft to be submitted to Scientific Data.

Abstract

We present a data set of reconstructed three-dimensional (3D) englacial stratigraphic horizons in northern Greenland and explain how 3D horizons provide an improved basis for the interpretation of deformed radar stratigraphy. The data covers three different survey regions, which represent crucial ice-dynamic settings in Greenland: (a) the onset of the Peterman Glacier, (b) a region of deformed stratigraphy close to the ice divide in Northern Greenland and (c) the onset of the North East Greenland Ice Stream (NEGIS). We provide the data in different formats to enable a wide range of applications and reproduction of the results. The data set will be made available for download from PANGAEA.

Background

The Greenland Ice Sheet (GrIS) is one of the largest ice masses and holds 11 % of all ice on Earth (Allison et al., 2009). Over the last two decades, ice mass loss of the GrIS has accelerated and caused sea level to rise about 10.8 ± 0.9 millimetres (Shepherd et al., 2020). If ice mass loss continues as predicted by Church and White (2006), it has the potential to contribute as much as 9 cm of sea level rise by 2050. At the same time, the interior of the GrIS is thickening, partly as an ongoing dynamic response to the last deglaciation (MacGregor et al., 2016). This suggests that the behavior of the Greenland ice sheet is complex, and at the same time we see that climatic and dynamic effects of the past are preserved in the ice.

Ice flows from the centre towards the ocean via a network of glaciers and ice streams (Joughin et al., 2010). These corridors of fast ice flow are responsible

of discharging large amounts of ice and sediment (Bennett, 2003) and are thus considered to play a key role in the stability of the GrIS. The geometry, flow velocity and location of ice streams are controlled by a variety of factors, which can be difficult to identify (Winsborrow et al., 2010). Furthermore, it has been shown that ice stream behaviour can be highly dynamic and subject of rapid changes (Conway et al., 2002). As ice flows it deforms and as it deforms it leaves traces in the ice on the large and small scale. We are able to visualize a variety of structures in ice sheets are the result of cumulative deformation. Many are the result of inhomogeneities in ice flow and the structures can be preserved or overprinted over time.

For instance, folding in ice sheets can be identified with ice-penetrating radar data. The depth-varying reflections of radar waves by englacial layers are interpreted as isochrones (i.e. layers deposited as snow at the same time; e.g. Cavitte et al. 2016) and provide

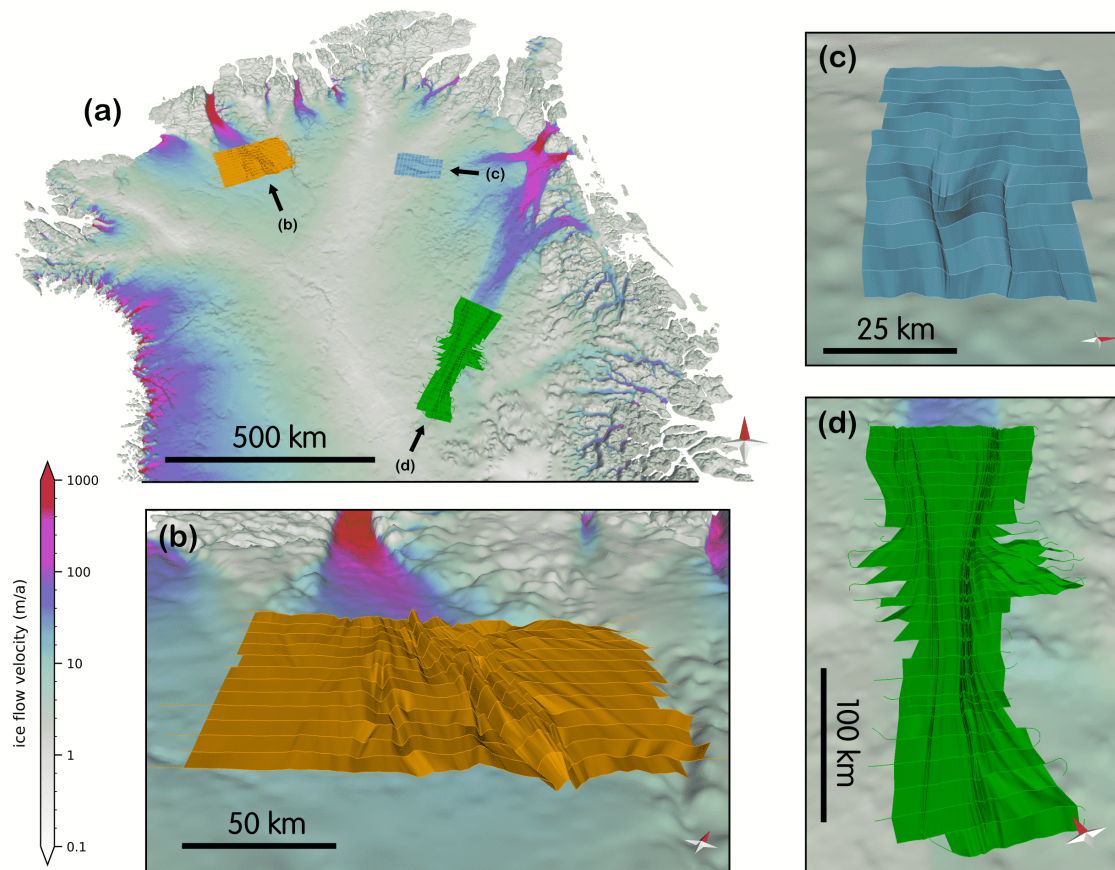


Figure L.1: Overview of the locations of the three data sets of 3D englacial stratigraphy horizons in northern Greenland (a). The survey region at the onset of the Peterman Glacier is shown in panel (b). A set of reconstructed folds in northern Greenland is shown in panel (c) and the 3D reconstruction of two stratigraphic horizons covering the shear margins of the NEGIS in panel (d). The base map shows the bed topography [Morlighem et al. \(2017\)](#) overlain with a color map of the ice surface velocity [Joughin et al. \(2017\)](#) of Greenland. The map has a vertical exaggeration of $z = 10$ and the ice surface velocity is shown on a logarithmic scale.

insight into the ice-sheet history (e.g. [MacGregor et al., 2015](#); [Bons et al., 2016](#)). During the last decades, continuous progress in the quality and coverage of high-resolution radar data ([Rodríguez-Morales et al., 2014](#); [Gogineni et al., 2001](#)) improved the understanding of the englacial stratigraphic architecture of the Greenlandic and Antarctic Ice Sheet (GrIS and AIS).

Here we present a radar derived data set of folded three-dimensional (3D) stratigraphic horizons in northern Greenland. Our 3D horizons allow an extended interpretation for fold formation mechanisms, past ice flow patterns as well as processes at the shear margins of ice streams. We provide an overview of locations and glaciological setting of the 3D stratigraphic horizons, a detailed workflow on how the data were created and the data formats.

Material and methods

Study regions

The data presented in this study originate from three different ice dynamic settings in Northern Greenland (Figure L.1) and represents folded stratigraphic horizons, which were used to draw conclusions about past or recent ice movements. The study regions represent locations at the Greenland Ice Sheet, where fundamental research questions were answered: (a) at the onset of ice flow of the Peterman Glacier, (b) a region in Northern Greenland close to the ice divide and (c) the onset region of the Northeast Greenland Ice Stream (NEGIS).

The Petermann Glacier (PG) is one of Greenland's largest outlet glaciers draining about 4% of the GrIS ([Münchow et al., 2014](#)). The floating tongue of the PG is the longest in Greenland ([Rignot and Steffen, 2008](#)) and the upstream regions of fast flow are not topographically confined by a trough ([Morlighem et al., 2014](#)).

Table L.1: Radar data system specifications and acquisition parameters of the data used for 3D horizon construction.

Study	Platform	Instrument	Frequency Range	Acquisition Channels	Season
Bons et al., 2016	NASA DC-8	MCoRDS	189.15-198.65 MHz	8	2010
	NASA P-3B	MCoRDS 2	180-210 MHz	16	2011
Jansen et al., 2021 (Paper VI)	AWI Polar6	MCoRDS 5	180-210 MHz	8	2018
Franke et al., 2021 (Paper VII)	AWI Polar6	MCoRDS 5	180-210 MHz	8	2018

Chu et al. (2018) investigated the thermal conditions at the onset of the PG, which shows a complex thermal transition at the base near the onset of Petermann Glacier. In this context, Wolovick et al. (2014) used a thermomechanical model to simulate folds as they exist upstream of the PG with moving patches of subglacial slip. However, this approach was based on radargrams, which did not map the full geometry of the folds at the PG. Bons et al. (2016) used an extensive grid of OIB radar lines to construct the first 3D surfaces of stratigraphic horizons, which represent the outline of the true geometry of glacial folds. The authors demonstrated with this data set that converging flow and the anisotropic character of the ice was the cause for the large-scale folding at the onset of the PG. This data set is the first of three, which will be published in this paper.

The survey region in Figure L.1 b is located in Northern Greenland and extends from 79°N to 80°N and from 32°W to 40°W. Ice surface velocity in this region is almost zero in the western part at the ice divide and increases up to 15 m/a on the eastern edge. Two fold units in this area are partly covered by OIB radar profiles and have been subject to prior studies by Pantou and Karlsson (2015); Dow et al. (2018) and Leysinger Vieli et al. (2018) but never structurally analysed in depth. Franke et al., 2021 (Paper VII) used AWI UWB radar data of a systematic grid to create 3D horizons of the folded englacial stratigraphy. The geometry and spatial extent of the folds were linked to the glaciological setting and the current ice surface flow regime. The authors found that the folds were formed in a different ice-dynamic setting than the present one in northern Greenland and in several stages of formation. A key aspect of this study was the orientation of the fold axes, the shape of fold axes surfaces and the 3D shape of the folds regarding the direction of overturning.

The third data set (Figure L.1 c) of reconstructed radar stratigraphy published in this paper (a study by Jansen et al., 2021 (in prep.); Paper VI) is located at the onset of the Northeast Greenland Ice Stream (NEGIS). The genesis as well as the geometry and positioning of the shear margins of the NEGIS is not fully

understood and has been subject to several studies (e.g. Fahnestock, 2001; Christianson et al., 2014; Franke et al., 2021b) and this part of the GrIS represents one of the largest uncertainties for ice flow predictions in Greenland (Aschwanden et al., 2016). The data set covers an area of 150 km upstream and 100 km downstream of the deep drilling site on the ice stream (EastGRIP; <https://eastgrip.org>). In the survey area the ice stream accelerates from 12 m/a to 75 m/a. The reconstructed horizons focus on the deformation patterns of the shear margins and show steep undulations, which are intensified downstream with ongoing shear. The 3D representation of the folded stratigraphic layers show how new folds are formed when the ice stream widens and that older structures are preserved inside of the ice stream where shearing decreases. The study links the change of shape of the 3D horizons with the strain rate field calculated from the surface flow velocities.

Workflow

Data acquisition

The most suitable radar data to image the deep stratigraphy and folded structures in the GrIS and AIS are available from multichannel coherent depth sounders (MCoRDS; Gogineni et al. 1998). The Centre of Remote Sensing of Ice Sheets (CREGIS) collected an enormous amount of high-quality radar data over the GrIS and AIS over the last decades during Operation Ice Bridge (OIB; Shi et al. 2010). Furthermore, the Alfred-Wegener-Institute, Helmholtz Centre for Polar and Marine Research (AWI) operates an analogous airborne ultra-wideband (UWB) radar system since 2015 (Hale et al., 2016). The radar system consists of an array of eight antennas elements (oriented in HH polarization) which are installed on the fuselage of the AWIPolar6 Basler BT-67 aircraft. The capabilities of imaging complex englacial structures and large units of folded stratigraphy have been demonstrated by Kjær et al. (2018); Franke et al. (2020, 2021b).

Bons et al. (2016) used OIB data from the seasons 2010 and 2011 for their analysis. The data in the study of Franke et al., 2021 (Paper VII) and Jansen et al., 2021

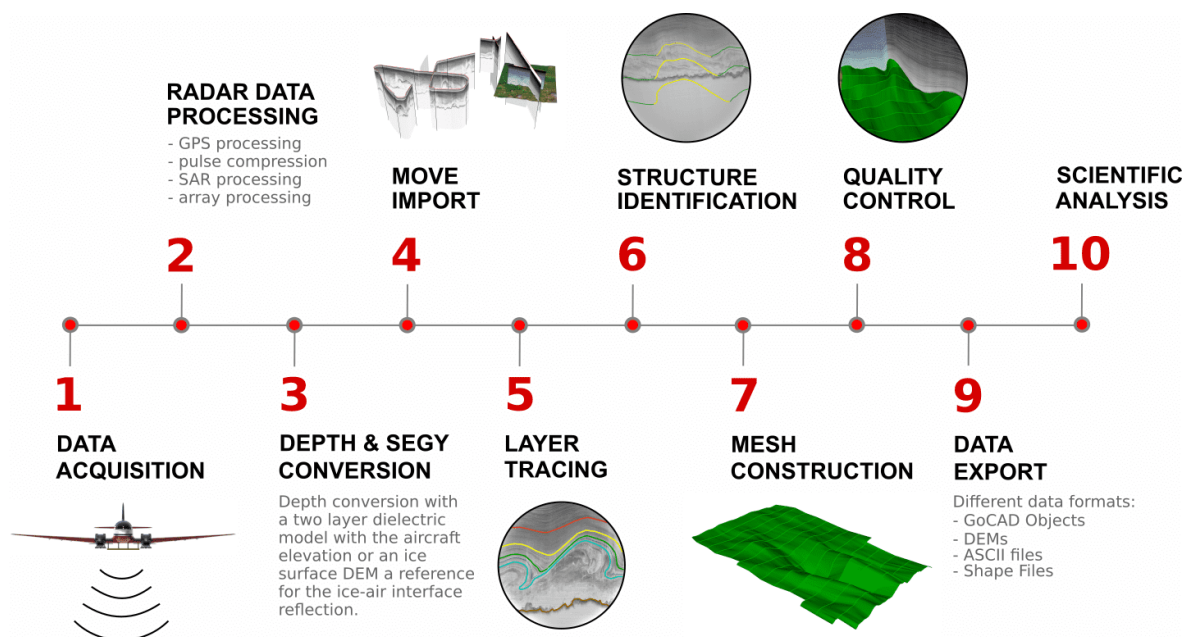


Figure L.2: Workflow sequence for 3D horizon construction.

(Paper VI) were generated on the basis of AWI UWB data in 2018 (see Table L.1).

Radar data processing

For the construction of 3D surfaces we apply radar data processing in three spatial domains:

1. Pulse compression of the chirped waveform in the vertical range to improve the range signal quality and the signal-to-noise ratio (SNR).
2. Along-track Synthetic Aperture Radar (SAR) processing (fk migration) to locate reflection energy back to the target location.
3. Cross-track processing(array processing), which is a coherent combination of the return signals of the antenna array to increase SNR and reduce surface clutter.

An important basis for accurate radar measurements are high-precision geographical positioning data of the aircraft. For the studies with the AWI UWB radar, we use the data of four Novatel dual-frequency GNSS (Global Navigation Satellite System) receivers, which is recorded with 20Hz sampling interval. Data are post-processed with the Precise Point Positioning (PPP) method using the commercial software package *Waypoint 8.4*. The flight trajectories are combined with the Radar data within the SAR processing. Details of radar data processing for both AWI UWB data sets are described by Franke et al. (2020).

Radar data are typically processed in the two-way travel time (TWT) domain. To construct 3D surfaces we convert the TWT axis into an elevation axis with a two dimensional dielectric constant (ϵ_r) model for air with $\epsilon_r = 1$ and for ice with $\epsilon_r = 3.15$. The radar reflection of the air-ice interface represents the boundary between the two dielectric constants. Two different workflows have been used to enable the direct import of radar data to the 3D model building software. Bons et al. (2016) used elevation corrected radargram sections with a subsequently produced coordinate system. For the study of Franke et al., 2021 (Paper VII) and Jansen et al., 2021 (Paper VI), we converted the elevation-corrected radar data to the SEGY format with the *ObsPy* Python framework Beyreuther et al. (2010).

3D surface construction in move

The construction of 3D horizons, which represent an internal reflection horizon (IRH), starts with the layout of survey lines. We achieve the best result when englacial structures (e.g. folds) are oriented with their fold axis 90° to the survey lines.

The depth-converted SEGY radar data can be imported as sections in the Move 3D canvas. Internal layers are traced manually. The philosophy behind the construction of 3D horizons is the segmentation of the traced layers into segments of coherent geometric features. A common feature would be an anticline, which

is visible in several adjacent radargrams. These segments can then be combined to form a coherent structure, such as the anticline of a fold. An appropriate way to check if the geometry of the interpolated is correct, it is possible to compare the 3D horizon with a radar profile which is oriented perpendicular to the actual radar sections.

Data records

Peterman Glacier

Four 3D horizons are provided for the onset region of the PG. Horizon P1 is 11.7 ka old and represents the transition from the glacial to the holocene and is located ~ 1 km below the ice surface. The horizon is mainly characterized by open cylindrical folds with the fold axis oriented parallel to ice flow. Horizons P2 and P3 are located deeper and show asymmetric and overturned folds with respective ages of 37.5 ka and 87.0 ka. Horizon P4 represents strongly disturbed ice stratigraphy of the basal unit.

Northern Greenland

The data set in Northern Greenland represents two fold units, which are located close to the ice divide and are oriented towards the main glacier outlet system in Northeast Greenland. Three 3D horizons (F1, F2 and F3; labelled from young to old) were constructed to outline the geometry and extension of the folds as well as to display the deformation of stratigraphic horizons with increasing depth. The horizons have a respective age of 45.5 ka, 52.2 ka as well as 60 ka and extend 85 km in the direction parallel to the fold axis and 50–60 km in 90° to the fold axis. Horizon F3 is smaller than the two younger horizons because the radar horizon could not be traced in all radargrams.

NEGIS onset

The data set at the onset of the NEGIS comprises two 3D horizons extending ~250 km in the direction of ice flow and between 30–70 km and ZZ km across ice flow. The two horizons have a respective age of 7.3 ka and 12.8 ka and are labelled N1 (for the younger horizon) and N2 (for the older horizon). The main characteristic of these horizons is the representation of the deformation structure at the shear margins.

Technical validation

The 3D horizons of the three data sets were created on the basis of parallel radar profiles between which the individual structures were linearly interpolated. In

addition, the radar profiles are oriented perpendicular to the fold axis, as this produces the best results. In order to check whether the interpolated geometries are as consistent as possible, they are compared with obliquely oriented radar profiles, if these are available. This was performed for all three data sets and no significant deviations of the 3D geometries were found. No significant deviations of the 3D geometries were found.

Data formats and usage notes

3D horizons are provided in different data formats (see Table L.3). Some of the data formats can be used with standard and open source software (e.g. GeoTIFFs or ASCII xyz files) but others require specialised and often also commercial software (e.g. GoCAD Objects or CAD format). In the following, we discuss the possible applications, advantages, and disadvantages of the data formats:

1. **GoCAD (Geological Objects)** is a common file format for (mostly) commercial geological modeling software. The 3D horizons can be exported and imported directly in the TSURF (.ts) format, which stores the shape as well as meta-data of the horizon. A great advantage of many commercial geology software with a 3D canvas is the simultaneous use and display of different data formats like radar sections, geo-coded raster files, shapefiles as well as well-data. Another advantage to pure 3D software is the incorporation of 3D structures and the georeferenced canvas. For the data presented in this paper, we provide the 3D horizons in the TSURF format and as a point set, where the surface is represented by a point cloud with xyz coordinates in EPSG:3413. Furthermore, the single radar layers, which are the basis for the 3D reconstruction are provided as xyz data.
2. **CAD (Computer Aided Design)** files in the Drawing Exchange Format (.dxf). CAD surface objects preserve the 3D nature of the horizons presented here as triangulated objects and can be handled by several commercial and open-source CAD software. One disadvantage in comparison to the GoCAD format is that geographical information is lost and that the file size is larger.
3. **Digital Elevation Models (DEMs)** are provided in the GeoTIFF and .nc format in the EPSG:3413 coordinate system. DEMs are not exported directly but interpolated from the xyz point data with a cell size of 100m. Because it is not possible to represent overturning structures (such as in Figure L.3 e), we only provide DEMs for 3D

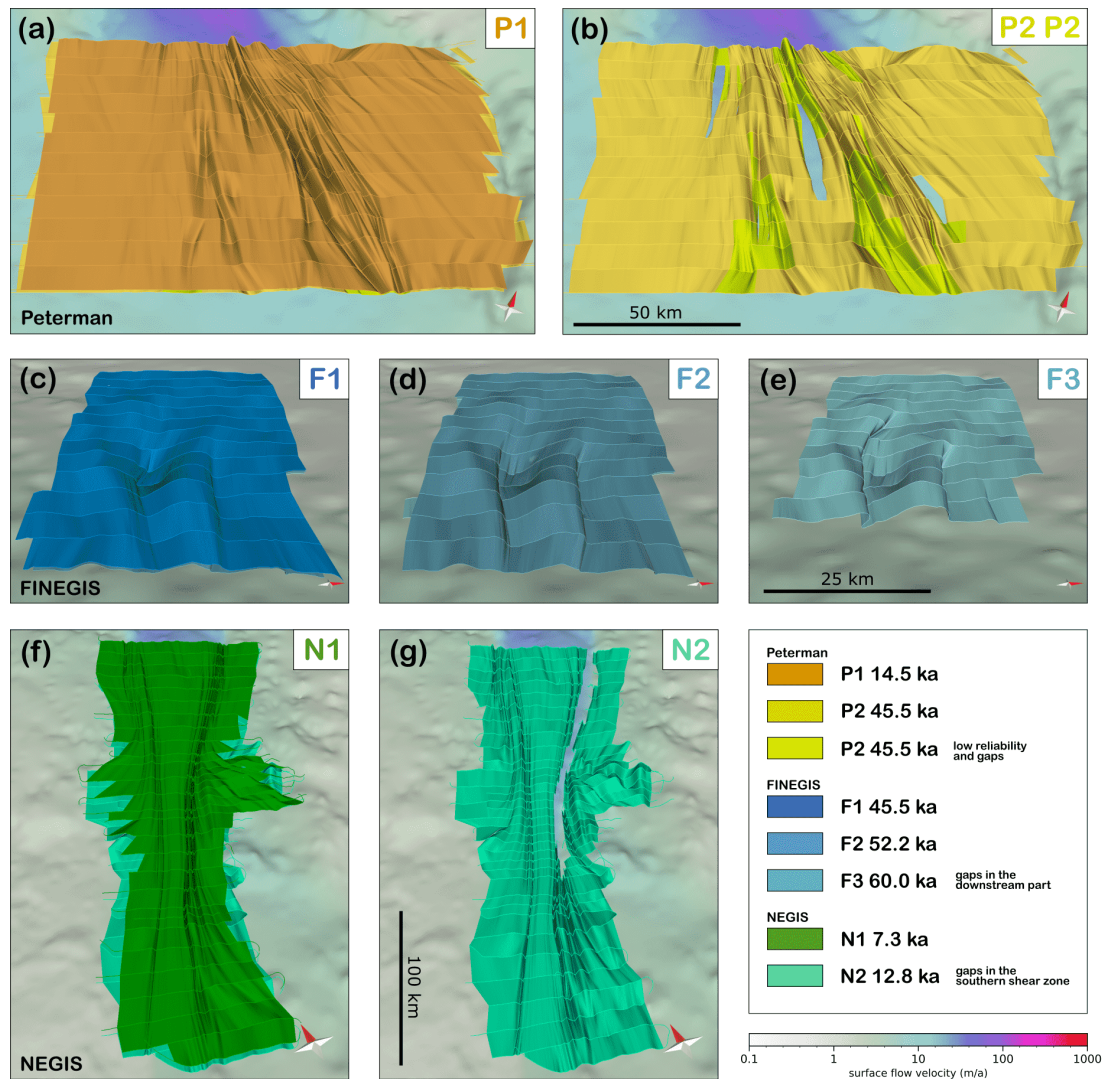


Figure L.3: Individual horizons published with this manuscript. Panels (a) and (b) represent the horizons from the onset of the Peterman Glacier, (c)–(e) the horizons upstream of the northern catchment of the 79° NG and (f) and (g) the horizons at the onset of the NEGIS, centered at the EGRIP drill site. The map in the background shows the bed topography Morlighem et al. (2017) overlain with a color map of the surface ice flow velocity of Greenland Joughin et al. (2017).

horizons where this is not the case. The 3D character of the DEMs can be

4. **Shape Files** are provided for radar section lines as well as point sets for the 3D horizons. The z-value is stored in the attribute table.

The entire data set is available at the PANGAEA Data Repository.

Code and data availability

The CReSIS-toolbox is available under <https://github.com/CReSIS/> and the main documentation can be found at <https://ops.cresis.ku.edu/wiki/>. The

radar data, which was used to build the 3D horizons is available at the following locations: The radar depth sounder data used for the Peterman Glacier can be obtained at the CReSIS Data Products website: <https://data.cresis.ku.edu/>. The EGRIP-NOR-2018 radar data products (onset of the NEGIS) are available at the PANGAEA Data Publisher (<https://doi.pangaea.de/10.1594/PANGAEA.928569>; Franke et al. 2021a). The MEaSURES Greenland Ice Sheet Velocity Map from InSAR Data, Version 2 from Joughin et al. (2017) is available from <https://doi.org/10.5067/OC7B04ZM9G6Q> and the BMv3 bed topography DEM from (Morlighem et al., 2017) is available at the National Snow and Ice Data Center (NSIDC): <https://doi.org/10.5067/2CIX82HUV88Y>.

Table L.2: 3D horizon specifications of the three survey regions.

Study	Region	Horizon	Horizon Age	Surface Area
Bons et al., 2016	Peterman Glacier onset	P1	14.5 ka	13 762 km ²
		P2	45.5 ka	12 235 km ²
Franke et al., 2021 (Paper VII)	Northern Greenland	F1	45.5 ka	5 402 km ²
		F2	52.2 ka	5 325 km ²
		F3	60.0 ka	4 781 km ²
Jansen et al., 2021 (Paper VI)	NEGIS onset	N1	7.3 ka	15 451 km ²
		N2	12.8 ka	16 311 km ²

Table L.3: Data format specifications, description and usage.

Data Type	Data Format	Description	Usage
Geological Object (GoCAD Object)	TSURF (.ts)	TSURF data files are triangulated based surface objects containing vertex coordinates and triangle to vertex connectivities	Mostly commercial geological modelling software with a 3D canvas
	Point Set (.dat)	Points with coordinates (x,y,z) and scalar/vector properties saved in ASCII file format for 3D surfaces	Generic ASCII data format
	Line (.dat)		
Computer Aided Design (CAD)	Drawing Exchange Format (.dxf)	Triangulated based surface objects in the standard exchange format for CAD applications	Commercial and non-commercial CAD Software. A disadvantage to the 3D Geo-Modelling Software is that DXF coordinates are always without dimensions.
Digital Elevation Model (DEM)	GeoTIFF (.tif)	Raster file generated from the 3D surface in a georeferenced TIFF file (only available for structures which are not overturning)	Native file format for many scientific programming languages as well as GIS applications
	NetCDF (.nc)		Native file format for many scientific programming languages as well as GIS applications
Shape File	Point Set (.shp)	Analogue data to the ASCII point set but in the Shape File format	Native file format for many GIS applications and geo-libraries
	Line Set (.shp)	Analogue data to the ASCII line but in the Shape File format	Native file format for many GIS applications and geo-libraries

Bibliography

- Allison, I., Alley, R., Fricker, H., Thomas, R., and Warner, R. Ice sheet mass balance and sea level. *Antarctic Science*, 21(5):413–426, 2009. doi: 10.1017/S0954102009990137. URL <https://doi.org/10.1017/S0954102009990137>.
- Aschwanden, A., Fahnestock, M. A., and Truffer, M. Complex Greenland outlet glacier flow captured. *Nature Communications*, 7(1), feb 2016. doi: 10.1038/ncomms10524. URL <https://doi.org/10.1038/ncomms10524>.
- Bennett, M. R. Ice streams as the arteries of an ice sheet: their mechanics, stability and significance. *Earth-Science Reviews*, 61(3):309–339, 2003. ISSN 0012-8252. doi: 10.1016/S0012-8252(02)00130-7. URL <https://www.sciencedirect.com/science/article/pii/S0012825202001307>.
- Beyreuther, M., Barsch, R., Krischer, L., Megies, T., Behr, Y., and Wassermann, J. ObsPy: A Python Toolbox for Seismology. *Seismological Research Letters*, 81(3):530–533, may 2010. doi: 10.1785/gssrl.81.3.530. URL <https://doi.org/10.1785/gssrl.81.3.530>.
- Bons, P. D., Jansen, D., Mundel, F., Bauer, C. C., Binder, T., Eisen, O., Jessell, M. W., Llorens, M.-G., Steinbach, F., Steinhage, D., and Weikusat, I. Converging flow and anisotropy cause large-scale folding in Greenland's ice sheet. *Nature Communications*, 7(1), apr 2016. doi: 10.1038/ncomms11427. URL <https://doi.org/10.1038/ncomms11427>.
- Cavitte, M. G. P., Blankenship, D. D., Young, D. A., Schroeder, D. M., Parrenin, F., Lemeur, E., MacGregor, J. A., and Siegert, M. J. Deep radiostratigraphy of the east antarctic plateau: connecting the dome c and vostok ice core sites. *Journal of Glaciology*, 62(232):323–334, 2016. doi: 10.1017/jog.2016.11. URL <https://doi.org/10.1017/jog.2016.11>.
- Christianson, K., Peters, L. E., Alley, R. B., Anandakrishnan, S., Jacobel, R. W., Riverman, K. L., Muto, A., and Keisling, B. A. Dilatant till facilitates ice-stream flow in northeast Greenland. *Earth and Planetary Science Letters*, 401: 57–69, sep 2014. doi: 10.1016/j.epsl.2014.05.060. URL <https://doi.org/10.1016/j.epsl.2014.05.060>.
- Chu, W., Schroeder, D. M., Seroussi, H., Creyts, T. T., and Bell, R. E. Complex Basal Thermal Transition Near the Onset of Petermann Glacier Greenland. *Journal of Geophysical Research: Earth Surface*, 123(5):985–995, may 2018. doi: 10.1029/2017jf004561. URL <https://doi.org/10.1029/2017jf004561>.
- Church, J. A. and White, N. J. A 20th century acceleration in global sea-level rise. *Geophysical Research Letters*, 33(1), 2006. doi: <https://doi.org/10.1029/2005GL024826>. URL <https://agupubs.onlinelibrary.wiley.com/doi/abs/10.1029/2005GL024826>.
- Conway, H., Catania, G., Raymond, C. F., Gades, A. M., Scambos, T. A., and Engelhardt, H. Switch of flow direction in an Antarctic ice stream. *Nature*, 419(6906):465–467, oct 2002. ISSN 0028-0836. doi: 10.1038/nature01081. URL <http://www.nature.com/articles/nature01081>.
- Dow, C. F., Werder, M. A., Babonis, G., Nowicki, S., Walker, R. T., Csatho, B., and Morlighem, M. Dynamics of Active Subglacial Lakes in Recovery Ice Stream. *Journal of Geophysical Research: Earth Surface*, 123(4):837–850, 2018. doi: <https://doi.org/10.1002/2017JF004409>. URL <https://agupubs.onlinelibrary.wiley.com/doi/abs/10.1002/2017JF004409>.
- Fahnestock, M. High Geothermal Heat Flow Basal Melt, and the Origin of Rapid Ice Flow in Central Greenland. *Science*, 294(5550):2338–2342, dec 2001. doi: 10.1126/science.1065370. URL <https://doi.org/10.1126/science.1065370>.
- Franke, S., Jansen, D., Binder, T., Dörr, N., Helm, V., Paden, J., Steinhage, D., and Eisen, O. Bed topography and subglacial landforms in the onset region of the Northeast Greenland Ice Stream. *Annals of Glaciology*, pages 1–11, mar 2020. doi: 10.1017/aog.2020.12. URL <https://doi.org/10.1017/aog.2020.12>.
- Franke, S., Binder, T., Jansen, D., Paden, J. D., Dörr, N., Gerber, T., Miller, H., Dahl-Jensen, D., Helm, V., Steinhage, D., Weikusat, I., Wilhelms, F., and Eisen, O. [DATASET] Ultra-wideband radar data over the shear margins and along flow lines at the onset region of the Northeast Greenland Ice Stream (NEGIS), 2021a. URL <https://doi.pangaea.de/10.1594/PANGAEA.928569>.
- Franke, S., Jansen, D., Beyer, S., Neckel, N., Binder, T., Paden, J., and Eisen, O. Complex basal conditions and their influence on ice flow at the onset of the northeast greenland ice stream. *Journal of Geophysical Research: Earth Surface*, 126(3):e2020JF005689, 2021b. doi: 10.1029/2020JF005689. URL <https://agupubs.onlinelibrary.wiley.com/doi/abs/10.1029/2020JF005689>.
- Gogineni, S., Chuah, T., Allen, C., Jezek, K., and Moore, R. K. An improved coherent radar depth sounder. *Journal of Glaciology*, 44(148):659–669, 1998. doi: 10.3189/S0022143000002161. URL <https://doi.org/10.3189/S0022143000002161>.
- Gogineni, S., Tammana, D., Braaten, D., Leuschen, C., Akins, T., Legarsky, J., Kanagaratnam, P., Stiles, J., Allen, C., and Jezek, K. Coherent radar ice thickness measurements over the Greenland ice sheet. *Journal of Geophysical Research: Atmospheres*, 106(D24):33761–33772, dec 2001. doi: 10.1029/2001jd900183. URL <https://doi.org/10.1029/2001jd900183>.
- Hale, R., Miller, H., Gogineni, S., Yan, J. B., Rodriguez-Morales, F., Leuschen, C., Paden, J., Li, J., Binder, T., Steinhage, D., Gehrmann, M., and Braaten, D. Multi-channel ultra-wideband radar sounder and imager. In *2016 IEEE International Geoscience and Remote Sensing Symposium (IGARSS)*. IEEE, jul 2016. doi: 10.1109/igarss.

- 2016.7729545. URL <https://doi.org/10.1109%2Ffigarss.2016.7729545>.
- Joughin, I., Smith, B. E., Howat, I. M., Scambos, T., and Moon, T. Greenland flow variability from ice-sheet-wide velocity mapping. *Journal of Glaciology*, 56(197):415–430, 2010. ISSN 0022-1430. doi: 10.3189/002214310792447734. URL <http://dx.doi.org/10.3189/002214310792447734>.
- Joughin, I., Smith, B. E., and Howat, I. M. A complete map of Greenland ice velocity derived from satellite data collected over 20 years. *Journal of Glaciology*, 64(243):1–11, nov 2017. doi: 10.1017/jog.2017.73. URL <https://doi.org/10.1017%2Fjog.2017.73>.
- Kjær, K. H., Larsen, N. K., Binder, T., Bjørk, A. A., Eisen, O., Fahnestock, M. A., Funder, S., Garde, A. A., Haack, H., Helm, V., Houmark-Nielsen, M., Kjeldsen, K. K., Khan, S. A., Machguth, H., McDonald, I., Morlighem, M., Mouginot, J., Paden, J. D., Waight, T. E., Weikusat, C., Willerslev, E., and MacGregor, J. A. A large impact crater beneath Hiawatha Glacier in northwest Greenland. *Science Advances*, 4(11):ear8173, nov 2018. doi: 10.1126/sciadv.aar8173. URL <https://doi.org/10.1126%2Fsciadv.aar8173>.
- Leysinger Vieli, G. J.-M. C., Martín, C., Hindmarsh, R. C. A., and Lüthi, M. P. Basal freeze-on generates complex ice-sheet stratigraphy. *Nature Communications*, 9(1), nov 2018. doi: 10.1038/s41467-018-07083-3. URL <https://doi.org/10.1038%2Fs41467-018-07083-3>.
- MacGregor, J. A., Fahnestock, M. A., Catania, G. A., Paden, J. D., Gogineni, S. P., Young, S. K., Rybarski, S. C., Mabrey, A. N., Wagman, B. M., and Morlighem, M. Radiostratigraphy and age structure of the Greenland Ice Sheet. *Journal of Geophysical Research: Earth Surface*, 120(2):212–241, feb 2015. doi: 10.1002/2014jef003215. URL <https://doi.org/10.1002%2F2014jef003215>.
- MacGregor, J. A., Colgan, W. T., Fahnestock, M. A., Morlighem, M., Catania, G. A., Paden, J. D., and Gogineni, S. P. Holocene deceleration of the Greenland ice sheet. *Science*, 351(6273):590–593, 2016. ISSN 0036-8075. doi: 10.1126/science.aab1702. URL <https://science.sciencemag.org/content/351/6273/590>.
- Morlighem, M., Rignot, E., Mouginot, J., Seroussi, H., and Larour, E. Deeply incised submarine glacial valleys beneath the Greenland ice sheet. *Nature Geoscience*, 7(6):418–422, may 2014. doi: 10.1038/ngeo2167. URL <https://doi.org/10.1038%2Fng2167>.
- Morlighem, M., Williams, C. N., Rignot, E., An, L., Arndt, J. E., Bamber, J. L., Catania, G., Chauché, N., Dowdeswell, J. A., Dorschel, B., Fenty, I., Hogan, K., Howat, I., Hubbard, A., Jakobsson, M., Jordan, T. M., Kjeldsen, K. K., Millan, R., Mayer, L., Mouginot, J., Noël, B. P. Y., O'Cofoigh, C., Palmer, S., Rysgaard, S., Seroussi, H., Siegert, M. J., Slabon, P., Straneo, F., van den Broeke, M. R., Weinrebe, W., Wood, M., and Zinglensen, K. B. BedMachine v3: Complete Bed Topography and Ocean Bathymetry Mapping of Greenland From Multibeam Echo Sounding Combined With Mass Conservation. *Geophysical Research Letters*, 44(21):11,051–11,061, nov 2017. doi: 10.1002/2017gl074954. URL <https://doi.org/10.1002%2F2017gl074954>.
- Münchow, A., Padman, L., and Fricker, H. A. Interannual changes of the floating ice shelf of Petermann Gletscher North Greenland, from 2000 to 2012. *Journal of Glaciology*, 60(221):489–499, 2014. doi: 10.3189/2014jog13j135. URL <https://doi.org/10.3189%2F2014jog13j135>.
- Panton, C. and Karlsson, N. B. Automated mapping of near bed radio-echo layer disruptions in the Greenland Ice Sheet. *Earth and Planetary Science Letters*, 432:323–331, dec 2015. doi: 10.1016/j.epsl.2015.10.024. URL <https://doi.org/10.1016%2Fj.epsl.2015.10.024>.
- Rignot, E. and Steffen, K. Channelized bottom melting and stability of floating ice shelves. *Geophysical Research Letters*, 35(2), jan 2008. doi: 10.1029/2007gl031765. URL <https://doi.org/10.1029%2F2007gl031765>.
- Rodriguez-Morales, F., Byers, K., Crowe, R., Player, K., Hale, R. D., Arnold, E. J., Smith, L., Gifford, C. M., Braaten, D., Panton, C., Gogineni, S., Leuschen, C. J., Paden, J. D., Li, J., Lewis, C. C., Panzer, B., Alvestegui, D. G.-G., and Patel, A. Advanced Multifrequency Radar Instrumentation for Polar Research. *IEEE Transactions on Geoscience and Remote Sensing*, 52(5):2824–2842, may 2014. doi: 10.1109/tgrs.2013.2266415. URL <https://doi.org/10.1109%2Ftgrs.2013.2266415>.
- Shepherd, A., Ivins, E., Rignot, E., Smith, B., van den Broeke, M., Velicogna, I., Whitehouse, P., Briggs, K., Joughin, I., Krinner, G., Nowicki, S., Payne, T., Scambos, T., Schlegel, N., A. G., Agosta, C., Ahlstrøm, A., Babonis, G., Barletta, V. R., Bjørk, A. A., Blazquez, A., Bonin, J., Colgan, W., Csatho, B., Cullather, R., Engdahl, M. E., Felikson, D., Fettweis, X., Forsberg, R., Hogg, A. E., Gallee, H., Gardner, A., Gilbert, L., Gourmelen, N., Groh, A., Gunter, B., Hanna, E., Harig, C., Helm, V., Horvath, A., Horwath, M., Khan, S., Kjeldsen, K. K., Konrad, H., Langen, P. L., Lecavalier, B., Loomis, B., Luthcke, S., McMillan, M., Melini, D., Mernild, S., Mohajerani, Y., Moore, P., Mottram, R., Mouginot, J., Moyano, G., Muir, A., Nagler, T., Nield, G., Nilsson, J., Noël, B., Otsuka, I., Pattie, M. E., Peltier, W. R., Pie, N., Rietbroek, R., Rott, H., Sandberg Sørensen, L., Sasgen, I., Save, H., Scheuchl, B., Schrama, E., Schröder, L., Seo, K. W., Simonsen, S. B., Slater, T., Spada, G., Sutterley, T., Talpe, M., Tarasov, L., van de Berg, W. J., van der Wal, W., van Wessem, M., Vishwakarma, B. D., Wiese, D., Wilton, D., Wagner, T., Wouters, B., and Wuite, J. Mass balance of the Greenland Ice Sheet from 1992 to 2018. *Nature*, 579(7798):233–239, 2020. ISSN 14764687. doi: 10.1038/s41586-019-1855-2. URL <https://doi.org/10.1038/s41586-019-1855-2>.
- Shi, L., Allen, C. T., Ledford, J. R., Rodriguez-Morales, F., Blake, W. A., Panzer, B. G., Prokopiack, S. C., Leuschen, C. J., and Gogineni, S. Multichannel coherent radar depth sounder for NASA operation ice bridge. *International Geoscience and Remote Sensing Symposium (IGARSS)*, pages 1729–1732, 2010. doi: 10.1109/IGARSS.2010.5649518. URL <http://dx.doi.org/10.1109/IGARSS.2010.5649518>.

- Winsborrow, M. C., Clark, C. D., and Stokes, C. R. What controls the location of ice streams? *Earth-Science Reviews*, 103(1):45–59, 2010. ISSN 0012-8252. doi: <https://doi.org/10.1016/j.earscirev.2010.07.003>. URL <https://www.sciencedirect.com/science/article/pii/S0012825210000838>.
- Wolovick, M. J., Creyts, T. T., Buck, W. R., and Bell, R. E. Traveling slippery patches produce thickness-scale folds in ice sheets. *Geophysical Research Letters*, 41(24):8895–8901, dec 2014. doi: 10.1002/2014gl062248. URL <https://doi.org/10.1002/2014gl062248>.